

PACIFIC EARTHQUAKE ENGINEERING RESEARCH CENTER

Experimental Investigation of the Behavior of Vintage and Retrofit Concentrically Braced Steel Frames under Cyclic Loading

Barbara G. Simpson

Stephen A. Mahin

Jiun-Wei Lai

Department of Civil and Environmental Engineering
University of California, Berkeley

PEER Report No. 2017/12
Pacific Earthquake Engineering Research Center
Headquarters at the University of California, Berkeley

December 2017

Disclaimer

The opinions, findings, and conclusions or recommendations expressed in this publication are those of the author(s) and do not necessarily reflect the views of the study sponsor(s), the Pacific Earthquake Engineering Research Center, or the Regents of the University of California.

Experimental Investigation of the Behavior of Vintage and Retrofit Concentrically Braced Steel Frames under Cyclic Loading

Barbara G. Simpson

Stephen A. Mahin

Jiun-Wei Lai

Department of Civil and Environmental Engineering
University of California, Berkeley

PEER Report No. 2017/12
Pacific Earthquake Engineering Research Center
Headquarters at the University of California, Berkeley

December 2017

ABSTRACT

The parallel evolution of seismic design provisions and braced-frame research has led to inconsistencies between the design and construction of braced frames and the development of modern seismic design codes and now-typical detailing requirements. Since literature on concentrically braced frames (CBFs) spans over several decades, existing older or *vintage* concentrically braced frames—especially those designed prior 1988—may be prone to a number of deficiencies that are now limited in new CBFs due to contemporary seismic design requirements.

The number and range of these deficiencies and their likely interdependence, makes assessing the likely behavior of vintage braced frame systems problematic. Recent research has focused on improving the seismic behavior of modern braced frame systems, such as the Special Concentrically Braced Frame (SCBF). In contrast, relatively little research has focused on existing braced frames, even though vintage CBFs may be characterized by distinctly different behavior from modern SCBFs. Component tests of non-compact braces and connections and documented failures during past earthquakes have shown that vintage CBFs may be vulnerable to a number of complex damage states, including limited deformability and energy-dissipation capacity of the braces, potentially brittle connection failures, beam yielding in V- or chevron configurations, etc.

To improve this situation, experiments of complete sub-assemblages of vintage braced frame systems are needed to improve understanding of seismic response, assess the feasibility and efficacy of possible retrofit strategies, and calibrate computational models for future parametric studies. This report presents results of experiments and related analyses performed on vintage CBF specimens. Cyclic quasi-static tests were performed on three full-scale CBF specimens. A common two-story, one-bay configuration was adopted. The first specimen was representative of a pre-1988 CBF incorporating hollow HSS braces. The second specimen was similar, but the HSS braces were filled with concrete. The third specimen incorporated a mast (or *strongback*) retrofit and other features intended to mitigate the weak-story behavior observed in the first two specimens.

The first test structure utilized square HSS braces placed in a “chevron” configuration with one column oriented in strong-axis bending and the other in weak-axis bending. The first specimen was designed according to the 1985 Uniform Building Code; as such, it did not satisfy many requirements of current seismic design codes. These inadequacies were typical of vintage construction and included high brace width-to-thickness ratios, weak gusset connections lacking adequate yield-lines, weak beams designed without consideration of an unbalanced load that may arise due to brace buckling, and no capacity design considerations in proportioning members or connections. This specimen formed a weak story in the second floor, while the rest of the frame experienced only minor yielding and little permanent damage. Both second-story braces buckled—exhibiting considerable local buckling at the brace midpoint—and then fractured within a few additional cycles. Since the imposed story drifts were modest, the frame was subsequently repaired. The fractured second-story braces and gussets were replaced with the same sections.

The new braces in the “second” test specimen were filled with low-strength concrete in an effort to postpone brace local buckling and fracture observed during the first experiment. Net section reinforcement was also added at all the brace-to-gusset connections. Testing of the

second specimen also resulted in a weak-story mechanism but in the bottom story. Delayed local buckling and subsequent fracture was observed in one of the bottom-story braces. After fracture of this brace, the frame tended to behave like an eccentrically braced frame (EBF) with a long link beam. This beam provided a relatively weak and flexible energy-dissipating mechanism. Many different local failure mechanisms were observed during subsequent loading cycles, including nearly-complete fracture at one column-to-baseplate interface, significant local buckling, and multiple connection weld and base metal failures.

The third specimen utilized a “strongback” (SB) retrofit aimed at alleviating the weak-story behavior seen in both the first and second experimental tests. The SB system employs a steel truss “backbone” that is designed to remain essentially elastic. This truss enforces similar drift demands in adjacent stories to delay or prevent weak-story behavior. The retrofit design was composed of two halves: an “inelastic” truss utilizing a buckling-restrained brace (BRB) that dissipated seismic input energy and an “elastic” vertical truss designed to control weak-story behavior. The specimen was successful in imposing nearly uniform drifts over the full height of the frame throughout the duration of the test. These preliminary experimental results show that the SB system can be an effective means in limiting weak-story mechanisms.

A number of numerical simulations were calibrated to the experimental results. These analytical models are capable of predicting the observed behavior. The models developed adequately simulated the observed brace global buckling, braces fatigue, column-to-baseplate fracture, and the overall global response of the test specimens.

ACKNOWLEDGMENTS

This experimental report would not have been possible without the insight and advice of a number of outside contributors, including numerous individuals, companies, and organizations whose time, expertise, and services were essential to the completion of these experimental tests.

The design of all three test specimens was based on a number of relevant discussions from practicing engineers and fellow researchers whose feedback was invaluable to this project. A special thanks goes to Rafael Sabelli, James Malley, Paxti Uriz, Steve Powell, and Brett Manning for their advice on the design and construction of this project.

The third experimental test would not have been possible without the donation of steel and fabrication by Schuff Steel. The buckling-restrained brace used in the third test specimen was donated by StarSeismic. The donations of these contributors are greatly appreciated. Engineers Mark Sencich and Jon Sanguinetti of Schuff Steel and Tim Nordstrom of StarSeismic offered invaluable input on the construction and design of the third test specimen; their time on the project is greatly appreciated.

Laboratory support provided by the NEES@berkeley Laboratory was essential to the completion of all three experimental tests. A special thanks goes to the laboratory engineers and technicians, including Dr. Shakhzod Takhirov, Dr. Selim Gunay, Jose Robles, and Robert Cerney, whose help and support in preparing the test specimen and conducting the tests was irreplaceable. Outside support with material testing from Cruz Carlos in the Davis Hall Structural Laboratory is also greatly appreciated.

This work is the result of an international collaborative project titled, “Collaborative Developments for Seismic Rehabilitation of Vulnerable Braced Frames,” funded by the National Science Foundation (Grant Number CMMI 1208002) through the research program of the George E. Brown Jr. Network for Earthquake Engineering Simulation. The overall Principal Investigator for this project was Professor Charles Roeder of the University of Washington, Seattle. This project involved similar tests of specimens at the University of Washington and the National Taiwan University. The overall research program was regularly discussed in-person or via video-conference with Professors Charles Roeder, Jeffrey Berman, and Dawn Lehman of the University of Washington, Seattle, and Keh-Chyuan Tsai of the National Taiwan University.

Any opinions, findings, and conclusions or recommendations expressed in this report are those of the authors and do not necessarily reflect the views of the National Science Foundation, other participants in the overall research program, or the Pacific Earthquake Engineering Research Center at the University of California, Berkeley.

CONTENTS

ABSTRACT	iii
ACKNOWLEDGMENTS	v
TABLE OF CONTENTS	vii
LIST OF TABLES	xiii
LIST OF FIGURES	xvii
1 INTRODUCTION	1
1.1 Background	1
1.2 Research Program Objectives	2
1.3 Report Scope and Organization	3
2 LITERATURE REVIEW	5
2.1 Introduction	5
2.2 Evolution of U.S. Earthquake Provisions: 1985 to the 1988 UBC to the present	5
2.2.1 Braced Frame Design Demands.....	6
2.2.2 Inelastic Behavior of Braces	8
2.2.2.1 <i>Slenderness Ratio</i>	10
2.2.2.2 <i>Width-to-Thickness Ratio</i>	11
2.2.3 Story Mechanism Behavior.....	14
2.2.4 Weak Beam and the Concept of an Unbalanced Load	16
2.2.5 Connection Design.....	18
2.2.6 Summary	20
2.3 Braced Frame Behavior in Past Earthquakes	21
2.3.1 1971 San Fernando, California, Earthquake	21
2.3.2 1978 Miyagi-ken Oki, Japan, Earthquake.....	21
2.3.3 1994 Northridge, California, Earthquake.....	22
2.3.4 1995 Hyogo-ken Nanbu, Japan, Earthquake.....	25
2.3.5 Summary of Braced Frame Behavior in Past Earthquakes.....	29
3 SPECIMEN DESIGN AND CONSTRUCTION	31
3.1 Introduction	31

3.2	Test Specimens	31
3.2.1	NCBF-B-1: Initial Specimen Design	32
3.2.1.1	<i>Brace Design</i>	32
3.2.1.2	<i>Column Design</i>	34
3.2.1.3	<i>Beam Design</i>	34
3.2.1.4	<i>Connection Design</i>	35
3.2.1.5	<i>Erection and Fabrication</i>	35
3.2.2	NCBF-B-2: Concrete-Filled Braced Frame	36
3.2.2.1	<i>Concrete-Filled Brace Design</i>	37
3.2.2.2	<i>Erection and Fabrication</i>	38
3.2.3	NCBF-B-3SB: Strongback Retrofit	41
3.2.3.1	<i>Strongback Configuration</i>	43
3.2.3.2	<i>Kinematic Considerations</i>	45
3.2.3.3	<i>Brace Design</i>	45
3.2.3.4	<i>Column Design</i>	47
3.2.3.5	<i>Beam Design</i>	48
3.2.3.6	<i>Connection Design</i>	48
3.2.3.7	<i>Erection and Fabrication</i>	49
4	EXPERIMENTAL SET-UP AND TEST PROGRAM.....	51
4.1	Introduction.....	51
4.2	Test Set-Up	51
4.3	Instrumentation.....	52
4.3.1	Data Reduction.....	54
4.3.1.1	<i>Global</i>	54
4.3.1.2	<i>Braces</i>	55
4.3.1.3	<i>Columns</i>	56
4.3.1.4	<i>Beams</i>	57
4.3.1.5	<i>Connections</i>	58
4.4	Loading Protocol.....	58
4.4.1	NCBF-B-1 & NCBF-B-2 Loading Protocol.....	59
4.4.2	NCBF-B-3SB Loading Protocol.....	60
5	EXPERIMENTAL RESULTS.....	63
5.1	Introduction.....	63
5.2	NCBF-B-1: Baseline Test Specimen	63
5.2.1	Event Points, Observations, and Photographs	63
5.2.2	Summary of Key Observations for NCBF-B-1	70

5.3	NCBF-B-2: Specimen Upgrade	71
5.3.1	Event Points, Observations, and Photographs	71
5.3.2	Summary of Key Observations for NCBF-B-2	85
5.4	NCBF-B-3SB: Strongback Retrofit	87
5.4.1	Event Points, Observations, and Photographs	87
5.4.2	Summary of Key Observations for NCBF-B-3SB.....	99
6	ANALYSIS OF TEST RESULTS	101
6.1	Introduction	101
6.2	NCBF-B-1: Baseline Test Specimen	101
6.2.1	Global Behavior	102
6.2.2	Hollow Steel Brace Response.....	107
6.2.2.1	<i>Hollow Brace Local Buckling and Fracture</i>	107
6.2.2.2	<i>Brace Design Comparison</i>	108
6.2.3	Beam Response.....	112
6.2.4	Column Response	116
6.2.5	Connection Response.....	117
6.2.5.1	<i>Shear Tab Behavior</i>	118
6.3	NCBF-B-2: Specimen Upgrade	118
6.3.1	Global Behavior	121
6.3.2	Concrete-Filled Brace Response.....	125
6.3.2.1	<i>Concrete-Filled Brace Local Buckling and Fracture</i>	126
6.3.2.2	<i>Brace Design Comparison</i>	128
6.3.3	Beam Response.....	130
6.3.4	Column Response	135
6.3.5	Connection Response.....	137
6.3.5.1	<i>Shear Tab Behavior</i>	138
6.4	NCBF-B-3SB Strongback Retrofit	139
6.4.1	Global Behavior	139
6.4.2	Elastic Brace Response	145
6.4.3	Buckling Restrained Brace Response	145
6.4.3.1	<i>Assessment of BRB by AISC 341-10 Criteria</i>	147
6.4.4	Beam Response.....	151
6.4.5	Column Response	156

6.4.6	Connection Response.....	158
6.4.6.1	<i>Shear Tab Behavior</i>	158
6.5	Comparison of Specimen Behavior	160
6.5.1	Global Behavior	160
6.5.2	Weak-Story Tendency	162
6.5.3	Energy Dissipation.....	165
7	OPENSEES NUMERICAL CALIBRATION.....	171
7.1	Numerical Calibration.....	171
7.1.1	Experimental Tests.....	171
7.2	Numerical Model.....	173
7.2.1	Constraints and Boundary Conditions	173
7.2.2	Material.....	173
7.2.2.1	<i>Concrete Material</i>	173
7.2.2.2	<i>BRB Material</i>	174
7.2.2.3	<i>Low-Cycle Fatigue Material</i>	174
7.2.3	Sections.....	175
7.2.4	Elements.....	175
7.3	Discussion of Calibration Results	176
7.3.1	Discussion of NCBF-B-1 Simulation	176
7.3.2	Discussion of NCBF-B-2 Simulation	178
7.3.3	Discussion of NCBF-B-3SB Simulation	180
7.4	Continued Work.....	182
8	SUMMARY, CONCLUSIONS, AND FUTURE RESEARCH.....	185
8.1	Summary of Experimental Results.....	185
8.1.1	Summary of NCBF-B-1 Baseline Response.....	185
8.1.2	Summary of NCBF-B-2 CFT Upgrade Response	186
8.1.3	Summary of NCBF-B-3SB Strongback Response	187
8.2	Future Work.....	188
8.2.1	Evaluation of Vintage Braced Frames	188
8.2.2	Optimization of the Strongback System	188
	REFERENCES.....	191

APPENDIX A	PLOTS OF THE NCBF-B-1 TEST	197
APPENDIX B	PLOTS OF THE NCBF-B-2 TEST	219
APPENDIX C	PLOTS OF THE NCBF-B-3SB TEST	241
APPENDIX D	INSTRUMENTATION DRAWINGS (ELECTRONIC APPENDIX)	
APPENDIX E	DESIGN EXAMPLE CALCULATIONS (ELECTRONIC APPENDIX)	
APPENDIX F	TEST SPECIMEN SHOP DRAWINGS (ELECTRONIC APPENDIX)	

LIST OF TABLES

Table 1.1	Collaborative testing matrix.....	2
Table 1.2	University of California, Berkeley, testing matrix.....	3
Table 2.1	Historical trend for braced frame response modification factors.....	8
Table 2.2	Historical trend for brace slenderness limits.....	11
Table 2.3	Historical trend for brace width-to-thickness limit.....	13
Table 2.4	Historical trend for the expected post-buckling strength of the braces.....	17
Table 2.5	Historical trend for capacity design of the connection.....	19
Table 2.6	Description of braced frame damage in past earthquakes.....	21
Table 2.7	Summary of braced frame damage during the 1994 Northridge earthquake [Tremblay et al. 1995].....	23
Table 2.8	Examples of braced frame damage from the Hyogo-ken-Nanbu earthquake [Tremblay et al. 1996].....	27
Table 2.9	Braced frame configurations and damage states from the Hyogo-ken- Nanbu earthquake [AIJ 1995].....	27
Table 2.10	Brace sections and damage states from the Hyogo-ken-Nanbu earthquake [AIJ 1995].....	27
Table 3.1	Summary of experimental test specimens.....	32
Table 3.2	Brace properties of NCBF-B-1.....	34
Table 3.3	Material properties of NCBF-B-1.....	36
Table 3.4	Brace properties of NCBF-2.....	38
Table 3.5	Material properties of NCBF-B-2.....	39
Table 3.6	Compressive strength of cylindrical concrete specimens: NCBF-B-2 members, first- and second-story braces.....	39
Table 3.7	Split cylinder concrete test summary: NCBF-B-2 members, first- and second-story braces.....	39
Table 3.8	Concrete slump test on day of concrete pour: NCBF-B-2.....	40
Table 3.9	Elastic brace properties of NCBF-B-3SB.....	47
Table 3.10	Properties of buckling restrained brace (NCBF-B-3SB).....	47
Table 3.11	Material properties of NCBF-B-3SB.....	50

Table 4.1	Sensor list and corresponding response quantity.....	53
Table 4.2	Roof drift ratios corresponding to AISC deformation quantities.....	60
Table 5.1	Legend for representation of damage in each test specimen.	63
Table 5.2	NCBF-B-1 observations at various event points during the test.....	64
Table 5.3	NCBF-B-1: List of figures grouped by location.	65
Table 5.4	NCBF-B-2 observations at various event points during the test.....	72
Table 5.5	NCBF-B-2: List of figures grouped by locations	73
Table 5.6	NCBF-B-3SB observations at various event points during the test.....	88
Table 5.7	NCBF-B-3SB: List of figures grouped by location.	89
Table 6.1	Legend for label definitions.	101
Table 6.2	NCBF-B-1 legend of symbols for significant event points.	102
Table 6.3	NCBF-B-1 peak base shear at each cycle.	103
Table 6.4	NCBF-B-1 approximate base shear after significant damage events.	103
Table 6.5	NCBF-B-1 description of event points.	105
Table 6.6	NCBF-B-1 brace critical variables.....	108
Table 6.7	NCBF-B-1 brace compression strength degradation.	109
Table 6.8	NCBF-B-2 legend of symbols for significant event points.	119
Table 6.9	NCBF-B-2 peak base shear at each cycle.....	122
Table 6.10	NCBF-B-2 approximate base shear after significant damage events.	122
Table 6.11	NCBF-B-2 description of event points.	123
Table 6.12	NCBF-B-2 brace compression strength degradation.	125
Table 6.13	NCBF-B-2 brace critical variables.....	128
Table 6.14	NCBF-B-2 estimate of brace composite (EI) _{eff}	129
Table 6.15	NCBF-B-3SB legend of symbols for significant event points.....	139
Table 6.16	NCBF-B-3SB peak base shears at each cycle.....	140
Table 6.17	NCBF-B-3SB description of event points.	140
Table 6.18	NCBF-B-3SB BRB critical variables.	146
Table 6.19	Ratio of maximum compression force, C_{max} , to the maximum tension force, T_{max} for each cycle.	148
Table 6.20	Cumulative plastic deformation calculations for the first-story east BRB on each cycle of loading.	150

Table 6.21	Beam peak unbalanced load and vertical mid-span displacement.....	152
Table 6.22	Summary of experimental test results.....	161
Table 7.1	Uniaxial material <i>Steel4</i> input parameters for BRBs.....	174
Table 7.2	Buckling brace initial perturbation.	175
Table 7.3	Fatigue material input parameters.....	176
Table A.1	NCBF-B1: Values used for labels in plots.....	197
Table B.1	NCBF-B-2: values used for labels in plots.	219
Table C.1	NCBF-B-3SB: values used for labels in plots.	241

LIST OF FIGURES

Figure 2.1	Design response spectrum comparison of ASCE 7-10 and the 1985 UBC. Note: spectral accelerations for the ASCE 7-10 response spectrum were generated from USGS mapped acceleration values for zip code 94720. Mapped accelerations will vary according to site location, and this spectrum reflects one of the possible spectra that can be generated.7	7
Figure 2.2	Idealized hysteretic behavior of a brace under cyclic axial loading (based on diagram found in Bruneau et al. [2011]).....9	9
Figure 2.3	Local buckling in hollow cross sections [graphic courtesy of Liu and Goel 1988].12	12
Figure 2.4	Local buckling in concrete-filled cross sections [graphic courtesy of Liu and Goel 1988].....12	12
Figure 2.5	Idealized weak-story behavior (a) and soft-story behavior (b) of a braced frame with equivalent braces in each story.....15	15
Figure 2.6	Diagram illustrating post-buckling strength degradation of the brace and the unbalanced load on the beam.18	18
Figure 2.7	Diagram of connection types: (a) vintage CBF gusset plate without yield-line; (b) SCBF gusset plate with linear yield-line; and (c) SCBF gusset plane with elliptical yield-line.20	20
Figure 2.8	Photographed damage from the 1978 Miyagi-Ken Oki earthquake: (a) damaged steel frame furniture warehouse located on the outskirts of Sendai with rupture at bolt holes; and (b) Sendai Unyu Soko warehouse showing perimeter bracing with unbraced center bays [photographs courtesy of EERI 1978].22	22
Figure 2.9	Photographs of a four-story commercial building damage after the 1994 Northridge earthquake: (a) fracture of brace near connection region; (b) and (c) failure of slotted brace to gusset weld; (d) local buckling of brace near connection region; and (e) fracture at midpoint of brace [photographs courtesy of Bonneville and Bartoletti 1996].....24	24
Figure 2.10	Photographs of damage to seven-story braced frame structure under the Hyogo-ken-Nanbu earthquake: (a) overall view; (b) brace fracture at net section area of bolted region; and (c) fracture of bracing member [photographs courtesy of Tremblay et al. 1996].....26	26
Figure 2.11	Photographs of damage to five-story braced frame structure under the Hyogo-ken-Nanbu earthquake: (a) rupture of square tube brace; (b) local buckling of square tube brace; (c) out-of-plane buckling of gusset plate; (d) severe beam distortion of beam with out-of-plane buckling of gusset plate; (e) fracture of welded gusset to column interface; and (f) failure of bolted gusset to column interface [photographs courtesy of Tremblay et al. 1996].28	28

Figure 3.1	Test specimen schematic with dimensions, materials, and member sizes: NCBF-B-1.....	33
Figure 3.2	Overall views from north side of NCBF-B-1 before test: (a) west view; (b) center fisheye; and (c) east view.....	33
Figure 3.3	Erection of NCBF-B-1: (a) parts after final shop fabrication; and (b) field welding after erection.	36
Figure 3.4	Test specimen schematic with dimensions, materials, and member sizes: NCBF-B-2.....	37
Figure 3.5	Demolition of NCBF-B-1 damaged second-story braces and gusset plates.	40
Figure 3.6	Final second-story demolition state: (a) west gusset plate removal; (b) middle gusset plate removal; and (c) east gusset plate removal.	40
Figure 3.7	Repair of second story of NCBF-B-1: (a) erection of braces; and (b) added net-section reinforcement.....	41
Figure 3.8	Formwork for concrete pour: (a) first-story middle formwork; (b) and (c) first-story east formwork; and (d) first-story west formwork.	41
Figure 3.9	Examples of plastic mechanism: (a) conventional braced frame and (b) SB system.	42
Figure 3.10	Possible SB configurations: (a) “chevron” SB; (b) double-story X SB; and (c) offset double-story X SB.	42
Figure 3.11	Preliminary design configurations: (a) “chevron” SB; (b) double-story X SB; (c) lambda SB; (d) offset lambda SB.	43
Figure 3.12	Test specimen schematic with dimensions, materials, and member sizes: NCBF-B-3SB.....	44
Figure 3.13	Overall views from north side of NCBF-B-3SB before test: (a) west view; (b) center fisheye; and (c) east view.	44
Figure 3.14	Kinematic relations of an idealized SB system with a lambda brace configuration.	45
Figure 3.15	Deformed shape at incipient collapse under a triangular load distribution: (a) positive applied force; and (b) negative applied force.	46
Figure 3.16	Moment diagram at incipient collapse under a triangular load distribution: (a) positive applied force and (b) negative applied force.	46
Figure 3.17	Axial force diagram at incipient collapse under a triangular load distribution: (a) positive applied force and (b) negative applied force.	47
Figure 3.18	Free body diagram of middle connection of NCBF-B-3SB.	48
Figure 3.19	Original gusset plate “remnants” from NCBF-B-1 at first floor west connection of NCBF-B-3SB.	49
Figure 3.20	Erection of NCBF-B-3SB: parts after final shop fabrication.....	49

Figure 4.1	Test set-up: isometric drawing.....	52
Figure 4.2	Diagram of global response quantities.....	55
Figure 4.3	Internal force sign convention (positive moment, M , is counter-clockwise).....	55
Figure 4.4	Diagram for the estimation of column base moment, M_{bot}	57
Figure 4.5	Diagram for the estimation of beam end moments, M_{end} and M_{mid}	58
Figure 4.6	Lateral force distribution for loading protocol.....	59
Figure 4.7	Displacement control loading protocol at roof of NCBF-B-1.	59
Figure 4.8	Displacement control loading protocol at roof of NCBF-B-2.	60
Figure 4.9	Displacement control loading protocol at roof of NCBF-B-3SB.	61
Figure 5.1	NCBF-B-1 applied roof drift ratio during the test.	64
Figure 5.2	Sequence of brace behavior: (a) buckling of both braces with crack initiation in the west brace; (b) crack propagation in the west brace; (c) west-brace fracture; and (d) east-brace fracture.....	65
Figure 5.3	West brace behavior: (a) brace buckling; (b) crack initiation; (c) crack propagation; and (d) brace fracture.....	66
Figure 5.4	Final fracture state of the east brace.	66
Figure 5.5	Final fracture state of the west brace.	66
Figure 5.6	Base of east column at the second story.	66
Figure 5.7	Base of west column at second story.	67
Figure 5.8	Damage to the second-floor shear tabs: (a) north-face east gusset; (b) south-face east gusset; (c) north-face west gusset; and (d) south-face west gusset.....	67
Figure 5.9	East gusset plate at the second story.	67
Figure 5.10	West gusset plate at the second story.....	68
Figure 5.11	Center gusset plate at the roof.....	68
Figure 5.12	Twisting of center gusset plate at the roof.	68
Figure 5.13	Base of the east column.	68
Figure 5.14	East column web at second story behind the gusset plate.	69
Figure 5.15	Typical flaking at net section.	69
Figure 5.16	Typical flaking near the tip of the gusset plates.	69
Figure 5.17	Top of roof beam above the center gusset.	69
Figure 5.18	Closure of roof beam–column gap.....	70

Figure 5.19	NCBF-B-1: (a) schematic of collapse mechanism and (b) hierarchy of damage.	71
Figure 5.20	NCBF-B-2 applied roof drift ratio during the test.	71
Figure 5.21	Sequence of first-story east-brace behavior: (a) east-brace global buckling; (b) east-brace local buckling; (c) east-brace crack initiation; (d) east-brace fracture; (e) meeting of east brace in compression (positive roof drift); and (f) separation of east brace in tension (negative roof drift).	74
Figure 5.22	(a) Final fracture state of the east brace; and (b) bending of the east gusset plate.	75
Figure 5.23	(a) Global buckling of the west brace; and (b) local buckling of the west gusset plate.	76
Figure 5.24	Sequence of first-floor beam behavior: (a) positive (upward) beam displacement (negative roof drift); (b) negative (downward) beam displacement (positive roof drift); (c) beam-flange local buckling; and (d) beam double curvature.	77
Figure 5.25	Final first-floor beam state: (a) double curvature; (b) local buckling; and (c) twisting of gusset.	78
Figure 5.26	East base-plate slip.	78
Figure 5.27	Twisting of first-floor beam at east connection after shear tab tear.	79
Figure 5.28	Weld fracture at the first-story center gusset.	79
Figure 5.29	Curvature and final downward displacement of the first-floor beam.	79
Figure 5.30	Yielding of east-column web near the column base behind first-story lower gusset plate.	80
Figure 5.31	Tearing of east-column web behind the second-story lower gusset plate.	80
Figure 5.32	First-story east-brace behavior: (a) and (b) outward local buckling; (c) crack propagation; and (d) brace fracture.	80
Figure 5.33	Second-story east connection.	81
Figure 5.34	Second-story west connection.	81
Figure 5.35	Local buckling and crack initiation of the second-story east brace.	82
Figure 5.36	Fracture at the second-story west gusset-to-beam weld.	82
Figure 5.37	First-story east connection.	82
Figure 5.38	First-story west connection.	83
Figure 5.39	Fracture at the west gusset-to-baseplate weld.	83
Figure 5.40	Fracture at the west gusset-to-baseplate weld.	83
Figure 5.41	Fracture at the west column base.	84
Figure 5.42	Fracture at the west column flange.	84

Figure 5.43	Damage to the first-floor shear tabs (south face) at: (a) the east gusset and (b) west gusset; and damage to second-floor shear tabs (south face) at (c) the east gusset and (d) west gusset.....	84
Figure 5.44	Damage to first-floor shear tabs (north face) at (a) the east gusset and (b) west gusset; and damage to second-floor shear tabs (north face) at (c) east gusset and (d) west gusset.....	85
Figure 5.45	NCBF-B-2: (a) schematic of collapse mechanism and (b) hierarchy of damage.....	86
Figure 5.46	NCBF-B-3SB applied roof drift ratio during test.....	87
Figure 5.47	Damage sequence of first-floor east shear tab (welded): (a) initial state (0% drift ratio); (b) initial crack formation at bottom of weld (+1.5% drift ratio, first cycle); (c) crack propagation (+1.5% drift ratio, first cycle); and (d) full fracture of weld (-1.5% drift ratio, first cycle).....	90
Figure 5.48	Final damage state of first-floor east shear tab (welded): (a) from north side; (b) from south side; (c) beam after removal of shear tab plate; and (d) erection bolt hole elongation.....	90
Figure 5.49	Final fracture state of weld of shear tab (welded) after plate removal.....	91
Figure 5.50	Damage sequence of first-floor east shear tab (welded repair): (a) after initial weld repair (part of 2014-10-25 repair); (b) gross section yielding of shear tab plate (+1.5% drift ratio, second cycle); (c) crack formation at top and bottom of shear tab near column weld line (-1.5% drift ratio, second cycle); and (d) close up of defective weld.....	91
Figure 5.51	Damage sequence of first-floor east shear tab (with slotted holes): (a) initial state; (b) and (c) beam rotating through slotted holes (+3% and -3% drift ratio, respectively, first cycle); (d) final damage state; and (e) holes after demolition.....	91
Figure 5.52	First-floor east shear tab (with slotted holes): (a) slotted plate repair (part of 2014-10-26 repair); original beam top and bottom holes in Figure 5.50; new middle standard size holes drilled in beam during repair; (b) rotation of beam through slotted holes (+3.5% drift ratio); and final damage state of slotted shear tab of (c) north face and (d) south face.....	92
Figure 5.53	Second-floor east shear tab (welded): (a) additional welds added top and bottom of plate at plate-to-beam interface (part of 2014-10-25 repair); and final damage state of (b) north face and (c) south face.....	92
Figure 5.54	Second-floor east shear tab behavior during test: (a) separation of shear tab and column during test (-2.5% drift ratio, first cycle); and (b) unstable behavior of beam after shear tab had slipped away from column (-3% drift ratio, first cycle).....	93
Figure 5.55	Shear tab final damage states: (a) first floor east; (b) second-floor east weld fracture; (c) first floor west; and (d) second floor west.....	93

Figure 5.56	Final damage state of center connection and plastic hinging at first-floor east beam.....	94
Figure 5.57	Web buckling of beam: (a) from below and (b) facing west.	94
Figure 5.58	East first-floor beam plastic hinge: (a) initial plastic hinge formation; local buckling at: (b) north face; and (c) south face.	94
Figure 5.59	Damage at column base: (a) east column front; (b) west column front; (c) east column exterior; and (d) west column exterior.....	95
Figure 5.60	Whitewash flaking: (a) west column flange at base gusset plate; (b) lower first-story east brace net reduced section region; (c) west edge stiffeners at center connection; and (d) lower second-story east brace net section region.	96
Figure 5.61	Final bulging of BRB casing.....	97
Figure 5.62	Final damage state of upper second-story east brace connection: whitewash flaking at lower flange of beam, net reduced section region of brace, and at flanges of column.	98
Figure 5.63	(a) Extension of BRB at 2% drift ratio; and (b) and (c) whitewash flaking at upper BRB gusset connection.	98
Figure 5.64	Whitewash flaking at west first-floor gusset (potentially left from original frame before strongback “retrofit”).	98
Figure 5.65	Whitewash flaking behind weak-axis west column at roof gusset plate.	99
Figure 5.66	NCBF-B-3SB: (a) schematic of collapse mechanism and (b) hierarchy of damage.	100
Figure 6.1	NCBF-B-1 base shear versus roof drift ratio.	104
Figure 6.2	NCBF-B-1 hysteretic loop breakdown by cyclic amplitude.	105
Figure 6.3	NCBF-B-1 base shear versus roof drift ratio of brace buckling behaviour.	106
Figure 6.4	NCBF-B-1 base shear versus roof drift ratio after second-story west brace buckling (at -0.41% on first cycle to 0.5%).	106
Figure 6.5	NCBF-B-1 story shear versus story drift ratio.	107
Figure 6.6	Second-story east brace: (a) crack propagation; (b) second-story west brace low-cycle fatigue striations; and (c) corner tear, possibly upon load reversal.	109
Figure 6.7	Second-story east brace section fracture: (a) transverse section; and (b)-(d) longitudinal section.	110
Figure 6.8	Second-story west brace section fracture: (a) transverse section; and (b)-(d) longitudinal section.	110
Figure 6.9	NCBF-B-1 estimated brace axial force versus axial deformation (brace length is the work-point-to-work-point length).	111

Figure 6.10	NCBF-B-1 estimated brace axial force versus out-of-plane displacement.....	112
Figure 6.11	NCBF-B-1 beam estimated unbalanced load versus story drift.....	113
Figure 6.12	NCBF-B-1 beam vertical mid-span displacement versus story drift. Note: Unbalanced load is positive upward.	113
Figure 6.13	NCBF-B-1 beam end rotations versus story rotation.....	114
Figure 6.14	NCBF-B-1 second floor east and west half-beam estimated end moment time histories (estimated at beam end and at half-beam depth outside middle connection).....	115
Figure 6.15	NCBF-B-1 column estimated axial force versus roof drift ratio.	116
Figure 6.16	NCBF-B-1 column normalized axial moment interaction, (estimated at half the column depth above the second-story gusset plate connection).	117
Figure 6.17	NCBF-B-1 second-floor beam estimated end moment versus end rotation.	118
Figure 6.18	NCBF-B-2 base shear versus roof drift ratio.	119
Figure 6.19	NCBF-B-2 hysteretic loop breakdown by cyclic amplitude.....	120
Figure 6.20	NCBF-B-2 base shear versus roof drift ratio up to first-story east brace fracture (at -0.60% on second cycle to -0.75%).....	123
Figure 6.21	NCBF-B-2 base shear versus roof drift ratio after first-story east brace fracture (at -0.60% on second cycle to -0.75%).....	124
Figure 6.22	NCBF-B-2 story shear versus story drift ratio.....	124
Figure 6.23	Inner concrete after test at local buckling location: (a) and (b) second-story west brace; and (c) and (d) second-story east brace.	127
Figure 6.24	Inner concrete after test after global buckling of first-story west brace.	127
Figure 6.25	Local buckling of first-story east brace: (a) outward local buckling; crack propagation (b) west side and (c) south side; and (d) complete fracture.	128
Figure 6.26	NCBF-B-2 estimated brace axial force versus axial deformation.	129
Figure 6.27	NCBF-B-2 estimated brace axial force versus out-of-plane displacement.....	130
Figure 6.28	NCBF-B-2 beam estimated unbalanced load versus story drift ratio. Note: Unbalanced load is positive upward.	131
Figure 6.29	NCBF-B-2 beam vertical mid-span displacement versus story drift ratio.....	131
Figure 6.30	NCBF-B-2 first-floor east half-beam estimated shear versus story drift ratio (where L is the distance from the beam end to the edge of the middle connection).....	132
Figure 6.31	NCBF-B-2 beam end rotations versus story rotation.....	133
Figure 6.32	NCBF-B-2 first-floor east and west half-beam estimated end moment time histories (estimated at beam end and at half-beam depth outside middle connection).....	134

Figure 6.33	NCBF-B-2 column estimated axial force versus roof drift ratio.	136
Figure 6.34	NCBF-B-2 column normalized axial moment interaction (estimated at half the column depth above the second-story gusset plate connection). Here, M_p is the plastic moment capacity of the column, and P_y is the yield strength of the column equal to AF_y , where; A is the cross-sectional area, and F_y is the yield strength found from the coupon tests.....	137
Figure 6.35	NCBF-B-2 first-floor beam estimated end moment versus end rotation.....	138
Figure 6.36	NCBF-B-3SB base shear versus roof drift ratio.	141
Figure 6.37	NCBF-B-3SB hysteretic loop breakdown by cyclic amplitude.....	142
Figure 6.38	NCBF-B-3SB base shear versus roof drift ratio prior to rupture of BRB (@+1.45% on first cycle to +2.5%).	143
Figure 6.39	NCBF-B-3SB base shear versus roof drift ratio after rupture of BRB (@+1.45% on first cycle to +2.5%).	143
Figure 6.40	NCBF-B-3SB story shear versus story drift ratio: (a) second story; and (b) first story (BRB rupture at +1.45% on first cycle to +2.5%).	144
Figure 6.41	NCBF-B-3SB estimated elastic west braces axial force versus axial deformation (% brace length is the work-point-to-work-point length).	145
Figure 6.42	NCBF-B-3SB estimated BRB axial force versus axial deformation (% brace length is the work-point-to-work-point length).....	147
Figure 6.43	Example calculation for the cumulative plastic deformation for idealized cycles at amplitude increment $n = 3$	151
Figure 6.44	NCBF-B-3SB first-floor east $\frac{1}{2}$ -beam estimated shear versus story drift ratio (where L is the distance from the beam end to the edge of the middle connection).....	153
Figure 6.45	NCBF-B-3SB first-floor beam: (a) unbalanced load and (b) vertical mid-span displacement versus story drift ratio. Note: Unbalanced load is positive upward.	153
Figure 6.46	NCBF-B-3SB beam end rotations versus story rotation.....	154
Figure 6.47	NCBF-B-3SB first-floor east and west $\frac{1}{2}$ -beam estimated end moment time histories (estimated at beam end and at a half-beam depth outside middle connection).....	155
Figure 6.48	NCBF-B-3SB column estimated axial force versus roof drift ratio.	157
Figure 6.49	NCBF-B-3SB column normalized axial moment interaction (estimated at half the column depth above the second-story gusset plate connection). Here M_p is the plastic moment capacity of the column and P_y is the yield strength of the column equal to AF_y , where A is the cross-sectional area and F_y is the yield strength found from the coupon tests.....	158
Figure 6.50	NCBF-B-3SB first-floor east beam estimated end moment versus end rotation: (a) welded shear tab and (b) slotted shear tab. Error! Bookmark not defined.	

Figure 6.51	NCBF-B-3SB second-floor east welded shear tab estimated moment versus rotation at east end.	160
Figure 6.52	Base shear versus roof drift ratio envelopes for all three test specimens.	162
Figure 6.53	Story shear versus story drift ratio envelopes for all three test specimens.	163
Figure 6.54	Comparison between the ratio of the first-story drift ratio to the sum of the first- and second-story drift ratios at peak cyclic amplitudes.	164
Figure 6.55	Comparison between the ratio of the column shear and the story shear at peak cyclic amplitudes.	164
Figure 6.56	Energy dissipation in NCBF-B-1.	165
Figure 6.57	Energy dissipation in NCBF-B-2.	166
Figure 6.58	Energy dissipation in NCBF-B-3SB.	166
Figure 6.59	Comparison of the energy dissipation in each half-cycle for each test specimen.	167
Figure 6.60	Comparison of the cumulative energy dissipation in each test specimen.	167
Figure 6.61	Comparison of energy dissipation of the buckled second-story braces in the NCBF-B-1 test.	168
Figure 6.62	Comparison of energy dissipation of the buckled braces in the NCBF-B-2 test.	169
Figure 6.63	Energy dissipation in the BRB of the NCBF-B-3SB test.	170
Figure 7.1	Schematic of simulations: (a) NCBF-B-1 & 2 and (b) NCBF-B-3SB.	172
Figure 7.2	NCBF-B-1 comparison of numerical and experimental results of global hysteresis.	177
Figure 7.3	NCBF-B-1 comparison of numerical and experimental results of brace hysteresis.	178
Figure 7.4	NCBF-B-2 comparison of numerical and experimental results of global hysteresis.	179
Figure 7.5	NCBF-B-2 comparison of numerical and experimental results of brace hysteresis.	180
Figure 7.6	NCBF-B-3SB comparison of numerical and experimental results of global hysteresis.	181
Figure 7.7	NCBF-B-3SB comparison of numerical and experimental results of brace hysteresis.	182

Figure A.1	NCBF-B-1 Story shear time histories.	198
Figure A.2	NCBF-B-1 Story drift ratio time histories.	199
Figure A.3	NCBF-B-1 estimated brace axial force time histories.	200
Figure A.4	NCBF-B-1 brace out-of-plane displacement time histories.	201
Figure A.5	NCBF-B-1 Brace axial deformation time histories (L_b is the work-point-to-work-point length).	202
Figure A.6	NCBF-B-1 second-story east brace estimated moment time histories (measured at top and bottom $\frac{1}{4}$ -points of brace length).	203
Figure A.7	NCBF-B-1 second-story east brace out-of-plane end rotation time histories.	203
Figure A.8	NCBF-B-1 first-story east brace estimated moment time histories (measured at top and bottom $\frac{1}{4}$ -points of brace length).	204
Figure A.9	NCBF-B-1 first-story east brace out-of-plane end rotation time histories.	204
Figure A.10	NCBF-B-1 second-story west brace estimated moment time histories (measured at top and bottom $\frac{1}{4}$ -points of brace length).	205
Figure A.11	NCBF-B-1 second-story west brace out-of-plane end rotation time histories.	205
Figure A.12	NCBF-B-1 first-story west brace estimated moment time histories (measured at top and bottom $\frac{1}{4}$ points of brace length).	206
Figure A.13	NCBF-B-1 first-story west brace out-of-plane end rotation time histories.	206
Figure A.14	NCBF-B-1 brace estimated shear time histories.	207
Figure A.15	NCBF-B-1 estimated unbalanced load time histories.	208
Figure A.16	NCBF-B-1 beam vertical mid-span displacement time histories.	208
Figure A.17	NCBF-B-1 first-floor east $\frac{1}{2}$ -beam estimated moment history (measured at 3 ft-0 in. from ends).	209
Figure A.18	NCBF-B-1 first-floor west $\frac{1}{2}$ -beam estimated moment history (measured at 3 ft-0 in. from ends).	209
Figure A.19	NCBF-B-1 second-floor east $\frac{1}{2}$ -beam estimated moment history (measured at 3 ft-0 in. from ends).	210
Figure A.20	NCBF-B-1 second-floor west $\frac{1}{2}$ -beam estimated moment history (measured at 3 ft-0 in. from frame centerline and 1 ft-6 in. from west end).	210
Figure A.21	NCBF-B-1 beam axial deformation time histories.	211
Figure A.22	NCBF-B-1 second-floor beam end rotation time histories.	211
Figure A.23	NCBF-B-1 first-floor beam end rotation time histories.	212
Figure A.24	NCBF-B-1 beam estimated shear time histories.	213
Figure A.25	NCBF-B-1 column estimated axial force time histories.	214

Figure A.26	NCBF-B-1 east column estimated moment history (measured at 3 ft-0 in. from the column ends).	215
Figure A.27	NCBF-B-1 west column estimated moment history (measured at 3 ft-0 in. from the column ends).	216
Figure A.28	NCBF-B-1 column estimated shear time histories.	217
Figure B.1	NCBF-B-2 story shear time histories.....	220
Figure B.2	NCBF-B-2 story drift ratio time histories.....	221
Figure B.3	NCBF-B-2 estimated brace axial force time histories.	222
Figure B.4	NCBF-B-2 brace out-of-plane displacement time histories.....	223
Figure B.5	NCBF-B-2 brace axial deformation time histories. (L_b is the work-point-to-work-point length).	224
Figure B.6	NCBF-B-2 second-story east brace estimated moment time histories (measured at top and bottom $\frac{1}{4}$ -points of brace length).	225
Figure B.7	NCBF-B-2 second-story east brace out-of-plane end rotation time histories.	225
Figure B.8	NCBF-B-2 first-story east brace estimated moment time histories (measured at top and bottom $\frac{1}{4}$ -points of brace length).	226
Figure B.9	NCBF-B-2 first-story east brace out-of-plane end rotation time histories.	226
Figure B.10	NCBF-B-2 second-story west brace estimated moment time histories (measured at top and bottom $\frac{1}{4}$ -points of brace length).	227
Figure B.11	NCBF-B-2 second-story west brace out-of-plane end rotation time histories.	227
Figure B.12	NCBF-B-2 first-story west brace estimated moment time histories (measured at top and bottom $\frac{1}{4}$ -points of brace length).	228
Figure B.13	NCBF-B-2 first-story west brace end rotation time histories.	228
Figure B.14	NCBF-B-2 brace estimated shear time histories.....	229
Figure B.15	NCBF-B-2 first-floor beam estimated unbalanced load history.	230
Figure B.16	NCBF-B-2 Beam vertical mid-span displacement time histories.....	230
Figure B.17	NCBF-B-2 first-floor east $\frac{1}{2}$ -beam estimated moment history (measured at 3 ft-0 in. from ends).	231
Figure B.18	NCBF-B-2 first-floor west $\frac{1}{2}$ -beam estimated moment history (measured at 3 ft-0 in. from ends).	231
Figure B.19	NCBF-B-2 second-floor east $\frac{1}{2}$ -beam estimated moment history (measured at 3 ft-0 in. from ends).....	232

Figure B.20	NCBF-B-2 second-floor west $\frac{1}{2}$ -beam estimated moment history (measured at 3 ft-0 in. from end from frame centerline and 1 ft-6 in. from west end).	232
Figure B.21	NCBF-B-2 beam axial deformation time histories.	233
Figure B.22	NCBF-B-2 second-floor beam end rotation time histories.	233
Figure B.23	NCBF-B-2 first-floor beam end rotation time histories.	234
Figure B.24	NCBF-B-2 beam estimated shear time histories (where L is the distance from the beam end to the edge of the middle connection).	235
Figure B.25	NCBF-B-2 column estimated axial force time histories.	236
Figure B.26	NCBF-B-2 east column estimated moment history (measured at 3 ft-0 in. from the column ends).	237
Figure B.27	NCBF-B-2 west column estimated moment history (measured at 3 ft-0 in. from the column ends).	238
Figure B.28	NCBF-B-2 column estimated shear time histories.	239
Figure C.1	NCBF-B-3SB story shear time histories.	242
Figure C.2	NCBF-B-3SB story drift ratio time histories.	243
Figure C.3	NCBF-B-3SB estimated brace axial force time histories.	244
Figure C.4	NCBF-B-3SB brace out-of-plane displacement time histories.	245
Figure C.5	NCBF-B-3SB Brace axial deformation time histories (L_b is the work-point-to-work-point length).	246
Figure C.6	NCBF-B-3SB first-story east brace estimated moment time histories (measured at top and bottom $\frac{1}{4}$ -points of brace length).	247
Figure C.7	NCBF-B-3SB first-story east brace out-of-plane end rotation time histories.	247
Figure C.8	NCBF-B-3SB second-story west brace estimated moment time histories (measured at top and bottom $\frac{1}{4}$ points of brace length).	248
Figure C.9	NCBF-B-3SB second-story west brace out-of-plane end rotation time histories.	248
Figure C.10	NCBF-B-3SB first-story west brace estimated moment time histories (measured at top and bottom $\frac{1}{4}$ -points of brace length).	249
Figure C.11	NCBF-B-3SB first-story west brace out-of-plane end rotation time histories.	249
Figure C.12	NCBF-B-3SB brace estimated shear time histories.	250
Figure C.13	NCBF-B-3SB first-floor beam estimated unbalanced load history.	251
Figure C.14	NCBF-B-3SB first-floor beam vertical mid-span displacement history.	251

Figure C.15	NCBF-B-3SB first-floor east $\frac{1}{2}$ beam estimated moment history (measured at 3 ft-0 in. from the east end and 1 ft-6 in. from the west end).....	251
Figure C.16	NCBF-B-3SB first-floor west $\frac{1}{2}$ beam estimated moment history (measured at 1 ft-6 in. from the east end and 3 ft-0 in. from the west end).....	252
Figure C.17	NCBF-B-3SB second- floor beam estimated moment history (measured at 3 ft-0 in. from the east end and 3 ft.-0 in. west of the beam midpoint).	252
Figure C.18	NCBF-B-3SB beam axial deformation time histories.	253
Figure C.19	NCBF-B-3SB first-floor beam end rotation time histories.....	254
Figure C.20	NCBF-B-3SB beam estimated shear time histories (where L is the distance from the beam end to the edge of the middle connection).....	255
Figure C.21	NCBF-B-3SB column estimated axial force time histories.....	256
Figure C.22	NCBF-B-3SB east column estimated moment history (measured at 3 ft-0 in and 4 ft-0 in. from the column ends).	257
Figure C.23	NCBF-B-3SB west column estimated moment history (measured at 3 ft-0 in. and 4 ft-0 in from the column ends).	258
Figure C.24	NCBF-B-3SB Column estimated shear time histories.....	259

1 Introduction

1.1 BACKGROUND

Extensive research was conducted in the United States and Japan in the late 1970s and 1980s on the inelastic behavior of steel braces and concentrically braced frames (CBFs) (e.g., Black et al. [1980], Astaneh et al. [1985], Liu and Goel [1988], and Foutch et al. [1987]). This and subsequent research prompted significant changes to the seismic design requirements for CBFs. These changes were introduced gradually, beginning in California in the late 1970s [SEAOC 1978], before becoming nationally accepted in the United States in the late 1980s [ICBO 1988]. Since 1988, the seismic provisions for CBFs have been updated regularly. However, many existing braced frames, herein referred to as *vintage* if designed prior to 1988, were designed before or during this update and revision process [Malley 1989].

Modern code provisions attempt to create lateral load-resisting systems that have sufficient ductility to resist severe seismic excitations safely. Current codes include a variety of provisions to achieve this ductility, including ones that:

1. Stipulate limits on material properties, brace slenderness ratios, and section compactness ratios to achieve adequate inelastic behavior;
2. Require beams and columns to develop the expected loads from the redistribution of forces as braces yield or buckle;
3. Prescribe connection details capable of developing the capacity of the attached braces as well as the rotations associated with brace buckling and frame action; and
4. Restrict the bracing configurations permitted in order to reduce the dependence of the overall system behavior on the direction of loading.

Modern versions of these requirements were adopted nationally after 1988. While these changes should result in far more ductile behavior in CBFs, existing braced frames, especially those designed prior to 1988, may include a range of deficiencies that limit their ductility when subjected to strong ground shaking. Such deficiencies have been confirmed in several post-earthquake reconnaissance reports [Tremblay et al. 1995; Tremblay et al. 1996; and Rai and Goel 2003].

While recent studies have sought to understand the behavior of SCBF systems [Lehman et al. 2008; Uriz and Mahin 2008; Clark 2009; Lumpkin et al. 2009; Yoo et al. 2009; Chen and Mahin 2010; and Lai and Mahin 2013], vintage braced frame systems have been comparatively neglected. In the 1980s, researchers conducted sub-assembly experiments on six-story braced

frames as part of the U.S.-Japan Cooperative Program [Foutch et al. 1987, Fukuta et al. 1989]. The full-scale CBF-phase of this program was concluded after limited yielding in the surrounding frame. The CBF was then modified and tested as an eccentrically braced frame utilizing the same specimen. Later experiments of now vintage CBFs were tested under greater inelastic demands but utilized half- or smaller-scale specimens. Current standards for CBFs [e.g., ASCE/SEI-41 (2013)] were generally developed based on data obtained from experimental observations and numerical analyses of CBFs designed to post-1997 code provisions [Tremblay 2002; Lee and Bruneau 2005, Lehman et al. 2008; Uriz and Mahin 2008; Stoakes and Fahnestock 2012; and Lai and Mahin 2013]. Relatively few test results are available for CBF sub-assemblages designed to earlier seismic provisions.

A thorough assessment the behavior of vintage CBFs designed according to older building codes is limited by the lack of data. The large number of possible deficiencies and the deteriorating and potentially brittle inelastic behavior of vintage braced frames complicates determination of their seismic response. Thus, a integrated experimental and analytical research program was undertaken to holistically study the behavior of typical vintage and retrofit CBF systems.

1.2 RESEARCH PROGRAM OBJECTIVES

An experimental study assessing the vulnerability of vintage CBF systems was undertaken to address the following issues:

1. Improve understanding of the hierarchy of damage and failures in vintage CBF systems;
2. Holistically assess the relationship between the member, connection, and frame behavior;
3. Calibrate numerical models to simulate expected CBF behavior; and
4. Identify promising retrofit strategies to improve performance of deficient CBF systems.

This investigation was part of larger research program that included a series of tests done under the *George E. Brown Jr., Network for Earthquake Engineering Simulation (NEES)* Small Group Project titled “Collaborative Developments for Seismic Rehabilitation of Vulnerable Braced Frames” between the National Center for Research on Earthquake Engineering (NCREE) in Taiwan, the University of Washington (UW), and the University of California, Berkeley (UCB). Tests at UCB were carried out in the nees@berkeley equipment site. Details of the specimens tested at each of these laboratories are presented in Table 1.1. This report focuses on the tests done by UCB in the nees@berkeley laboratory.

Table 1.1 Collaborative testing matrix.

Facility	Test Description	Emphasis
UW	1-story vulnerable and retrofit vintage CBF tests	Member and connection testing
nees@berkeley	2-story vulnerable and retrofit vintage CBF tests	System testing without concrete slab
NCREE	3-story vulnerable and retrofit vintage CBF tests	System testing with concrete slab

1.3 REPORT SCOPE AND ORGANIZATION

Three two-story, one-bay vintage CBF deficient and retrofit frames were tested in this investigation; see Table 1.2. All three tests employed one column oriented in weak-axis bending and one column oriented in strong-axis bending. The first test (NCBF-B-1) was considered the baseline test specimen and was designed according to the 1985 Uniform Building Code (UBC) [ICBO 1985]. The second specimen (NCBF-B-2) upgraded the first specimen with concrete-filled braces and net section details to improve the behavior observed during the baseline test. The third specimen (NCBF-B-3SB) consisted of an overall retrofit of the first two specimens, making use of a “strongback” retrofit design to distribute story drifts more uniformly over the height of the frame.

Chapter 2 provides an overview of procedures typically used in the design of vintage concentrically braced frames and examines their limitations. Chapter 2 also provides a summary of damage observed in older braced frames during past earthquakes. Chapter 3 describes the design and construction of each of the test specimens. Chapter 4 defines the experimental program, test set-up, loading protocol, and instrumentation used in the experiments. Observations of local and global response and accumulated damage in the frames are summarized in Chapter 5. Chapter 6 analyzes and compares data from the tests. Chapter 7 examines efforts to develop and calibrate a numerical model to the experimental results. Finally, results and recommendations for future research are summarized in Chapter 8.

The appendices supplementing this report provide more detailed information on the design and testing results. In particular, Appendices A, B, and C contain response-history plots of test data not included in Chapter 6. Appendix D (electronic appendix) provides detailed lists and drawings of the instruments used in the test. Appendix E (electronic appendix) includes example calculations used in determining the member sizes and connection details. Appendix F (electronic appendix) shows the shop drawings for the specimens.

Table 1.2 University of California, Berkeley, testing matrix.

Test designation	Test site	Experiment description	Test date
NCBF-B-1	nees@berkeley	Baseline vintage CBF specimen	10-11-2013
NCBF-B-2	nees@berkeley	NCBF-B-1 upgrade: (1) CFT braces; (2) Net section reinforcement	02-10-2014 02-25-2014
NCBF-B-3SB	nees@berkeley	“Strongback” retrofit	09-25-2014 09-26-2014 09-27-2014

2 Literature Review

2.1 INTRODUCTION

This chapter describes some of the potential deficiencies associated with older braced frames, herein termed *vintage* braced frames if designed to codes in effect prior to the 1988 UBC. Section 2.2 highlights important developments in the U.S. building code from 1985 to the present, identifying potential concerns regarding the seismic behavior of vintage braced frames. Section 2.3 then discusses damage observed in braced frames following past earthquakes, highlighting damage most relevant to braced frames designed in the late 1970s through the mid-1980s.

2.2 EVOLUTION OF U.S. EARTHQUAKE PROVISIONS: 1985 TO THE 1988 UBC TO THE PRESENT

Concentrically braced frames became increasingly popular in the late 1960s and 1970s for the design and construction of low- and mid-rise structures. The design of steel concentrically braced frames was considered uncomplicated and allowed for easy fabrication and construction. The bracing members were generally idealized with pinned ends, allowing for straightforward elastic analysis with limited regard to flexural bending. The connections between members utilized simple gusset plates that did not require the labor and other costs associated with moment connections. The inverted-V or “chevron” configuration of braces was considered to be the most efficient bracing system [Cheng and Juang 1985], with the added benefit of easy accommodation for the placement of architectural elements such as doors and windows.

Current seismic design provisions include special regulations to ensure that braced frames adequately dissipate energy, even in the post-buckling inelastic range. Detailing requirements, such as maximum slenderness (kl/r) and width-to-thickness (b/t) ratios, aid the braces in developing an acceptable hysteretic response under strong ground motions; see Section 2.2.2. The beam in a chevron configuration is now required to have adequate capacity under the unbalanced load resulting from the difference in the vertical components of the forces in the tension brace and post-buckled compression brace in the story below; this is examined in Section 2.2.4. Capacity-design principles now reduce the likelihood of premature connection failures and allow the braces to achieve their full capacity; see Section 2.2.5.

These improved seismic design provisions were introduced gradually. Research conducted during the late 1970s and 1980s on bracing components and connections led to new

design recommendations that were eventually included in the 1988 UBC [Black et al. 1980; Lee and Goel 1987]; prior editions of the UBC addressed braced frames in a limited fashion. Thus, it is important to understand CBF design provisions prior to the 1988 UBC in order to understand the possible deficiencies associated with existing vintage braced frame designs.

This section compares current design standards to those used to design existing braced frames and discusses potential deficiencies in older braced frames, as listed below:

Section 2.2.1: Braced frame design demands

Section 2.2.2: Inelastic behavior of the bracing members

Section 2.2.2.1: Influence of the brace global slenderness, or kl/r , ratio

Section 2.2.2.2: Influence of the brace local width-to-thickness, or b/t , ratio

Section 2.3.3: Story mechanism behavior

Section 2.2.4: Weak- and strong-beam mechanisms and the effect of the unbalanced load

Section 2.2.5: Connection design

Finally, an overall summary can be found in Section 2.2.6.

2.2.1 Braced Frame Design Demands

To understand the development of code-prescribed seismic demands, this section outlines current methods for determining reduced seismic design forces and compares calculations for the required design base shear strength in modern and vintage building codes.

Current evaluation of building behavior depends on the estimated severity of the earthquake for a building site. Generally, the most severe earthquake effects considered by ASCE 7-10 [2010] (including adjustments for targeted risk) is a risk-targeted maximum considered earthquake (MCE_R). Based on mapped pseudo-accelerations provided by the United States Geological Survey (USGS), engineers can generate an elastic pseudo-acceleration response spectrum for a design-basis earthquake (DBE) based on a building site and a derived MCE_R response spectrum. Modern structures are then designed for reduced seismic forces based on the DBE spectral ordinate at the structure's fundamental period, an importance factor, and a response modification coefficient or R factor.

This R factor is used to approximate inelastic response as a function of the expected ductility, over-strength, damping, and energy dissipation of the desired system; see Figure 2.1. Modern special concentrically braced frames (SCBFs) are expected to exhibit more ductile behavior than ordinary concentrically braced frames (OCBFs), a concept reflected in their R factors of 6 and 3.25, respectively. While current code provisions such as ASCE 7-10 explicitly require structures to be designed for one level of ground shaking, it is implicitly assumed that the structures will also reach other performance objectives—such as collapse prevention—for MCE_R -level shaking.

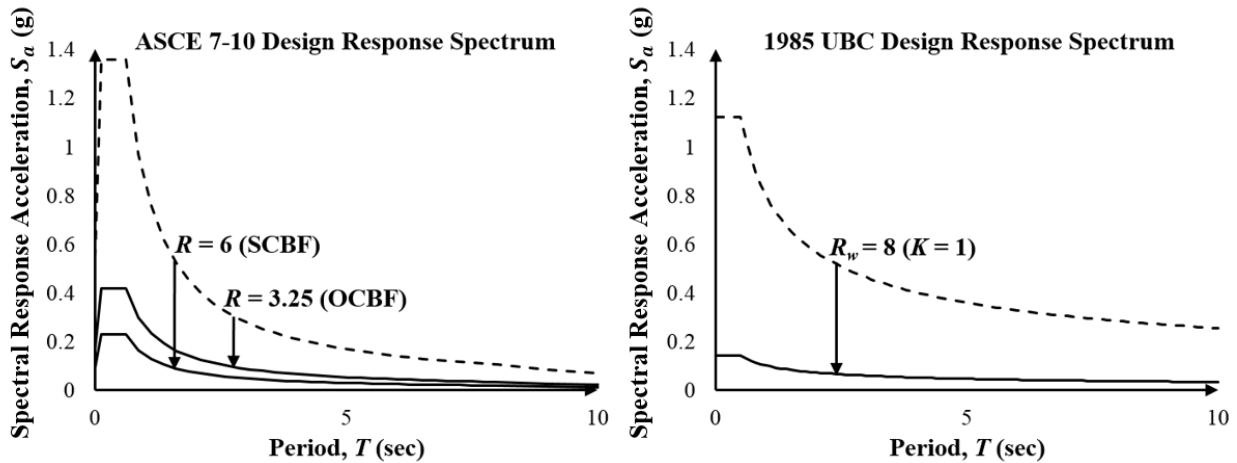


Figure 2.1 Design response spectrum comparison of ASCE 7-10 and the 1985 UBC. Note: spectral accelerations for the ASCE 7-10 response spectrum were generated from USGS mapped acceleration values for zip code 94720. Mapped accelerations will vary according to site location, and this spectrum reflects one of the possible spectra that can be generated.

In comparison, the design base shear, V_b , in the 1988 UBC was based on the following equation:

$$V_b = ZIKCSW \quad (2.1)$$

where Z is the seismic zone factor depending on the structures location; I is the importance factor; C is a numerical coefficient depending on the soil conditions of the site and the period of the structure; S is a soil profile coefficient; W is the seismic weight of the structure; and K is a factor representing the expected ductility of the system. The Z coefficient denotes a seismic zone factor of 1 through 4. Zone 4 structures were located in what was considered to be high seismic areas; the required base shear was increased by a factor of 4 in these regions.

The value of K in vintage building codes has a similar meaning to the R factor in modern building codes. This factor was introduced in the 1959 SEAOC “Blue Book” based on types of construction that had been found to perform better in past earthquakes. Braced frames were not addressed by these K factors and fell under an “all other buildings except...” category with $K = 1.0$. The 1988 UBC replaced this K factor with an R_w factor, defined by the following:

$$R_w = \frac{8}{K} \quad (2.2)$$

Generally, this R_w factor was equivalent to the K factor but additionally provided an explicit R_w for braced frames, clarifying the code-level strength requirements for CBFs. The R_w factor was considered a better representation of inelastic demands because it divided rather than multiplied the equation for design base shear.

The values for the modern R factor were determined largely from calibration with past practice. A direct comparison between response modification factors can be made using the following equation for a moment-resisting frame [ATC 1995]:

$$R_w = 1.54R = \frac{7.86}{K} \approx \frac{8}{K} \quad (2.3)$$

From this equation and the ductility factors tabulated in Table 2.1, it can be observed that the design base shear calculated per vintage building codes can be smaller than that calculated per modern seismic codes depending on the site location. This difference in design-level forces is also highlighted by the conceptual dissimilarity in the base shear parameters, Z , C , and S , and the parameters used to generate modern response spectra. An approximate comparison between the design response spectra generated according to ASCE 7-10 and the 1985 UBC can be seen in Figure 2.1.

This variation in design level forces can result in differences between the capacity of vintage braced frames and modern seismic design loads. Vintage braced frames were designed to lower design forces than current U.S. code requirements. As such, these structures may have insufficient strength for the expected level of ground shaking depending on the building location.

Table 2.1 Historical trend for braced frame response modification factors.

Building code	Ductility factor	
1979–1985 UBC	$K = 1$	
1988 UBC	$R_w = 8$	
1992 AISC 341	$R = 5$	
Braced-frame type ¹	OCBF	SCBF
1997 AISC 341	$R = 5$	$R = 6$
2002 AISC 341	² $R = 5$	$R = 6$
2005 AISC 341	$R = 3.25$	$R = 6$
2010 AISC 341	$R = 3.25$	$R = 6$

¹ Specific specifications for SCBFs and OCBFs did not appear until the 1997 AISC seismic provisions.

² Provisions for OCBFs were eliminated in the 2002 AISC seismic provisions, except what was previously required for low-rise or roof structures designed with an amplified seismic load of $\Omega_0 E$.

2.2.2 Inelastic Behavior of Braces

The asymmetric behavior of brace compression buckling and tensile yielding can be described by the simplified hysteretic plot in Figure 2.2. The example brace is loaded axially from compression to tension starting from point O. Line O-ii represents the linear elastic region of the brace prior to buckling. The brace is able to unload back to point O within this region. Once the brace reaches its compression capacity, C_u , at point (i), the brace buckles.

If this buckling is elastic, the brace exhibits the plateau region i-ii, and slender braces are still able to unload elastically along line ii-i-O. Upon buckling, the brace develops moments along its length because of the out-of-plane deformation, Δ , with a maximum moment at the brace midpoint. Once this maximum moment has reached the plastic moment of the brace, a plastic hinge forms at point (ii). Localized plastic hinge rotations under further axial displacement, δ , cause a small kink to form. From the equation $M = P\Delta$, the load-carrying

capacity, P , of the brace must decrease to sustain the same plastic moment with an increasing out-of-plane displacement, Δ . A nonlinear decrease in axial capacity can be seen along line ii-iii corresponding to the interaction between the axial load and the brace's moment capacity.

At point (iv) at $P = 0$, the brace exhibits both a lateral residual deformation from the kink as well as residual axial shortening. Line iv-v represents the elastic recovery that takes place as the brace is pulled in tension and begins to straighten. At point (v), the plastic moment capacity is reached at the midpoint of the brace. The plastic hinge rotations, however, are opposite in direction to the plastic hinge rotations seen during the previous compression cycle. The out-of-plane Δ decreases, rather than increases, as the brace attempts to straighten back to its initial undeformed position as it is pulled in tension. If $M = P\Delta$ is again applied, the load is allowed to continue to increase even after the plastic moment capacity of the brace has been reached. This tension force is then capped in line vi-vii by the tension yielding capacity of the brace.

Even though the brace is straightened in tension, a small residual deformation is left upon reloading into the next compression cycle. This is because the applied tension force is limited by the brace yielding capacity, and the brace can never completely re-straighten. This residual deformation often causes the second cycle's compression capacity, C_u' , to be smaller than the initial buckling capacity, C_u , leading to a degradation in compression strength upon subsequent cycles. This process is described in more detail in Bruneau et al. [2011].

The importance of the post-buckling behavior of the bracing members was first noted in small-scale experimental component tests performed in the 1970s and early 1980s [Wakabayashi et al. 1970; Higginbotham 1973; Popov et al. 1976; and Black et al. 1980]. These studies showed that brace behavior largely depends on the actual yield capacity of the steel, the slenderness of the bracing member, and the width-to-thickness ratio of the brace cross section. Modern seismic provisions attempt to achieve adequate energy dissipation in the braces through stringent requirements related to all three of these factors, but no such provisions existed for vintage braced frames.

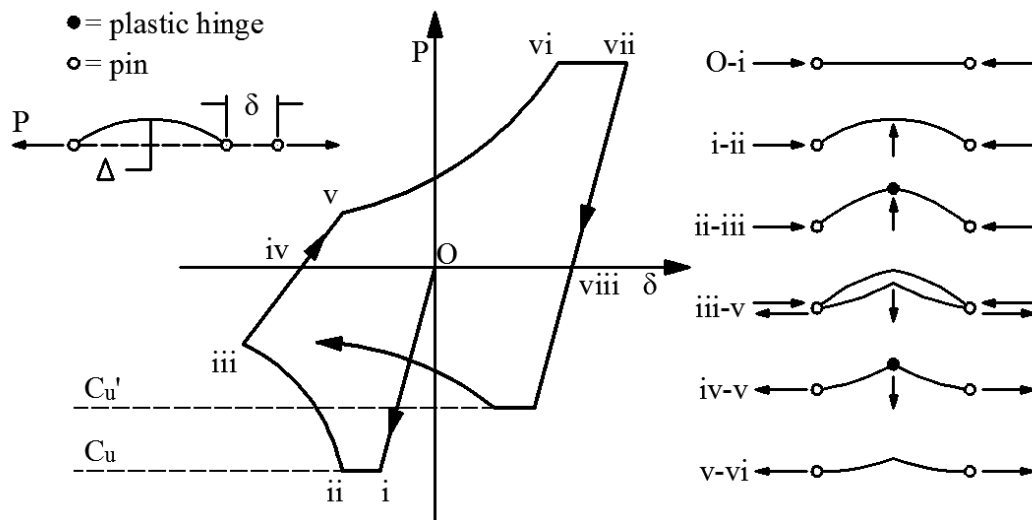


Figure 2.2 Idealized hysteretic behavior of a brace under cyclic axial loading (based on diagram found in Bruneau et al. [2011]).

Designs of vintage braced frames typically did not account for the post-buckling brace response. Brace members were designed based on a static elastic analysis under reduced forces derived from the procedure outlined in Section 2.2.1. Bracing members were then proportioned on the basis of allowable stress design. The surrounding elements were designed under similar prescribed force demands. These demands did not account for capacity-based design principles or the expected force re-distributions resulting from brace buckling. In CBFs, the inelastic behavior of the braces often governs the inelastic behavior of the system. Moreover, force re-distributions that occur upon brace buckling cannot be captured by an elastic analysis. Thus, vintage CBFs may exhibit inadequate brace hysteretic behavior. Surrounding elements may also be insufficiently designed to develop re-distributed demands resulting from brace buckling.

2.2.2.1 Slenderness Ratio

Brace slenderness plays a dominant role in the shape of the brace hysteretic loop and has significant impact on the energy-dissipation capacity of the bracing member. As shown in Figure 2.2, i-ii represents the elastic buckling region of the brace hysteretic loop. With increasing slenderness, this plateau region lengthens and buckling capacity decreases. For stocky braces, the opposite is true, and line i-ii may be absent in the hysteretic loop in the case of inelastic buckling. Herein, braces with $kl/r < 60$ are considered stocky while braces with $kl/r > 120$ are considered slender. Braces in between these limits are considered intermediately slender.

The hysteretic response of stocky braces is considered “full” or “stable” and is associated with larger energy-dissipation capacity compared to that of slender braces. In comparison, slender braces have a smaller buckling capacity and a pinched hysteretic response. If slender enough ($kl/r > 300$), slender braces have minimal compression capacity, resulting in tension-only brace behavior. Many researchers in the early 1980s preferred stocky braces to slender braces because of their similar yielding and buckling strengths and larger energy-dissipation capacity [Black et al. 1980; Ghanaat 1980; Aoyama 1981; and Nordenson 1984]. The limited compression capacities in slender braces also results in accumulated residual elongation when the brace is stretched in tension and is not shortened as much in compression during cycles of inelastic loading. This behavior has resulted in restrictions on maximum brace slenderness. Modern seismic provisions often restrict slenderness to the stocky-to-intermediate slenderness range.

Though stocky braces tend to dissipate more energy, stocky braces can exhibit a shorter fatigue life when compared to slender braces. Under similar story drift demands, stocky braces require larger plastic rotations and strains at the plastic-hinge region to achieve similar elongation and shortening in slender braces. This increases localized demands in the plastic-hinge region, potentially resulting in a shortened fatigue life. This behavior led some researchers in the early 1980s to prefer slender to stocky braces [Shepard 1973; Jain et al. 1978]. A more recent study done by Tremblay [2002] hypothesized that a stockier brace could cause earlier fracture in stockier braces compared to slender braces. The study proposed that a minimum, as well as a maximum, slenderness ratio should be considered for stocky braces.

Table 2.2 lists the historic trend in brace slenderness limits in U.S. building codes. Modern seismic provisions tend to limit slenderness to the stocky to intermediate range [SEAONC 1985]. In contrast, the 1985 UBC recognized the limited ductility of slender bracing elements through:

1. An increase in the design base shear through a larger K factor ($K = 1$ for braced frames and $K = 0.67$ for ductile moment-resisting space frames);
2. A 1.25 factor increase on the prescribed axial force on each brace, and
3. A slenderness limit of 200.

While this slenderness limit of 200 is similar to current code requirements for SCBF systems, it is difficult to determine whether this slenderness limit would significantly impact brace inelastic behavior. Higher brace slenderness could increase fatigue life, but other factors—such as the width-to-thickness ratio of the brace section—could also impact fatigue. As such, deficiencies in the brace response due to slenderness alone is inconclusive.

Table 2.2 Historical trend for brace slenderness limits.

Building code	kl/r limit	
1979–1985 UBC	200 ³	
1988 UBC	200	
1992 AISC 341	$720/\sqrt{F_y}$	
Braced frame type ¹	OCBF	SCBF
1997 AISC 341	$720/\sqrt{F_y}$	$1000/\sqrt{F_y}$
2002 AISC 341	$720/\sqrt{F_y}^2$	$1000/\sqrt{F_y}$
2005 AISC 341	$720/\sqrt{F_y}$	$680/\sqrt{F_y}$ or 200 ⁴
2010 AISC 341	$680/\sqrt{F_y}^5$	200

¹ Specific specifications for SCBFs and OCBFs did not appear until the 1997 AISC seismic provisions.

² Provisions for OCBFs were eliminated in the 2002 AISC seismic provisions, except what was previously required for low-rise or roof structures designed with an amplified seismic load of $\Omega_0 E$, where $\Omega_0 = 2$.

³ Specific slenderness limits were made for all compression elements and were not made specifically for bracing elements.

⁴ The 200 limit was permitted where columns were designed considering the maximum expected load transferred by the brace (considering the expected material strength of $R_y F_y$).

⁵ Only required for V or inverted-V (“chevron”) configurations.

2.2.2.2 Width-to-Thickness Ratio

Research on hollow steel tubes began in the late 1970s [Kahn and Hanson 1976] with small-scale tests on hollow rectangular sections. These tests closely matched the behavior of theoretical hysteretic loops and were associated with a relatively long fatigue life. Later studies, however, found that the presence of local buckling in large-scale steel members highly affects the fatigue life of hollow steel tubes [Gugerli and Goel 1982; Lee and Goel 1987; and Liu and Goel 1988]. High width-to-thickness ratios, b/t , associated with non-compact sections can lead to early local buckling and localized strains, causing earlier brace fracture compared to that of seismically compact sections.

2.2.2.2.1 Hollow Braces

Rectangular hollow sections, a common brace section in vintage as well as modern buildings, are especially susceptible to local buckling behavior. The wall of the compression flange of the rectangular tube buckles inward while the webs of the tube buckle outward, as can be seen in the hollow cross section in Figure 2.3 [Liu and Goel 1988]. As local buckling occurs, a concentration of local strains develops at the section corners. Small cracks are initiated at the corners, eventually propagating across the face of the tube wall. Upon later tension cycles, the brace will ultimately fracture as the crack spreads across the remainder of the section. With decreasing b/t (and thus increasing material thickness per length of wall), local buckling becomes less of a concern, and fatigue life generally increases.

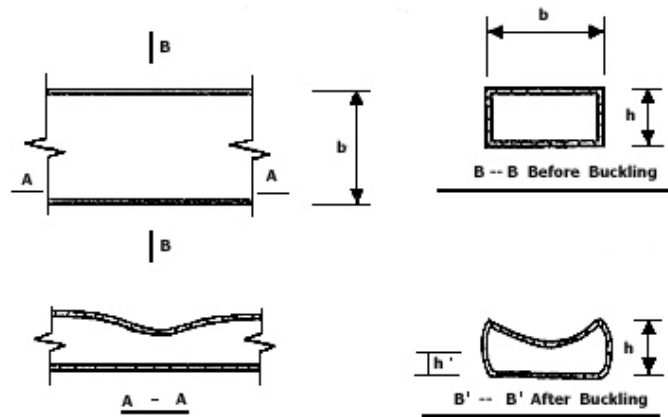


Figure 2.3 Local buckling in hollow cross sections [graphic courtesy of Liu and Goel 1988].

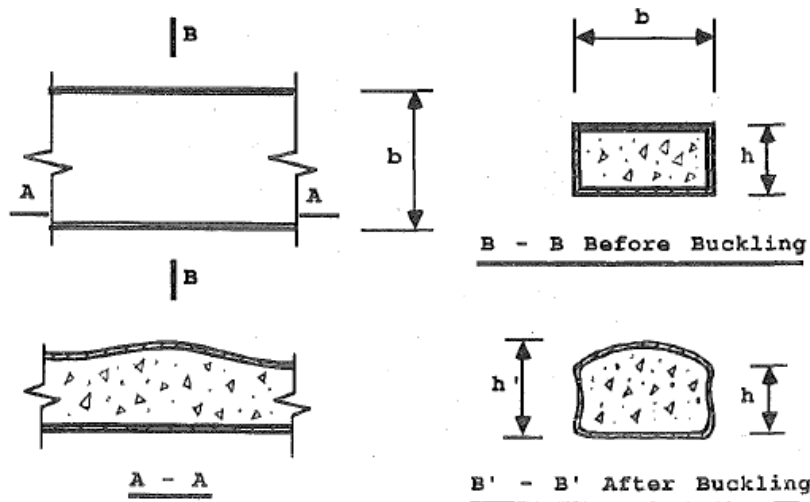


Figure 2.4 Local buckling in concrete-filled cross sections [graphic courtesy of Liu and Goel 1988].

Table 2.3 Historical trend for brace width-to-thickness limit.

Building Code		Width-to-thickness limit					
		Square HSS (b/t)		Round HSS (D/t)		Wide flange	
		Hollow	CFT ²	Hollow	CFT ²	Flange ($b/2t$)	Web (h/t_w)
1979–1985 UBC ¹		$\frac{238}{\sqrt{F_y}}$	N/A	$\frac{3300}{\sqrt{F_y}}$	N/A	$\frac{95}{\sqrt{F_y}}$	$\frac{253}{\sqrt{F_y}}$
1988 UBC		$\frac{238}{\sqrt{F_y}}$	N/A	$\frac{3300}{\sqrt{F_y}}$	N/A	$\frac{95}{\sqrt{F_y}}$	$\frac{253}{\sqrt{F_y}}$
1992 AISC		$\frac{110}{\sqrt{F_y}}$	N/A	$\frac{1300}{\sqrt{F_y}}$	N/A	$\frac{52}{\sqrt{F_y}}$	$\frac{P_u}{\phi P_y} \leq 0.125 \quad \frac{520}{\sqrt{F_y}} \left[1 - 1.54 \frac{P_u}{\phi P_y} \right]$ $\frac{P_u}{\phi P_y} > 0.125 \quad \frac{191}{\sqrt{F_y}} [2.33 - 1.54] \geq \frac{253}{\sqrt{F_y}}$
1997 AISC		$\frac{110}{\sqrt{F_y}}$	$\frac{240^3}{\sqrt{F_y}}$	$\frac{1300}{\sqrt{F_y}}$	$\frac{481^4}{\sqrt{F_y}}$	$\frac{52}{\sqrt{F_y}}$	Same as 1992
2002 AISC		$\frac{109}{\sqrt{F_y}}$	$\frac{240^3}{\sqrt{F_y}}$	$\frac{1276}{\sqrt{F_y}}$	$\frac{481^4}{\sqrt{F_y}}$	$\frac{52}{\sqrt{F_y}}$	$\frac{P_u}{\phi P_y} \leq 0.125 \quad \frac{535}{\sqrt{F_y}} \left[1 - 1.54 \frac{P_u}{\phi P_y} \right]$ $\frac{P_u}{\phi P_y} > 0.125 \quad \frac{191}{\sqrt{F_y}} \left[2.33 - \frac{P_u}{\phi P_y} \right]$
2005 AISC		$\frac{109}{\sqrt{F_y}}$	$\frac{240^3}{\sqrt{F_y}}$	$\frac{1276}{\sqrt{F_y}}$	$\frac{4350^4}{\sqrt{F_y}}$	$\frac{52}{\sqrt{F_y}}$	Same as 1992
2010 AISC	Moderately ductile members	$\frac{109}{\sqrt{F_y}}$	$\frac{384}{\sqrt{F_y}}$	$\frac{1276}{\sqrt{F_y}}$	$\frac{4350^4}{\sqrt{F_y}}$	$\frac{52}{\sqrt{F_y}}$	$\frac{P_u}{\phi P_y} \leq 0.125 \quad \frac{640}{\sqrt{F_y}} \left[1 - 2.75 \frac{P_u}{\phi P_y} \right]$ $\frac{P_u}{\phi P_y} > 0.125 \quad \frac{191}{\sqrt{F_y}} \left[2.33 - \frac{P_u}{\phi P_y} \right] \geq \frac{253}{\sqrt{F_y}}$
	Highly ductile members	$\frac{94}{\sqrt{F_y}}$	$\frac{238}{\sqrt{F_y}}$	$\frac{1108}{\sqrt{F_y}}$	$\frac{2204^4}{\sqrt{F_y}}$	$\frac{52}{\sqrt{F_y}}$	$\frac{P_u}{\phi P_y} \leq 0.125 \quad \frac{417}{\sqrt{F_y}} \left[1 - 0.93 \frac{P_u}{\phi P_y} \right]$ $\frac{P_u}{\phi P_y} > 0.125 \quad \frac{131}{\sqrt{F_y}} \left[2.93 - \frac{P_u}{\phi P_y} \right] \geq \frac{253}{\sqrt{F_y}}$

¹ Older specifications allowed for a reduction in the allowable stress for a compression element when the sections did not meet the specified width-to-thickness ratio requirements.

² CFT is defined as a concrete-filled tube.

³ Derived from the minimum wall thickness required for concrete-filled composite columns: $t \geq b\sqrt{F_y/2E}$.

⁴ Width-to-thickness ratios are presented for concrete-filled round HSS members from AISC 360-10 were deemed to be adequate according to the commentary of AISC 341-10.

The fatigue properties of the brace, as stated in Section 2.2.2.1, also depend on the global slenderness of the bracing member. Overall curvature of a brace loaded in compression tends to be smaller for braces with larger slenderness. Smaller curvatures correspond to smaller strains near the plastic hinge region at the middle of the bracing member [point (ii) in Figure 2.2]. Thus, similar b/t ratios tend to exhibit longer fatigue life with increasing kl/r [Liu and Goel 1988; Tremblay 2002]. As listed in Table 2.3, modern code requirements make no distinction between width-to-thickness limits for stocky and slender braces. In all cases of slenderness, modern width-to-thickness ratios are limited to that of highly ductile members.

Older code provisions, like the 1985 UBC, have significantly higher limits for brace width-to-thickness ratios; see Table 2.3. For example, AISC 341-10 requires rectangular section with a yield strength of 46 ksi to have a b/t ratio less than 13.8 to satisfy code requirements for seismic compactness. The 1985 UBC allows b/t ratios of 35.1 with the additional option of using a reduced allowable stress for higher b/t ratios. Thus, bracing members in older CBFs may be susceptible to severe local buckling, which could lead to earlier brace fracture compared to seismically compact bracing elements.

2.2.2.2 Concrete-Filled Tube (CFT) Braces

Researchers have studied the effect of filling hollow steel sections with concrete to delay or prevent local buckling in tubular bracing members [Lee and Goel 1987; Broderick et al. 2005; Fell 2008]. In these studies, the addition of concrete was found to delay and decrease the severity of local buckling. Unlike local buckling in hollow sections, the concrete in concrete-filled tubes (CFTs) forces local buckling to occur outward rather than inward; see Figure 2.4. This outward local buckling decreases the severity of the strain concentrations at the corners of the tube, potentially resulting in increased fatigue life. Crack initiation at the tube corners commences upon crushing of the inner concrete fill.

Past studies of CFT brace have found this degree of improvement to be variable. While the strength of the concrete has little effect on brace fatigue, the b/t and kl/r ratios of the external steel tube both affect the fracture life of CFT braces. As local b/t and global kl/r increase, the presence of the concrete has also been found to be less effective in delaying fracture [Liu and Goel 1988]. Width-to-thickness limits for hollow and CFTs are shown in Table 2.3. Although experimental tests for concrete-filled tube (CFT) braces regarding their benefit are often inconclusive, filling hollow braces with concrete allows an increased b/t limit of 35.1 for a yield strength of 46 ksi according to current code provisions (e.g. AISC 341 [2010]).

2.2.3 Story Mechanism Behavior

Braced frames designed in accordance with modern building codes (e.g., AISC [2010]) are expected to be able to withstand several large cycles of reversed loading into the inelastic range without significant reduction in strength or stiffness. However, numerical studies (e.g., Khatib et al. [1988]; Sabelli [2001]; Tremblay [2003]; Uriz and Mahin [2008]; Hines et al. [2009]; Chen and Mahin [2010]; and Lai and Mahin [2015]), experimental tests (e.g., Foutch et al. [1987] and Uang and Bertero [1986]), and post-earthquake observations (e.g., Rai and Goel [2003]) have indicated that concentrically braced frames tend to concentrate damage in a few “weak” stories in response to strong earthquake shaking.

An idealized diagram demonstrating both weak- and soft-story behavior is shown in Figure 2.5. The braces are oriented in a “chevron” configuration with equivalent braces in each story. It is assumed that the majority of the stiffness and strength of the story comes from the braces framed in that story (i.e., the contribution of column shear to the story shear is ignored).

In Figure 2.5(a), an inverted triangular load distribution is laterally applied to the frame assuming equal mass and stiffness at each story. If the braces in every story have similar compression capacities, C_n , the first-story brace will buckle first under the story shear demand, D_1 . After brace buckling, the strength of the first-story compression brace will decrease during subsequent inelastic cycles; see Section 2.2.2. If the capacity of the buckled brace decreases to 30% of its original compression capacity, C_n , and the force in the tension brace is less than or equal to its tension capacity, T_n , then the first story will remain relatively weaker than the upper stories where the braces did not buckle. This relative reduction in story strength will promote concentrations of demands in the first story. Similarly, the decrease in strength of the post-buckled brace can be associated with a decrease in story stiffness; see Figure 2.5(b). The smaller relative story stiffness in the first story will lead to greater concentrations of drift demands in the softened story.

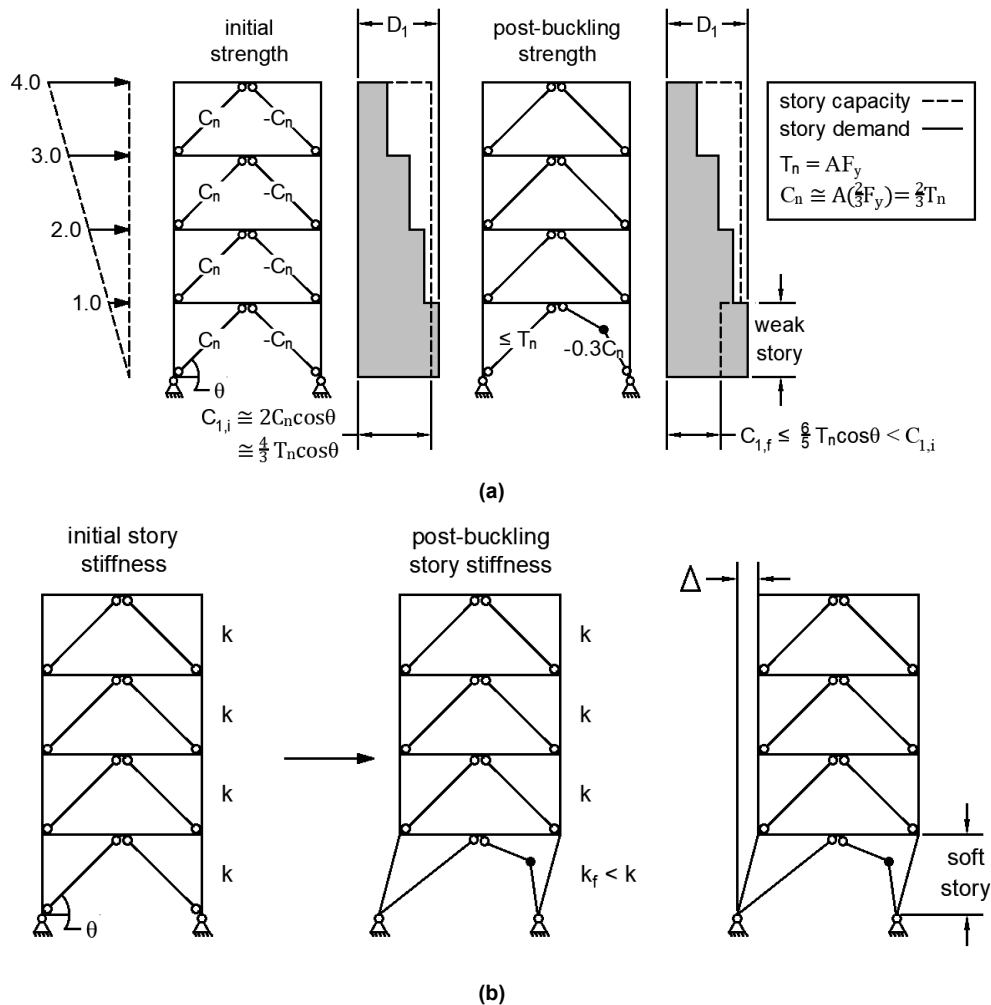


Figure 2.5 Idealized weak-story behavior (a) and soft-story behavior (b) of a braced frame with equivalent braces in each story.

Unless these demands can be re-distributed to other stories, this concentration of demands will lead to a story mechanism. While the extent of this phenomenon is dependent on a variety of factors (e.g., the size, slenderness, and configuration of the braces, the type of ground motion, and the number of stories), story mechanisms often arise because of the poor hysteretic response of the braces. These concentrations in demand trigger greater localized structural and nonstructural damage, can cause earlier element failure and significant residual displacements, and may lead to extensive or impractical repairs. The larger story drift demands can also influence P - Δ effects and further amplify the story drift under high gravity loads.

Vintage, as well as modern, braced frames are susceptible to story-mechanism behavior. Modern designs attempt to mitigate story mechanisms by specifying uniform demand-to-capacity ratios over the building height. Uniformity in demand-to-capacity ratios was not often considered in the design of older braced frames, and vintage CBFs may be especially vulnerable to story-mechanism behavior.

2.2.4 Weak Beam and the Concept of an Unbalanced Load

The post-buckling behavior of the braces affects the demands on the surrounding elements, especially in "chevron" configurations. The diagrams in Figure 2.6 show the development of an "unbalanced load" on the beam in V or inverted-V ("chevron") configurations. The tension capacity, T_n , is assumed approximately equal to the compression capacity, C_n , of the opposite brace.

An elastic free body diagram of the beam is shown on the left of Figure 2.6. In this diagram, the vertical components of the compression and tension brace are equal and opposite, and cancel when the vertical components are summed. The free body diagram of the beam after brace buckling is shown on the right of Figure 2.6. After one brace buckles and experiences strength degradation, the vertical components of the compression and tension brace force no longer cancel. The post-buckled compression component and potentially yielding and strain hardening tension component create an "unbalanced load" that tends to pull down on the beam.

Modern codes require the beam be designed for enough flexural capacity to remain elastic under the bending moments developed by this unbalanced load. This results in the "strong" beam plastic mechanism shown in the bottom right diagram of Figure 2.6. Strong beam mechanisms are the favored response in current building codes. In the case of CBFs with strong beams, the majority of the energy dissipation occurs through compression buckling and tension yielding of the braces. Strong beams also aid the tension brace in yielding after buckling occurs in the compression brace.

Prior to 1988, beams in "chevron" configurations were designed without consideration of an unbalanced load. The unbalanced load on the beam cannot be detected by traditional elastic analysis. As such, the beams in vintage CBFs were often designed as if the braces in the story below acted as a vertical support for tributary gravity loads. This caused beams in vintage braced frame to be relatively weaker compared to beams in modern braced frames. "Weak" beam plastic mechanism, like that shown in the bottom left diagram of Figure 2.6, can dissipate energy through plastic hinging in the beam. The occurrence of this "weak beam" phenomenon in multistory CBFs has been well demonstrated by Foutch et al. [1987], Fukuta et al. [1989], Khatib et al. [1988], Bradley et al. [2014], and Sen et al. [2016].

A strong beam mechanism utilizes brace buckling and yielding to dissipate energy. Some researchers have hypothesized that this may be a less capable form of energy dissipation compared to beam flexural yielding [e.g., Khatib et al. 1988]. Beams designed to carry the unbalanced load can also become unreasonably oversized and strengthened, impacting the capacity design of the surrounding columns. On the other hand, weak beam mechanisms lead to plastic hinge formation in the beam. This results in potentially large vertical deflections that may cause unwanted damage in the slab and floor diaphragm. Vertical deflections may also increase axial shortening in the braces, possibly leading to larger deformation demands in the bracing elements.

Table 2.4 Historical trend for the expected post-buckling strength of the braces.

Building code	Expected post-buckling brace compression strength	
	OCBF	SCBF
1979-1985 UBC	N/A	
1988 UBC	N/A	
1992 AISC 341	N/A	
Braced Frame Type ¹	OCBF	SCBF
1997 AISC 341	N/A	$0.3\phi_c C_n^{3,4}$
2002 AISC 341	N/A ²	$0.3\phi_c C_n^{3,4}$
2005 AISC 341	N/A	$0.3C_n^3$
2010 AISC 341	Note ⁵	$0.3 * \min \left\{ \begin{array}{l} R_y F_y A_g^{6,7} \\ 1.14 F_{cre} A_g \end{array} \right.$

N/A is defined as not-applicable as there were no provisions provided for the post-buckling strength of the brace.

¹ Specific specifications for SCBFs and OCBFs did not appear until the 1997 AISC seismic provisions.

² Provisions for OCBFs were eliminated in the 2002 AISC seismic provisions, except what was previously required for low-rise or roof structures designed with an amplified seismic load of $\Omega_0 E$, where $\Omega_0 = 2$.

³ Only required for V or inverted-V configurations.

⁴ $\phi_c = 0.85$ for 2002 and earlier editions.

⁵ Designed for amplified seismic load of $\Omega_0 E$, where $\Omega_0 = 2$.

⁶ Commentary states that two separate analyses are required in order to find the maximum demand on each member of the system: (1) all braces at maximum forces, (2) tension braces at maximum strength and compression braces at their low post-buckling strength.

⁷ F_{cre} is F_{cr} determined per AISC 360 Chapter E using expected yield stress $R_y F_y$, in lieu of F_y .

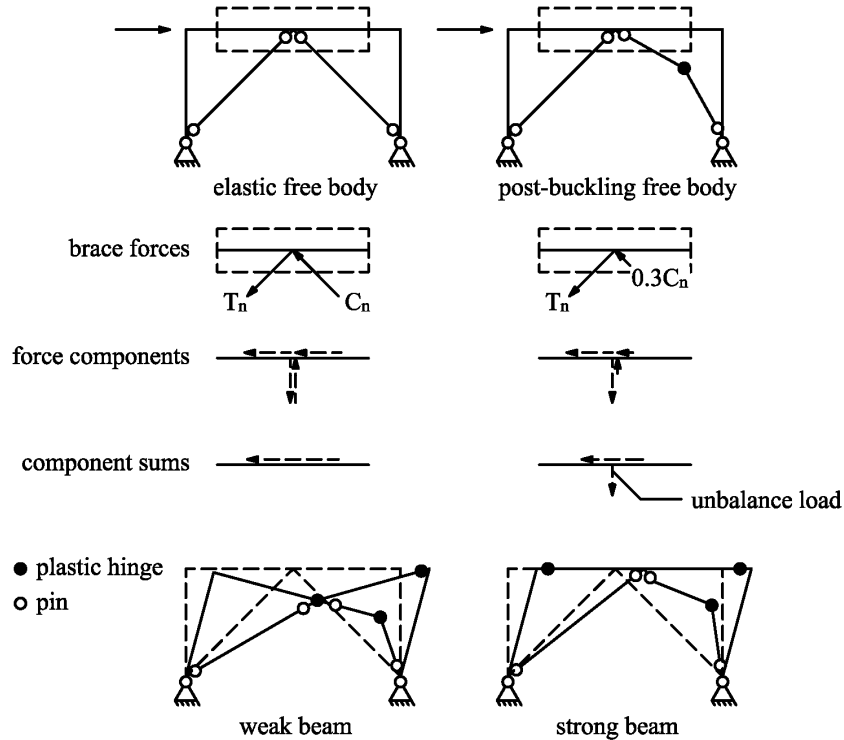


Figure 2.6 Diagram illustrating post-buckling strength degradation of the brace and the unbalanced load on the beam.

Table 2.4 shows the evolution of code requirements for the consideration of the post-buckled brace response and its impact on the surrounding frame elements. SEAONC began to discourage the use of K-braced frames, or “chevron” configurations, in the 1980s [SEAONC 1985]. The unbalanced load on the beam was initially addressed in the 1988 UBC through the following three design requirements:

- Braces must be designed for 1.5 times the prescribed forces
- Beams must be continuous between columns
- Inverted V bracing should not carry gravity loads

Explicit consideration of the effects of an “unbalanced load” on the beam was introduced in 1997 [AISC 1997], and more comprehensive “capacity design” requirements have been added in more recent provisions.

2.2.5 Connection Design

In current code provisions, connections are designed to develop the expected capacity of the members framing into them. These modern capacity principles for gusset connections were introduced in the 1992 AISC seismic provisions; see Table 2.5. Earlier provisions allowed the connections to be designed for a minimum of either the nominal tensile capacity of the brace or an increased load derived from the design base shear and the equivalent lateral force procedure. This often led to small, compact connections that could fail before the brace buckled in compression or yielded in tension; see Figure 2.7(a).

These vintage connections were commonly designed by a simplified force distribution scheme that uses the horizontal and vertical components of the brace force to design welds or bolts at the beam or column interface [Naeim 1989]. Welds often utilized non-notch tough welding material with little deformability, potentially leading to abrupt and brittle weld failures. Net section failure was initially introduced in AISC 1997. However, specific requirements for net-section reinforcement were not introduced until AISC 2002. As such, net-section failures could also be a potential failure mode in vintage CBFs.

Figure 2.7 compares a typical vintage connections to modern SCBF connections. Yield-lines in modern gusset designs account for the brace-end rotation associated with buckling. Yield-lines can be either linear [Astaneh-Asl 1982] or elliptical [Lehman et al. 2008]. Tapered SCBF connections can become large to account for the required yield-line, and too-conservative gusset plates have been found to increase the demand on the surrounding framing members. A balanced design procedure has been developed to create gusset plates that are strong enough to satisfy capacity-design principles, but not excessively strong to increase the demand on surrounding regions [Roeder et al. 2011].

Table 2.5 Historical trend for capacity design of the connection.

Building code	Required connection strength					
	Tension		Moment ³		Compression	
1979-1985 UBC	$\min \left\{ F_y A_g^{7,8} \right.$		1.25P ^{7,8}		N/A	
1988 UBC	$\left. \min \left\{ A_g F_y^7 \right. \right.$		3/8 R _w P ⁷		N/A	
1992 AISC 341	A _g F _y		M _n		N/A	
Braced frame type ¹	OCBF	SCBF	OCBF	SCBF	OCBF	SCBF
1997 AISC 341	A _g R _y F _y	A _g R _y F _y	1.1 R _y M _p	1.1 R _y M _p	GS ⁵	GS ⁵
2002 AISC 341	A _g R _y F _y	A _g R _y F _y	N/A ²	1.1 R _y M _p	N/A ²	GS ⁵
2005 AISC 341	A _g R _y F _y	A _g R _y F _y	N/A	1.1 R _y M _p	N/A	1.1 R _y P _n
2010 AISC 341	Note ⁴	A _g R _y F _y	Note ⁴	1.1 R _y M _p	Note ⁴	1.1 * min $\left\{ \begin{array}{l} R_y F_y A_g^6 \\ 1.14 F_{cre} A_g \end{array} \right.$

¹ Specific specifications for SCBFs and OCBFs did not appear until the 1997 AISC seismic provisions.

² Provisions for OCBFs were eliminated in the 2002 AISC seismic provisions, except what was previously required for low-rise or roof structures designed with an amplified seismic load of Ω₀E, where Ω₀ = 2.

³ Except when brace connection can accommodate inelastic rotation associated with brace post-buckling deformations.

⁴ Designed for amplified seismic load of Ω₀E, where Ω₀ = 2.

⁵ Generic Statement: "The design of gusset plates shall include consideration of buckling.

⁶ F_{cre} is F_{cr} determined per AISC 360-10 Chapter E using expected yield stress R_yF_y, in lieu of F_y.

⁷ P is the maximum demand delivered to the connection as calculated from the equivalent lateral force procedure from the design base shear.

⁸ Does not allow for 1/3 increase in member stress allowed in ASD design.

Vintage gusset connections lack yield-lines, potentially inhibiting the brace from rotating out-of-plane and leading to increased connection and brace demands. Compact gusset plates without yield-lines may also cause plastic hinging to form in other regions, like the ends of the brace or at the beam and column. The lack of capacity-design principles may lead to gusset plate designs with inadequate strength, possibly leading to connection failures prior to yielding or buckling of the bracing element.

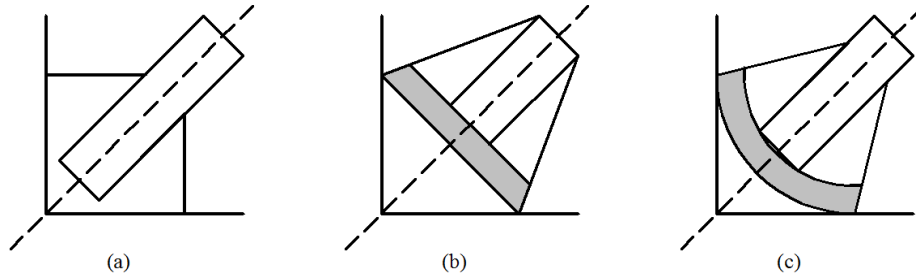


Figure 2.7 Diagram of connection types: (a) vintage CBF gusset plate without yield-line; (b) SCBF gusset plate with linear yield-line; and (c) SCBF gusset plate with elliptical yield-line.

2.2.6 Summary

The deficiencies in vintage braced frames designed prior to the 1988 UBC can be categorized as follows:

1. Smaller design forces leading to members with inadequate strength. This could be alleviated in designed where elements were conservatively designed for these forces.
2. Large width-to-thickness limits that could lead to severe local buckling and potentially brace fracture. This problem could be moderated with concrete-filled tube braces or braces with large global slenderness.
3. No consideration of the demand-to-capacity ratio of each story as it is related to the entire system, potentially leading to weak-story behavior.
4. Weak beams in “chevron” configurations that were not designed to remain elastic under demands developed from an unbalanced load. This could potentially change the damage mechanism to include beam yielding.
5. Inadequate gusset plate connections that may fail before the brace buckles in compression or yields in tension. Such connections did not utilize yield-lines to account for out-of-plane brace buckling, were not designed based on capacity-design principles, and may lack net-section reinforcement where that failure mode controls. These deficiencies may be exacerbated in connections that utilized non-notch tough welding material.

The large number of possible deficiencies and the deteriorating and potentially brittle behavior of vintage braced frames complicates quantifying their seismic response. The assessment of such structures is difficult since failures in a local component or connection may not result in an overall system failure. Moreover, the retrofit of an individual failure mode may shift failures to other modes. As such, vintage CBFs require holistic assessment of sub-assembly system behavior.

2.3 BRACED FRAME BEHAVIOR IN PAST EARTHQUAKES

The following section presents documented braced frame damage during past earthquakes. Careful evaluation of this damage could provide important insight into the dynamic behavior of vintage CBFs during an actual seismic event. A summary of the described earthquake damage in this section is provided in Table 2.6.

2.3.1 1971 San Fernando, California, Earthquake

While the majority of the damage after the magnitude 6.6 San Fernando earthquake was reported in reinforced-concrete structures, there were a few observed cases of brace buckling and rupture [Steinbrugge et al. 1971]. One case was of flat bar braces in a temporary wall in a mixed-use construction building. The other case was of buckling of steel double-angle X-bracing damage in a three-story metal skin building. The damage observed after the San Fernando earthquake provides an example brace buckling behavior of vintage braced frames during moderate ground shaking.

Table 2.6 Description of braced frame damage in past earthquakes.

Year	Location	Magnitude	Description of damage
1971	San Fernando (California, USA)	6.6	Buckling and fracture of bar and double angle braces.
1978	Miyagiken-Oki (Japan)	7.4	Buckling and fracture of bar and double angle braces. Premature connections failures.
1994	Northridge (California, USA)	7.7	Local buckling and fracture of bracing members. Premature connection failures. Deformation of beam. Uplift at column base. Weak-story behavior.
1995	Hyogo-ken Nanbu (Japan)	7.2	Local buckling and fracture of small and large section braces. Premature connection failures. Distortion of beam near connection region. Significant yielding of beam.

2.3.2 1978 Miyagi-ken Oki, Japan, Earthquake

The 1978 Miyagi-ken Oki Earthquake was a magnitude 7.4 event that occurred just outside Sendai City, Japan. The majority of the steel buildings were relatively new braced frames and were typical of design standards in Japan during that time, consisting of bar or double-angle braces with bolted gusset plate connections. The gusset connections were usually welded to the beams and columns. These braced frames were commonly found in long-span structures, such as factories, warehouses, or gymnasiums.

Two studies investigating damage following the earthquake noted that severe damage was largely confined to one- to two-story braced frame systems [Kato et al. 1980; Tanaka et al. 1980]. The studies categorized this damage into (1) premature connection failures and (2) local fracture of the brace components. The damage was concluded to be primarily due to the following:

1. Inadequate connection capacity causing premature connection failures that precluded yielding of the bracing members. Connection failures included failures at bolted connections due to inadequate shear strength of the fasteners or insufficient strength of the net effective area of the bolted regions. Poor workmanship in the welded regions further limited connection strength and the ability of the connection region to transfer forces from the braces to the surrounding structure. Fracture was also observed in the column-to-footing connection regions.
2. Insufficient regard to the inelastic strength of the braces, leading to their inadequate capacity and fracture. Reference was also made to unbalanced brace configurations, leading to a non-uniform demand-to-capacity ratio over the frame height that limited the strength of the entire structure to the capacity of its weakest brace component.

In response to the Miyagi-ken Oki Earthquake, in 1979 the Ministry of Construction in Japan recommended earthquake design lateral force be increased by a factor of 1.5 for braced frames and that connection forces be 1.2 times larger than the yield strength of the braces designed for those lateral forces.

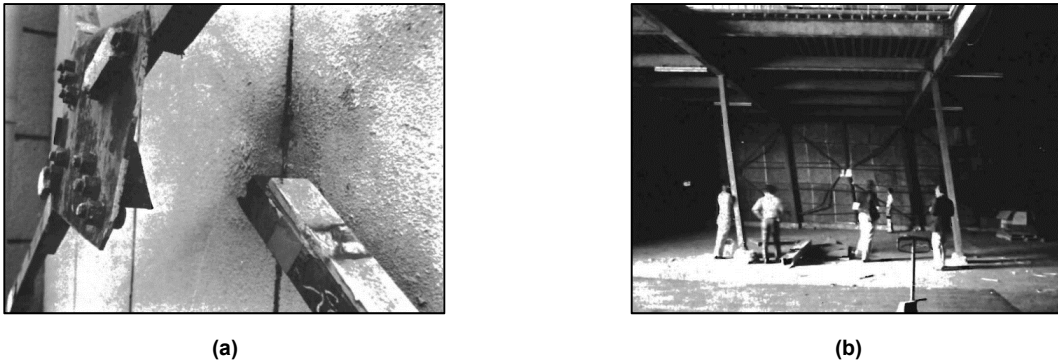


Figure 2.8 Photographed damage from the 1978 Miyagi-Ken Oki earthquake: (a) damaged steel frame furniture warehouse located on the outskirts of Sendai with rupture at bolt holes; and (b) Sendai Unyu Soko warehouse showing perimeter bracing with unbraced center bays [photographs courtesy of EERI 1978].

2.3.3 1994 Northridge, California, Earthquake

The damage observed after the 1994 Northridge earthquake highlighted a variety of unexpected damage states in steel structural systems. A meticulous study of documented braced frame damage can be found in Tremblay et al. [1995] and is summarized in Table 2.7. Emphasis herein is placed on those cases of unexpected failures; the reader is referred to that document to find more information of other damage cases.

In general, damage to braced frames associated with the 1994 Northridge earthquake can be classified as follows:

1. Severe local buckling and fracture of the braces: this damage mechanism was related to those braces designed with high width-to-thickness ratios leading to severe local buckling and brace fracture.

2. Premature connection failures: these connection failures were found at the brace-to-gusset welds and in some instances at the beam-to-column connections. It is unclear whether these failures were related to poor workmanship of the weld or inadequate weld strength.
3. Significant uplift in a number of braced frame structures leading to brittle failures of the baseplate connection region.
4. Weak-story behavior.

While there were no reported cases of structural collapse among braced frames, some cases did instigate alarm and raised questions of the braced frame's integrity under strong ground motions. For instance, a four-story irregular building with a concentrically "chevron" brace configuration suffered a variety of undesirable failure modes [Bonnevillle and Bartoletti 1996; Rai and Goel 2003; Kelly et al. 2000; and Krawinkler et al. 1996]. The building was constructed in 1986 according to the 1980 Los Angeles Building code (essentially equivalent to the 1985 UBC) and is typical of the vintage CBFs being investigated in this study.

The building was built on firm soil, and damage to the building was attributed to strong-motion shaking and not geotechnical settlement. Damage was essentially isolated to the second-story braces oriented in the north-south direction, indicative of weak-story behavior. Fracture occurred in the 12×12×3/8-in. square tube bracing members. It is assumed that this fracture was due to severe local buckling. The braces had high width-to-thickness ratios of 32, which are much larger than current code provisions for ductile braced frames; see Figure 2.9(a) and (e).

Table 2.7 Summary of braced frame damage during the 1994 Northridge earthquake [Tremblay et al. 1995].

Structure	Type	Structural damage
Two-story First Interstate Bank Building at Northridge	CBF	Buckling of brace connecting plates; possible yielding of anchor bolts
Four-story Student Union Building, California State University at Northridge	CBF	No structural damage observed
Four-story Oviatt Library, California State University at Northridge	CBF	Failure of brace connecting plates; cracking of baseplates; yielding of anchor bolts
Three-story building under construction in Van Nuys	CBF, MRF	Buckling of bracing members
Four-story No. 2 Brewhouse, Anheiser-Busch Inc.	CBF	Buckling of bracing members
Department of Water and Power San Fernando Generating Station	CBF	No structural damage observed
Four-story commercial office structure	CBF	Buckling and failure of bracing members; failures of brace welded connections; failure of beam-column moment connections
Two-story fashion plaza	CBF, MRF	Cracking in floor slab; buckling of bracing members

Connection failures were also observed at the brace-to-gusset slotted welded connections. It is unclear whether this connection failure was caused by insufficient fusion of the welds or the design strength of the welds; see Figure 2.9(b) and (c). There was also an instance of fracture of a full penetration weld at one of the collector moment beam-to-column connections. While the majority of the building remained plumb following the earthquake, the second-story story drift was measured to be approximately 0.2 in. The frame was retrofitted with new wide-flange braces as a zipper frame [Khatib et al. 1988].

Tremblay et al.'s [1995] report highlights other case studies associated with braced frame damage. The First Interstate Bank Building was a two-story steel frame built in the mid-1970s and retrofitted in 1991. The building had double angle X-bracing oriented in the north-south direction. While there was no evidence of inelastic behavior in the braces, severe buckling and bending was noted at the connecting plate where the two braces met in the X-bracing configuration. Evidence of uplift was also noted at the base of the building.

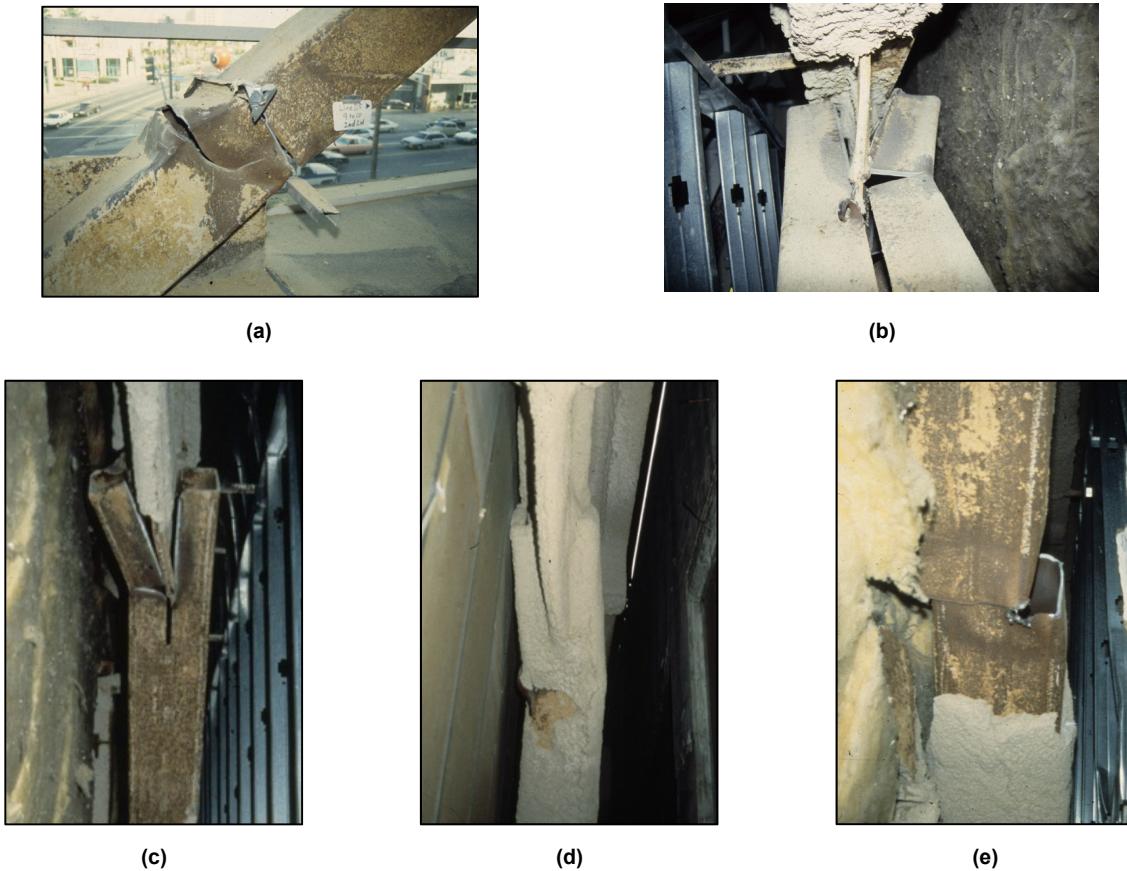


Figure 2.9 Photographs of a four-story commercial building damage after the 1994 Northridge earthquake: (a) fracture of brace near connection region; (b) and (c) failure of slotted brace to gusset weld; (d) local buckling of brace near connection region; and (e) fracture at midpoint of brace [photographs courtesy of Bonneville and Bartoletti 1996].

Damage was also noted in a three-story building under construction with a single bay “chevron” configuration with back-to-back channel braces. These braces exhibited significant out-of-plane buckling, but no sign of plastic hinging was noted at the beams. Another example of unexpected damage was documented for the Oviatt Library built in 1991. While the majority of the Oviatt Library remained undamaged, close observation revealed failures in the welded gusset-to-baseplate connection and fracture in the 3-in.-thick baseplates [WJE 1998]. Finally, a two-story fashion plaza representative of an existing steel frame constructed circa-1980 remained relatively undamaged but showed nominal global buckling in an exposed wide-flange brace at the rear of the structure.

2.3.4 1995 Hyogo-ken Nanbu, Japan, Earthquake

A detailed report of the damage following the magnitude 6.8 Hyogo-ken Nanbu earthquake outside of Kobe, Japan, can be found in a study performed by Tremblay et al. [1996], which compares the 1995 Canadian and Japanese code provisions; see Table 2.8 for examples of the damage sustained by braced frames in this earthquake. The study summarizes the results of an extensive survey of 988 damaged modern steel buildings compiled by the Architectural Institute of Japan [1995]. Of these 988 buildings, 168 or 17% were classified as braced frames; 46% of these braced frames were classified as severely damaged, and 6% of these braced frames were classified as collapsed; see Table 2.9 for the distribution of the type of braced frame configuration and the damage associated with that configuration. The damage state categories used in the survey are defined as follows:

Minor: No damage to beams and columns. Minor buckling of rod or flat bar tension-only braces. No permanent residual deformations.

Moderate: Buckling and rupture of bracing members. Yielding of surrounding columns and beams. Small residual deformations (less than 1%).

Severe: Serious damage to the surrounding columns, beams, and connections. Significant residual drifts that would be difficult to repair.

Collapse: Collapse of a story or the entire building.

X-bracing constituted 100% of the braced frame collapse states. Chevron configurations were documented as behaving considerably better. Note that X-bracing configurations most likely used tension-only bracing members with very slender bracing elements. The survey also categorized structural damage by brace section; see Table 2.10. Though not explicitly quantified in the survey, if smaller brace sections are associated with older braced frame designs, a correlation exists between the section type and the age of the building. Note that connections were usually bolted connections. In the case of a connection of a brace to the center of a beam, the connection was often designed as a moment connection.

Based on Tremblay et al.’s report [1996] and the survey performed by AIJ [1995], damage to steel braced frames during the Hyogo-Ken Nanbu earthquake can be generalized as follows:

1. Premature connections failures: this includes buckling of the gusset plates in compression, rupture of the gusset plates in tension, and failures at both bolted and welded connection interfaces.

2. Brace member failures either due to severe local buckling or brace fracture in tension.
3. Significant yielding and local buckling of the beam at the brace-to-beam connection region.
4. Brittle rupture at the column-to-baseplate interface.

The report by Tremblay et al. summarized specific case studies where damage to braced frame buildings was severe. One of these case studies was of a seven-story braced frame in downtown Kobe with wide-flange (or H-shaped) braces; see Figure 2.10. The braces met the ductile width-to-thickness ratios and slenderness ratios of 32 from the 1994 Canadian Standard Association for the design of steel structures. The braces exhibited (1) fracture at the midpoint of the braces; (2) fracture of the bolted brace-to-gusset connection at the net section area; (3) fracture at the welds of the gusset to frame interface; and (4) significant yielding of beam at the brace-to-beam moment connections. In the case of the connection failures, it was shown that the brace connection could not adequately develop the full yielding capacity of the braces.

Observations from a four-story chevron braced parking structure revealed cases of gusset plate tensile fracture after the gusset plates buckled out-of-plane when the brace was in compression. Another five-story X-braced parking structure with square-tube braces experienced the following damage: (1) fractured braces; (2) local buckling at the brace ends; (3) failures of the bolt fasteners in the connection region; and (4) distortions of the beam at the bracing connections; see Figure 2.11. Several cases of notable buckling and brittle fracture of the column at the baseplate were also noted in a number of damaged buildings.

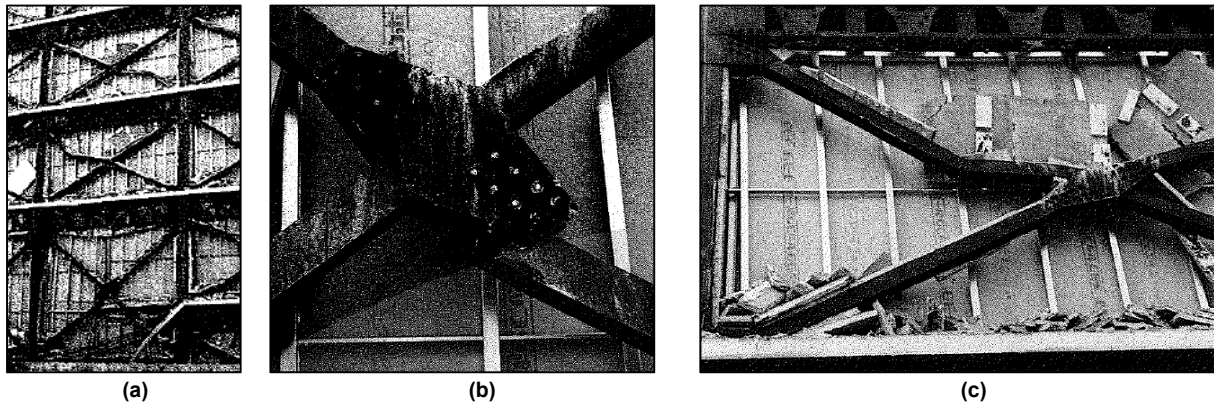


Figure 2.10 Photographs of damage to seven-story braced frame structure under the Hyogo-ken-Nanbu earthquake: (a) overall view; (b) brace fracture at net section area of bolted region; and (c) fracture of bracing member [photographs courtesy of Tremblay et al. 1996].

Table 2.8 Examples of braced frame damage from the Hyogo-ken-Nanbu earthquake [Tremblay et al. 1996].

Structure	Type	Structural damage
Seven-story braced frame building	CBF	Fracture of braces; failures of bolted connections; failures of welded connections; severe distortions of beam
Four-story chevron braced parking structure	CBF	Fracture of gusset plates
Five-story X-braced parking structure	CBF	Fracture of braces; local buckling at brace ends; failures of bolted connections; severe distortions of beam

Table 2.9 Braced frame configurations and damage states from the Hyogo-ken-Nanbu earthquake [AIJ 1995].

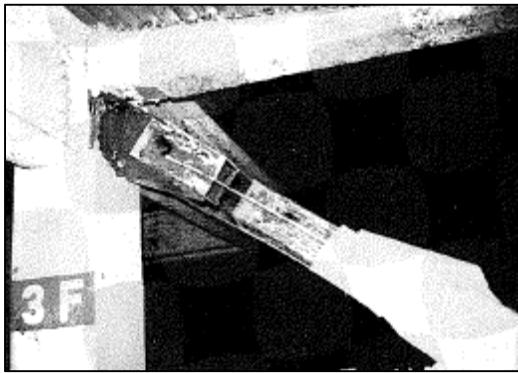
Bracing configuration	Damage state				Total damaged
	Collapse	Severe	Moderate	Minor	
M-B1	8	63	45	18	134
X-Bracing	8	59	39	15	121
Chevron-bracing	0	0	4	1	5
B-B2	3	15	11	5	34
X-bracing	2	11	6	4	23
Chevron-bracing	0	3	4	1	8
X/Chevron-bracing	0	0	1	0	1
Total	11	78	56	23	168

¹ M-B: Braced framing in one direction and moment framing in opposite direction.

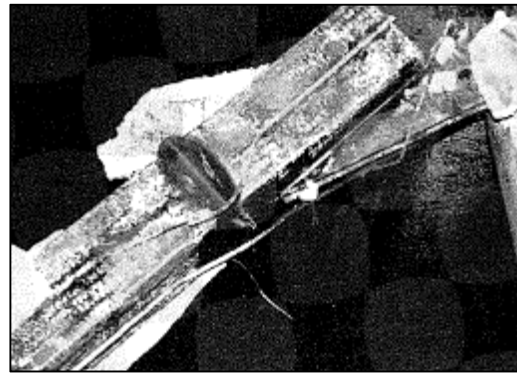
² B-B: Braced framing in both directions.

Table 2.10 Brace sections and damage states from the Hyogo-ken-Nanbu earthquake [AIJ 1995].

Brace Section	Damage State				Total Damaged
	Collapse	Severe	Moderate	Minor	
Rods	9	37	20	11	77
Angles	4	18	19	3	44
Flat bars	1	25	13	5	44
Sub-total (small braces)	14	80	52	19	165
Round tubes	0	7	22	13	42
Wide-flange	0	5	3	0	8
Square tubes	0	0	4	2	6
Channels	0	2	2	0	4
Sub-total (larger braces)	0	14	31	15	60
Unknown	15	47	51	114	227
Total	29	141	134	148	452



(a)



(b)



(c)



(d)



(e)



(f)

Figure 2.11 Photographs of damage to five-story braced frame structure under the Hyogo-ken-Nanbu earthquake: (a) rupture of square tube brace; (b) local buckling of square tube brace; (c) out-of-plane buckling of gusset plate; (d) severe beam distortion of beam with out-of-plane buckling of gusset plate; (e) fracture of welded gusset to column interface; and (f) failure of bolted gusset to column interface [photographs courtesy of Tremblay et al. 1996].

2.3.5 Summary of Braced Frame Behavior in Past Earthquakes

Damage during past earthquakes have shown that concentrically braced frames, especially vintage braced frames, can be susceptible to damage under strong ground motions. A summary of the damage can be listed as follows:

- Connection failures
- Brace local buckling and fracture
- Damage to surrounding elements outside the braces
- Weak-story behavior

Connection failures were observed during several earthquake events. These connection failures often resulted from inadequate strength in the design of the connection region. This lack of strength led to connections that were unable to develop full strength of the connecting braces.

Severe local buckling was observed in a number of vintage braced frames. In some instances, local buckling led to brace fracture. This local buckling did not always occur at the midpoint of the brace and was frequently observed at the brace ends near the connection region. Out-of-plane buckling of the braces also caused damage to surrounding nonstructural elements; e.g., cladding and wall partitions.

Yielding, and in some instances failure, was also noted in the elements surrounding the bracing members. This includes cracks in the floor diaphragms, failures in the connection regions, torsional deformations of the beams, and tensile fracture of anchor bolts or baseplates. While it is hypothesized that uplift and rocking at the foundation may have its own energy dissipative effects, this behavior will not be studied in this literature review; the reader is referred to other sources [Filiatrault et al. 1992].

Any failure along the lateral load path can reduce a CBF's ability to resist seismic demands. One important example of this behavior can be seen in the weak-story mechanism of the four-story commercial building during the 1994 Northridge earthquake [Bonneville and Bartoletti 1996]. In this building, damage was severe in the second-story, and the remaining structure exhibited minor damage, indicative of weak second-story behavior.

3 Specimen Design and Construction

3.1 INTRODUCTION

Chapter 2 illustrated the variety of potential deficiencies in vintage CBF systems. Unlike the SCBF, which has prescribed connection and member details, vintage CBFs were not typically designed with ductile details or consideration of capacity-design principles. As such, vintage CBFs typically do not have a clear hierarchy of damage states and can be susceptible to interdependent failures in the braces, connections, and beams. Vintage CBF designs are also variable, making the hierarchy and variety of damage uncertain as their design could change dramatically from building to building. The large number of possible deficiencies and the localized, deteriorating, and potentially brittle behavior of vintage braced frames makes their behavior difficult to quantify without the use of computationally expensive continuum models. Even then, these models must be verified by experimental tests to ensure that they properly capture vintage CBF behavior.

Vintage CBFs require a holistic study to evaluate the variety of interrelated inadequacies. However, little data is available for sub-assembly experiments of vintage braced frames. Thus, this study conducted three full-scale planar experiments to study the behavior and the hierarchy of damage of vintage CBFs.

3.2 TEST SPECIMENS

An experimental study assessing the vulnerability of vintage CBF systems was undertaken to achieve the following: (1) gain an understanding of the hierarchy of damage and failures in vintage CBF systems; (2) holistically assess the relationship between the component members, connections, and entire frame; and (3) evaluate the behavior of a potential retrofit “strongback” (SB) strategy under quasi-static cyclic loading conditions. As such, three test types were selected for the experimental study: a baseline vintage CBF test (Section 3.2.1), a vintage CBF upgrade with CFT braces and net section details (Section 3.2.2), and an extensive SB retrofit (Section 3.2.3); see Table 3.1 for a summary of all three tests. Example calculations can be found in Appendix E (electronic appendix), and shop drawings of the test specimens can be found in Appendix F (electronic appendix).

Table 3.1 Summary of experimental test specimens.

Specimen name	Description
NCBF-B-1	Baseline vintage CBF specimen
NCBF-B-2	NCBF-B-1 upgrade: (i) CFT braces; (ii) Net section reinforcement
NCBF-B-3SB	CBF retrofit: SB system

3.2.1 NCBF-B-1: Initial Specimen Design

The first test specimen, designated NCBF-B-1, consisted of a one-bay two-story concentrically braced frame designed and detailed in compliance with the UBC [1985] and the AISC ASD-78 *Specification for the Design, Fabrication and Erection of Structural Steel Buildings* [1978]. The braces were chosen to be oriented in an inverted-V, or “chevron,” configuration, reflecting a common configuration in vintage braced frame construction documents. The UW surveyed twelve vintage braced frames designed during the 1980s, of which 70% consisted of chevron configurations [Sloat 2014]. The chevron configuration also emphasized the effect of a vertical unbalanced load on the beam, reflecting a potential vulnerability in vintage braced frames; see Section 2.2.4.

The story heights and bay widths were constrained by the previously built test set-up [Lai and Mahin 2013], limited laboratory space, and the proportions of a previous test on unbraced steel frames that utilized the existing test set-up in the nees@berkeley laboratory [Dusicka et al. 2012–2013]. The frame consisted of irregular story heights of 10 ft-2 in. and 9 ft-2 in., beam centerline-to-centerline for the first and second floors, respectively, and a bay width of 20 ft-0 in., column centerline-to-centerline. Figure 3.1 shows connection details, member sizes, and material specifications; the view is to the north, looking south at the frame. Elements on the left side of the frame are to the nominal east side of the specimen, while those on the right side are to the nominal west side of the specimen. Views of the constructed specimen, prior to testing, are shown in Figure 3.2.

3.2.1.1 Brace Design

Member sizes were selected based on the maximum base shear capacity of the test set-up of 600 kips with the actuators acting in an inverted triangular distribution over the height of the frame; see Section 4.4. The braces were designed using allowable stress design for an estimated permitted brace stress based on the frame’s geometry, the test set-up maximum base shear, and an assumed overstrength factor, Ω_0 , of 2.0, similar to the overstrength factor in AISC 341-10 [2010] for OCBFs. Brace sizes were further designed with a 1.33 increase in allowable stress. The brace size for the first story was selected to be the same section as the baseline NCBF-INV-1 test specimen designed and tested by the UW [Sen et al. 2016].

Brace properties and local and global slenderness limits are shown in Table 3.2. Brace slenderness (kl/r) ratios were about 50 for both stories and are representative of stocky braces; see Section 2.2.2.1. This global slenderness is less than the maximum permitted for pre-1988 CFBs ($kl/r < 200$) [ICBO 1985] or current provisions for new CBFs [AISC 2010]. As shown in

Table, 3.2, brace width-to-thickness (b/t) ratios are about 30 and representative of non-seismically compact sections (per length of section wall). Although these values satisfy the limits imposed by the 1985 UBC, they are more than twice the current limit for SCBFs; see Section 2.2.2.2.

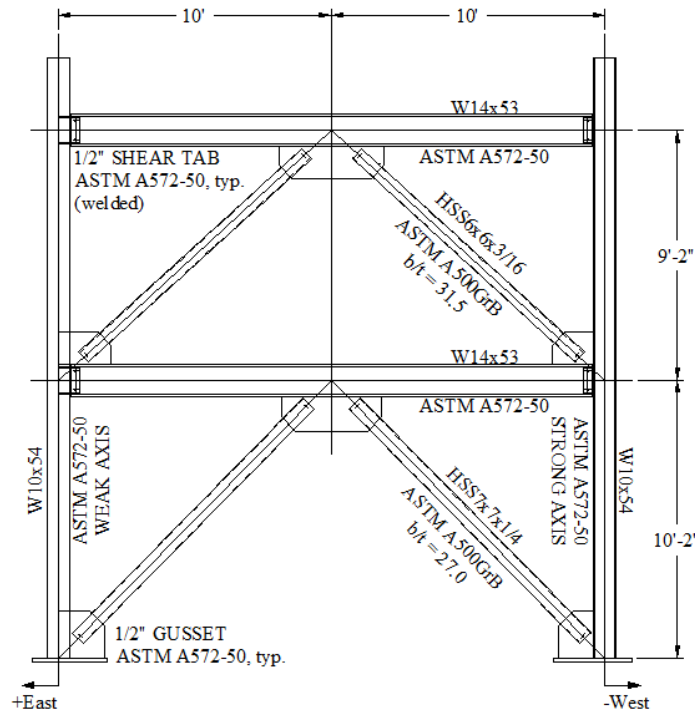


Figure 3.1 Test specimen schematic with dimensions, materials, and member sizes: NCBF-B-1.

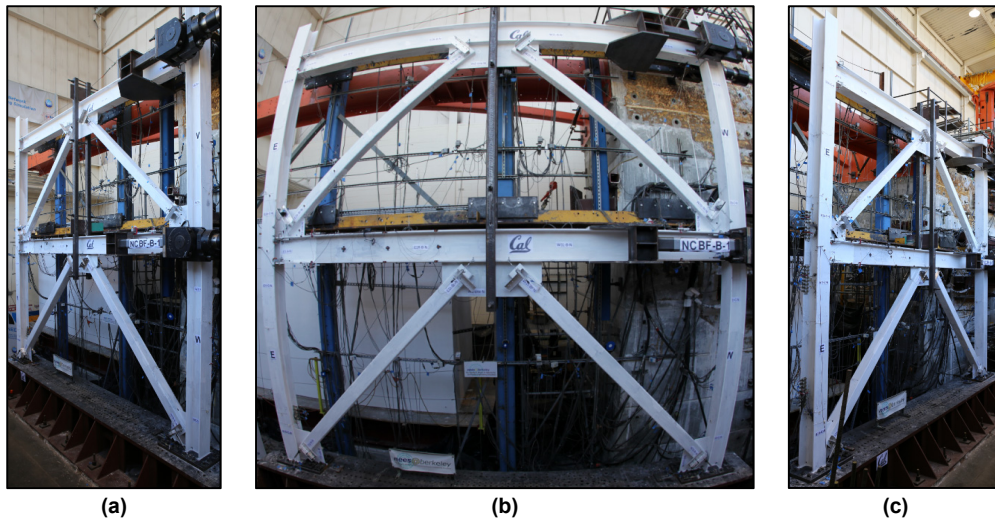


Figure 3.2 Overall views from north side of NCBF-B-1 before test: (a) west view; (b) center fisheye; and (c) east view.

Table 3.2 Brace properties of NCBF-B-1.

Member	Section	Cross-sectional area (in. ²)	Width-to-thickness ratio (b/t)			Approximate slenderness ratio (k/l) ¹
			Design	2010 limit ²	1988 limit ³	
First-story brace	HSS7x7x1/4	6.17	27.0	13.8	35.1	52.5
Second-story brace	HSS6x6x3/16	3.98	31.5	13.8	35.1	56.0

¹ $k=1.0$ and brace length, l , is the brace length from the shop drawings.

² Limits according to AISC 341-10 [2010].

³ Limits according to UBC [1985, 1988]. . A reduction in allowable stress was allowed if sections did not meet this limit.

3.2.1.2 Column Design

Columns were designed following the same basic assumptions as the braces. A survey done by the UW on twelve existing vulnerable braced frames designed during the 1980s found that half of the frames surveyed had columns oriented in weak-axis bending [Sloat 2014; Bonneville and Bartoletti 1996]. Both vintage code provisions and current design codes have no requirements for whether columns should be oriented in strong- or weak-axis bending. While some studies have investigated gusset plate to weak-axis column connections [Gross and Cheok 1988; Brown 1988], few system-level experiments have incorporated weak-axis column orientations; i.e., McManus et al. [2013].

To explore the effect of column orientation on connection behavior, the east (left) column in Figure 3.1 was oriented in weak-axis bending, while the west (right) column was oriented in strong-axis bending. This allowed the test to make an immediate comparison between the strong- and weak-axis columns, while also representing asymmetrical column orientations in a corner bay. Additional gravity loads tributary to the columns were not considered in the design or testing. While the column web does satisfy current seismic requirements, the column flanges do not satisfy current width-to-thickness requirements for highly ductile sections [AISC 2010]. Similar tests on vulnerable braced frames performed by the UW at the NCREE laboratory in Taiwan utilized columns in strong-axis bending, offering a comparison between weak- and strong-axis behavior in columns [Sen et al. 2016].

3.2.1.3 Beam Design

Both beams were designed for the maximum axial load that could be delivered to the floors by the actuators of 400 kips at the roof and 200 kips on the first floor. The beams were designed to be non-composite, representative of a beam in a system with a weak diaphragm like wood decking. The tests performed by the UW utilized a concrete slab and offer a possible comparison of behavior under the presence of a concrete slab [Sen et al. 2016].

Because the beam was designed without consideration of an “unbalanced load,” it does not follow the “strong” beam principle used in modern CBF designs; see Section 2.2.4. The beams were designed assuming the braces below the beams did not exist [ICBO 1988]; hence, these beams are weaker in bending than those that would be found in contemporary CBFs.

The beams were laterally restrained as required by code at the columns and at their mid-span; see Figure 3.2. This minimal arrangement satisfies contemporary lateral bracing

requirements (AISC 341-10 [2010]). The beam sections used in the specimens satisfy current seismic provisions for moderately ductile sections (AISC 341-10 [2010]).

3.2.1.4 Connection Design

The connections of the vintage CBF system were designed according to the *Seismic Design Handbook* [Naeim 1989] using the vertical and horizontal component of the brace force to calculate the demands at the gusset-to-column and -beam interfaces. Welds were designed using a 1.25 increase in applied load without a 1.33 allowed increase in weld strength. None of the connection details considered the expected capacity of the braces. Gusset plates were designed without a yield-line to allow for out-of-plane buckling. The braces terminated with a 1-in. clearance to the adjacent column, resulting in compact, square gusset plates; see Section 2.2.5. The slotted connection between the HSS brace and gusset plate resulted in a reduced net section for a short region of the brace. Reinforcement was not provided at the net-section regions as it was not explicitly required by the 1985 UBC; current requirements would require reinforcement at these locations (AISC 341-10 [2010]). While the connection details for this test were designed with welds, connections used by the UW used a variety of bolted connection details [Hsiao et al 2011; Sen et al. 2016; and Johnson 2014].

Shear tabs were designed as welded to be compatible with the welds used for the gusset-to-column interface. Two bolts were added to the shear tabs for erection purposes. Comparatively, note that the UW utilized a common plate for the gusset-to-column and beam-to-column detail in some of their experimental tests [Hsiao et al 2011; Sen et al. 2016; and Johnson 2014]. The column to baseplate connection was designed with a CJP weld and was considered to be a fixed-base detail.

3.2.1.5 Erection and Fabrication

Beams and columns were delivered to the laboratory after shop assembly had been completed. The columns were erected first, followed by the beams, and finally the braces. All members were connected through erection bolts before being field welded *in situ* in the laboratory; see Figure 3.3.

The shop fabrication of the test specimen was performed by a professional contractor, and all welds were laid by certified welders. All welds were specified as notch tough (AWS-A5.20: E71-T8 self-shielded flux cored wire), as the fabricators and erectors were not able to procure weld consumables representative of construction practices in the 1970s and 1980s. Note that the use of notch-tough welding consumables may not reflect standard practice in the design of vintage connections, and non-notch tough welding material may behave much worse than the notch-tough welding material used for these tests. Tests performed by the UW with non-notch tough welding material indicated abrupt and brittle failures at the welded region [Hsiao et al. 2011; Sen et al. 2016; and Johnson 2014]. While vintage braced frames commonly used material with a yield strength of 36 ksi, standard modern materials were used for the beams, columns, braces, and connection plates, as detailed in Table 3.3.



(a)



(b)

Figure 3.3 Erection of NCBF-B-1: (a) parts after final shop fabrication; and (b) field welding after erection.

Table 3.3 Material properties of NCBF-B-1

Member	Section	Material	Yield stress, F_y (ksi)		Ultimate stress, F_u (ksi)	
			Mill cert. ⁴	Coupon test ¹	Mill cert. ⁴	Coupon test ¹
Column (weak axis)	W10x54	ASTM A572-50	56.0	60.3	76.0	75.9
Column (strong axis)						
Beams	W14x53	ASTM A572-50	54.0	56.5	71.0	71.0
First-story brace	HSS7x7x1/4	ASTM A500 Gr. B	55.8	51.7	69.7	67.7
Second-story brace	HSS6x6x3/16	ASTM A500 Gr. B	49.0	46.8	68.0	65.4
Gusset plate	PL1/2"	A572-50	67.0	66.9	84.8	82.5
Shear tabs	PL1/2"	A572-50	67.0	66.9	84.8	82.5
Base plate	PL2"	A572-50	52.5	- ²	77.0	- ²
Field weld consumables	CORESHIELD 8	AWS A5.20; E71T-8-D; ASME SFA 5.20 ³				

¹ Average of two tensile coupon tests performed according to ASTM E8.

² Coupon test not performed.

³ Notch tough welding material.

⁴ From mill certificates provided by GK Welding.

3.2.2 NCBF-B-2: Concrete-Filled Braced Frame

The premise of the second CBF test, designated NCBF-B-2, was to upgrade the NCBF-B-1 test frame to improve the behavior observed during the first baseline NCBF-B-1 test. The baseline test showed significant local buckling and fracture in the second-story braces. Buckling of the braces in the second story, followed by degradation of the brace strength and story-shear capacity in the second story, led to weak-story behavior. A more detailed discussion of the

results from the NCBF-B-1 test can be found in Chapter 6; the first test is addressed here to emphasize the development of the design for the second NCBF-B-2 upgrade.

The second-story braces in the first specimen fractured in the testing protocol. The test was ended before significant yielding or damage occurred elsewhere in the frame. The damaged second-story braces and gusset plates were replaced with the same sections and sizes as those used in the original test. The columns, beams, and first-story braces and gusset plates were re-used for the NCBF-B-2 test specimen. The second-story braces and gusset plates were removed and replaced with new braces and gusset plates with the same sections and sizes as those used in the original test.

Fracture of the braces was then addressed by filling all four braces with concrete. Additionally, the demand-to-capacity ratio for net-section fracture was calculated to be higher than other connection failure modes. The net-section region was considered vulnerable, so reinforcement was added at all four brace ends in order to mitigate an unwanted failure at the reduced section of the braces. The final bracing configuration in Figure 3.4 was similar to NCBF-B-1, as shown in Figures 3.1 and 3.2.

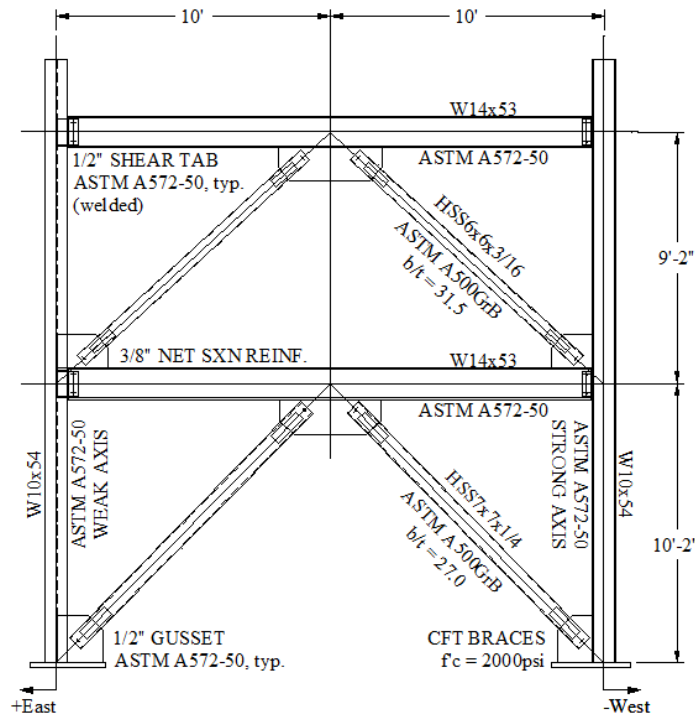


Figure 3.4 Test specimen schematic with dimensions, materials, and member sizes: NCBF-B-2.

3.2.2.1 Concrete-Filled Brace Design

The purpose of filling the braces with concrete was to delay local buckling. It was hypothesized that delaying local buckling would also result in delayed fracture, thereby addressing the short fatigue life observed in the braces during the first test. The composite strength of the CFT brace, however, was limited by the maximum lateral capacity of the test set-up of about 600 kips of base shear. Thus, low-strength concrete with a nominal compression capacity of 2000 psi was

used to limit over-strengthening the braces and overloading of the test set-up. Brace strength was calculated using current design procedures for composite, concrete-filled sections [AISC 360-10 2010]. With the added concrete-fill, the braces satisfied current b/t requirements for highly ductile members; see Table 3.4. The concrete filled the entire brace length in an effort to also reinforce the gusset-plate connections.

Another method of filling the braces while limiting the brace composite action was performed by the UW in their NCBF1-R5 member test [Sloat 2014]. Their test did not fill the braces from end to end. Upon loading, the steel section de-bonded from the inner concrete fill; allowing the use of nominal 4000 psi concrete strength while not overloading the test set-up.

Table 3.4 Brace properties of NCBF-2.

Member	Section	Cross-sectional area (in ²)	Width-to-thickness ratio (b/t)	
			Design	Limit ²
First-story brace	HSS7x7x1/4	6.17	27.0	35.2
Second-story brace	HSS6x6x3/16	3.98	31.5	35.2

¹ $k = 1.0$ and brace length, l , is the brace length from the shop drawings.

² Limits according to AISC 341-10 [2010]. Limit did not exist in the 1988 UBC.

3.2.2.2 Erection and Fabrication

Photographs of the demolition and subsequent repair of the second-story steel braces are shown in Figures 3.5, 3.6, and 3.7. The second-story braces were first removed from the original NCBF-B-1 specimen. Any leftover edges were ground down. New braces were then erected and field welded in the original position of the damaged gusset plates and braces. Finally, net-section reinforcement was added to the front, back, and ends of all the braces in both the first and second story.

After the steel had been repaired, the brace-end slot, erection holes, and the bottom of the braces were closed with wooden formwork that was clamped into place. Gaps were further filled with epoxy to keep the wet concrete encased in the brace. Photographs of the formwork can be found in Figure 3.8.

The low-strength concrete was made according to a mix design created by a local professional concrete contractor, Sugar City Building Materials Co. (the same company that mixed and delivered the concrete). Concrete was poured into the top end of all four braces using a concrete pump and a funnel. The braces were vibrated with rubber mallets to ensure the braces were filled from end-to-end. The first-story east brace was poured first, followed by the first-story west brace, and finally the second-story braces in the same order.

On the day of the pour, several concrete cylinders were made and two slump tests were performed before and after the pour. At 26 days, the concrete had an average compressive strength of 2200 psi and an average tensile strength of 310 psi, according to concrete cylindrical compression and splitting tensile tests as specified in ASTM C39 (ASTM 2011a) and C496 (ASTM 2011b) standards. Steel material properties can be found in Table 3.5. Concrete cylinder tests and the results from the slump tests can be found in Tables 3.6, 3.7, and 3.8.

Table 3.5 Material properties of NCBF-B-2.

Member	Section	Material	Yield stress, F_y (ksi)		Ultimate stress, F_u (ksi)	
			Mill cert. ⁴	Coupon test ¹	Mill cert. ⁴	Coupon test ¹
Column (weak axis)		Same as NCBF-B-1 ⁵ (Table 3.3)				
Column (strong axis)						
Beams						
First-story brace						
Gusset plate						
Shear tabs						
Base plate						
Second-story brace repair						
Second-story gusset plate repair	PL1/2"	A572-50	67.0	-. ²	76.0	-. ²
Net section reinforcement	PL3/8"	A572-50	70.0	-. ²	87.5	-. ²
Field weld consumables	CORESHIELD 8	AWS A5.20; E71T-8-D; ASME SFA 5.20 ³				

¹ Average of two tensile coupon tests performed according to ASTM E8.

² Coupon test not performed.

³ Notch tough welding material.

⁴ From mill certificates provided by GK Welding.

⁵ Re-used members from specimen NCBF-B-1.

Table 3.6 Compressive strength of cylindrical concrete specimens: NCBF-B-2 members, first- and second-story braces.

Day	Units	Cylinder number ¹			Average
		1	2	3	
7	(psi)	1015	1390	1365	1257
14	(psi)	1758	1592	1082	1675
26	(psi)	1970	1804	2762	2179

¹ Compressive strength determined according to ASTM C39.

Table 3.7 Split cylinder concrete test summary: NCBF-B-2 members, first- and second-story braces.

Day	Units	Cylinder number ¹			Average
		1	2	3	
26	(psi)	334	270	340	314

¹ Tensile strength determined according to ASTM C496

Table 3.8 Concrete slump test on day of concrete pour: NCBF-B-2.

Day	Units	Test no. ³	
		1 ¹	2 ²
1	(in.)	8	6.5

¹ Slump taken before initial pour

² Slump taken after pour was completed

³ Sequence of pour: first-story west brace, first-story east brace; and second-story west brace, second-story east brace.

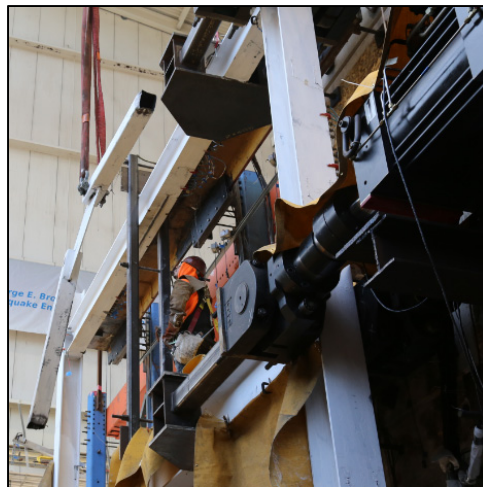


Figure 3.5 Demolition of NCBF-B-1 damaged second-story braces and gusset plates.

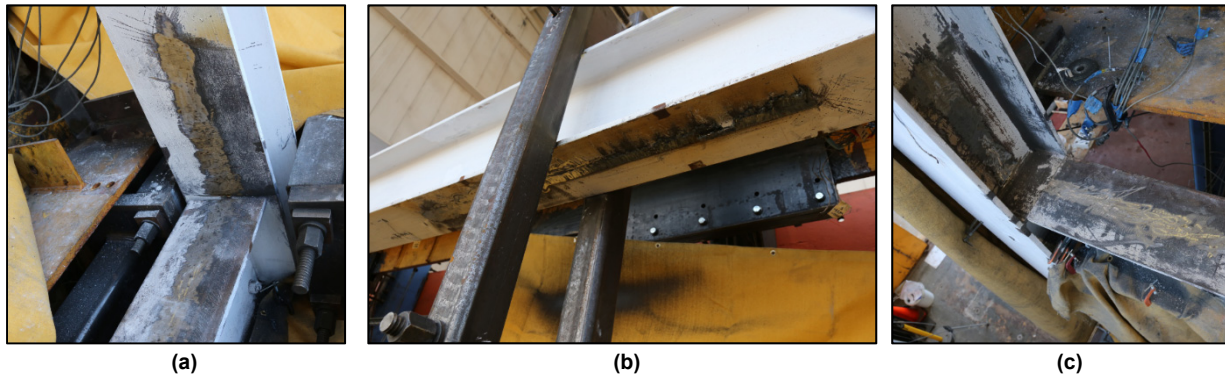


Figure 3.6 Final second-story demolition state: (a) west gusset plate removal; (b) middle gusset plate removal; and (c) east gusset plate removal.



Figure 3.7 Repair of second story of NCBF-B-1: (a) erection of braces; and (b) added net-section reinforcement.

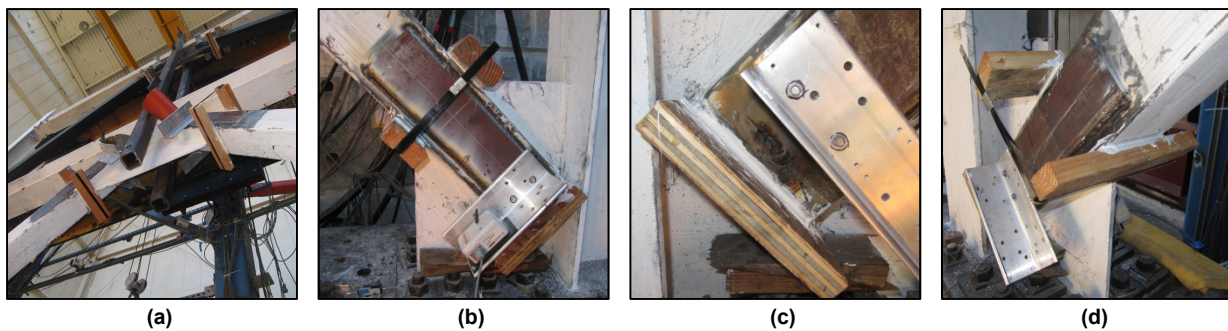


Figure 3.8 Formwork for concrete pour: (a) first-story middle formwork; (b) and (c) first-story east formwork; and (d) first-story west formwork.

3.2.3 NCBF-B-3SB: Strongback Retrofit

The first two specimens both exhibited weak-story behavior in the second and first story, respectively, limiting the drift capacity of both the baseline vintage CBF and the CFT upgrade (see Chapter 5). Thus, the third test specimen implemented a “strongback” (SB) retrofit scheme aimed at improving vintage CBF performance by reducing the weak-story tendency common in both modern and vintage braced frames. Story mechanisms arise because of the limited ability of the system to re-distribute the inelastic demand over the building’s height, concentrating it instead in a single story; see Section 2.2.3 and Figure 3.9(a). Thus, the SB system imposes a uniform drift distribution over the height of the frame to delay or prevent concentrations of demand in a few stories; see Figure 3.9(b).

The SB method examined in this study is a hybrid of the zipper frame [Khatib et al. 1988], tied eccentric braced frame [Popov et al. 1992], and elastic truss system [Merzouq and Tremblay 2006; Tremblay and Poncet 2005; Mar 2010; and Takeuchi et al. 2015] that utilizes a vertical steel “backbone” to mitigate weak-story behavior. The SB system described herein is a simple and economic modification of the conventional braced frame that utilizes two vertical trusses; see Figure 3.9(b). The “inelastic” truss is detailed to dissipate energy through either buckling and yielding in conventional braces or yielding in buckling-restrained braces. The opposite “elastic” truss, or strongback, is intended to control the distribution of story drifts and inelastic demands, thereby delaying or preventing weak-story behavior. The strongback is detailed to be pinned at its base and designed to remain essentially elastic during an earthquake

so that story drifts over the height of the structure remain nearly uniform. Some other SB configurations are shown in Figure 3.10. Alternatively, the SB truss could be represented by a concrete or steel plate shear wall [Qu et al. 2012; Djojo et al. 2014; and Grigorian and Grigorian 2016].

Research-to-date on “masted” systems like the SB system has focused primarily on applications to new construction, employing analytical rather than experimental methods to examine the implementation of a building spine or backbone [Martini et al. 1990; Popov et al. 1992; Tremblay 2003; Tremblay and Merzouq 2004; Mar 2010; MacRae 2011; Lai and Mahin 2013; and Panian et al. 2015]. Thus, a full-scale experimental test, labeled NCBF-B-3SB, was conducted in order to: (1) evaluate the behavior of an SB system under quasi-static, cyclic loading conditions; (2) establish whether weak-story behavior could be mitigated with an SB system; and (3) calibrate analytical models to obtain a range of expected SB system behaviors.

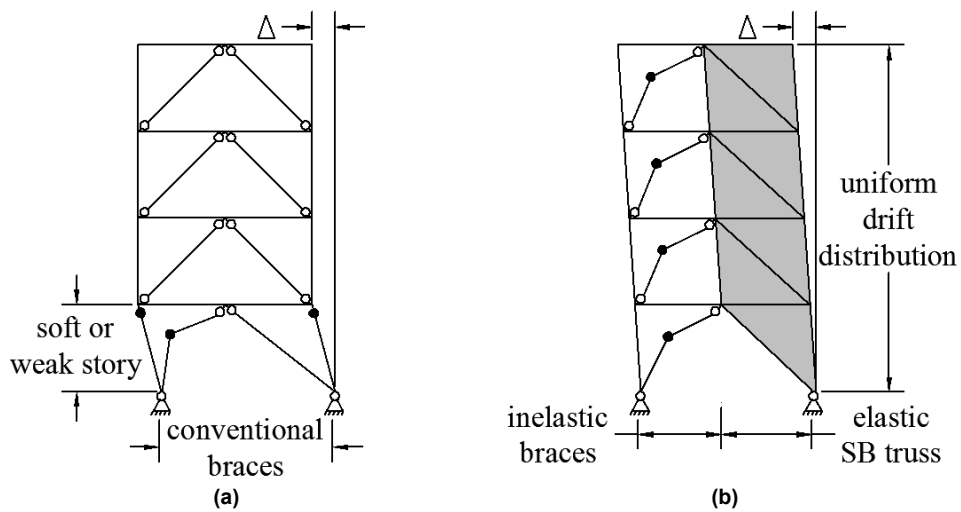


Figure 3.9 Examples of plastic mechanism: (a) conventional braced frame and (b) SB system.

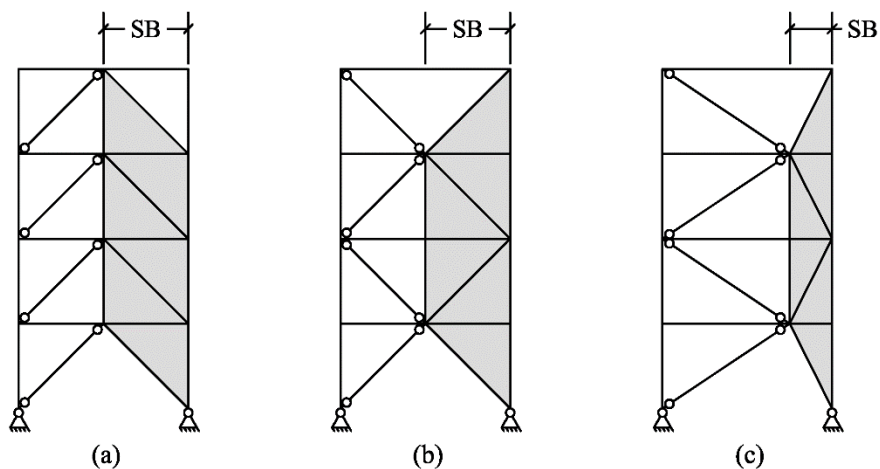


Figure 3.10 Possible SB configurations: (a) “chevron” SB; (b) double-story X SB; and (c) offset double-story X SB.

3.2.3.1 Strongback Configuration

The retrofit design of the NCBF-B-3SB test specimen was based on the original design of the two tested vintage braced frames, NCBF-B-1 and 2. It was decided that the beams, columns, and shear tabs would remain the same as the original test specimens. This would hypothetically minimize the need for demolition and shoring in an actual retrofit situation.

The braces and gusset plates were re-oriented in a new “strongback” geometry. An array of configurations were proposed; see Figure 3.11. While configuration (a) and (b) could be extended from a two-story building to a multi-story building, configuration (c) was chosen because of its simplicity and need for fewer connections. Option (d), while advantageous in reducing the strains in the BRB and plastic rotations of the first-floor beam, was discarded because the out-of-plane support of the existing test set-up was already located at the middle of the frame, and it was unlikely that an existing lateral support would be moved in an actual retrofit situation.

The new lambda configuration, (c), consisted of two halves:

1. The column, braces, and half-beam on the west (right) side of the frame in Figure 3.12 were designed to remain essentially elastic throughout the test. The west column and braces were intended to act like a strong backbone (or “strongback”) for the system and distribute story drifts in a nearly uniform fashion over both stories.
2. The lateral load-resisting system on the east (left) side of the frame consisted of a single buckling-restrained brace (BRB) prop that acted as the primary energy-dissipating device in the system. Other plastic deformations were expected at the ends of the east (left) lower level half-beam, the base of the east (left) column, and the east (left) shear tab connections at the lower and roof beams.

The constructed specimen, prior to testing, is shown in Figure 3.13.

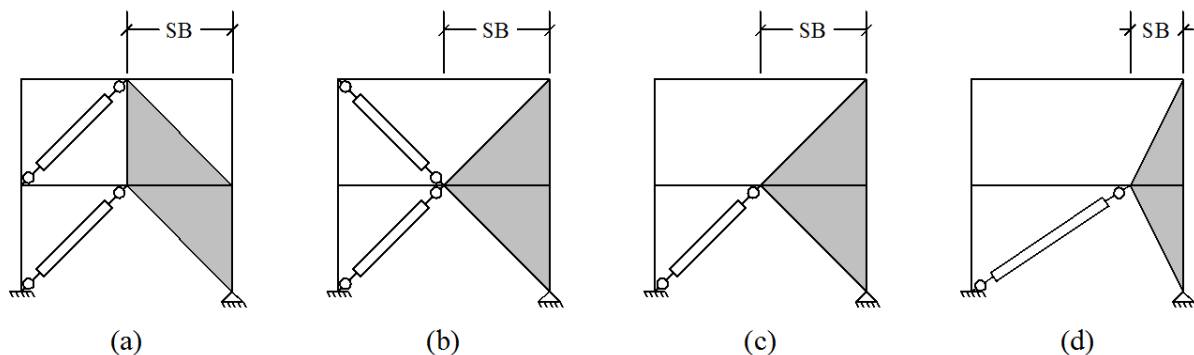


Figure 3.11 Preliminary design configurations: (a) “chevron” SB; (b) double-story X SB; (c) lambda SB; (d) offset lambda SB.

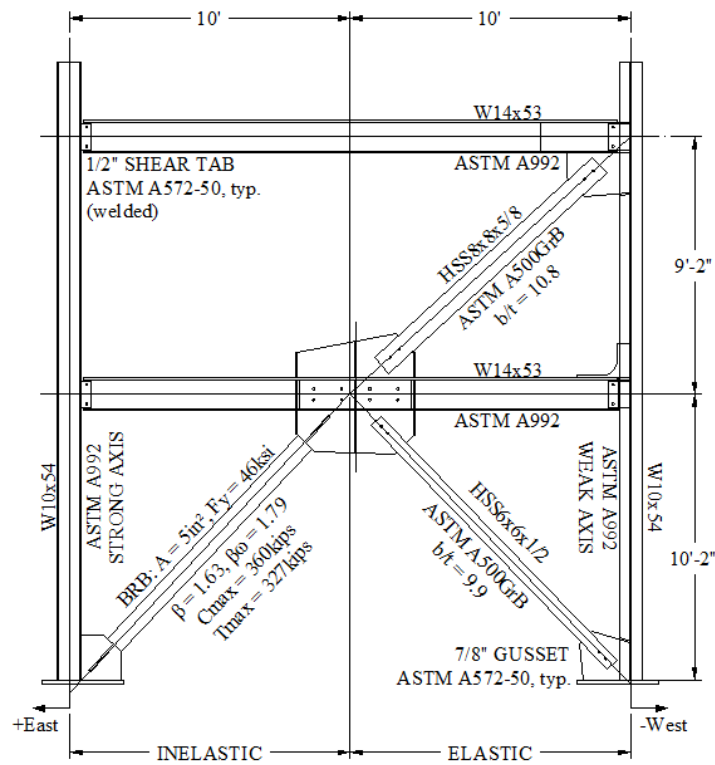


Figure 3.12 Test specimen schematic with dimensions, materials, and member sizes: NCBF-B-3SB.

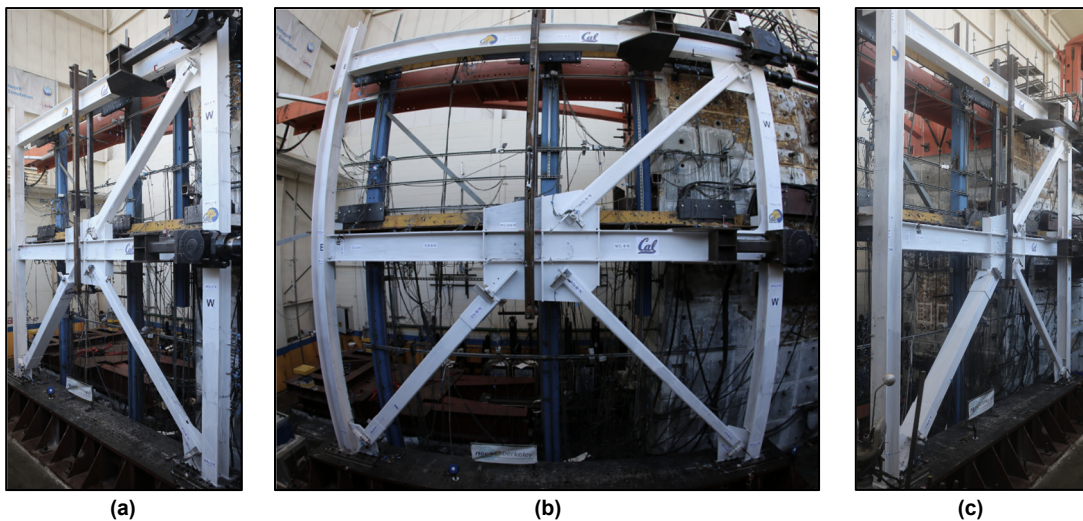


Figure 3.13 Overall views from north side of NCBF-B-3SB before test: (a) west view; (b) center fisheye; and (c) east view.

3.2.3.2 Kinematic Considerations

The benefit of the strongback system lies in its tendency to impose nearly uniform drifts in each story. However, note from simple kinematic considerations (Figure 3.14) that the plastic and shear tab rotations at the east end of the first-floor beam and the strains in the inelastic brace of the lambda configuration will be about double the rotations and strains of a conventional chevron configuration with a “strong beam” (see Section 2.2.4) at the same lateral displacement. Thus, special attention should be placed in the design of these regions and elements due to the large inelastic demands caused by the kinematic behavior of the SB system.

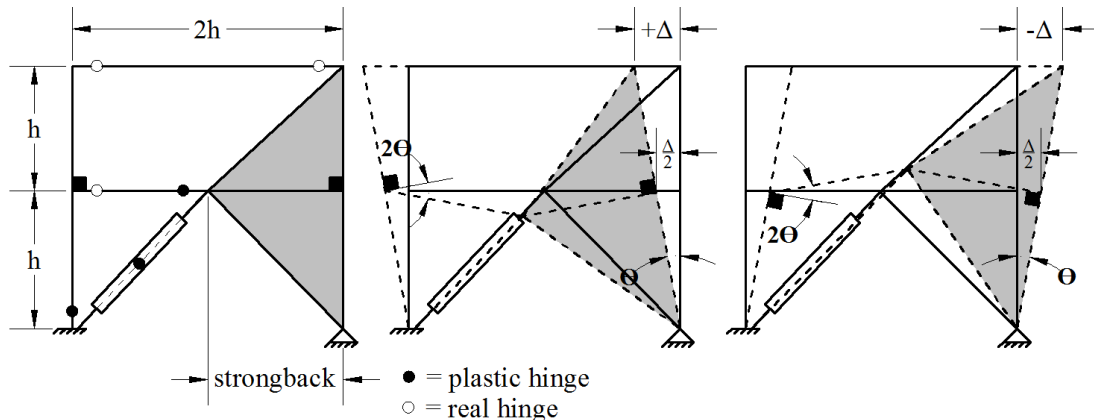


Figure 3.14 Kinematic relations of an idealized SB system with a lambda brace configuration.

3.2.3.3 Brace Design

A BRB was selected as the inelastic brace because of its ability to have similar compression and tension capacities, making it relatively independent of the direction of loading. It was assumed that the asymmetric SB configuration would consist of two mirrored bays along the same column line, creating symmetric lateral resistance in compression and tension for conventional buckling braces in a full building. The BRB allowed this frame to be tested in a single-bay configuration without the need for a mirrored frame to account for differences in compression and tension as the frame was loaded in both the positive and negative directions.

The inelastic BRB provided the majority of the strength and stiffness in the frame. As such, the BRB was first selected based on the maximum base shear capacity of the test set-up of 600 kips; see Section 4.4. This limiting base shear was considered to be similar to situations where a retrofit’s capacity is limited by the capacity of the existing original collectors.

For design purposes, the expected compression capacity of the BRB was designed to be less than 550 kips, ensuring that the total capacity of the frame would not exceed the lateral capacity of the test set-up. The design stiffness of the BRB was increased by 70% to account for the additional stiffness outside the yielding length of the steel core. It was also assumed that the compression strength of the BRB was 10% greater than its tension strength.

The remaining braces in the elastic half of the bracing configuration were then chosen based on plastic analysis, assuming the plastic hinges shown in Figure 3.15. Shear tabs and brace end connections were assumed to be simple connections. The elastic braces were designed to be 1.1 times the force delivered to the braces at incipient collapse based on the assumed maximum

capacity of the BRB and an assumed triangular force distribution; see Section 4.4. Preliminary design moments and forces at incipient collapse are shown in Figures 3.16 and 3.17. In these diagrams, positive moments are counterclockwise and positive axial forces are tensile. Because they were expected to remain elastic, net-section reinforcement and compact sections were not strict requirements in the selection of the elastic brace sections. Final properties for the elastic braces are shown in Table 3.9.

Based on these preliminary calculations, a BRB was selected to have a core area of 5 in.² in order to have an adjusted compression capacity less than 550 kips. The weld-connected StarSeismic Wildcat BRB was chosen for its large erection tolerances considered suitable for a retrofit situation. This preliminary analysis was then further verified using a fiber-based numerical model created in OpenSees [McKenna et al. 2010]. Final BRB properties as provided by StarSeismic can be found in Table 3.10. Note that the design approach utilized herein is not a design methodology and would not be suitable for an SB systems subjected to dynamic loading.

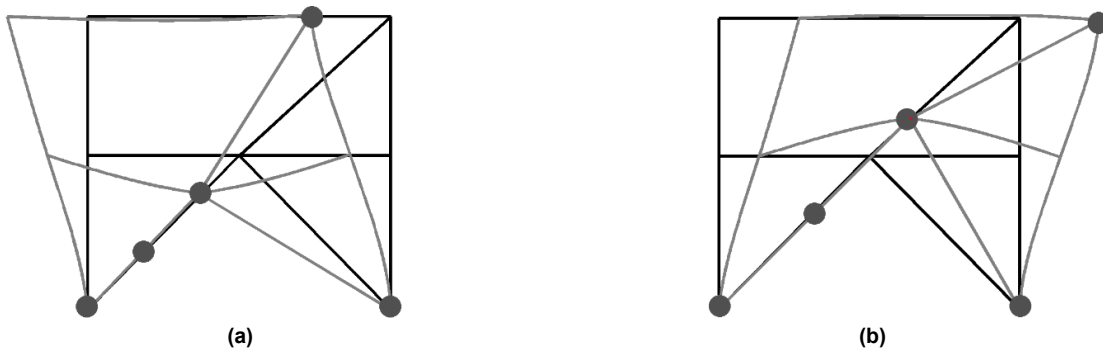


Figure 3.15 Deformed shape at incipient collapse under a triangular load distribution: (a) positive applied force; and (b) negative applied force.

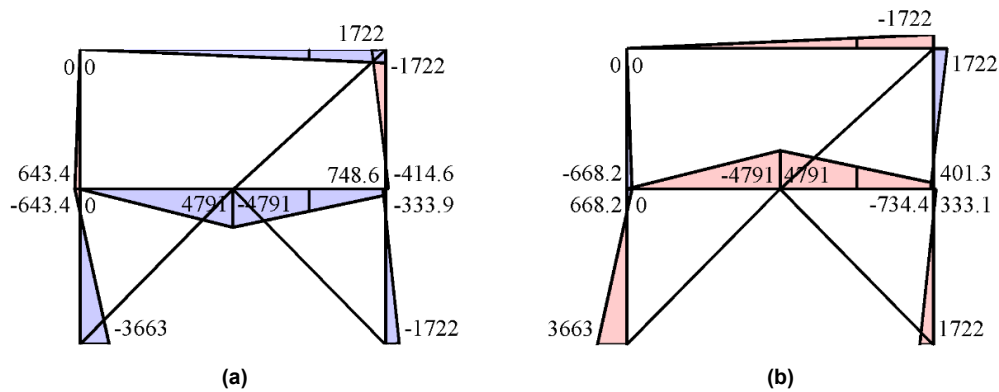


Figure 3.16 Moment diagram at incipient collapse under a triangular load distribution: (a) positive applied force and (b) negative applied force.

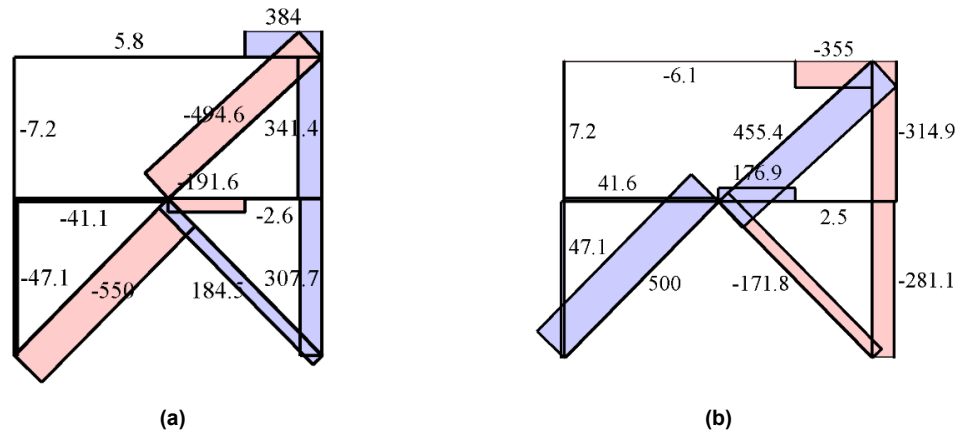


Figure 3.17 Axial force diagram at incipient collapse under a triangular load distribution: (a) positive applied force and (b) negative applied force.

Table 3.9 Elastic brace properties of NCBF-B-3SB.

Member	Section	Cross-sectional area (in ²)	Width-to-thickness ratio (b/t) ²	Approximate slenderness ratio (kl/r) ^{1,2}
First-story brace	HSS6x6x1/2	9.74	9.9	64.0
Second-story brace	HSS8x8x5/8	16.4	10.8	42.9

¹ $k=1.0$ and brace length, l , is the brace length from the shop drawings.

² No specific limits as braces in the strongback system are expected to remain elastic.

Table 3.10 Properties of buckling restrained brace (NCBF-B-3SB).

Member	Section	Material	Core area (in ²)	Yield length (in.)	ω ^{2,1}	$\beta\omega$ ^{3,1}
First-story east BRB	StarSeismic Wildcat BRB	ASTM A36 Low Yield	5.0	75.6	1.63	1.79

¹ As provided by StarSeismic Steel.

² Tension adjustment factor.

³ Compression adjustment factor.

3.2.3.4 Column Design

The column sections were kept the same as the original NCBF-B-1 test specimen. Large plastic rotations were anticipated at the base of the west column in the strongback (Figure 3.14); hence, the west column was oriented in weak-axis bending to mimic a “pinned” connection while achieving the same axial capacity of a column in strong-axis bending. Stiffeners were added to the column web at the base, first, and roof level gusset plate regions to address other local web punching failures observed during the NCBF-B-2 test; see Section 6.3.5.

3.2.3.5 Beam Design

The beams were kept the same as in the original NCBF-B-1 design. A plastic hinge was expected to develop near the center connection of the first-floor beam after the BRB had yielded; see Figure 3.14. Though the BRB was intended to be the primary energy-dissipating component, the lower beam was also expected to dissipate some energy through flexural yielding. To account for these expected inelastic demands, the east half of the first-floor beam was treated like a long beam link in an eccentrically braced frame. The beam was checked to ensure it had adequate shear strength to develop anticipated plastic moment demands. While the beam web was adequate for the shear generated by these plastic hinge, the beam web was considered inadequate for the concentrated forces induced by the braces framing into the center and roof west gusset plate regions. To prevent web crippling, a doubler plate was provided on the web of the lower beam for the full length of the center gusset plate, and web stiffeners were provided at both ends of the gusset plate; see Figure 3.18.

3.2.3.6 Connection Design

New gusset connections were designed for the ends of all bracing members using current AISC 341-10 [2010] provisions and basic capacity-design principles, using 1.1 times the maximum force that could be delivered by the braces. The corner gusset plates were designed using the Uniform Force Method, while the middle connection was designed using a free-body diagram to calculate the internal force distribution; see Figure 3.18. The first-floor west connection retained “remnants” of the initial gusset connection as if the original braces of NCBF-B-1 had been cut out in preparation for the new retrofit; see Figure 3.19. This was designed to reflect the unlikelihood that the original gusset connections would be removed in an actual retrofit situation and served as secondary reinforcement of that connection region. All welded shear tabs were kept the same as the NCBF-B-1 design, as outlined in Section 3.2.1.4.

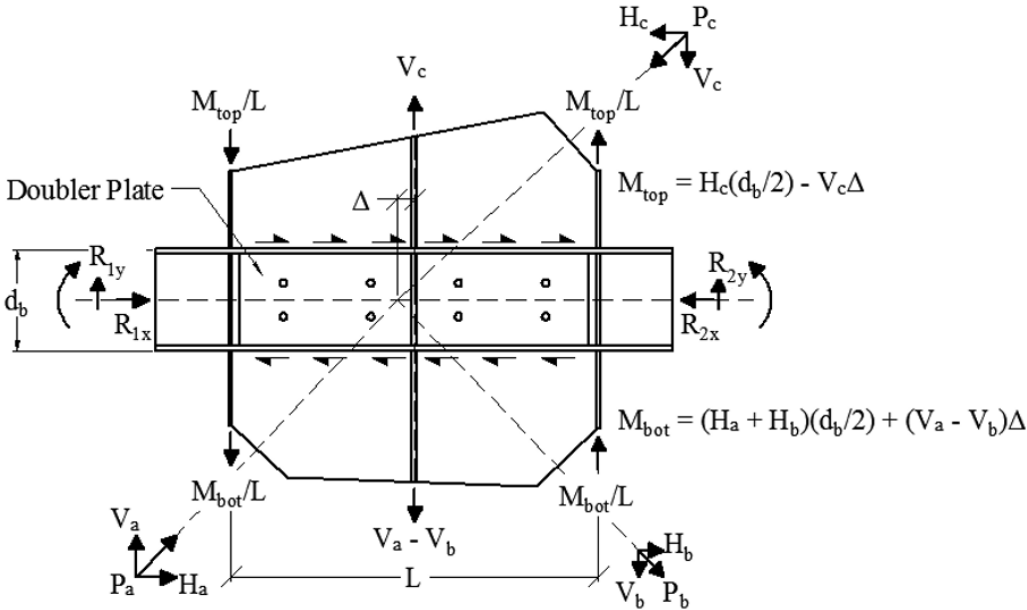


Figure 3.18 Free body diagram of middle connection of NCBF-B-3SB.



Figure 3.19 Original gusset plate “remnants” from NCBF-B-1 at first floor west connection of NCBF-B-3SB.

3.2.3.7 Erection and Fabrication

While the NCBF-B-3SB test specimen was designed as a retrofit, for the sake of economy fabrication and erection were treated as if it was new construction. The beams and columns were delivered to the laboratory with the appropriate connections and plates shop welded to the members even though the gusset plates would have been field welded in an actual retrofit situation; see Figure 3.20. The columns were erected first, followed by the beams, and finally the braces. All members were connected through erection bolts before being field welded *in situ* in the laboratory.

The shop fabrication of the test specimen was performed by a professional contractor, and all welds were laid by certified welders. The BRB was manufactured according to the specifications outlined by StarSeismic. All welds were specified as notch tough (AWS-A5.20: E71-T8 self-shielded flux cored wire). Material properties for the members can be found in Table 3.11; see Table 3.10 for the material properties of the BRB.



Figure 3.20 Erection of NCBF-B-3SB: parts after final shop fabrication.

Table 3.11 Material properties of NCBF-B-3SB.

Member	Section	Material	Yield stress, F_y (ksi)		Ultimate stress, F_u (ksi)	
			Mill Cert. ⁴	Coupon Test ¹	Mill Cert. ⁴	Coupon Test ¹
Column (weak axis)	W10x54	ASTM A572-50	55.5	51.4	78.0	67.8
Column (strong axis)						
Beams	W14x53	ASTM A572-50	56.5	54.2	73.0	69.4
First-story west brace	HSS6x6x1/2	ASTM A500 Gr. B	59.6	- ²	69.3	- ²
Second-story west brace	HSS8x8x5/8	ASTM A500 Gr. B	64.6	67.0	78.9	76.5
First-story east BRB	StarSeismic Wildcat BRB	ASTM A36 Low Yield	42.7 ⁵	39.9 ⁵	62.0 ⁵	64.8 ⁵
Gusset Plate	PL7/8"	A572-50	61.0	- ²	83.5	- ²
Shear Tabs	PL1/2"	A572-50	54.8	- ²	72.3	- ²
Base plate	PL2"	A572-50	57.0	- ²	82.5	- ²
Field weld consumables	CORESHIELD 8	AWS A5.20; E71T-8-D; ASME SFA 5.20 ³				

¹ Average of two tensile coupon tests performed according to ASTM E8. Coupon tests were performed on material taken from the elastic regions of the damaged test specimen after the test.

² Coupon test not performed.

³ Notch tough welding material.

⁴ From mill certificates provided by Schuff Steel, except as noted.

⁵ As provided by StarSeismic mill certificates and material tests.

4 Experimental Set-Up and Test Program

4.1 INTRODUCTION

This chapter discusses the experimental program. Information on the test set-up can be found in Section 4.2. Instrumentation and a brief discussion of data reduction are shown in Section 4.3.1. A detailed sensor lists and sensor locations for each test can be found in Appendix D (electronic appendix). The load protocol for each test is also discussed in Section 4.4.

4.2 TEST SET-UP

The test set-up was adapted from a previous study illustrated in Figure 4.1. The reconfigurable reaction wall (see item “1” in Figure 4.1) is made up of thirty grouted concrete blocks that were pre-tensioned horizontally and vertically to the strong floor (see “2”). Two MTS 220-kip actuators (see “4”) with 72 in. (± 36 in.) of static stroke were located at each floor level and connected to the quarter-points of the beams through heavy transfer brackets (see “5”) at each floor. Fixed conditions were provided at the column baseplates through CJP welds at the baseplate-to-column interface. The 2-in. baseplates were anchored to a heavy built-up beam (see “3”), which helped spread the concentrated reaction forces along the strong floor.

Lateral out-of-plane support was provided for the specimen by a stiff support frame (see “6”). The test specimen was attached to the support frame through heavy T-sections (see “7”) that were allowed to slide horizontally in a direction parallel to the intended lateral movement of the test specimen. The T-sections at each floor were attached to both columns through steel plates that acted like transverse shear tabs (see “8”), which allowed beam elongation and shortening through yielding of the plates. A center support (see “9”) running vertically along the frame centerline was also attached to the T-sections in the same fashion. This center support was connected to the T-sections and provided out-of-plane lateral stability to the beams while permitting vertical movement.

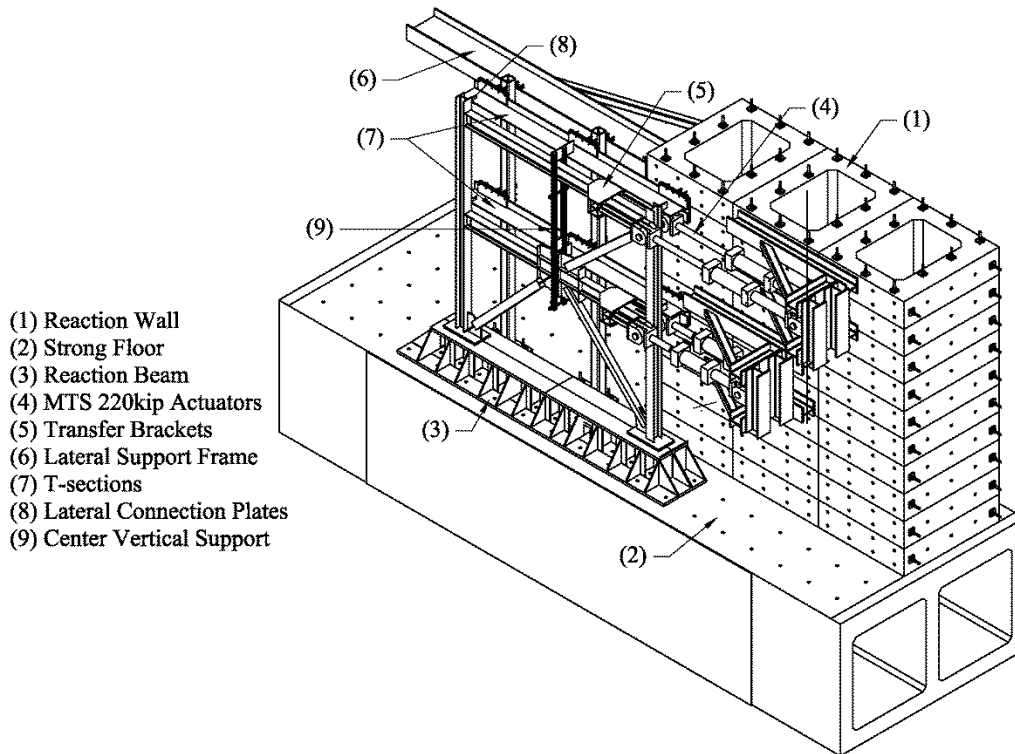


Figure 4.1 Test set-up: isometric drawing.

4.3 INSTRUMENTATION

Instrumentation consisted of over 200 measurement devices, including linear strain gages, strain gage rosettes, linear variable differential transformers (LVDTs), wire pots, and tilt-meters. As detailed in Table 4.1, these instruments attempted to capture critical behaviors in each test specimen such as connection and beam rotations, brace axial deformations, member forces, and global displacements.

Instruments communicated to the PI6000 Data Acquisition System (DAS) through cables connected to junction boxes located near the specimen. Noise in the data was reduced via 40-Hz filters installed on the hardware boards of the DAS. Data was read from the DAS system via the software application, PI660-6000_XPS. The voltage read by each instrument was calibrated before the test. Strain gages were balanced through the software to ensure that they were working correctly. Position instruments were calibrated using a linear relationship between the voltage reading and a known physical value of measurement. The actuators were controlled by a real-time digital MTS Structural Test System (STS) controller, utilizing proportional-integral-derivative (PID) closed loop control with a differential pressure transducer feedback signal.

The frame's behavior was additionally documented through six high-resolution digital single-lens reflex (DSLR) cameras that were triggered to take still photos every 10 sec during the test. A high-definition (HD) video camera was also used to capture sudden inertial behaviors in the braces like buckling and fracture. The global deformed shape of the frame was also captured through two three-dimensional Leica HDS-2500 laser scanners at significant damage points throughout the loading protocol.

Each specimen was painted with a light coat of white wash, detectable in Figures 3.2 and 3.13, to aid in identifying locations of high strain. Any data collected not available in the plots of this report can be found under the NEEShub archive.

Table 4.1 Sensor list and corresponding response quantity.

Location	Sensor type	Response quantity
Global response monitoring	Internal load cell (actuators)	Applied lateral force Story shear
	Internal position transducer (actuators) String potentiometer	Lateral story drift
Braces	Linear strain gages ¹	Axial force Bending moment Reduced section yielding (NCBF-B1 only)
	Linear position transducer String potentiometer	End rotation Axial deformation Out-of-plane displacement [two-dimensional (2D) triangulation]
Columns	Linear strain gages ¹	Axial force Bending moment Weak-axis web yielding
	Tri-axial rosette ²	Story shear Panel zone shear
Beams	Linear strain gages ¹ inear	Axial force Bending moment
	Linear position transducer	End rotation
	String potentiometer (3D triangulation)	Horizontal displacement Vertical displacement Out-of-plane displacement Middle gusset rotation
Gusset plates	Tri-axial rosette ²	Connection stress/strain Doubler plate stress/strain (NCBF-B-3SB only)
Test set-up monitoring	Linear position transducer	Reaction beam slip Base-plate slip
	Tilt meter	Actuator transfer bracket rotation

¹ Linear strain gages were purchased from Texas Measurements, designated FLA-5-11-3LT.

² Strain gage rosettes were purchased from Texas Measurements, designated FRA-5-11-3LT.

4.3.1 Data Reduction

Correction and manipulation of the data from individual instruments was done using MATLAB *Version 9.3.0* (2017). Strains and displacements obtained from the DAS were plotted in history diagrams. This data was used to derive specific response quantities to obtain meaningful information from the instrumentation during each test.

4.3.1.1 Global

Global response quantities at the top of each story were obtained from both internal instruments in the actuators on the west side of the test set-up and external string potentiometers located on the east side of the test set-up. Story shears and story drifts came from the data monitored from the feedback of the actuators. These measurements were taken as the average of two actuators located at each story. The string potentiometers verified the data obtained from the actuator internal position transducer while the frame was behaving elastically. Differences between the potentiometers and the actuator transducers were used to estimate axial elongation and shortening of the beam.

Global response quantities are shown in Figure 4.2. V_1 and V_2 are the story shears in the first and second story, respectively. The base shear, V_b , is calculated as the sum of the story shears from the force feedback of the actuators. The sign convention for all plots using moments and rotations is positive counter-clockwise. Figure 4.3 describes the sign convention used for internal forces, where N is the axial force, V is the shear force, and M is the moment.

The roof drift ratio, θ_R , is defined as the lateral displacement of the top level divided by the total height of the specimen. First- and second-story drift ratios, θ_1 and θ_2 , are defined as the lateral displacement of the cited floor minus the displacement of the floor below divided by the appropriate story height, as defined in the following equations:

$$\theta_R = \frac{\Delta_R}{h_1 + h_2} \times 100 \quad (4.1)$$

$$\theta_1 = \frac{\Delta_1}{h_1} \times 100 \quad (4.2)$$

$$\theta_2 = \frac{\Delta_R}{h_2} \times 100 = \frac{\Delta_R - \Delta_1}{h_2} \times 100 \quad (4.3)$$

Several instruments were also used to monitor the test set-up to ensure that it was behaving as expected and to ensure the safety of the testing program. Such instruments included position transducers monitoring slip in the baseplates and the reaction beam and tilt meters monitoring the in-plane rotation of the actuators.

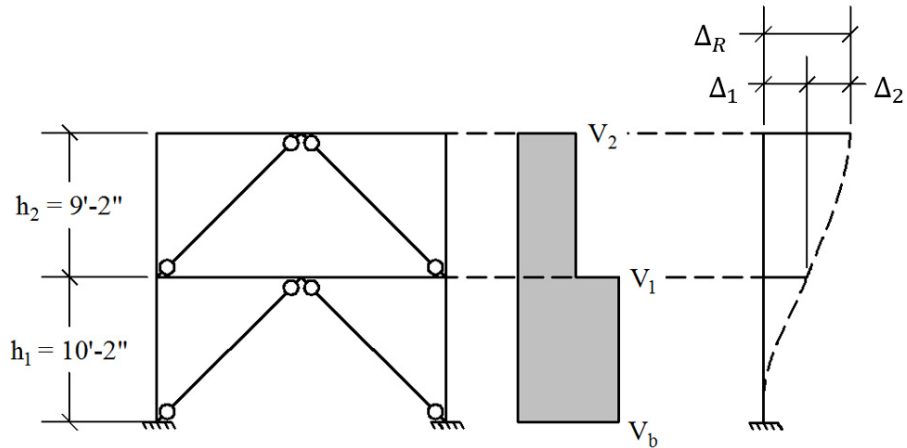


Figure 4.2 Diagram of global response quantities.

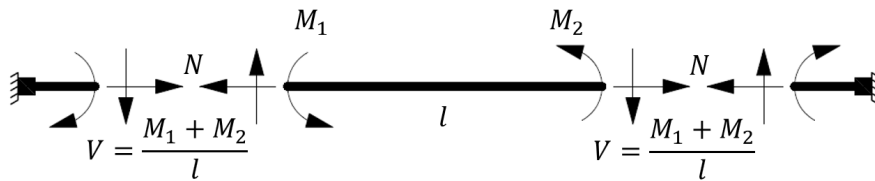


Figure 4.3 Internal force sign convention (positive moment, M , is counter-clockwise).

4.3.1.2 Braces

Since load cells could not be used to monitor the axial force in the braces, brace axial force was estimated via the average of four strain gages located at the lower quarter points of the brace length. Strain gages located at this location were placed in expected elastic regions. The axial force was approximated based on the average strain of the four strain gages, ε , and the modulus of elasticity of steel, E , times the area of the brace cross section, A .

$$P = A\sigma \quad (4.4)$$

where the stress, σ , equals $E\varepsilon$.

This quantity was compared to the revolved brace force determined from the story shears minus the column shears. The effective modulus of elasticity, E , was then calibrated to the horizontal component of this revolved brace force. Both calculations gave similar results and were considered to be relatively accurate at low displacement levels.

Moments at the end of the braces could be approximated using the strains measured from strain gages located at either side of the upper and lower quarter points of the brace, ε_1 and ε_2 , divided by the brace depth, d , to get the curvature, κ . This curvature can then be used to estimate the moment at a section, M , by the following equation:

$$M = \kappa EI \quad (4.5)$$

where $\kappa = (\varepsilon_1 - \varepsilon_2) / d$.

Brace shears were then calculated from the moment distribution along the member length. Because the moment diagram is linear, the member shear diagrams are constant. They

can be calculated as the moments at the strain gages offset from the ends of the member, M_1 and M_2 , divided by the distance between the strain gages, l , along the member length, as shown in Figure 4.3. Shear, V , was calculated from the following equation:

$$V = \frac{M_1 + M_2}{l} \quad (4.6)$$

To facilitate this calculation, strain gages were located in regions that were expected to remain elastic.

Axial elongation of the braces was monitored using the average of two wirepots located on two sides of each brace. These wirepots were offset from the brace centerline to allow for brace out-of-plane displacements. Both ends of the brace were further monitored through linear displacement transducers and, in the case of the BRB in the third NCBF-B-3SB specimen, wirepots. Two linear instruments were located on either side of the gusset plates from the end of the brace to the nearest “rigid” element; i.e., either the beam flange, column flange, or baseplate. The rotation at the ends of the brace was then determined from the difference in these two linear measurements divided by the normal distance between the two instruments.

Out-of-plane displacement of the braces was calculated from two wirepots at each brace using 2D triangulation. The wirepots were located on the lateral support frame and were connected to mid-length at each brace. The area between the deformed brace and the undeformed brace was assumed to remain the same throughout the test. Thus, the out-of-plane deformation, d , could be calculated from the equation:

$$d = \frac{\text{Area}}{c} \quad (4.7)$$

where c is the distance between the two wirepots. In the case of NCBF-B-1, the reduced section region of the braces was monitored with linear strain gages to determine if this region yielded during the test.

4.3.1.3 Columns

Internal moments, shears, and axial forces in the columns were calculated from strain gages using the same equations as used for the braces: Equations (4.4), (4.5), and (4.6). Story shears were also calculated using tri-axial rosettes located on the columns. These quantities were very similar to the results obtained from linear strain gages at the same location. Rosettes were used to monitor the shears developed in the column panel zones. Linear strain gages located along the weak-axis column web behind the gusset connection were also used to monitor strains in the column web. The moment at the column base, M_{bot} , at half the column depth, $d_c/2$, was projected from moments recovered from the strain gages and the slope calculated between these moments assuming a linear moment distribution; see Figure 4.4. The moment at the bottom of the second-story columns was calculated in a similar fashion.

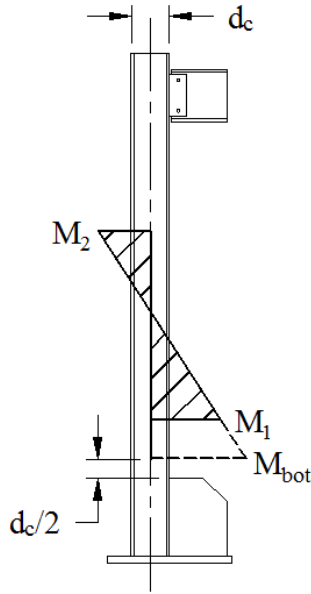


Figure 4.4 Diagram for the estimation of column base moment, M_{bot} .

4.3.1.4 Beams

Internal moments and axial forces in the columns were calculated from strain gages using the same equations as used for the braces and columns, Equations (4.4), (4.5), and (4.6). Beam shears were also calculated the same as the column shears. The difference between the shears on either side of the middle connection were used to also estimate the unbalanced load on the beam.

Three-dimensional (3D) triangulation was used to monitor the 3D displacement and rotations of the middle connection from a total of six wirepots. Three wirepots were located on the lateral support frame with targets on the lower beam flange to either side of the middle connection. A transformation matrix was used after the test to change the orientation of the measurements to a standard X -, Y -, and Z -coordinate system. The vertical displacement of the beam was calculated using the average Y -measurement from all six wirepots.

Beam-end rotations were calculated from linear displacement transducers located on the top and bottom beam flanges. Rotations were derived from the difference in the reading from the two instruments, divided by the distance between the instruments. The moments at the beam ends, M_{end} , were projected from moments recovered from the strain gages and the slope calculated between these moments assuming a linear moment distribution; see Figure 4.5. M_{mid} was calculated in a similar fashion at a distance of a half-beam depth, $d_b/2$, from the middle connection.

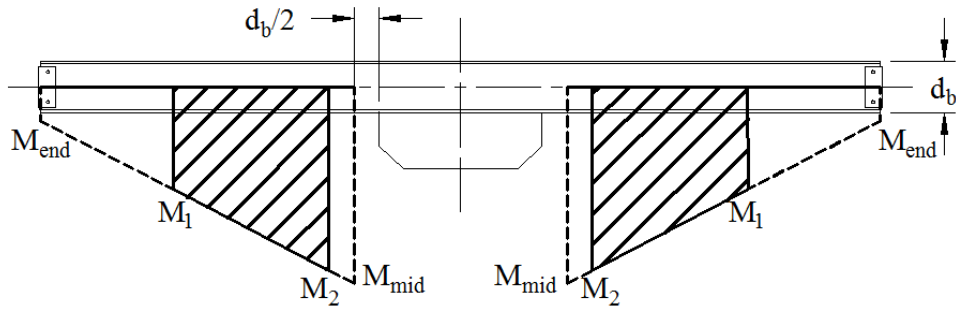


Figure 4.5 Diagram for the estimation of beam end moments, M_{end} and M_{mid} .

4.3.1.5 Connections

Select gusset plates had an array of tri-axial rosettes that measured the strains at specific points on the plate. Rosettes also monitored the strains in the doubler plates used in NCBF-B-3SB. These strains will be used to verify strains in future numerical models. Shear-tab rotations were calculated using the same position transducers monitoring the beam-end rotations, as described in Section 4.3.1.4.

4.4 LOADING PROTOCOL

The global horizontal displacement of the roof floor beam was used to control the specimen during the test. The roof actuators were displacement-controlled and the first-floor actuators were force-controlled. The forces in the lower level actuators were set to be half the force feedback from the load cells in the roof actuators. This arrangement maintained an inverted triangular load distribution over the height of the frame. The maximum base shear capacity of the loading system was 600 kips; see Figure 4.6.

All three experiments were quasi-static cyclic tests. The roof-level actuator was programmed to move with a constant velocity of 0.01 in./sec through the entire test. Displacements are considered positive when the frame moves in the east (left) direction of the laboratory and negative when the frame moves in the west (right) direction. The test was paused during the loading process to document any frame damage, such as yielding, local buckling, and brace or weld fracture; these pauses were taken out of the test data for the sake of coherency. Elastic tests were performed prior to the final test date to ensure that the test set-up and instruments were behaving as intended.

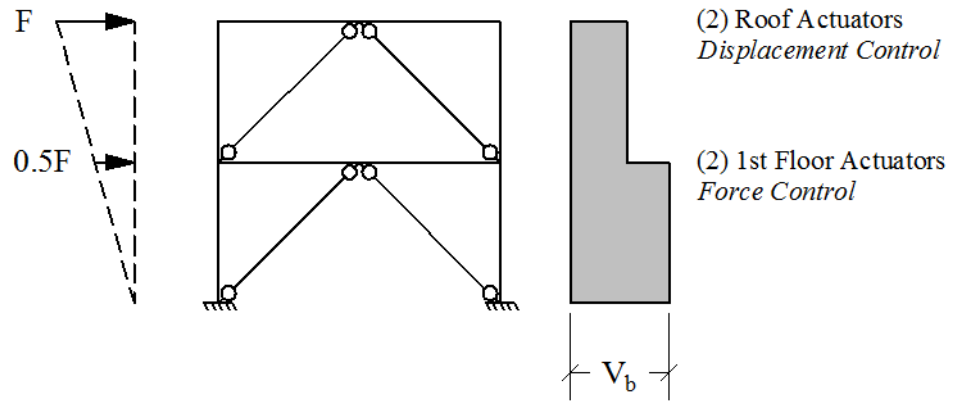


Figure 4.6 Lateral force distribution for loading protocol.

4.4.1 NCBF-B-1 & NCBF-B-2 Loading Protocol

Both the NCBF-B-1 and NCBF-B-2 test specimens followed the same loading protocol. The cyclic loading protocol was selected based on the predicted yield roof drift ratio, θ_y , of the frame of about 0.5%. Figures 4.7 and 4.8 show the loading protocol for both specimens. Note that the NCBF-B-2 test specimen was tested over more cycles at larger displacement amplitudes.

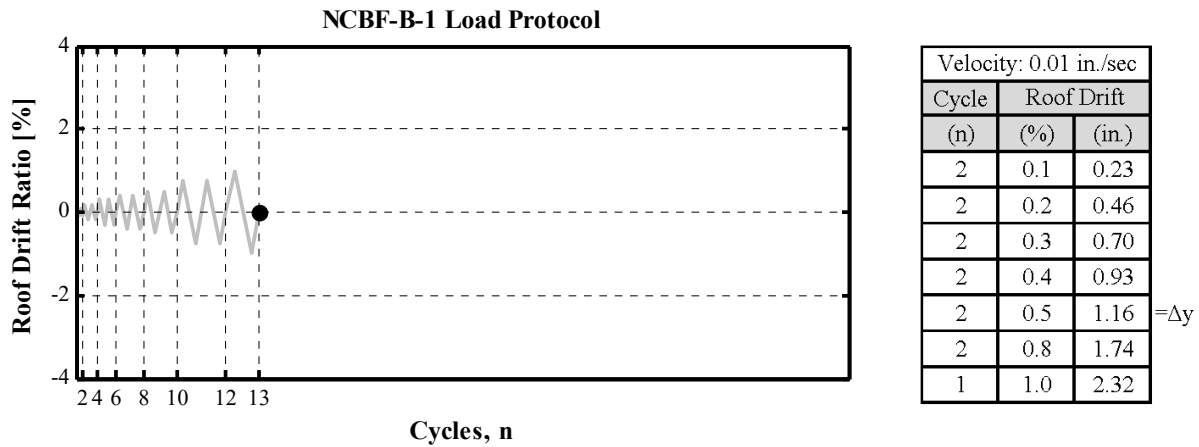


Figure 4.7 Displacement control loading protocol at roof of NCBF-B-1.

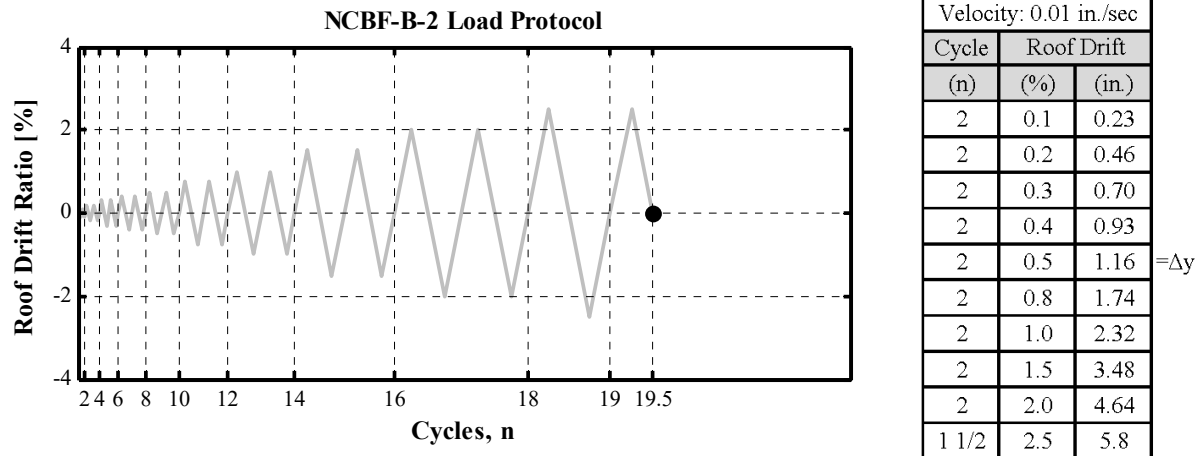


Figure 4.8 Displacement control loading protocol at roof of NCBF-B-2.

4.4.2 NCBF-B-3SB Loading Protocol

The NCBF-B-3SB test followed a loading protocol similar to the buckling-restrained brace loading sequence found in Chapter K3.4c of AISC 341-10 [2010]. The provision defines a predefined sequence of displacement cycles with progressively increasing peak amplitudes to be imposed on a brace or braced frame sub-assembly. Additional amplitude cycles were added to the end of the qualification testing protocol to observe damage at larger roof displacements. Two additional amplitude cycles were also added at a roof drift ratio of 0.75% to reflect the amplitude cycles used in the loading protocol of the NCBF-B-1 and 2 tests. This was done to monitor the strongback behavior under deformations similar to that imposed on the vintage-era braced frame specimens.

The AISC 341-10 standard [2010] includes acceptance criteria for the qualification of individual BRBs and BRB sub-assemblages. Under the provisions, the test specimen must satisfy a set of acceptance criteria under a prescribed loading sequence up two cycles at $2\theta_{bm}$, where θ_{bm} corresponds to the BRB deformations at a target design roof drift ratio of 2%. The values of roof drift ratio corresponding to these BRB deformation quantities can be seen in Table 4.2 and are included in the loading protocol of Figure 4.9.

Table 4.2 Roof drift ratios corresponding to AISC deformation quantities.

Deformation quantity	Roof drift ratio
θ_{by} ¹	0.2%
θ_{bm} ²	1%
$2\theta_{bm}$	2%

¹ θ_{by} is the deformation at yield.

² θ_{bm} is the design deformation ($\theta_{bm} = C_d\theta_{bys}$, where C_d is 5.0 for a BRB).

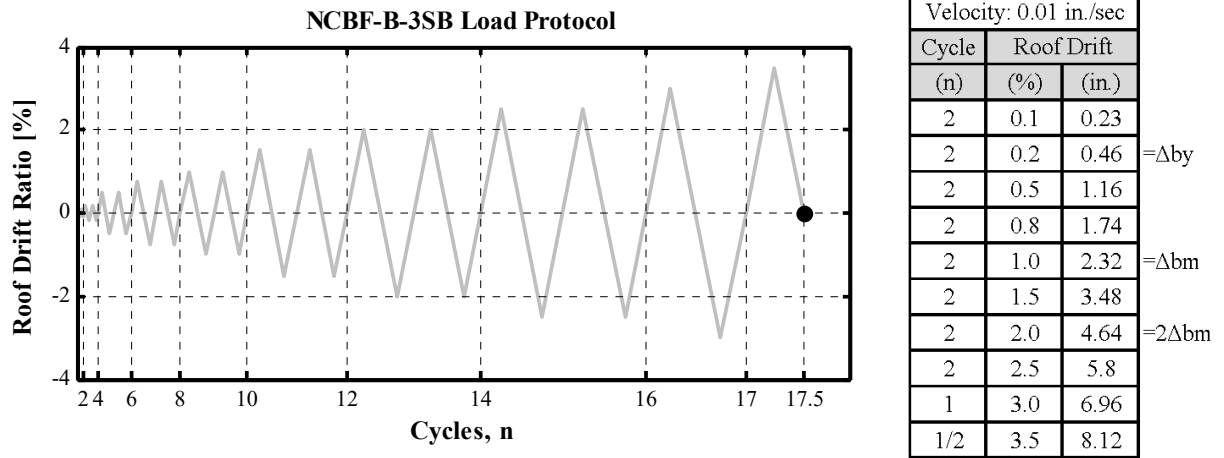




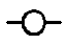



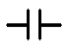

Figure 4.9 Displacement control loading protocol at roof of NCBF-B-3SB.

5 Experimental Results

5.1 INTRODUCTION

This chapter presents observations and photographs of each experimental test. The propagation of damage for each test specimen over the course of the loading protocol can be seen in Figures 5.19, 5.45, and 5.66. The variations in shaded regions represent increased damage over the course of the test, and fracture is represented by the removal of those sections, as defined by the legend in Table 5.1.

Table 5.1 Legend for representation of damage in each test specimen.

↔ Cyclic Loading (+E, -W)			
	Brace Global Buckling		Minor Yielding
	Brace Local Buckling		Moderate Yielding
	Brace Crack Initiation		Severe Damage
	Brace Rupture		Fracture

5.2 NCBF-B-1: BASELINE TEST SPECIMEN

The first experimental test, NCBF-B-1, was conducted on October 11th, 2013, in the nees@berkeley laboratory. This specimen served as the baseline test for vintage braced frames; see Section 3.2.1. The global hysteretic behavior of the frame during the entire test can be seen in the hysteretic loop of Figure 6.1 in Chapter 6.

5.2.1 Event Points, Observations, and Photographs

Table 5.2 provides a brief narrative description of major observed events that occurred during the testing process. The points in the loading protocol where these events occurred are indicated in Figure 5.1. In most cases, the narrative description is based on observations made at the peak amplitude of a cycle. Thus, events described at a point may have occurred earlier during that

cycle. All drift ratios provided in the table correspond to roof drift ratios, as specified in Section 4.3.1.1.

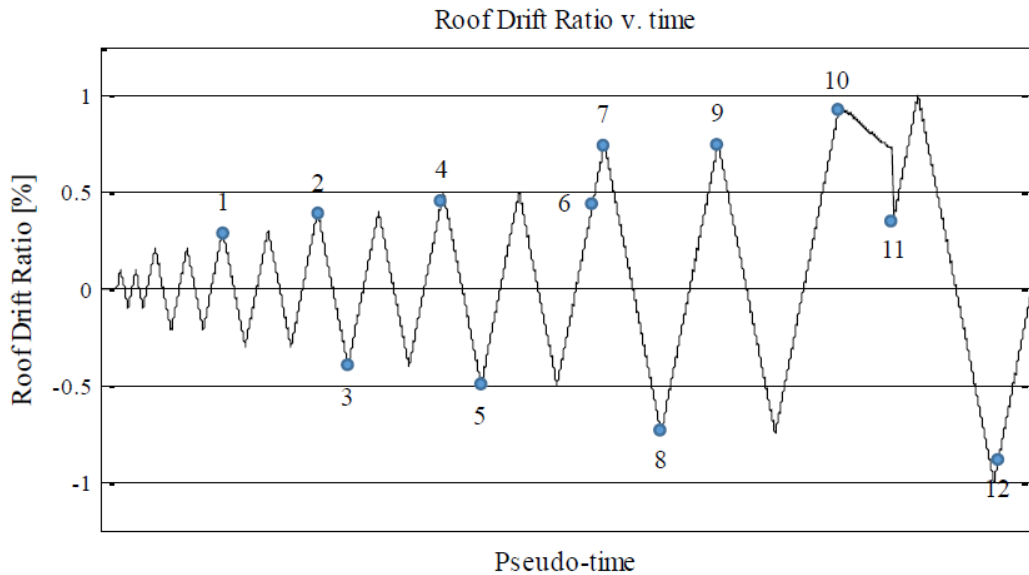


Figure 5.1 NCBF-B-1 applied roof drift ratio during the test.

Table 5.2 NCBF-B-1 observations at various event points during the test.

Event point	Figure no.	Observations
1	5.13	Minor flaking at the base of the east column web.
2		Flaking at the east weak-axis column near the beam column connection region at the first floor.
3		Flaking at the east and west side bottom gusset plates near the baseplates.
4	5.2 and 5.3	East second-story brace buckles (+0.44%).
5	5.2 and 5.3	West second-story brace buckles (-0.41%).
6	5.2 and 5.3	Crack initiates in the west second-story brace.
7	5.9, 5.10, 5.11, and 5.14	Flaking at the second-story bottom gusset plates. Flaking near the gusset to roof beam weld at the middle gusset plate. Vertical yield line appears along the web of the east weak axis column behind the gusset plate.
8	5.9, 5.10, and 5.18	Gap at the west roof beam-column connection observably closes. More flaking at all of the second-story gusset plates.
9	5.2 and 5.3	Crack propagates in the second-story west brace.
10	5.2, 5.3, 5.5, 5.8, 5.9, 5.10, 5.12, and 5.15	West second-story brace fractures (+0.90%). Hydraulics are shut down. Flaking at the roof shear tabs. Some flaking at the net section at the second-story braces. Observable yield-line at gusset plates and twisting of roof center gusset plate.
11	-	Frame reloads (0.48%) to next cyclic peak after hydraulics were shut down at point (10).
12	5.2 and 5.4	East second-story brace fractures (-0.87%).

Table 5.3 NCBF-B-1: List of figures grouped by location.

Figure no.	Location captured by each photograph
5.2–5.5	Second-story braces
5.6, 5.7, 5.13, and 5.14	Columns
5.15–5.18	Connection regions
5.8	Shear tabs
5.9–5.12	Gusset plates
5.13	Baseplates

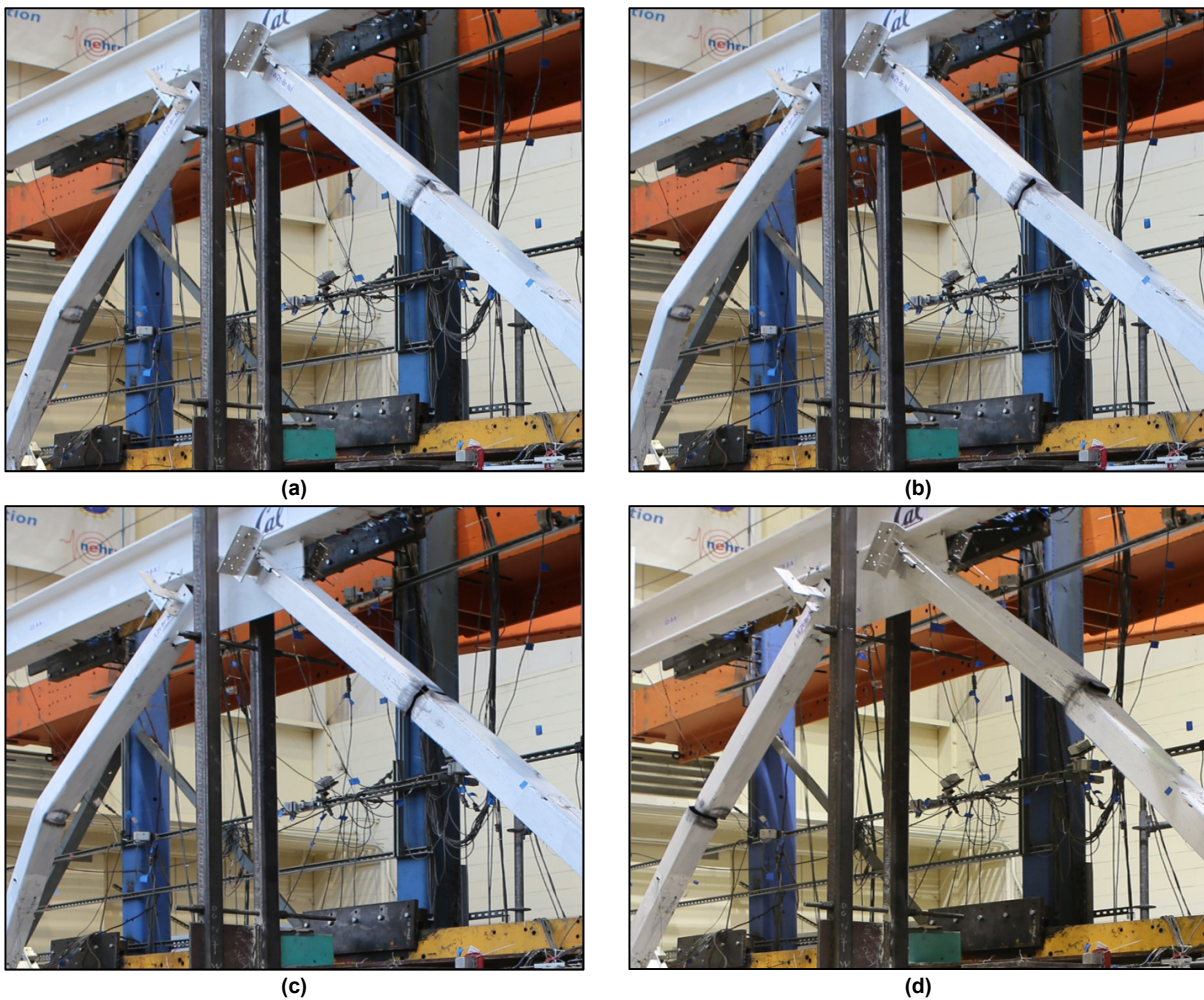


Figure 5.2 Sequence of brace behavior: (a) buckling of both braces with crack initiation in the west brace; (b) crack propagation in the west brace; (c) west-brace fracture; and (d) east-brace fracture

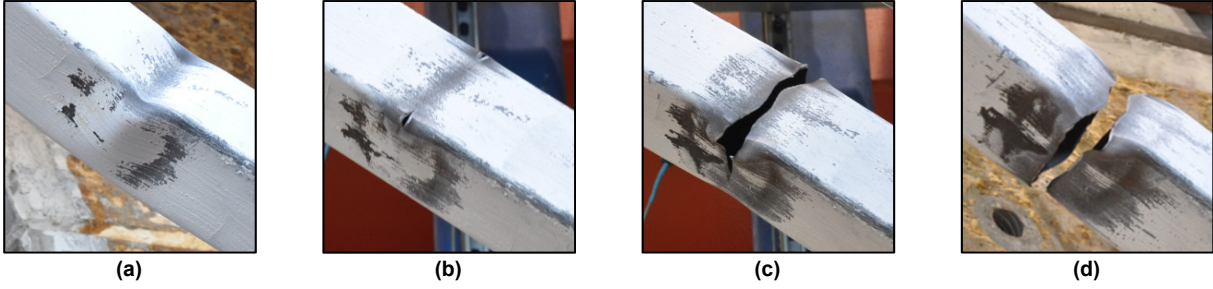


Figure 5.3 West brace behavior: (a) brace buckling; (b) crack initiation; (c) crack propagation; and (d) brace fracture.

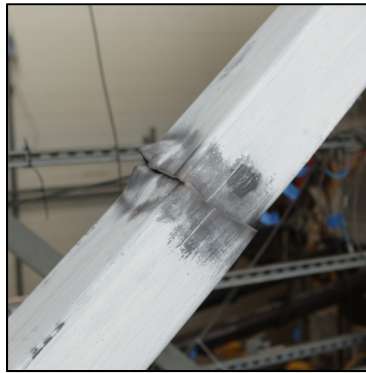


Figure 5.4 Final fracture state of the east brace.



Figure 5.5 Final fracture state of the west brace.

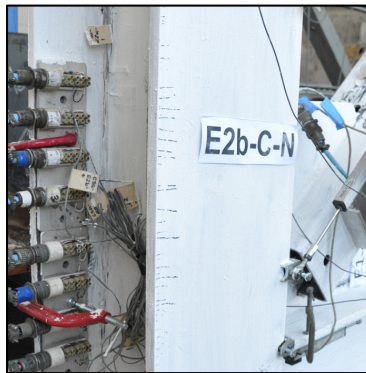
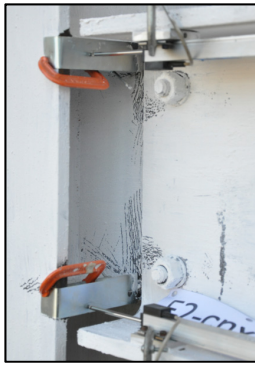


Figure 5.6 Base of east column at the second story.



Figure 5.7 Base of west column at second story.



(a)



(b)



(c)



(d)

Figure 5.8 Damage to the second-floor shear tabs: (a) north-face east gusset; (b) south-face east gusset; (c) north-face west gusset; and (d) south-face west gusset.



Figure 5.9 East gusset plate at the second story.



Figure 5.10 West gusset plate at the second story.



Figure 5.11 Center gusset plate at the roof.

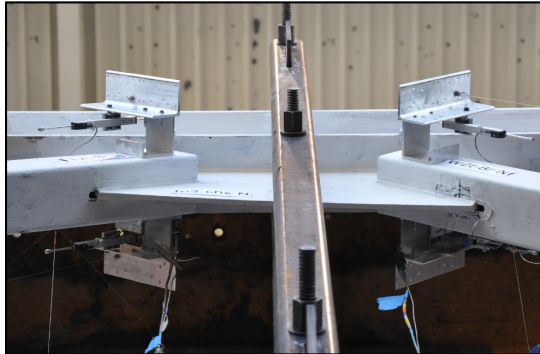


Figure 5.12 Twisting of center gusset plate at the roof.

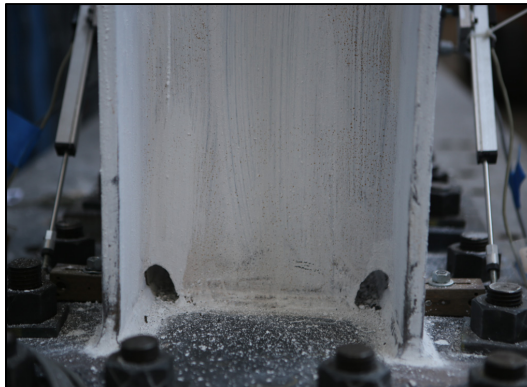


Figure 5.13 Base of the east column.

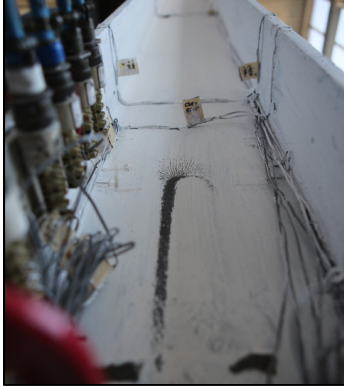


Figure 5.14 East column web at second story behind the gusset plate.

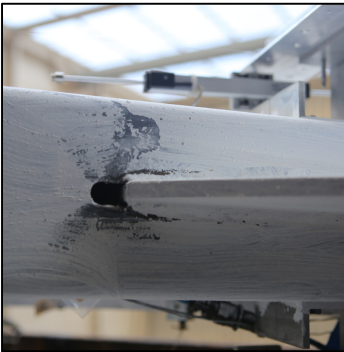


Figure 5.15 Typical flaking at net section.



Figure 5.16 Typical flaking near the tip of the gusset plates.



Figure 5.17 Top of roof beam above the center gusset.

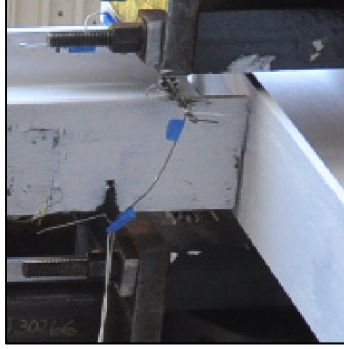


Figure 5.18 Closure of roof beam–column gap.

5.2.2 Summary of Key Observations for NCBF-B-1

This section will provide a summary for key event points of the test, as shown in Figure 5.19.

$\theta_R < \theta_y = 0.5\%$ Several elastic cycles were completed to check that the instrumentation was performing as expected. Whitewash flaking was observed at the base of the east column web and at the gusset plates near the gusset-to-baseplate connection.

$\theta_R = \theta_y = 0.5\%$ The second-story east brace locally buckled on the first half cycle to +0.5%. The second-story west brace locally buckled during that same cycle to -0.5%.

$\theta_R = 0.75\%$ Cracks initiated at the corners of the second-story west brace at the local buckle location on the first half cycle to +0.75%. During the second-half cycle to +0.75%, these cracks propagated along the face of the second-story west brace.

Flaking was observed at the second-story gusset plates. Yielding was observed behind the bottom east gusset plate along the web of the weak axis column.

$\theta_R = 1.0\%$ The second-story west brace fractured on the first half cycle to +1.0%. The actuators were shut down due to instability problems associated with high gains. The second-story east brace fractured during that same cycle to -1.0%.

The second-floor middle gusset plate showed observable twisting. Elliptical yield-lines were observed at the second-story gusset plates where the brace buckled out-of-plane. Yielding was observed in the second-floor shear tabs.

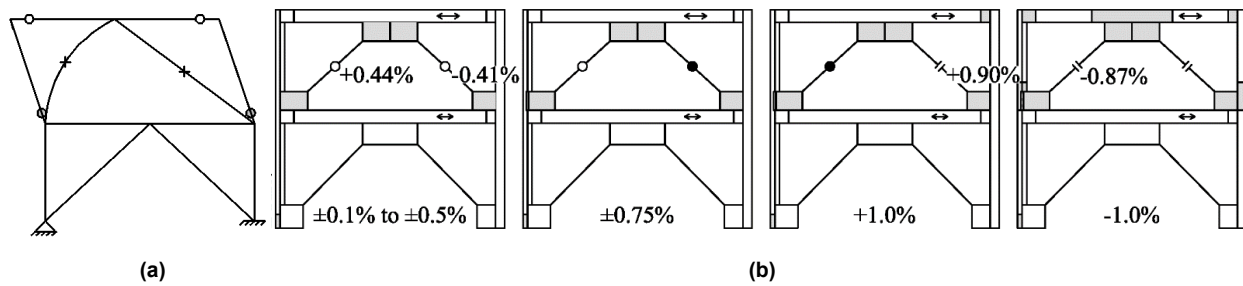


Figure 5.19 NCBF-B-1: (a) schematic of collapse mechanism and (b) hierarchy of damage.

5.3 NCBF-B-2: SPECIMEN UPGRADE

The second experimental test, NCBF-B-2, was conducted in two parts on February 10, 2014, and February 25, 2014, in the nees@berkeley laboratory. This specimen served as a concrete-filled brace upgrade as described in Section 3.2.2. The global hysteretic behavior of the frame during the entire test can be seen in the hysteretic loop of Figure 6.18 in Chapter 6.

5.3.1 Event Points, Observations, and Photographs

Table 5.4 provides a brief narrative description of major observed events that occurred during the testing process. The points in the loading protocol where these events occurred are indicated in Figure 5.20. In most cases, the narrative description is based on observations made at the peak amplitude of a cycle. Thus, events described at a point may have occurred earlier during that cycle. All drift ratios provided in the table correspond to roof drift ratios, as specified in Section 4.3.1.1.

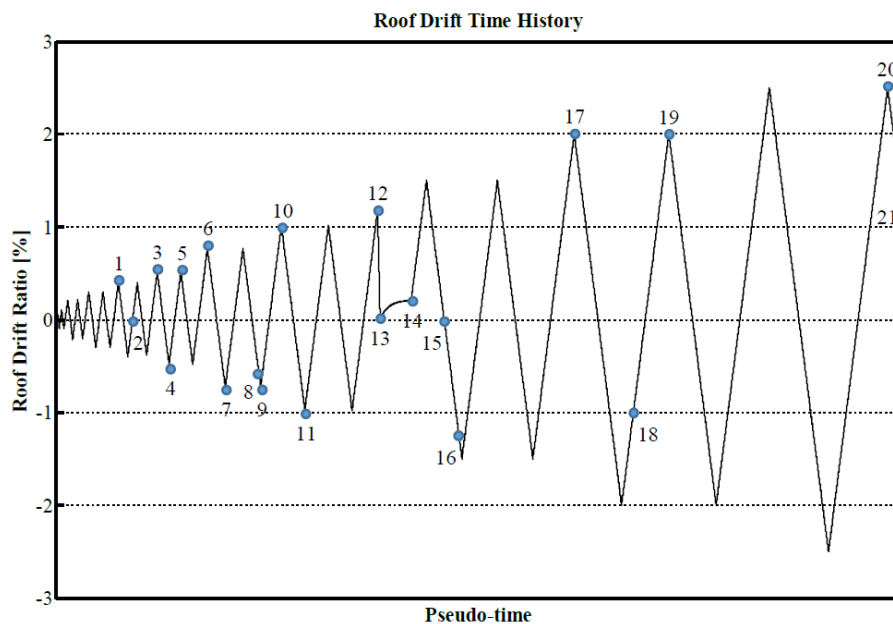


Figure 5.20 NCBF-B-2 applied roof drift ratio during the test.

Table 5.4 NCBF-B-2 observations at various event points during the test.

Event point	Figure no.	Observations
0		Loading protocol cycles around around second-story residual displacement (-0.227 in.) from NCBF-B-1 test.
1	5.26	0.13 in. slip at east baseplate (+0.4%).
2		Test paused at zero force. Both baseplates welded to floor beam with ¼-in. fillet welds, full length, both sides.
3	5.21 and 5.32	East first-story brace (global) buckling (+0.51%).
4	5.37	Whitewash flaking at east first-story gusset plate. Concrete in east brace appears to be unbonded.
5	5.37	More flaking at east first-story gusset plate. Flaking at middle first-story gusset plate at east corner of beam. Flaking near yield-line of east gusset.
6	5.21 and 5.32	East first-story brace local buckles (+0.55%).
7	5.23	West first-story brace (global) buckling (-0.73%)
8	5.21, 5.22, and 5.32	East first-story brace crack initiation.
9	5.21, 5.22, and 5.32	East first-story brace fractures (-0.60%).
10	5.21 and 5.24	First-floor beam visibly lowers (1.96 in.) and starts to form plastic hinge. Brace fracture closes.
11	5.24	First-floor beam visibly raises (1.04 in.).
12		Beam hits William rods at center support before peak roof drift is reached.
13		Test paused and hydraulics are shut down. Center support is adjusted to allow for increased beam vertical displacement.
14		Test resumes on 02-25-2014. Frame reloads to next cyclic peak after hydraulics were shut down at point (13), with second-story residual displacement (0.53%).
15	5.24, 5.25, 5.34, and 5.38	First-floor beam begins to twist. Noticeable flaking at west column above first-floor gusset plate and column base.
16	5.24, 5.40, and 5.43	Crack visibly opens in east first-floor shear tab. Crack opens at west gusset to baseplate weld. Local buckling at beam near middle gusset plate.
17	5.23(b), 5.35, 5.38, and 5.39	Whitewash flaking at second-story east brace near net section. Free-edge buckling at bottom-west gusset plate. Local buckling at bottom of second-story east brace.
18	5.24, 5.25, 5.27, 5.29, 5.34, 5.38, 5.39, and 5.40	First-story west column flange local buckles. First-story beam continues to twist. Crack propagates at toe of west gusset plate. Local buckling at bottom of second-story west brace.
19	5.28 and 5.31	First-floor shear tab pushes through weak-axis column (+1.94%). Crack forms at first-floor beam near center gusset plate.
20	5.42	West column cracks near baseplate.
21	5.38, 5.39, 5.40, 5.41, and 5.42	West column completely fractures at baseplate (+2.33%). Test ends with a residual roof displacement of 3.055 in.

Table 5.5 NCBF-B-2: List of figures grouped by locations

Figure no.	Location captured by each photograph
5.21, 5.22, 5.23, and 5.32	First-story braces
5.24, 5.25, and 5.29	First-floor beam
5.30 and 5.31	Columns
5.27	Connection regions
5.22, 5.23, 5.28, 5.33, 5.34, 5.35, and 5.36	Gusset plates
5.26, 5.37, 5.38, 5.39, 5.40, 5.41, and 5.42	Baseplates
5.43 and 5.44	Shear tabs

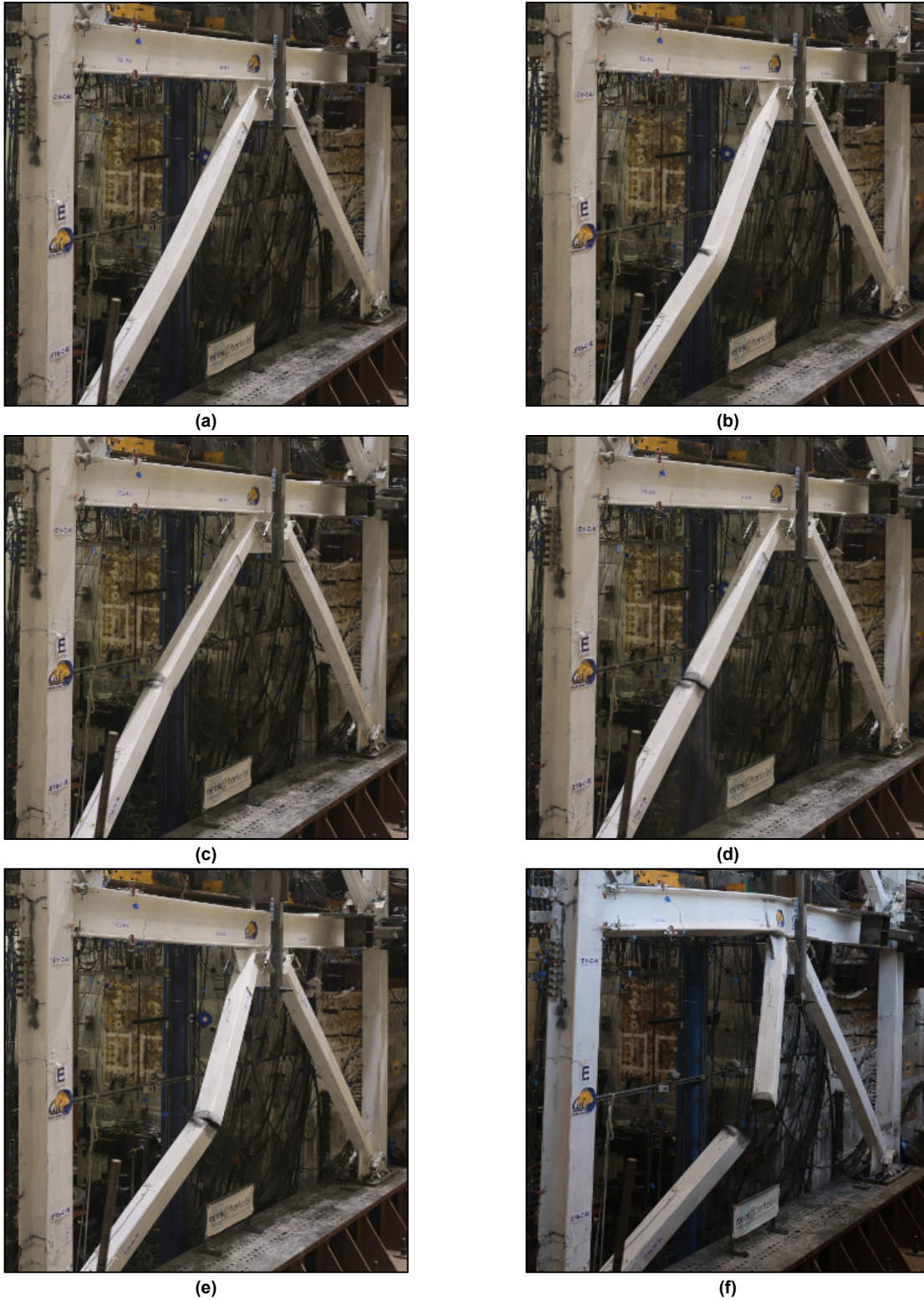
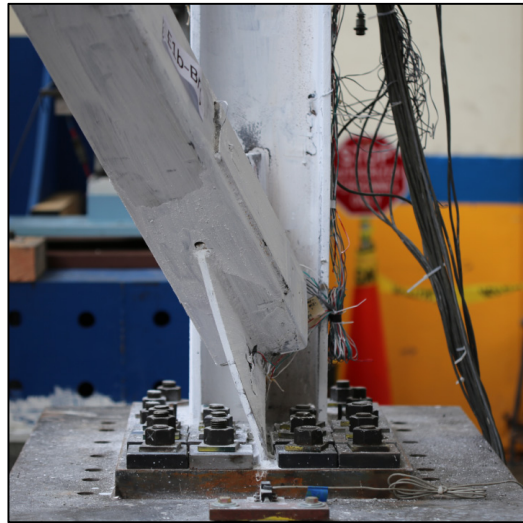


Figure 5.21 Sequence of first-story east-brace behavior: (a) east-brace global buckling; (b) east-brace local buckling; (c) east-brace crack initiation; (d) east-brace fracture; (e) meeting of east brace in compression (positive roof drift); and (f) separation of east brace in tension (negative roof drift).

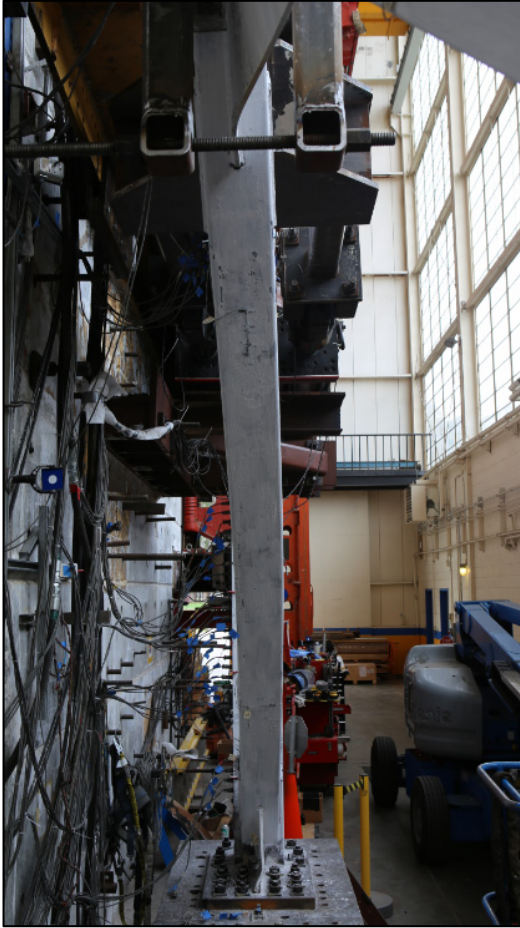


(a)

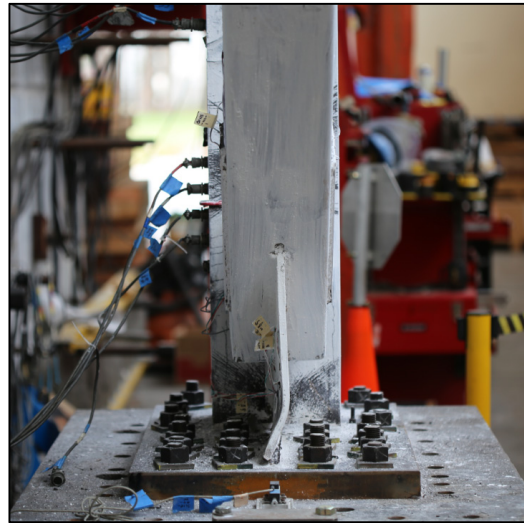


(b)

Figure 5.22 (a) Final fracture state of the east brace; and (b) bending of the east gusset plate.



(a)



(b)

Figure 5.23 (a) Global buckling of the west brace; and (b) local buckling of the west gusset plate.



(a)



(b)



(c)



(d)

Figure 5.24 Sequence of first-floor beam behavior: (a) positive (upward) beam displacement (negative roof drift); (b) negative (downward) beam displacement (positive roof drift); (c) beam-flange local buckling; and (d) beam double curvature.



(a)



(b)



(c)

Figure 5.25 Final first-floor beam state: (a) double curvature; (b) local buckling; and (c) twisting of gusset.

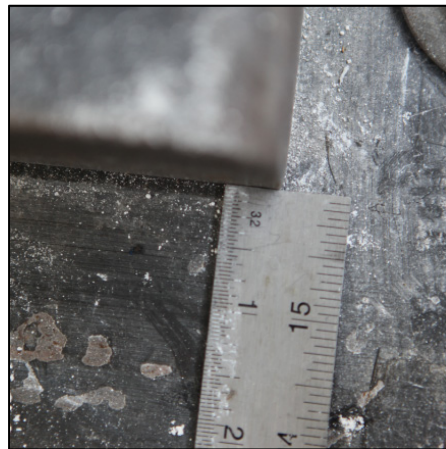


Figure 5.26 East base-plate slip.



Figure 5.27 Twisting of first-floor beam at east connection after shear tab tear.



Figure 5.28 Weld fracture at the first-story center gusset.



Figure 5.29 Curvature and final downward displacement of the first-floor beam.



Figure 5.30 Yielding of east-column web near the column base behind first-story lower gusset plate.



Figure 5.31 Tearing of east-column web behind the second-story lower gusset plate.

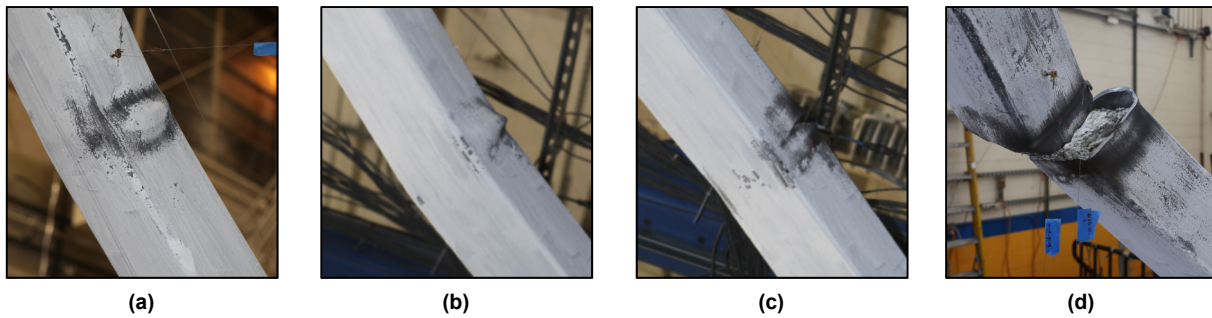


Figure 5.32 First-story east-brace behavior: (a) and (b) outward local buckling; (c) crack propagation; and (d) brace fracture.



Figure 5.33 Second-story east connection.



Figure 5.34 Second-story west connection.



Figure 5.35 Local buckling and crack initiation of the second-story east brace.



Figure 5.36 Fracture at the second-story west gusset-to-beam weld.



Figure 5.37 First-story east connection.



Figure 5.38 First-story west connection.



Figure 5.39 Fracture at the west gusset-to-baseplate weld.



Figure 5.40 Fracture at the west gusset-to-baseplate weld.



Figure 5.41 Fracture at the west column base.

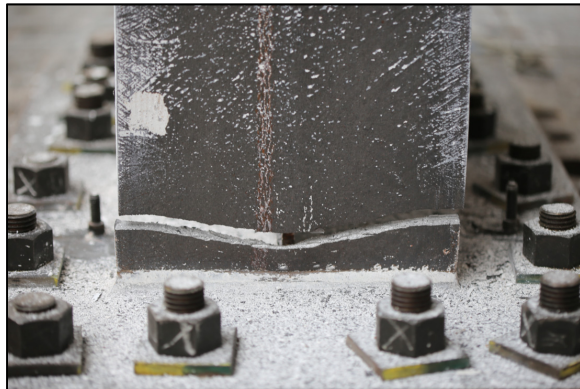


Figure 5.42 Fracture at the west column flange.

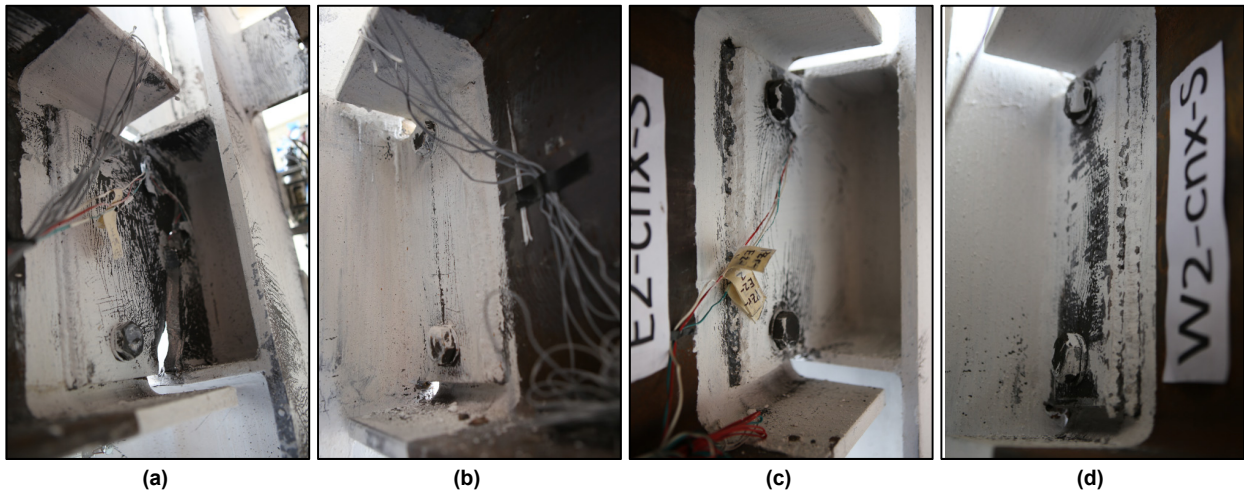


Figure 5.43 Damage to the first-floor shear tabs (south face) at: (a) the east gusset and (b) west gusset; and damage to second-floor shear tabs (south face) at (c) the east gusset and (d) west gusset.

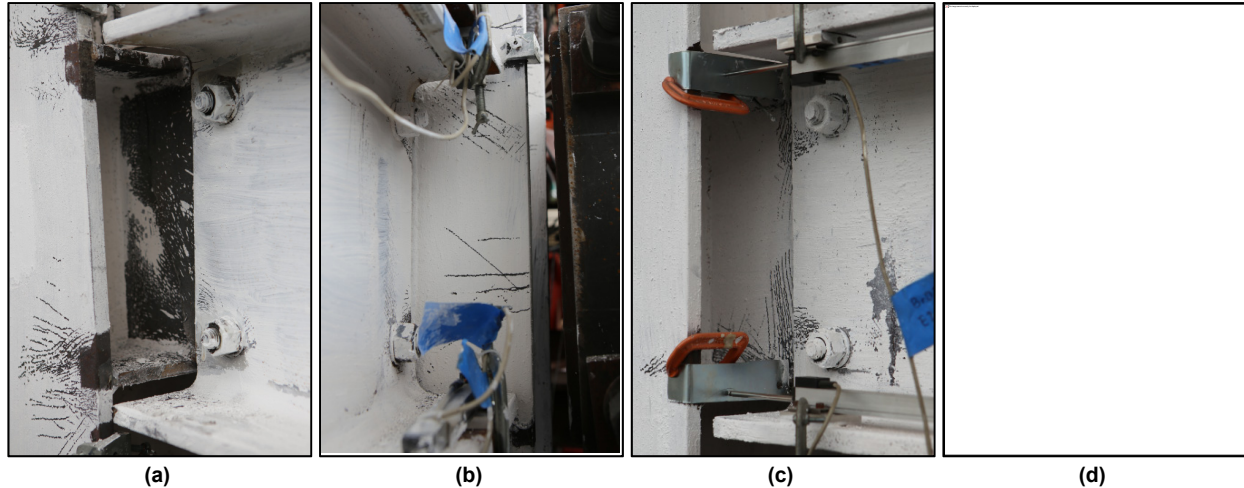


Figure 5.44 Damage to first-floor shear tabs (north face) at (a) the east gusset and (b) west gusset; and damage to second-floor shear tabs (north face) at (c) east gusset and (d) west gusset.

5.3.2 Summary of Key Observations for NCBF-B-2

This section will provide a summary for key event points of the test, as shown in Figure 5.45 below.

$\theta_R < \theta_y = 0.5\%$ Several elastic cycles were completed to check that the instrumentation was performing as expected. Original whitewash flaking from the NCBF-B-1 test was kept “as-is” and was unchanged for the NCBF-B-2 test. The east baseplate slipped on the first half-cycle to +0.4%. The test was paused, and the baseplates were welded to the floor beam. The test was resumed to the next peak cycle of -0.4%.

$\theta_R = \theta_y = 0.5\%$ The first-story east brace globally buckled on the first half cycle to +0.5%. During the second cycle to +0.5%, the first-story east brace locally buckled. Whitewash flaking was observed at all first-story gusset plates.

$\theta_R = 0.75\%$ The first-story west brace globally buckled on the first cycle to -0.75%. Initial cracks in the first-story east brace were observed on the second cycle to +0.75% before fracturing in that same half-cycle to +0.75%.

$\theta_R = 1.0\%$ The first-floor beam began to move upward and downward. Plastic hinging became apparent at the first-floor beam outside the middle connection.

$\theta_R = 1.5\%$ During the first half-cycle to +1.5%, the beam lowered and hit the center support of the test set-up. The test was paused until the center support could be modified for larger beam vertical displacements. The test was resumed to a roof drift amplitude of +1.5%.

The first-floor beam noticeably twisted out-of-plane on the resumed cycle to

+1.5%. During that same first cycle to -1.5%, a crack opened in the east first-floor shear tab, a small crack initialized at the first-story east gusset-to-base-plate weld, and local buckling was apparent at the first-floor beam to the east of the middle gusset plate.

$\theta_R = 2.0\%$

The second-story east column locally buckled above the second-story east gusset plate on the first half-cycle to 2.0%. Free-edge buckling was also observed at the first-story west gusset plate.

The second-story west column locally buckled above the second-story west gusset plate during the next half-cycle to -2.0%. The west column flange also buckled near the base plate. The crack at the first-story gusset-to-baseplate weld propagated through the entire gusset plate.

During the second cycle to +2.0%, the second-story east gusset plate punched through the west weak-axis column web.

$\theta_R = 2.5\%$

During the second cycle to +2.5%, the west column fractured just above the column to baseplate weld along the west flange and web. The east flange remained attached to the baseplate.

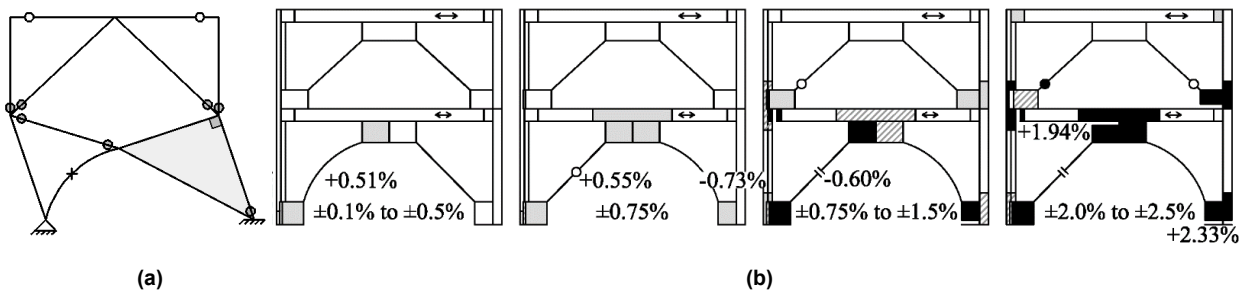


Figure 5.45 NCBF-B-2: (a) schematic of collapse mechanism and (b) hierarchy of damage.

5.4 NCBF-B-3SB: STRONGBACK RETROFIT

The third experimental test, NCBF-B-3SB, was conducted in three parts on September 24, 25, and 27, 2014, in the nees@berkeley laboratory. This specimen served as a strongback retrofit of the baseline vintage braced frames as described in Section 3.2.3. The global hysteretic behavior of the frame during the entire test can be seen in the hysteretic loop of Figure 6.36 in Chapter 6.

5.4.1 Event Points, Observations, and Photographs

Table 5.6 provides a brief narrative description of major observed events that occurred during the testing process. The points in the loading protocol where these events occurred are indicated in Figure 5.46. In most cases, the narrative description is based on observations made at the peak amplitude of a cycle. Thus, events described at a point may have occurred earlier during that cycle. All drift ratios provided in the table correspond to roof drift ratios, as specified in Section 4.3.1.1.

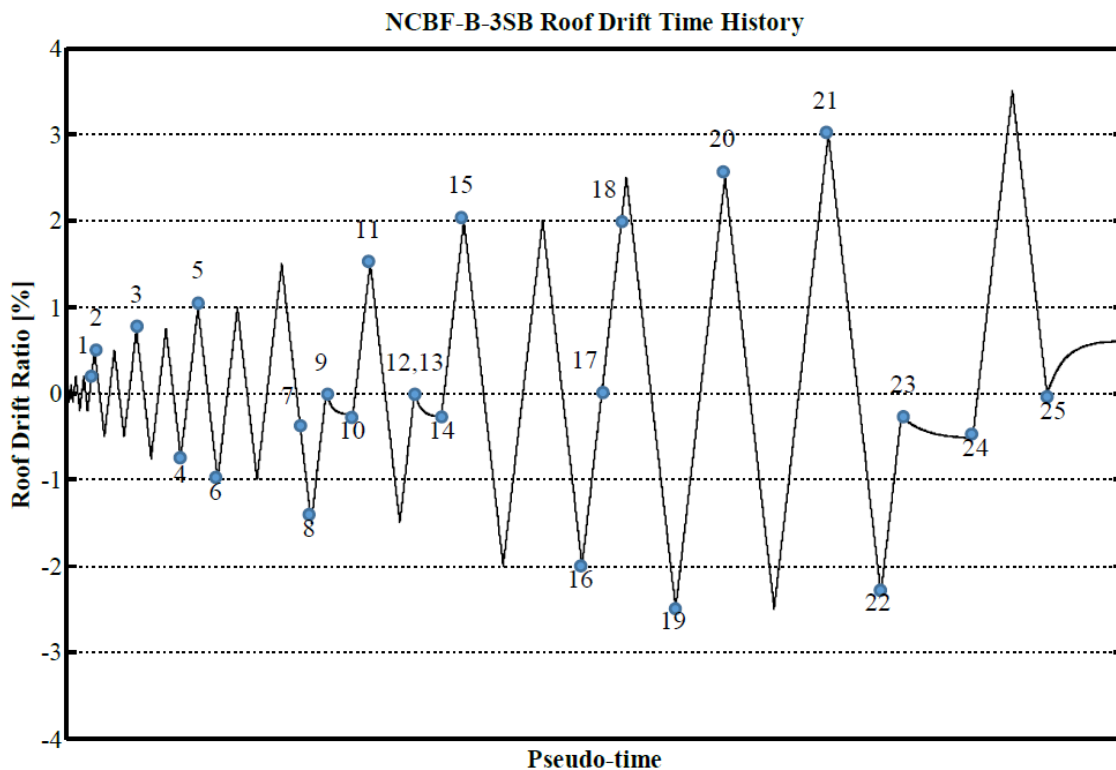


Figure 5.46 NCBF-B-3SB applied roof drift ratio during test.

Table 5.6 NCBF-B-3SB observations at various event points during the test.

Event point	Figure no.	Observations
0		Test begins 2014-10-24.
1		BRB yields (+0.21% drift ratio).
2	5.60(c)	Observed flaking in first-level beam flanges, near center where there is a stiffener at the west end of the gusset plate. Whitewash flaking on north side of east column flange near base.
3	5.65	Some whitewash flaking behind west weak-axis column web near roof gusset plate. Increased whitewash flaking at east column flange near base and center connection stiffeners. Slight increase in stiffness in hysteretic loop.
4	5.63(a)	First-level beam observed to move up and down ≈ 0.5 in. Visually noticeable extension of BRB.
5	5.47(b) and 5.58(a)	Plastic-hinge formation on south side of east beam near center connection. Extensive yielding (whitewash flaking) at first-floor east shear tab.
6		First-floor beam moves up ≈ 1 in. at its center.
7	5.47, 5.48, and 5.49	Loud bang noise heard. Fracture of first-floor east shear tab to beam weld (-1.43%).
8	5.47, 5.48, and 5.49	Both (2) erection bolts of first-floor east shear tab failed in shear (-3.41 in.).
9	5.50(a) and 5.53(a)	Hydraulic system shut down (at 0% drift ratio). First-floor east welded shear tab was repaired (replaced with new welded shear tab). Welds were added at roof east shear tab.
10		Test resumes on 2014-10-25 (residual roof drift ratio of -0.24%).
11	5.50(b) and 5.60(b)	Yielding in plate of first-floor east shear tab. Increased plastic hinging in first-floor east beam near center connection. Some whitewash flaking at net section of first-floor west brace.
12	5.50(c) and (d)	Observed crack in first-floor east shear tab-to-column weld near bottom and top of weld line. Defective weld (apparent lack of fusion between new shear tab and weld metal). Discussion with welder confirmed that the polarity was mistakenly reversed during the welding process.
13	5.52(a)	Hydraulic system shut down (at 0% drift ratio). Damaged shear tab was replaced with slotted beam-to-column shear tab connection detail.
14		Test resumes 2014-10-27 (residual roof drift ratio of -0.27%).
15	5.51(b) and (c), 5.59(d), 5.60(a), and 5.63(b).	Whitewash flaking at bottom BRB connection gusset region. Slight bolt bearing observed at edge of first-floor east shear tab. Mid-span of first-floor beam moved down ≈ 2.5 in. Vertical yield lines noted on external web of west weak-axis column and baseplate gusset connection. Whitewash flaking at flange of strong-axis column above gusset plate.
16	5.58(a), and 5.63(a)	Whitewash flaking at base of east column on exterior flange. Upper end of BRB appears to be extending more than lower end. More axial displacement between end cap relative to lower end BRB casing observed in compression over tension cycle [Figure 5.61(a)] possibly due to HSS/concrete restraining assembly slipping down BRB during tension cycle. Prominent yielding (whitewash flaking) on north and south face of beam web near central gusset plate in first-story east half-beam. More flaking on south face of beam web than north face.
17		BRB satisfies AISC 341-10 K3.4c testing requirement of $2\Delta_{bm}$.
18	5.58(b) and (c), and 5.61	Bulging in casing of BRB (+1.45% drift ratio). Drastic decrease in frame stiffness. BRB fails in compression well beyond design maximum compression capacity. Initial local buckling in first-floor east half beam top flange.
19	5.58(b) and (c) and 5.55(b)	Local buckling in first-floor east half-beam bottom flange at center gusset plate. BRB core appears to have ruptured in tension and no longer contributes to load capacity in negative (west) displacement loading cycle. East roof level shear tab fractures at shear tab to column shop weld.

Event point	Figure no.	Observations
20	5.54	Fractured shear tab at east roof beam bears on east column. Stiffening in hysteretic loop as BRB core touches in compression. Severe local buckling in first-floor east half-beam near center gusset plate.
21	5.57	Severe buckling of first-floor east half-beam web in plastic-hinge region near center gusset connection.
22	5.54	Roof shear tab completely pulls away from east column resulting in substantial vertical displacement at the east end of the roof beam. Further roof displacements in negative (west) direction deemed unsafe.
23		Hydraulic system shut down for inspection of specimen.
24		Test resumed for final +3.5% amplitude cycle.
25		Test ends (at 0% drift ratio). Residual roof displacement of +0.61%.

Table 5.7 NCBF-B-3SB: List of figures grouped by location.

Figure no.	Location captured by each photograph
5.47–5.55	Shear tabs
5.47–5.49	First-floor east shear tab (welded)
5.50	First-floor east shear tab (welded repair)
5.51 and 5.52	First-floor east shear tab (with slotted holes)
5.53 and 5.54	Roof east shear tab
5.55	Final damage state of all shear tabs
5.56–5.58	First-floor beam
5.59	Baseplates
5.61 and 5.63	BRB
5.60, 5.62, 5.64, and 5.65	Connection regions

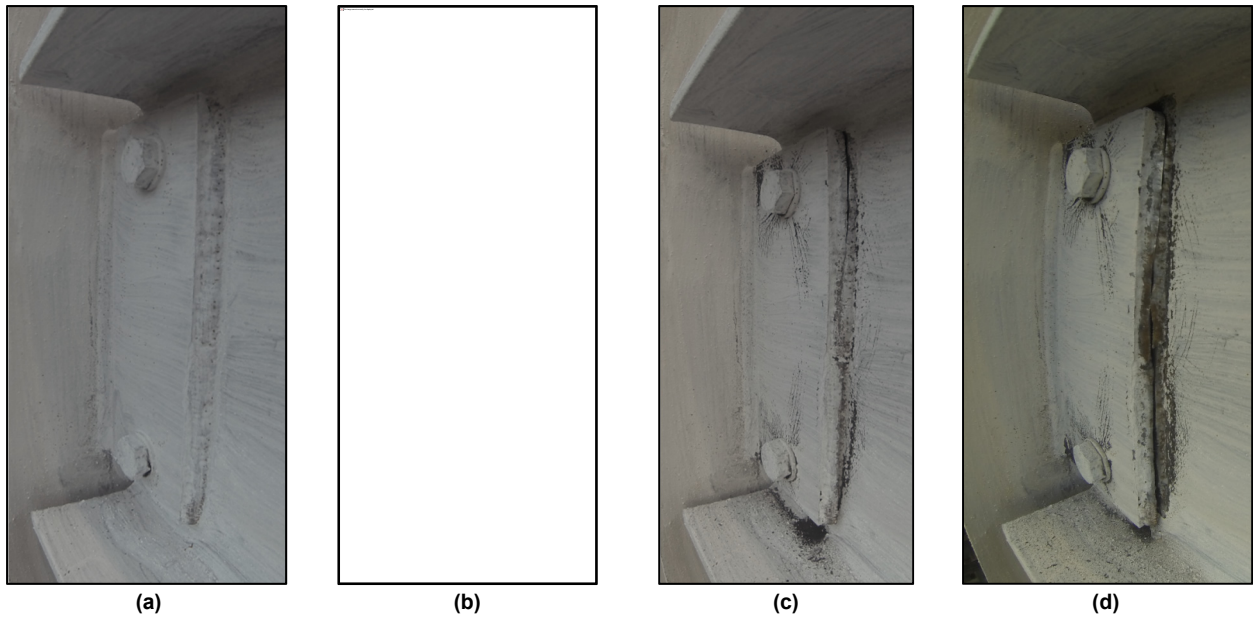


Figure 5.47 Damage sequence of first-floor east shear tab (welded): (a) initial state (0% drift ratio); (b) initial crack formation at bottom of weld (+1.5% drift ratio, first cycle); (c) crack propagation (+1.5% drift ratio, first cycle); and (d) full fracture of weld (-1.5% drift ratio, first cycle).

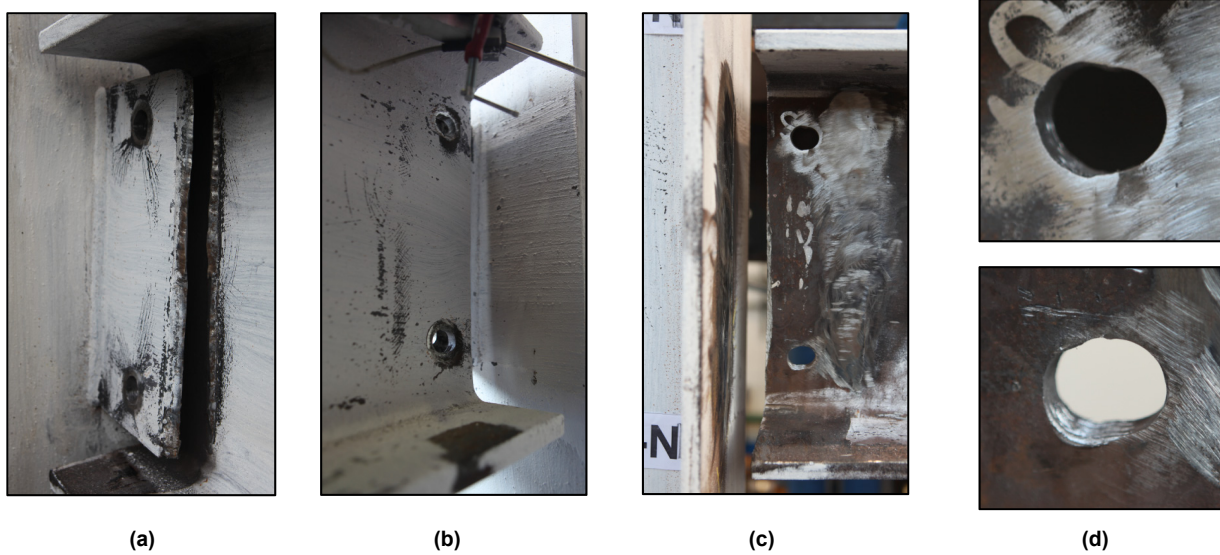


Figure 5.48 Final damage state of first-floor east shear tab (welded): (a) from north side; (b) from south side; (c) beam after removal of shear tab plate; and (d) erection bolt hole elongation.

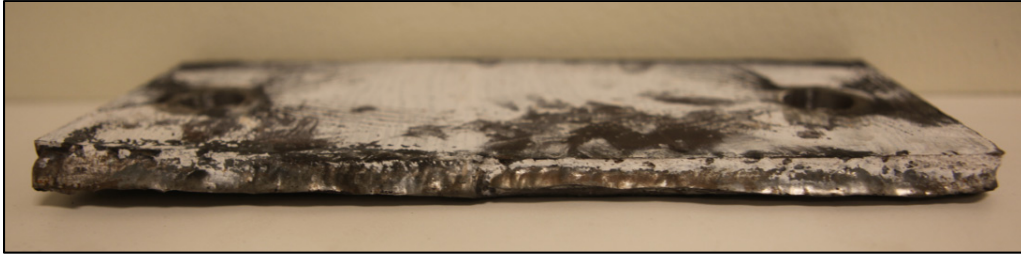


Figure 5.49 Final fracture state of weld of shear tab (welded) after plate removal.

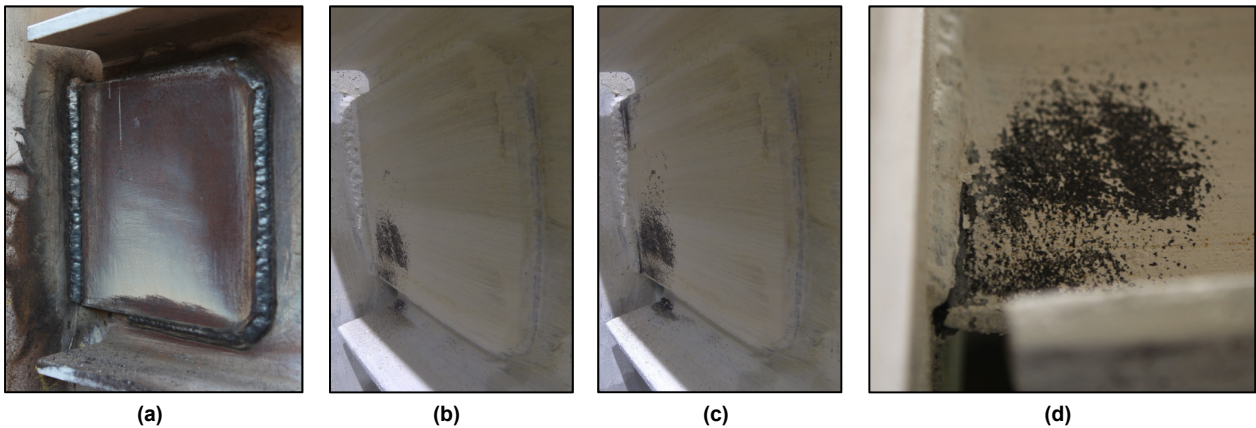


Figure 5.50 Damage sequence of first-floor east shear tab (welded repair): (a) after initial weld repair (part of 2014-10-25 repair); (b) gross section yielding of shear tab plate (+1.5% drift ratio, second cycle); (c) crack formation at top and bottom of shear tab near column weld line (-1.5% drift ratio, second cycle); and (d) close up of defective weld.

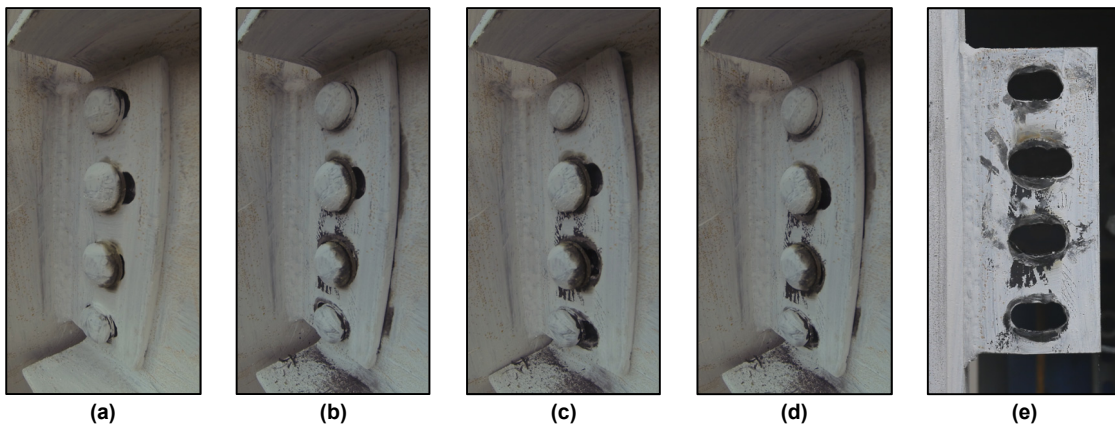


Figure 5.51 Damage sequence of first-floor east shear tab (with slotted holes): (a) initial state; (b) and (c) beam rotating through slotted holes (+3% and -3% drift ratio, respectively, first cycle); (d) final damage state; and (e) holes after demolition.

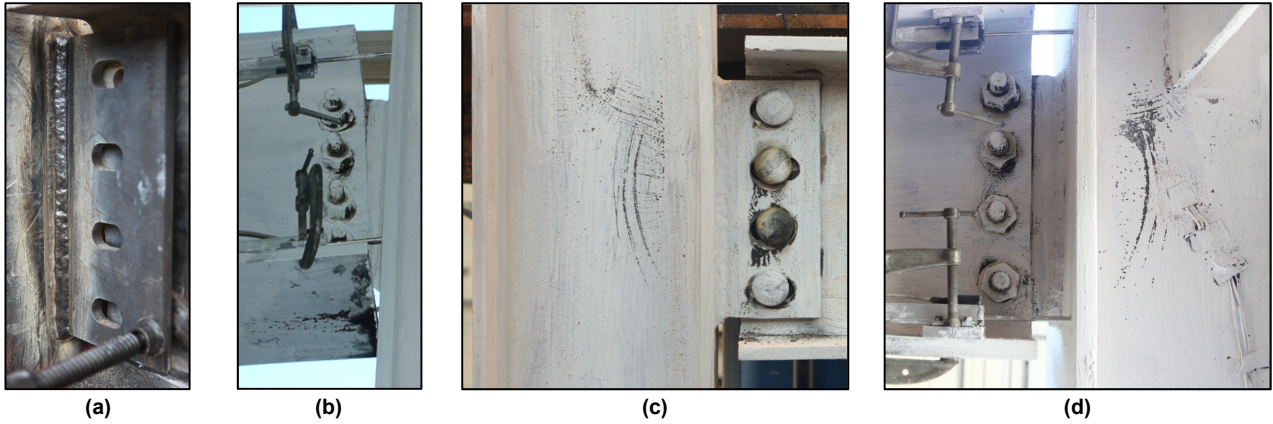


Figure 5.52 First-floor east shear tab (with slotted holes): (a) slotted plate repair (part of 2014-10-26 repair); original beam top and bottom holes in Figure 5.50; new middle standard size holes drilled in beam during repair; (b) rotation of beam through slotted holes (+3.5% drift ratio); and final damage state of slotted shear tab of (c) north face and (d) south face.

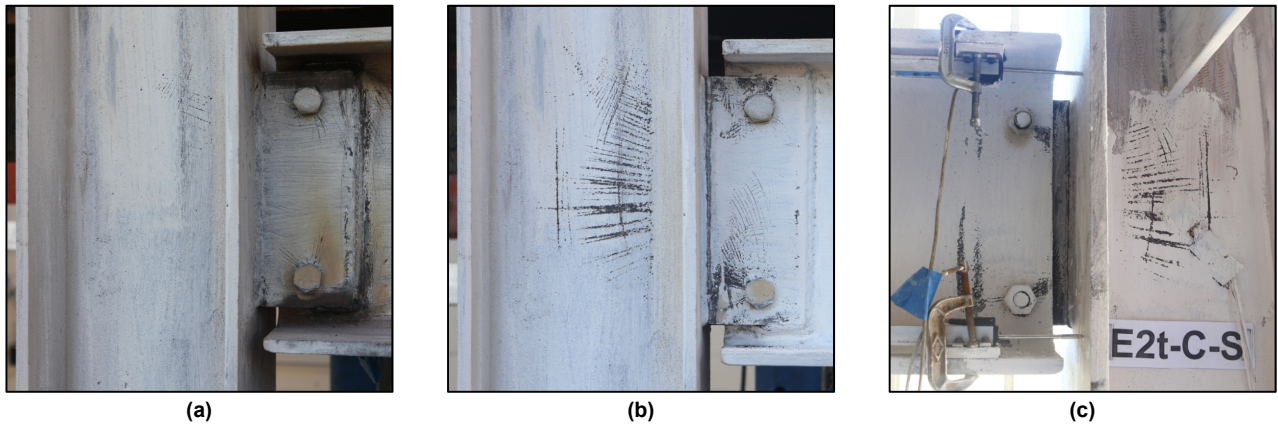


Figure 5.53 Second-floor east shear tab (welded): (a) additional welds added top and bottom of plate at plate-to-beam interface (part of 2014-10-25 repair); and final damage state of (b) north face and (c) south face.



(a)



(b)

Figure 5.54 Second-floor east shear tab behavior during test: (a) separation of shear tab and column during test (-2.5% drift ratio, first cycle); and (b) unstable behavior of beam after shear tab had slipped away from column (-3% drift ratio, first cycle).



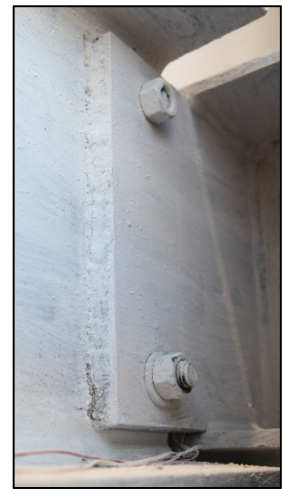
(a)



(b)



(c)

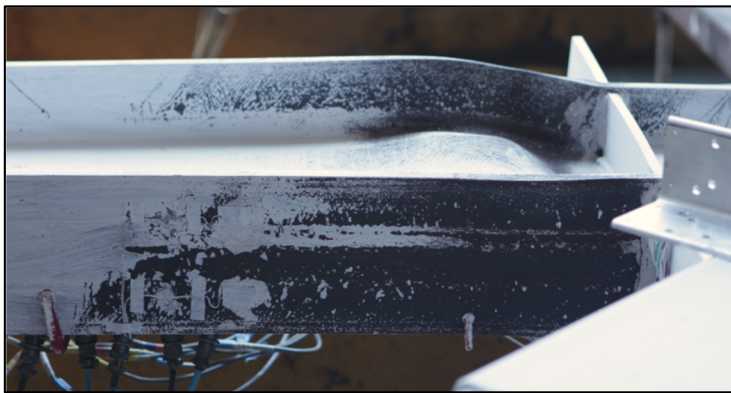


(d)

Figure 5.55 Shear tab final damage states: (a) first floor east; (b) second-floor east weld fracture; (c) first floor west; and (d) second floor west.



Figure 5.56 Final damage state of center connection and plastic hinging at first-floor east beam.



(a)

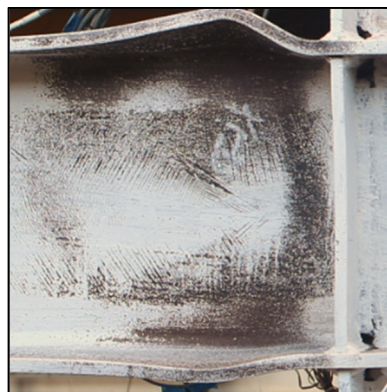


(b)

Figure 5.57 Web buckling of beam: (a) from below and (b) facing west.



(a)



(b)



(c)

Figure 5.58 East first-floor beam plastic hinge: (a) initial plastic hinge formation; local buckling at: (b) north face; and (c) south face.



(a)



(b)



(c)

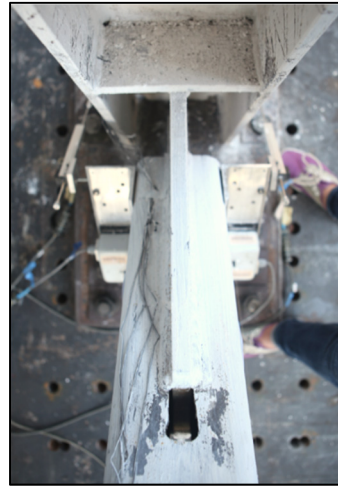


(d)

Figure 5.59 Damage at column base: (a) east column front; (b) west column front; (c) east column exterior; and (d) west column exterior.



(a)



(b)



(c)



(d)

Figure 5.60 Whitewash flaking: (a) west column flange at base gusset plate; (b) lower first-story east brace net reduced section region; (c) west edge stiffeners at center connection; and (d) lower second-story east brace net section region.



Figure 5.61 Final bulging of BRB casing.

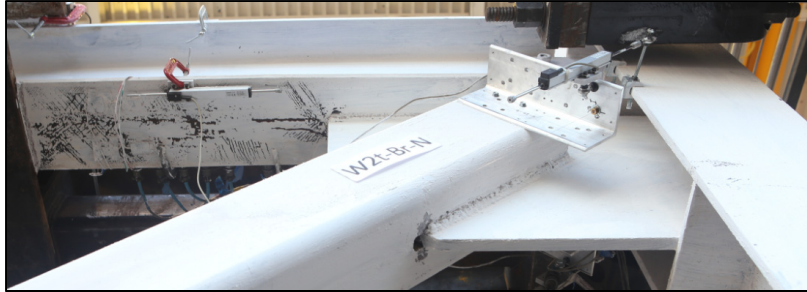


Figure 5.62 Final damage state of upper second-story east brace connection: whitewash flaking at lower flange of beam, net reduced section region of brace, and at flanges of column.

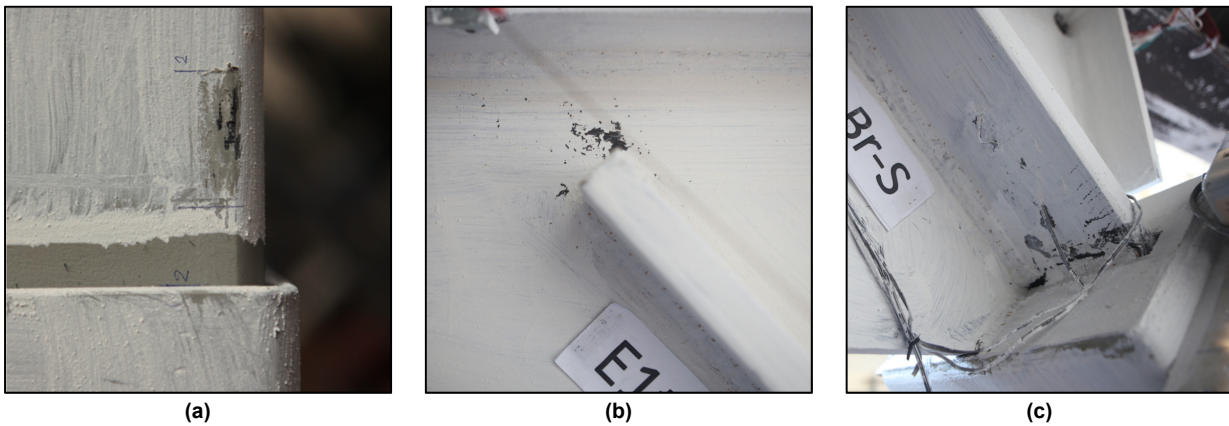


Figure 5.63 (a) Extension of BRB at 2% drift ratio; and (b) and (c) whitewash flaking at upper BRB gusset connection.



Figure 5.64 Whitewash flaking at west first-floor gusset (potentially left from original frame before strongback “retrofit”).



Figure 5.65 Whitewash flaking behind weak-axis west column at roof gusset plate.

5.4.2 Summary of Key Observations for NCBF-B-3SB

This section will provide a summary for key event points of the test, as shown in Figure 5.66 below.

$\theta_R = \theta_y = 0.2\%$ The first-story east BRB yields in compression on first half-cycle to +0.2%.

$\theta_R = 0.5\%$ Whitewash flaking at first-floor beam was observed near middle connection and near base of east column flange.

$\theta_R = 0.75\%$ The first-floor beam visibly began to move up and down.

$\theta_R = 1.0\%$ Extensive yielding could be seen at the first-floor east shear tab connection due to whitewash flaking in that region. Noticeable whitewash flaking was also observed to the east of the middle connection of the first-floor beam.

$\theta_R = 1.5\%$ The original shear tab connection design from NCBF-B-1 fractured at the first-floor east beam-to-shear tab weld on the first cycle to -1.5%. The test was paused, and the shear tab was replaced with a new shear tab with a larger area for gross section yielding. The test was resumed to the next peak cyclic amplitude of +1.5%.

During the second cycle to -1.5%, the shear tab exhibited noticeable cracks in the new welds that were later deemed to be from defective field welds. The test was paused and the shear tab was replaced with a shear tab connection with slotted holes. The test was resumed to the next peak cyclic amplitude of +2.0%.

$\theta_R = 2.0\%$ At the end of the second cycle of 2.0%, the BRB exceeded a lateral drift ratio requirement of $2\Delta_{bm}$ of 2.0% defined by the AISC 341-10 testing criteria.

Increased whitewash flaking was further observed near the plastic-hinge region of the first-floor beam to the east of the middle gusset plate connection.

$\theta_R = 2.5\%$

During the first half-cycle to +2.5%, a noticeable bulging occurred in the outer HSS casing of the BRB in conjunction with a decrease in the frame's compression capacity, as shown in Figure 6.39. During the same cycle to -2.5%, the BRB displayed negligible tension capacity, as shown in Figure 6.42.

During the next half-cycle to -2.5%, the east roof column-to-shear tab weld fractured. Local buckling was observed at the plastic-hinge region of the first-floor beam to the east of the middle connection.

$\theta_R = 3.0\%$

Severe local buckling appeared at the plastic-hinge region of the first-floor beam.

On the first half-cycle to -3.0%, the fractured roof shear tab pulled away from the beam, and the test was deemed unsafe for cycles in the negative direction. The test was paused before being resumed to a half-cycle at +3.5%.

$\theta_R = +3.5\%$

After the final half-cycle to +3.5%, the test ended

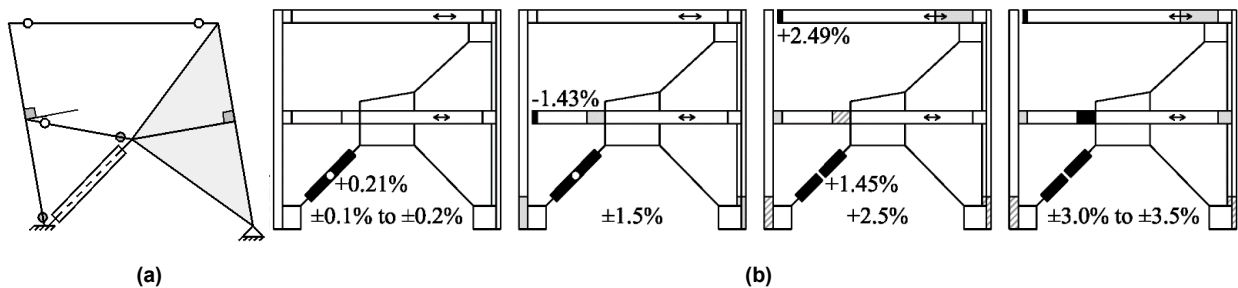


Figure 5.66 NCBF-B-3SB: (a) schematic of collapse mechanism and (b) hierarchy of damage.

6 Analysis of Test Results

6.1 INTRODUCTION

This chapter discusses the test results and contains plots derived from the instrumentation used to monitor the test specimen. Definitions for the labels used to describe locations on the test specimens and certain behaviors used throughout this chapter can be found in Table 6.1.

Response history plots not shown in this chapter can be found in Appendix A for the first NCBF-B-1 test specimen, Appendix B for the second NCBF-B-2 test specimen, and Appendix C for the third NCBF-B-3SB test specimen. Maximum and minimum values are shown in the pseudo-histories in each of these appendices. Definitions and values for member capacities, M_p , M_y , C_n , T_n , C_{max} , and T_{max} , labeled on the plots are called out in Tables A.1, B.1, and C.1 for each test specimen.

Table 6.1 Legend for label definitions.

Label	Definition	Label	Definition
1F	First floor / story	Δ_R	Roof drift amplitude
2F	Second floor / story	Δ_1	First-story drift
E	East side	Δ_2	Second-story drift
W	West side	Δ_y	Roof drift at yield
N	North side	Δ_{by}	Yield drift of BRB
S	South side	Δ_{bm}	Design drift of 1.0%
T	Tensile load	θ_R	Roof drift ratio
C	Compression load	θ_1	First-story drift ratio
Y	Yielding	θ_2	Second-story drift ratio
B	Global buckling		
LB	Local buckling		
Fr	Fracture		

6.2 NCBF-B-1: BASELINE TEST SPECIMEN

Table 6.2 shows the legend of symbols used to describe significant events in the plots for the NCBF-B-1 test. Values for these points are detailed in Table 6.5. The global hysteretic behavior of the frame during the entire test can be seen in the hysteretic loop of Figure 6.1, and

documentation of the events during the test can be found in Section 5.2. A breakdown of the hysteretic cycles at each peak roof drift amplitude can be found in Figure 6.2.

Table 6.2 NCBF-B-1 legend of symbols for significant event points.

○	2F E Brace Buckling
○	2F W Brace Buckling
*	2F W Brace Fracture
○	Frame Reloading
*	2F E Brace Fracture
●	Test End

6.2.1 Global Behavior

The baseline test, NCBF-B-1, was representative of a vintage braced frame. Though minor flaking was observed at the column web and gusset near the east and west base plate, there was little other observable yielding prior to buckling of the second-story braces. The inelastic behavior of the NCBF-B-1 test specimen was initialized by local buckling of the second-story east brace at +0.44% roof drift ratio when the brace was in compression. The second-story west brace then buckled during the same cycle at -0.41% roof drift ratio when the loading was reversed, and the opposite west brace was put into compression.

The braces exhibited immediate local buckling with little indication of global buckling behavior; Figure 6.2 shows a breakdown of the system hysteretic loop at each cyclic amplitude. The relationship between the roof drift ratio and base shear appears linear until the cycle at amplitude 0.5%, when the first brace exhibits local buckling. This local buckling resulted in approximately a 40% decrease in load-carrying capacity, as shown in Table 6.4, the hysteretic loops of subsequent cycles, and in Table 6.3, which shows the peak base shears during each cycle and the ratio between the peak base shear of that cycle, V , to the maximum base shear, V_{max} , observed during the entire test. At brace buckling, the base shear was equal V_{max} , and this ratio was equal to 1.0. After brace buckling, this ratio decreased from 1.0 as the brace strength degraded upon subsequent cycles. The difference in system behavior before and after both braces buckled can be seen in Figures 6.3 and 6.4.

Damage was concentrated in the second story after the first brace buckled, forming a weak story in the second story, as shown in the story hysteretic behavior of Figure 6.5 and the schematic of Figure 5.19(a). The first story exhibits a nearly linear relationship, indicating roughly elastic behavior, while the second story provides most of the system's energy-dissipation capacity after brace local buckling was initiated.

The system exhibited a decrease in strength at a cyclic amplitude of 1.0% upon brace fracture, corresponding to approximately 50% decrease in strength before and after brace fracture. The base shear was reduced to 30% of V_{max} ; see Table 6.4. The second-story west brace fractured in tension upon the first cyclic amplitude to +1.0% at +0.9% roof drift ratio. The opposite east brace then fractured in tension at -0.87% roof drift ratio on the next half-cycle to -1.0%.

The test was ended with small residual drifts in the second story, as can be seen by the "Test End" marker in Figures 6.1 and 6.5. Due to the nearly elastic behavior of the remainder of

the frame, the test was stopped after both second-story braces fractured. This allowed for reuse of the undamaged portion of specimen for testing of NCBF-B-2.

Table 6.3 NCBF-B-1 peak base shear at each cycle.

Cycle	Roof drift amplitude	V ¹	V/V _{max}	Event	Roof drift amplitude	V ¹	V/V _{min}	Event
(n)	(%)	(kips)			(%)	(kips)		
1	+0.1	105.7	0.27		-0.1	-105.8	0.27	
2	+0.1	107.0	0.28		-0.1	-106.0	0.27	
3	+0.2	210.5	0.54		-0.2	-221.7	0.57	
4	+0.2	219.9	0.57		-0.2	-221.8	0.57	
5	+0.3	289.9	0.75		-0.3	-304.3	0.79	
6	+0.3	302.0	0.78		-0.3	-305.9	0.79	
7	+0.4	367.4	0.95		-0.4	-381.7	0.99	
8	+0.4	374.3	0.97		-0.4	-375.4	0.97	
9	+0.5	386.7	1.00	2F E (LB)	-0.5	-387.1	1.00	2F W (LB)
10	+0.5	239.0	0.62		-0.5	-246.7	0.64	
11	+0.75	279.4	0.72		-0.75	-283.6	0.73	
12	+0.75	267.5	0.69		-0.75	-270.9	0.70	
13	+1.0	250.9	0.65	2F W (Fr)	-1.0	-236.9	0.61	2F E (Fr)
$V_{max} =$		386.7	kips		$V_{min} =$	-387.1	kips	

¹ Max base shear in each half-cycle.

Table 6.4 NCBF-B-1 approximate base shear after significant damage events.

Cycle	Roof drift amplitude	V	V _L ¹	V _L /V _{max,min}	Event
(n)	(%)	(kips)	(kips)		
9	+0.5	386.7	232.1	0.60	2F E (LB)
9	-0.5	-387.1	-253.1	0.65	2F W (LB)
13	+1.0	250.9	122.3	0.32	2F W (Fr)
13	-1.0	-236.9	-117.9	0.30	2F E (Fr)

¹ Approximate base shear after significant decrease in maximum V in a half-cycle.

Table 6.5 NCBF-B-1 description of event points.

Event Point	Event	Amplitude	Cycle no.	θ_R	θ_1	θ_2
		(%)		(%)	(%)	(%)
1	2F E brace (LB)	+0.5	1	+0.44	+0.41	+0.46
2	2F W brace (LB)	-0.5	1	-0.41	-0.41	-0.42
3	2F W brace (Fr)	+1.0	1	+0.90	+0.20	+1.67
5	2F E brace (Fr)	-1.0	1	-0.87	-0.22	-1.58

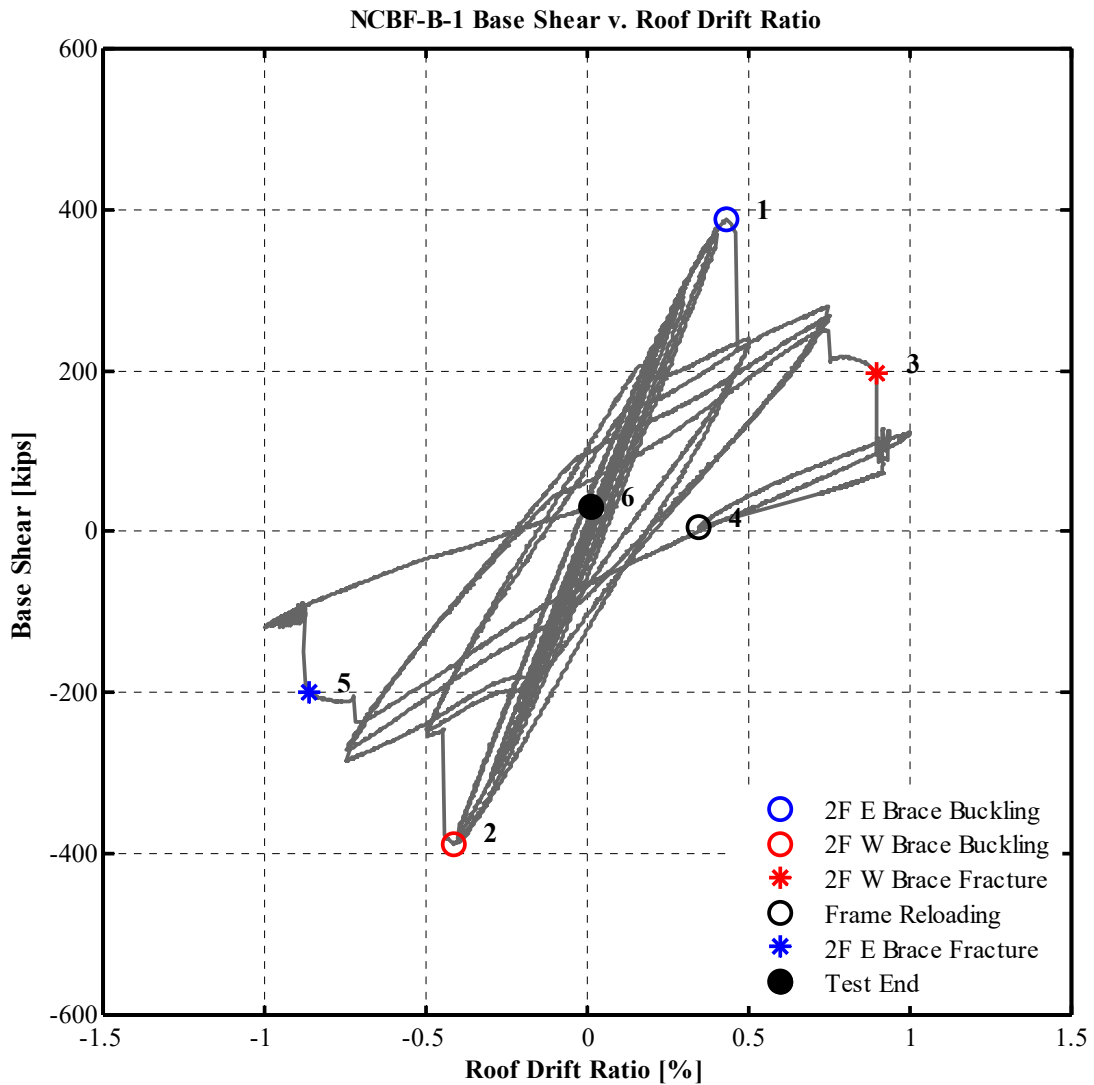


Figure 6.1 NCBF-B-1 base shear versus roof drift ratio.

Table 6.5 NCBF-B-1 description of event points.

Event Point	Event	Amplitude	Cycle no.	θ_R	θ_1	θ_2
		(%)		(%)	(%)	(%)
1	2F E brace (LB)	+0.5	1	+0.44	+0.41	+0.46
2	2F W brace (LB)	-0.5	1	-0.41	-0.41	-0.42
3	2F W brace (Fr)	+1.0	1	+0.90	+0.20	+1.67
5	2F E brace (Fr)	-1.0	1	-0.87	-0.22	-1.58

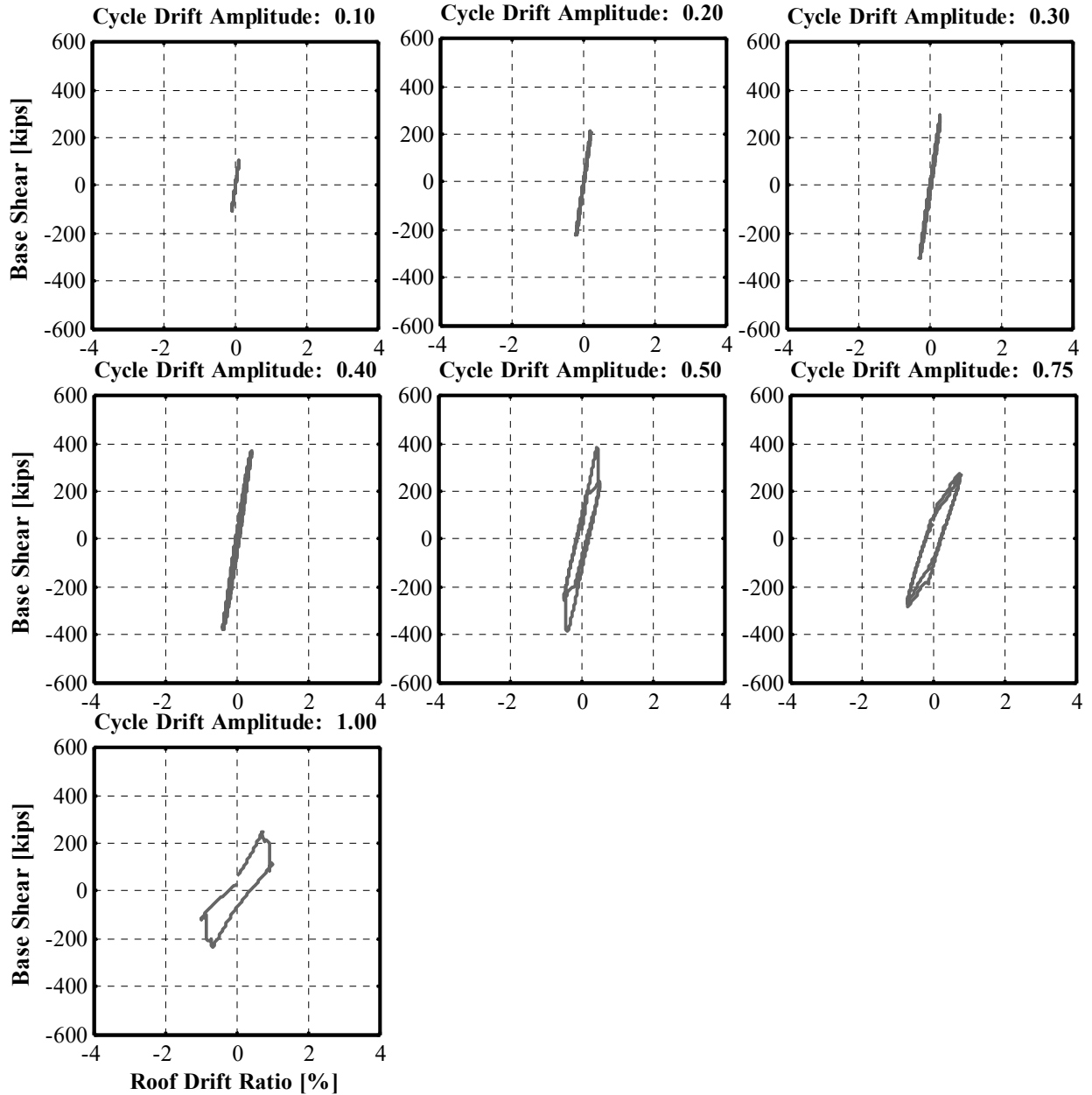


Figure 6.2 NCBF-B-1 hysteretic loop breakdown by cyclic amplitude.

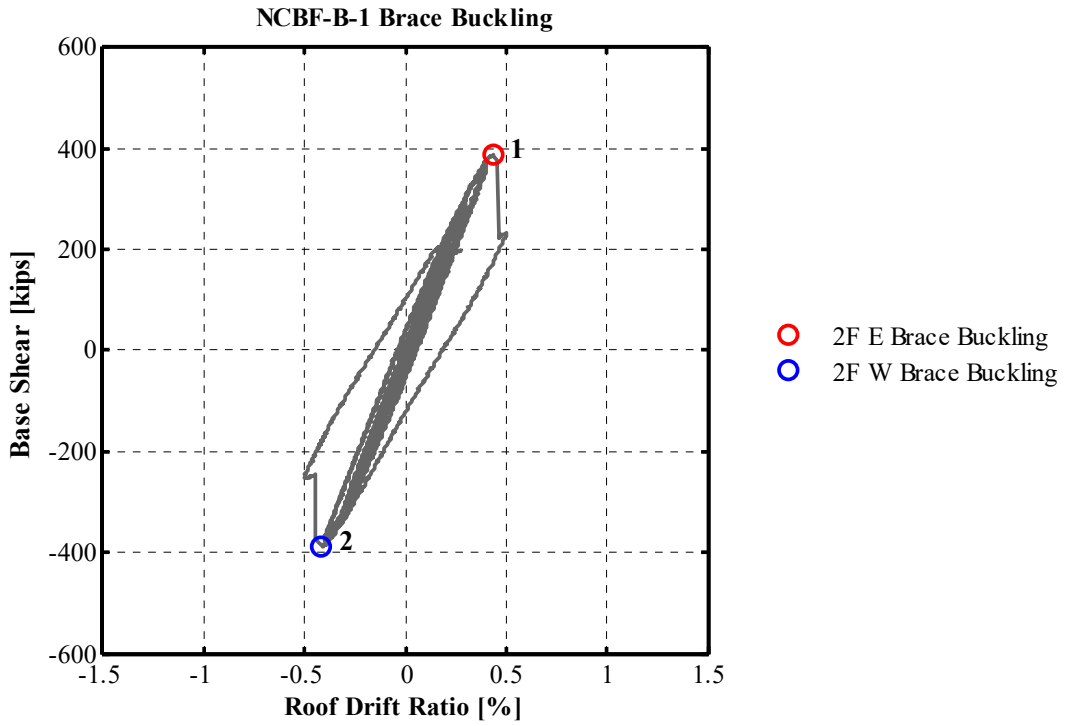


Figure 6.3 NCBF-B-1 base shear versus roof drift ratio of brace buckling behaviour.

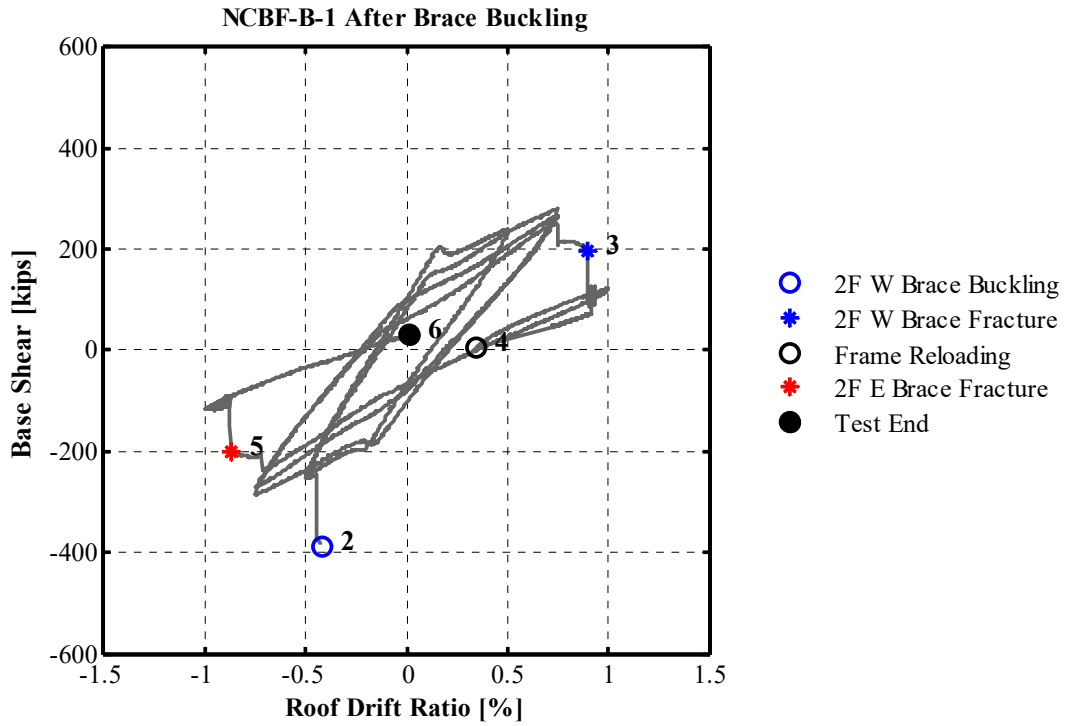


Figure 6.4 NCBF-B-1 base shear versus roof drift ratio after second-story west brace buckling (at -0.41% on first cycle to 0.5%).

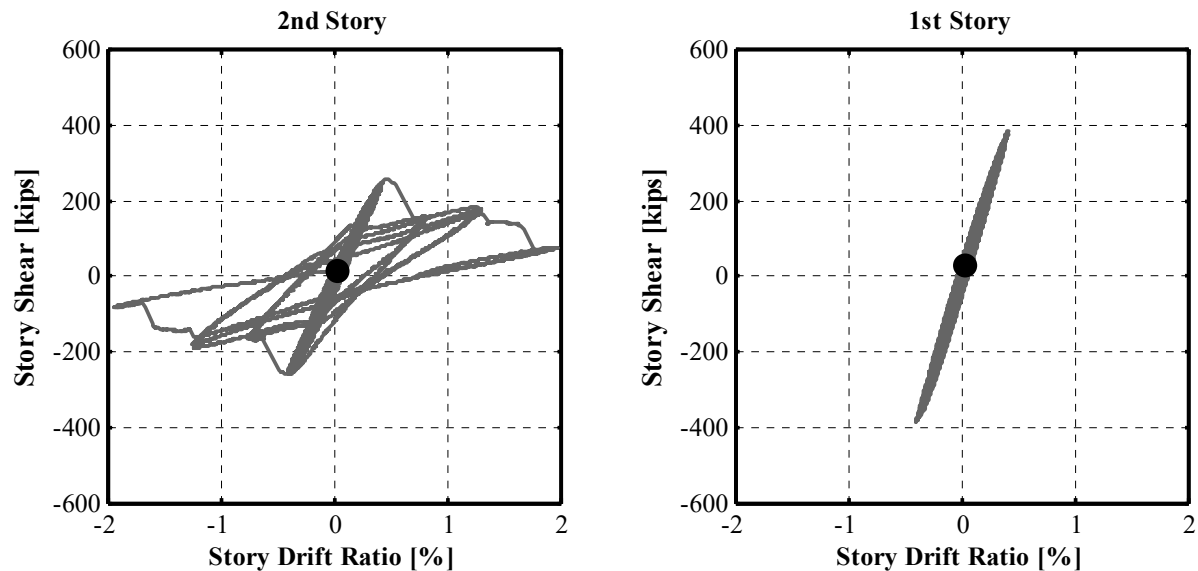


Figure 6.5 NCBF-B-1 story shear versus story drift ratio.

6.2.2 Hollow Steel Brace Response

Even though Figure A.3 indicates that the first-story braces may have been close to their buckling capacity, neither of the first-story braces buckled in compression or exhibited significant yielding in tension. The first-story braces provided little energy dissipation after initial buckling of the second-story east brace. This behavior can be seen in the nearly linear plots of the first-story braces in Figure 6.9.

Both upper-story braces buckled in opposite directions from one another. The east brace displaced a maximum of 4.7 in. to the north, and the west brace displaced a maximum of 3.6 in. to the south before fracture; see Figures 6.10 and A.4. The second-story braces did not exhibit tensile yielding, as shown in Figures 6.9 and 6.10. After local buckling, the strength of both second-story braces decreased upon each repeated cycle. The compression capacity of the braces decreased to approximately 40% of the initial buckling capacity during the loading cycle after local buckling initiated. The brace post-buckling strength continued to decrease upon subsequent compression cycles, as shown in the C/P_{cr} ratio of Table 6.7. The variable, C , is the peak compression demand in a cycle, and P_{cr} is the peak buckling load estimated during the test.

6.2.2.1 Hollow Brace Local Buckling and Fracture

The braces fractured when the brace was in tension after four consecutive cycles following the onset of local buckling. Local buckling in the tubes was severe, as shown in Figure 6.6(a). The inner “flange” of the hollow steel tube buckled inward while the “webs” of the tube buckled outward, causing high strain concentrations at the corners of the steel section. This behavior is similar to the local buckling behavior for hollow tubular sections described in Section 2.2.2.2.1.

The local buckling and fracture behavior of the west brace is shown in the photographs of Figure 5.3. Brace fracture followed quickly after local buckling. Cracks formed at the corners of the steel tube before propagating along the length of one “flange” and through the entire brace section. These cracks initiated on the concave side of the buckled brace at the location of local

buckling. Photographs of the final fracture state of the brace can be seen in Figures 5.4, 5.5, 6.7, and 6.8. While the photographs are similar for both braces, the second-story west brace shows some later damage due to the fractured edges coming in contact when the brace was reloaded in compression. This is possibly the cause of the corner tear evident in Figure 6.6(c).

6.2.2.2 Brace Design Comparison

The solid black lines in Figures 6.9 and 6.10 designate the brace tension capacity, T_n , and compression capacity, C_n , calculated from AISC 360-10 [2010] using the yield strength found from the coupon tests. These values are called out in Table 6.6. The variable, C_n , is calculated using an equivalent length factor, k , of 1.0.

The elastic stiffness, K , of each brace was calculated by fitting a linear relationship to elastic cycles at 0.1% roof drift ratio. The axial deformation at brace buckling D_{cr} was estimated from the following equation, assuming bilinear behavior:

$$D_{cr} = P_{cr} / K \quad (6.1)$$

A new effective length factor, k , was back-calculated from the P_{cr} value, which was estimated from the experimental data using the length of the bracing member from the shop drawings and the equations for inelastic buckling from AISC 360-10 [2010]. From this estimate, it can be inferred that the strong- and weak-axis columns—and their respective the shorter and longer gusset plates—influenced the effective length factors of the braces.

Note that the axial force in the braces is an estimated quantity, which is derived from strain gages located at the quarter points of the braces and a modulus of elasticity calibrated to the horizontal component of the story shear minus the column shears; see Section 4.3.1.2. As such, specific values for the brace axial force can describe relative trends of estimated brace behavior but may not represent the exact axial load of the braces during the experiment.

Table 6.6 NCBF-B-1 brace critical variables.

Brace Location	P_{cr}	K	D_{cr}	T_n^1	C_n^2	k
	(kips)	(kips/in.)	(in.)	(kips)	(kips)	
First-story east brace	– ³	– ³	– ³	319	259	– ³
First-story west brace	– ³	– ³	– ³			– ³
Second-story east brace	187	862	0.22	209	164	0.7
Second-story west brace	161	834	0.19			1.0

¹ Tension capacity using the tensile coupon yield strength as specified by AISC 360-10 [2010].

² Compression capacity using the coupon yield strength with $k = 1$ as specified by AISC 360-10 [2010].

³ Brace did not buckle.

Table 6.7 NCBF-B-1 brace compression strength degradation.

		2F east brace				2F west brace			
Cycle	Amplitude	T^1	C^2	C/P_{cr}	Event	T^1	C^2	C/P_{cr}	Event
(n)	(%)	(kips)	(kips)			(kips)	(kips)		
3	0.2	33.4	-74.9	0.40		72.2	-71.0	0.44	
4	0.2	70.8	-75.3	0.40		70.6	-71.2	0.44	
5	0.3	70.2	-111.7	0.60		102.7	-102.4	0.64	
6	0.3	96.6	-113.4	0.61		100.9	-103.7	0.64	
7	0.4	96.8	-157.3	0.84		139.3	-145.5	0.90	
8	0.4	133.1	-161.5	0.86		138.2	-146.6	0.91	
9	0.5	131.3	-187.1	1.00	2F E (LB)	153.5	-160.9	1.00	2F W (LB)
10	0.5	136.2	-72.0	0.38		95.8	-65.4	0.41	
11	0.75	97.5	-50.0	0.27		141.1	-51.0	0.32	
12	0.75	125.5	-27.5	0.15		129.6	-21.8	0.14	
13	1.0	119.7	-22.2	0.12		118.5	0.0	0.00	
		$P_{cr}^3 =$	-187.1	kips			$P_{cr}^3 =$	-160.9	kips

¹ Maximum tension force in each cycle.

² Maximum compression force in each cycle.

³ Approximate critical buckling load.

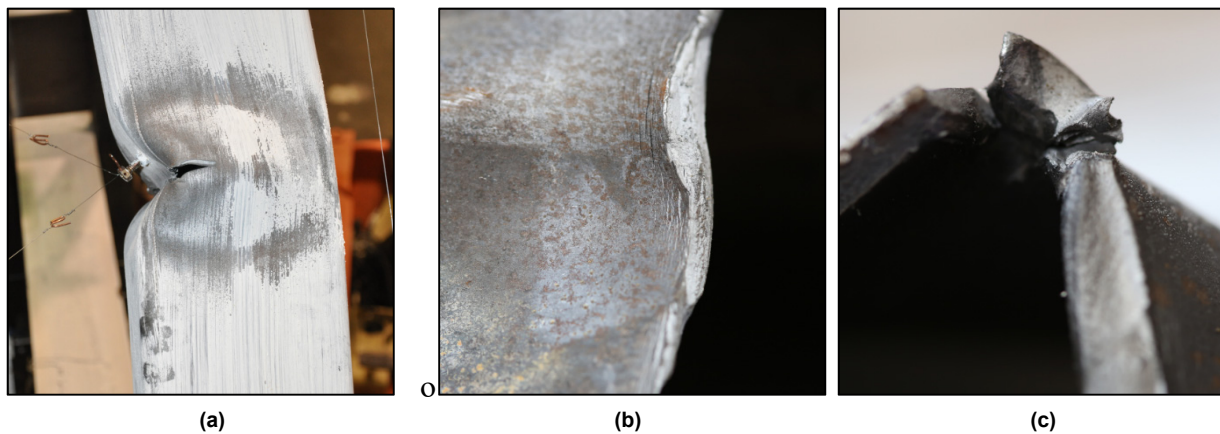


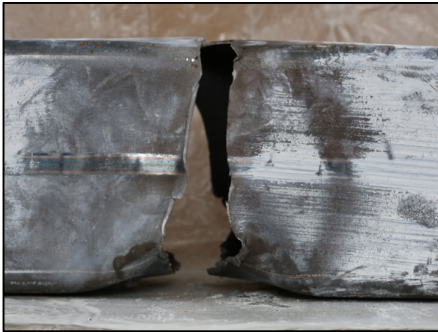
Figure 6.6 Second-story east brace: (a) crack propagation; (b) second-story west brace low-cycle fatigue striations; and (c) corner tear, possibly upon load reversal.



(a)



(b)



(c)



(d)

Figure 6.7 Second-story east brace section fracture: (a) transverse section; and (b)-(d) longitudinal section.



(a)



(b)



(c)



(d)

Figure 6.8 Second-story west brace section fracture: (a) transverse section; and (b)-(d) longitudinal section.

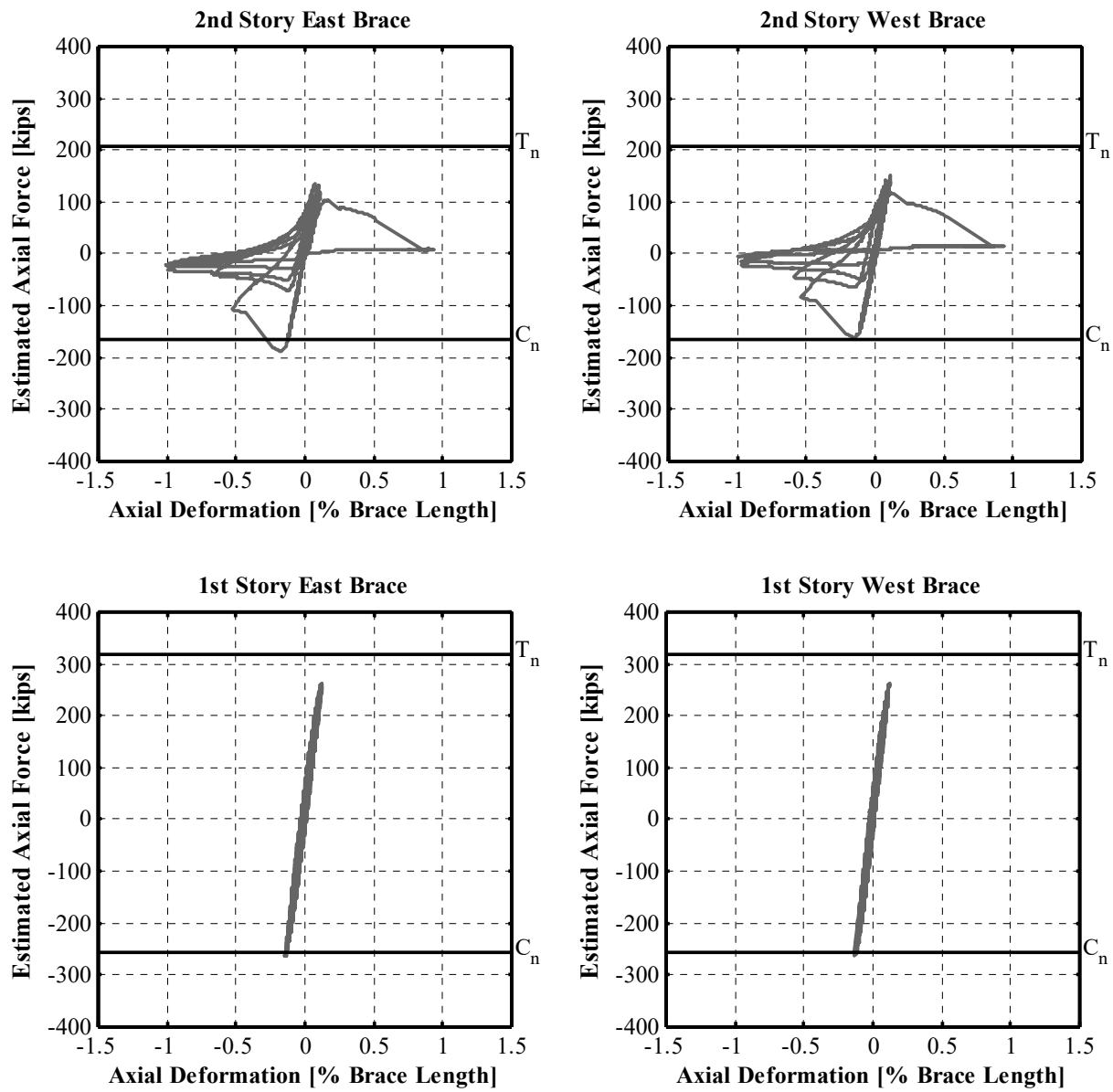


Figure 6.9 NCBF-B-1 estimated brace axial force versus axial deformation (brace length is the work-point-to-work-point length).

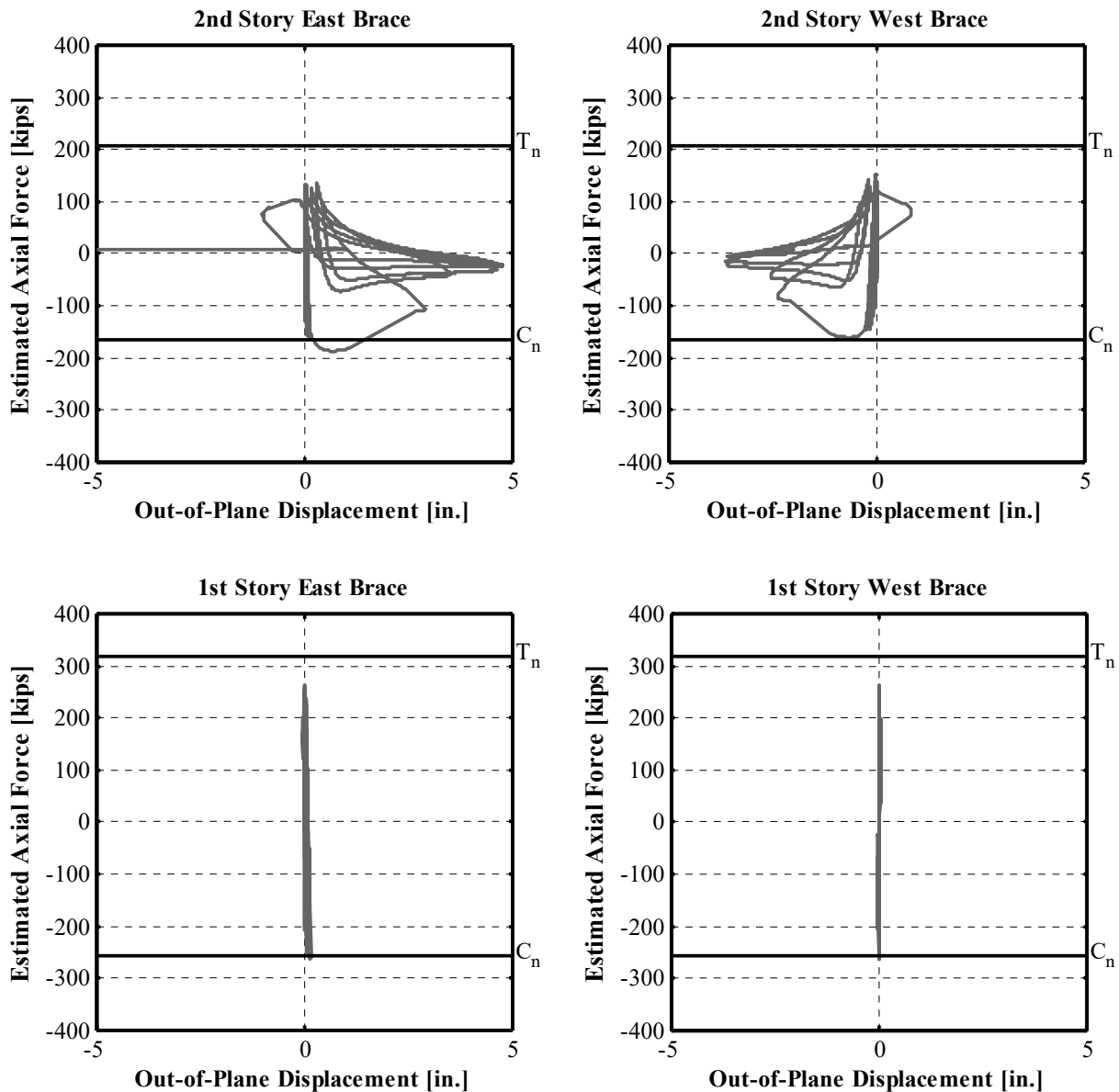


Figure 6.10 NCBF-B-1 estimated brace axial force versus out-of-plane displacement.

6.2.3 Beam Response

The beam exhibited minor yielding and whitewash flaking at the roof level above the second-story buckled braces and remained primarily elastic at the first floor above the first-story braces. The maximum displacement of the weak roof beam was -0.94 in.; see Figures 6.12 and A.16. The majority of this motion was downward in response to the unbalanced load due to brace buckling in the second story; as shown in Figures 6.11 and A.15. Residual vertical displacements of the beam at the end of test were considered minor. The rapid deterioration and fracture of the braces are believed to have contributed to the small vertical displacement of the roof beam.

The estimated moments at the ends of the east and west first-floor half-beams are shown in Figure 6.14. These moments were estimated according to Section 4.3.1.4. Small moments developed near the end beam-column connections. Moments to either side of the middle connection are moderately large but still below the yield moment of the beam, M_y . Minor whitewash flaking was observed near the middle gusset plate; see Figure 5.17.

The rotations at the second-floor beam ends corresponded roughly to the story rotation of the second story; see Figure 6.13. Maximum rotations were about 0.02 radians at their peak. The rotations at either end of the roof beam were opposite and nearly symmetric as the beam was pulled down by the unbalanced load.

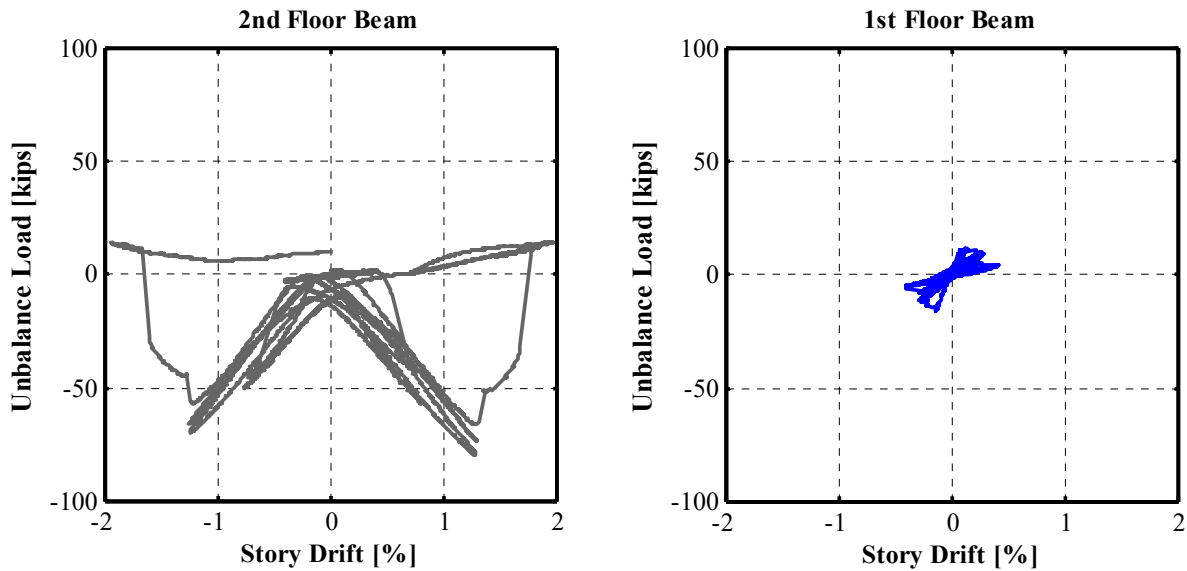


Figure 6.11 NCBF-B-1 beam estimated unbalanced load versus story drift.

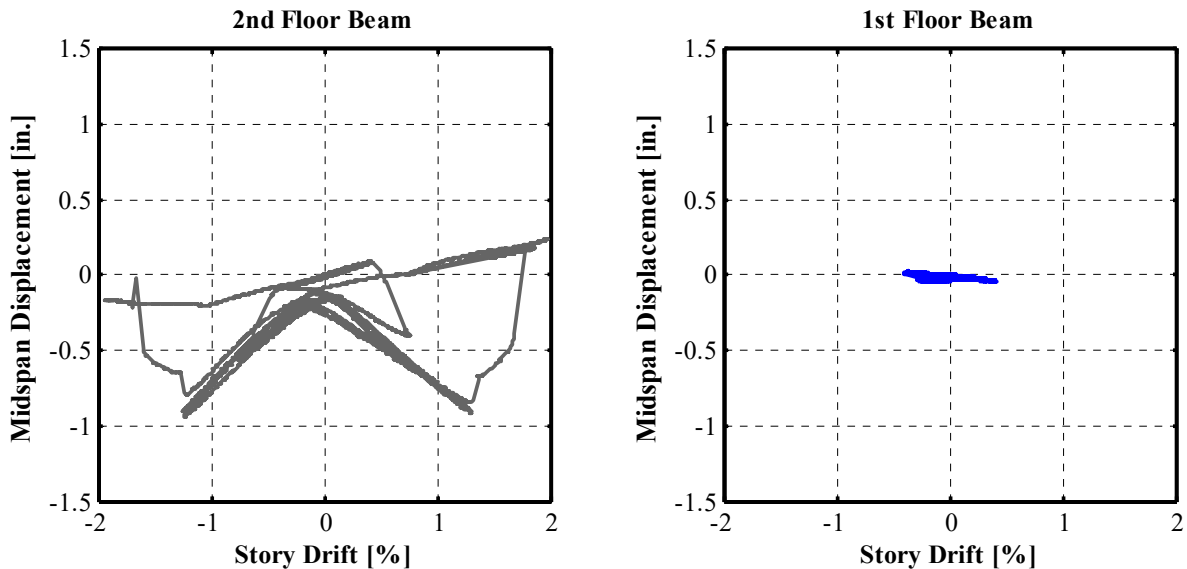


Figure 6.12 NCBF-B-1 beam vertical mid-span displacement versus story drift. Note: Unbalanced load is positive upward.

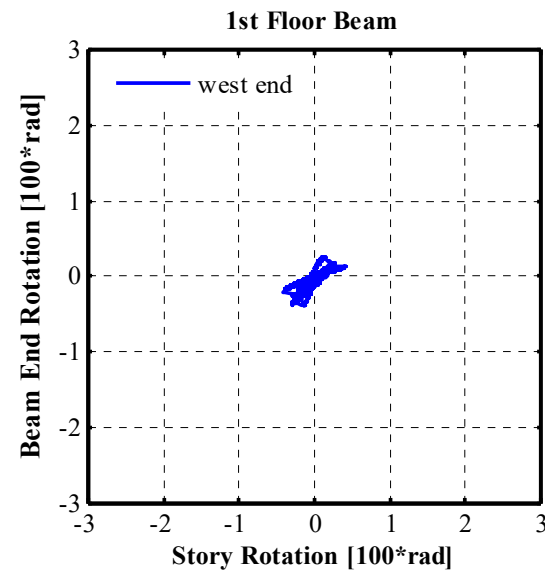
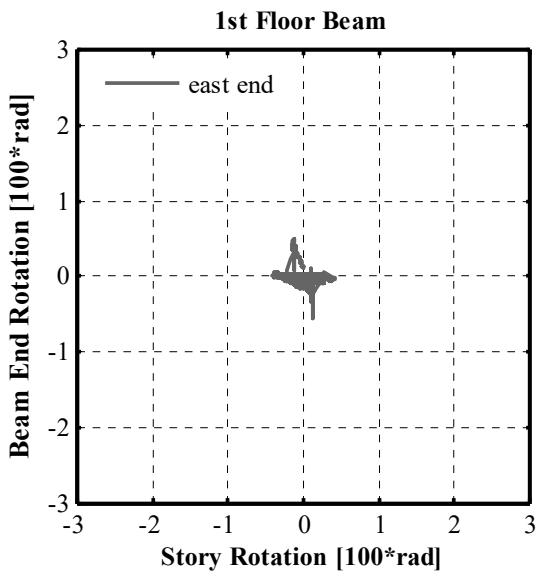
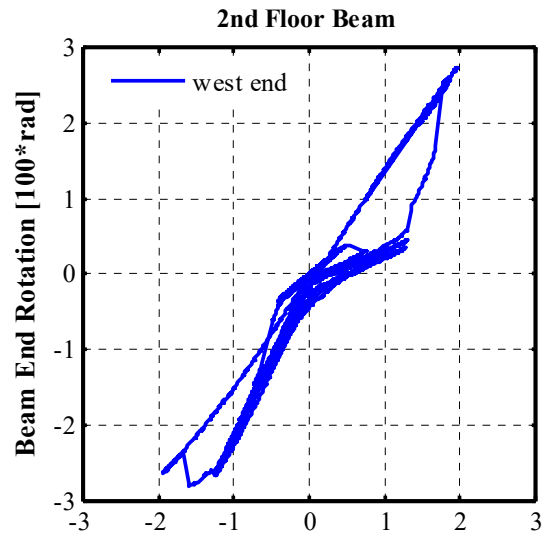
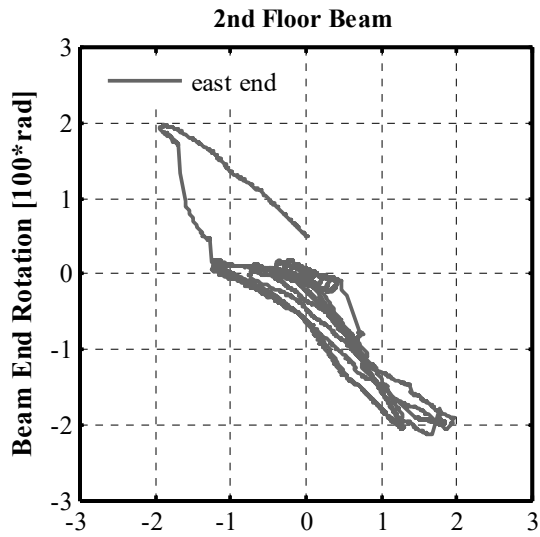


Figure 6.13 NCBF-B-1 beam end rotations versus story rotation.

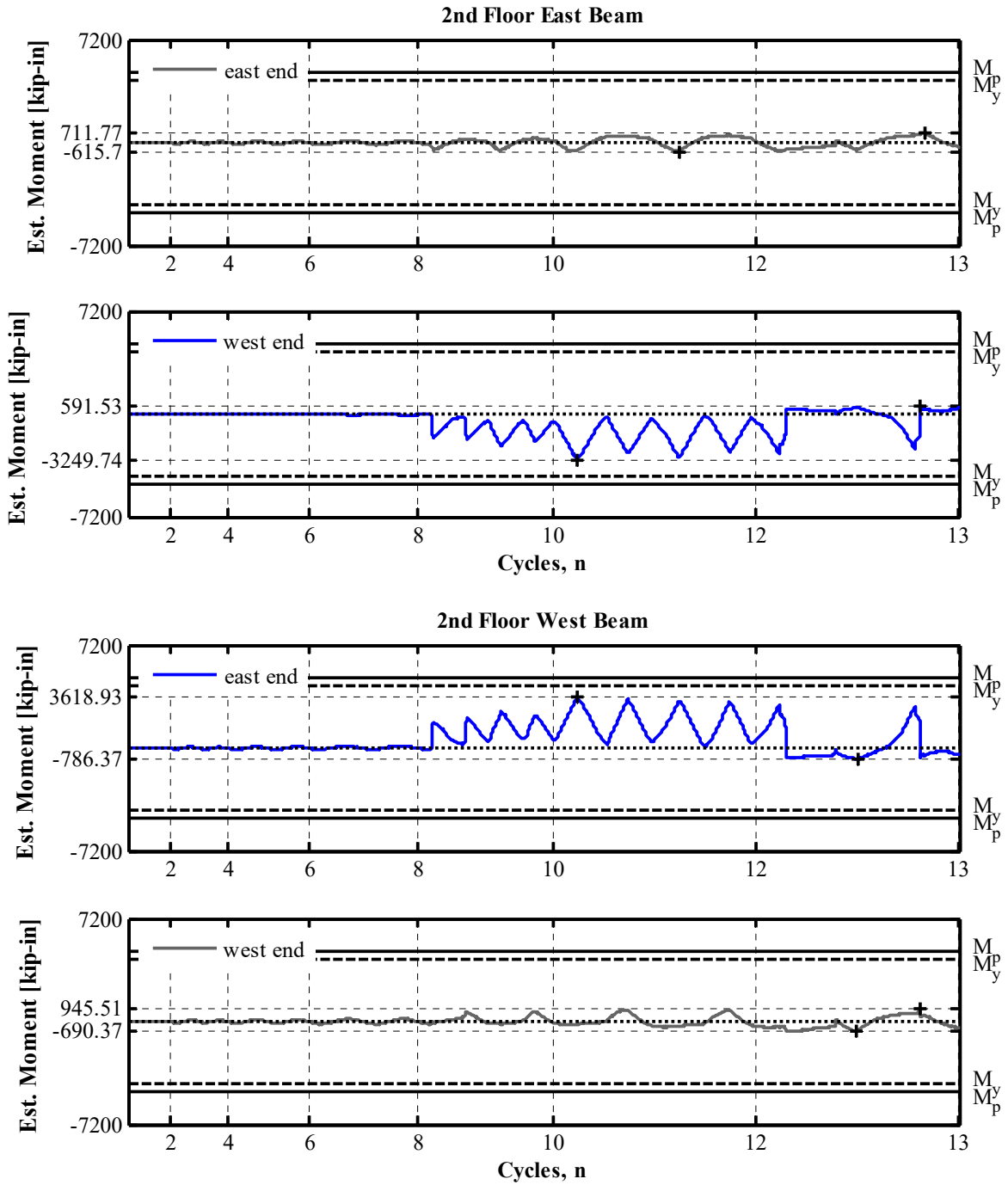


Figure 6.14 NCBF-B-1 second floor east and west half-beam estimated end moment time histories (estimated at beam end and at half-beam depth outside middle connection).

6.2.4 Column Response

The columns exhibited minor yielding and whitewash flaking during the beginning of the test at the column base; see Figure 5.13. At the end of the test, whitewash flaking was observed at the second story above the first-floor beam on both the strong- and weak-axis columns, as shown in Figures 5.6 and 5.7, and at the gusset plate tips near the gusset-to-column interface, as shown in Figure 5.16.

During the first positive amplitude to roof drift ratio +0.75%, a vertical yield line appeared on the west column web behind the first-floor west gusset plate; see Figure 5.14. This gusset plate region was not stiffened.

Figure 6.15 plots the column axial force versus roof drift ratio. The behavior of the weak- and strong-axis columns is approximately equal in compression and tension. This symmetric behavior appears to indicate limited, minor yielding in both columns. Figure 6.16 shows interaction diagrams between the column axial force and moment. The method used to calculate the moments in these diagrams is outlined in Section 4.3.1.3.

Here, M_p is the plastic moment capacity of the column and P_y is the yield strength of the column equal to AF_y , where A is the cross-sectional area and F_y is the yield strength found from the coupon tests.

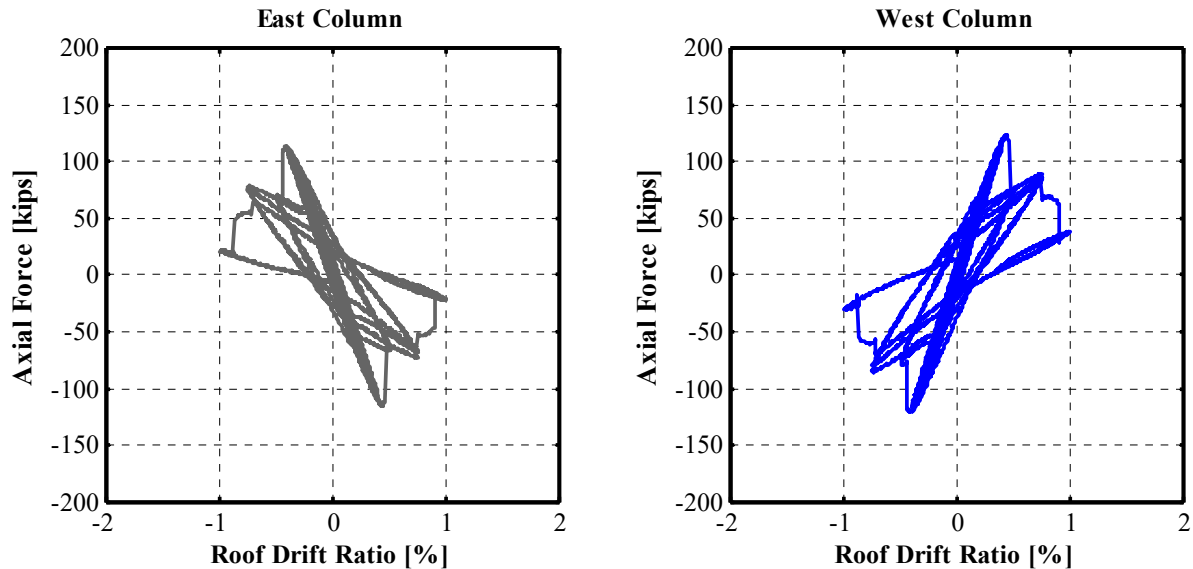


Figure 6.15 NCBF-B-1 column estimated axial force versus roof drift ratio.

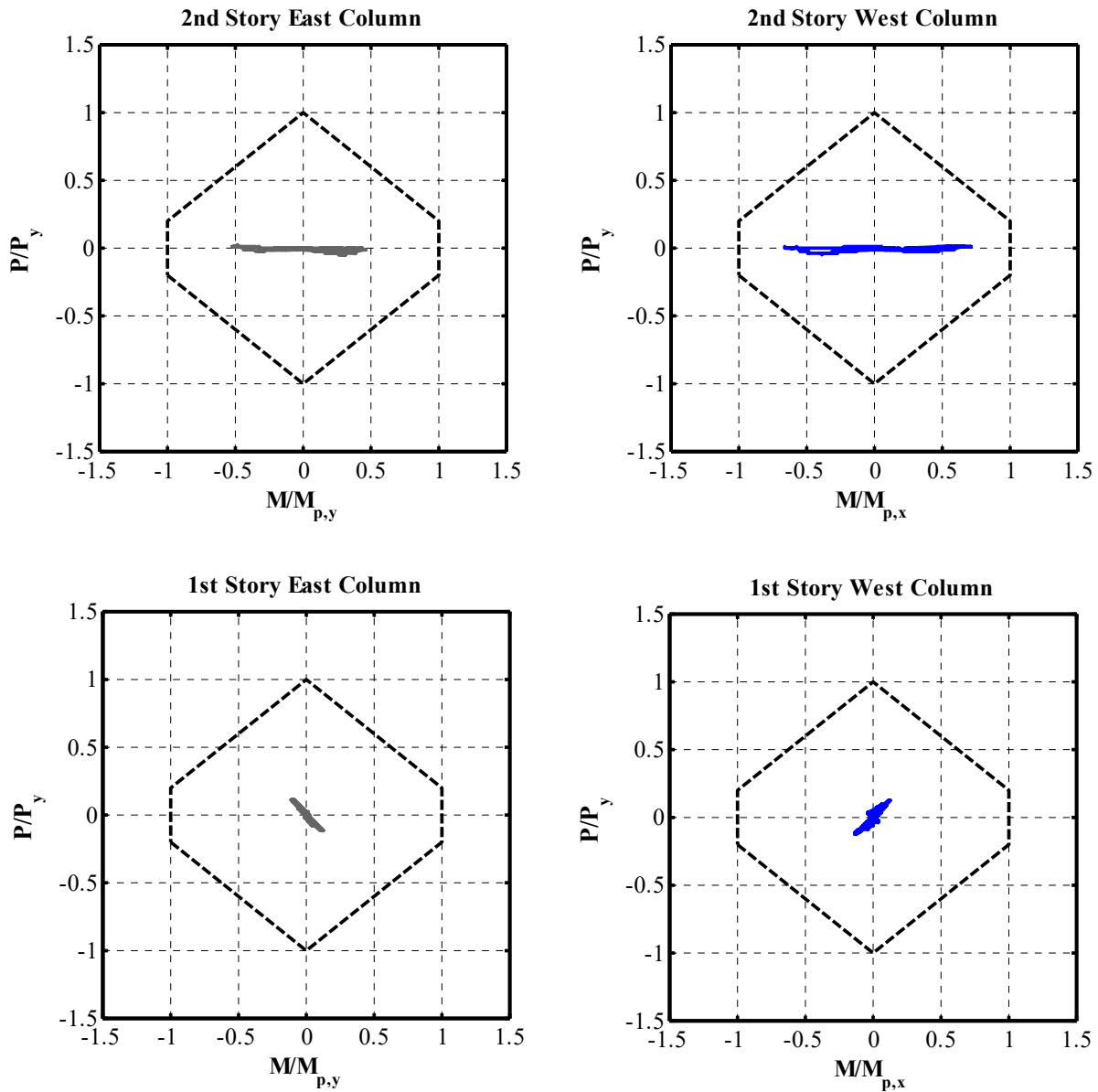


Figure 6.16 NCBF-B-1 column normalized axial moment interaction, (estimated at half the column depth above the second-story gusset plate connection).

6.2.5 Connection Response

All three 0.5 in. second-story gusset plates exhibited observable flaking due to out-of-plane buckling of the braces: see Figures 5.9 and 5.10. The middle gusset plate at the roof indicated some twisting at the end of the test as the braces buckled in opposite out-of-plane directions, as shown in Figure 5.12.

Some flaking at the net section of all the second-story brace-to-gusset connections was observed at the end of the test; see Figure 5.15. Note that vintage braced frames have no requirement for net-section reinforcement. Net-section rupture could have played a more

dominant role in the frame's behavior if brace buckling had not been the dominant limit state. Also of note: the connections for this test utilized notch-tough welding consumables, and more severe connection failures may occur with the non-notch tough welding consumables typical of vintage braced frame construction.

6.2.5.1 Shear Tab Behavior

Minor yielding of the roof shear tabs was observed at the end of the test: see Figure 5.8. Plots of the estimated beam end moment versus end rotation at the shear tab locations are shown in Figure 6.17. Neither of the roof shear tabs reached a rotational demand of 0.03 radians and moment demands are considered to be small.

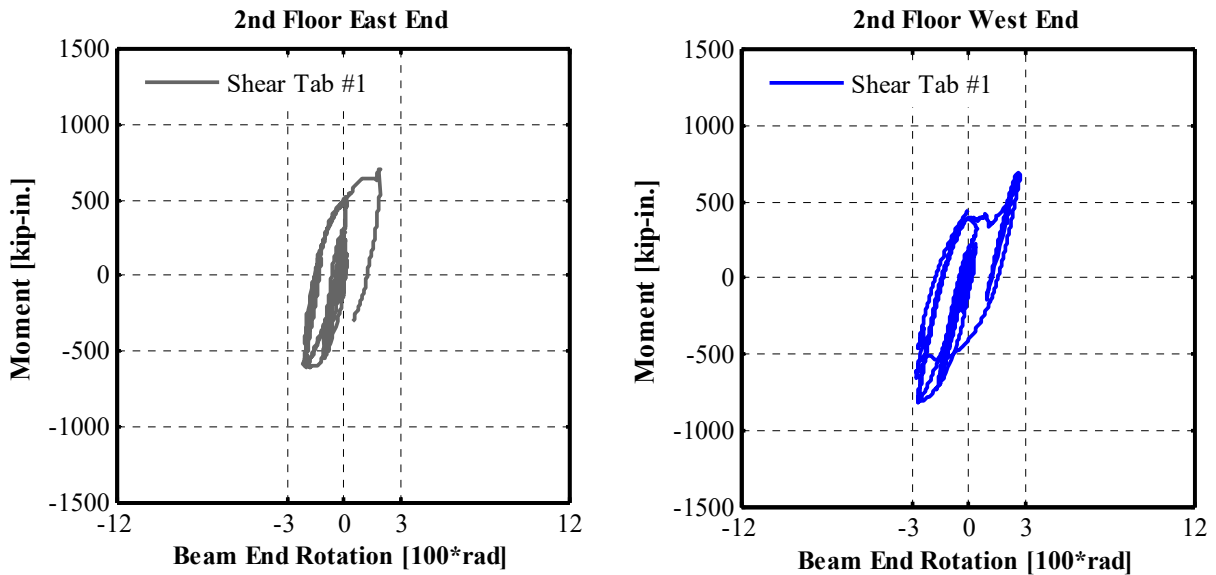


Figure 6.17 NCBF-B-1 second-floor beam estimated end moment versus end rotation.

6.3 NCBF-B-2: SPECIMEN UPGRADE

Table 6.8 shows the legend of symbols used to describe significant events in the plots for the NCBF-B-2 test. Values for these points are called out in Table 6.11. The global hysteretic behavior of the frame during the entire test can be seen in the hysteretic loop of Figure 6.18, and documentation of the events during the test can be found in Section 5.3. A breakdown of the hysteretic cycles at each peak roof drift amplitude can be found in Figure 6.19.

Table 6.8 NCBF-B-2 legend of symbols for significant event points.

- + 1E Brace Global Buckling
- 1E Brace Local Buckling
- + 1W Brace Global Buckling
- * 1E Brace Fracture
- + 1F E Column Web Failure
- Frame Reloading
- * West Column Fracture
- Test End

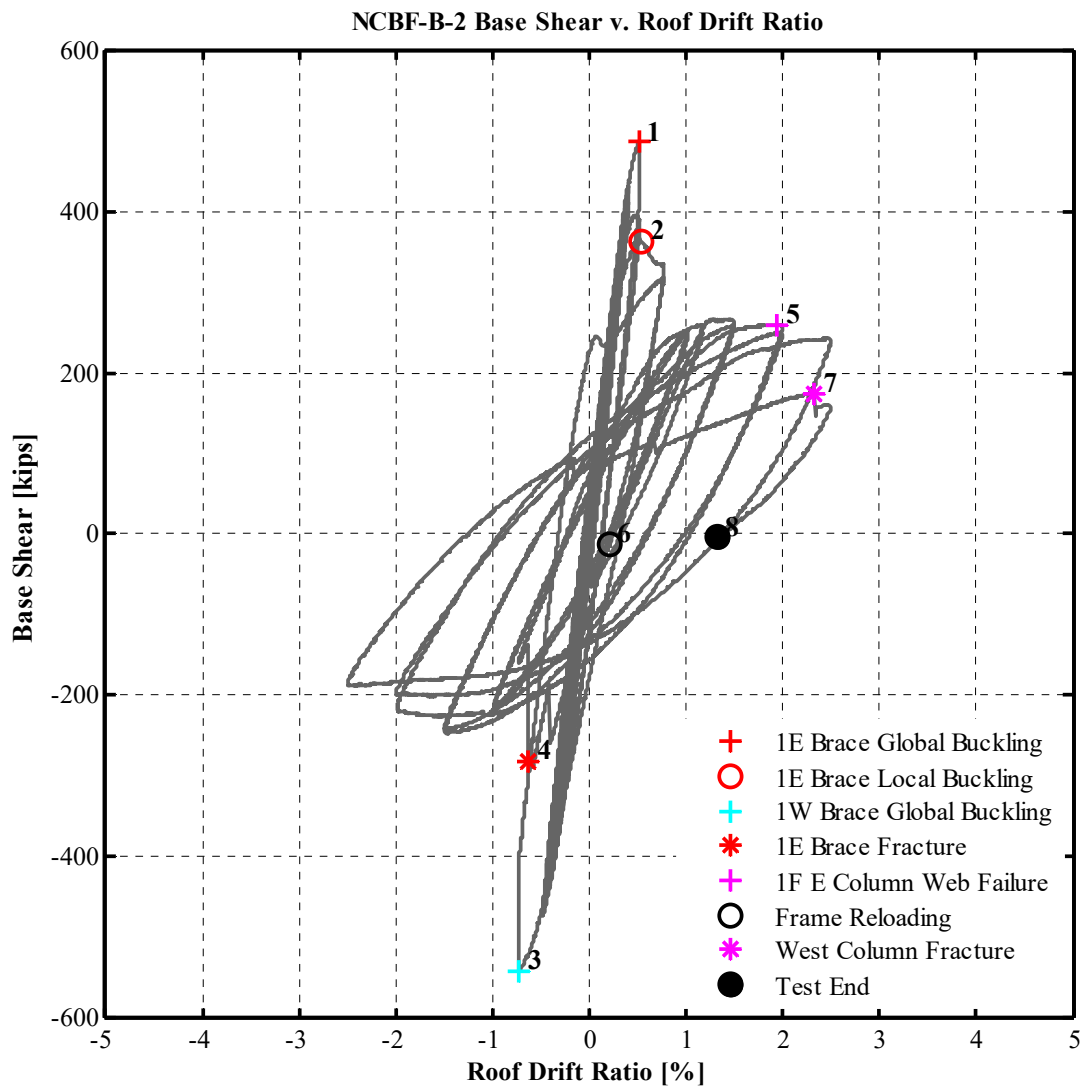


Figure 6.18 NCBF-B-2 base shear versus roof drift ratio.

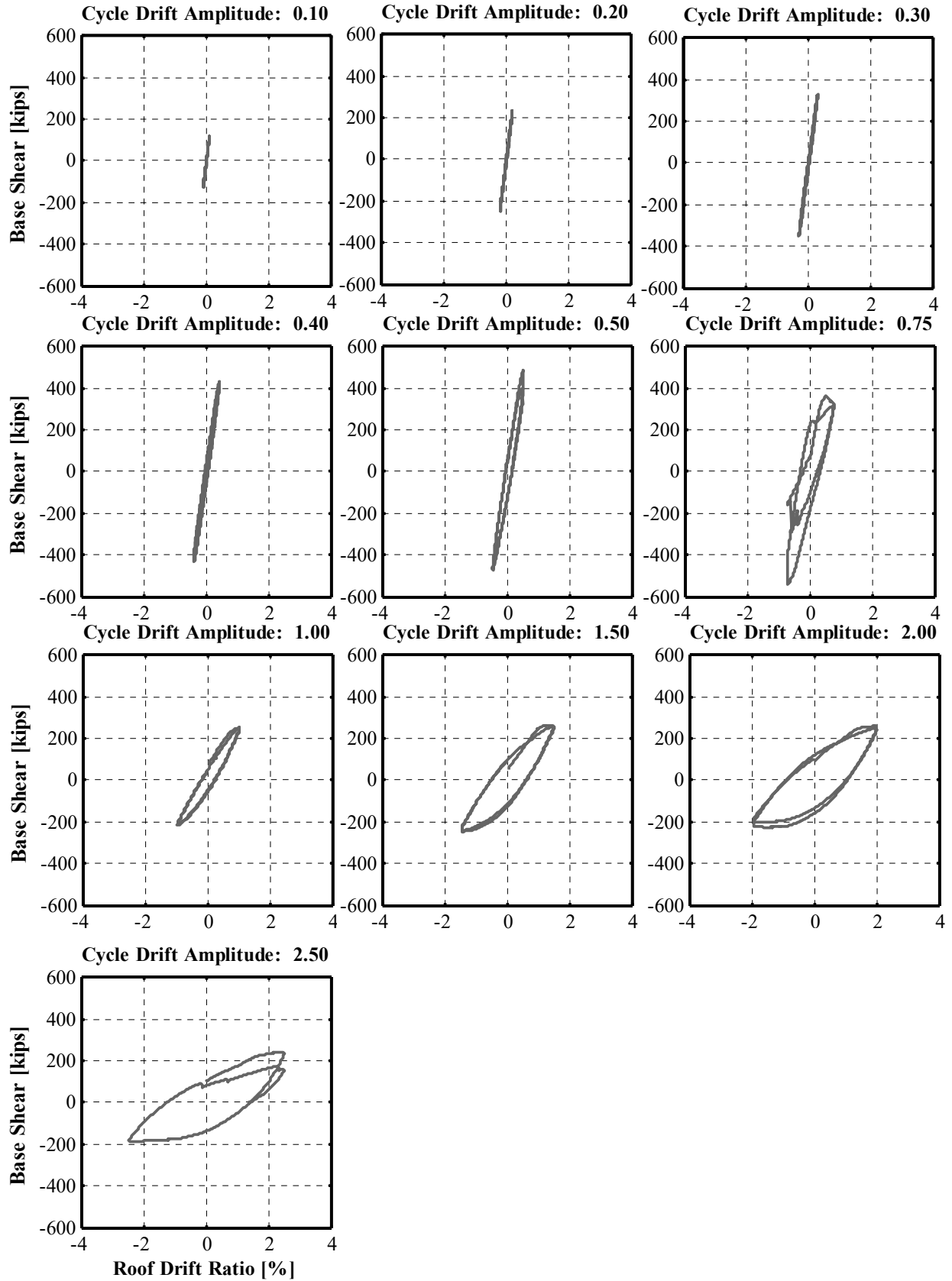


Figure 6.19 NCBF-B-2 hysteretic loop breakdown by cyclic amplitude.

6.3.1 Global Behavior

The second NCBF-B-2 test upgraded the NCBF-B-1 test specimen by filling all four braces with low-strength concrete to delay brace local buckling and potentially increase the fatigue life of the braces to observe other damage states. While initial buckling occurred at a similar roof drift ratios as observed during the NCBF-B-1 test, the added concrete increased the elastic stiffness of the overall frame. Inelastic behavior was initialized by buckling of the east first-story brace in compression at +0.51% roof drift ratio and 486 kips of base shear, approximately 25% higher than the peak base shear of the NCBF-B-1 specimen. In contrast to the local buckling observed in the hollow braces of the NCBF-B-1 test, buckling in the east CFT exhibited stable global buckling over two complete cycles before local buckling occurred mid-length of the brace.

Damage was concentrated in the first story after the first brace globally buckled, forming a weak story in the first story; see Figure 5.45(a). The second story dissipated little energy, while the first story contributed most of the energy-dissipation capacity after brace buckling was initialized; see Figure 6.22.

Degradation of the system hysteresis loops can be seen in Tables 6.9 and 6.10. After initial global buckling of the first-story east brace, the base shear decreased to 84% of V_{max} . This decrease in shear strength is less than that observed upon local buckling of the hollow braces in the NCBF-B-1 test. Upon local buckling in the first-story east brace, the base shear decreased to 69% of V_{max} , which is a value similar to that of NCBF-B-1 upon local buckling (about 60% of V_{max}).

After local buckling was observed in the east brace, the opposite first-story west brace exhibited global buckling a half-cycle later at the maximum base shear seen during the loading protocol of 542 kips. It is unclear whether the west brace would have buckled if the test had not been paused for the Leica Laser Scanner to capture the frame's deformed shape. No visible local buckling was observed in the first-story west brace during the remainder of the test.

Fracture occurred in the east brace at a roof drift ratio of -0.60% in tension, one cycle after global buckling occurred in the west brace. The two fractured ends of the east brace came in contact in compression during a portion of the next cycle, increasing the stiffness and strength of the frame. After that first post-fracture cycle, the two halves of the fractured brace were pushed apart, and the first-story east brace no longer contributed to the lateral resistance of the frame [see Figure 5.21(f)]. Upon fracture of the brace, the base shear in the system decreased to about 30% of V_{max} , which was similar to the NCBF-B-1 test at brace fracture.

After fracture of the first-story east brace, the first story acted like an eccentric braced frame with a very long link of the east half of the first-floor beam length. Plastic rotations were observed at the two ends of the east half of the beam; see Figure 5.45(a). The hysteretic loops before and after the first-story east brace fracture can be seen in Figures 6.20 and 6.21. These plots demonstrate that even though the stiffness and strength of the system had decreased after fracture of the first-floor east brace, the frame was still able to dissipate energy through flexural yielding of the beam. The west half of the first story—including the half-beam, first-story column, and remaining west brace—behaved like a nearly rigid body that rotated about the base of the strong-axis west column. Frame action affected both second-story braces; localized buckling was observed in the region just above the brace-to-gusset connection (see Figure 5.35). This caused the second story to contribute some energy-dissipation capacity late in the test, as

can be seen in the second-story shear plot of Figure 6.22. The frame continued to dissipate energy through plastic hinging in the first floor beam and at the column bases at reduced shear strength. Substantial tearing was observed at the beam–column shear tab connection. The west column fractured at the interface between the column base and baseplate at +2.33%.

Table 6.9 NCBF-B-2 peak base shear at each cycle.

Cycle	Amplitude	V ¹	V/V _{max}	Event	Amplitude	V ¹	V/V _{min}	Event
(n)	(%)	(kips)			(%)	(kips)		
1	+0.1	121.3	0.25		-0.1	-125.2	0.23	
2	+0.1	121.2	0.25		-0.1	-124.8	0.23	
3	+0.2	240.5	0.49		-0.2	-254.4	0.47	
4	+0.2	242.9	0.50		-0.2	-252.6	0.47	
5	+0.3	327.8	0.67		-0.3	-348.9	0.64	
6	+0.3	329.8	0.68		-0.3	-343.3	0.63	
7	+0.4	409.5	0.84		-0.4	-429.8	0.79	
8	+0.4	429.9	0.88		-0.4	-391.6	0.72	
9	+0.5	485.9	1.00	1F E (B)	-0.5	-473.3	0.87	
10	+0.5	395.9	0.81		-0.5	-467.8	0.86	
11	+0.75	366.3	0.75	1F E (LB)	-0.75	-541.6	1.00	1F W (B)
12	+0.75	318.1	0.65		-0.75	-288.5	0.53	1F E (Fr)
13	+1.0	253.5	0.52		-1.0	-216.7	0.40	
14	+1.0	252.6	0.52		-1.0	-214.8	0.40	
15	+1.5	265.7	0.55		-1.5	-247.0	0.46	
16	+1.5	258.3	0.53		-1.5	-241.8	0.45	
17	+2.0	259.8	0.53		-2.0	-225.8	0.42	
18	+2.0	250.0	0.51		-2.0	-200.5	0.37	
19	+2.5	242.8	0.50		-2.5	-187.4	0.35	
20	+2.5	174.1	0.36	W Col (Fr)				
	V _{max} =	485.9	kips		V _{min} =	-541.6	kips	

¹ Maximum base shear in each half-cycle.

Table 6.10 NCBF-B-2 approximate base shear after significant damage events.

Cycle	Amplitude	V	V _L ¹	V _L /V _{max,min}	Event
(n)	(%)	(kips)	(kips)		
9	+0.5	485.9	406.1	0.84	1F E (B)
11	+0.75	366.3	333.9	0.69	1F E (LB)
11	-0.75	-541.6	-401.2	0.74	1F W (B)
12	-0.75	-288.5	-159.3	0.29	1F E (Fr)
20	+2.5	174.1	159.3	0.33	W Col (Fr)

¹ Approximate base shear after significant decrease in maximum V in a half-cycle.

The test was concluded after the peak amplitude cycle of 2.5% roof drift ratio at the zero force point of the actuators. The relaxed frame exhibited a residual roof drift of 1.3%, as can be seen by the “Test End” marker in Figure 6.18. Almost all of this residual drift ratio was concentrated in the first story; see Figure 6.22.

Table 6.11 NCBF-B-2 description of event points.

Event point	Event	Amplitude	Cycle no.	θ_R	θ_1	θ_2
		(%)		(%)	(%)	(%)
1	1F E brace (B)	+0.5	1	+0.51	+0.50	+0.53
2	1F E brace (LB)	+0.75	1	+0.55	+0.68	+0.39
3	1F W brace (B)	-0.75	1	-0.73	-0.76	-0.70
4	1F E brace (Fr)	-0.75	2	-0.60	-0.86	-0.37
5	1F E column web (Fr)	+1.0	2	+1.94	+3.37	+0.36
7	W column base (Fr)	+2.5	2	+2.33	+3.83	+0.67
8	Test End			+1.32	+2.21	+0.33

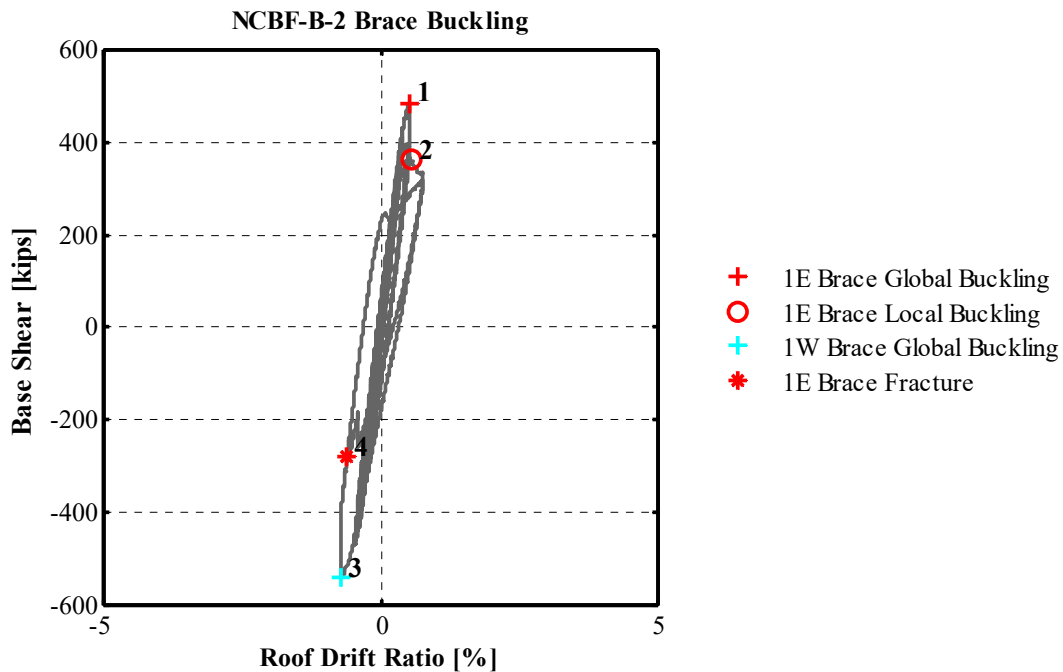


Figure 6.20 NCBF-B-2 base shear versus roof drift ratio up to first-story east brace fracture (at -0.60% on second cycle to -0.75%).

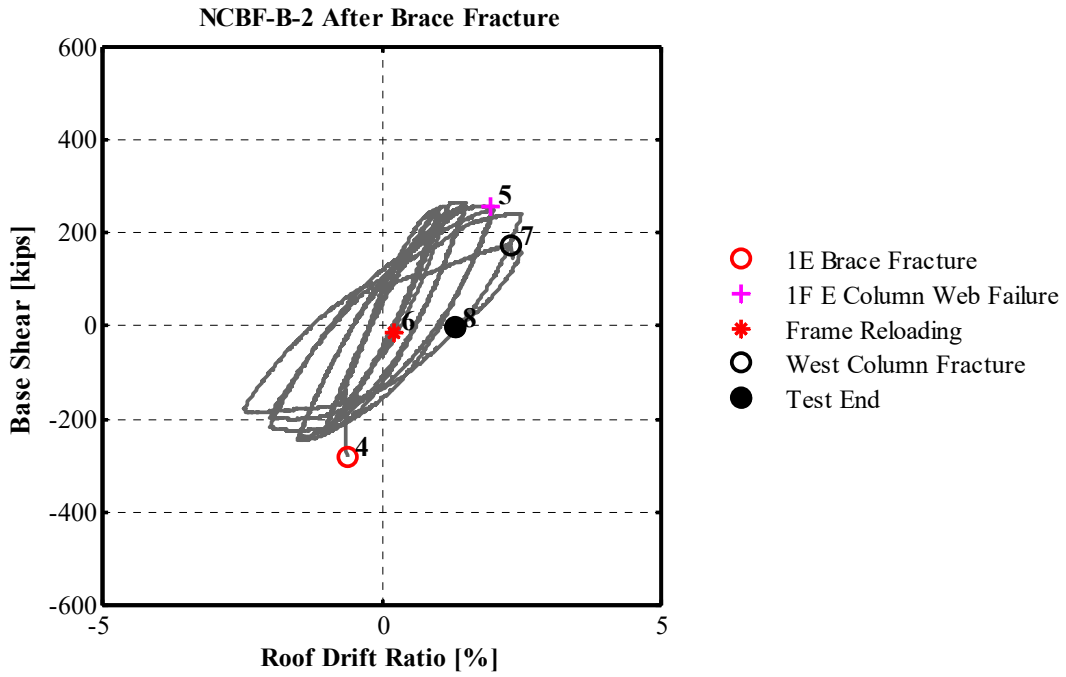


Figure 6.21 NCBF-B-2 base shear versus roof drift ratio after first-story east brace fracture (at -0.60% on second cycle to -0.75%).

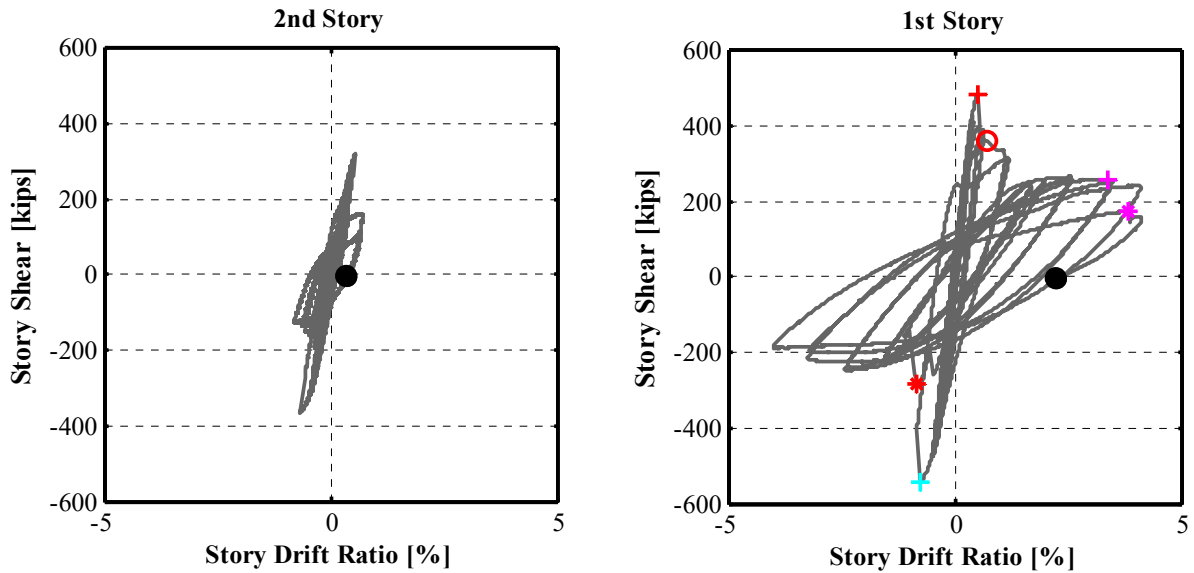


Figure 6.22 NCBF-B-2 story shear versus story drift ratio.

6.3.2 Concrete-Filled Brace Response

Both first-story braces buckled in the same direction to the north. The west brace displaced 1.65 in. out-of-plane and the east brace displaced a maximum of 12.66 in. out-of-plane, as shown in Figures 6.27 and B.4. Neither of the first-story braces appeared to have exhibited significant tensile yielding. All four braces contributed some energy dissipation to the system, but this contribution was delayed for the second-story braces until local buckling developed from frame action near the bottom ends of the braces, as shown in Figures 6.26 and 6.27.

Table 6.12 shows the ratio between the first-story east and west braces' peak compression load in each cycle, C , and their buckling capacity, P_{cr} . After global buckling, the estimated force in first-story east brace decreased to 21% of its buckling capacity upon the next cycle, followed by another 8% upon local buckling, and another 8% upon brace fracture. As the east brace decreased in strength, so did the strength of the overall system; therefore, less force was delivered to the first-story west brace. As a result of the rapid strength degradation of the first-story east brace, after slight global buckling, the first-story west brace remained essentially elastic during the remainder of the test.

Table 6.12 NCBF-B-2 brace compression strength degradation.

Cycle	Amplitude	1F E Brace				1F West Brace				
		T^1	C^2	C/P_{cr}	Event	T^1	C^2	C/P_{cr}	Event	
(n)	(%)	(kips)	(kips)			(kips)	(kips)			
3	0.2	73.0	-138.0	0.40		144.5	-140.5	0.44		
4	0.2	138.3	-148.9	0.43		143.3	-141.5	0.44		
5	0.3	137.5	-218.0	0.63		197.6	-192.8	0.60		
6	0.3	188.9	-216.9	0.63		199.6	-197.1	0.62		
7	0.4	190.7	-276.3	0.80		249.6	-250.4	0.78		
8	0.4	233.7	-306.1	0.89		255.8	-226.4	0.71		
9	0.5	196.1	-344.9	1.00	1F E (B)	299.9	-281.2	0.88		
10	0.5	240.5	-273.5	0.79		245.6	-284.6	0.89		
11	0.75	237.6	-244.5	0.71	1F E (LB)	262.0	-319.8	1.00	1F W (B)	
12	0.75	261.4	-215.6	0.63	1F E (Fr)	245.3	-175.2	0.55		
13	1.0	0	0	0		234.4	-194.2	0.61		
14	1.0	0	0	0		231.7	-192.7	0.60		
15	1.5	0	0	0		264.5	-207.1	0.65		
16	1.5	0	0	0		257.4	-187.7	0.59		
17	2.0	0	0	0		304.9	-157.7	0.49		
18	2.0	0	0	0		296.0	-123.4	0.39		
19	2.5	0	0	0		329.7	-88.5	0.28		
20	2.5	0				241.9				
		$P_{cr}^3 =$	-344.9	kips			$P_{cr}^3 =$	-319.8	kips	

6.3.2.1 Concrete-Filled Brace Local Buckling and Fracture

While the concrete-fill was successful in delaying local buckling, it did not prevent local buckling behavior and brace fracture. Figures 5.21 and 6.25 show the propagation of fracture in the first-story east brace. Unlike the hollow braces, local buckling in the CFT occurred outward rather than inward because of the presence of the concrete-fill. This local buckling behavior is similar to that of previous member tests performed on grout and concrete-filled braces [Lee and Goel 1987; Broderick et al. 2005; and Fell 2008].

While this outward local buckling appears to be less severe than the inward local buckling observed in the hollow braces, crack initiation and brace fracture still occurred within a few cycles after the initiation of local buckling. The first-story east brace fractured 1-1/2 cycles after local buckling. The rupture propagated more quickly in the CFT than in the hollow HSS section, which fractured three to four cycles after local buckling. As both the concrete and the steel were loaded in compression, the concrete tended to expand outward. This expansion was confined by the steel tube, leading to an increase in the brace composite compression capacity. This effect, however, also decreased how much additional stress could be achieved by the surrounding steel tube, especially as the steel tube was secondarily used to confine the interior concrete while still resisting axial demands [Gardner and Jacobson 1967]. This effect may be exacerbated in tubes with large width-to-thickness ratios, where there is less steel to meet these additional demands from the concrete-fill.

After completion of the test, the second-story braces and first-story west brace were skinned to reveal the damage to the inner concrete, as shown in Figures 6.23 and 6.24. Concrete crushing is apparent near the local buckled location of the second-story braces. The first-story west brace appears to have some crushing along the compression side of the globally buckled brace.



(a)



(b)



(c)



(d)

Figure 6.23 Inner concrete after test at local buckling location: (a) and (b) second-story west brace; and (c) and (d) second-story east brace.



Figure 6.24 Inner concrete after test after global buckling of first-story west brace.

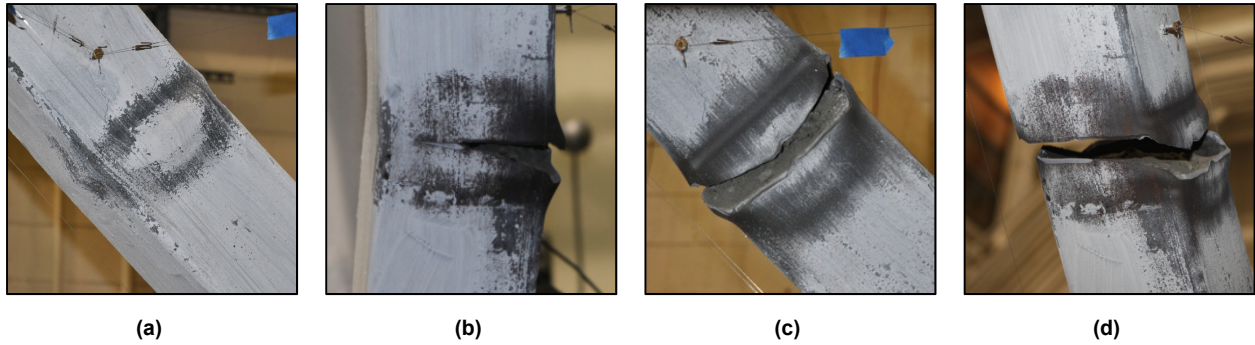


Figure 6.25 Local buckling of first-story east brace: (a) outward local buckling; crack propagation (b) west side and (c) south side; and (d) complete fracture.

6.3.2.2 Brace Design Comparison

As introduced in Section 6.2.2.2, the solid black lines in Figures 6.26 and 6.27 represent the tension and compression capacities of the CFT braces as specified by AISC 360-10 [2010]. Values for the quantities can be found in Table 6.13.

Similar to that described in Section 6.2.2.2 for the hollow steel braces, an effective length factor, k , was back calculated from the estimated buckling capacity of each brace and compression capacity for composite sections provided in AISC 360-10 [2010]. Effective length factors for the first-story braces were similar to the NCBF-B-1 second-story braces, highlighting that the effective length factor, k , depends on the brace boundary conditions and may be affected by whether the gusset plate was connected to a strong- or weak-axis column.

An estimation for the effective secant stiffness, $(EI)_{\text{eff}}$, used to calculate the composite Euler buckling load was made by comparing the first few elastic cycles at 0.1% roof drift ratio to the story shears minus the column shears, as described in Section 4.3.1.2. These values were found to be similar to the specifications for CFTs as specified by AISC 360-10 [2010]; see Table 6.14. Note that the axial force in the braces is an estimated quantity as described in Section 4.3.1.2. Specific values for the brace axial force can describe relative trends of estimated brace behavior but may not represent exact forces developed during the experiment.

Table 6.13 NCBF-B-2 brace critical variables.

Brace location	P_{cr}	K	D_{cr}	T_n^1	C_n^2	k
	(kips)	(kips/in.)	(in.)	(kips)	(kips)	
First-story east brace	344	1458	0.24	319	323	0.8
First-story west brace	320	1469	0.22			1.0

¹ Tension capacity using the tensile coupon yield strength as specified by AISC 360-10 [2010].

² Compression capacity using the coupon yield strength with $k = 1$ as specified by AISC 360-10 [2010] for composite CFT sections.

Table 6.14 NCBF-B-2 estimate of brace composite $(EI)_{eff}$.

Brace location	$(EI)_{eff}$	
	Experiment	AISC 360-10
	(kip-in. ²)	(kip-in. ²)
First-story brace	1,607,300	1,688,477
Second-story brace	699,060	830,371

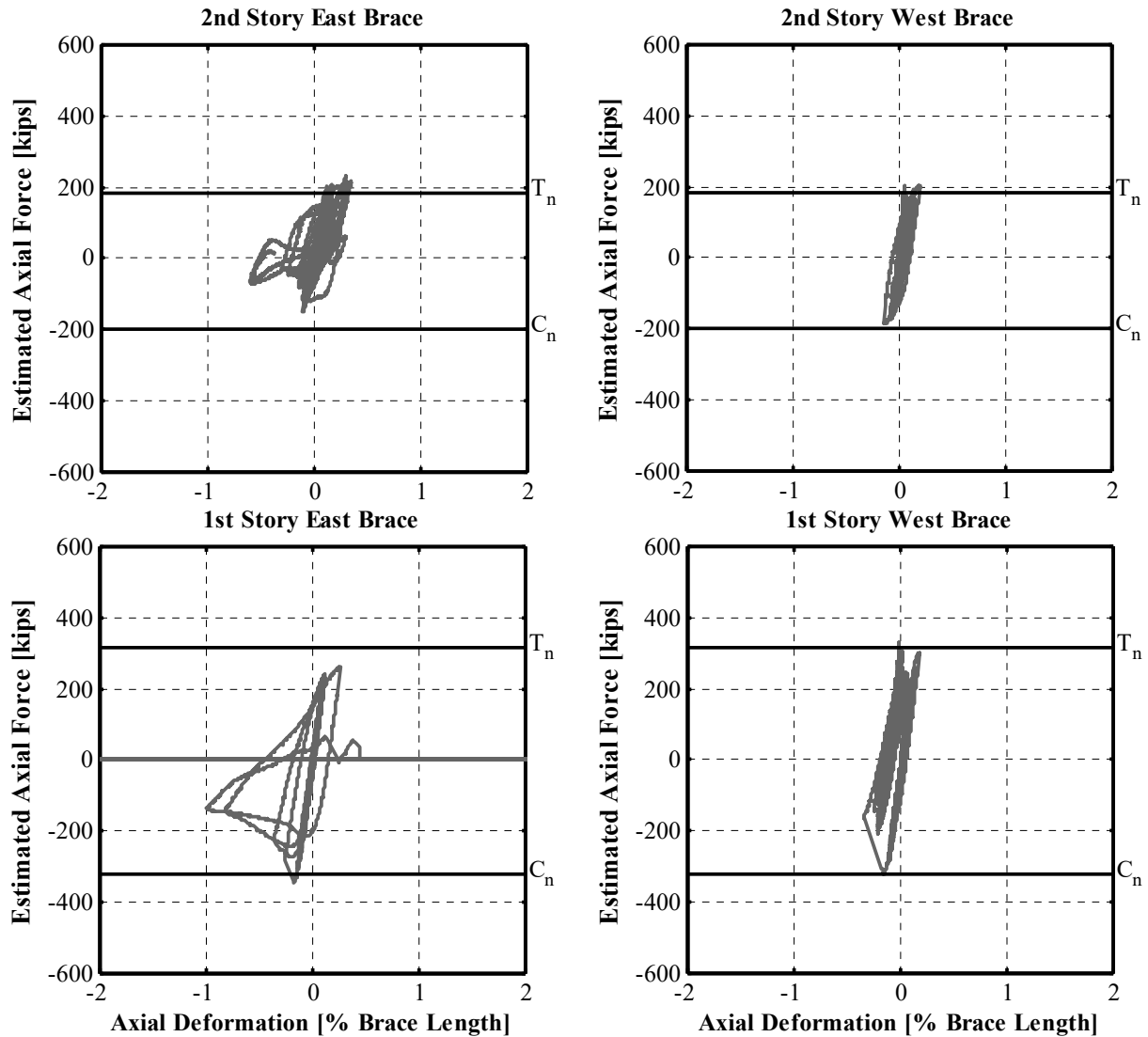


Figure 6.26 NCBF-B-2 estimated brace axial force versus axial deformation.

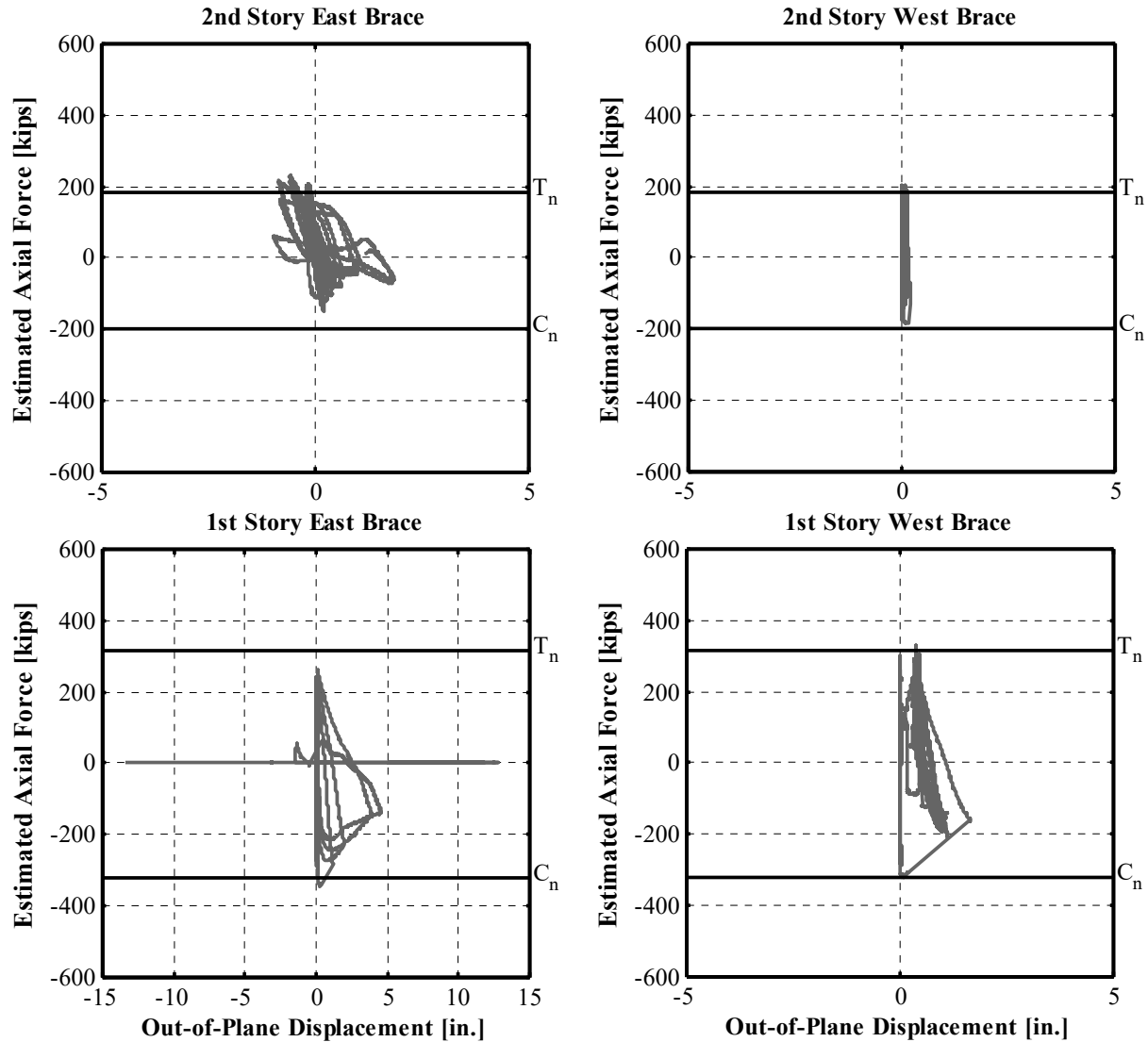


Figure 6.27 NCBF-B-2 estimated brace axial force versus out-of-plane displacement.

6.3.3 Beam Response

The unbalanced load on the beam was both upward and downward, rather than strictly downward as in the case of the NCBF-B-1 test, as shown in Figure 6.28. Note that positive story drift corresponds to a negative (downward) unbalanced load. The first-floor beam moved down a maximum of -4.78 in. when the remaining west brace was in tension and moved up a maximum of 3.27 in. when the west brace was in compression, as can be seen in Figures 5.24, 6.29, and B.16. This was due to nearly “rigid” body rotation of the west half of the first story (i.e., the induced EBF-like beam link behavior shown in Figure 5.45(a)). As the frame moved to the right of this figure, the center of the lower beam moved upward. As the frame moved to the left, the center of the beam moved downward. This behavior is fundamentally different from the case typically assumed for “strong” beams designed to resist an “unbalanced load” due to brace buckling; see Section 2.2.4. At the end of the test, the residual vertical displacement of the beam was measured at -2.90 in. in the downward direction.

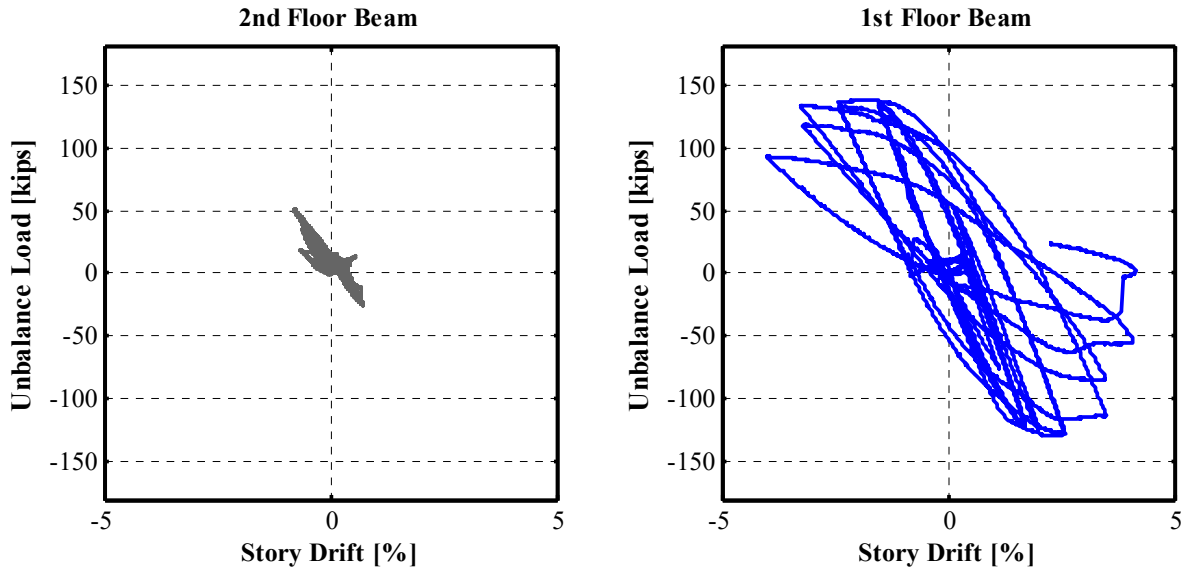


Figure 6.28 NCBF-B-2 beam estimated unbalanced load versus story drift ratio. Note: Unbalanced load is positive upward.

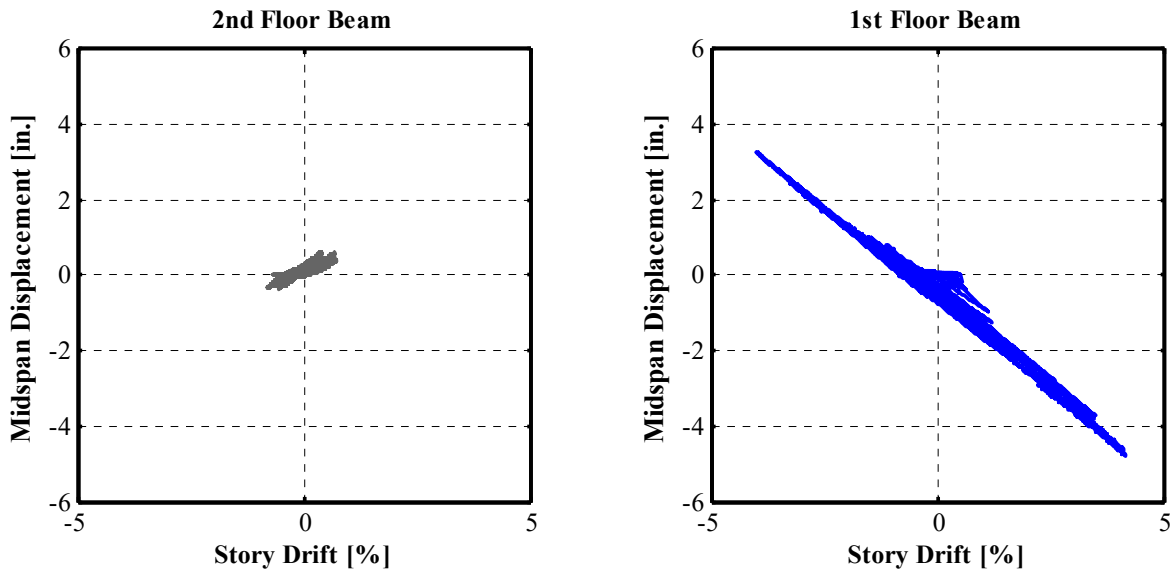


Figure 6.29 NCBF-B-2 beam vertical mid-span displacement versus story drift ratio.

While the beam displayed double curvature (out-of-plane) and substantial flange local buckling when in compression, it was successively straightened when the beam was in tension; see Figure 5.25(a) and Figure 5.29. Upon completion of the test, whitewash flaking due to plastic hinging was visible to either side of the center gusset plate.

The estimated moments at the ends of the east and west first-floor half-beams are shown in Figure 6.32. These moments were estimated according to the description provided in Section 4.3.1.4. Moments at the end beam–column connection are larger than the second-floor roof beam

of the NCBF-B-1 test. This is likely because of the presence of the second-story gusset plates that reinforce these shear tab connections. Estimated moments to either side of the middle connection appear to have exceeded the plastic moment capacity of the beam, M_p .

The west end of the first-floor beam rotated very little during the test, remaining at an approximate right angle to the column face, as shown in the rotation plots of Figure 6.31. In contrast, the east end of the beam rotated in both the clockwise and counterclockwise directions. The rotation of the east end of the beam are higher than the first-story story drift ratio.

A plot of the estimated shear in the east half of the first-floor beam is shown in Figure 6.30. The maximum shear approaches $1.5M_p/L$ as the beam reaches its plastic moment capacity near the middle connection. This observed shear decreases when a crack opened in the first-floor east gusset plate and the east second-story gusset plate punched through the east column web, as specified by the pink “+” in the plot. In this case, L is the length of the link defined as the distance from the beam end to the edge of the middle connection. The plastic shear develop by moments in the beam link is below the nominal shear capacity of the beam, $V_{n,beam}$, as specified by the solid black line on the plot of 154 kips.

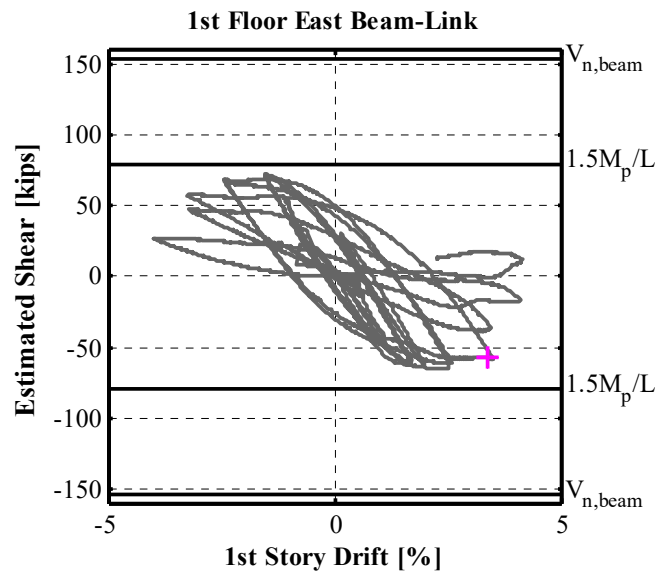


Figure 6.30 NCBF-B-2 first-floor east half-beam estimated shear versus story drift ratio (where L is the distance from the beam end to the edge of the middle connection).

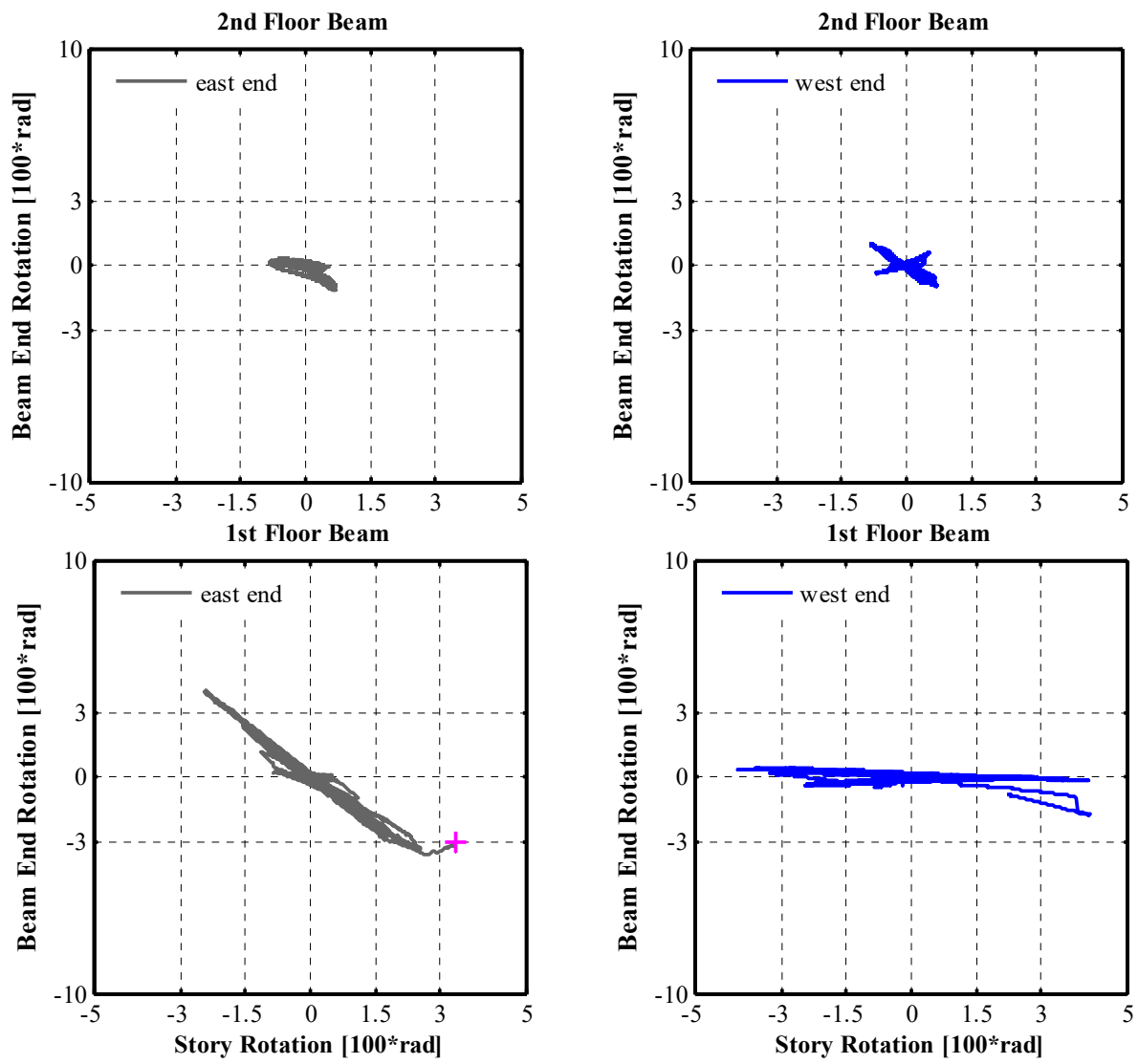


Figure 6.31 NCBF-B-2 beam end rotations versus story rotation.

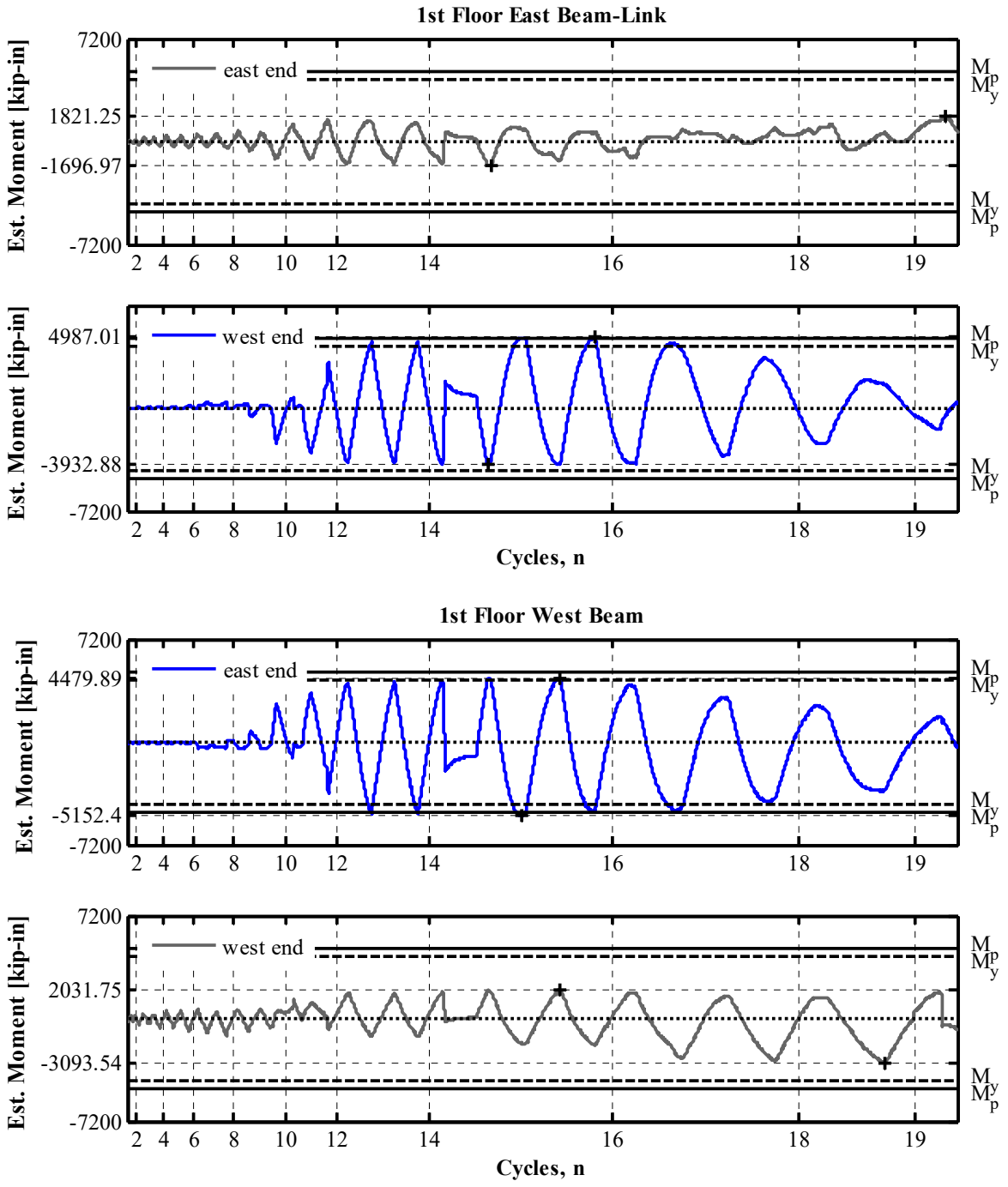


Figure 6.32 NCBF-B-2 first-floor east and west half-beam estimated end moment time histories (estimated at beam end and at half-beam depth outside middle connection).

6.3.4 Column Response

The difference in axial demand in the strong- and weak-axis columns can be seen in Figure 6.33. While both columns appear to have similar axial forces prior to buckling of the first-story east brace, after fracture of the first-story east brace the axial force in the west column decreases and the columns have different axial demands.

The east weak-axis column approaches yield moment M_y at the base of both the first and second story, as shown by the whitewash flaking evident in Figures 5.33 and 5.37 and the interaction diagrams in Figure 6.34. The west strong-axis column exceeds its plastic moment capacity at the base of the second story. Whitewash flaking was evident at this location; see Figure 5.34. During the last cycle of the second test, the west strong-axis column fractured along its flange and web, leaving the single interior column flange still connected to the west baseplate, as shown in Figures 5.41 and 5.42.

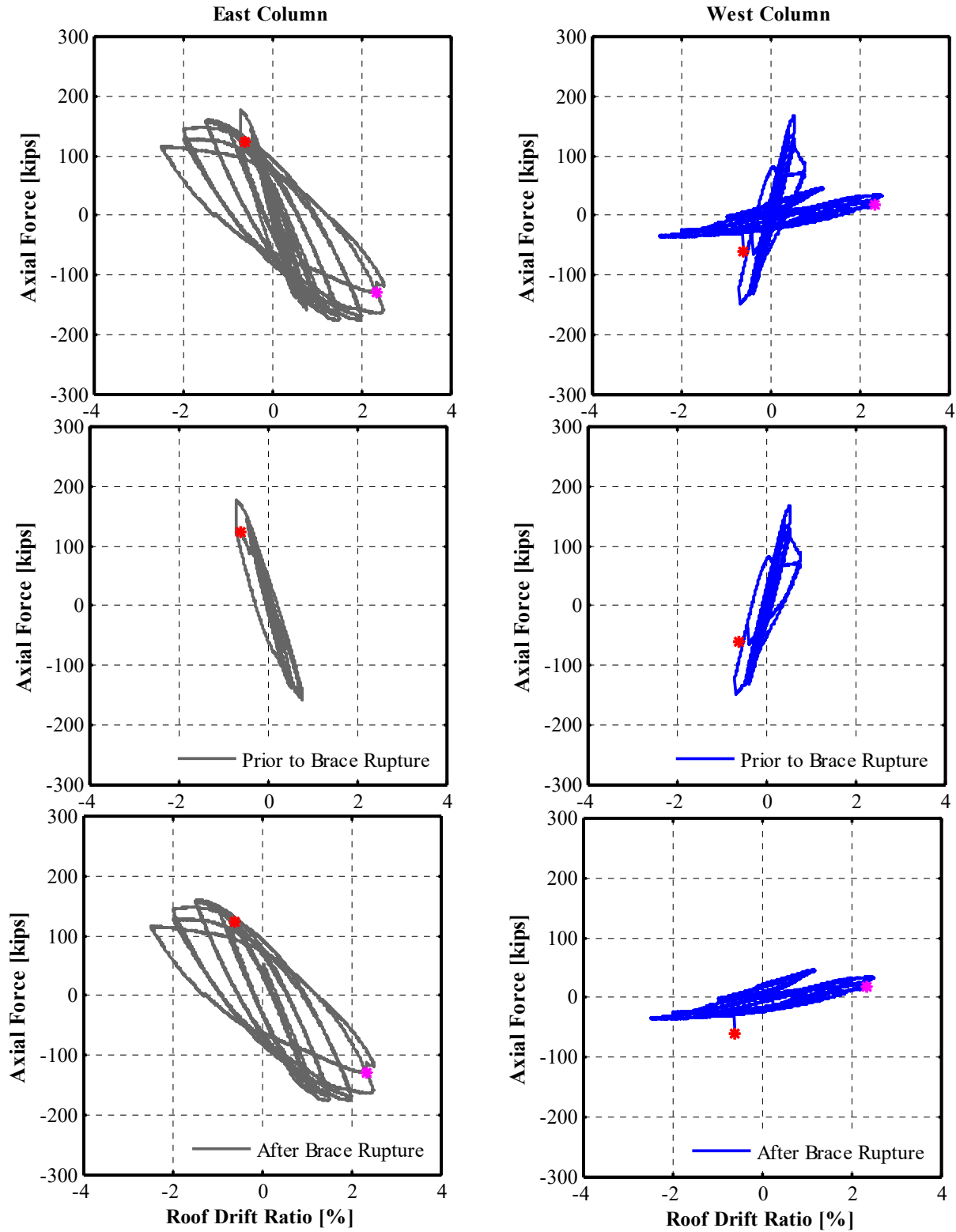


Figure 6.33 NCBF-B-2 column estimated axial force versus roof drift ratio.

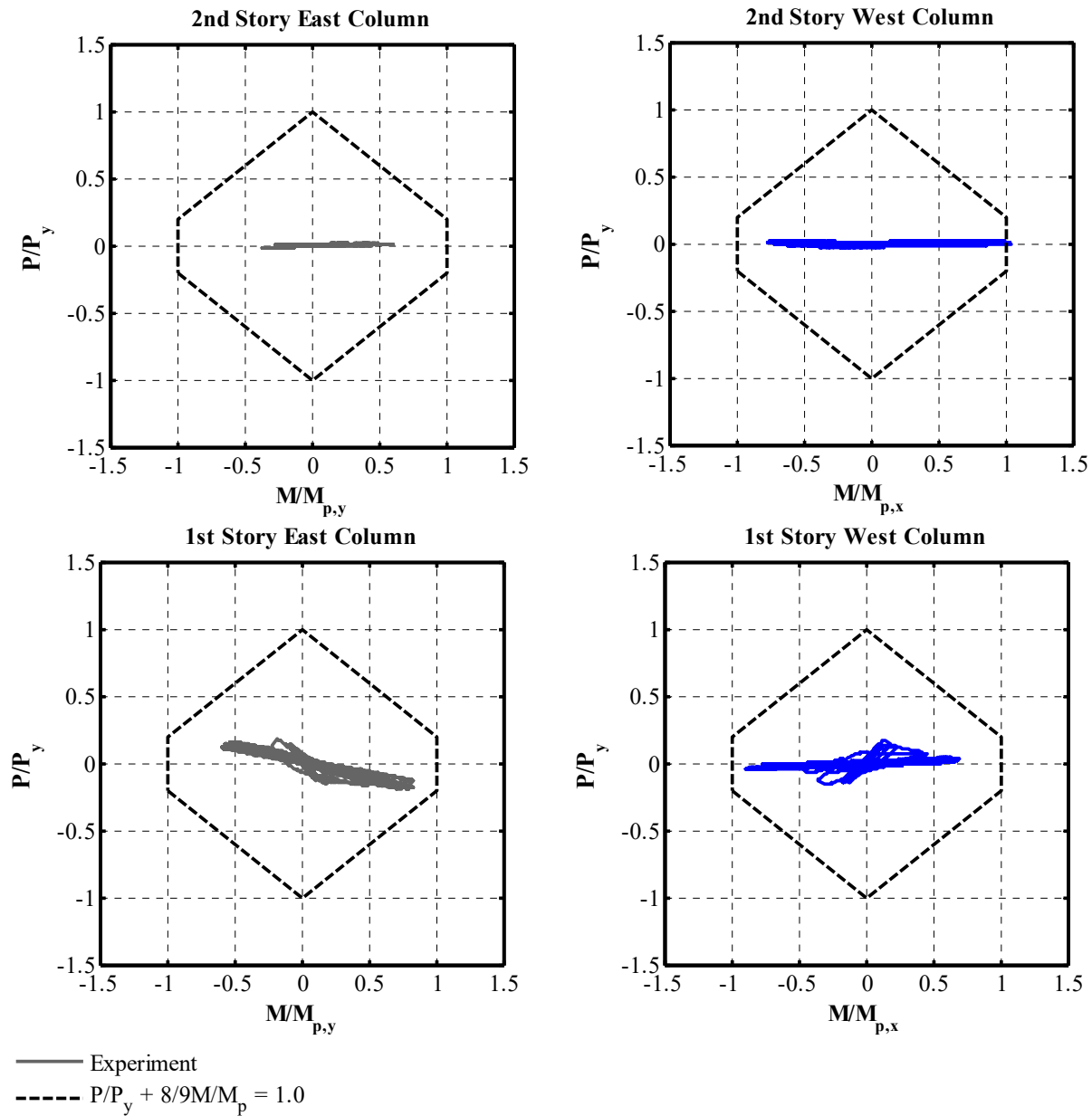


Figure 6.34 NCBF-B-2 column normalized axial moment interaction (estimated at half the column depth above the second-story gusset plate connection). Here, M_p is the plastic moment capacity of the column, and P_y is the yield strength of the column equal to AF_y , where; A is the cross-sectional area, and F_y is the yield strength found from the coupon tests.

6.3.5 Connection Response

Many types of connection failures were observed during the NCBF-B-2 test. This is in part due to the larger number of cycles and lateral drifts experienced by this specimen. The two gusset plates connected to the first-story east brace both showed significant out-of-plane behavior as the brace buckled to the north; see Figure 5.22(b) and Figure 5.28. The first-story west gusset plate showed localized buckling near the gusset to baseplate interface, as shown in Figure 5.23(b).

The welds at the first-story middle gusset-to-beam (Figure 5.28), east gusset-to-baseplate (Figure 5.39), and second-story east gusset-to-beam (Figure 5.36) connections exhibited partial or complete fracture. Although under-sized, these welds did correspond to notch-tough welding consumables. Note that the connections for this test utilized notch-tough welding consumables, and more severe connection failures may dominate using the non-notch tough welding consumables typical of vintage braced frame construction. The unstiffened second-story east lower gusset plate also punched through the web of the weak-axis column as the east connection area attempted to rotate in-plane about the column-beam work-point (see Figure 5.31).

6.3.5.1 Shear Tab Behavior

The welded first-floor east shear tab fractured, beginning at the edge of the lower stiffener along the bottom of the shear tab and extending to the stiffener at the top of the shear tab, as shown in Figures 5.43(a) and 5.44(a). When the crack opened at this location, the beam tended to rotate as if it were pinned in-plane and twist about its longitudinal axis; see Figure 5.28. This connection was not designed to resist the forces that developed due to overall frame action and the local forces created by the observed EBF-like beam link behavior; see Figure 5.45(a).

The moment-rotation relationship of the first-story east shear tab can be seen in Figure 6.35. The moment at the shear tab connection was higher than the roof shear tab connection of the NCBF-B-1 test. This is most likely because of the additional moment capacity provided by the second-story gusset plate above that shear tab location. As the crack opened in the shear tab base metal, the moment at the end of the beam was reduced. This crack opening and corresponding moment reduction occurred at approximately 0.03 radians of rotation. The pink “+” in the plot represents the loss of instrumentation monitoring the rotation of that region when the second-story east gusset plate punched through the weak-axis column web just above the shear tab location. The first-floor east shear tab had already showed crack initiation before this pink “+” symbol.

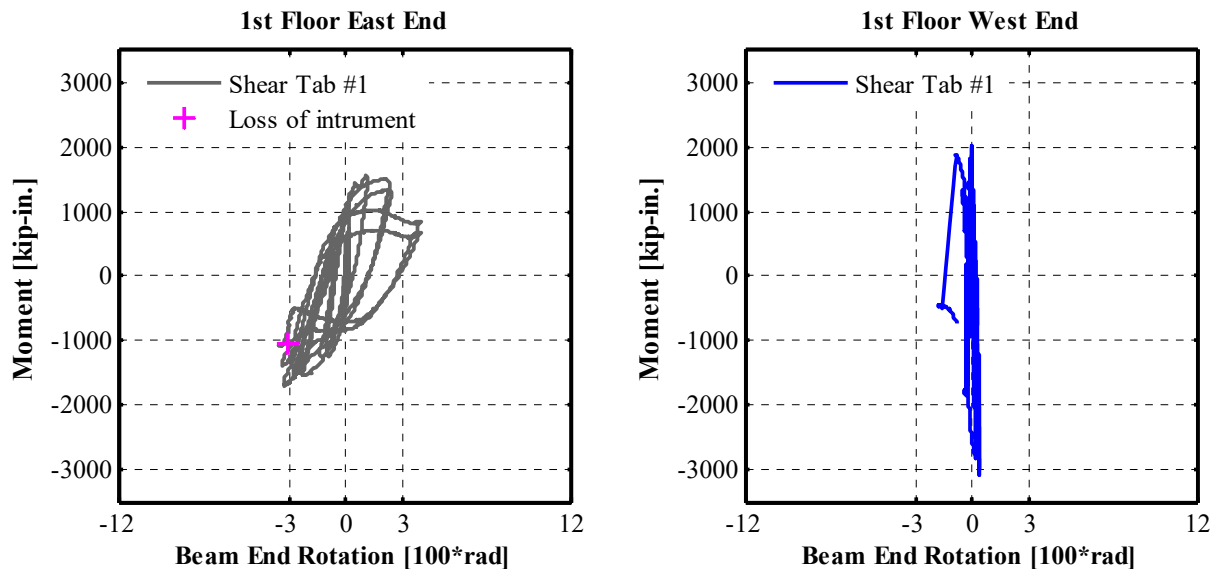


Figure 6.35 NCBF-B-2 first-floor beam estimated end moment versus end rotation.

6.4 NCBF-B-3SB STRONGBACK RETROFIT

Table 6.15 shows the legend of symbols used to describe significant events in the plots for the NCBF-B-3SB test. Values for these points are called out in Table 6.17. The global hysteretic behavior of the frame during the entire test can be seen in the hysteretic loop of Figure 6.36, and documentation of the events during the test can be found in Section 5.4. A breakdown of the hysteretic cycles at each peak roof drift amplitude can be found in Figure 6.37.

Table 6.15 NCBF-B-3SB legend of symbols for significant event points.

+	1F Shear Tab Failure
○	Reload
●	BRB satisfies AISC
*	BRB Failure
+	2F Shear Tab Failure
●	Test End

6.4.1 Global Behavior

The NCBF-B-3SB specimen consisted of a retrofit “strongback” design whose aim was to mitigate the weak-story behavior observed in both the NCBF-B-1 and NCBF-B-2 test specimens. The SB system performed as intended and engaged both stories in energy dissipation throughout the entire loading protocol, as can be seen in the nearly linear behavior in the story hysteresis loops of Figure 6.40 and the schematic in Figure 5.66(a). Inelastic behavior was initiated upon yielding of the BRB in compression at 0.21%. The hysteretic loops through the 2% roof drift ratio cycles were full and stable (Figure 6.38) and behaved much like a typical BRB frame. In contrast, the first two specimens exhibited significant deterioration in strength and stiffness after local buckling was observed in the braces at roof drift ratios of 0.44% and 0.77%. In this case, significant deterioration is defined when the specimen’s capacity decreased below 80% of the maximum capacity, V_{max} , as shown in Tables 6.16 for the NCBF-B-3SB test.

During the first quarter-cycle to a roof drift ratio of 2.5%, the outer casing of the BRB bulged, and the frame exhibited a softening response, as shown in the later hysteresis loops of roof drift ratios of 2.5% and larger in Figure 6.37. The difference in system behavior before and after BRB rupture can be seen in Figures 6.38 and 6.39. Prior to this softening, the system exhibited strain hardening, as shown by the increasing $V/V_{max,min}$ ratio in Table 6.16. In spite of this softening response, the strongback prevented a weak-story response throughout the remainder of the test. While the stiffness and strength of the frame was reduced, the frame was still able to dissipate energy through smaller but stable hysteretic loops produced by the stiffness and strength of the remaining members.

Plastic hinges formed where expected in the system: at both column bases and at the first-floor east beam near the center connection, as predicted by the kinematic diagram of Figure 3.14. Residual drift ratios at the end of the test are detailed in Table 6.17 and by the “Test End” marker in Figures 6.36 and 6.40. Residual drift ratios in both the first and second stories were similar and approximately 0.6% at the end of the test.

Table 6.16 NCBF-B-3SB peak base shears at each cycle.

Cycle (n)	Amplitude (%)	V (kips)	V/V _{max}	Event	Amplitude (%)	V (kips)	V/V _{min}	Event	
									1
2	+0.1	104.7	0.20		-0.1	-103.8	0.22		
3	+0.2	201.7	0.39		-0.2	-194.5	0.42		
4	+0.2	198.3	0.38		-0.2	-193.3	0.42		
5	+0.5	252.1	0.48	BRB (Y)	-0.5	-245.4	0.53		
6	+0.5	270.0	0.52		-0.5	-262.0	0.56		
7	+0.75	324.4	0.62		-0.8	-316.1	0.68		
8	+0.75	335.5	0.64		-0.8	-321.8	0.69		
9	+1.0	372.0	0.71		-1.0	-359.2	0.77		
10	+1.0	377.5	0.72		-1.0	-359.7	0.77		
11	+1.5	424.8	0.82		-1.50	-400.6	0.86		
12	+1.5	468.5	0.90		-1.50	-430.7	0.93		
13	+2.0	514.1	0.99		-2.0	-464.3	1.00		
14	+2.0	521.2	1.00		-2.0	-453.7	0.98		
15	+2.5	497.8	0.96	BRB (Fr)	-2.5	-258.3	0.56		
16	+2.5	303.9	0.58		-2.5	-242.3	0.52		
17	+3.0	314.5	0.60		-3.0	-216.0	0.47		
18	+3.5	364.1	0.70						
V _{max} =		521.2	kips		V _{min} =		-464.3	kips	

¹ Maximum base shear in each half-cycle.

Table 6.17 NCBF-B-3SB description of event points.

Event point	Event	Amplitude	Cycle no.	θ_R	θ_1	θ_2
		(%)		(%)	(%)	(%)
0	1F BRB (Y)	+0.5	1	+0.21	+0.18	+0.25
1	1F E shear tab (Fr)	-1.5	1	-1.43	-1.38	-1.49
6	1F E BRB (Fr)	+2.5	1	+1.45	+1.37	+1.56
7	2F E shear tab (Fr)	+2.5	1	+2.49	+2.42	+2.56
8	Test end			+0.61	+0.58	+0.65

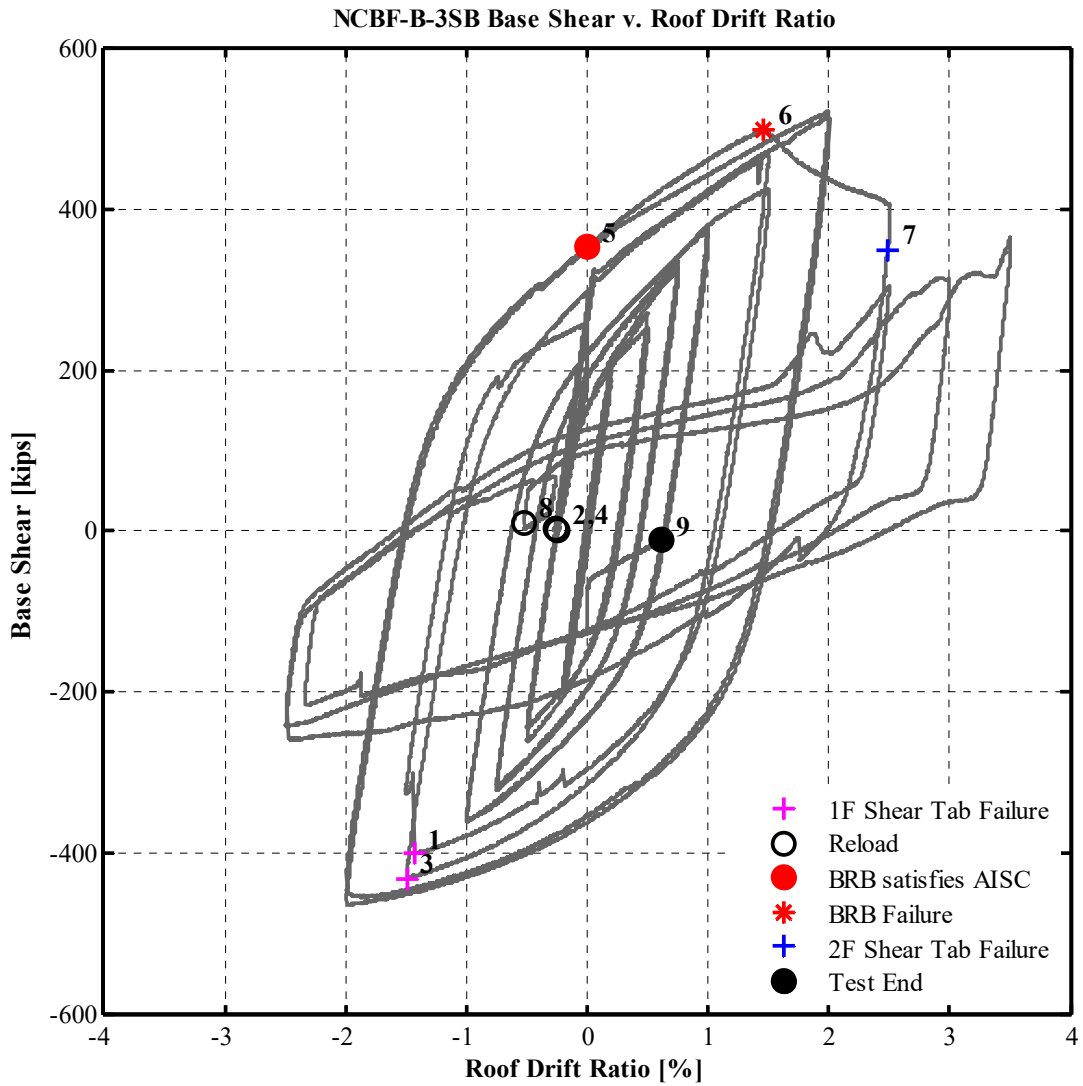


Figure 6.36 NCBF-B-3SB base shear versus roof drift ratio.

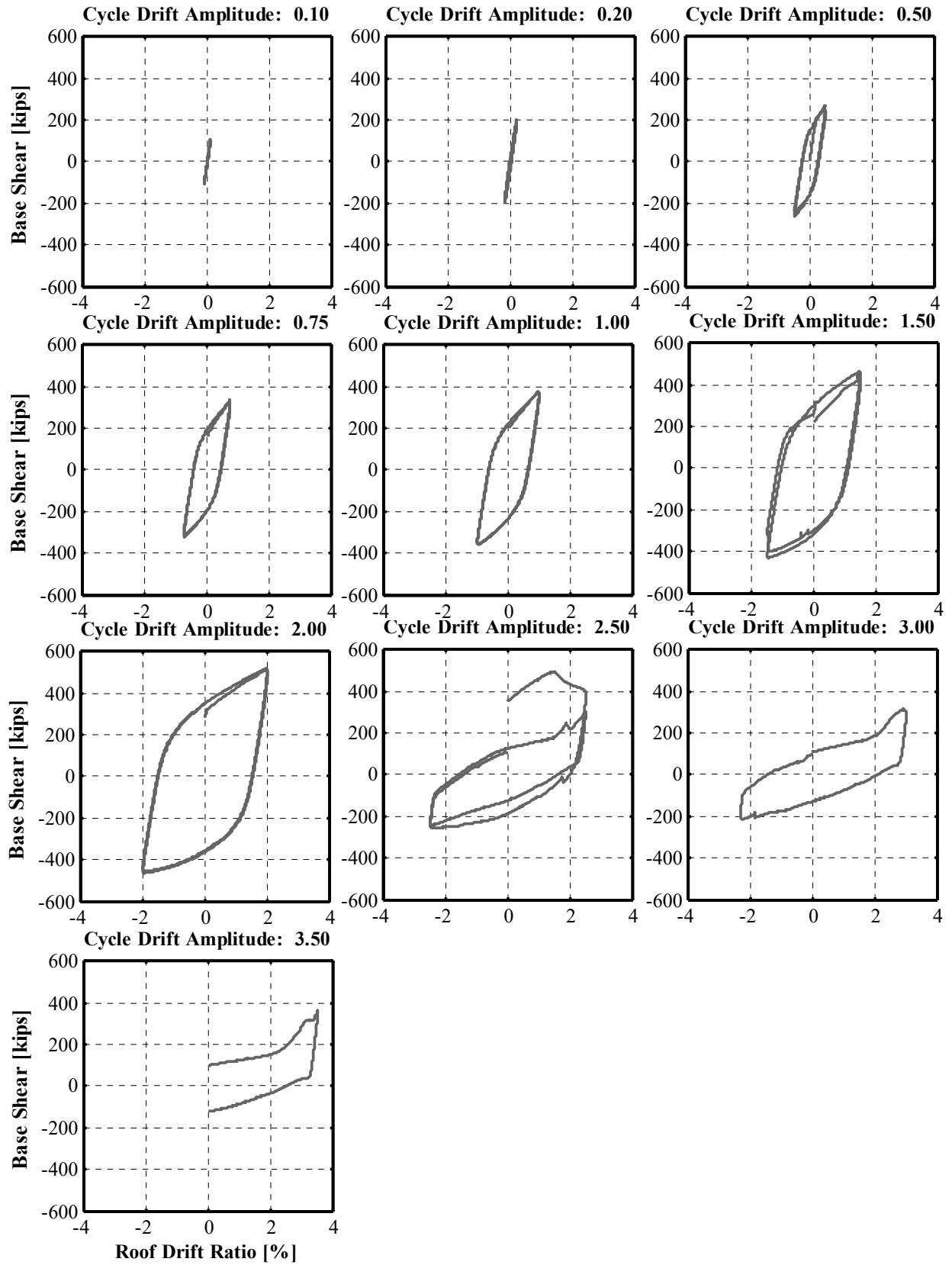


Figure 6.37 NCBF-B-3SB hysteretic loop breakdown by cyclic amplitude.

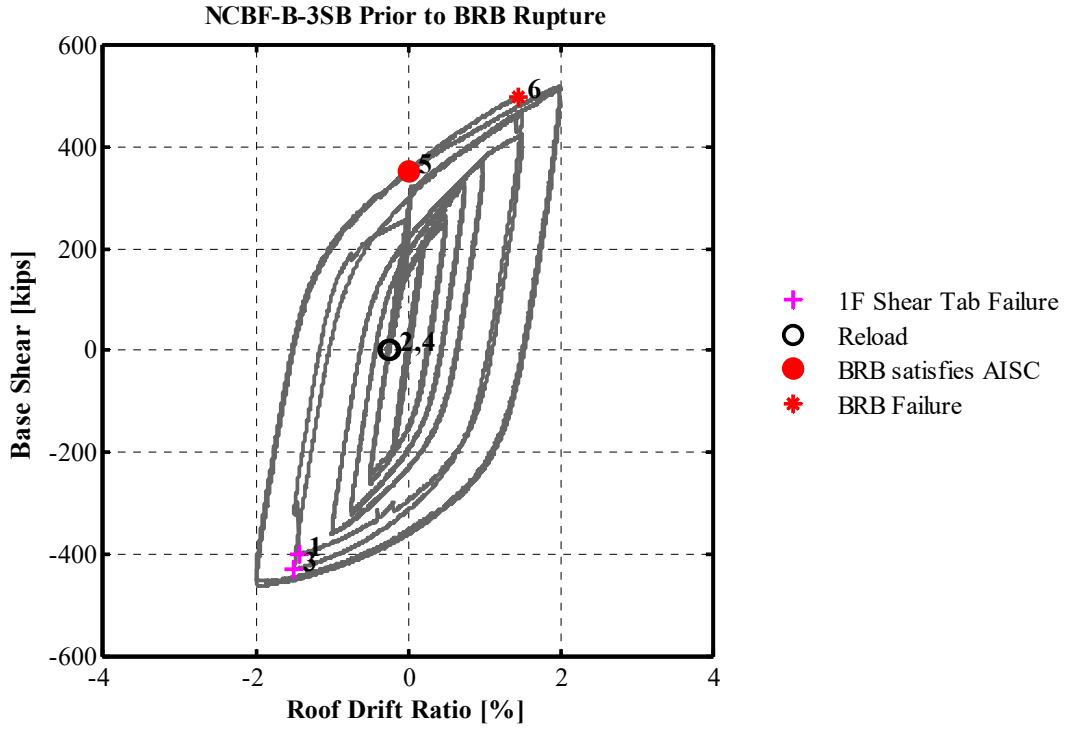


Figure 6.38 NCBF-B-3SB base shear versus roof drift ratio prior to rupture of BRB (@+1.45% on first cycle to +2.5%).

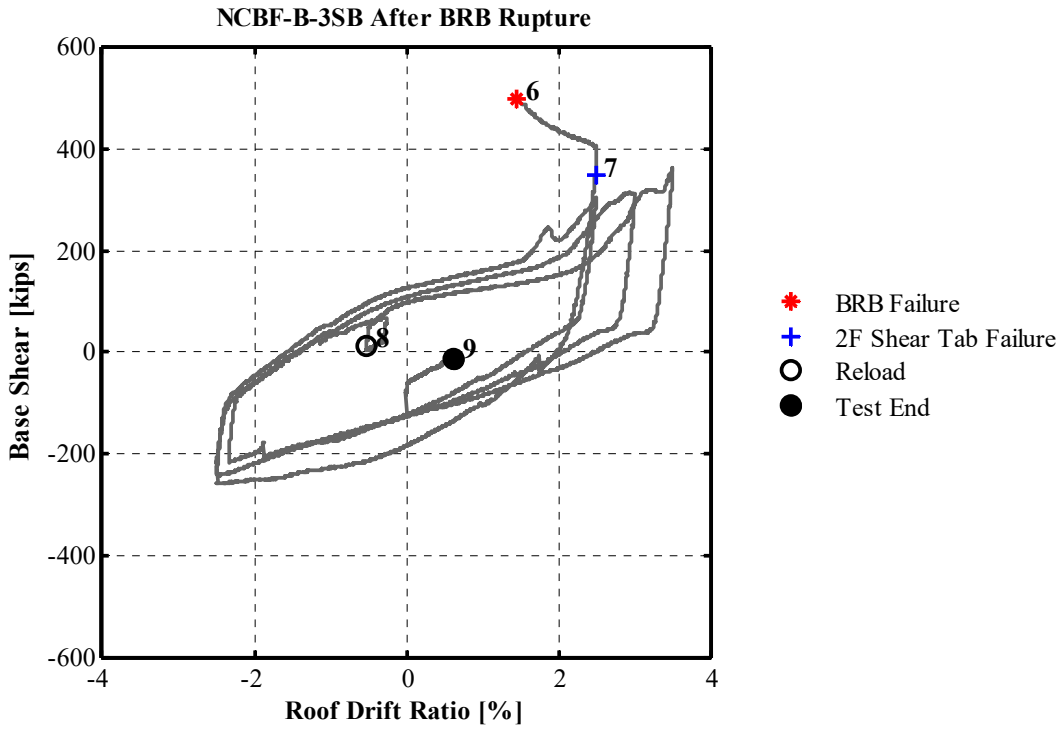


Figure 6.39 NCBF-B-3SB base shear versus roof drift ratio after rupture of BRB (@+1.45% on first cycle to +2.5%).

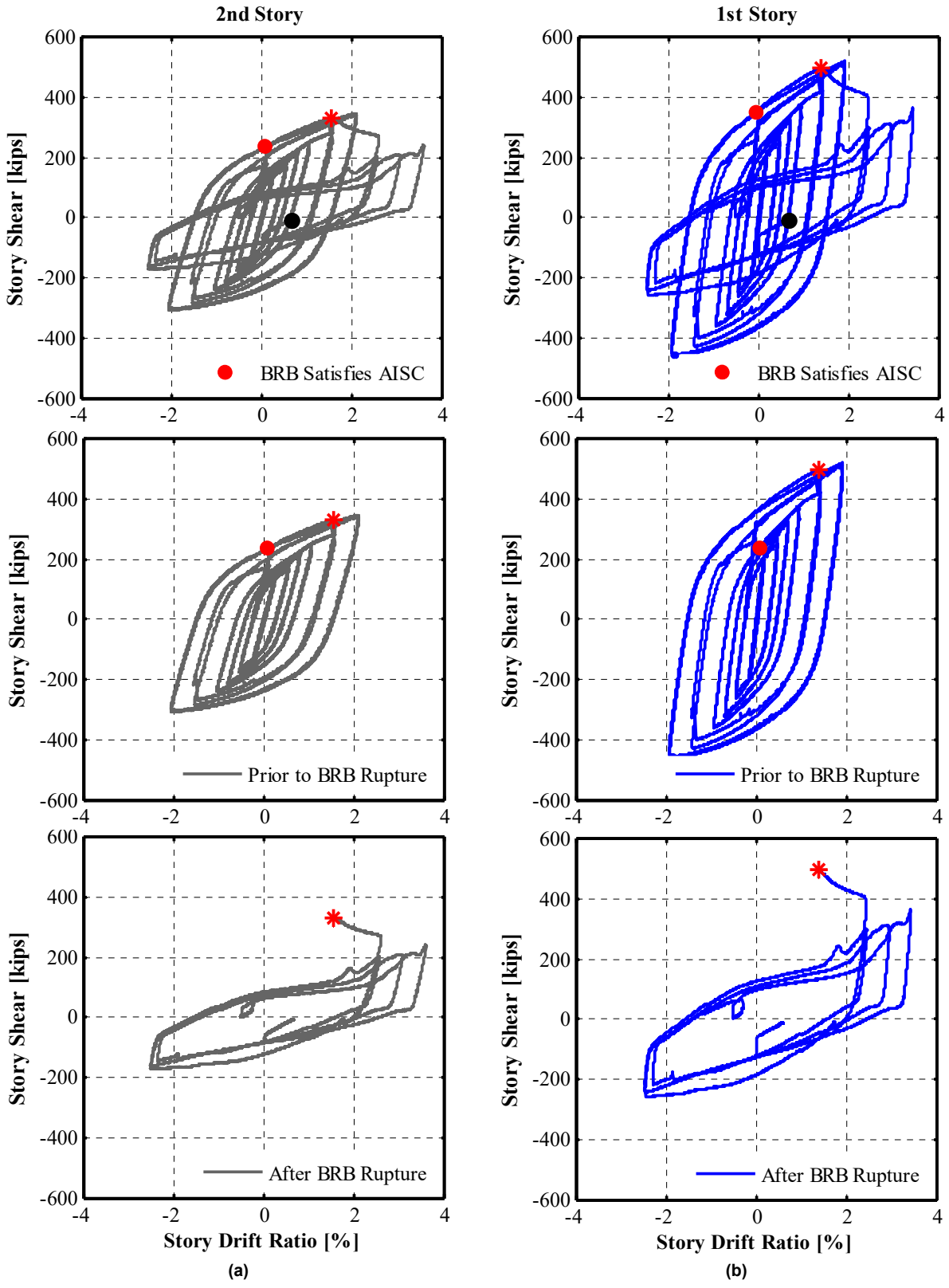


Figure 6.40 NCBF-B-3SB story shear versus story drift ratio: (a) second story; and (b) first story (BRB rupture at +1.45% on first cycle to +2.5%).

6.4.2 Elastic Brace Response

Both braces in the “strongback” half of the system remained elastic, as indicated by the roughly linear relationship shown in Figure 6.41 and the plots of Figures C.4 and C.5. Design for the elastic braces was conservative, as shown by the solid black lines representing the nominal tension, T_n , and compression, C_n , capacities of the elastic braces as provided by AISC 360-10 [2010]. Further optimization of the elastic half of the system could provide smaller, yet still adequate, brace sections. Note, however, that these demands could be significantly different under dynamic loading conditions.

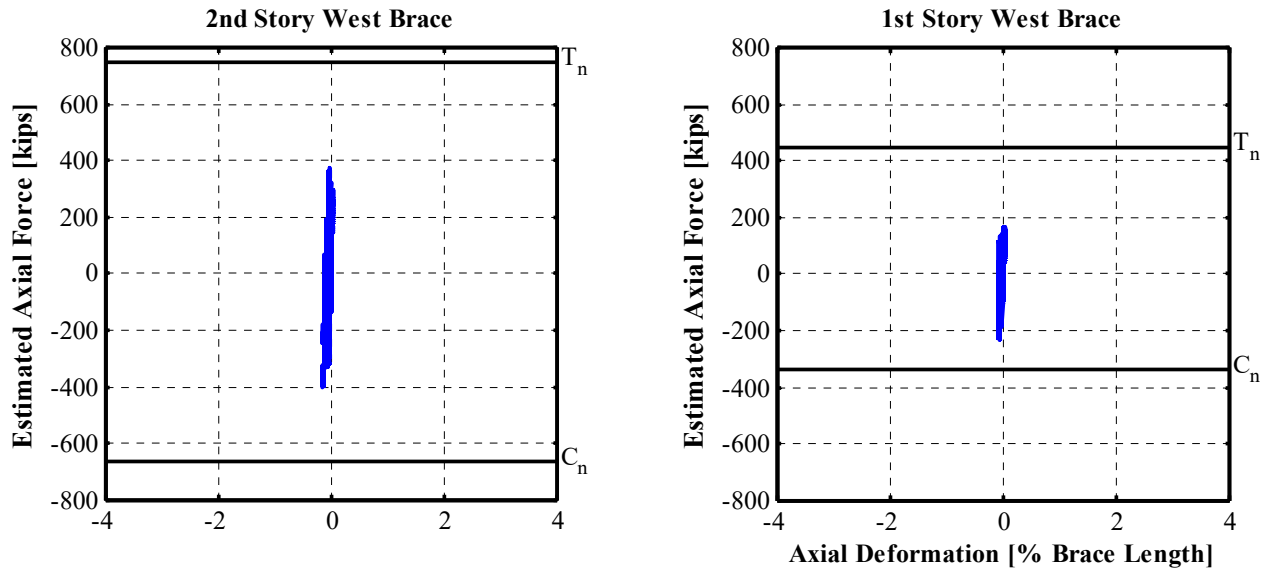


Figure 6.41 NCBF-B-3SB estimated elastic west braces axial force versus axial deformation (% brace length is the work-point-to-work-point length).

6.4.3 Buckling Restrained Brace Response

The BRB exhibited full and stable hysteretic loops and substantial isotropic and kinematic hardening after yielding at 0.21% roof drift ratio in compression, as shown in the BRB hysteresis loops of Figure 6.42.

A decrease in the load-carrying capacity of the BRB was observed during the first cycle to a roof drift ratio of +2.5% when the outer casing of the BRB bulged in compression. It is inferred from the subsequent loss of tensile capacity that the BRB core ruptured in tension during that same cycle to -2.5%. In spite of this, the BRB continued to contribute to the SB frame’s resistance when the ruptured portions of the fractured core came in contact with one another in compression as shown in the post-rupture cycles of Figure 6.42.

Comparisons between experimental values and the nominal values for the yield force and adjusted compression and tension capacities of the BRB can be found in Table 6.18. The yield deformation, Δ_{by} , is calculated by Equation (6.3). Note that the axial force for the BRB is an estimated quantity, as described in Section 4.3.1.2. As such, specific values for the BRB axial force can describe relative trends of estimated brace behavior and may not represent the exact

loads seen by the brace. Discrepancies between the nominal and experimental values likely come from inaccuracies in estimating the axial force in the BRB.

The BRB experienced negligible moment and shear and was loaded almost entirely in axial compression and tension; see Figures C.6 and C.12. After the test, the BRB core was removed from the casing to examine the ruptured region. The steel core had ruptured at the location of the bulge in the outer BRB casing; this occurred at approximately mid-length. Residual necking of the steel core was noticeable above and below the ruptured region, indicating that local buckling occurred at other locations along the BRB yield length. Despite high axial strains, the BRB satisfied current cyclic testing requirements for BRBs (AISC 341-10 [2010]) up to and including the target amplitude of 2.0%.

Table 6.18 NCBF-B-3SB BRB critical variables.

First-story east BRB	Nominal	Experiment
P_y^1 (kips)	230	209
Δ_{by} (in.)	0.16	0.15
C_{max}^1 (kips)	357	435
T_{max}^1 (kips)	327	386

¹ T_{max} and C_{max} correspond to the maximum compression and tension capacity of the BRB as specified by StarSeismic ($T_{max} = \omega P_y$; $C_{max} = \beta \omega P_y$, where P_y is the force required to yield the steel core of 5 in.²).

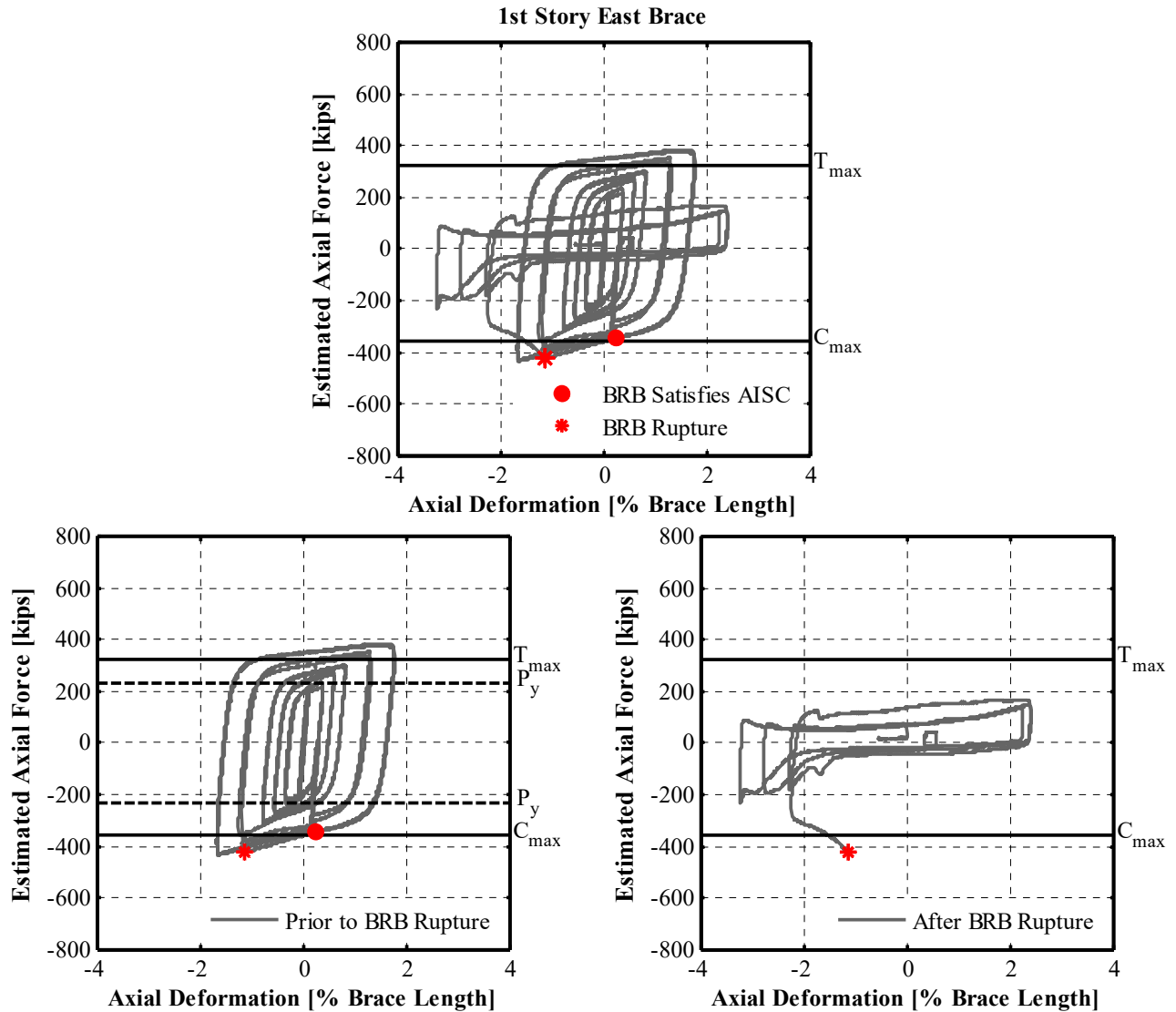


Figure 6.42 NCBF-B-3SB estimated BRB axial force versus axial deformation (% brace length is the work-point-to-work-point length).

6.4.3.1 Assessment of BRB by AISC 341-10 Criteria

The following acceptance criteria must be satisfied for the BRB and BRB sub-assembly to be deemed acceptable by the AISC 341-10 [2010] provisions. This section uses the definitions for Δ_{by} and Δ_{bm} as defined in Table 4.2.

1. The plot showing the applied load versus displacement history shall exhibit stable, repeatable behavior with positive incremental stiffness.

Both the BRB and sub-assembly frame met this requirement up to $2\Delta_{bm}$, as can be seen by the hysteretic plots in Figures 6.38 and 6.42.

2. There shall be no rupture, brace instability, or brace end connection failure.

The BRB showed no signs of rupture or strength deterioration prior to $2\Delta_{bm}$, as can be seen by the hysteretic plots in Figures 6.38 and 6.42.

3. For brace tests, each cycle to a deformation greater than Δ_{by} the maximum tension and compression forces shall not be less than the *nominal strength* of the core.

The nominal strength of the core can be calculated from the following equation:

$$P_y = F_y A_{sc} = 230 \text{ kips} \quad (6.2)$$

where $F_y = 46 \text{ ksi}$ and $A_{sc} = 5 \text{ in.}^2$ are the yield strength and the area of the core, respectively. The first cycle after Δ_{by} did not exceed P_y , and the axial load was 217 kips in tension and 219 kips in compression. Every other subsequent cycle after these two initial cycles exceeded this quantity prior to $2\Delta_{bm}$. The compression and tension forces can be compared to the dotted line in Figure 6.42, which denotes the quantity P_y with respect to the estimated brace axial force.

4. For brace tests, each cycle to a deformation greater than Δ_{by} the ratio of the maximum compression force to the maximum tension force shall not exceed 1.3.

Table 6.19 shows that the BRB satisfied this criterion during every loading cycle. The compression strength of the BRB never exceeded the tension strength of the BRB (C_{max}/T_{max}) by more than 1.3.

Table 6.19 Ratio of maximum compression force, C_{max} , to the maximum tension force, T_{max} for each cycle.

n	Roof drift ratio (%)	Cycle at amplitude, n	C_{max}/T_{max}
1	0.5	1	1.01
2		2	1.01
3	0.75	1	1.03
4		2	1.03
5	1	1	1.03
6		2	1.04
7	1.5	1	1.05
8		2	1.10
9	2	1	1.12
10		2	1.15

5. Additional complete cycles after $2\Delta_{bm}$ shall be applied to the test specimen as required for the brace to achieve a cumulative inelastic axial deformation of at least 200 times the yield deformation.

Table 6.20 shows the cumulative plastic deformation (CPD) of the BRB over each roof drift amplitude. It can be seen that the final CPD developed by the BRB exceeded the value of $200\Delta_{by}$, as required by AISC 341-10 [2010].

The yield deformation, Δ_{by} , for the BRB was estimated as 0.15 in. from the hysteretic loop in Figure 6.42. The axial deformation of the brace was generated from the average of two wire pots located on either side of the BRB extending the full length of the BRB from the collars at both ends. The estimated axial force was calculated from four

strain gages located near the lower end of the BRB. The lateral component of this axial force was also correlated to the total first-story shear minus the column shears and minus the lateral component of the axial force of the west first-floor brace. The procedure for determining the BRB force is further outlined in Section 4.3.1.2.

An estimate of the yield deformation was calculated by fitting a linear line to the elastic portion of the axial force-deformation plot. The slope of the fitted line determined the effective stiffness, k_e , of the BRB. This elastic portion was limited to the first two cycles of roof drift at $0.5\Delta_{by}$. The yield displacement was then calculated by the following formula:

$$\Delta_{by} = \frac{P_y}{k_e} = 0.147 \text{ in.} \quad (6.3)$$

where $k_e = 1415$ kips/in. and $p_y = 209$ kips as estimated from the yield force in the experimental data. Comparisons were additionally made between this method and a theoretical method for calculating the yield deformation. The theoretical method relied on calculating the individual stiffness of the BRB components and combining them in series [Black et al. 2002] as follows:

$$K_e = \frac{1}{\frac{1}{K_i} + \frac{2}{K_{con}} + \frac{2}{K_{tr}}} = 1444 \text{ kips/in.} \quad (6.4)$$

where K_i , K_{con} , and K_{tr} are the stiffness of the yielding core, the connection, and the transitional section of the brace respectively. A similar approach could then be taken to calculate the yield deformation as:

$$\Delta_{by} = \frac{P_y}{K_e} = 0.158 \text{ in.} \quad (6.5)$$

The first solution in Equation (6.3) varies from Equation (6.5) by 7.5%. Thus, it was deemed acceptable to use the axial deformation calculated from the linear fit of the data.

The CPD was then calculated by summing the normalized plastic deformations in each cycle. These plastic deformations did not include the elastic deformations observed upon reloading and unloading of the BRB. For simplicity, the effect of strain hardening on the lower bound of the plastic deformation was ignored, and this lower bound was assumed to be Δ_{by} . The formula used in calculating the CPD is as follows:

$$CPD = \sum_{i=1}^n i \frac{|\Delta_{\max,n}| - \Delta_{by}}{\Delta_{by}} = \sum_{i=1}^n i \frac{|\Delta_{p,n}|}{\Delta_{by}} \quad (6.6)$$

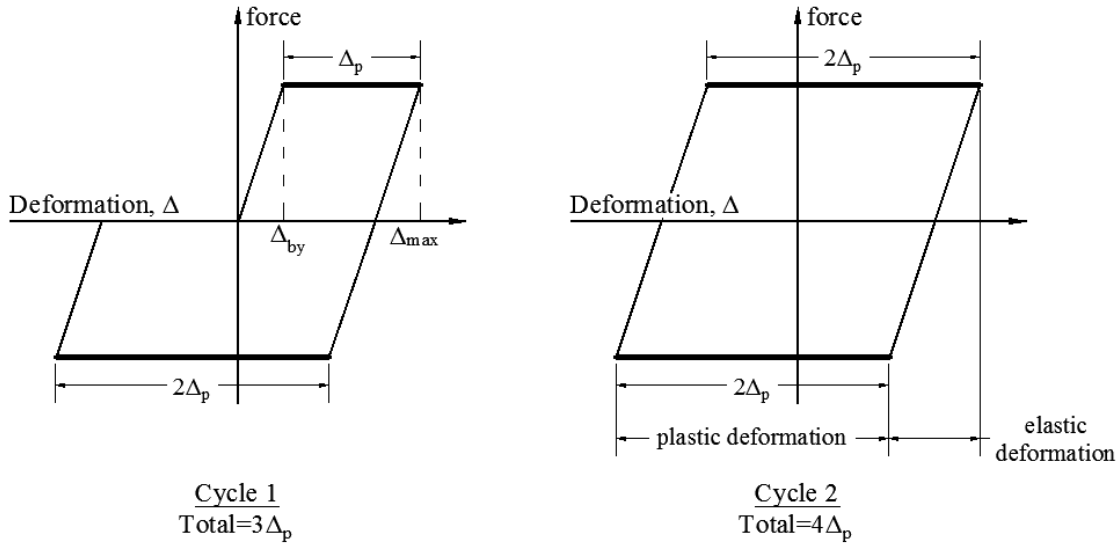
where i is an integer counting the number of movements towards a specific amplitude over the total number of cycles at that amplitude increment, n . The details of this calculation can be seen in Table 6.20, and an example calculation of an idealized cycle is shown in Figure 6.43.

Table 6.20 Cumulative plastic deformation calculations for the first-story east BRB on each cycle of loading.

Amplitude increment (n)	Peak cyclic roof drift ratio (%)	Cycle count	Normalized peak deformation		Normalized plastic deformation	Cumulative plastic deformation
			$\Delta_{min} / \Delta_{by}$	$\Delta_{max} / \Delta_{by}$	$\Delta_{p,n} / \Delta_{by}^2$	
1	0.1	1	0.51	0.48	0.0	0.0
		2	0.49	0.48		
2	0.2	3	1.12	1.12	0.0	0.0
		4	1.06	1.11		
3	0.5	5	4.33	4.37	$(3+4)(\Delta_{max,3} - \Delta_{by})/\Delta_{by} = 22.9$	22.9
		6	4.13	4.26		
4	0.75	7	6.71	6.82	$2*4(\Delta_{max,4} - \Delta_{by})/\Delta_{by} = 45.8$	68.7
		8	6.58	6.79		
5	1.0	9	9.29	9.42	$2*4(\Delta_{max,5} - \Delta_{by})/\Delta_{by} = 66.5$	135.2
		10	9.15	9.41		
6	1.5	11	14.70	15.39	$2*4(\Delta_{max,6} - \Delta_{by})/\Delta_{by} = 110.1$	245.3
		12	14.18	14.76		
7	2.0	13	19.60	20.30	$2*4(\Delta_{max,7} - \Delta_{by})/\Delta_{by} = 151.6$	396.8
		14	19.34	20.53		
8	2.5	15	13.27	0	$2(\Delta_{max,8} - \Delta_{by})/\Delta_{by} = 24.5$	421.4
		16 ¹	0	0	-	-
9	3	17	0	0	-	-
10	3.5	17.5	0	0	-	-

¹ The BRB exhibited a softening response before reaching the first peak at the amplitude of 2.5% roof drift ratio. The CPD was not calculated for further plastic deformation beyond point, but note that the fractured ends of the BRB contributed some capacity to the system in compression during subsequent cycles after BRB rupture.

² Example equations are provided for illustrative purposes and may not reflect calculated values taken from test data.



Example Calculation: $n = 3$

$$i = (3+4)$$

$$\Delta_{p,3}/\Delta_{by} = (3+4)(\Delta_{max,3} - \Delta_{by})/\Delta_{by}$$

Figure 6.43 Example calculation for the cumulative plastic deformation for idealized cycles at amplitude increment $n = 3$.

The maximum strain seen during the test was 4.0%. This was calculated through the following equation:

$$\varepsilon = \frac{\Delta}{L_i} \leq 2.5\%$$

where L_i is the yield length of the BRB core as provided by StarSeismic, and Δ is the maximum axial deformation estimated from the BRB experimental data. As noted in Section 3.2.3.2, the “lambda” SB configuration increases the strains in the BRB by a factor of more than twice that of a conventional braced frame configuration with a “strong” beam; see Section 2.2.4. Despite these large deformation demands, the BRB satisfied AISC 341-10 [2010] testing requirements and completed two cycles at the required drift level of $2\Delta_{bm}$ as shown by the red “*” in Figure 6.42 and the calculations provided in Section 6.4.3.1. The BRB was able to develop a CPD of 421 before exhibiting a softening response. This CPD value is greater than the AISC provision of 200 times the yield deformation, as discussed in Section 6.4.3.1(5). In summary, the BRB’s behavior satisfied the requirements in current AISC specifications.

6.4.4 Beam Response

A plastic hinge developed in the first-floor beam to the east of the middle gusset plate connection, as shown in Figure 5.56. This region performed well during the test and showed no signs of crack initiation or fracture. The beam exhibited secondary energy dissipation through plastic yielding and web and flange local buckling after rupture of the BRB.

The first-floor beam moved up and down during the test, behaving much like the beam of the NCBF-B-2 test, as shown in the plot of mid-span vertical displacement of Figure 6.45(b).

Like the NCBF-B-2 test, the estimated unbalanced load from the braces was also both up and down. The strongback effectively linked the vertical displacement of the center of the beam to the lateral displacement of the roof, moving a maximum of 2.76 in. upward and 3.78 in. downward. Table 6.21 compares the estimated unbalanced load and vertical displacement for each test specimen. The estimated moments at the ends of the east and west first-floor half-beams are shown in Figure 6.47. These moments were estimated according to the description provided in Section 4.3.1.4. The estimated moment to the east of the middle connection exceeded the plastic moment capacity of the beam, M_p , near the plastic hinge location. The jump in plots of the east half-beam are due to loss of strain gages that were replaced during the testing process.

The west end of the first- and second-floor beams rotated very little during the test, remaining at a right angle to the column face, as shown in the rotation plots of Figure 6.46. This behavior is much like the behavior observed in the first story of the second specimen due to the “rigid” motion shown in Figure 5.45. The east ends of the beam rotated in both clockwise and counterclockwise directions. This rotation was roughly double the story rotation at the first floor, as predicted by the kinematic diagram of Figure 3.14. At the roof, this rotation was approximately equal to the story rotation.

A plot of the estimated shear in the east half of the first-floor beam is shown in Figure 6.44(b). For comparison purposes, the beam shear of NCBF-B-2 is also shown in Figure 6.44(a) up to when the punching failure occurred at the weak-axis column, as called out by the pink “+” in that figure. Definitions for labels indicated on the plots are called out in Section 6.3.3. Like the NCBF-B-2 test, the east half-beam behaved like a long beam link in an eccentric braced frame. The maximum shear approaches $1.5M_p/L$. This induced shear was less than the shear capacity of the beam.

Table 6.21 Beam peak unbalanced load and vertical mid-span displacement.

Test specimen	Floor	Maximum unbalanced load (kips)		Vertical mid-span displacement (in.)	
		Maximum	Minimum	Maximum	Minimum
NCBF-B-1	Second floor	14.7	-79.7	0.24	-0.94
NCBF-B-2	First floor	138.2	-129.8	3.27	-4.78
NCBF-B-3SB	First floor	134.8	-87.9	2.76	-3.78

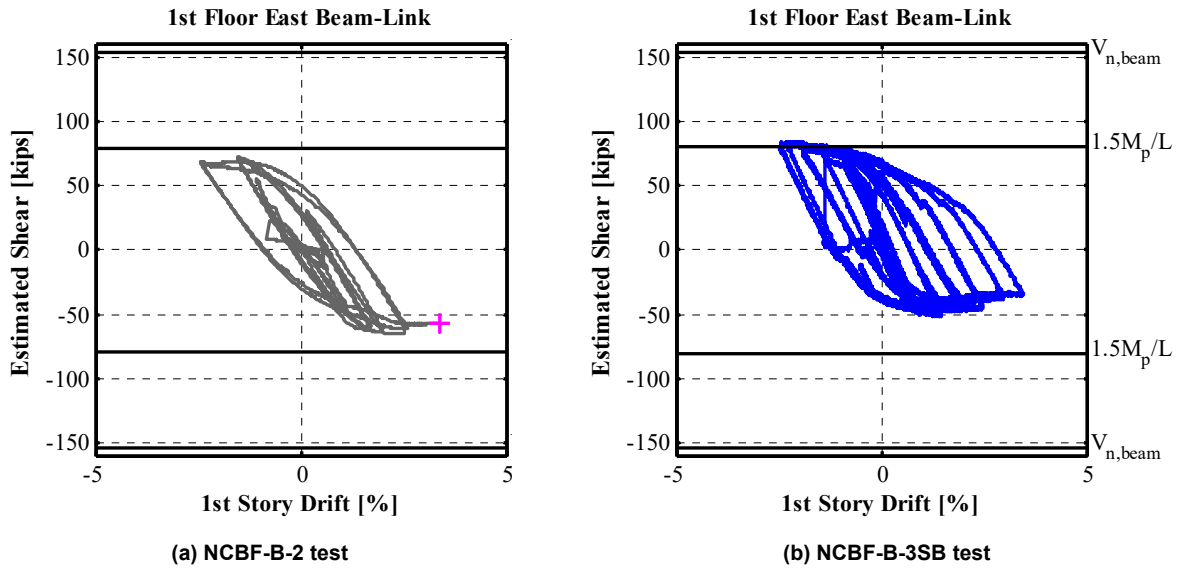


Figure 6.44 NCBF-B-3SB first-floor east $\frac{1}{2}$ -beam estimated shear versus story drift ratio (where L is the distance from the beam end to the edge of the middle connection).

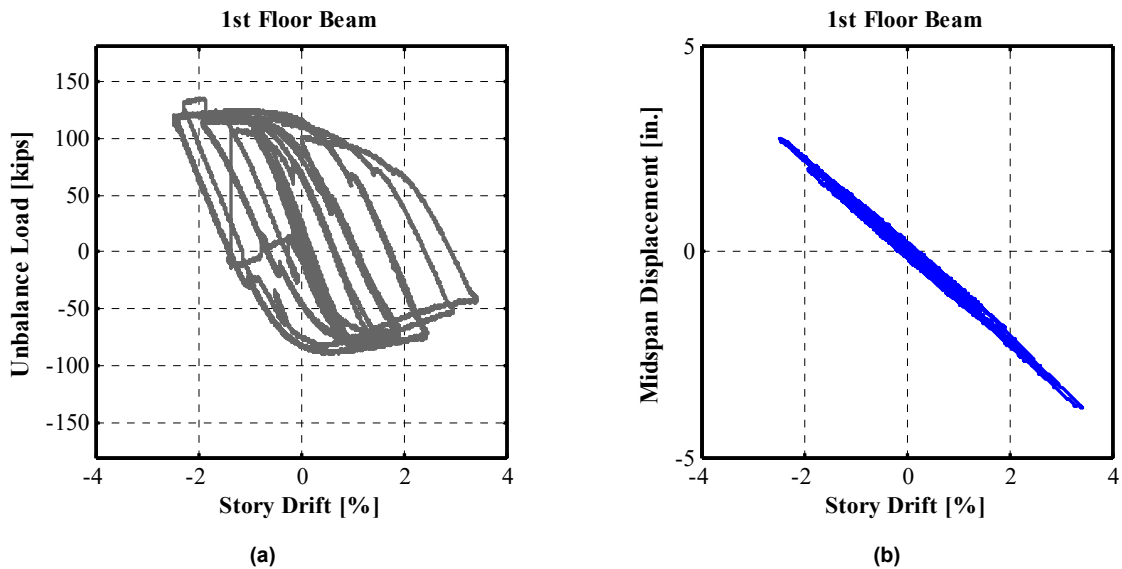


Figure 6.45 NCBF-B-3SB first-floor beam: (a) unbalanced load and (b) vertical midspan displacement versus story drift ratio. Note: Unbalanced load is positive upward.

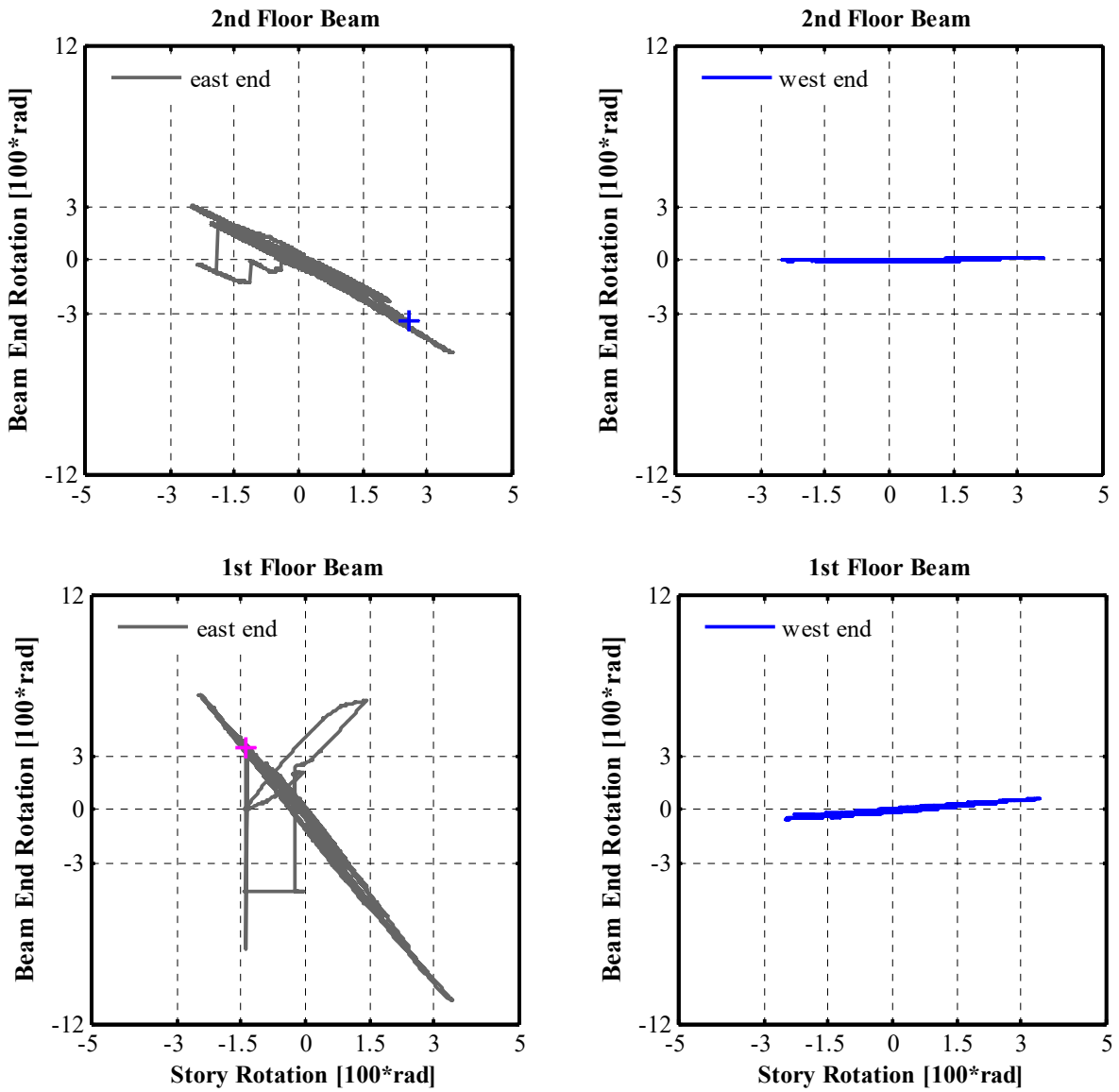


Figure 6.46 NCBF-B-3SB beam end rotations versus story rotation.

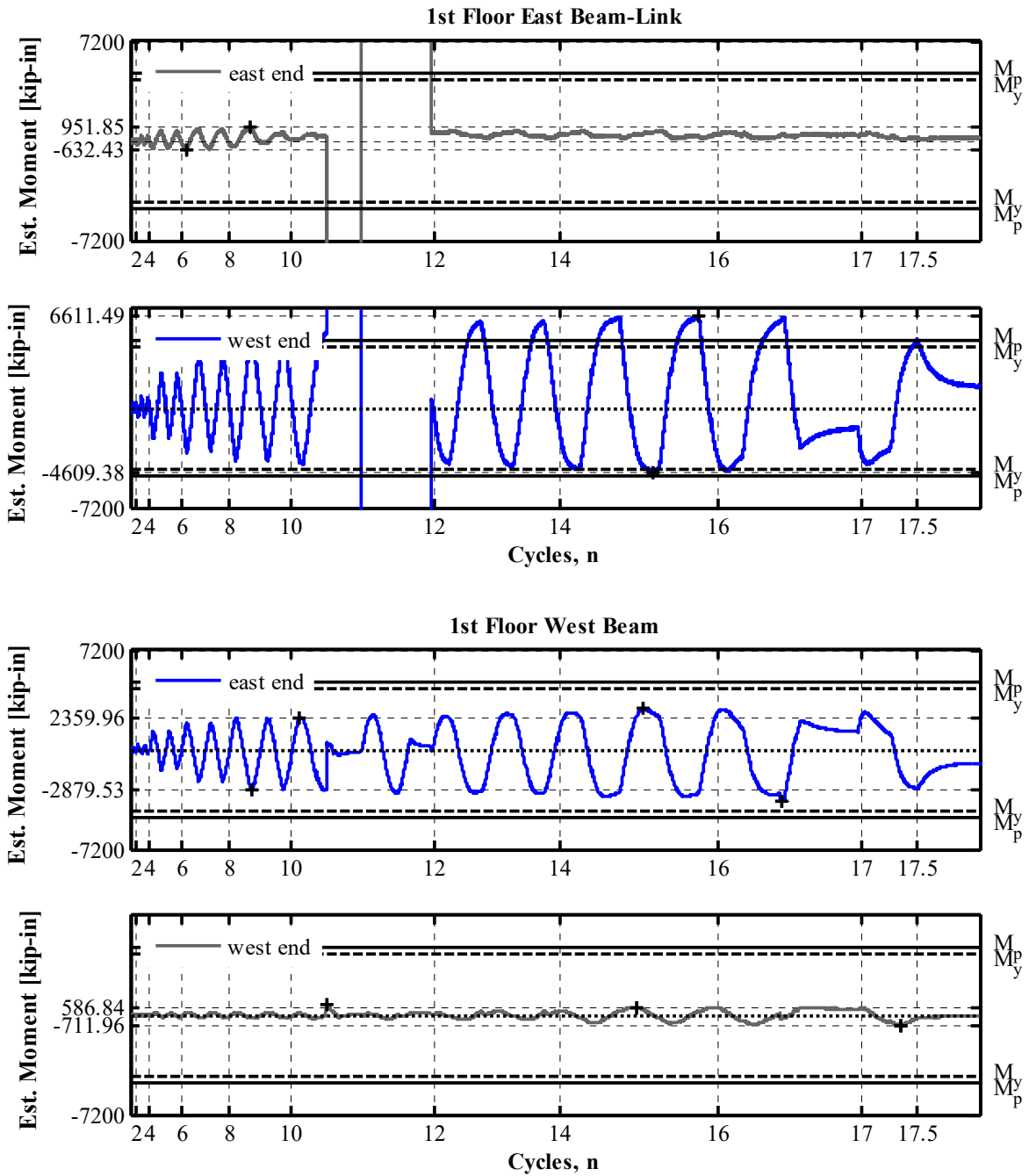


Figure 6.47 NCBF-B-3SB first-floor east and west 1/2-beam estimated end moment time histories (estimated at beam end and at a half-beam depth outside middle connection).

6.4.5 Column Response

For the lambda configuration used for the NCBF-B-3SB test, the axial forces in the east column were quite small compared to those in the west SB column (Figure 6.48). Axial force in the west column decreased after rupture of the BRB.

Plastic hinges developed at the base of both the east and west columns, as shown by the whitewash flaking evident in Figure 5.59. The east strong-axis column had small axial loads throughout the test (Figure 6.49), and most of the whitewash flaking (i.e., yielding) was isolated to the outer-most (east-side) column flange. The east weak-axis column had larger axial loads, but less moment demand. The estimated moment demand at the weak-axis column base approached M_y , as shown in Figure C.23; the weak-axis column was able to go through large rotational demand and acted much like a “pin” because of the small moment of inertia associated with the weak-axis bending direction.

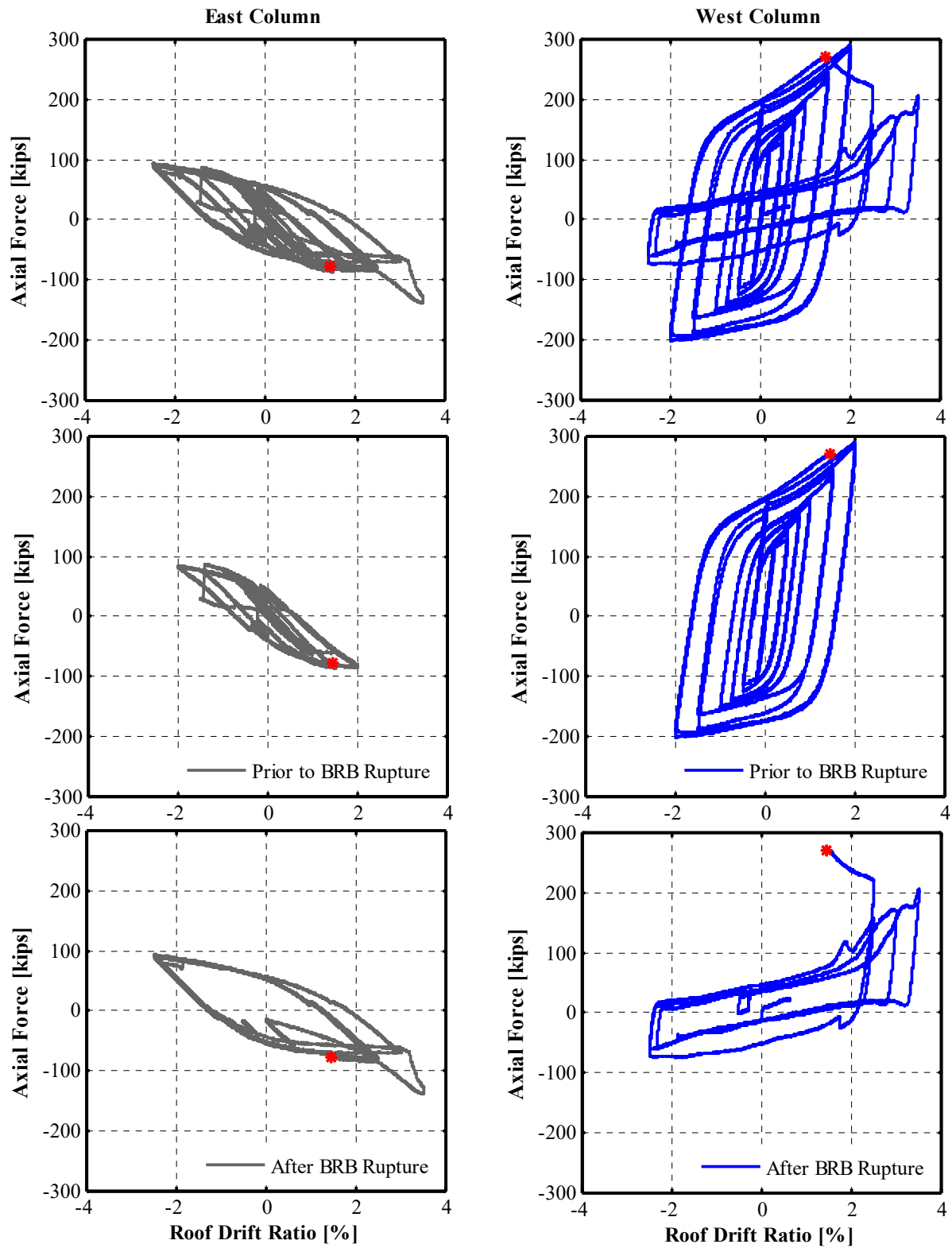


Figure 6.48 NCBF-B-3SB column estimated axial force versus roof drift ratio.

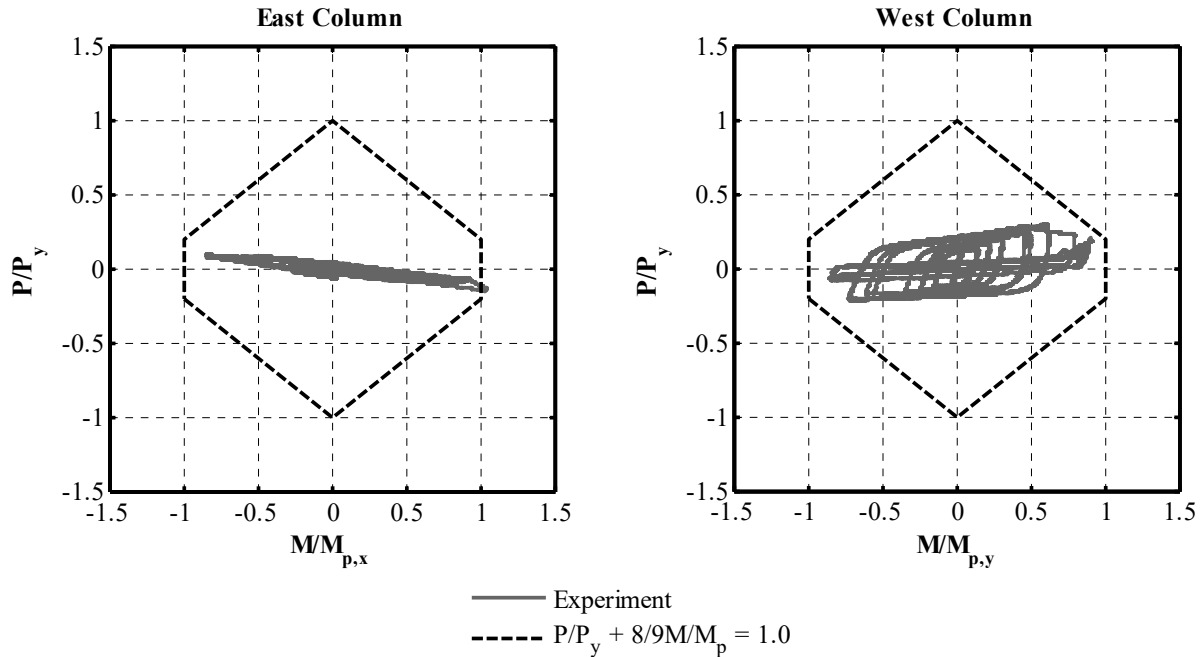


Figure 6.49 NCBF-B-3SB column normalized axial moment interaction (estimated at half the column depth above the second-story gusset plate connection). Here M_p is the plastic moment capacity of the column and P_y is the yield strength of the column equal to AF_y , where A is the cross-sectional area and F_y is the yield strength found from the coupon tests.

6.4.6 Connection Response

The majority of the connection regions behaved well during the test. The added edge stiffeners between the gusset plates and the weak-axis column flanges limited almost all yielding behind the external column web, and appeared to increase the web's performance at these regions compared to the first two test specimens. No vertical yield line appeared at the weak-axis column web, and the punching failure observed in the earlier tests seems to have been mitigated by the addition of these stiffeners.

Whitewash flaking at all of the gusset plates indicated minor yielding. Whitewash flaking was also observed at the net section region of the elastic braces; see Figure 5.60. The first-floor middle gusset plate connection exhibited little yielding at the end of the test. Other than the shear tab connections, the connections were considered to be “new” retrofitted details designed according to capacity design principles.

6.4.6.1 Shear Tab Behavior

Because of the failure of one of the shear tab connections, testing was interrupted and repairs (including upgraded details) were installed during the loading sequence. The effect of these repairs on the loading sequence can be seen in the unloading cycles of the roof drift ratio history plot in Figure 5.46.

The simple welded shear tab details at the east column on the first floor and roof level were both inadequate for the rotational demands induced in these regions. When these shear tabs

were initially designed, they were thought of as “existing” shear tabs from the original NCBF-B-1 baseline test specimen; see Section 3.2.3.6. A combination gusset-to-column weld and bolted beam-to-column connection was not considered common practice in these vintage CBF systems. As such, the shear tab was welded rather than bolted to be consistent with the weld at the gusset-to-column interface; see Section 3.2.1.4.

Due to the difficulty in acquiring non-notch tough welding consumables, the welds at the shear tab locations were specified as notch-tough and were consistent with today’s current welding standards. This welded detail did not have enough rotational capacity to meet the demands from the SB system (see Figures 3.14 and 6.46) and fractured on the first cycle to 1.5% roof drift ratio, corresponding to a rotational demand of 0.03 radians; see Figure 5.47.

The first-floor east welded shear tab was repaired with a new welded shear tab connection (Figure 5.50). Two new weld lines were also added to the top and bottom of the undamaged roof shear tab connection to preclude failures at the roof connection [Figure 5.53(a)]. The second shear tab was designed so the welds would be stronger than the gross section yielding of the shear tab plate. This would force the shear tab base metal to yield in a ductile manner before rupture of the welds. The shear tab was extended to create a larger gross section area for the shear tab to yield, and the welds were wrapped at the shear tabs top and bottom edges. However, the execution of the shear tab weld was deficient and the weld failed, so it is unclear whether this modified connection would have satisfied the rotational demands had these welds been adequate.

The third shear tab was designed with slotted holes to prevent large moment demands from developing at this region (Figure 5.52). The new connection behaved well and experienced minor yielding between the bolt holes of the shear tab connection. Note that the use of such a connection in an actual building would cause net elongation and shortening of the beam and would not be capable of transferring axial load.

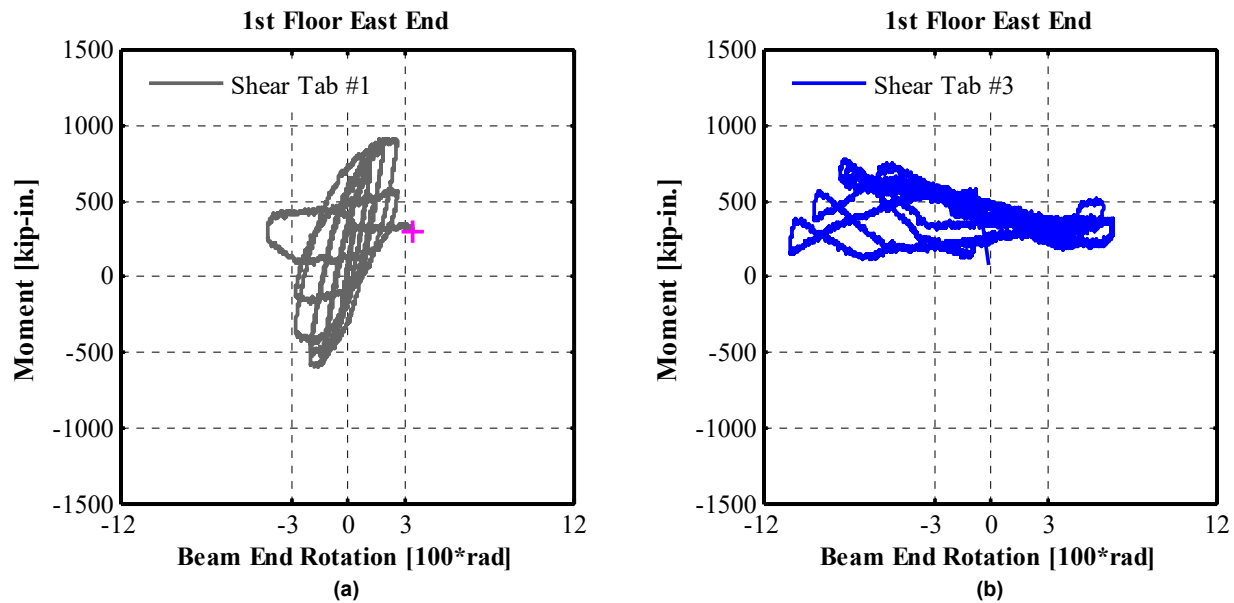


Figure 6.50 NCBF-B-3SB first-floor east beam estimated end moment versus end rotation: (a) welded shear tab and (b) slotted shear tab.

During the amplitude to 2.5% roof drift ratio, the east roof shop shear tab-to-column weld fractured; see Figures 5.53 and 5.54. This shear tab was not previously damaged and was presumed adequate since it had half of the rotational demands of the first-floor shear tab. After failure, the beam was allowed to cantilever off the west column roof level gusset plate connection for the remainder of the test.

Moment versus rotation plots for the first floor and roof east shear tabs are shown in Figures 6.50 and 6.51, respectively. Like the NCBF-B-2 test, the original welded shear tab appears to have a rotational capacity of roughly 0.03 radians for both the first floor and roof shear tabs. This rotational capacity was substantially increased upon replacement of the welded shear tab by the slotted shear tab, allowing this location to reach roughly 0.1 radians at its peak.

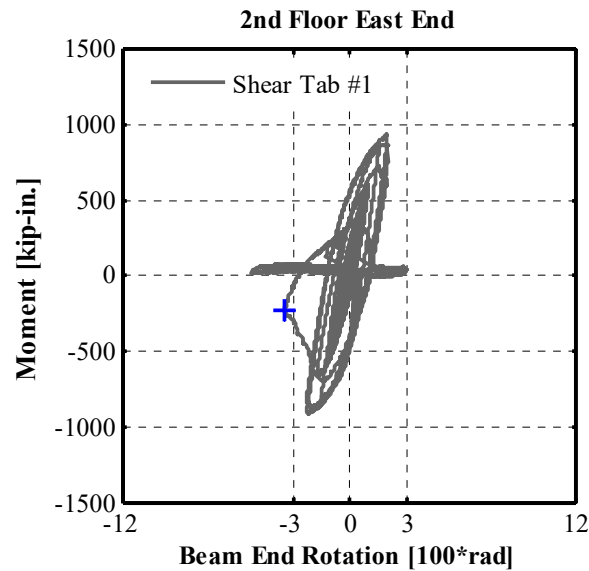


Figure 6.51 NCBF-B-3SB second-floor east welded shear tab estimated moment versus rotation at east end.

6.5 COMPARISON OF SPECIMEN BEHAVIOR

This section compares the behavior of all three specimens. Comparison plots were derived from data collected during the tests and the observations outlined in Chapter 5.

6.5.1 Global Behavior

The global behavior of each specimen was analyzed in Sections 6.2.1, 6.3.1, and 6.4.1 for the NCBF-B-1, NCBF-B-2, and NCBF-B-3SB specimens, respectively. This section presents a comparison of the test results in the form of overlaid backbone curves describing the peak values of the displacement amplitudes for each cycle. While these backbone curves reduce the clutter in the plots, it should be recognized that valuable information may be lost in showing only the peak displacement response. For the full hysteretic loops for each test, refer to Figures 6.1, 6.18, and 6.36 for the individual test specimens.

Table 6.22 lists the maximum base shear and roof drift ratio for each test specimen. This maximum base shear is calculated as the maximum value taken over the entire test. The maximum roof drift ratio is calculated as the maximum lateral roof drift ratio observed prior to significant strength degradation. Significant strength degradation is defined by a decrease in capacity of more than 80% of the maximum base shear capacity of the test specimen. The roof drift ratio at yield is also presented for illustrative purposes. Yielding reflects the initial point of dominant inelastic behavior such as brace buckling or yielding.

The vintage braced frame specimens yielded at a roof drift ratio more than double that of the SB test specimen; therefore, the first two test specimens remained elastic under larger drift demands than the third SB retrofit scheme. Inelastic behavior, though delayed in the first two tests, resulted in substantial decrease in system stiffness and strength due to brace buckling.

The backbone curves of Figure 6.52 show that strength degradation occurred quickly after brace buckling in the NCBF-B-1 and NCBF-B-2 test specimens. The lateral strength of NCBF-B-1 decreased by 40% after brace local buckling. The lateral strength of NCBF-B-2 decreased by 16% after brace global buckling and another 15% upon local buckling. Because of delayed local buckling, the second specimen was able to achieve a maximum roof drift ratio of 0.77% before significant strength degradation, while the first specimen was able to achieve 0.44% after initial local buckling. In contrast, the NCBF-B-3SB test specimen exhibited strain hardening after yielding until BRB rupture at a maximum roof drift ratio of 2.0%. The first sign of strength degradation occurred when the BRB ruptured and the lateral strength decreased by 39%.

In all three specimens, fracture of a brace was accompanied by a substantial decrease in strength and stiffness. In the case of the first two tests, brace fracture resulted in a decrease of strength to approximately 30% of the frame's original capacity. In the case of the second test specimen, NCBF-B-2, this decrease in strength was recovered upon repeated cycles as the beam began to act as a secondary energy-dissipation mechanism; however, this recovery was limited by other damage states, i.e., connection failures in other parts of the system. In the case of the third test specimen, this decrease in strength was not as severe. Upon BRB rupture, the system strength decreased to 61% of the maximum base shear. The beam additionally provided secondary energy-dissipation capacity, and the strongback engaged the energy-dissipation capacity of the remaining frame for the rest of the loading protocol.

Table 6.22 Summary of experimental test results.

Specimen name	Description	Maximum base shear (kips)	Roof drift ratio at yield¹	Maximum roof drift ratio²	Weak-story location
NCBF-B-1	Baseline vintage CBF specimen	387	0.41%	0.44%	second story
NCBF-B-2	CFT upgrade	542	0.51%	0.77%	first story
NCBF-B-3SB	SB retrofit	522	0.21%	2.0%	no weak story

¹ Yield corresponds to the first signs of dominant nonlinear behavior such as brace buckling or yielding.

² Maximum roof drift ratio prior to significant strength degradation defined when the measured base shear decreased below 80% of the specimen's maximum capacity.

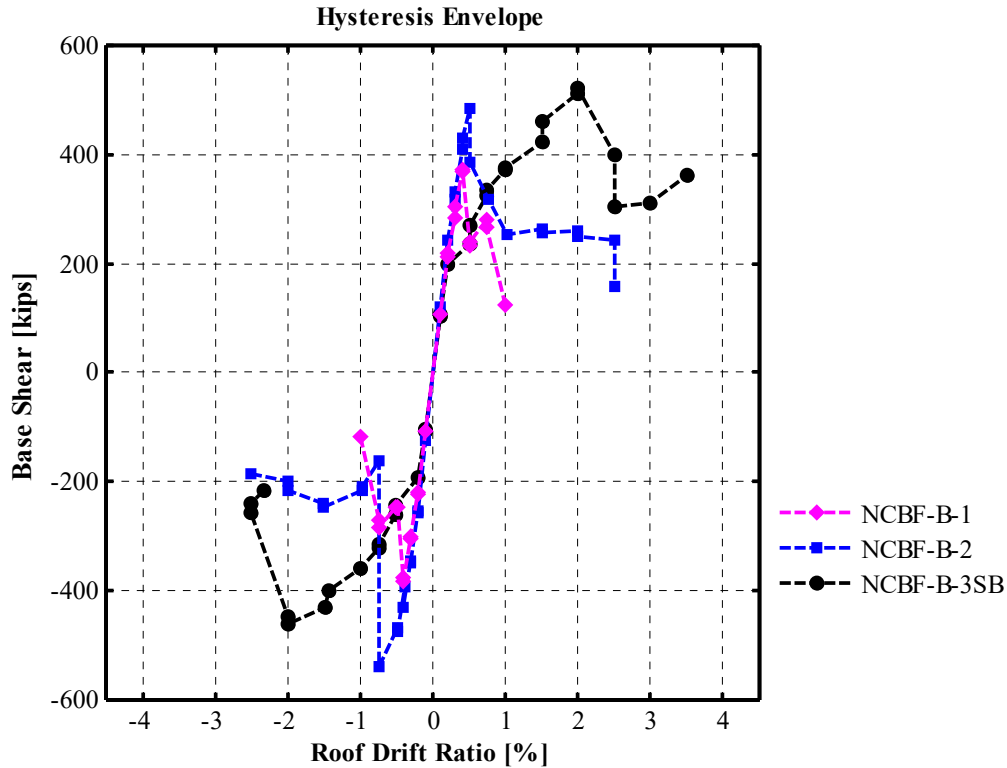


Figure 6.52 Base shear versus roof drift ratio envelopes for all three test specimens.

6.5.2 Weak-Story Tendency

Backbone curves for all three tests are shown for each story in Figure 6.53. From these plots it can be seen that the first, NCBF-B-1, test specimen exhibited nearly linear behavior in the first story while the second story achieved almost 2% story drift ratio. The second experimental test, NCBF-B-2, shows similar concentrations of drift demand in the first story. The second story was engaged only when large lateral displacements caused the second-story braces to buckle due to frame action. Both of these responses are indicative of weak-story behavior in the second and first stories for the NCBF-B-1 and NCBF-B-2 specimens, respectively.

The ratio of the first-story drift to the sum of the story drift at peak cyclic amplitudes for all three test specimens is plotted in Figure 6.54. This ratio represents the tendency of the system to form a weak story. The second and first story for the NCBF-B-1 and NCBF-B-2 tests, respectively, contribute disproportionately more to the total displacement after brace buckling. This ratio was lower when the actuators were moving in the negative (west) versus the positive (east) directions in the NCBF-B-2 test. This may be due to asymmetric behavior in the “weak” beam response; see Figure 5.45. In both cases, local buckling in a story corresponded to the largest decrease in that story’s contribution to the frame’s lateral resistance.

In contrast, the NCBF-B-3SB test specimen exhibited similar drift ratios in both stories throughout the entire test regardless of the direction of loading. The weak-story tendency in the SB frame varied little from the solid line at the 50% ratio in the plot, indicating nearly equal story drift response in both the first and second stories. This plot illustrates the ability of the SB

system to sustain a uniform drift distribution even after BRB fracture, designated by (Fr) in the plot.

The ratio between the column shear to the total story shear is plotted for all three tests in Figures 6.54 and 6.55. This ratio indicates how much lateral resistance is provided by the braces. The second-story braces in the NCBF-B-1 test dominate the lateral resistance for the second story with limited participation was observed by the braces in the first story (i.e., column shear was small). As the strength of the second-story braces decreased upon brace local buckling and fracture, the columns contributed increasingly more to the total shear resistance in the second story. In the case of the second NCBF-B-2 test, this behavior is reversed. The first-story braces contribute most of the first story's lateral resistance until brace local buckling and fracture. After brace local buckling and fracture, the columns play a more dominant role in both the second- and first-stories. In the third test specimen, NCBF-B-3SB, the columns contribute a higher percentage of the story shear after BRB rupture. In all three tests, the column contribution reflects degradation in the stiffness and strength of the braces, as shown in the decreases in strength in the hysteretic loops of Figures 6.52 and 6.53.

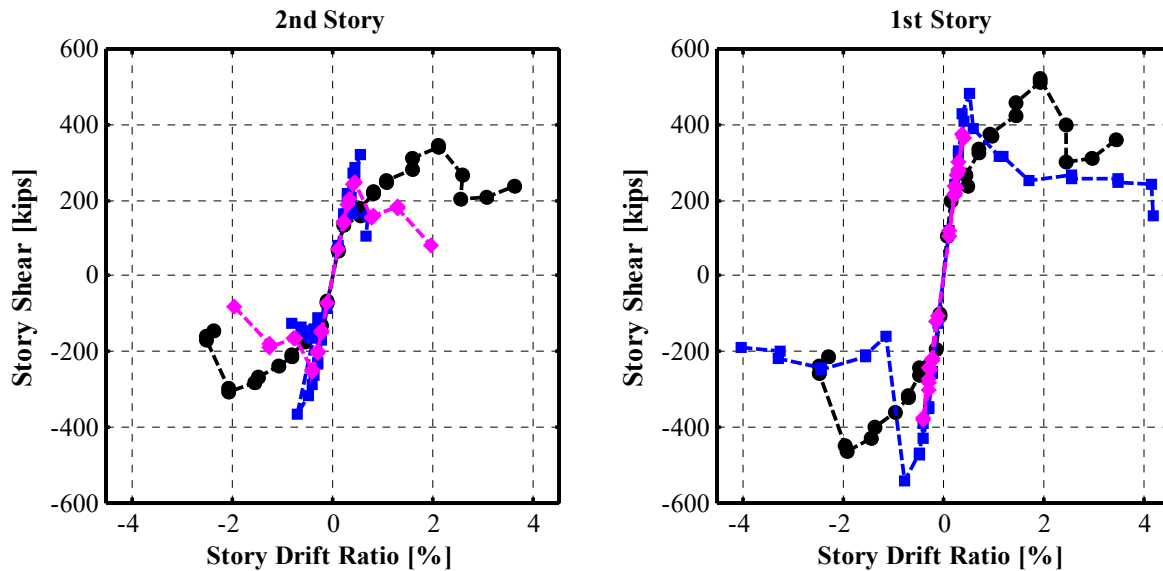


Figure 6.53 Story shear versus story drift ratio envelopes for all three test specimens.

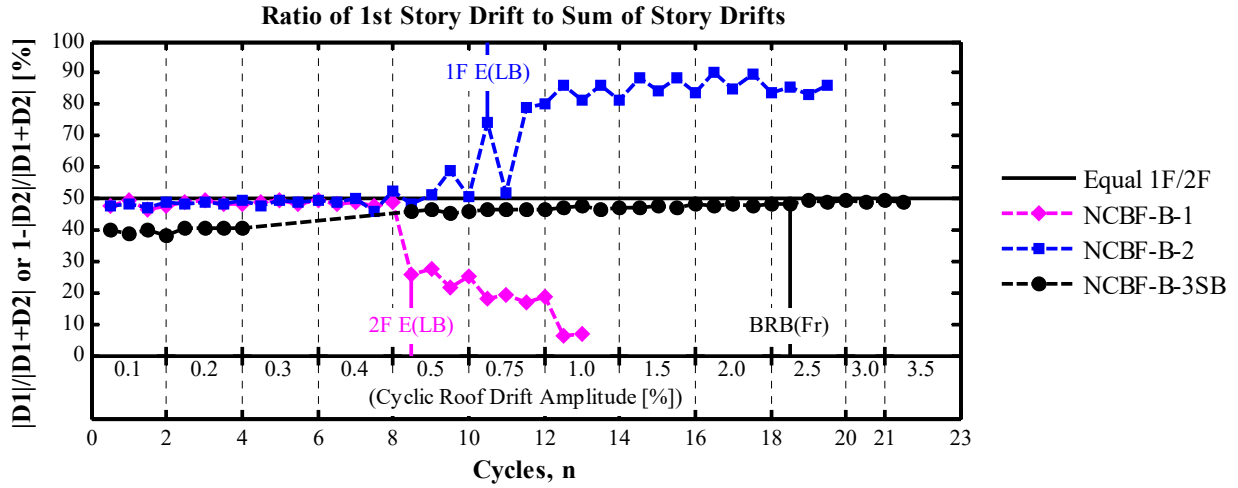


Figure 6.54 Comparison between the ratio of the first-story drift ratio to the sum of the first- and second-story drift ratios at peak cyclic amplitudes.

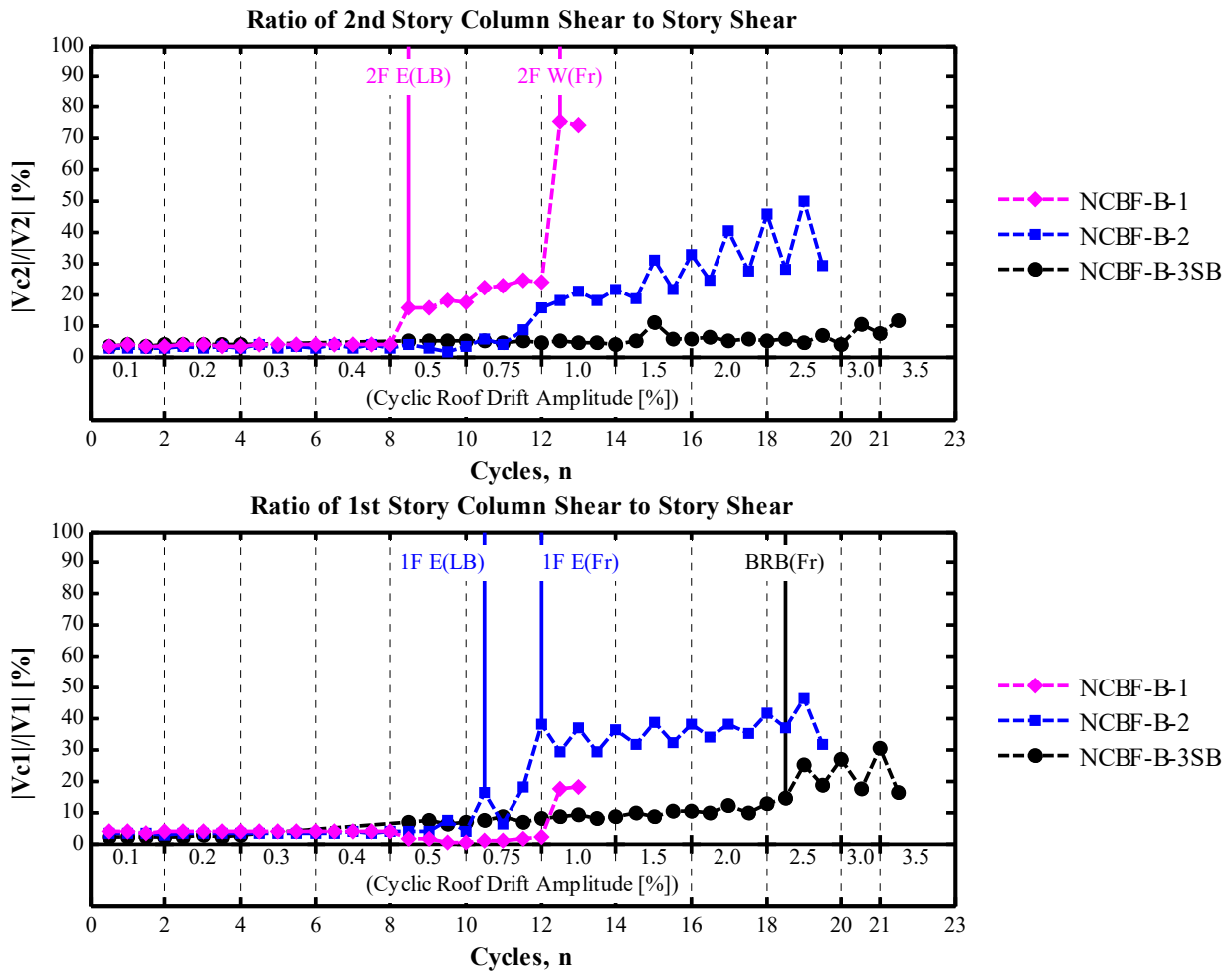


Figure 6.55 Comparison between the ratio of the column shear and the story shear at peak cyclic amplitudes.

6.5.3 Energy Dissipation

This section presents plots of the energy dissipation of each test specimen. In the case of these plots, energy dissipation is defined by the area under the global hysteretic loop calculated at each cycle of loading. This quantity is multiplied by 100 in the plots so that the cumulative energy dissipation and the energy dissipated in each cycle can be overlaid on the same plot. The energy dissipation from all three tests are plotted in one figure in Figures 6.59 and 6.60 for comparison purposes. The NCBF-B-3SB test specimen dissipated more energy than the first two test specimens; as can be surmised from non-degrading hysteretic peaks in Figure 6.52.

Energy dissipation from the braces are shown in Figures 6.61, 6.62, and 6.63. Focus was kept on braces that exhibited inelastic behavior (i.e., buckling or yielding). These plots demonstrate that energy dissipation for each brace is influenced by local buckling and fracture of the braces, which in turn influences the energy dissipation of the test specimens. In the case of NCBF-B-1, the second-story braces dissipated similar amounts of energy.

In the second test specimen the first-story east brace dissipated most of the energy prior to fracture. After fracture, the second-story braces were engaged by frame action and contributed some energy dissipation through local buckling. The first-level beam also participated in energy dissipation after brace fracture, though this contribution is not illustrated in the plots. The first-story west brace contributed slightly to the system throughout the duration of the test.

In the case of the third test specimen, NCBF-B-3SB, neither of the braces in the elastic “strongback” contributed any energy dissipation to the system. Energy dissipation was controlled almost entirely by the BRB until rupture, at which point the beam began to participate in energy dissipation; see Figure 6.63.

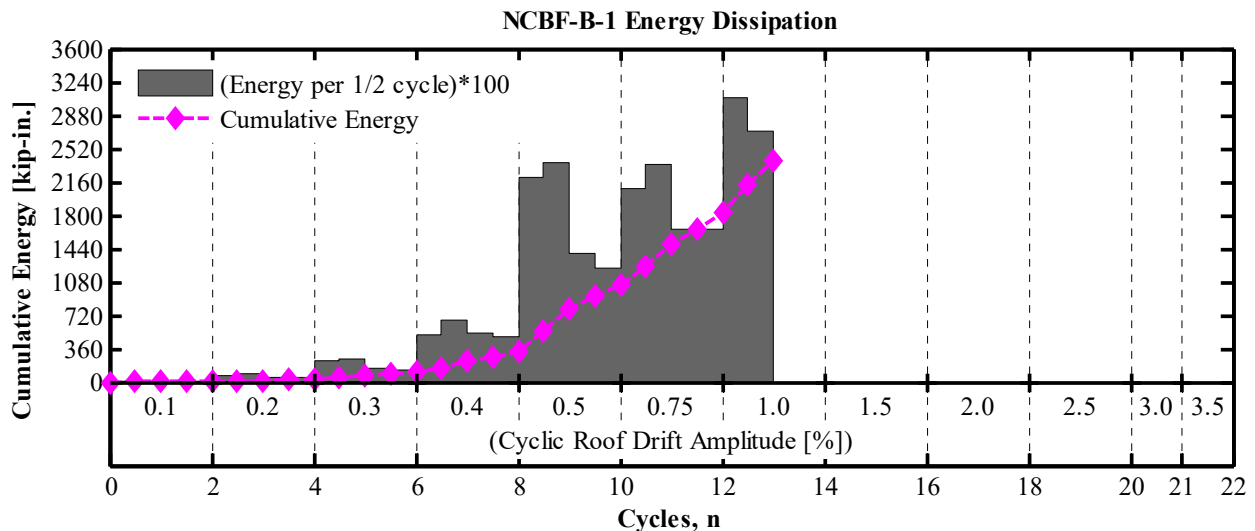


Figure 6.56 Energy dissipation in NCBF-B-1.

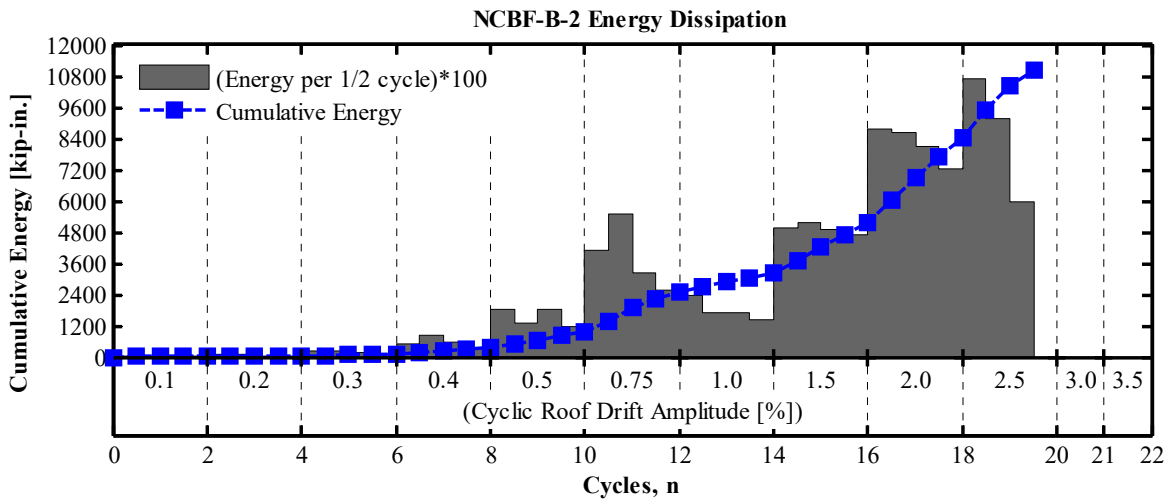


Figure 6.57 Energy dissipation in NCBF-B-2.

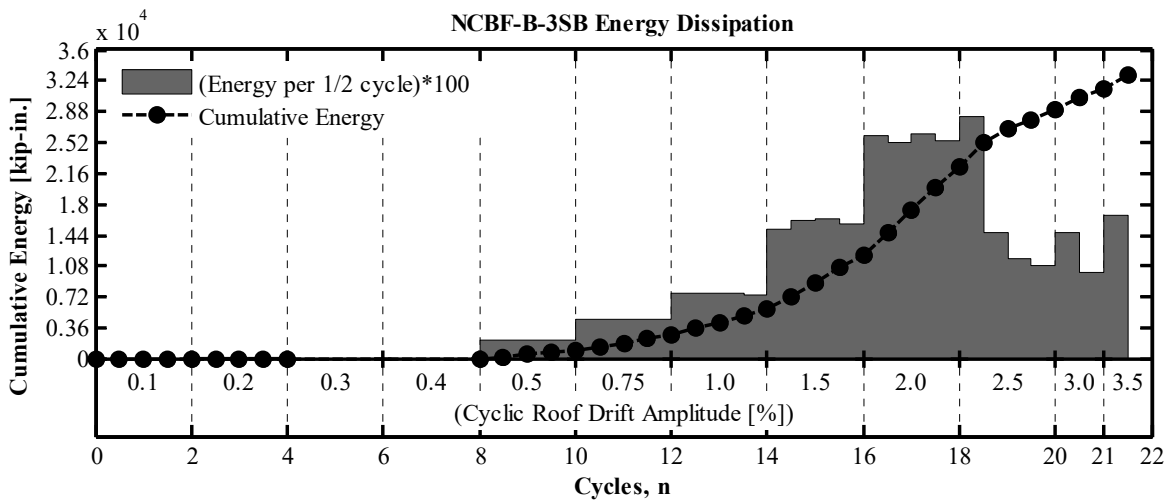


Figure 6.58 Energy dissipation in NCBF-B-3SB.

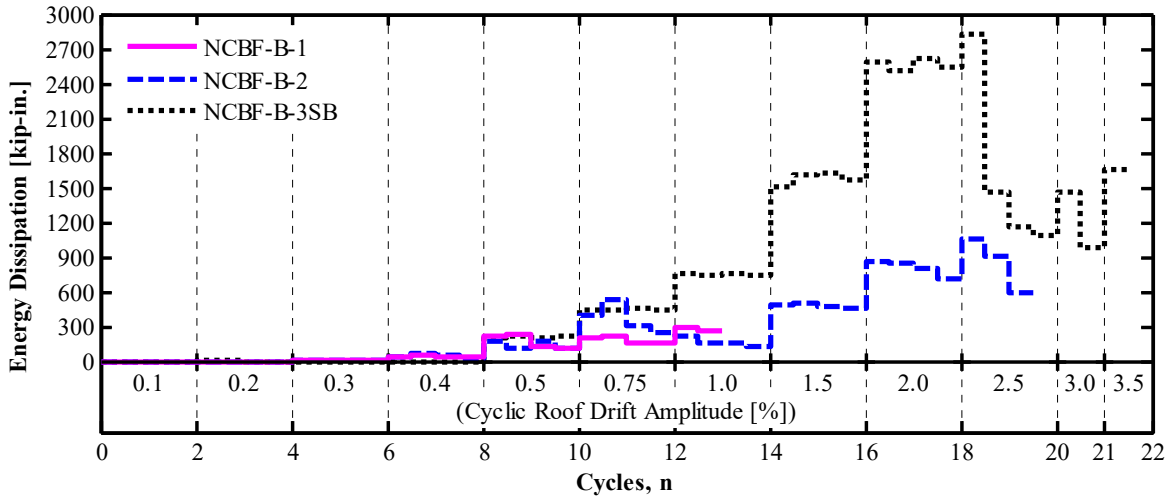


Figure 6.59 Comparison of the energy dissipation in each half-cycle for each test specimen.

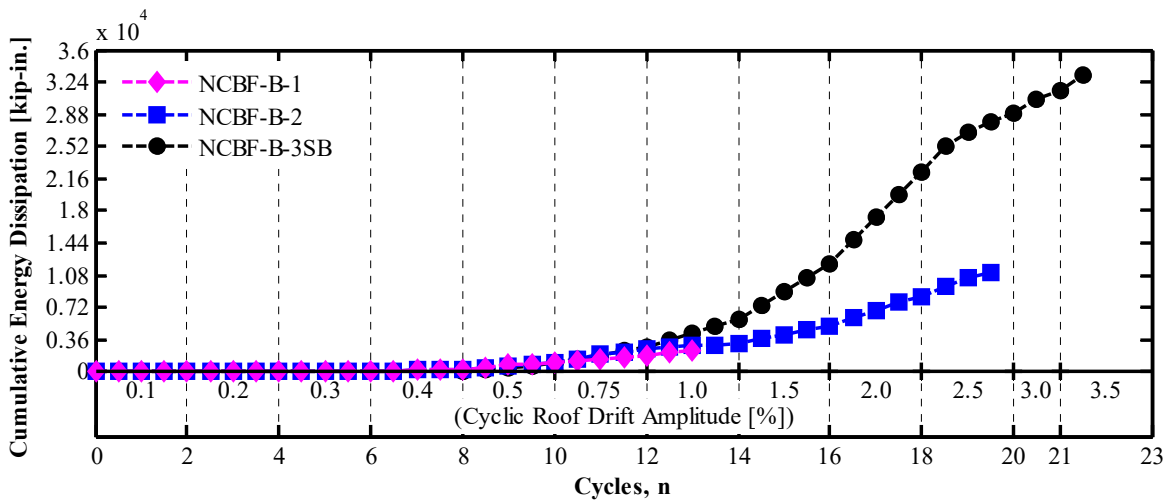


Figure 6.60 Comparison of the cumulative energy dissipation in each test specimen.

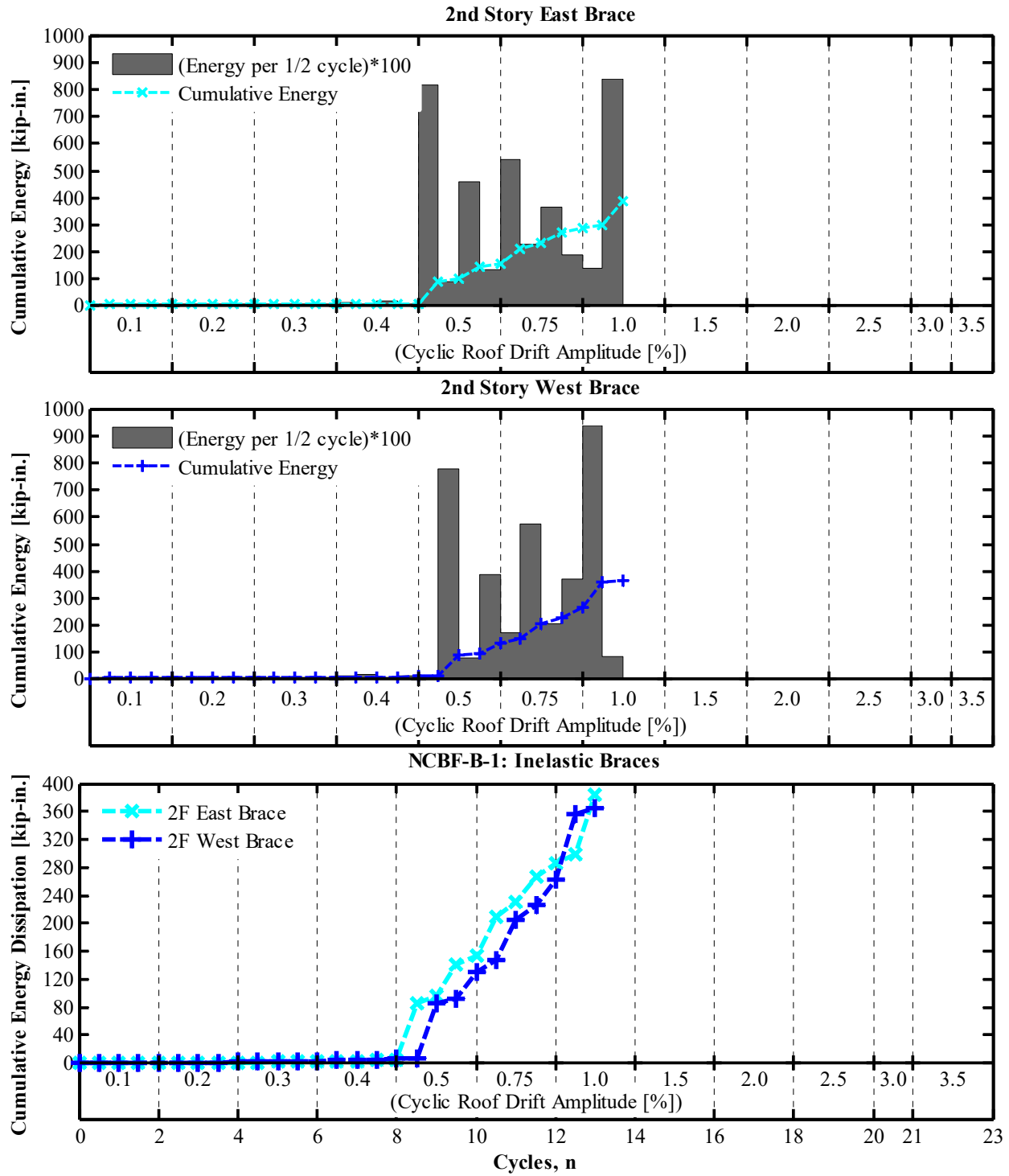


Figure 6.61 Comparison of energy dissipation of the buckled second-story braces in the NCBF-B-1 test.

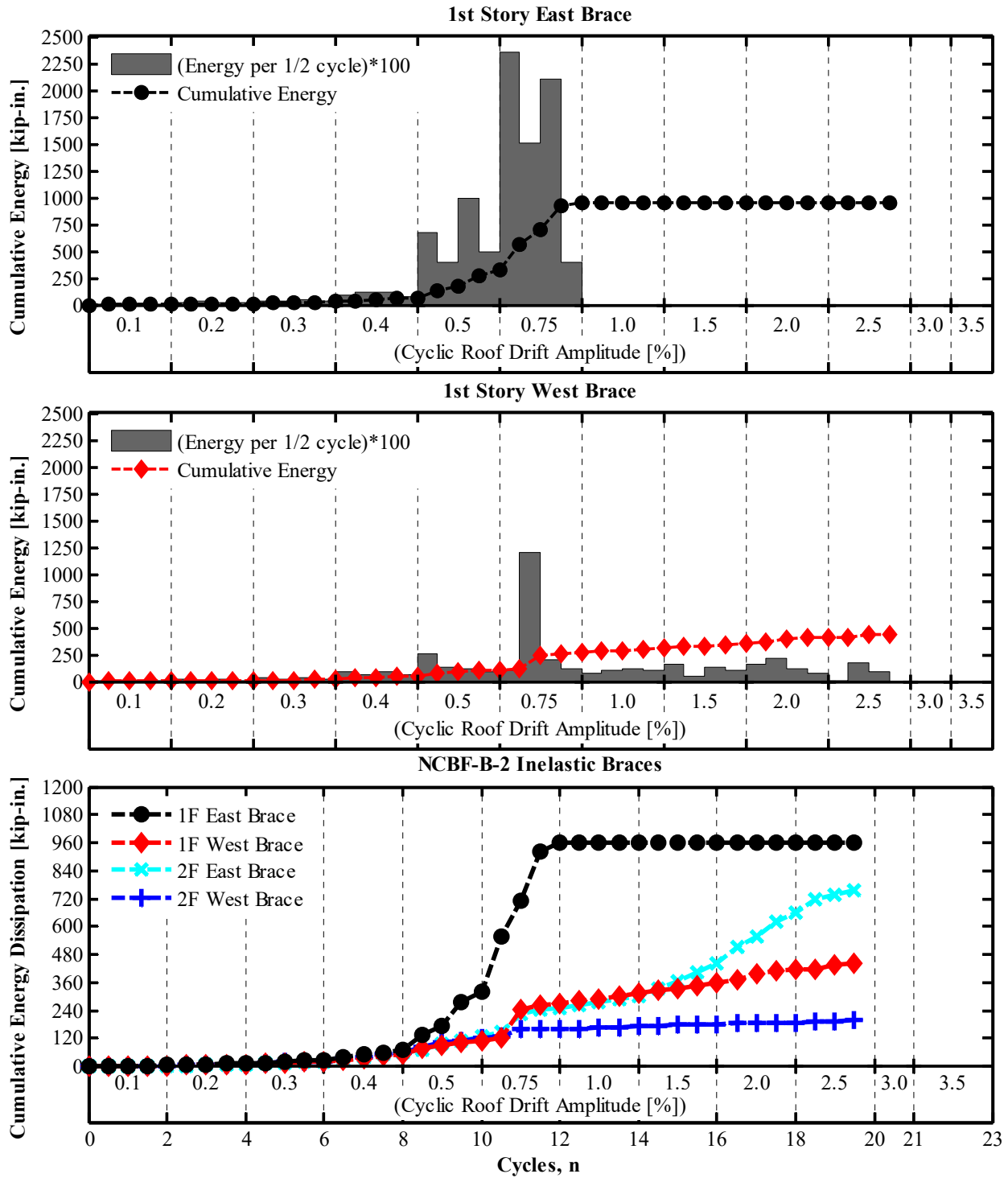


Figure 6.62 Comparison of energy dissipation of the buckled braces in the NCBF-B-2 test.

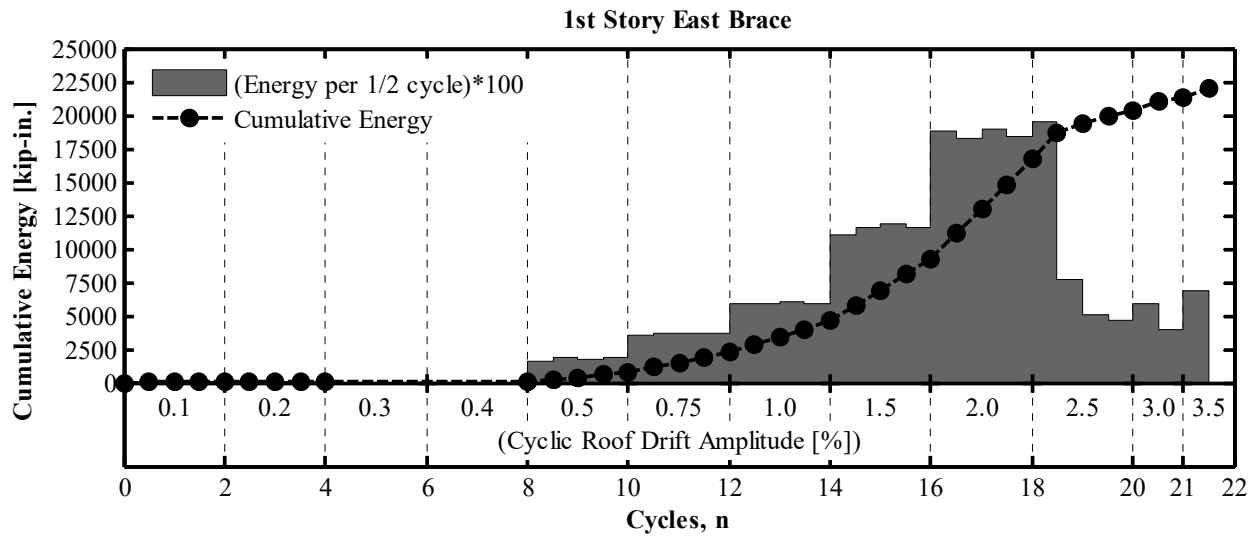


Figure 6.63 Energy dissipation in the BRB of the NCBF-B-3SB test.

7 OpenSees Numerical Calibration

7.1 NUMERICAL CALIBRATION

Numerical models were developed using the structural analysis program OpenSees [McKenna et al. 2010]. Verification of these models was performed through calibration of the numerical models to the experimental tests performed at UCB at the nees@berkeley laboratory.

7.1.1 Experimental Tests

A brief description of the test specimens are given to provide background to the calibration process.

1. *Specimen 1 (NCBF-B-1)*: The first specimen was designed according to the 1985 UBC and did not satisfy current seismic design requirements. These inadequacies were typical of vintage construction and included high brace width-to-thickness ratios, non-ductile gusset connections lacking adequate yield-lines, a weak beam designed without consideration of an unbalanced load that may arise due to brace buckling, and no capacity-design considerations in proportioning members or connections. This specimen formed a weak story in the second floor, while the rest of the frame experienced minor yielding and little permanent damage. Both second-story braces exhibited severe local buckling at the brace midpoint and then fractured within a few additional cycles.
2. *Specimen 2 (NCBF-B-2)*: Since the imposed story drifts from Specimen 1 were modest, the original frame was upgraded to include concrete-filled braces. The braces were filled with low-strength concrete to postpone local buckling and potentially delay brace fracture. Net-section reinforcement was additionally added to all brace-to-gusset connections. Testing resulted in a weak-story mechanism in the lower story. One brace fractured, causing the frame to behave like an eccentrically braced frame with a long link beam providing a weak and flexible energy-dissipating mechanism; see Figure 5.45. Many local failure mechanisms were observed during subsequent loading cycles, including nearly-complete fracture at one column-to-baseplate interface, significant local buckling in the beam, and multiple connection and weld failures.
3. *Specimen 3 (NCBF-B-3SB)*: The third specimen consisted of a “strongback” retrofit of the original NCBF-B-1 test specimen. Since this experiment was considered to be a retrofit of a vintage building design, the beams and columns were kept the same as the original test specimen. The four original braces of the NCBF-B-1 specimen were replaced with one

Buckling-Restrained Brace (BRB) as the primary energy-dissipation device and two conventional braces forming the essentially elastic “strongback.” The primary goal of this third test specimen was to mitigate weak-story behavior and distribute inelastic demands across both stories. The strongback was successful at mitigating a weak-story mechanism. The behavior of this specimen was characterized by full and stable hysteretic loops. Local buckling of the BRB casing and fracture of the BRB core were both observed before conclusion of the experiment. This behavior resulted in a softening response.

These test results were compared to the simulation results. Input parameters were adjusted sparingly to improve the fidelity of the simulations.

Valuable information about the modeling process was gained from the calibration of Specimen 1 (NCBF-B-1), including the behavior of the beams and columns, which had similar cross sections for all three tests. Calibration of the hollow brace buckling and fracture behavior from the NCBF-B-1 test also provided verification of the material and geometric parameters used to model the hollow braces. Specimen 2 (NCBF-B-2), with concrete-filled braces, further validated the behavior of the beams, columns, and braces, including fatigue observed in the strong-axis column-base and first-story west brace. Fracture of the BRB in the NCBF-B-3SB model was calibrated to the fatigue life of the BRB in the third experiment. In the case of all numerical models, local buckling and gusset connection failures were neglected. Note that incorporation of such failures would further refine the calibration results described herein.

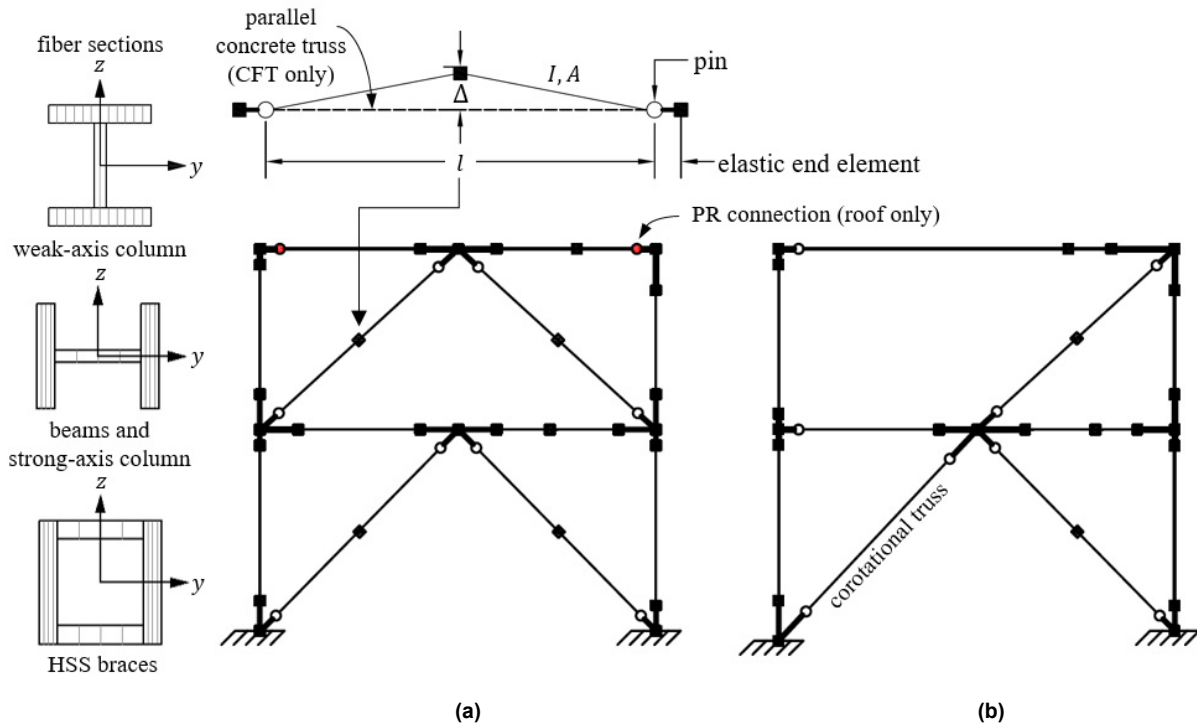


Figure 7.1 Schematic of simulations: (a) NCBF-B-1 & 2 and (b) NCBF-B-3SB.

7.2 NUMERICAL MODEL

This section describes the parameters used to simulate the behavior observed in the experiments. Schematic diagrams of the numerical models can be found in Figure 7.1.

7.2.1 Constraints and Boundary Conditions

All three models were developed as two-dimensional with three degrees-of-freedom (DOFs) per node. Beam–column connections attached to gusset plates were specified as fixed. Gusset-to-brace connections were specified as pins. Open circles in Figure 7.1 represent the locations for these pins.

The welded shear tabs for the roof level beam in NCBF-B-1 and 2 were modeled with partially restrained (PR) springs to represent the non-zero stiffness of these regions. The force-deformation relation for these PR connections was assumed to be bilinear. The PR yield deformation was based on the yield criteria of 0.005 radians as specified for bare steel connections in ASCE 41-13 [2013]. The strength for these regions was based on the minimum of gross yielding of the plate or beam web, rupture of the weld, or yielding or rupture of the base metal [AISC 360-10 2010]. For simplicity, possible connection failures at beam–column shear tabs with gusset plates were not modeled as they were not deemed significant to capturing the experiment’s global response prior to brace fracture. Note that these regions experienced local damage states that could affect the global hysteresis shape at large amplitude displacements. This is especially true of the calibration of the NCBF-B-2 experiment, which exhibited many localized and/or partial damage states.

Elastic end zones were used for regions where the beam–column connections and gusset plates intersect. Dimensions called out in the shop drawings of the test specimen were used to represent locations of these end zones. Elastic elements were assigned to be 10 times the moment of inertia and 1.0 times the area of the connecting member for the vintage braced frame tests. For the strongback test, end elements were representative of the ratio of the connection area to the connecting member area. Thick black lines in the schematic diagram of Figure 7.1 correspond to these end element regions.

7.2.2 Material

A uniaxial Giuffre-Menegotto-Pinto steel material model [Filippou et al. 1983] with 0.3% isotropic strain hardening was used for all the beams, columns, and braces, except for the BRB. Yield strengths reflect the average yield strength calculated from coupon tests and mill certificate reports; see Tables 3.3, 3.5, and 3.11. All other steel material values reflected default values in OpenSees.

7.2.2.1 Concrete Material

A concrete material model (*concrete01*) with zero tensile strength and degrading linear unloading/reloading stiffness was used to model the CFT braces in the second test specimen. This concrete material was assigned a concrete compressive strength, f'_c , based on the average compressive strength of cylinder tests performed on the day of the test of 2.2 ksi; see Table 3.6.

The concrete strain at maximum strength was specified as $\varepsilon_1 = 2 f'_c / E_c$ where E_c is the elastic stiffness of the concrete material based on its compressive strength ($E_c = 57\sqrt{f'_c}$). The concrete crushing strength was calibrated to the brace hysteretic behavior and was specified as $0.6 f'_c$ at a concrete strain at crushing strength of $5\varepsilon_1$.

7.2.2.2 BRB Material

The BRB utilized a steel Menegotto-Pinto material model capable of modeling the asymmetric isotropic and kinematic strain hardening associated with buckling-restrained braces (*steel4*) [Zsarnoczay 2013]. Material parameters for the BRB were calibrated to the test results and can be seen in Table 7.1. Note that these material properties are calibrated for the a buckling-restrained brace in a SB system undergoing larger strains than that of a typical BRB frame. As such, these material properties may not be generalizable to BRBs subject to cycles of smaller strain demands where kinematic and isotropic hardening occurs under smaller strain amplitudes.

Table 7.1 Uniaxial material *Steel4* input parameters for BRBs.

Asymmetric behavior	Kinematic hardening				Isotropic hardening				
	b_k	R_0	r_1	r_2	b_i	ρ_i	b_l	R_i	l_{yp}
Tension	0.003	22.0	0.925	0.15	0.003	1.0	0.0008	1.0	1.0
Compression	0.015	22.0	0.925	0.15	0.003	1.0	0.0008	1.0	-

b_k = kinematic hardening ratio, R_0, r_1, r_2 = transition from linear elastic to hardening asymptote, b_i = initial isotropic hardening ratio, ρ_i = intersection location between initial and saturated hardening asymptotes, b_l = saturated hardening ratio, R_i = exponential transition from initial isotropic to saturated asymptote, l_{yp} = length of yield plateau.

7.2.2.3 Low-Cycle Fatigue Material

The OpenSees low-cycle fatigue wrapper [Uriz and Mahin 2008] was used to model fracture of the braces and column base. These fatigue parameters were calibrated for those members that fractured during the experimental tests, including: (1) braces of the first test; (2) the brace and column base of the second test; and (3) the BRB of the third test. The calibrated parameters used for this fatigue model can be found in Table 7.2. The strain measures used for this fatigue model are non-objective and depend on the number, location, and weights of the element integration points used in the numerical model. This is emphasized by the difference between the fatigue parameters calibrated herein and those found by Uriz and Mahin [2008] ($m = -0.458, \varepsilon_0 = 0.091$ for HSS braces), which were calibrated to a greater number of brace sub-elements (see Section 7.2.4). Simulations using different brace modeling parameters would require re-calibration of the fatigue parameters reported herein.

Note that fiber models assume that plane sections remain plane and are not capable of modeling the local buckling behavior observed in the braces of the NCBF-B-1 and 2 tests and the casing of the BRB in the NCBF-B-3SB test. Differences between the experimental and numerical hysteretic loops after buckling emphasize this point.

7.2.3 Sections

Fiber sections were used for all the inelastic elements in the simulations except for the BRB. Beams and columns oriented in strong-axis bending used four fibers across the thickness of the flange and four fibers across the section depth. Columns oriented in weak-axis bending utilized twelve fibers across the flange width and two fibers along the thickness of the web. Tubular braces used four fibers across the thickness and depth of the four walls. These fibers were oriented in one direction to reflect the two-dimensional nature of the simulations; see Figure 7.1. The wall thickness of the fiber sections was modified to be equal to the gross cross-sectional area per AISC 360-10 [2010] to account for rounded corners not included in the idealized sections.

7.2.4 Elements

Nonlinear beam–column elements were used for the beams, columns, and braces. Buckling braces were modelled with two force-based nonlinear beam-column elements with initial imperfections and co-rotational transformations to simulate in-plane buckling. Initial imperfections, Δ , were tuned to the buckling strength of the brace observed in the experiments. Those braces that did not buckle had perturbations calibrated to the buckling load in AISC 360-10 [2010] using the simulated yield strength of the material. Values for calibrated perturbations can be found in Table 7.2. This calibration for the brace perturbation was not conducted for Specimen 3.

As established in Section 7.2.2.3, calibrated fatigue parameters depend on the strains derived at integration point locations along the element length. Two sub-elements with five integration points per sub-element using Gauss-Lobatto quadrature were utilized herein to lever the efficiency of force-based beam–column elements while providing a mid-length node to allow global brace buckling. This required re-calibration of the fatigue parameters m and ε_0 as the default values provided by Uriz and Mahin [2008] were derived using numerical models with a different number of integration points, brace properties, and number of sub-elements.

Table 7.2 Buckling brace initial perturbation.

Test	Member	Section	Yield Strength	Δ
NCBF-B-1	First-story brace	HSS6×6×3/16	49.0	$l/860$
	Second-story brace	HSS7×7×1/2	51.7	$l/860$
NCBF-B-2	First-story brace	HSS6×6×3/16 (CFT)	52.5	$l/860$
	Second-story brace	HSS7×7×1/2 (CFT)	51.7	$l/998$
NCBF-B-3SB	All buckling braces ^a	-	-	$l/1000$

^a same perturbation used for all buckling braces.

For the CFT braces, a co-rotational truss element was modeled in parallel to the fiber-element hollow braces to reflect the increased stiffness and strength associated with the concrete-filled braces. These parallel elements utilized the concrete material model described in Section 7.2.2.1 and were assigned an area equal to the hollow area of the steel HSS section. These concrete truss elements were programmed to be deleted through the `remove element` upon complete fracture of its respective steel fiber-based brace element. The fractured brace elements, nodes, constraints, and recorders were also removed after fracture using similar commands to improve convergence of the analysis. Modeling a separate element in parallel to the fiber brace section increased the stiffness and buckling strength of the bracing member without the computational expense required for a fully integrated concrete-filled tube fiber section.

The BRB in Specimen 3 was modeled with a single co-rotational truss element with a length equal to the experimental BRB length excluding the connection regions. The material stiffness of this truss was modified to account for the difference between this length, the yield length of the BRB core, and the additional stiffness provided by the transitions regions [Tsai et al. 2014]. Strain parameters used as inputs or extracted from the simulation were modified in a similar fashion to account for the actual yield length in the experiment; see Table 7.3.

Table 7.3 Fatigue material input parameters.

Test	Member	Section	m	ϵ_0
NCBF-B-1	Second-story brace	HSS6×6×3/16	-0.458	0.105
NCBF-B-2	First-story brace	HSS7×7×1/2 (CFT)	-0.458	0.105
	First-story west column	W10×54	-0.458	0.191
NCBF-B-3SB	BRB	-	-0.458	$0.15 l_T/l_y$ ^a

^a strain parameters multiplied by the ratio of the truss length, l_T , to the yield length, l_y , to adjust for the actual BRB yield length.

7.3 DISCUSSION OF CALIBRATION RESULTS

Plots of the hysteretic loops from the experimental tests and numerical models are compared in Figures 7.2 through 7.7. The solid grey and black lines in these figures represent the information from the experimental test and output from the OpenSees simulations, respectively.

7.3.1 Discussion of NCBF-B-1 Simulation

In general, the simulation of NCBF-B-1 adequately captured the observed experimental behavior. However, the initial stiffness of the numerical model was higher than the stiffness from the experimental test. This is especially noticeable in the story shear versus story drift ratio plots of the first story; see Figure 7.2.

The low-cycle fatigue material captured the rupture order of the second-story braces. Local buckling of the braces was neglected in the simulation as the fiber-based elements assume plane sections remain plane. The fatigue material ruptured the brace over several cycles, as can be observed by the smaller hysteretic loop in the second-story braces after initiation of fatigue in the outer-most fibers of the brace simulation; see Figure 7.3. Though this brace simulated behavior was different than the local buckling behavior exhibited during the experiment, gradual fatigue in each fiber of the simulated brace cross-section allowed the simulation to exhibit some strength degradation in the global hysteretic loops that well matched the global behavior observed during the experiment; see Figure 7.2.

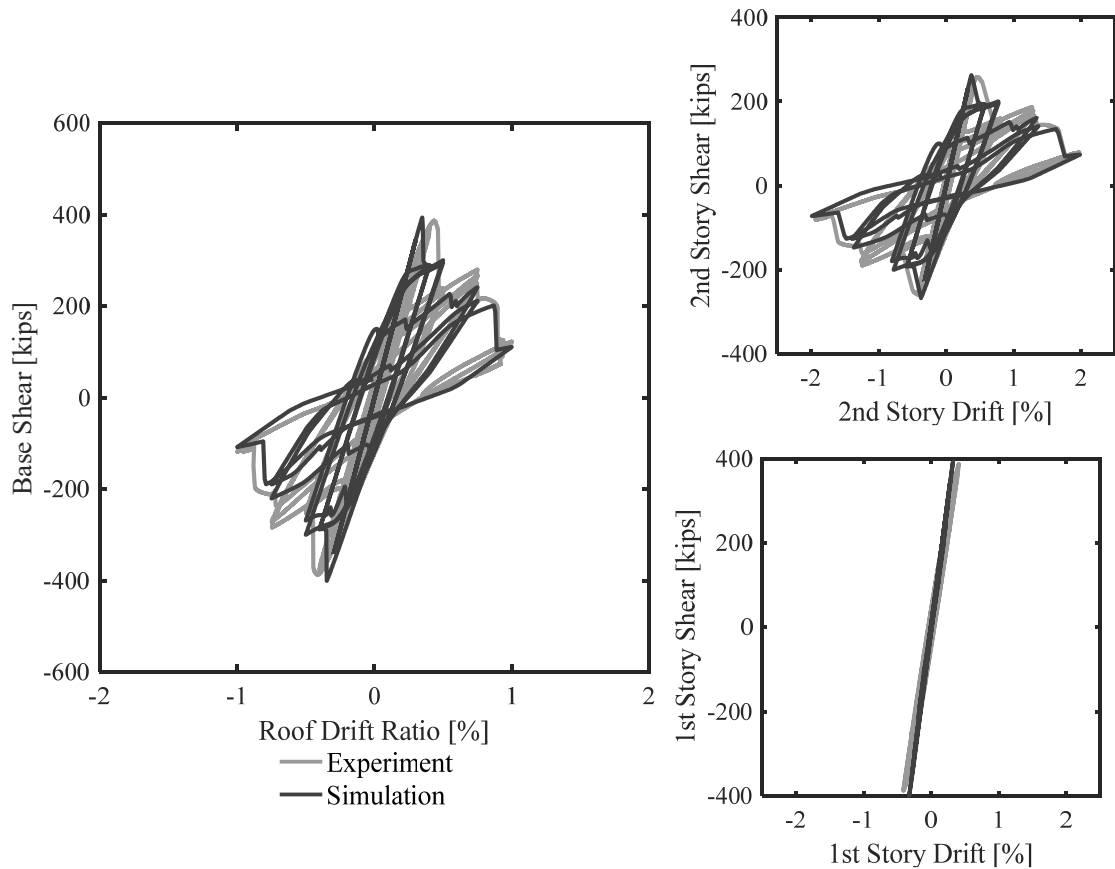


Figure 7.2 NCBF-B-1 comparison of numerical and experimental results of global hysteresis.

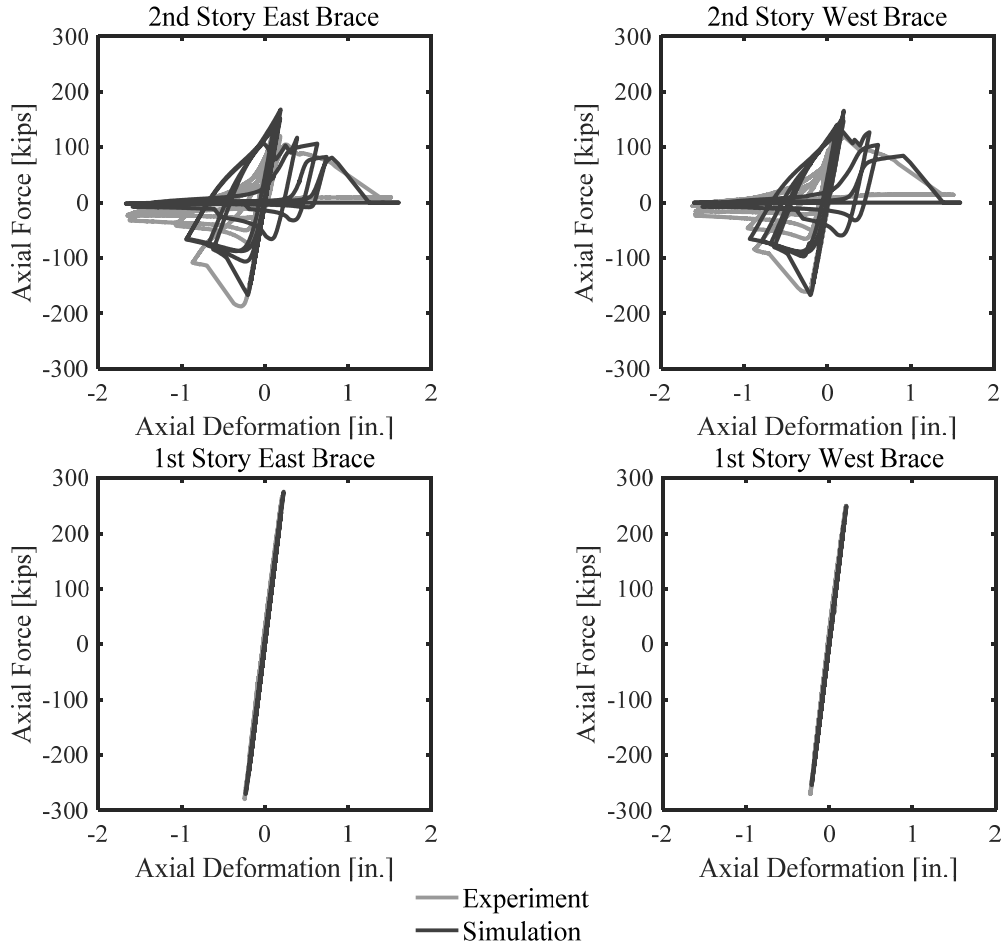


Figure 7.3 NCBF-B-1 comparison of numerical and experimental results of brace hysteresis.

7.3.2 Discussion of NCBF-B-2 Simulation

The parallel concrete and fiber-based brace elements adequately captured the CFT global behavior. Global buckling and subsequent fracture of the first-story east brace occurred at similar amplitude cycles in the simulation and the experiment. Partial fracture of the first-story east column also occurred during the same cycle in the experiment and the simulation. Though the simulation emulated the weak-beam mechanism observed during the experiment, the first-story west brace and second-story braces did not buckle in the simulation. Attempts to calibrate the behavior of the simulation to these other buckling responses was limited as buckling of the first-story west brace was minor and buckling in the second-story braces due to frame action required partially-restrained models for the brace-to-gusset regions.

The model adequately imitates the experimental results prior to brace fracture of the first-story east brace. However, after brace fracture, the hysteresis loops are fuller in the simulation than in the experiment. Subsequent simulated hysteretic loops did not include the many connection failures observed during the experimental test (e.g., weld failures, fracture of the east shear tab, punch through of the gusset through the weak-axis column web, etc.). These un-simulated damage states (including buckling modes in the first-story west and second-story

braces) caused the post-fracture hysteretic loops of the numerical model to be fuller than that of the experimental test.

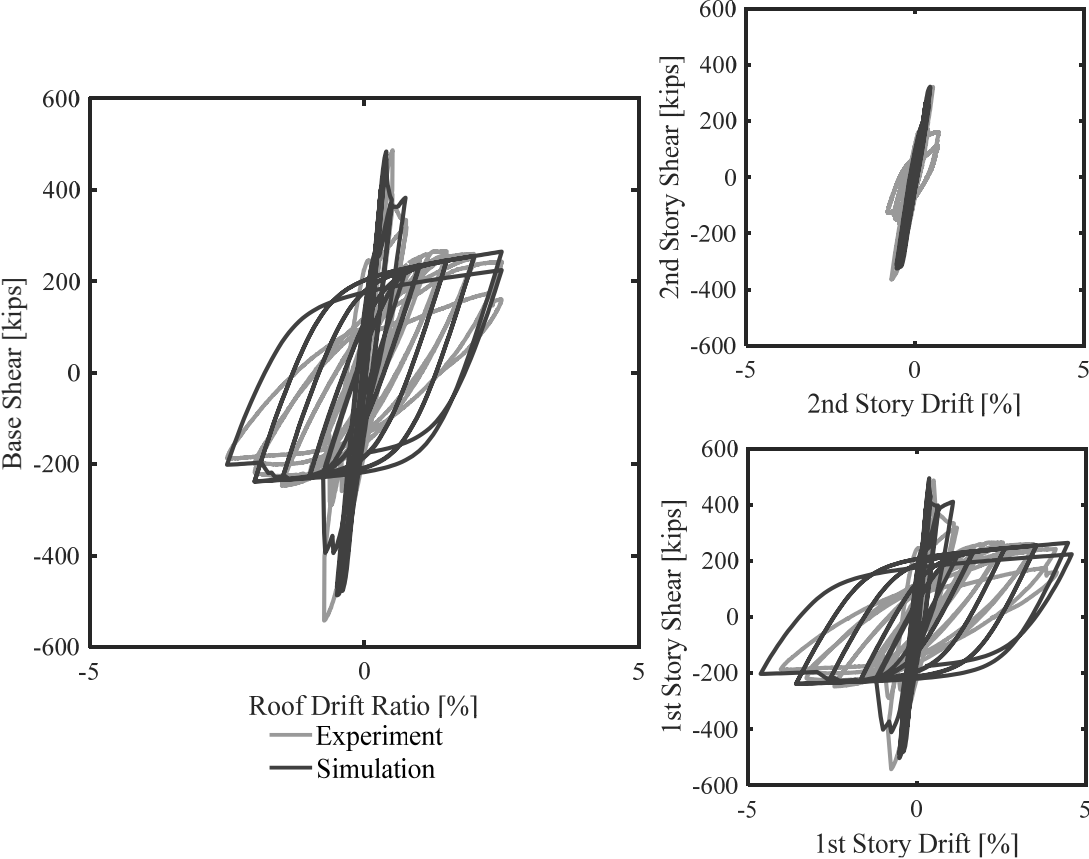


Figure 7.4 NCBF-B-2 comparison of numerical and experimental results of global hysteresis.

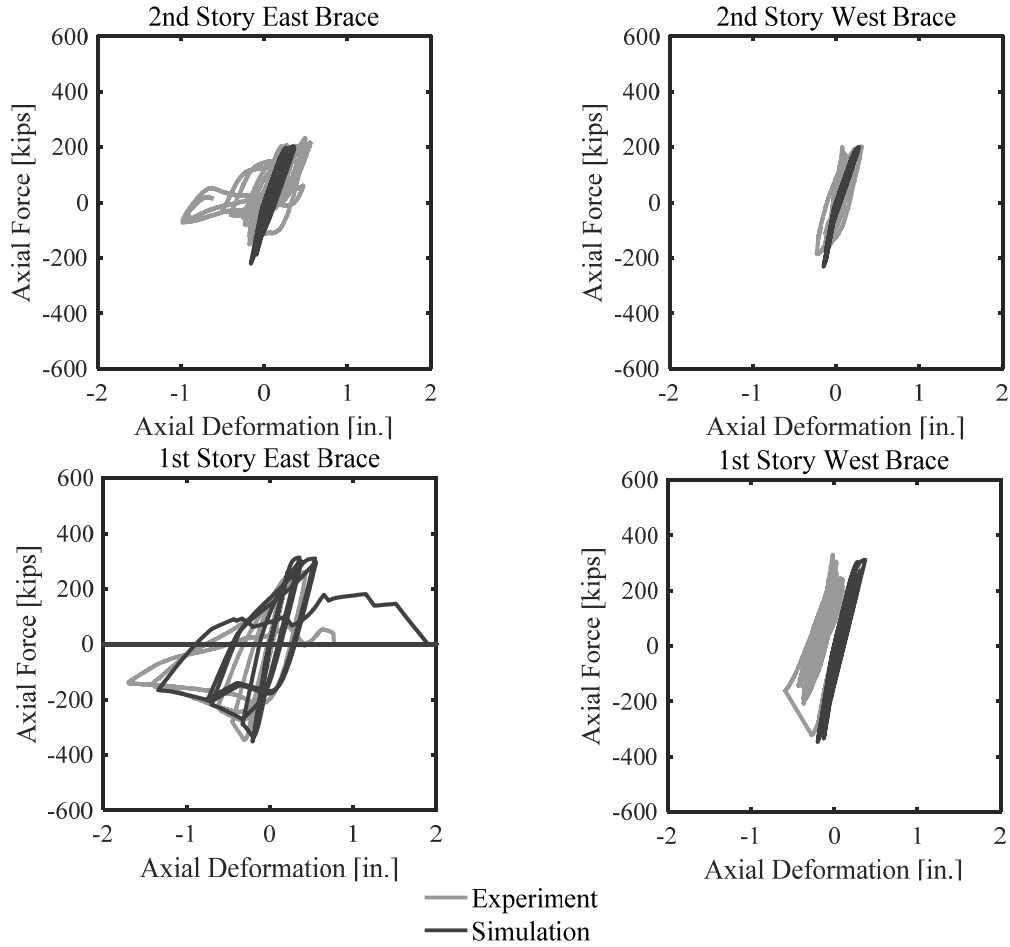


Figure 7.5 NCBF-B-2 comparison of numerical and experimental results of brace hysteresis.

7.3.3 Discussion of NCBF-B-3SB Simulation

The overall behavior of the NCBF-B-3SB experiment was well predicted by the simulation, including BRB rupture; see Figure 7.6. However, the low-cycle fatigue model used herein allows the BRB to only exhibit fatigue in tension. Thus, the softening response is a half-cycle delayed in the simulation as the BRB softened in compression during the experiment; see Figure 7.7. After BRB rupture, the BRB contributed no stiffness or strength to the global response of the numerical model. In the case of the experiment, some reserve capacity was intermittently observed in the test as the two fractured ends of the steel core came in contact in compression and then pulled apart in tension, as reflected in the hysteresis loops in Figure 6.42. This intermittent contact was not modeled in the analysis as shown by the differences in hysteretic cycles after BRB rupture.

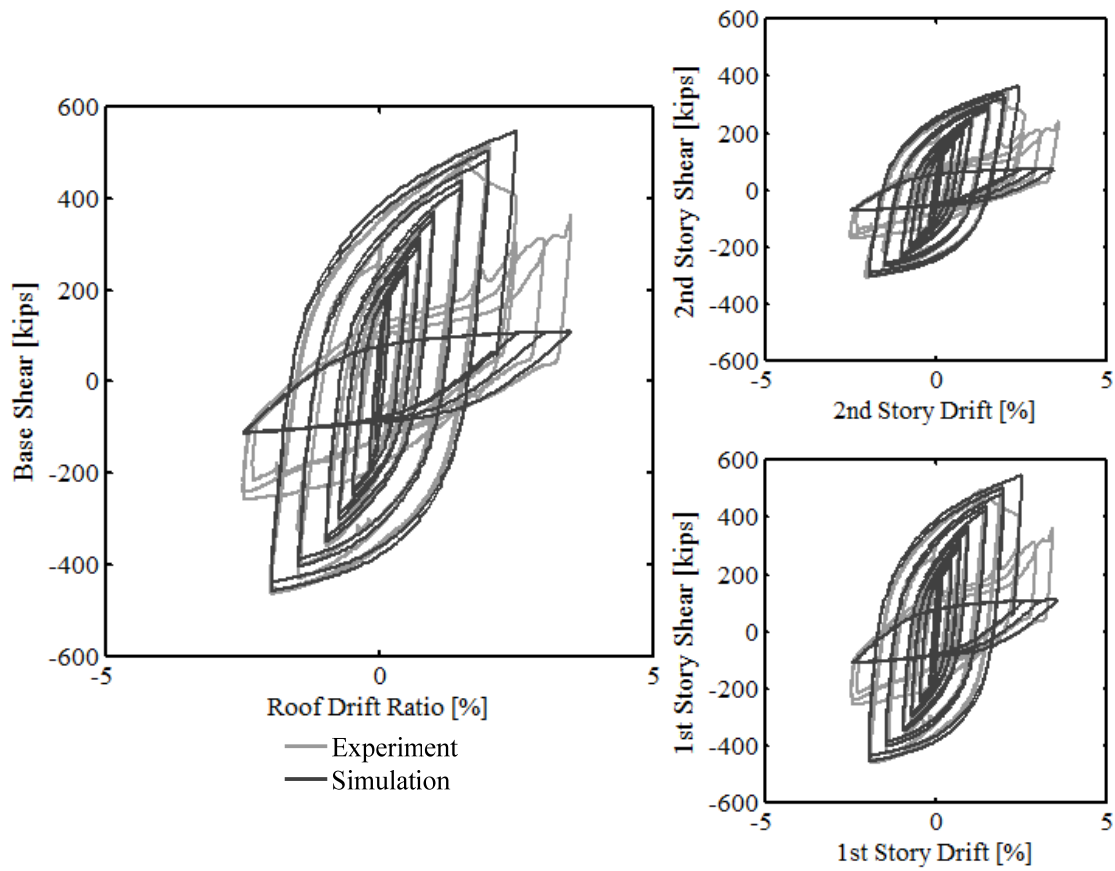


Figure 7.6 NCBF-B-3SB comparison of numerical and experimental results of global hysteresis.

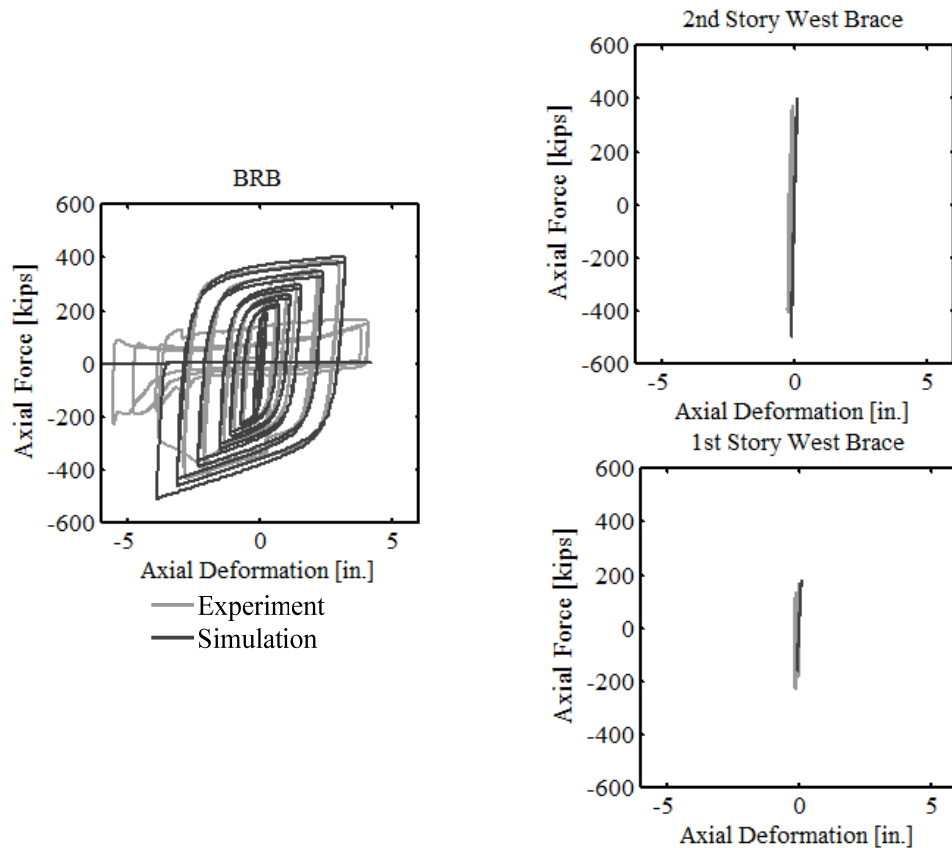


Figure 7.7 NCBF-B-3SB comparison of numerical and experimental results of brace hysteresis.

7.4 CONTINUED WORK

These calibrated numerical models captured the experimental results with adequate accuracy. Dynamic analyses using these calibrated models can be used to parametrically simulate the response of different vintage CBF designs under a range of ground motions. Such models could be used to quickly analyze a variety of input parameters. Additional parametric studies for different bracing configurations, number of stories, and brace sections may give valuable information on the adequacy of vintage braced frames and improve characterization of the behavior of the “strongback” system.

The use of an empirical low-cycle fatigue material well predicted the fracture observed in the experiments. Note, however, that this fatigue material model is dependent on the number of fibers, number of integration points, section shape, and element length used in the numerical simulations. Thus, use of the calibrated fatigue parameters from this study are reliable only for numerical models using similar simulation properties. As strain values needed for the fatigue material model non-objectively depend on the properties of the numerical simulations, numerical models with different properties must be re-calibrated to experimental results.

While the global behavior of the experiments was adequately captured by these OpenSees simulations, connection failures and local buckling were neglected in the simulations. More

sophisticated continuum models or empirically based springs representing connection regions may be necessary to better emulate these localized responses.

8 Summary, Conclusions, and Future Research

8.1 SUMMARY OF EXPERIMENTAL RESULTS

This study described the experimental results and numerical calibration of three cyclic experiments of concentrically braced frames. The first experiment represented an older braced frame typical of vintage designs in the mid-1980s. The second test implemented upgraded braces and details, including concrete-filled tube (CFT) braces and net-section reinforcement. Finally, the third test introduced a strongback retrofit scheme aimed at mitigating the weak-story behavior observed during the first two experiments.

8.1.1 Summary of NCBF-B-1 Baseline Response

This section presents a discussion of the key observations for the NCBF-B-1 test.

- Initial buckling of the second-story east brace led to a localized concentration of damage in the second story, indicative of a weak-story mechanism. The first story exhibited minor yielding and contributed little energy-dissipation capacity to the system. The peak story drift ratio of the second story was nearly 2%, and the first story exhibited small lateral displacements.
- The 40% decrease in the frame's shear capacity upon initial local buckling and the 70% decrease in the frame's shear capacity upon brace fracture indicate an abrupt and severe reduction in capacity that is largely dependent on the hysteretic response of the braces. Both of these reductions are significant, indicating that the baseline test frame had limited strength capacity beyond brace buckling.
- The braces were designed with high width-to-thickness ratios well above that of modern compactness requirements for highly ductile members. The braces exhibited severe local buckling, which led to brace fracture within only a few inelastic cycles. The braces did not exhibit gross section yielding but did show significant reduction in compression strength upon local buckling. Braces with high width-to-thickness ratios may be unable to sustain large cycles of inelastic displacement and maintain strength and stiffness after local buckling.
- Though minor yielding was observed in the connection regions, the use of non-notch tough welding consumables may lead to connection failures precluded by the notch-tough welding consumables used for this experiment. As such, more brittle connection failures could be expected in vintage braced frames. Whitewash flaking was observed near the

net-section region of the second-story braces and other failure modes could have been triggered had brace buckling not been the governing limit state.

8.1.2 Summary of NCBF-B-2 CFT Upgrade Response

This section presents a discussion of the key observations for the NCBF-B-2 test.

- Initial buckling of the first-story east brace led to a concentration of damage in the first story, indicative of a weak-story mechanism. The majority of the energy dissipation in the system was performed by the first-story east brace and first floor east half-beam, which behaved like a long beam link in an eccentrically braced frame. This beam link appeared capable of secondarily dissipating energy after brace fracture. Engagement of the second story was delayed until the second-story braces exhibited local buckling due to frame action under large drift demands. Even then, participation of the second story was minimal. The peak story drift ratio of the first story was 4.2%, five times larger than the peak story drift ratio of 0.8% in the second story. Damage to the first story was serious upon completion of the test, and residual displacements were six times larger in the first story than the second story.
- The frame's lateral strength decreased to approximately 80% of the maximum base shear upon global buckling, 70% upon local buckling, and 30% upon brace fracture. Like the baseline NCBF-B-1 test specimen, local buckling led to an abrupt decrease in the frame's strength and stiffness. After brace fracture, the frame's global response was defined by smaller hysteretic cycles with decreased strength and stiffness due to secondary energy dissipation through beam yielding. The reliability of this reserve capacity in vintage CBF is debatable, especially since the connections, first-story beam, and columns exhibited substantial damage upon completion of the experiment.
- While the addition of the concrete-fill delayed the onset of local buckling in the braces, brace fracture occurred at similar roof drift amplitudes to the hollow braces of the first test specimen. The results presented here and past research indicate that the benefit of the concrete-fill is reduced in sections with higher width-to-thickness ratios. To better understand the influence of the concrete-fill on the inelastic behavior of non-seismically compact braces, additional research is needed.
- The column oriented in strong-axis bending fractured near the baseplate in flexure towards the end of the experiment at a roof drift ratio of 2.33%. While this may be partly associated with the nearly rigid boundary conditions at the base of the columns used in the test set-up, the weak-axis column base showed substantially more rotational capacity under similar lateral displacements. Thus, weak-axis columns may be an appropriate solution for columns required to develop large rotational demands as part of braced bays. Note that vintage braced frames may experience uplift and could potentially dissipate energy through rocking on the foundation; however, potential rocking was considered outside the scope of these experiments.
- The net-section reinforcement used for the upgrade appears to have eliminated net-section yielding, as little whitewash flaking was observed at the net-section regions of the braces at the end of the test. The second-story east unstiffened gusset plate at the weak-

axis column punched through the column web, indicating that stiffeners may be required for improved behavior in gusset-to-weak-axis column connection regions. The welded shear tab detail used in this study showed significant damage. Further research to determine modeling and acceptance criteria for these types of connections is needed.

8.1.3 Summary of NCBF-B-3SB Strongback Response

This section presents a discussion of the key observations for the NCBF-B-3SB test.

- The SB system behaved well. As intended, it prevented the formation of a weak-story mechanism even after rupture of the BRB, the structure's primary source of energy dissipation. After rupture of the BRB, the SB system mobilized other portions of the structure to provide significant reserve strength, stiffness, and energy dissipation. The system's hysteretic loops were full and stable until the target roof drift ratio of 2%.
- The plastic-hinge regions were well predicted by a simple kinematic diagram of the frame's plastic mechanism. The lower-level beam formed a plastic hinge at the center gusset plate. The beam exhibited local buckling at this location (as would be expected at large plastic rotations). The use of a column oriented in the weak-axis direction at the base of the strongback truss resulted in satisfactorily ductile behavior. Other portions of the SB truss remained essentially elastic.
- The strain demands in the BRB were approximately double that of a conventional braced frame with a "strong" (flexurally rigid) beam, which results from the plastic mechanism associated with the frame's bracing configuration and geometry. The BRB satisfied current qualification testing protocols before rupture (e.g., AISC 341-10 [2010]), though maximum axial strain were greater than 4%. The failure mode consisted of crushing of the inner concrete, local buckling of the BRB outer casing, and subsequent rupture of the BRB steel core. Similar failure modes have been documented by Lin et al. [2015] on BRBs with rectangular core profiles.
- The welded shear tab beam-column connections from the original vintage structure could not develop the imposed rotations of the kinematic mechanism and fractured before the specimen was able to reach the target displacement in the loading protocol. This shear tab connection needed to be repaired several times during the test. This failure mode is similar to that observed during the NCBF-B-2 experiment and emphasizes the need for research on the rotational capacity of welded shear tabs.
- Residual drifts at the end of the test were about 0.6% in both the first and second stories. More extensive analyses are required to understand the behavior and performance of the strongback under dynamic loading conditions. The mechanism also allows for large vertical beam mid-span displacements that may be difficult to repair after a large earthquake. Note that re-centering capabilities may be implemented in the strongback to achieve enhanced performance goals.

8.2 FUTURE WORK

Future work can be split into two main categories: (1) evaluation of vintage braced frame systems based on experimental testing of baseline NCBF-B-1 and upgrade NCBF-B-2; and (2) refinement of the SB system as related to the NCBF-B-3SB test specimen.

8.2.1 Evaluation of Vintage Braced Frames

Future research is required before conclusions can be drawn about the behavior of vintage braced frames, including:

1. The effect of concrete in the braces was successful at delaying local buckling but not brace fracture. Further research is necessary before results can be deemed conclusive.
2. The plastic mechanism of the NCBF-B-2 test warrants further scrutiny. The weak beam in vintage braced frames allows plastic hinging in the beam (see Section 2.2.4), but it is unclear whether this behavior is desirable.
3. Welded shear tabs appeared to have much less rotational capacity than their bolted counterparts. Such connections are not explicitly considered in the current ASCE-41 [2013] modeling criteria. Further research is needed to assess the vulnerability of these types of connections at critical locations.
4. Numerical parametric studies need to be conducted to assess and improve current retrofit evaluation procedures for existing vintage braced frames (e.g., ASCE 41-13 [2013]).
5. While the fiber-element modeling techniques presented here may be capable of capturing global vintage CBF behavior, these models cannot capture local buckling or fracture unless they are calibrated to experimental tests. Continuum models are necessary to capture the localized behavior observed in the braces, beams, columns, and connections not captured in the numerical studies reported herein.
6. A probabilistic assessment needs to be carried out to determine the cost effectiveness of different retrofit and upgrade strategies, as with the FEMA P-58 [2012] methodology.

8.2.2 Optimization of the Strongback System

This preliminary study has demonstrated that the strongback system can be successful at mitigating weak-story behavior in steel braced frames. However, more research is still needed. Future research areas include:

1. Calibrated analytical studies computing the frame's displacement demands considering the system's design response spectrum and the structure's dynamic characteristics to determine the necessary strength needed for the strongback to remain essentially elastic. This includes collapse assessment (e.g., using FEMA P-695 [2009] methodology).
2. Additional parametric studies are needed to assess the impact of a range of strongback designs, including: alternative bracing configurations; different bracing types; the detailing of critical regions; and various number of stories and story heights.

3. Further optimization and refinement in the SB design concept, including simple and effective design recommendations to meet basic performance goals.
4. Additional studies and recommendations that allow the strongback system to reach enhanced performance goals; including advanced detailing or re-centering capabilities. An estimate of initial construction costs and the strongback's performance in terms of structural and nonstructural damage after an earthquake may provide valuable information about the feasibility of using this system in practice (e.g., use of FEMA P-58 [2012] methodology).

REFERENCES

- AIJ (1995). *Reconnaissance Report on Damage to Steel Building Structures Observed from the 1995 Hyogoken-Nanbu (Hanshin/Awaji) Earthquake*, Architectural Institute of Japan, Steel Committee of Kinki Branch.
- AISC (1978). *Specification for the Design, Fabrication and Erection of Structural Steel for Buildings*, American Institute of Steel Construction, Chicago, IL.
- AISC (1992). *Seismic Provisions for Structural Steel Buildings*, AISC/ANSI Standard 341, American Institute of Steel Construction, Chicago, IL.
- AISC (1997). *Seismic Provisions for Structural Steel Buildings*, AISC/ANSI Standard 341, American Institute of Steel Construction, Chicago, IL.
- AISC 341-10 (2010) *Seismic Provisions for Structural Steel Buildings*, AISC/ANSI Standard 341, American Institute of Steel Construction, Chicago, IL.
- AISC 360-10 (2010). *Specification for Structural Steel Buildings*, American Institute of Steel Construction, Chicago, IL.
- Aoyama H. (1981). Outline of earthquake provisions in the recently revised Japanese building code, *Bull. NZ Soc. Earthq. Eng.*, 14(2): 63–80.
- ASCE 41-13 (2013). *Seismic Rehabilitation of Buildings*, American Society of Civil Engineers, Reston, VA.
- ASCE 7-10 (2010). *Minimum Design Loads for Buildings and Other Structures*, American Society of Civil Engineers, Reston, VA.
- Astaneh-Asl A. (1982). *Cyclic Behavior of Double Angle Bracing Members with End Gusset Plates*, PhD. Thesis, Department of Civil Engineering, University of Michigan, Ann Arbor, MI.
- Astaneh-Asl A., Goel S., Hanson, R. (1985). Cyclic out-of-plane buckling of double-angle bracing, *ASCE, J. Struct. Eng.*, 10.1061/(ASCE) 0733-9445(1985)111:5(1135), 1135–1153.
- ASTM (2011a). “Standard test method for compressive strength of cylindrical concrete specimens, *ASTM C39/C39M-11a*, West Conshohocken, PA.
- ASTM (2011b). “Standard test method for splitting tensile strength of cylindrical concrete specimens, *ASTM C496/C496M-11*, West Conshohocken, PA.
- ATC (2012). *Performance Assessment Computation Tool (PACT-2)*, Applied Technology Council, Redwood City, CA, <https://www.atccouncil.org/downloads/atc58installation.html>.
- ATC (1995). *ATC-19: Structural Response Modification Factors*, Applied Technology Council, Redwood City, CA.
- Black C., Makris N., Aiken I. (2002). Component testing, stability analysis and characterization of buckling-restrained unbonded braces, *PEER Report No. 2002/08*, Pacific Earthquake Engineering Research Center, University of California, Berkeley, CA.
- Black R., Wenger W., Popov E. (1980). Inelastic buckling of steel struts under cyclic load reversals, *Report No. UCB/EERC-80/40*, Earthquake Engineering Research Center, University of California, Berkeley, CA.
- Bonneville D.; Bartoletti S. (1996). Case study 2.3: Concentric braced frame, Lankershim Boulevard, North Hollywood, 1994 Northridge earthquake: building case studies project. proposition 122: Degenkolb Engineers, Product 3.2, *SSC 94-06*, Seismic Safety Commission, State of California, pp. 305–324.
- Bradley C.R., Fahnestock L., Hines E.M., Sizemore J. (2014). Full-scale cyclic testing of low-ductility concentrically braced frames, *ASCE, J. Struct. Eng.*, 143(6): 0407029.
- Broderick B.M., Goggins J.M., Elghazouli A.Y. (2005). Cyclic performance of steel and composite bracing members, Elsevier, *J. Construct. Steel Res.*, 61: 493–514.
- Brown V. (1988). *Stability of Gusseted Connections in Steel Structures*, PhD Thesis, Department of Civil Engineering, University of Delaware, Newark, DE.

- Bruneau M., Uang C., Sabelli R. (2011). *Ductile Design of Steel Structures*, 2nd Ed., New York, NY: McGraw-Hill Companies, Inc.
- Chen C.H., Mahin S.A. (2012). Performance-based seismic demand assessment of concentrically braced steel frame buildings. Report No. PEER-2012/103, Pacific Earthquake Engineering Research Center, University of California, Berkeley, CA.
- Cheng F., Juang D.S. (1985). *Optimum Design of Braced and Unbraced Frames for Static, Seismic, and Wind Forces with UBC, ATC-3, and TJ-11*, Vol. 85, No. 10 of the Structural Series, University of Rolla, Missouri, 337 pgs.
- Clark K.A (2009). *Experimental Performance of Multi-Story X-Brace Systems*, Master's Thesis, Department of Civil and Environmental Engineering, University of Washington, Seattle, WA.
- Djojo G.S., Clifton G.C., Henry R.S. (2014). Rocking steel shear walls with energy dissipation devices, *Proceedings New Zealand Society for Earthquake Engineering Conf.*, New Zealand Society for Earthquake Engineering, Wellington, New Zealand.
- Dusicka P., Berman J., Purasinghe R. (2012-2013). NEESR-II: Toward rapid return to occupancy in unbraced steel frames, *NSF Award No: 0830313*, National Science Foundation, Reston, VA.
- EERI (1978). *Reconnaissance Report Miyagi-Ken-Okii*, Earthquake Engineering Research Institute, Berkeley, CA.
- Fell B.V. (2008). Large-Scale Testing and Simulation of Earthquake-Induced Low Cycle Fatigue in Bracing Members Subjected to Cyclic Inelastic Buckling, PhD thesis, Department of Civil and Environmental Engineering, University of California, Davis, CA.
- FEMA (2009). *Quantification of Building Seismic Performance Factors, FEMA P-695*, prepared by Applied Technology Council for Federal Emergency Management Agency, Washington, D.C.
- FEMA (2012). *Next-Generation Methodology for Seismic Performance Assessment of Buildings, prepared by the Applied Technology Council for the Federal Emergency Management Agency, Report No. FEMA P-58*, Washington, D.C.
- Filiatrault A., Anderson D.L., DeVall R.H. (1992). Effect of weak foundation on the seismic response of core wall type buildings, *Can. J. Civ. Eng.*, 19: 530–539.
- Filippou F.C., Popov E.P., Bertero V.V. (1983). Effects of bond deterioration on hysteretic behavior of reinforced concrete joints, Report No. EERC 83-19, Earthquake Engineering Research Center, University of California, Berkeley
- Foutch D., Goel S., Roeder C.W. (1987). Seismic testing of full-scale steel building—Part I, ASCE, *J. Struct. Eng.*, 10.1061/(ASCE)0733-9445 (1987)113:11(2111), 2111–2129.
- Fukuta T., Nishiyama I., Yamanouchi H., Kato B. (1989). Seismic performance of steel frames with inverted v braces, ASCE, *J. Struct. Eng.*, 10.1061/(ASCE)0733-9445(1989)115:8(2016), 2016–2028.
- Gardner N.J., Jacobson E.R. (1967). Structural behavior of concrete filled steel tubes, American Concrete Institute, *ACI J.*, 64(7): 404–412.
- Ghanaat Y. (1980). Study of X-braced steel structures under earthquake simulation, *UCB/EERC 80/08*, Earthquake Engineering Research Center, University of California, Berkeley, CA.
- Grigorian M., Grigorian C. (2016). An introduction to the structural design of rocking wall-frames with a view to collapse prevention, self-alignment and reparability, *Struct. Des. Tall Spec. Bldg.*, 25(2): 93–111.
- Gross J.L., Cheok G. (1988). Experimental study of gusseted connections for laterally braced steel buildings, *NISTIR 88-3849*, National Institute of Standards and Technology, Gaithersburg, MD.
- Gugerli H., Goel S.C. (1982). Inelastic cyclic behavior of steel bracing members, *UMEE 82R1 Report*, Department of Civil Engineering, University of Michigan, Ann Arbor, MI.
- Higginbotham A. (1973). *The Inelastic Cyclic Behavior of Axially-Loaded Steel Members*, PhD Thesis, Department of Civil Engineering, University of Michigan, Ann Arbor, MI.

- Hines E.M., Appel M.E., Cheever P.J. (2009). Collapse performance of low-ductility chevron braced steel frames in moderate seismic regions, *AISC Eng. J.*, 46(3): 149–180.
- Hsiao P.C., Lehman D.E., Berman J., Roeder C.W. (2014). Seismic vulnerability of older braced frames, *J. Perform. Constr. Fac.*, 28(1): 108–120.
- ICBO (1980). *Los Angeles Building Code*, International Conference of Building Officials, Whittier, CA.
- ICBO (1985). *Uniform Building Code*, International Conference of Building Officials, Whittier, CA.
- ICBO (1988). *Uniform Building Code*, International Conference of Building Officials, Whittier, CA.
- Jain A., Goel S., Hanson R. (1978). Hysteresis behavior of bracing members and seismic response of braced frames with different proportions, *UMEE 78R6 Report*, Department of Civil Engineering, University of Michigan, Ann Arbor, MI.
- Johnson M.M. (2014). *Seismic Evaluation of Bolted Connections in Non-Seismic Concentrically Braced Frames*, Master's Thesis, Department of Civil and Environmental Engineering, University of Washington, Seattle, WA.
- Kahn L.F., Hanson R.D. (1976). Inelastic cycles of axially loaded steel members, *ASCE, J. Struct. Div.*, 102(ST5): 947–959.
- Kato B., Tanaka A., Yamanouchi H. (1980). A field work investigation of steel building damage due to the 1978 Miyagiken-Oki earthquake, *Proceedings, 7th World Conference on Earthquake Engineering*, Istanbul, Turkey.
- Kelly D.J., Bonneville D., Bartoletti S. (2000). 1994 Northridge earthquake: Damage to a four-story steel braced frame building and its subsequent upgrade, *Proceedings, 12th World Conference on Earthquake Engineering*, Auckland, New Zealand.
- Khatib I. F., Mahin S.A., Pister K.S. (1988). Seismic behavior of concentrically braced steel frames, Report No. *UCB/EERC-88/01*, Earthquake Engineering Research Center, University of California, Berkeley, CA.
- Krawinkler H., Anderson J., Bertero V., Holmes W., Theil C. (1996). Steel buildings, *Earthq. Spectra*, 12(S1): 25–47.
- Lai J.W., Mahin S.A. (2013). Experimental and analytical studies on the seismic behavior of conventional and hybrid braced frames, *PEER Report No. 2013/10*, Pacific Earthquake Engineering Research Center, University of California, Berkeley, CA.
- Lai J.W., Mahin S.A. (2015). Strongback system: A way to reduce damage concentration in steel braced frames, *ASCE, J. Struct. Eng.*, 141(9): 0404223.
- Lee K., Bruneau M. (2005). Review of energy dissipation of compression members in concentrically braced frames, *Technical Report MCEER-02-0005*, Department of Civil and Environmental Engineering, SUNY Buffalo, NY.
- Lee S., Goel S.C. (1987). Seismic behavior of hollow and concrete filled square tubular bracing members, *Research Report UMCE 87-11*, Department of Civil Engineering, University of Michigan, Ann Arbor, MI.
- Lehman D.E., Roeder C.W., Herman D., Johnson S., Kotulka B. (2008). Improved seismic performance of gusset plate connections, *ASCE, J. Struct. Eng.*, 134(6): 890–901.
- Lin P.C., Tsai K.C., Chang C.A., Hsiao Y.Y., Wu A.C. (2015). Seismic design and testing of buckling-restrained braces with a thin profile, *Earthq. Eng. Struct. Dyn.*, no. DOI: 10.1002/eqe.2660.
- Liu Z., Goel S. (1988). Cyclic load behavior of concrete-filled tubular braces, *ASCE, J. Struct. Eng.*, 114(7): 1488–1506.
- Lumpkin E.J. (2009). *Enhanced Seismic Performance of Multi-Story Special Concentrically Braced Frames Using a Balanced Design Procedure*, Master's Thesis, Department of Civil and Environmental Engineering, University of Washington, Seattle, WA.
- MacRae G.A. (2011). The continuous column concept - Development and use, *Proceedings, 9th Pacific Conference on Earthquake Engineering*, Auckland, New Zealand.
- Malley J.O. (1989). *The 1988 UBC: Revisions and Additions to the Requirements for Braced Steel Frames*, Structural Engineers Association of California, Sacramento, CA.

- Mar D. (2010). Design examples using mode shaping spines for frame and wall buildings, *Proceedings, 9th US National and 10th Canadian Conference on Earthquake Engineering*, Toronto, Canada.
- Martini K., Amin N., Lee P., Bonowitz D. (1990). The potential role of non-linear analysis in the seismic design of building structures, *Proceedings, 4th US National Conference on Earthquake Engineering*, Palm Springs, CA.
- MATLAB Version 9.3.0 (2017) [Computer software]. The Mathworks Inc., Natick, MA,
- McKenna F., Scott M., Fenves G. (2010) .Nonlinear finite-element analysis software architecture using object composition, *ASCE, J. Comput. Civ. Eng.* , vol. 10.1061/(ASCE)CP.1943-5487-0000002, pp. 96–107.
- McManus P.S., MacMahon A., Puckett J.A. (2013). Buckling restrained braced frame with all-bolted gusset connections, *Eng. J.*, 50: 89–116.
- Merzouq S., Tremblay R. (2006). Seismic design of dual concentrically braced steel frames for stable seismic performance for multi-story buildings, *Proceedings, 8th U.S. National Conference on Earthquake Engineering*, EERI, Oakland, CA.
- Naeim F. (1989). *The Seismic Design Handbook*, Springer, New York.
- Nordenson G. (1984). Notes on the seismic performance of concentrically braced frames, *Proceedings, 8th World Conference on Earthquake Engineering*, pp. 395–402.
- OpenSees version 2.4.6 [Computer software]. Pacific Earthquake Engineering Research Center, Berkeley, CA.
- Panian L., Bucci N., Janhunen B. (2015). BRBM frames: An improved approach to seismic-resistant design using buckling-restrained braces, *Proceedings, ATC & SEI Conference on Improving the Seismic Performance of Existing Buildings and Other Structures*, San Francisco, CA.
- Popov E.P., Ricles J.M., Kasai K. (1992). Methodology for optimum EBF link design, *Proceedings, 10th World Conference on Earthquake Engineering*, Balkema, Rotterdam.
- Popov E.P., Takanashi K., Roeder C. (1976). Structural steel bracing systems: behavior under cyclic loading, *Report No. UCB/EERC-76/17*, Earthquake Engineering Research Center, University of California, Berkeley, CA.
- Qu Z., Wada A., Motoyui S., Sakata H., Kishiki S. (2012). Pin-supported walls for enhancing the seismic performance of building structures, *Earthq. Eng. Struct. Dyn.*, 41(14) 2075–2091.
- Rai D.C., Goel S.C. (2003). Seismic evaluation and upgrading of chevron braced frames, *J. Construct. Steel Res.*, 59: 971–994.
- Roeder C.W., Lumpkin E., Lehman D.E. (2011). A balanced design procedure for special concentrically braced frame connections, *J. Construct. Steel Res.*, 67(11): 1760–1772.
- Sabelli R. (2001). Research on improving the design and analysis of earthquake-resistant steel braced frames, *NEHRP Fellowship Rep. No. PF2000-9*, Earthquake Engineering Research Institute, Oakland, CA.
- SEAOC (1959). *SEAOC "Blue Book" Recommended Lateral Force Requirements*, Structural Engineers Association of California, Sacramento, CA
- SEAOC (1973). *SEAOC "Blue Book" Recommended Lateral Force Requirements*, Structural Engineers Association of California, Sacramento, CA.
- SEAOC (1978). *Tentative Lateral Force Requirements*, Seismology Committee, Structural Engineers Association of California, Sacramento, CA.
- SEAONC (1982). *Earthquake Resistant Design of Concentric and K-Braced Frames*, Structural Engineers Association of Northern California, Redwood City, CA.
- SEAONC (1985) *Tentative Lateral Force Requirements and Commentary*, Structural Engineers Association of Northern California, Redwood City, CA.
- Sen A.D., Roeder C.W., Berman J.W., Lehman D.E. (2016). Experimental investigation of chevron concentrically braced frames with yielding beams, *ASCE, J. Struct. Eng.*, 10.1061/(ASCE)ST.1943-541X.0001597, 4016123.
- Shepard R. (1973). Multiphase cross bracing in earthquake resistant structures, *Earthq. Eng. Struct. Dyn.*, 1: 311–324.

- Sloat A. (2014). *Evaluation and Retrofit of Non-Capacity Designed Braced Frames*, Master's Thesis, Department of Civil and Environmental Engineering, University of Washington, Seattle, WA.
- Steinbrugge K.V., Schader E.E., Beggles H.C., Weers C.A. (1971). San Fernando Earthquake February 9th, 1971, San Francisco, CA: Pacific Fire Rating Bureau.
- Stoakes C.D., Fahnestock L.A. (2011). Cyclic flexural testing of concentrically braced frame beam-column connections, *ASCE, J. Struct. Eng.*, 10.1061/(ASCE)ST.1943-541X.0000326, 739–747.
- Takeuchi T., Chen X., Matsui R. (2015). Seismic performance of controlled spine frames with energy-dissipating members, *J. Construct. Steel Res.*, 114: 51–65.
- Tanaka A., Morita K., Yamanouchi H. (1980). Damage of braced steel frames due to the 1978 Miyagiken-Oki earthquake, *Proceedings, 7th World Conference on Earthquake Engineering*, Istanbul, Turkey.
- Tremblay R. (2002). Inelastic seismic response of steel bracing members, Elsevier, *J. Constr. Steel Res.*, 58(5): 665–701.
- Tremblay R. (2003). Achieving a stable inelastic seismic response for multi-story concentrically braced steel frames, *AISC Eng. J.*, 40(2): 111–129.
- Tremblay R.; Bruneau M., Nakashima M., Prion H., Filiatrault A., DeVall R. (1996). Seismic design of steel buildings: lessons from the 1995 Hyogo-ken Nanbu earthquake, *Can. J. Civ. Eng.*, 23: 727–756.
- Tremblay R., Merzouq S. (2004). Dual buckling restrained braced steel frame for enhanced seismic response, *Proceedings, Passive Control Systems*, Yokohama, Japan.
- Tremblay R., Poncet L. (2005). Seismic performance of concentrically braced steel frames in multistory buildings with mass irregularity, *J. Struct. Eng.*, 10.1061/(ASCE)0733-9445(2005)131:9(1363), 1363–1375.
- Tremblay R., Timler N., Bruneau M., Filiatrault A. (1995). Performance of steel structures during the 1994 Northridge earthquake, *Can. J. of Civ. Eng.*, 22: 338–360.
- Tsai K., Wu A., Wei C., Lin P., Chuang M., Yu, Y. (2014). Welded end-slot connection and debonding layers for buckling-restrained braces, *Earthq. Eng. Struct. Dyn.*, 43(12): 1785–1807.
- Uang C.-M., Bertero, V.V. (1986). Earthquake simulation tests and associated studies of a 0.3 scale model of a six-story concentrically braced steel structure, *Report No. UCB/EERC-86/10*, Earthquake Engineering Research Center, University of California, Berkeley, CA.
- Uriz P., Mahin S.A. (2008). Toward earthquake-resistant design of concentrically braced steel-frame structures, *PEER Report No. 2008/08*, Pacific Earthquake Engineering Center, University of California, Berkeley, CA.
- Wakabayashi M., Matsui C., Manami K., Mitani I. (1970). Inelastic behavior of steel frames subjected to constant vertical and alternating horizontal loads, *Proceedings, World Conference on Earthquake Engineering*, pp. 1194–1197.
- WJE (1998). Oviatt Library, East and West Wings: Investigation of Base Plate Damage caused by the Northridge Earthquake, Wiss, Janney, Elstner Associates, Inc., *Task Order No. 175*, Emeryville, CA.
- Yoo J.H., Roeder C.W., Lehman D.E. (2009). Simulated behavior of multi-story X-braced frames, Elsevier, *Eng. Struct.*, 31: 182–197.
- Zsarnoczay A. (2013). *Experimental and Numerical Investigation of Buckling Restrained Braced Frames for Eurocode Conform Design Procedure Development*, Ph.D. Dissertation. Budapest University of Technology and Economics.

Appendix A Plots of the NCBF-B-1 Test

A.1 RESPONSE HISTORY PLOTS

The following plots show the maximum and minimum values of selected variables derived from the instrumentation. Time is broken into cycles to reflect the slow, static nature of the quasi-static test. Global plots of the story shears and drifts are shown in Section A.1.1. The derived axial force, shears, moments, and rotations at specified sections of the members are shown for the braces, beams, and columns in Sections A.1.2, A.1.3, and A.1.4, respectively. Labels used in the plots are defined by the values in Table A.1.

Table A.1 NCBF-B1: Values used for labels in plots.

Design axial capacity		Location	F_y (ksi) ¹	T_n (kips) ²	C_n (kips) ³
HSS7×7×1/4		First-story braces	51.7	319	259
HSS6×6×3/16		Second-story braces	52.5	209	164
Design moment		Location	F_y (ksi) ¹	M_y (kip-in.) ⁴	M_p (kip-in.) ⁵
W10×54	Strong axis	West column	60.3	3,618	4016
	Weak axis	East column		1242	1887
W14×53		Beam	56.3	4380	4904
HSS7×7×1/4		First-story braces	51.7	688	801
HSS6×6×3/16		Second-story braces	52.5	390	453

¹ From steel coupon tests

² Design tensile capacity from AISC 360 [2010]

³ Design compression buckling capacity from AISC 360 [2010] using the length of the brace from the shop drawings with an effective length factor of $k = 1$

⁴ Yielding moment: $M_y = F_y S$, where S is the elastic section modulus

⁵ Plastic moment: $M_p = F_y Z$, where Z is the plastic section modulus

A.1.1 Global Plots

The following section shows the plots for the global response parameters of each story, including story shears and displacements. Maximum and minimum values are called out on each plot.

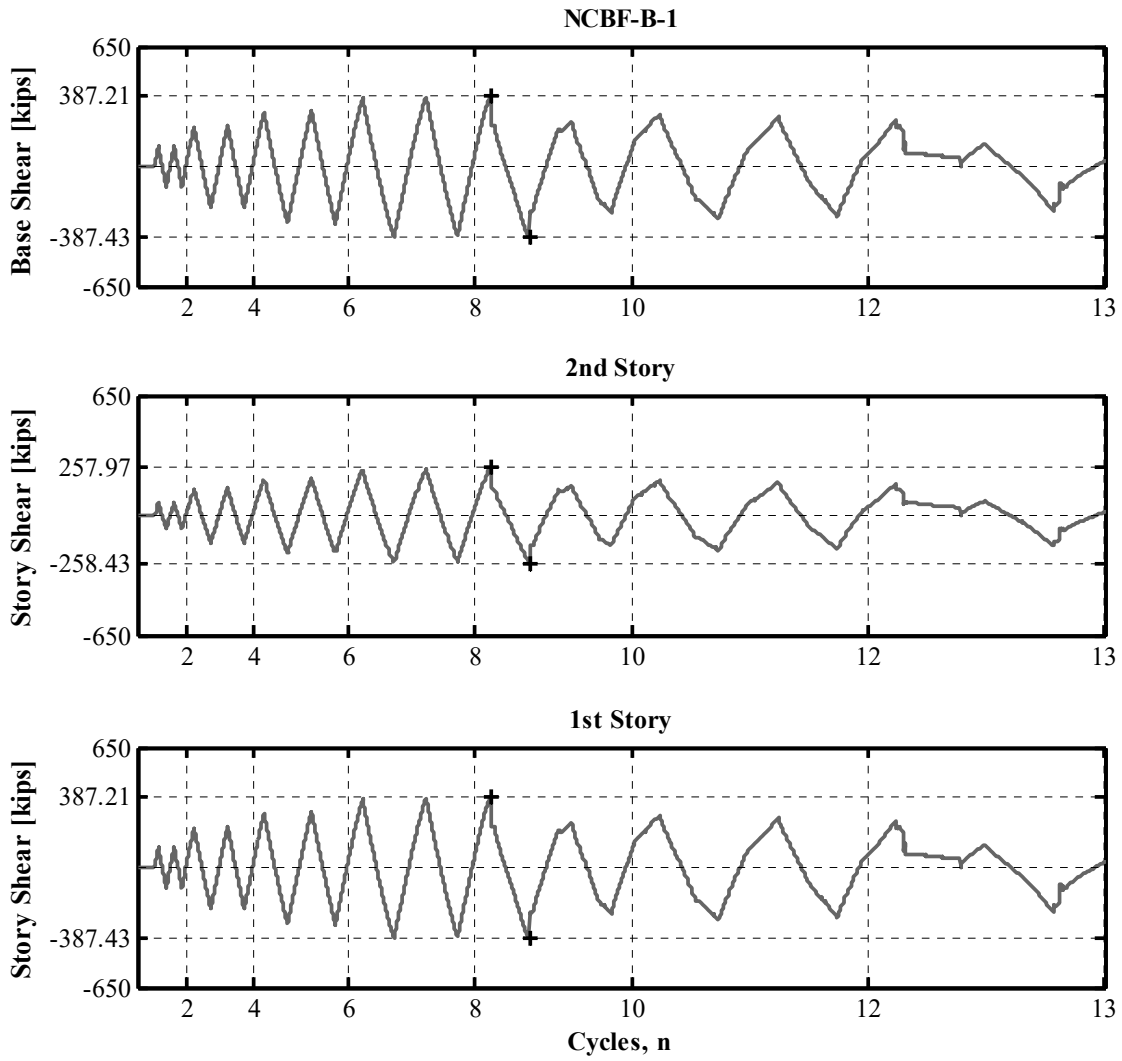


Figure A.1 NCBF-B-1 Story shear time histories.

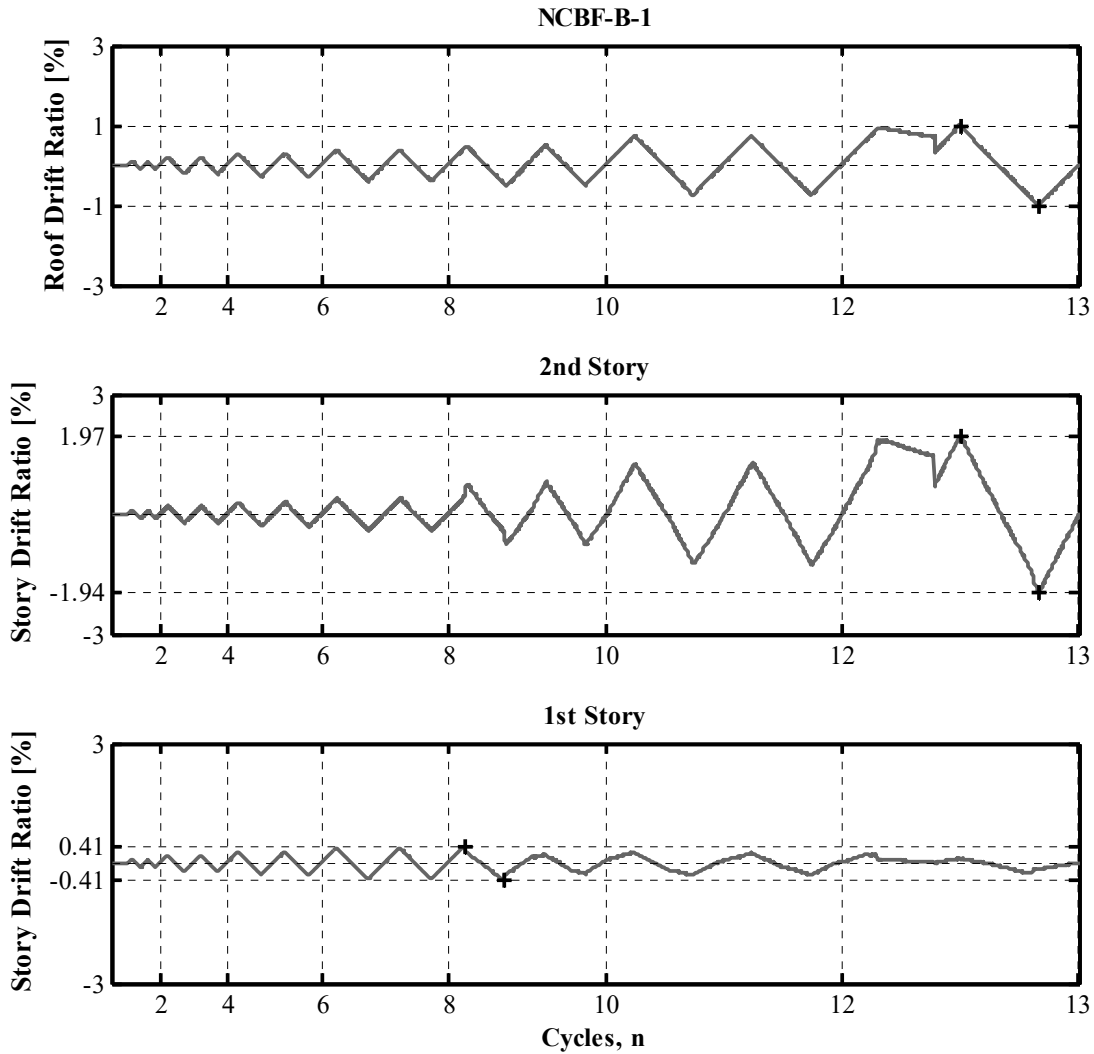


Figure A.2 NCBF-B-1 Story drift ratio time histories.

A.1.2 Brace Plots

The following section shows the plots for the brace response parameters. Plots include the response history for the brace estimated axial force, out-of-plane displacement, axial deformation, estimated moments, end rotations, and estimated shears. Maximum and minimum values are called out on each plot.

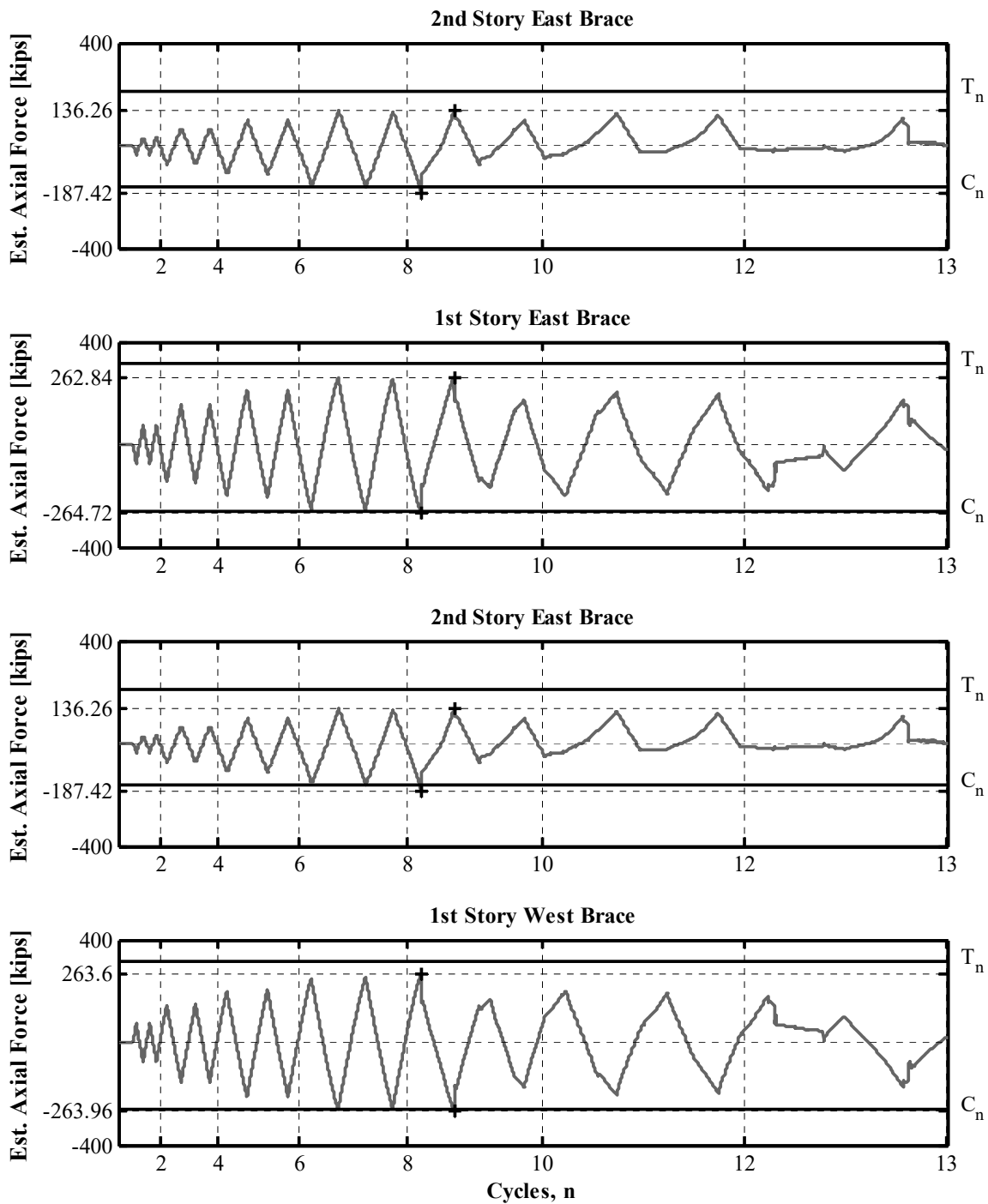


Figure A.3 NCBF-B-1 estimated brace axial force time histories.

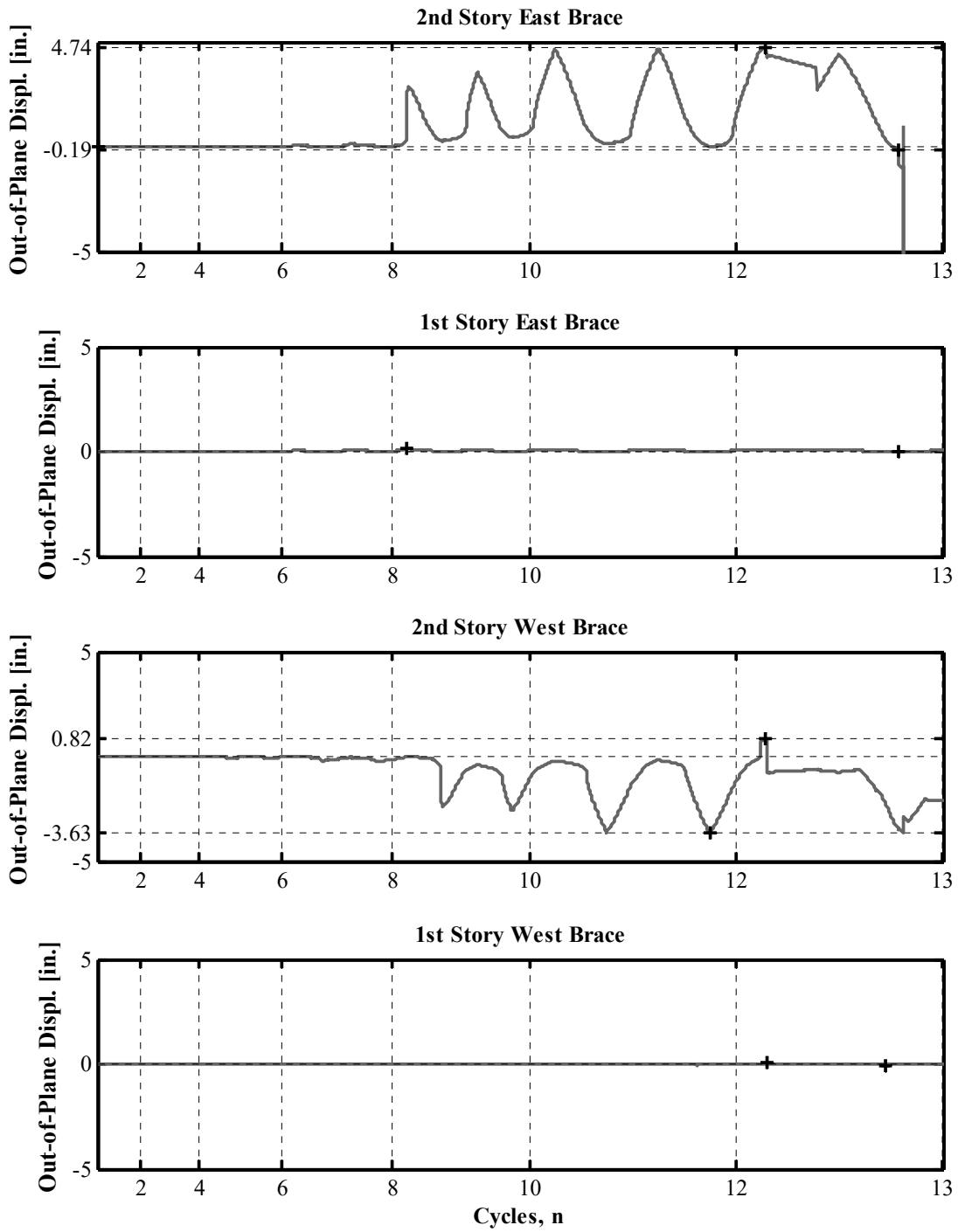


Figure A.4 NCBF-B-1 brace out-of-plane displacement time histories.

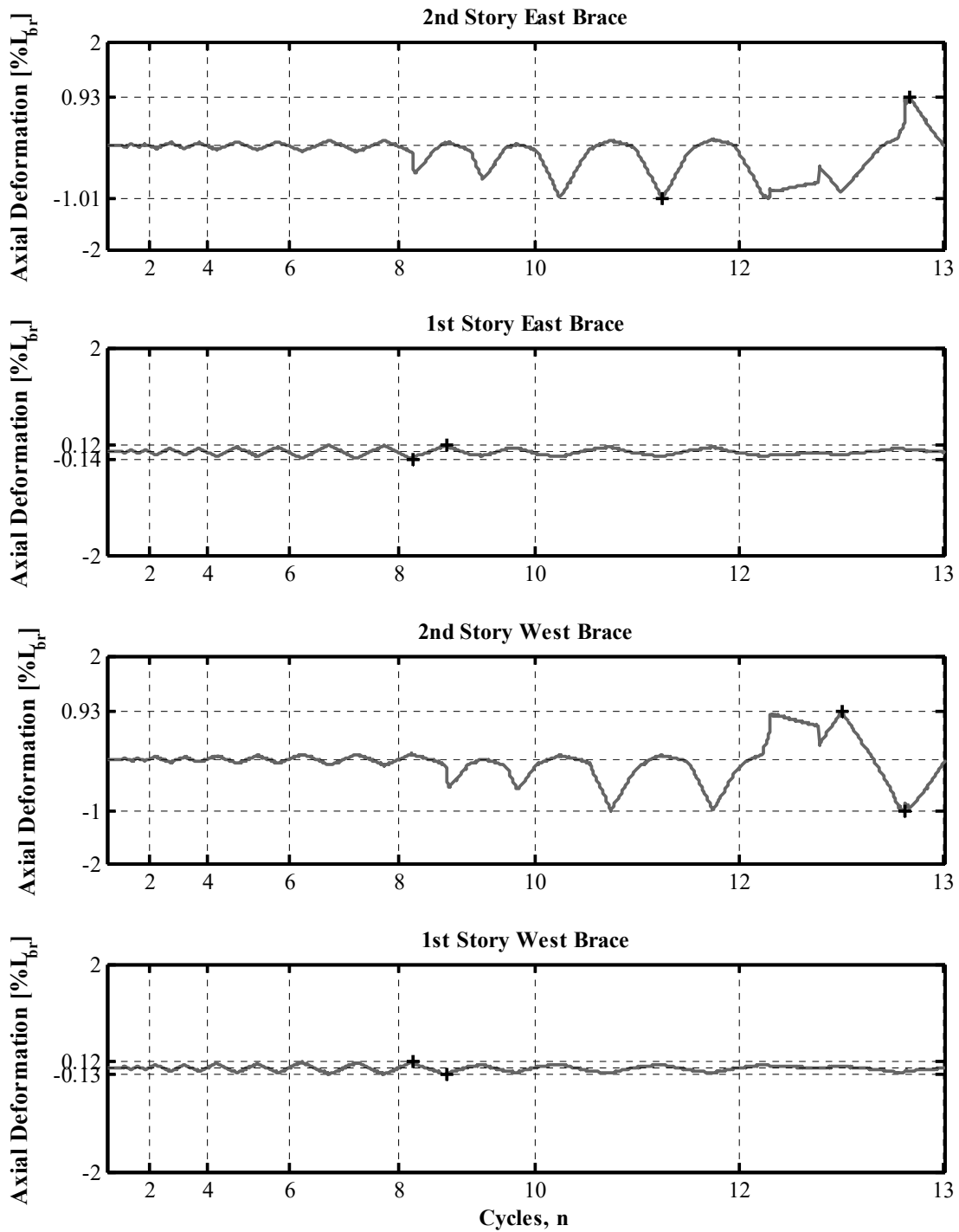


Figure A.5 NCBF-B-1 Brace axial deformation time histories (L_b is the work-point-to-work-point length).

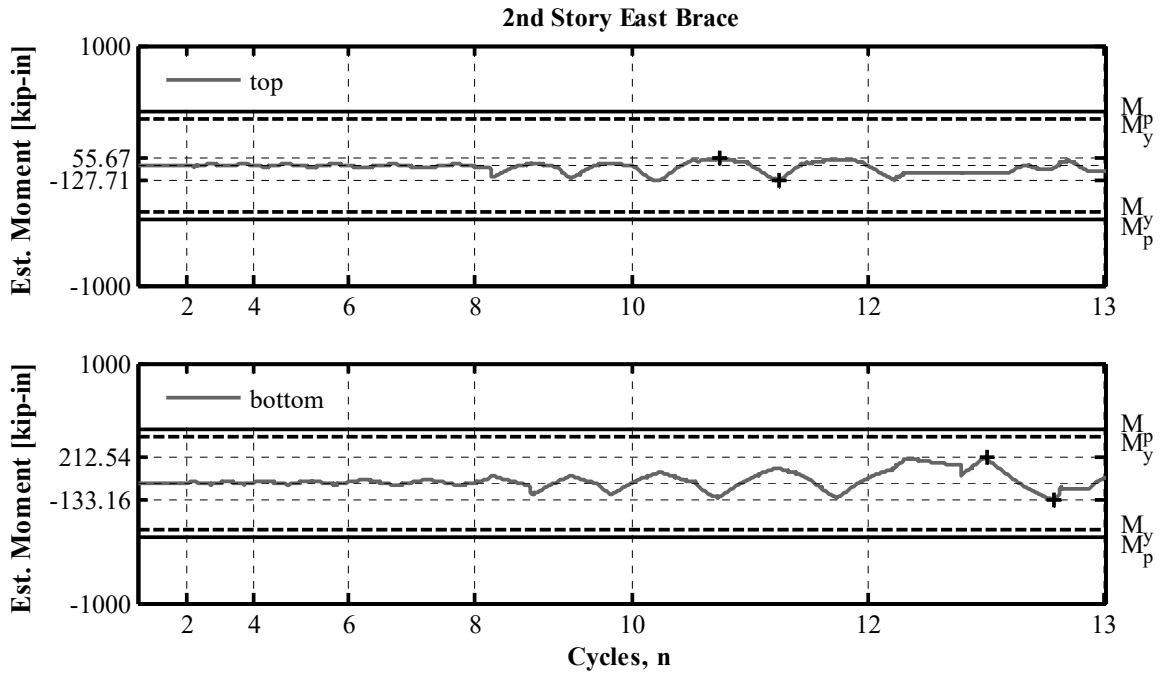


Figure A.6 NCBF-B-1 second-story east brace estimated moment time histories (measured at top and bottom ¼-points of brace length).

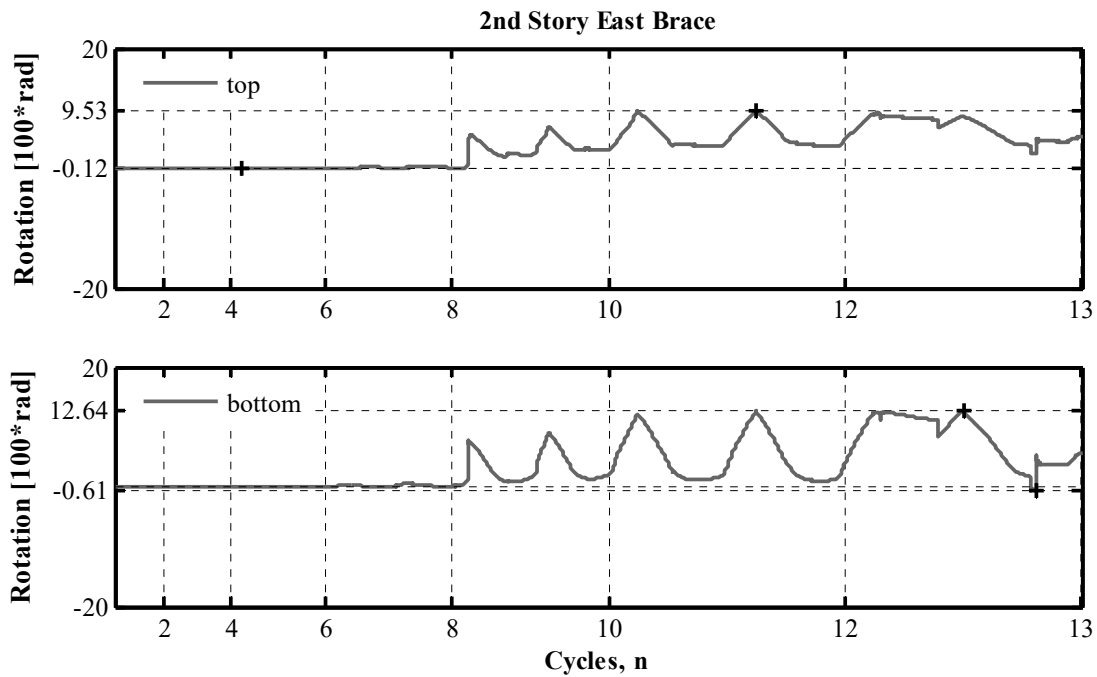


Figure A.7 NCBF-B-1 second-story east brace out-of-plane end rotation time histories.

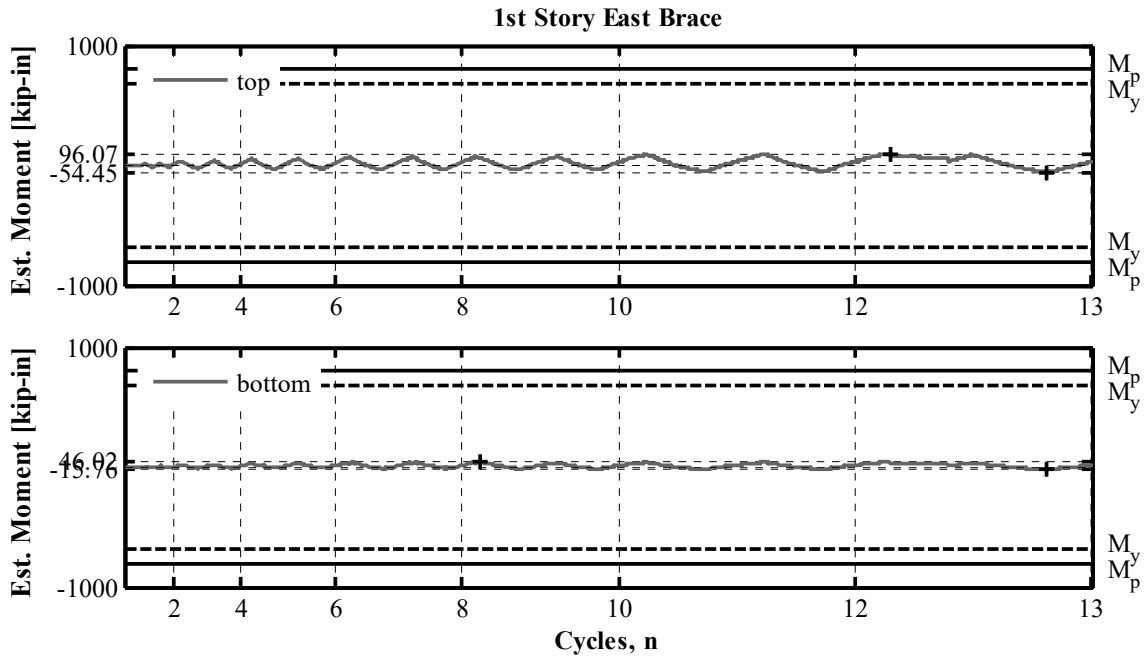


Figure A.8 NCBF-B-1 first-story east brace estimated moment time histories (measured at top and bottom ¼-points of brace length).

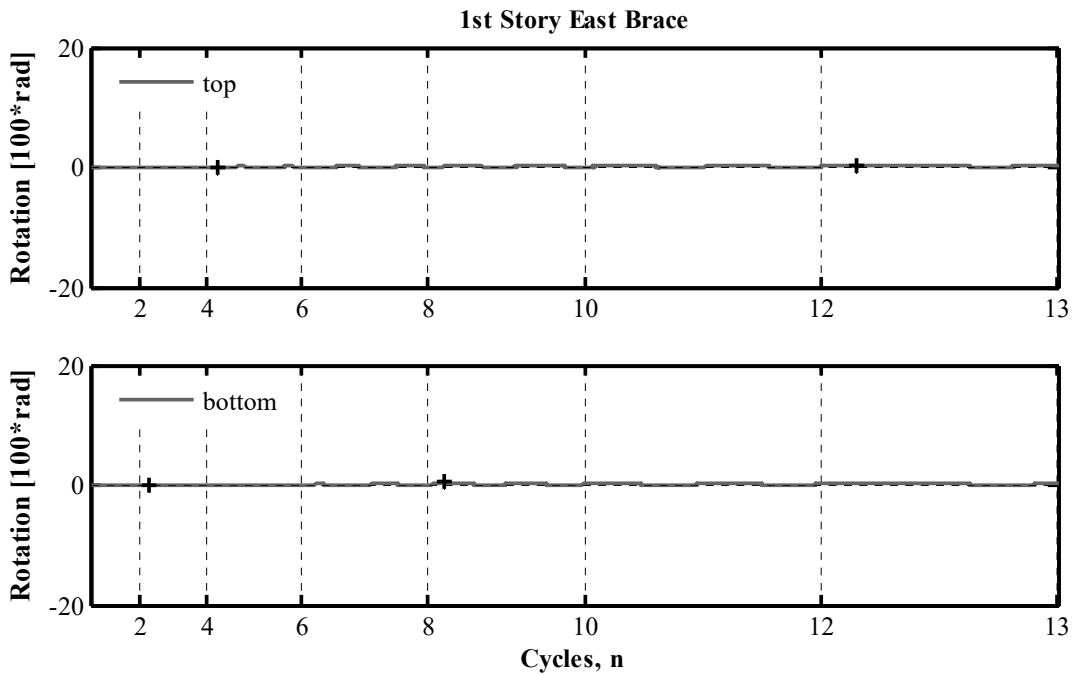


Figure A.9 NCBF-B-1 first-story east brace out-of-plane end rotation time histories.

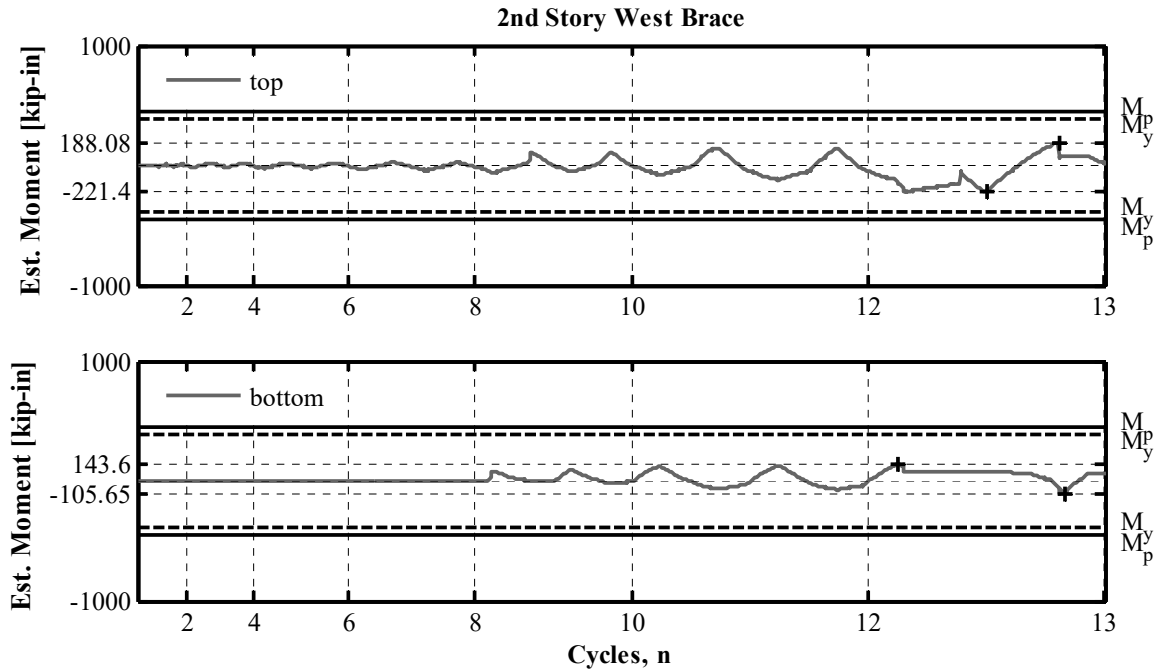


Figure A.10 NCBF-B-1 second-story west brace estimated moment time histories (measured at top and bottom ¼-points of brace length).

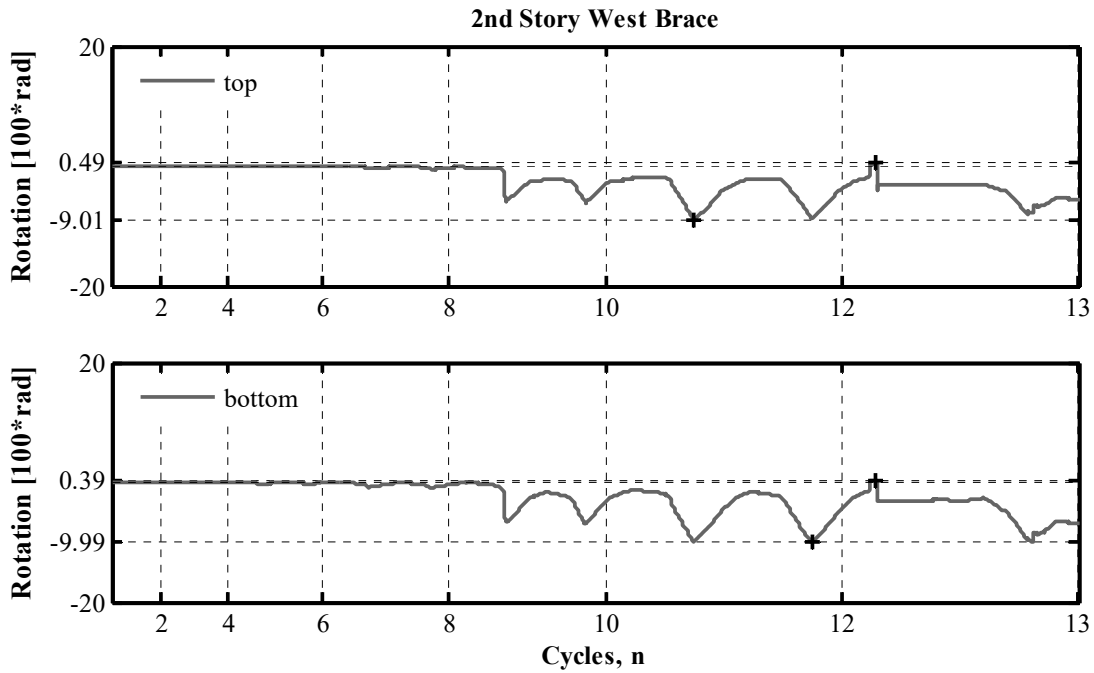


Figure A.11 NCBF-B-1 second-story west brace out-of-plane end rotation time histories

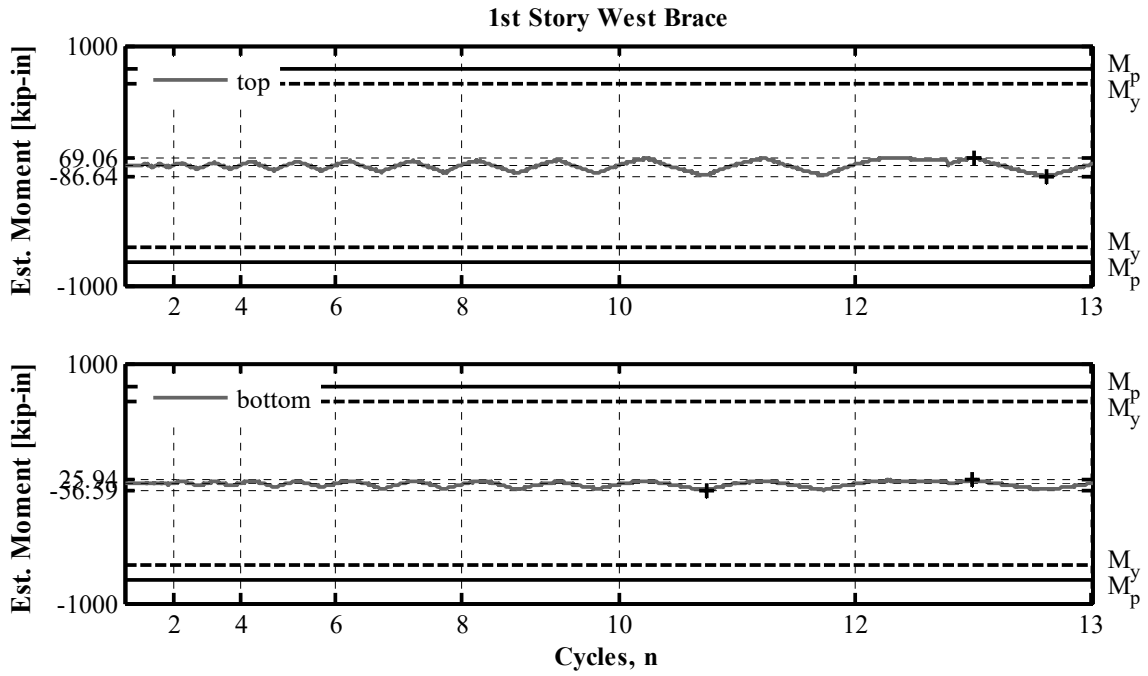


Figure A.12 NCBF-B-1 first-story west brace estimated moment time histories (measured at top and bottom ¼ points of brace length).

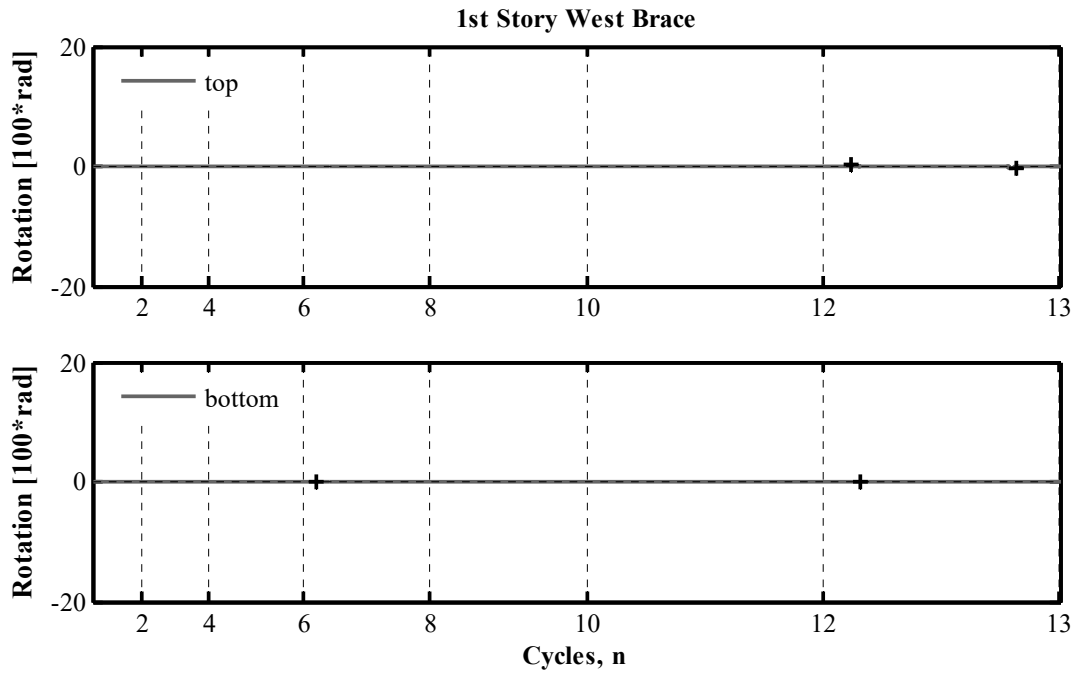


Figure A.13 NCBF-B-1 first-story west brace out-of-plane end rotation time histories.

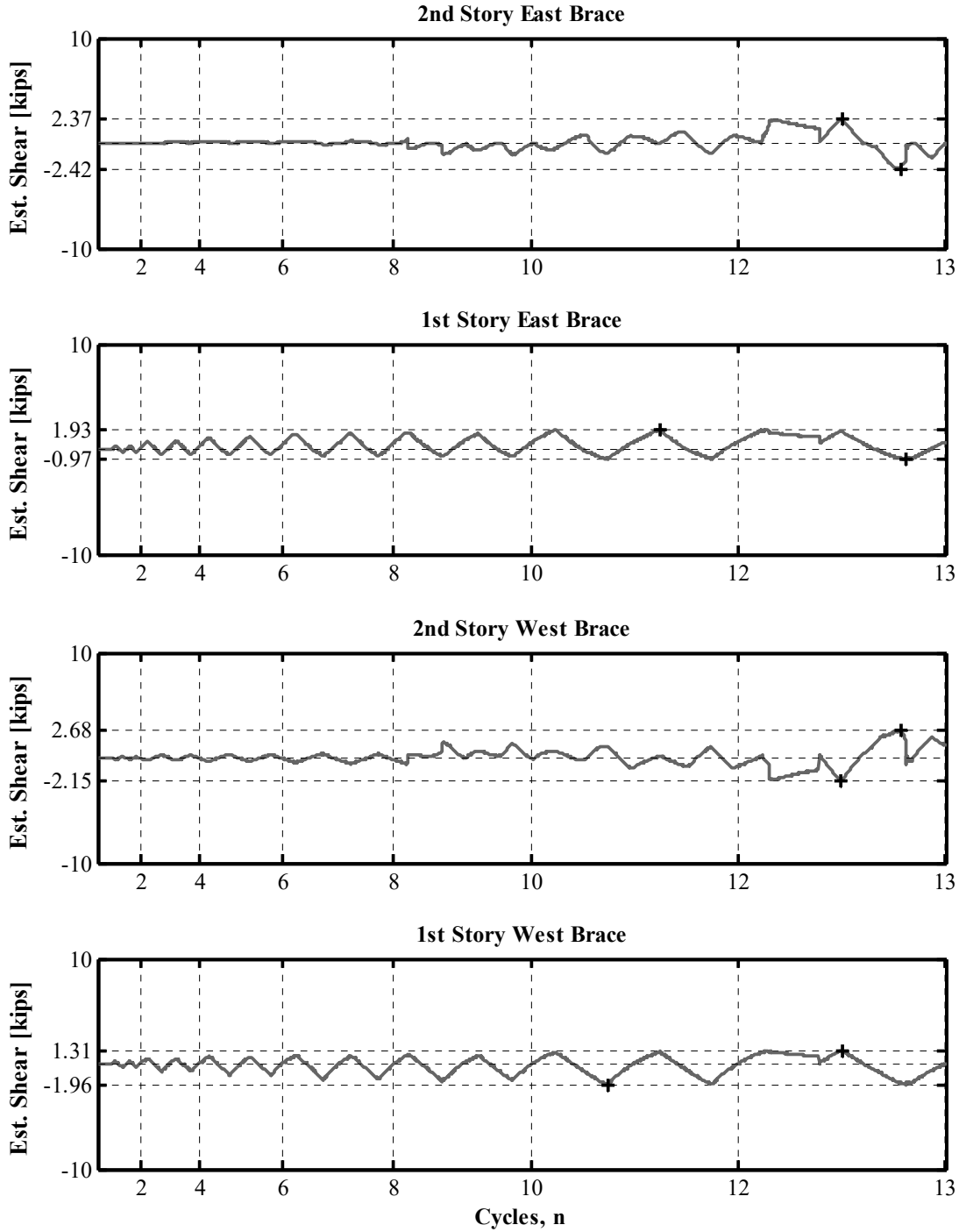


Figure A.14 NCBF-B-1 brace estimated shear time histories.

A.1.3 Beam Plots

The following section shows the plots for the brace response parameters. Plots include the response history for the beam estimated unbalanced load, mid-span displacement, estimated moment, axial deformation, moments, end rotations, and shears. Maximum and minimum values are called out on each plot.

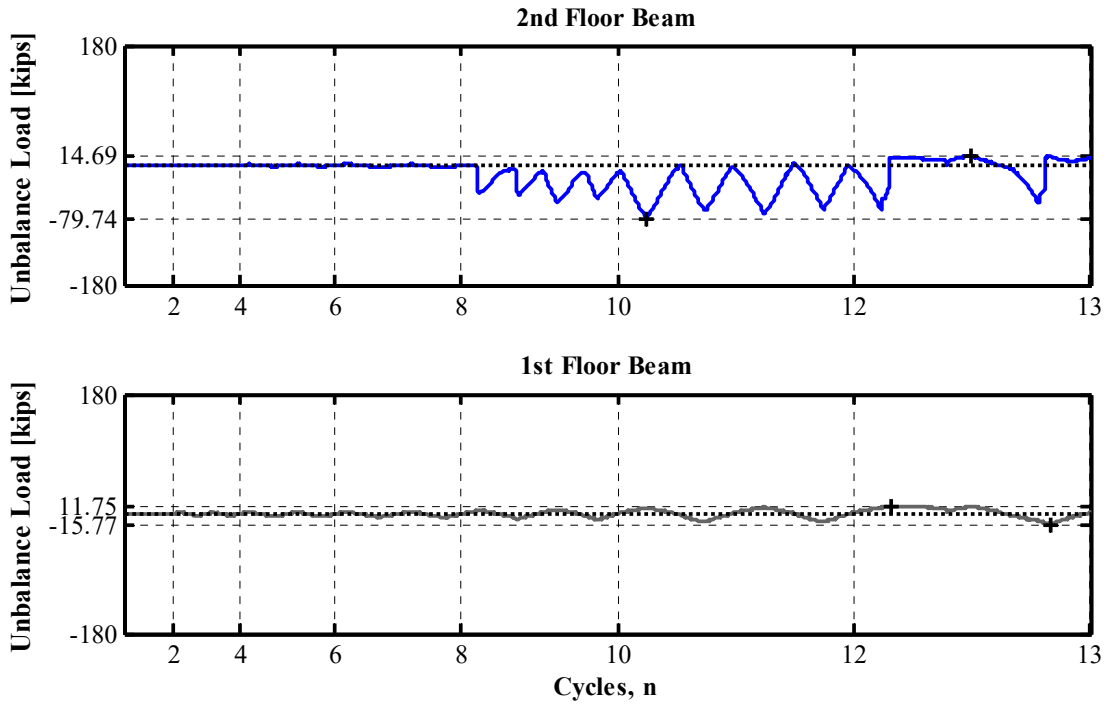


Figure A.15 NCBF-B-1 estimated unbalanced load time histories.

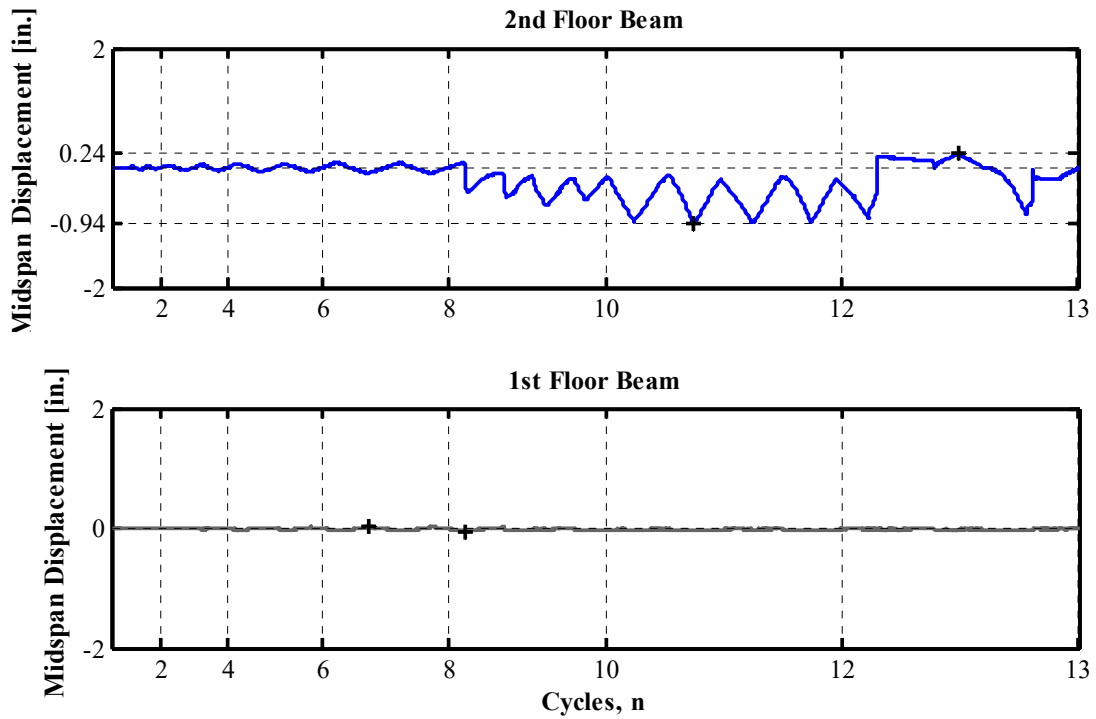


Figure A.16 NCBF-B-1 beam vertical mid-span displacement time histories.

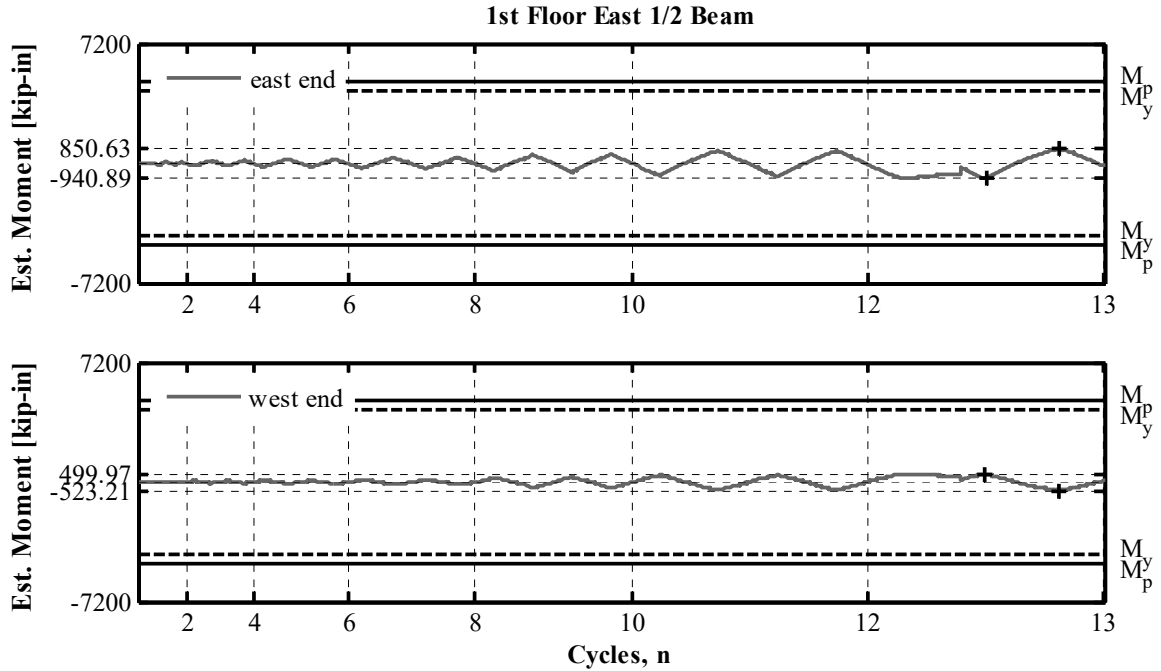


Figure A.17 NCBF-B-1 first-floor east 1/2-beam estimated moment history (measured at 3 ft-0 in. from ends).

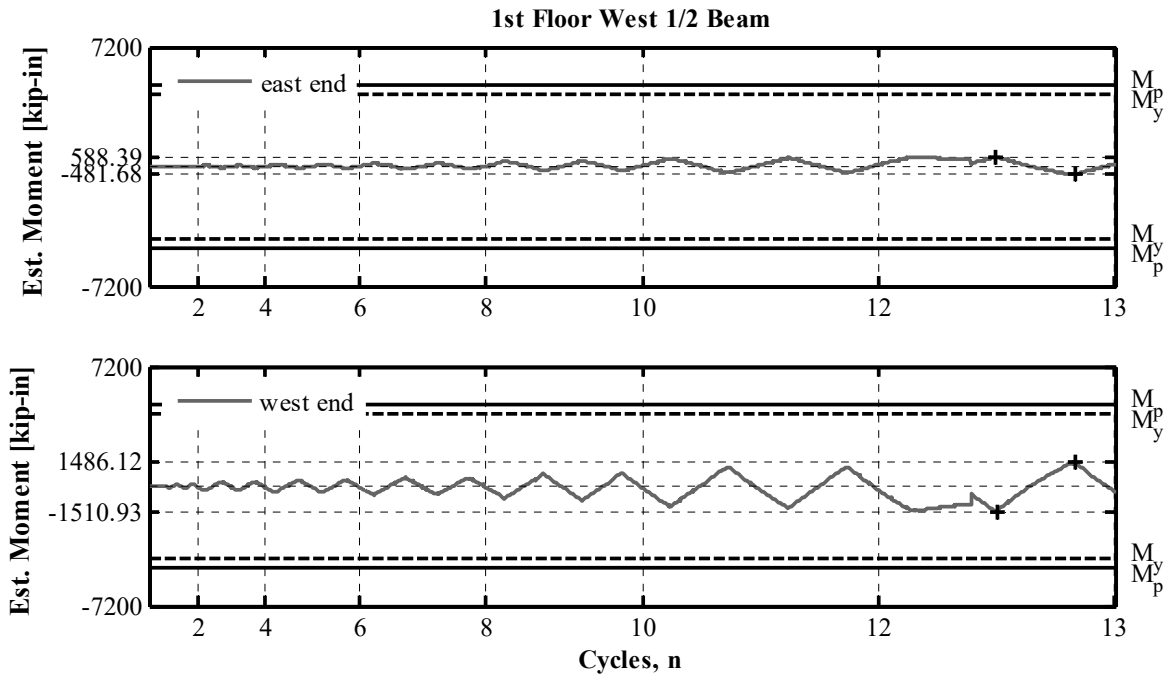


Figure A.18 NCBF-B-1 first-floor west 1/2-beam estimated moment history (measured at 3 ft-0 in. from ends).

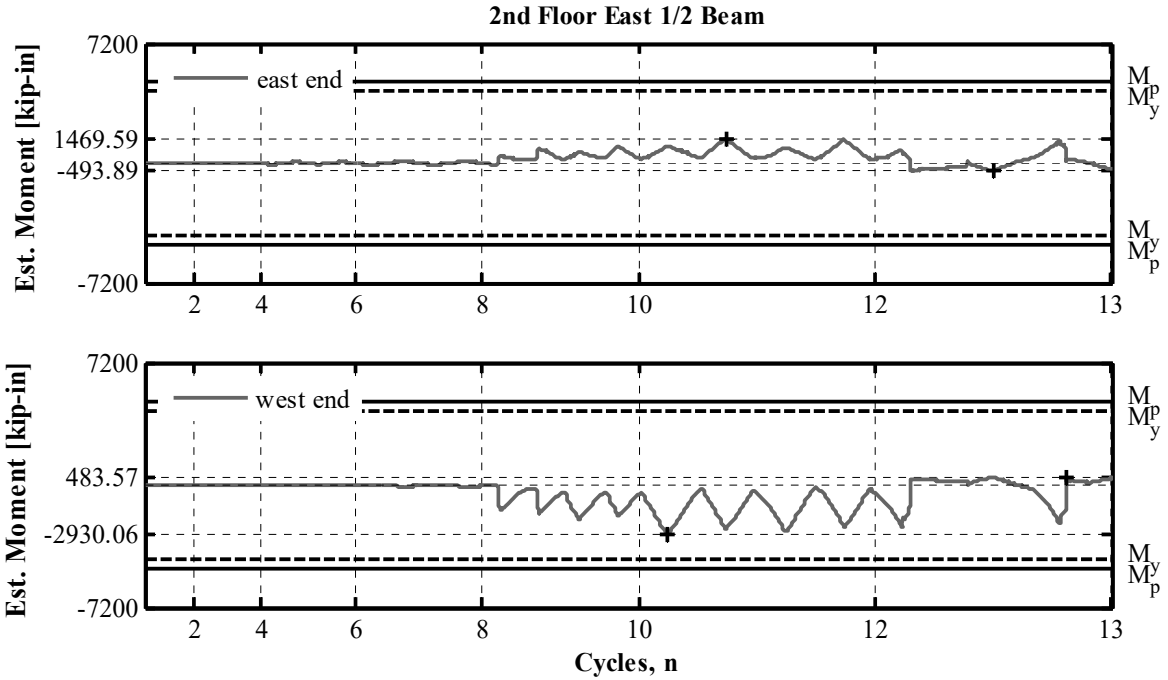


Figure A.19 NCBF-B-1 second-floor east 1/2-beam estimated moment history (measured at 3 ft-0 in. from ends).

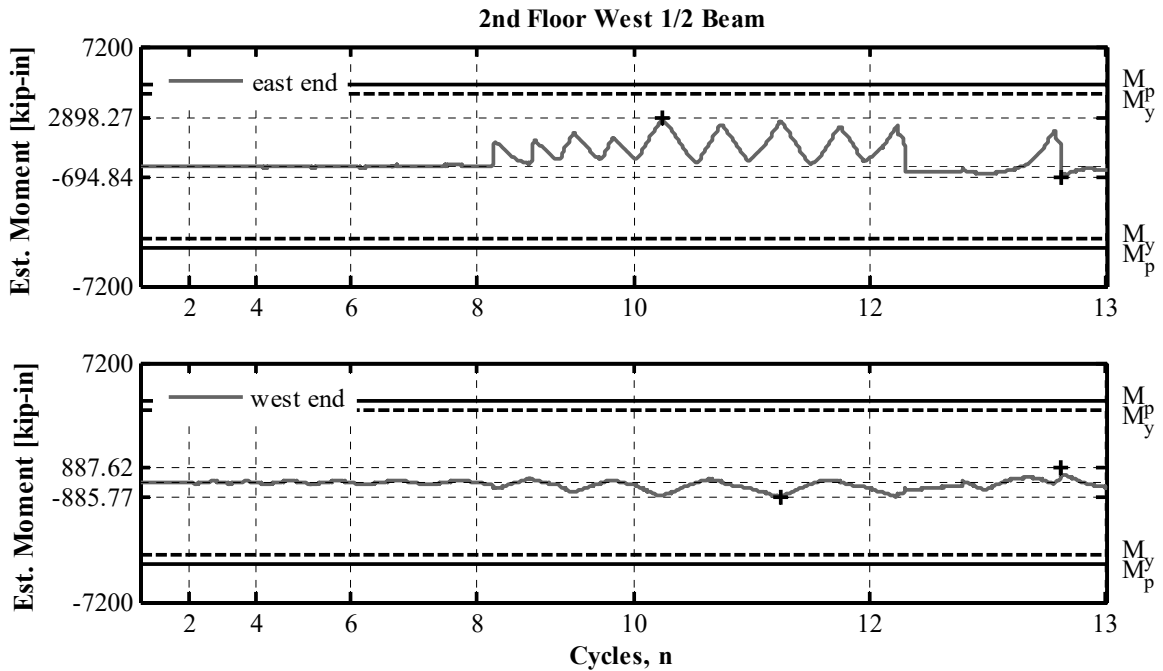


Figure A.20 NCBF-B-1 second-floor west 1/2-beam estimated moment history (measured at 3 ft-0 in. from frame centerline and 1 ft-6 in. from west end).

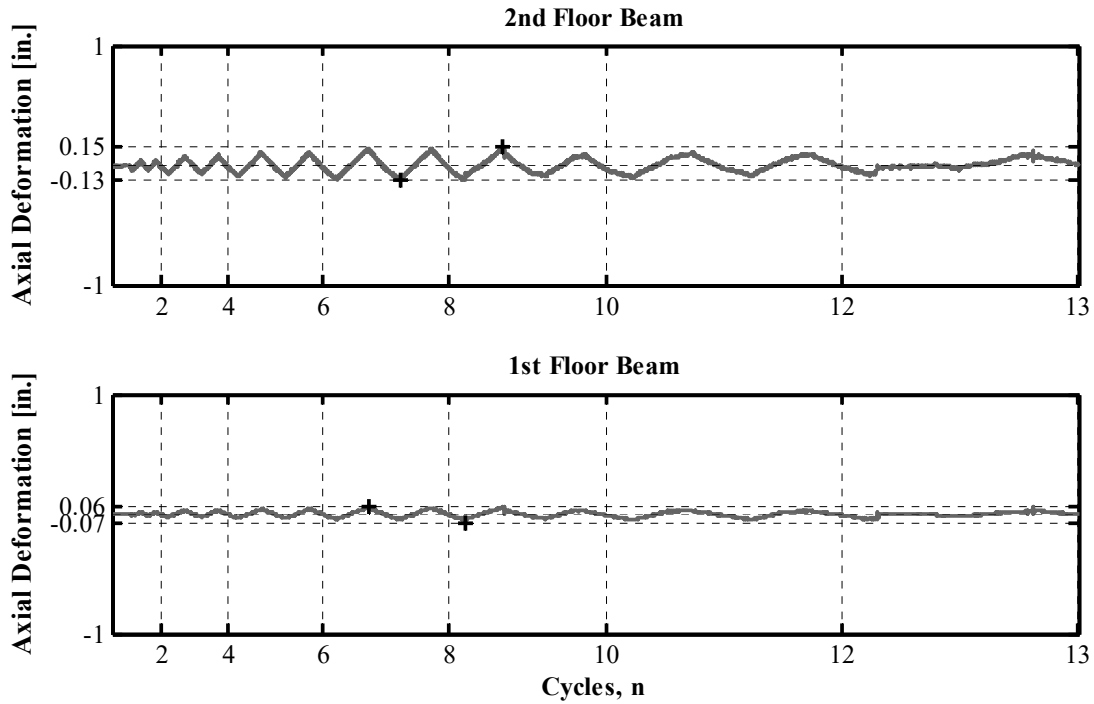


Figure A.21 NCBF-B-1 beam axial deformation time histories.

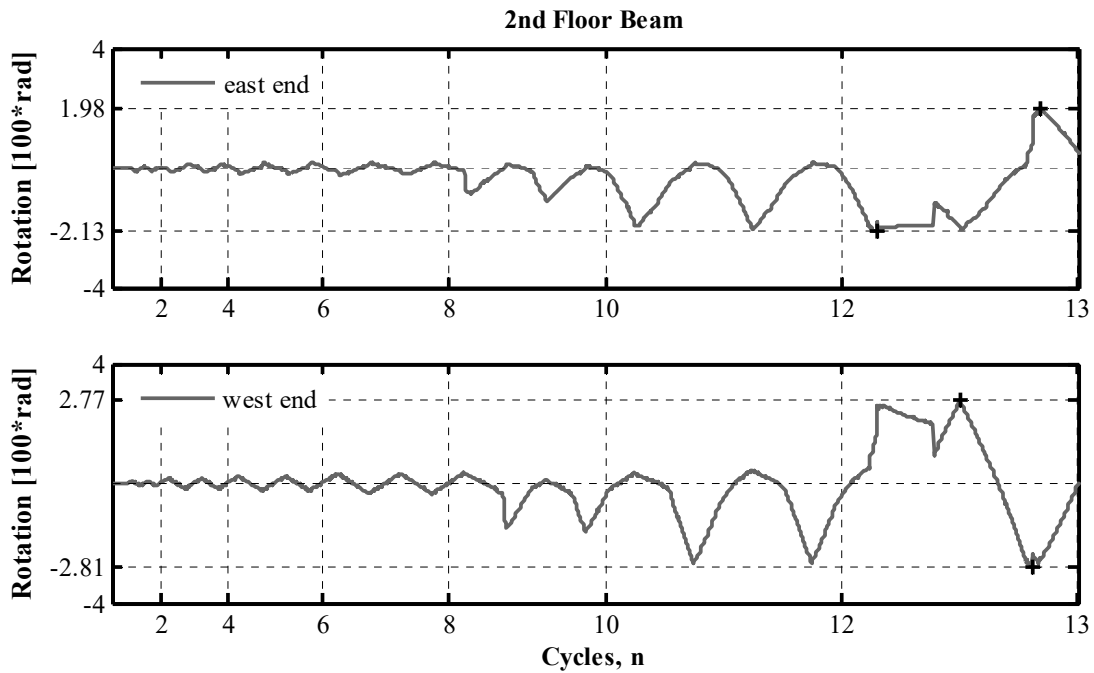


Figure A.22 NCBF-B-1 second-floor beam end rotation time histories.

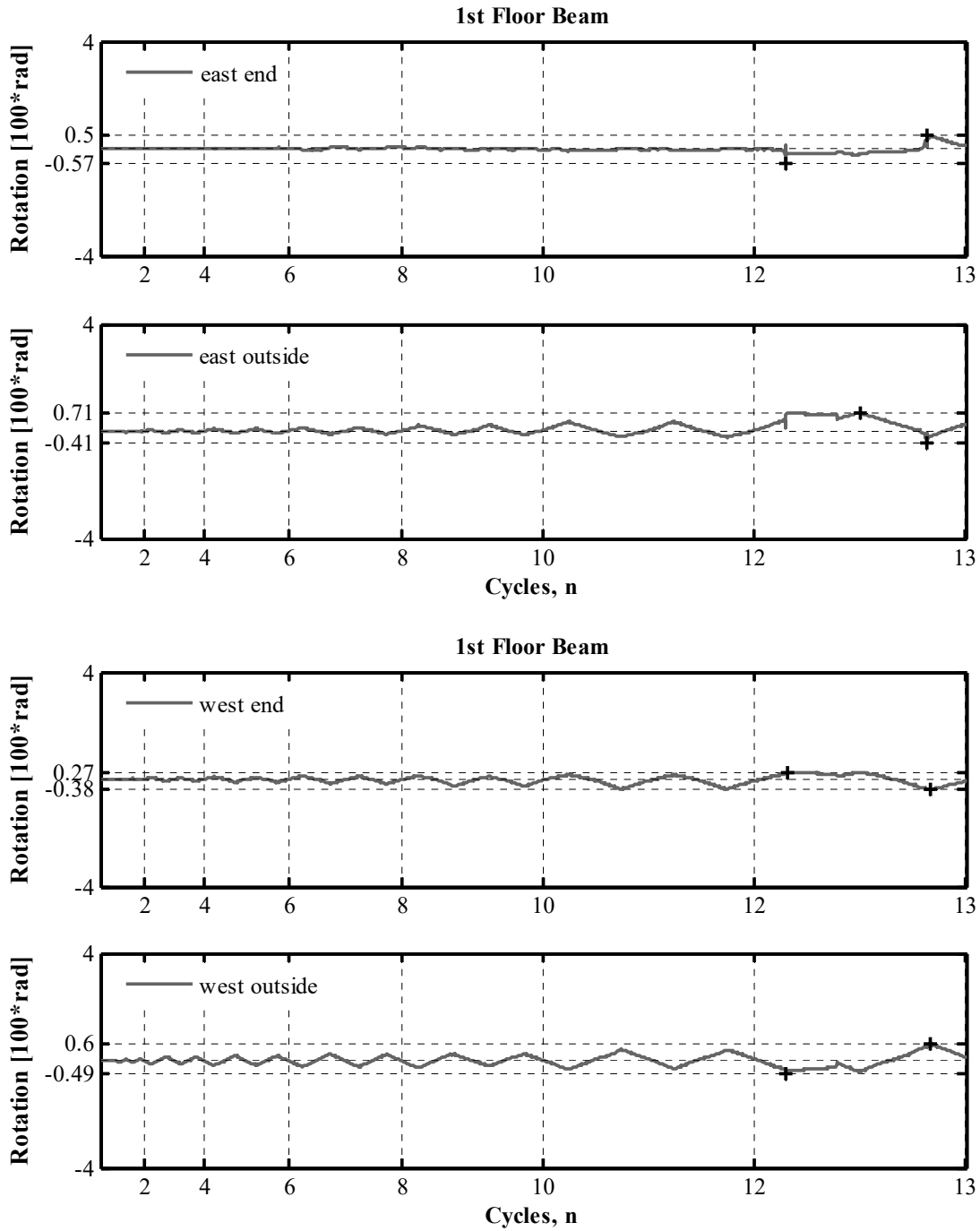


Figure A.23 NCBF-B-1 first-floor beam end rotation time histories.

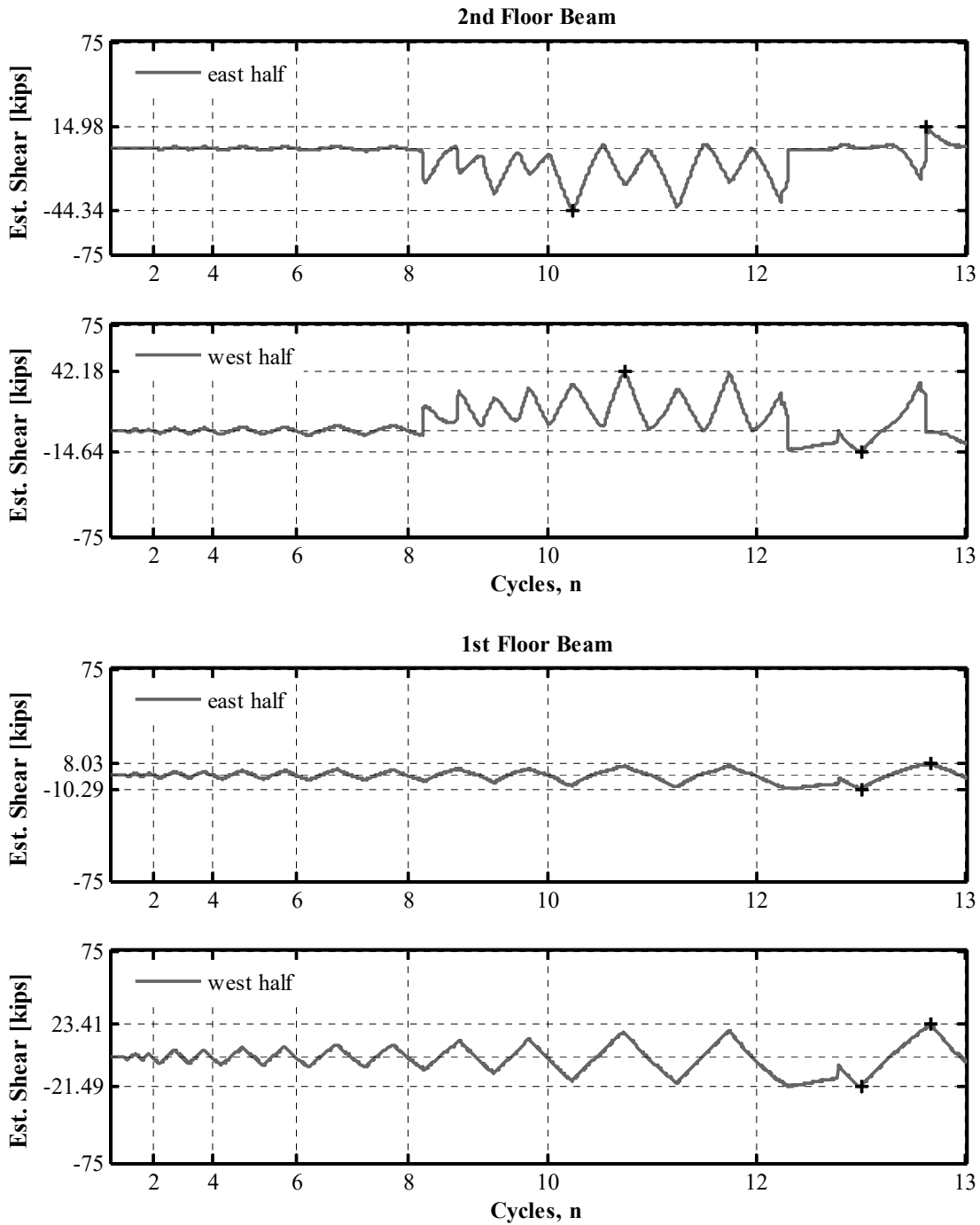


Figure A.24 NCBF-B-1 beam estimated shear time histories.

A.1.4 Column Plots

The following section shows the plots for the column response parameters. Plots include the response history for the column estimated axial force, estimated moments, and estimated shear. Maximum and minimum values are called out on each plot.

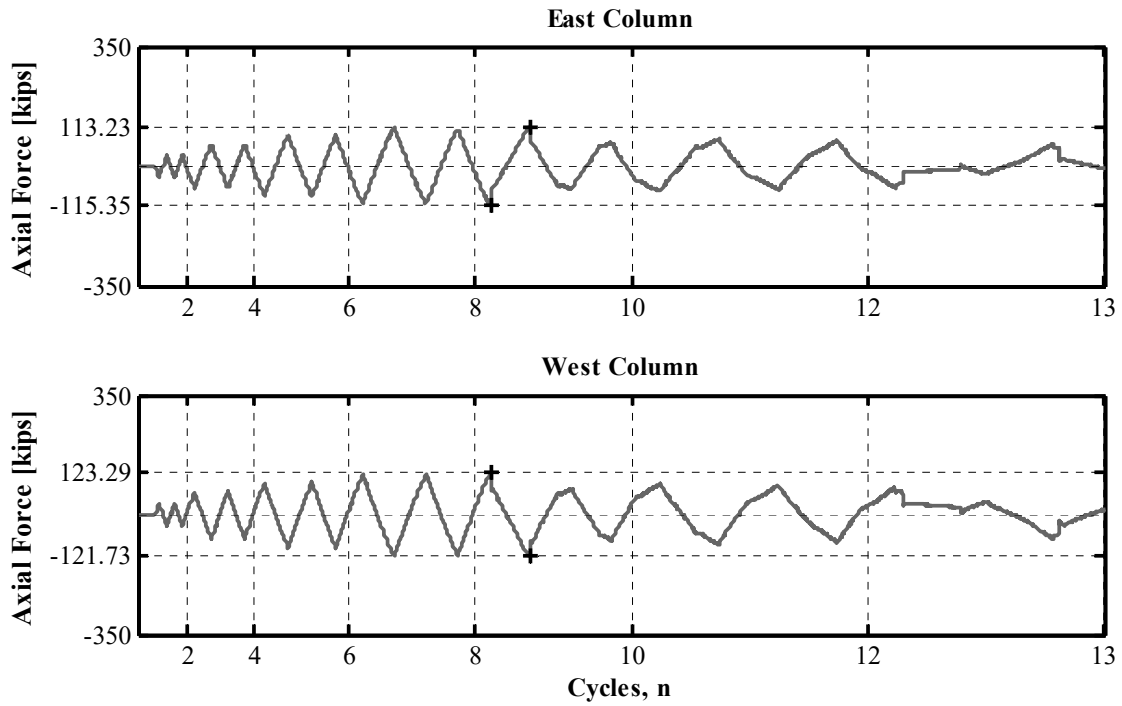


Figure A.25 NCBF-B-1 column estimated axial force time histories.

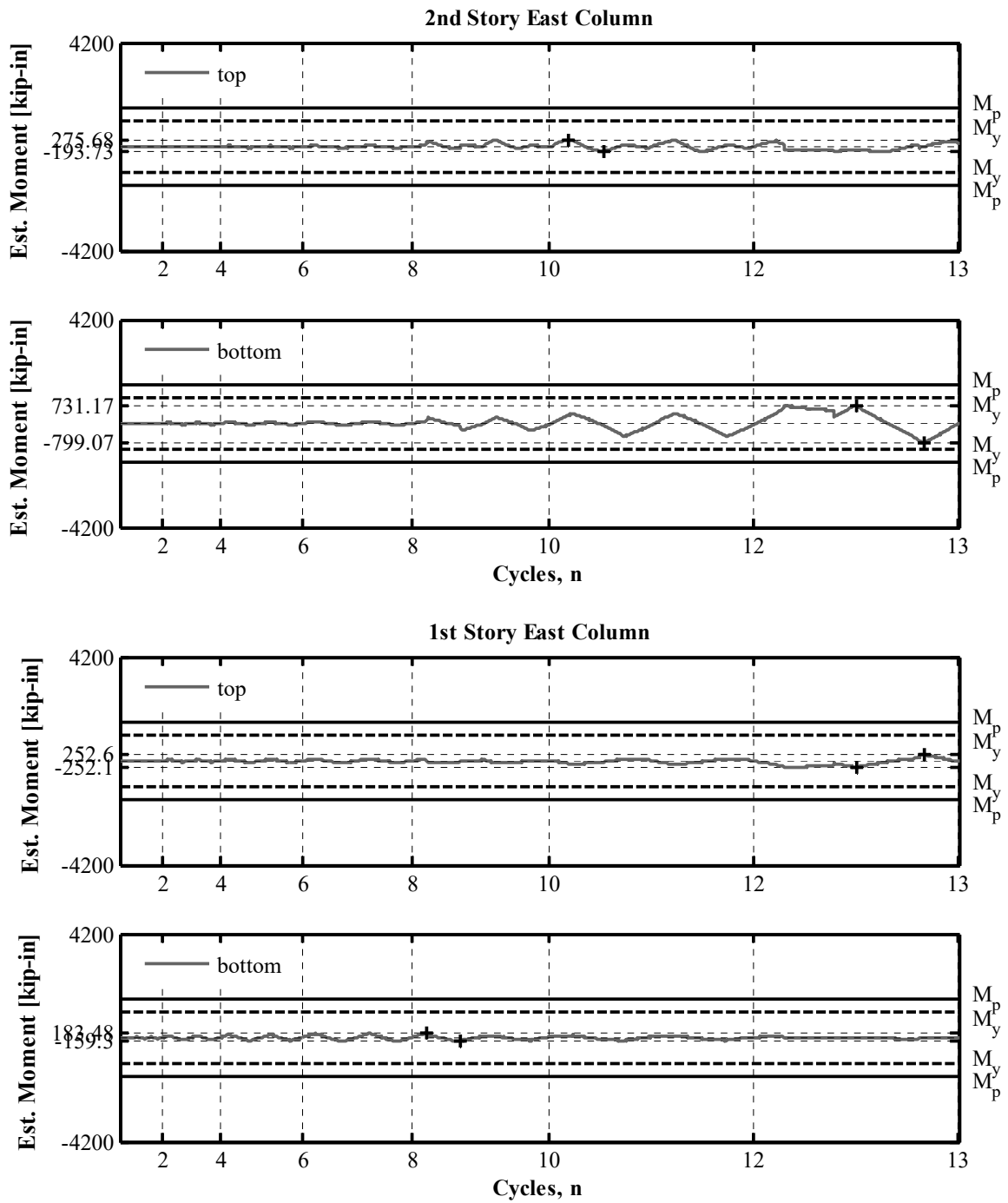


Figure A.26 NCBF-B-1 east column estimated moment history (measured at 3 ft-0 in. from the column ends).

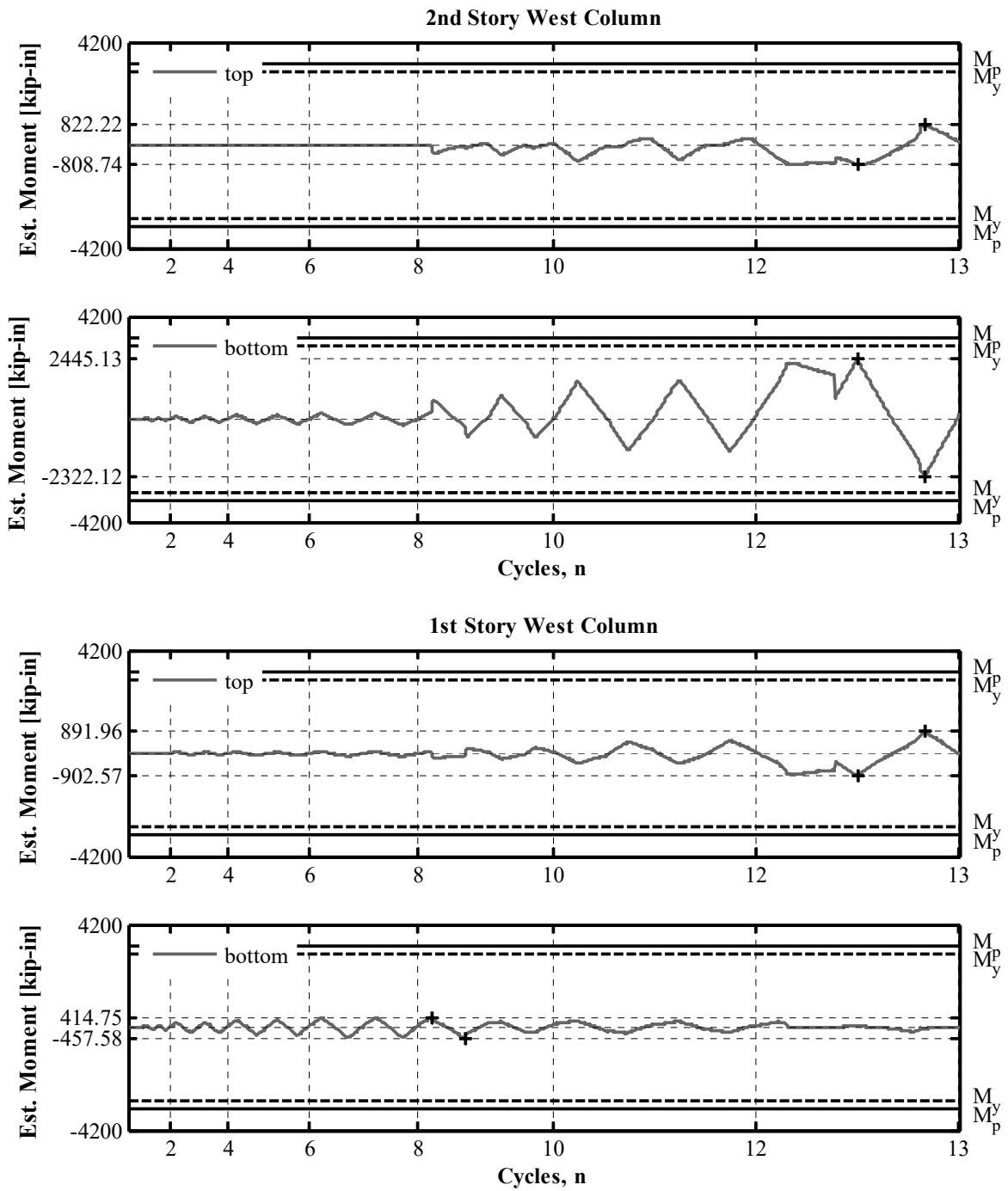


Figure A.27 NCBF-B-1 west column estimated moment history (measured at 3 ft-0 in. from the column ends).

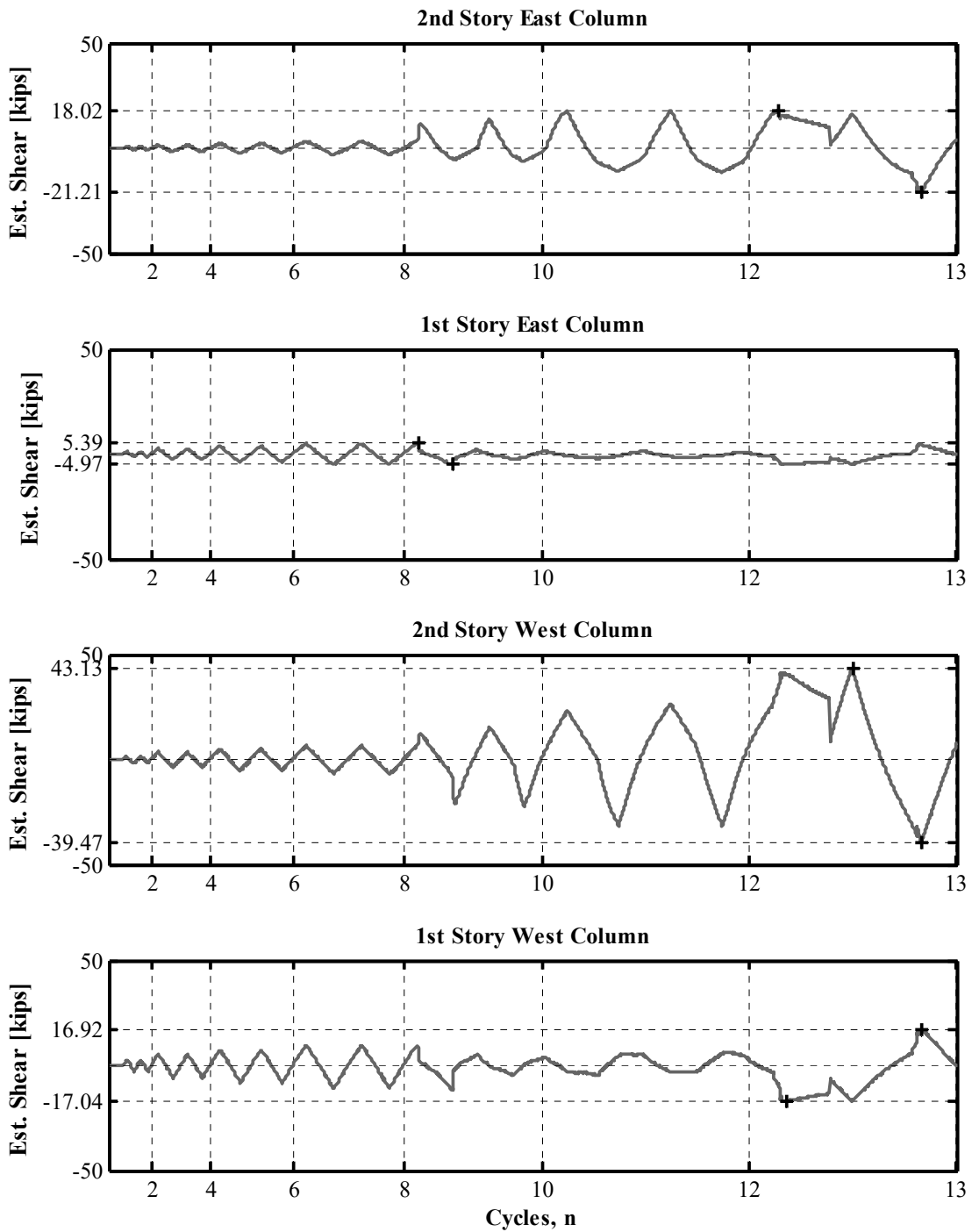


Figure A.28 NCBF-B-1 column estimated shear time histories.

Appendix B Plots of the NCBF-B-2 Test

B.1 RESPONSE HISTORY PLOTS

The following plots show the maximum and minimum values of selected variables derived from the instrumentation. Time is broken into cycles to reflect the slow, static nature of the quasi-static test. Global plots of the story shears and drifts are shown in Section B.1.1. The derived axial force, shears, moments, and rotations at specified sections of the members are shown for the braces, beams, and columns in Sections A.1.2, A.1.3, and A.1.4, respectively. Labels used in the plots are defined by the values in Table B.1.

Table B.1 NCBF-B-2: values used for labels in plots.

Design axial capacity		Location	F_y (ksi) ¹	T_n (kips) ²	C_n (kips) ³
HSS7×7×1/4 (CFT)		First-story braces	51.7	319	323
HSS6×6×3/16 (CFT)		Second-story braces	46.8	186	197
Design moment		Location	F_y (ksi) ¹	M_y (kip-in.) ⁴	M_p (kip-in.) ⁵
W10×54	Strong axis	West column	60.3	3618	4016
	Weak axis	East column		1242	1887
W14×53		Beam	56.3	4380	4904

¹ From steel coupon tests

² Design tensile capacity from AISC 360 [2010]

³ Design compression buckling capacity from AISC 360 [2010] for concrete-filled tubes (CFT) using the length of the brace from the shop drawings with an effective length factor of $k = 1$

⁴ Yielding moment: $M_y = F_y S$, where S is the elastic section modulus

⁵ Plastic moment: $M_p = F_y Z$, where Z is the plastic section modulus

B.1.1 Global Plots

The following section shows the plots for the global response parameters of each story, including story shears and displacements. Maximum and minimum values are called out on each plot.

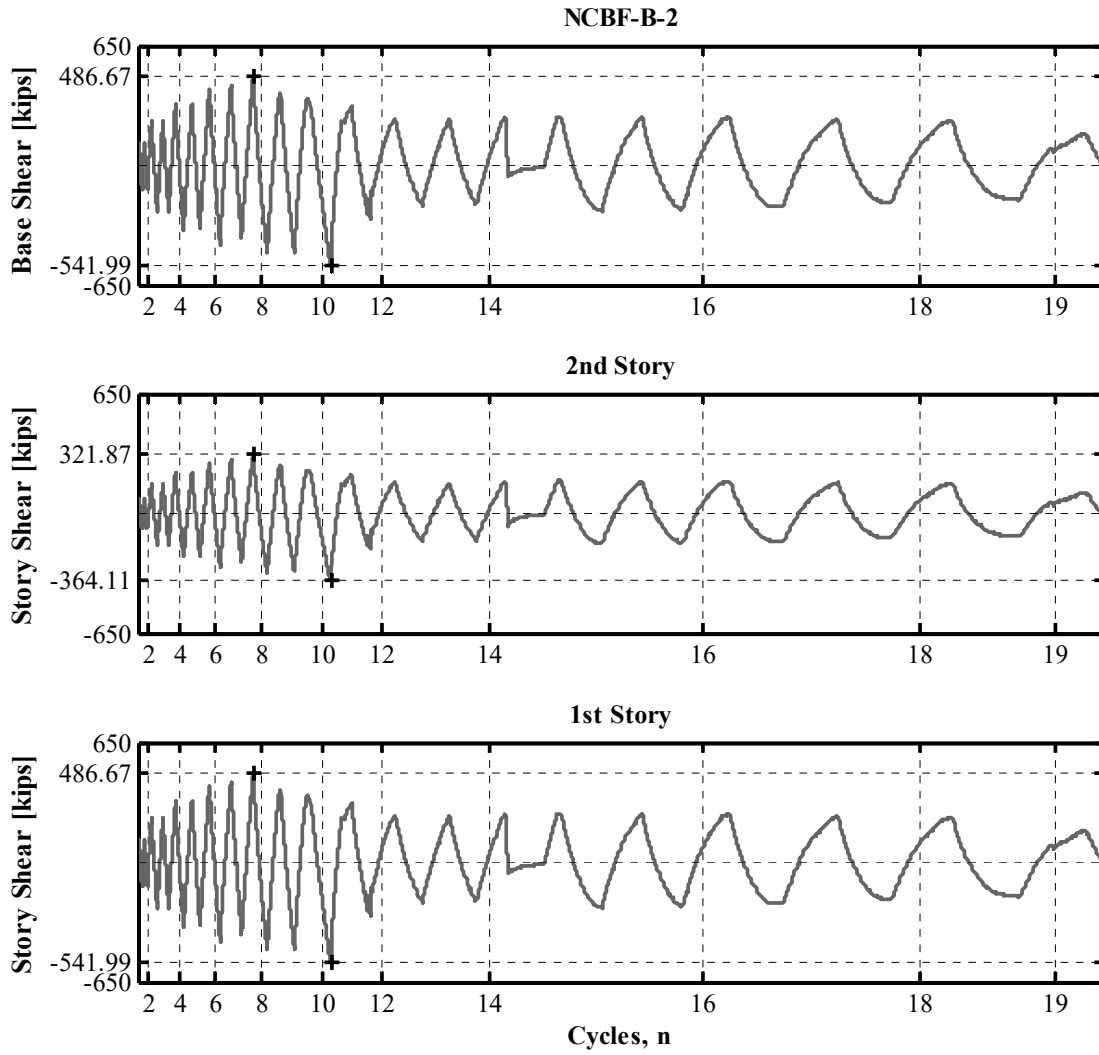


Figure B.1 NCBF-B-2 story shear time histories.

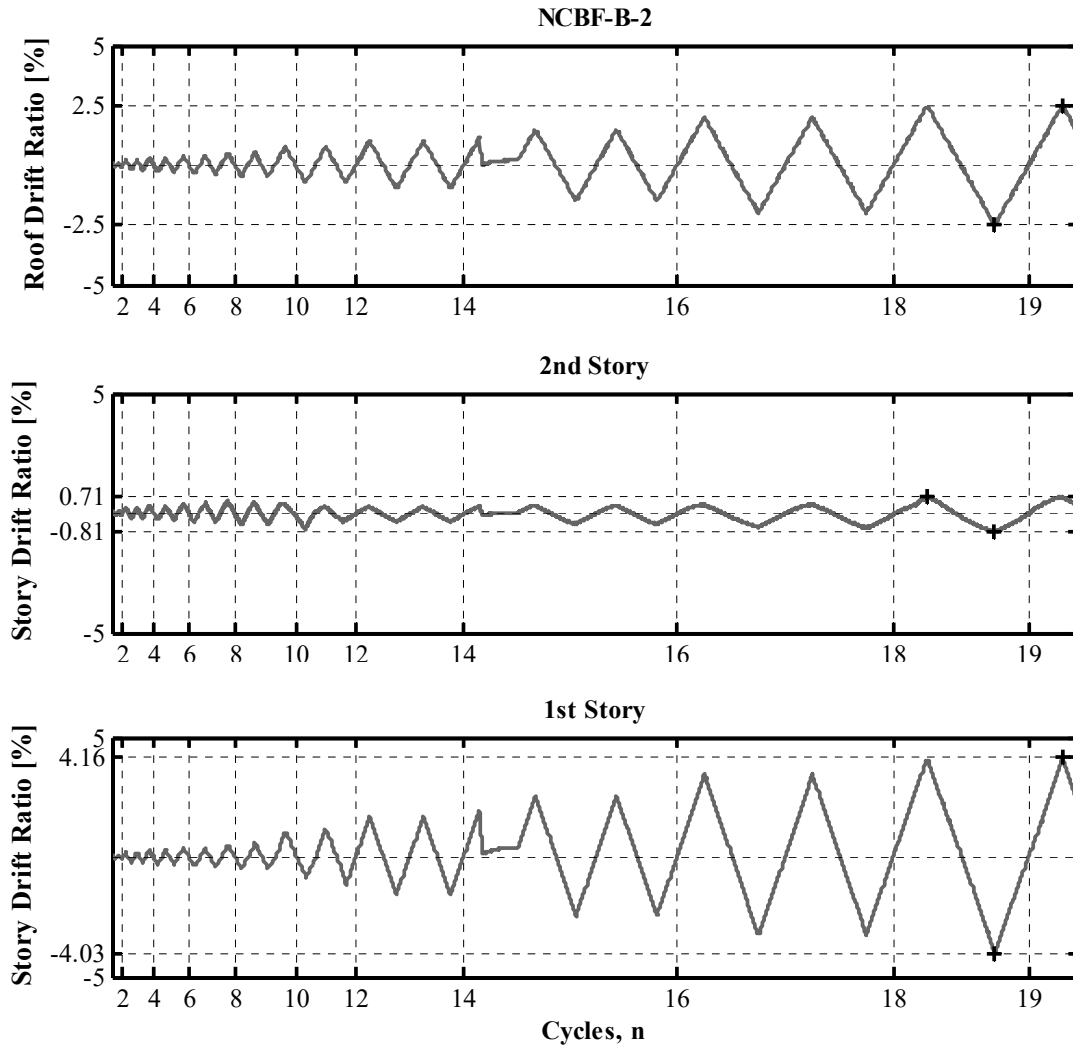


Figure B.2 NCBF-B-2 story drift ratio time histories.

B.1.2 Brace Plots

The following section shows the plots for the brace response parameters. Plots include the response history for the brace estimated axial force, out-of-plane displacement, axial deformation, estimated moments, end rotations, and estimated shears. Maximum and minimum values are called out on each plot.

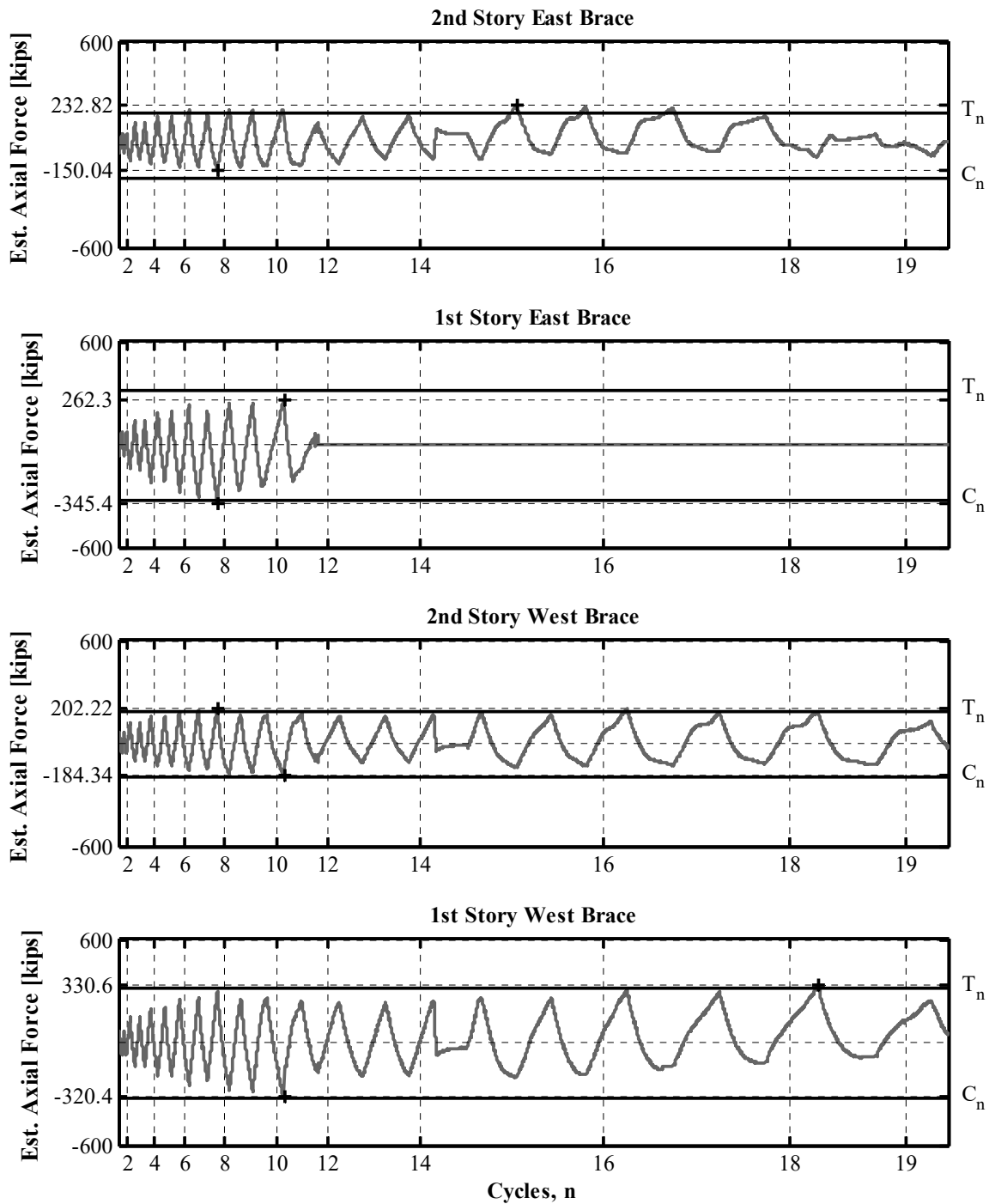


Figure B.3 NCBF-B-2 estimated brace axial force time histories.

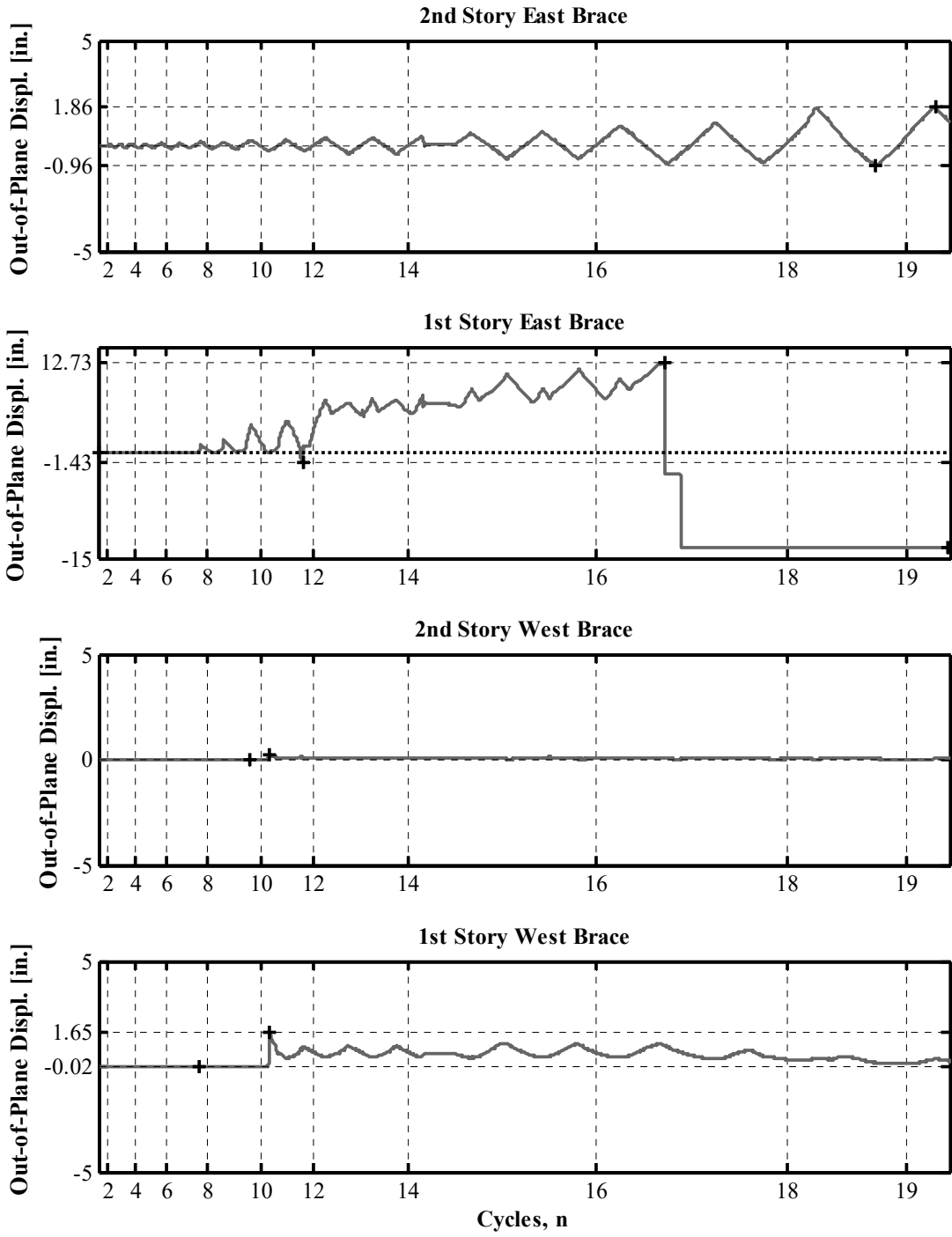


Figure B.4 NCBF-B-2 brace out-of-plane displacement time histories.

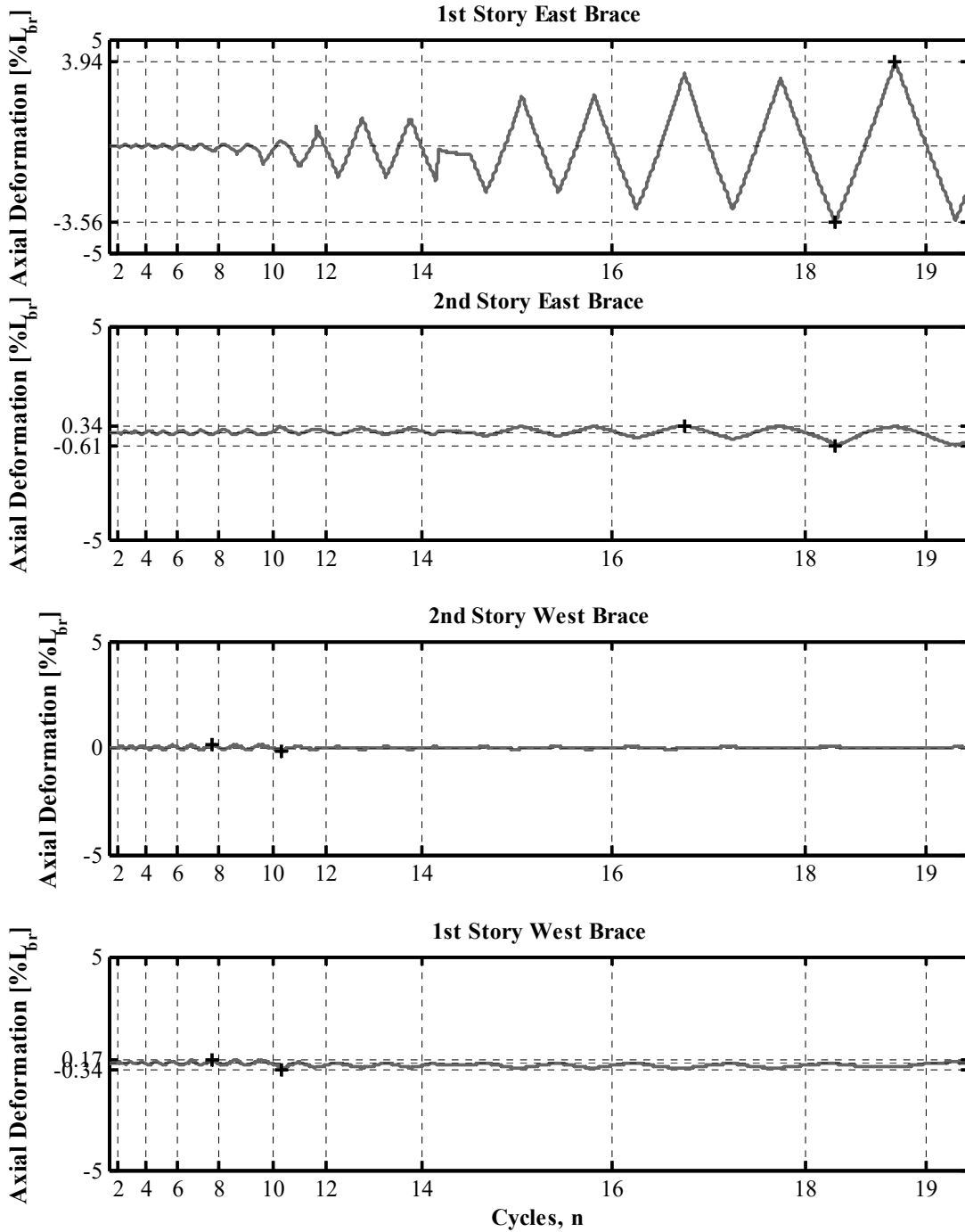


Figure B.5 NCBF-B-2 brace axial deformation time histories. (L_b is the work-point-to-work-point length).

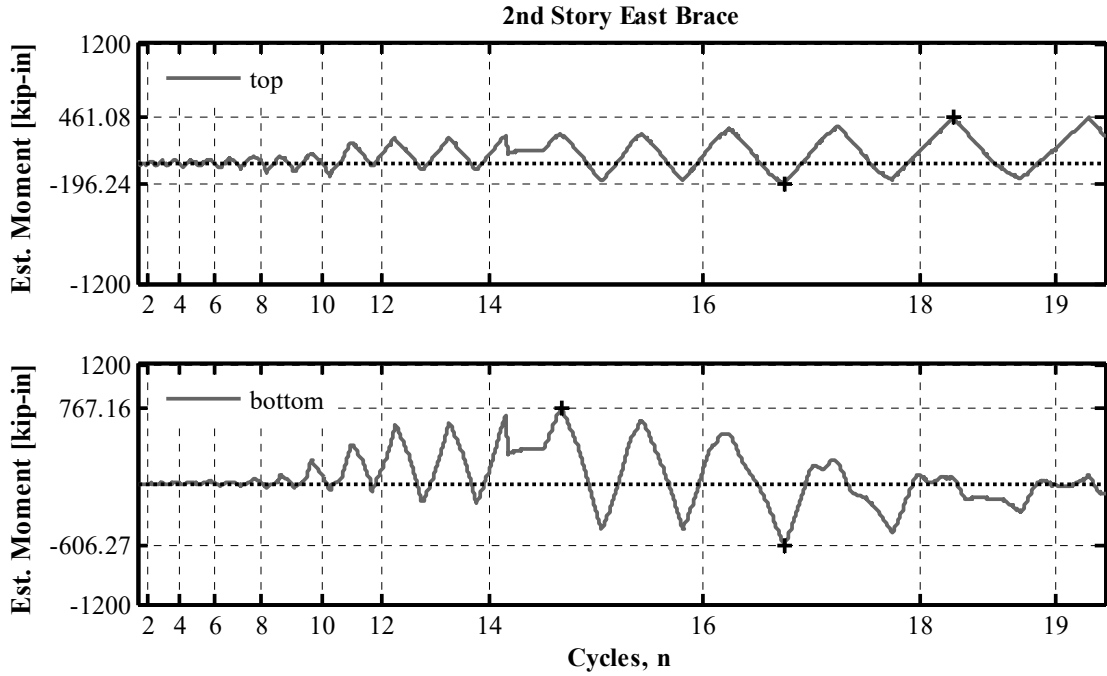


Figure B.6 NCBF-B-2 second-story east brace estimated moment time histories (measured at top and bottom ¼-points of brace length).

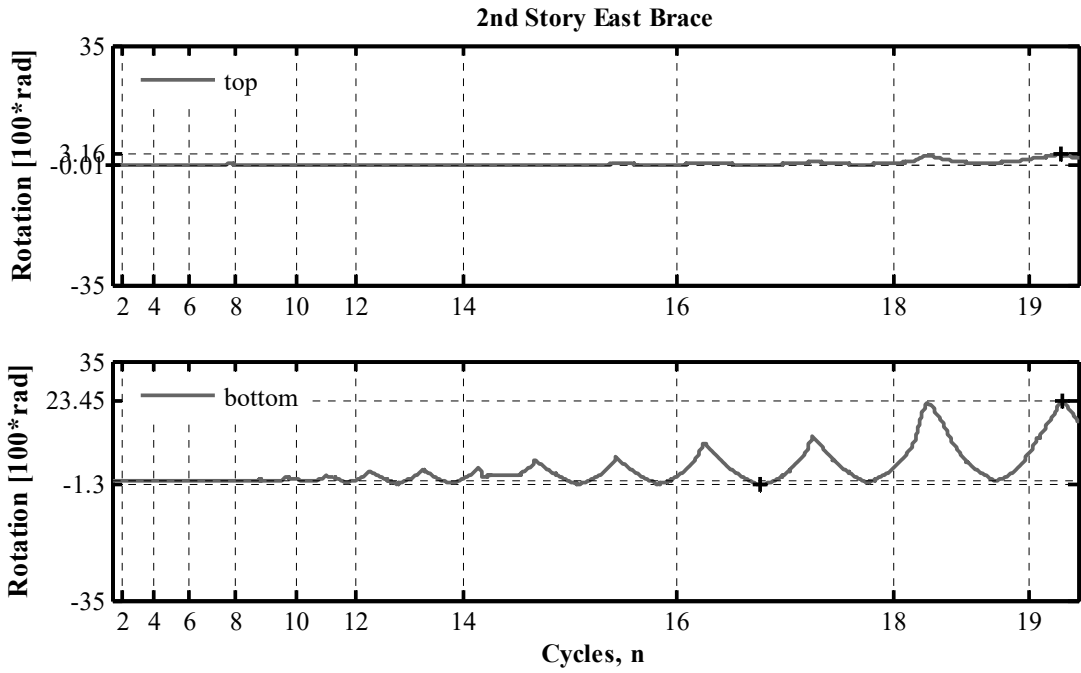


Figure B.7 NCBF-B-2 second-story east brace out-of-plane end rotation time histories.

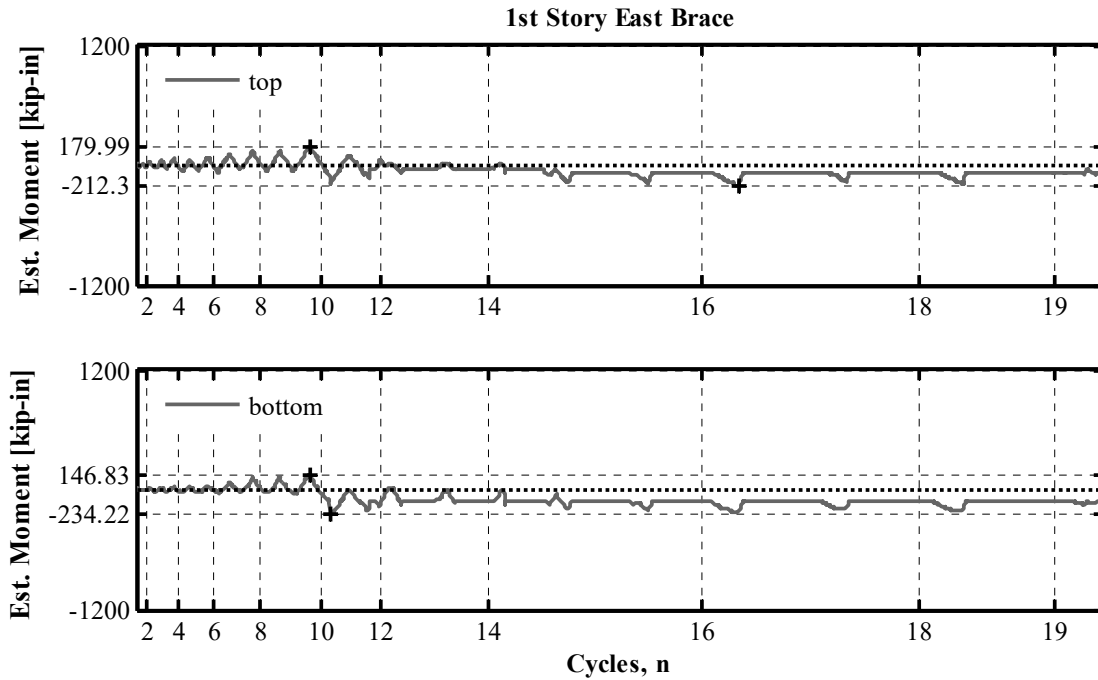


Figure B.8 NCBF-B-2 first-story east brace estimated moment time histories (measured at top and bottom ¼-points of brace length).

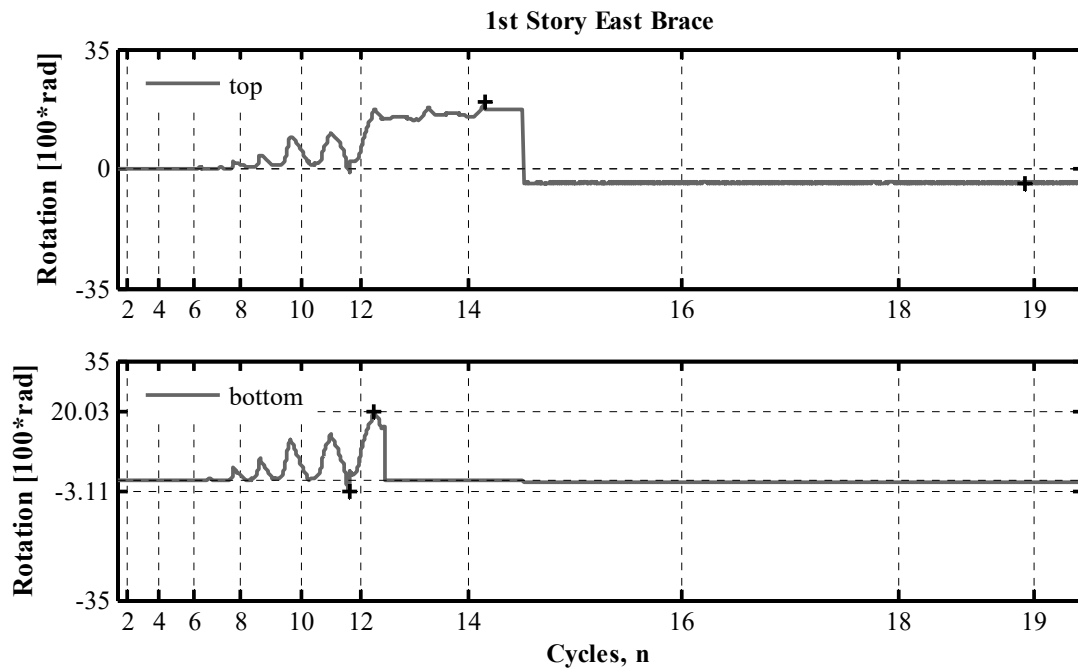


Figure B.9 NCBF-B-2 first-story east brace out-of-plane end rotation time histories.

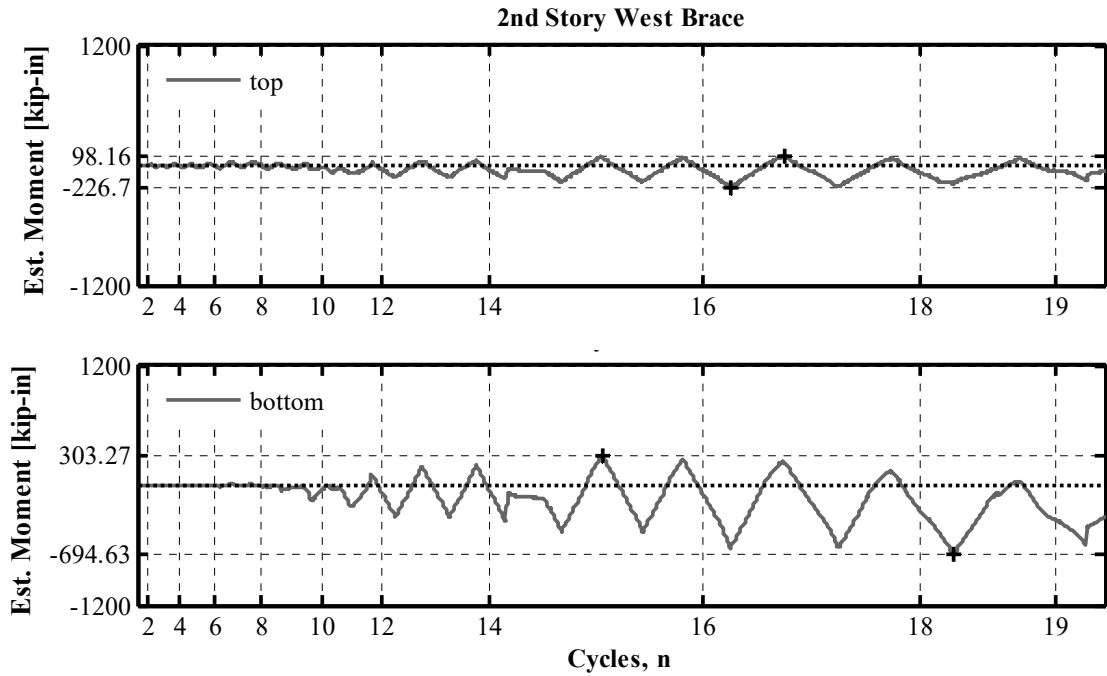


Figure B.10 NCBF-B-2 second-story west brace estimated moment time histories (measured at top and bottom ¼-points of brace length).

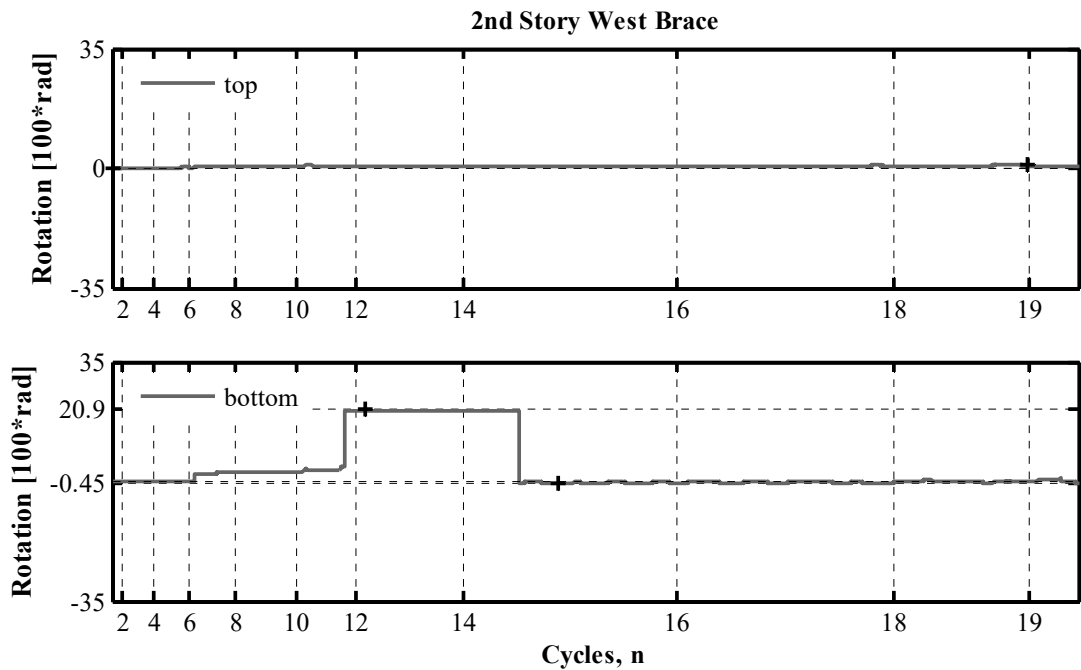


Figure B.11 NCBF-B-2 second-story west brace out-of-plane end rotation time histories.

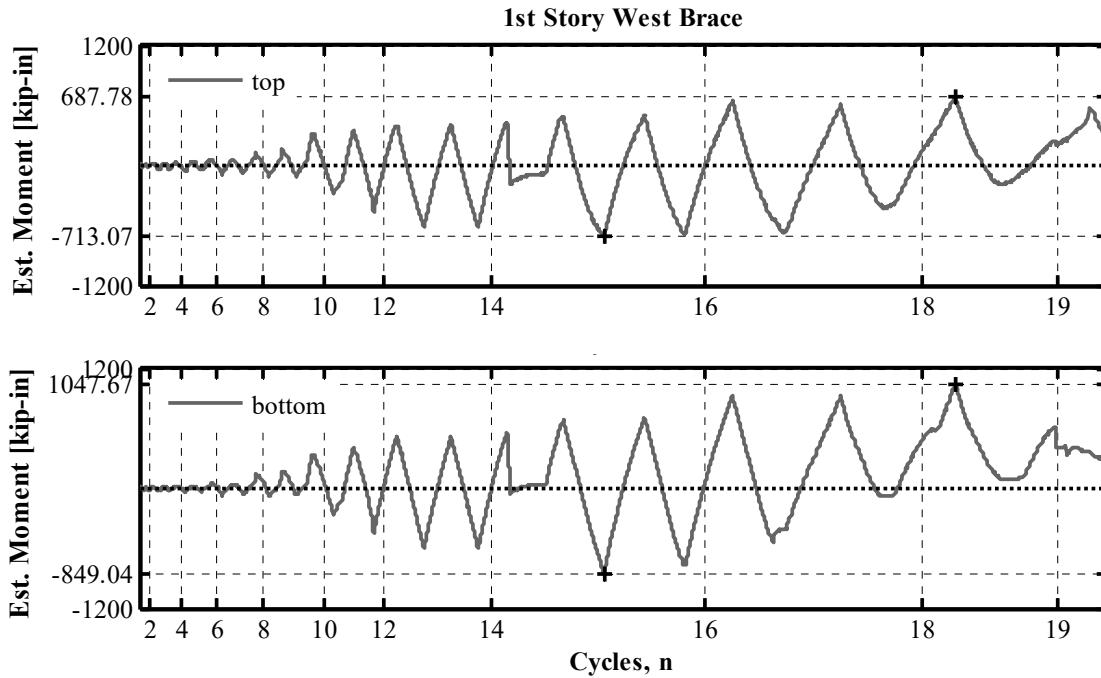


Figure B.12 NCBF-B-2 first-story west brace estimated moment time histories (measured at top and bottom ¼-points of brace length).

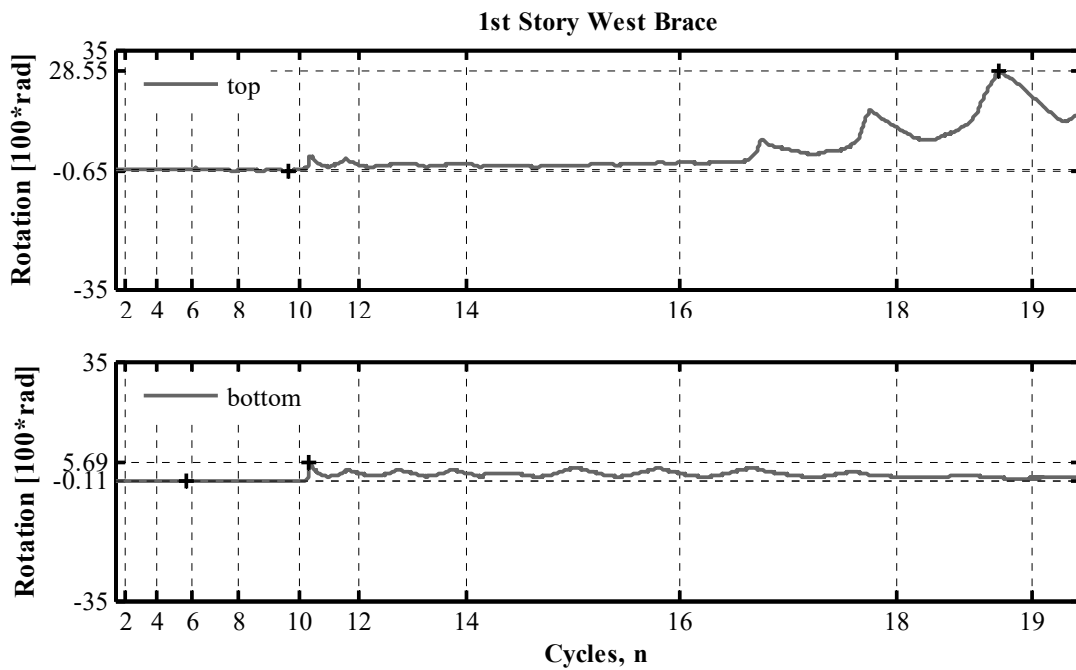


Figure B.13 NCBF-B-2 first-story west brace end rotation time histories.

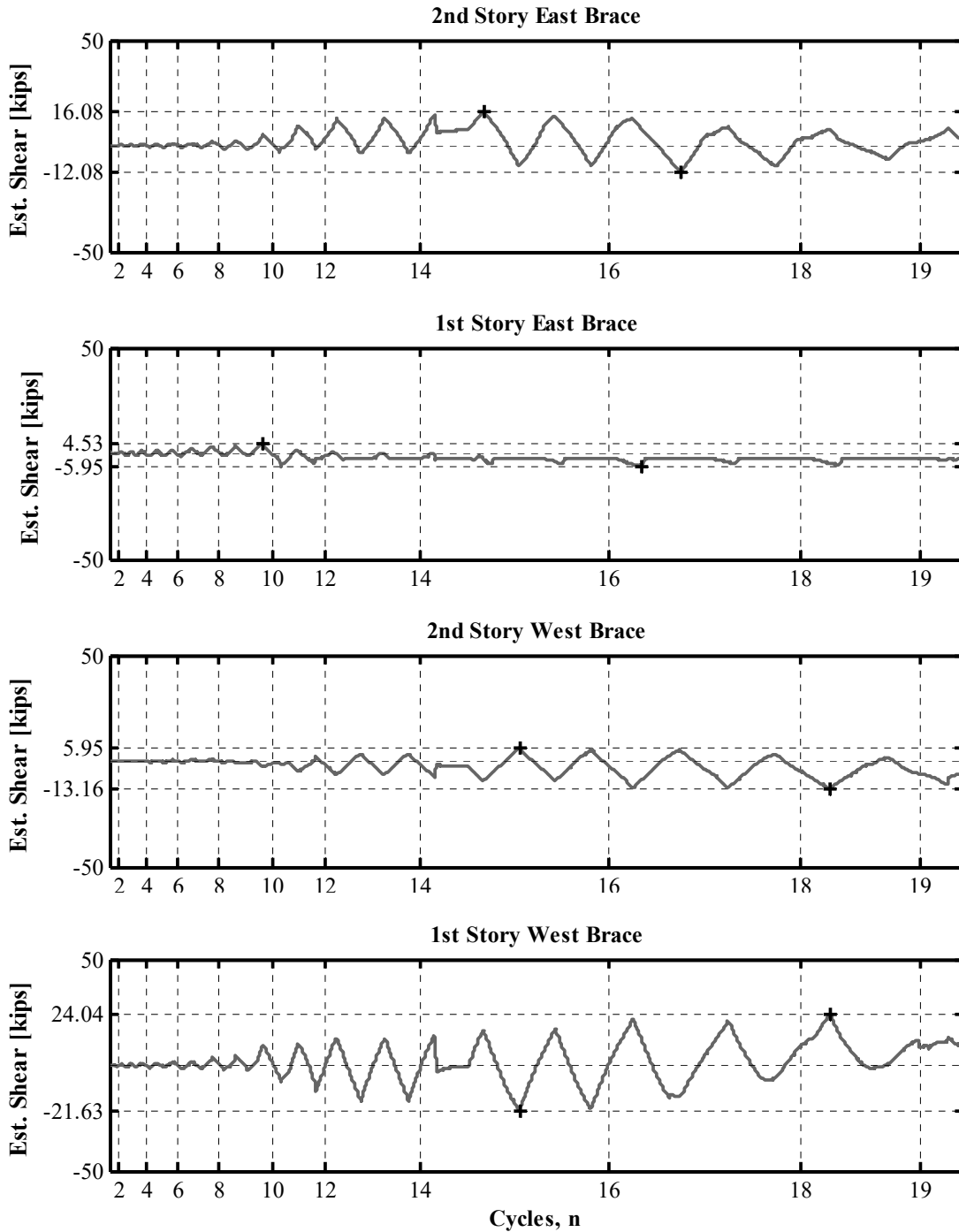


Figure B.14 NCBF-B-2 brace estimated shear time histories.

B.1.3 Beam Plots

The following section shows the plots for the brace response parameters. Plots include the response history for the beam estimated unbalanced load, mid-span displacement, estimated moment, axial deformation, moments, end rotations, and shears. Maximum and minimum values are called out on each plot.

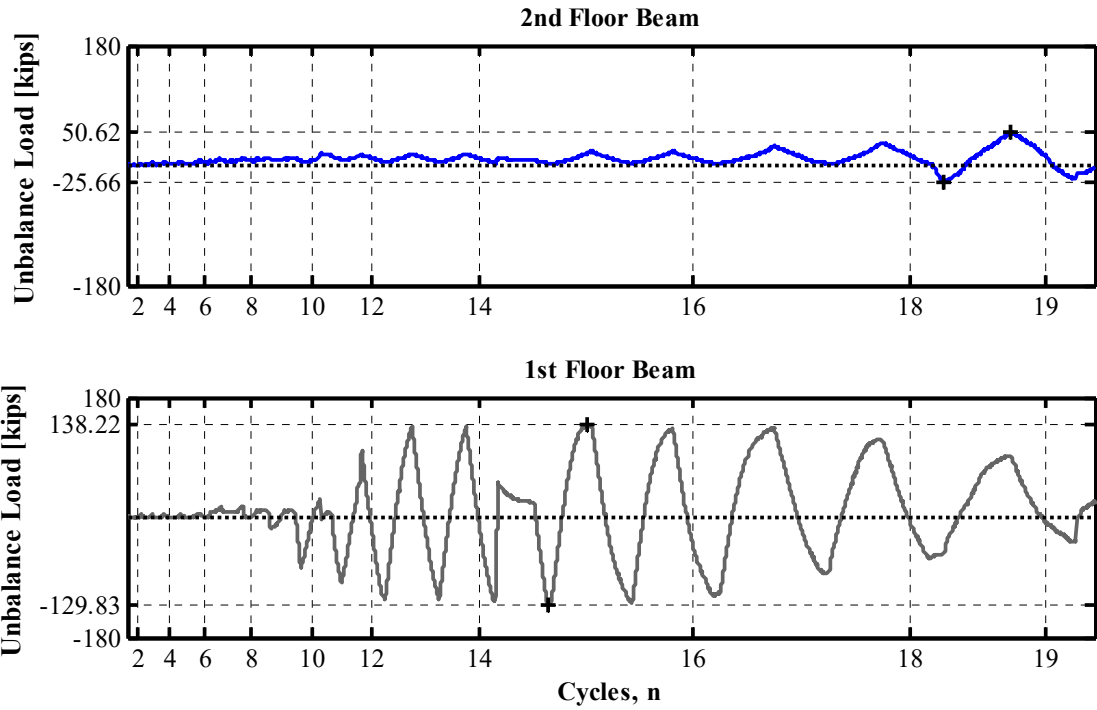


Figure B.15 NCBF-B-2 first-floor beam estimated unbalanced load history.

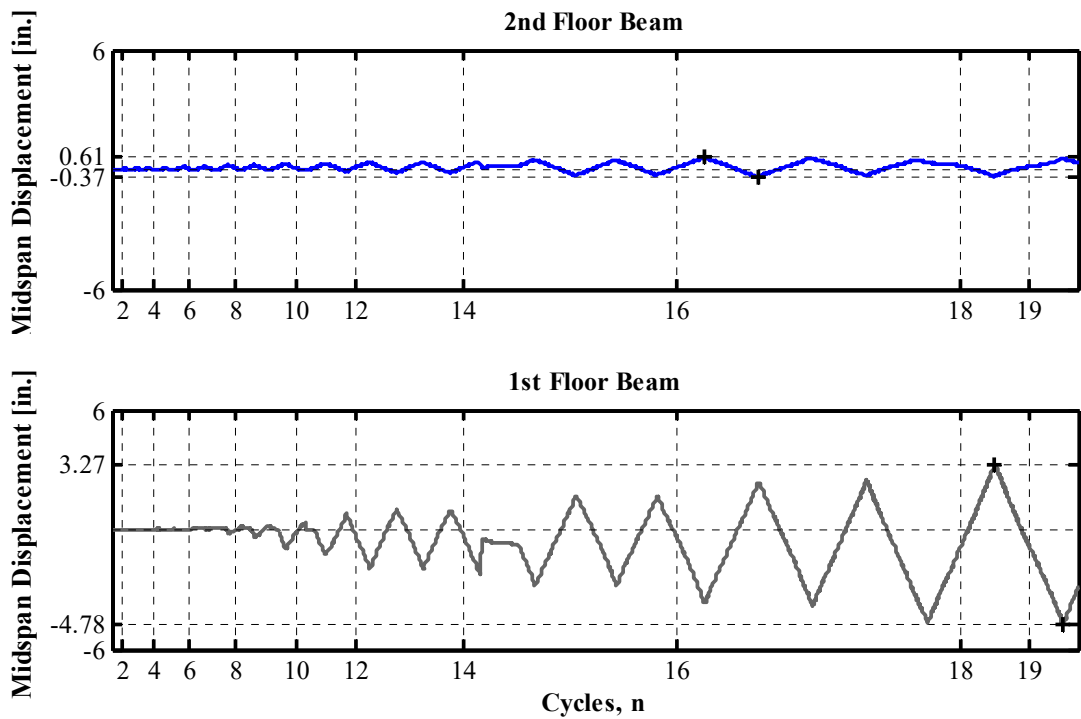


Figure B.16 NCBF-B-2 Beam vertical mid-span displacement time histories

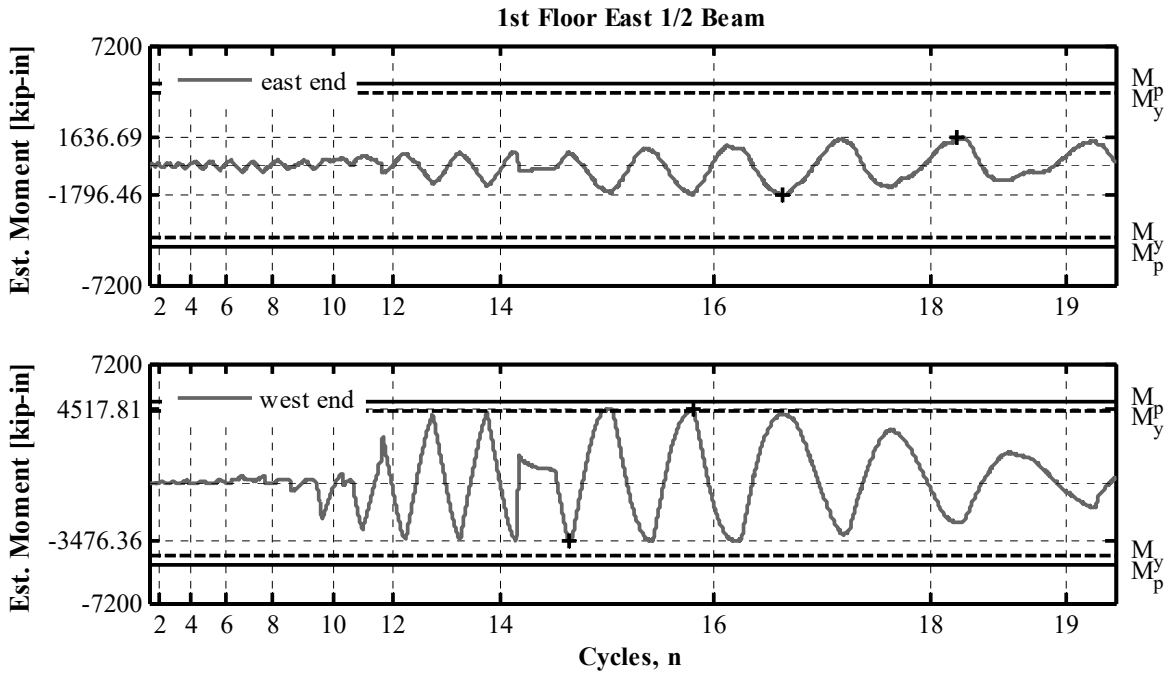


Figure B.17 NCBF-B-2 first-floor east 1/2-beam estimated moment history (measured at 3 ft-0 in. from ends).

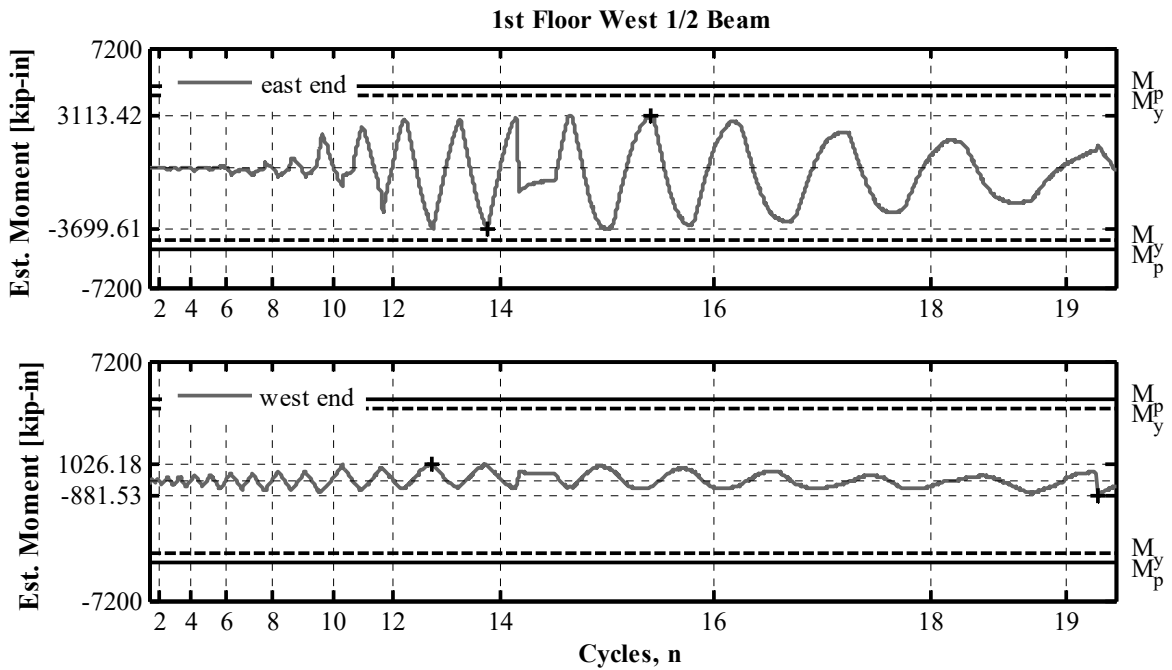


Figure B.18 NCBF-B-2 first-floor west 1/2-beam estimated moment history (measured at 3 ft-0 in. from ends).

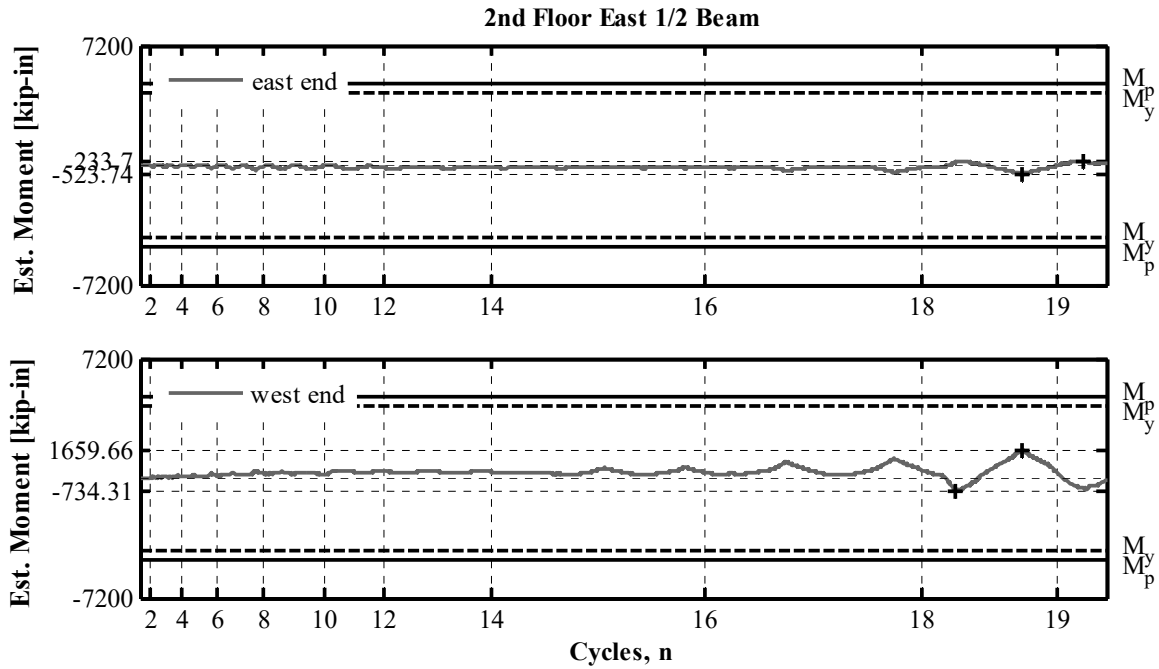


Figure B.19 NCBF-B-2 second-floor east 1/2-beam estimated moment history (measured at 3 ft-0 in. from ends).

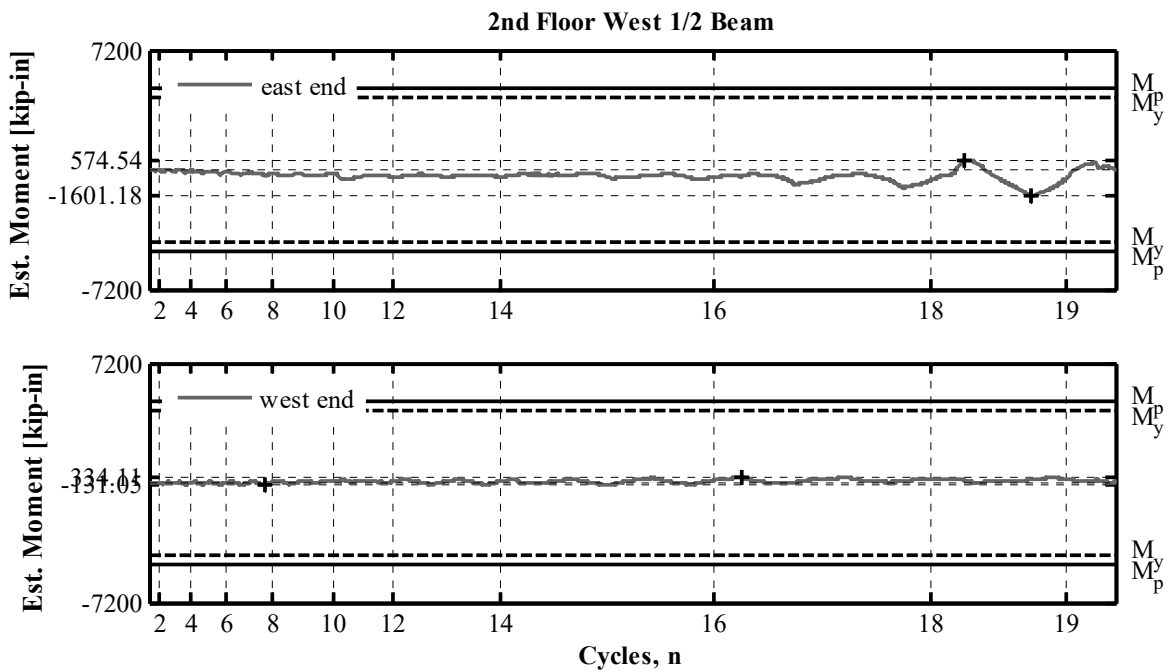


Figure B.20 NCBF-B-2 second-floor west 1/2-beam estimated moment history (measured at 3 ft-0 in. from end from frame centerline and 1 ft-6 in. from west end).

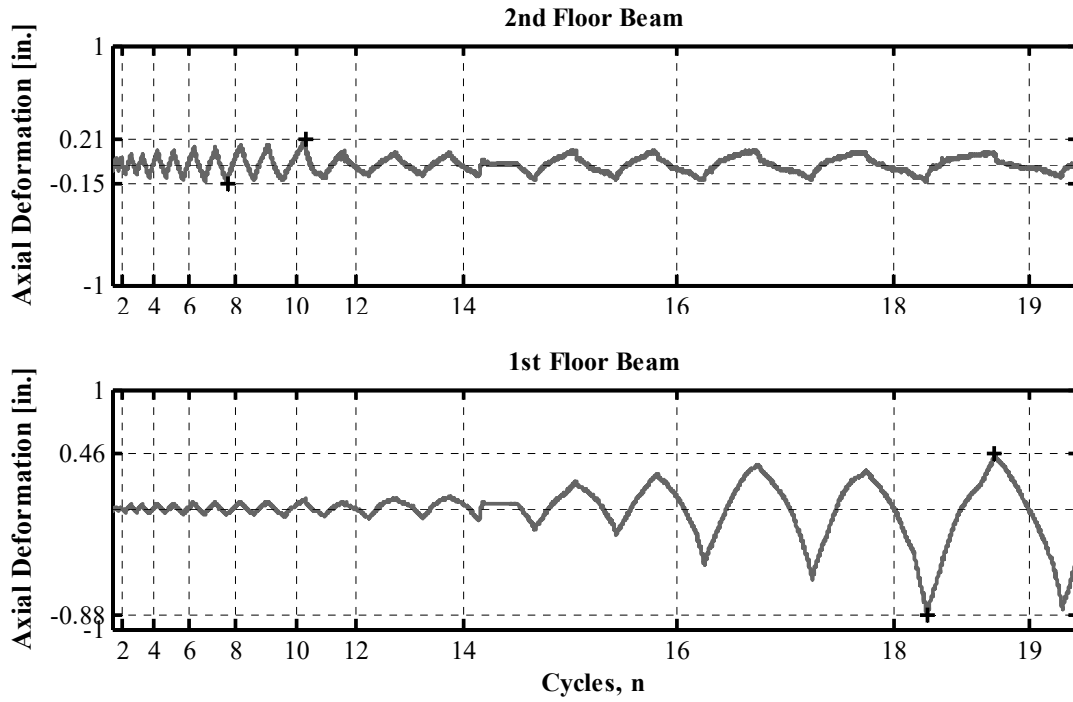


Figure B.21 NCBF-B-2 beam axial deformation time histories.

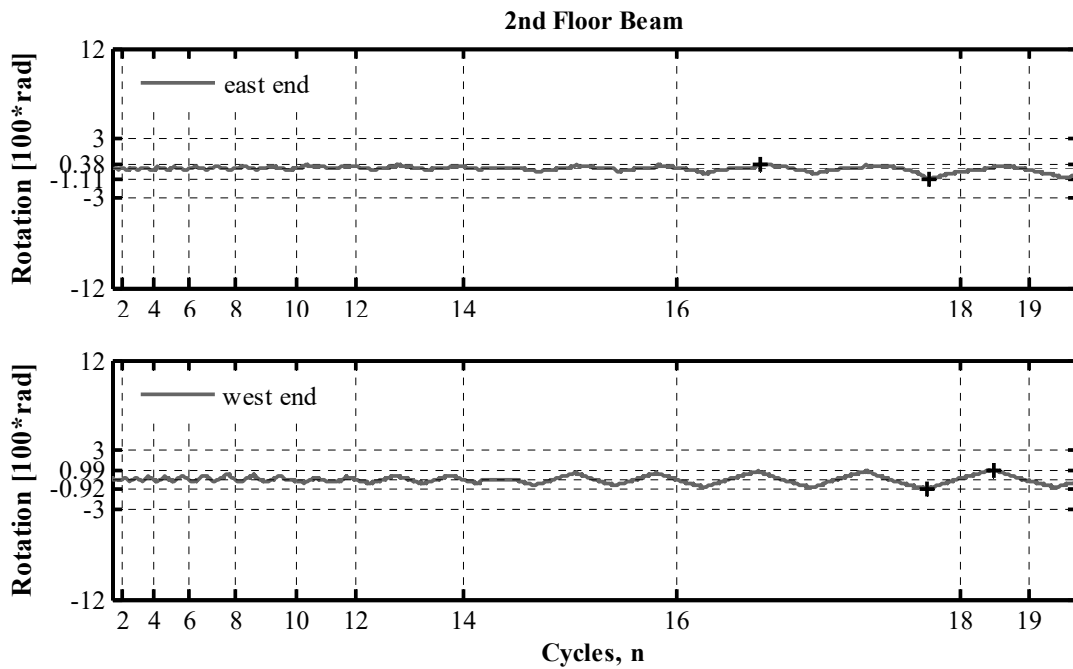


Figure B.22 NCBF-B-2 second-floor beam end rotation time histories.

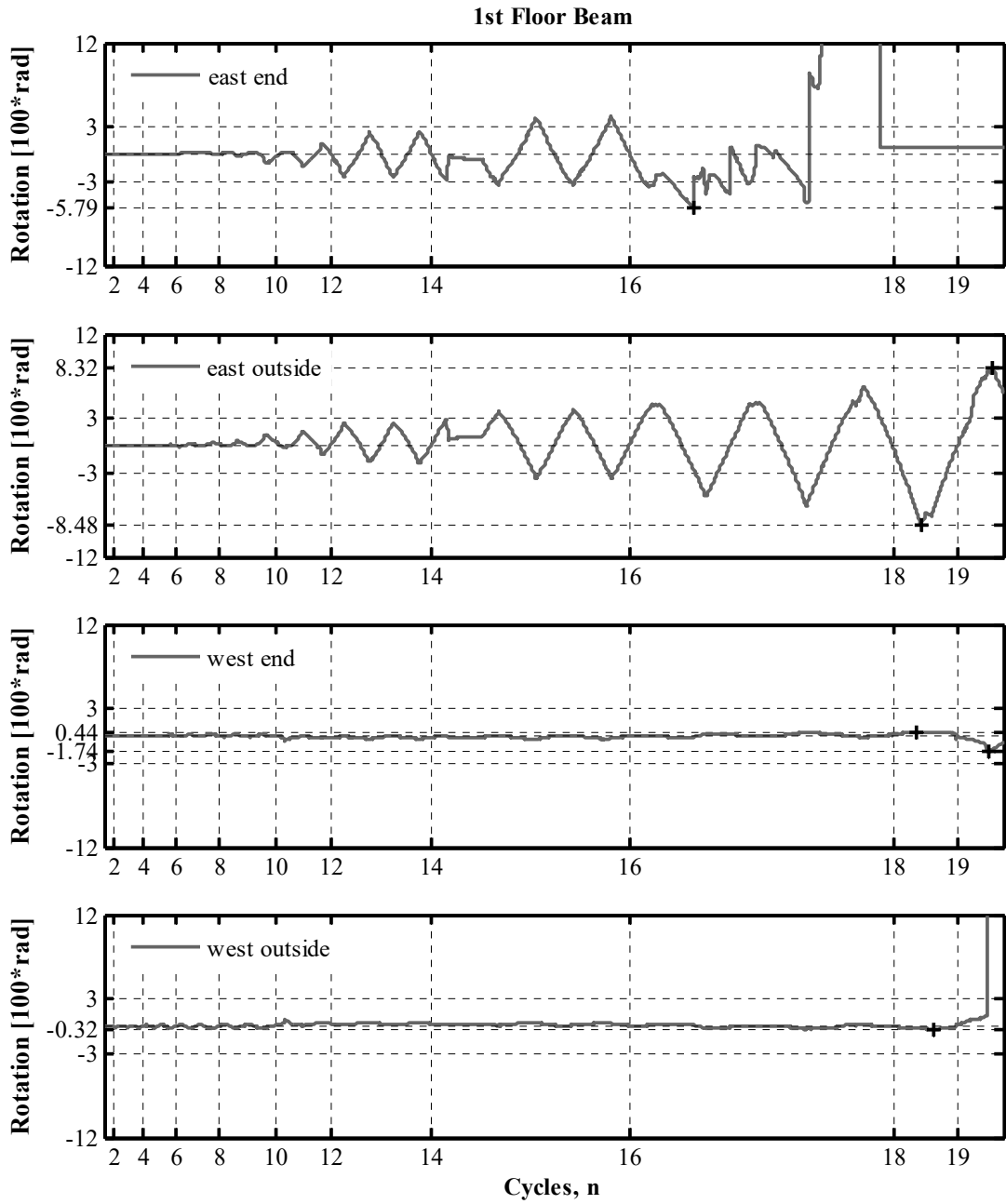


Figure B.23 NCBF-B-2 first-floor beam end rotation time histories.

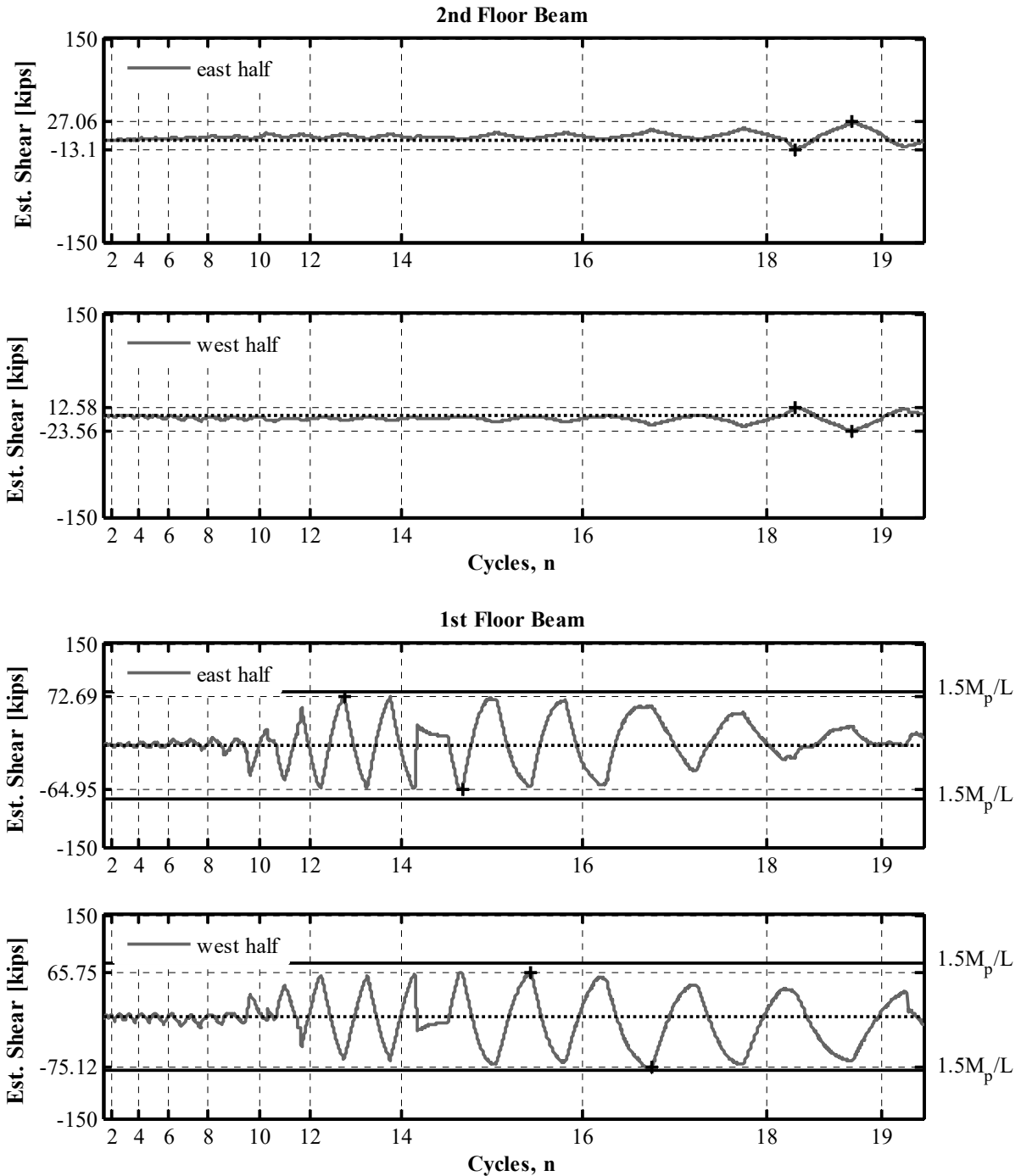


Figure B.24 NCBF-B-2 beam estimated shear time histories (where L is the distance from the beam end to the edge of the middle connection).

B.1.4 Column Plots

The following section shows the plots for the column response parameters. Plots include the response history for the column estimated axial force, estimated moments, and estimated shear. Maximum and minimum values are called out on each plot.

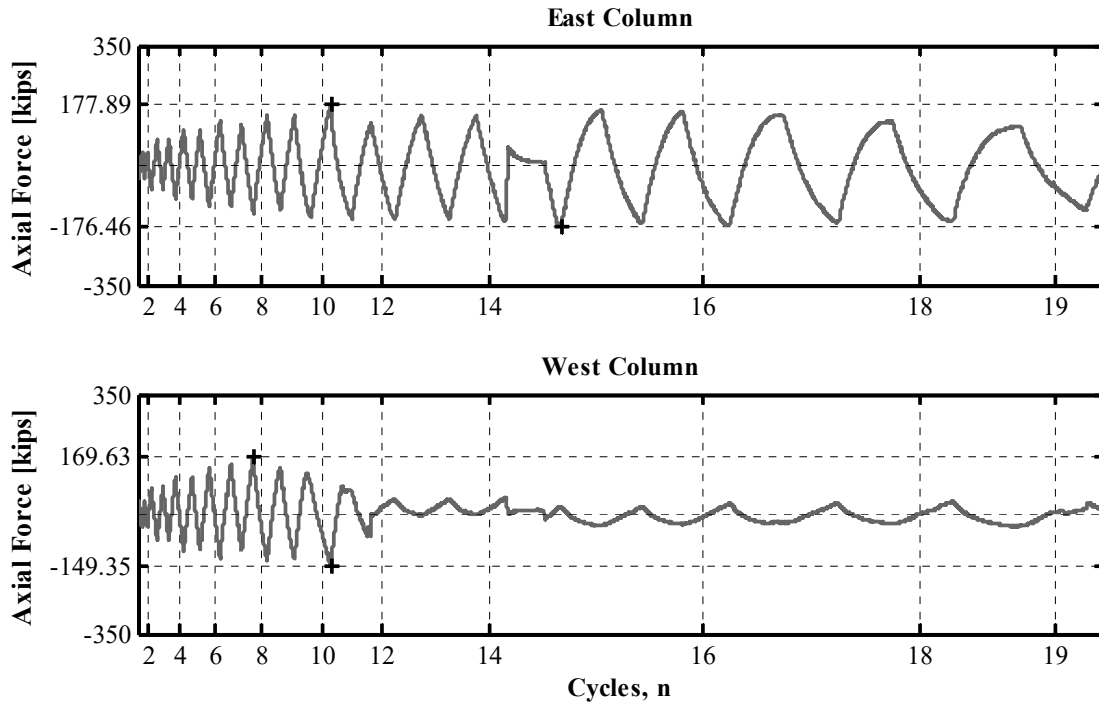


Figure B.25 NCBF-B-2 column estimated axial force time histories.

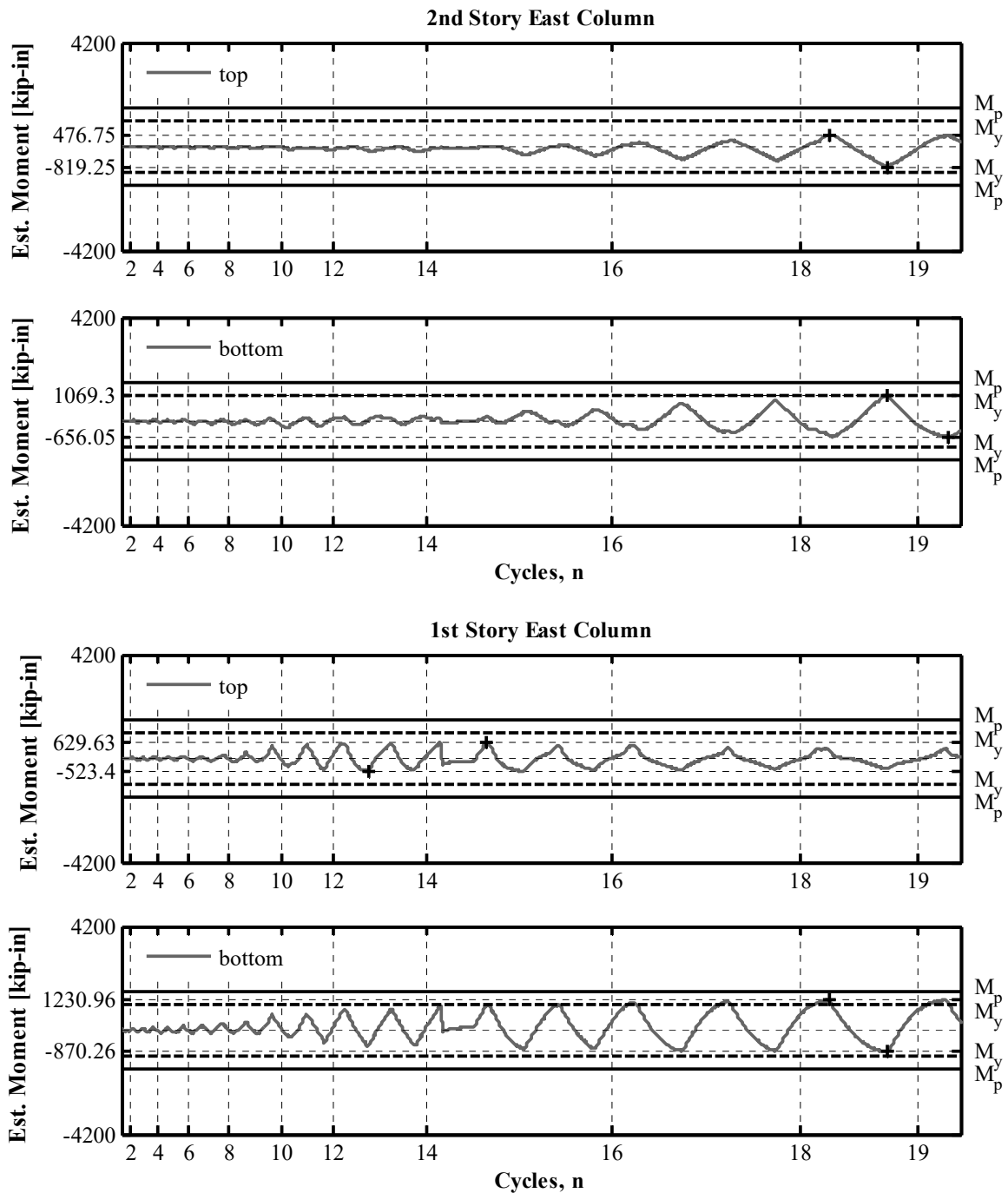


Figure B.26 NCBF-B-2 east column estimated moment history (measured at 3 ft-0 in. from the column ends).

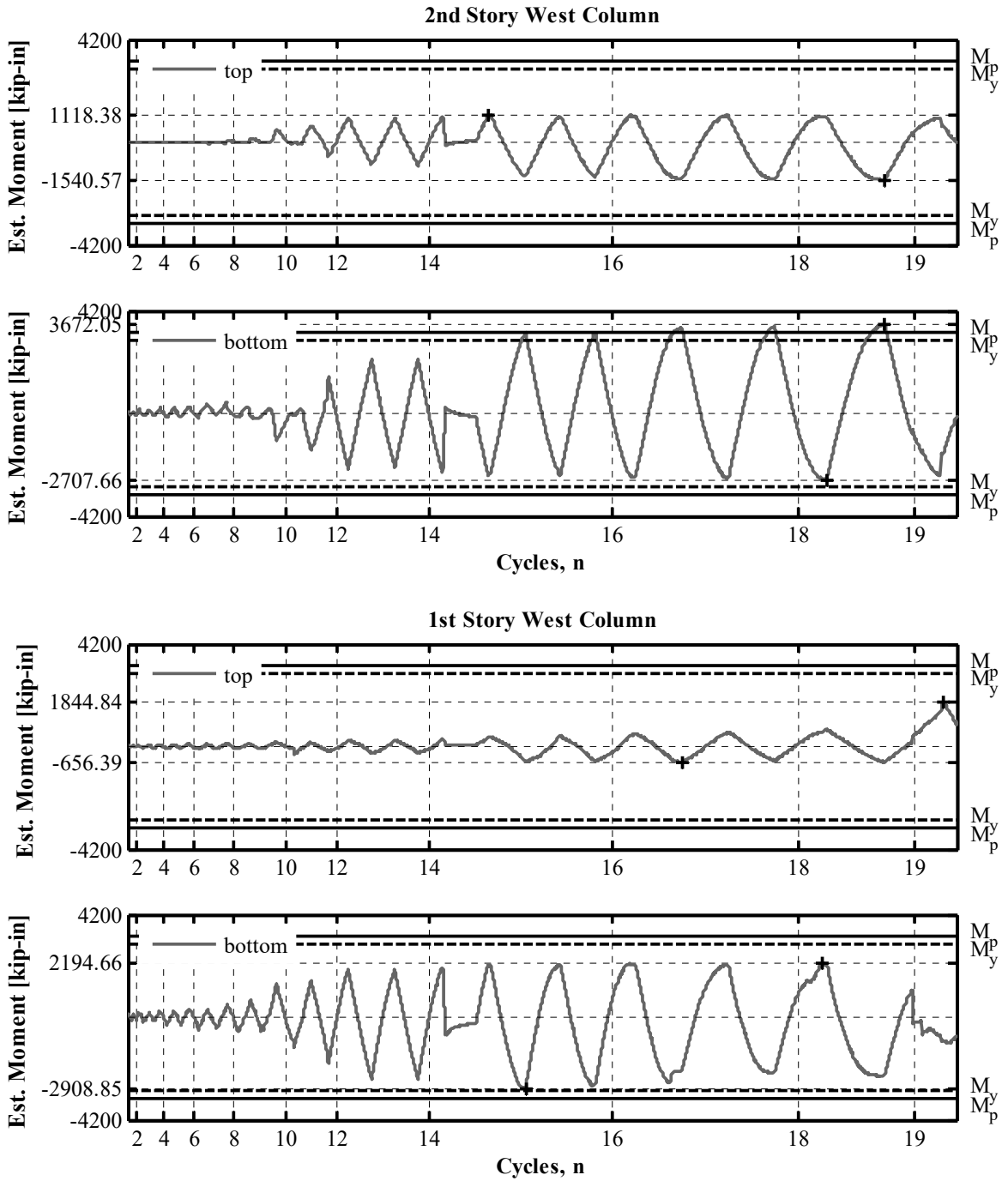


Figure B.27 NCBF-B-2 west column estimated moment history (measured at 3 ft-0 in. from the column ends).

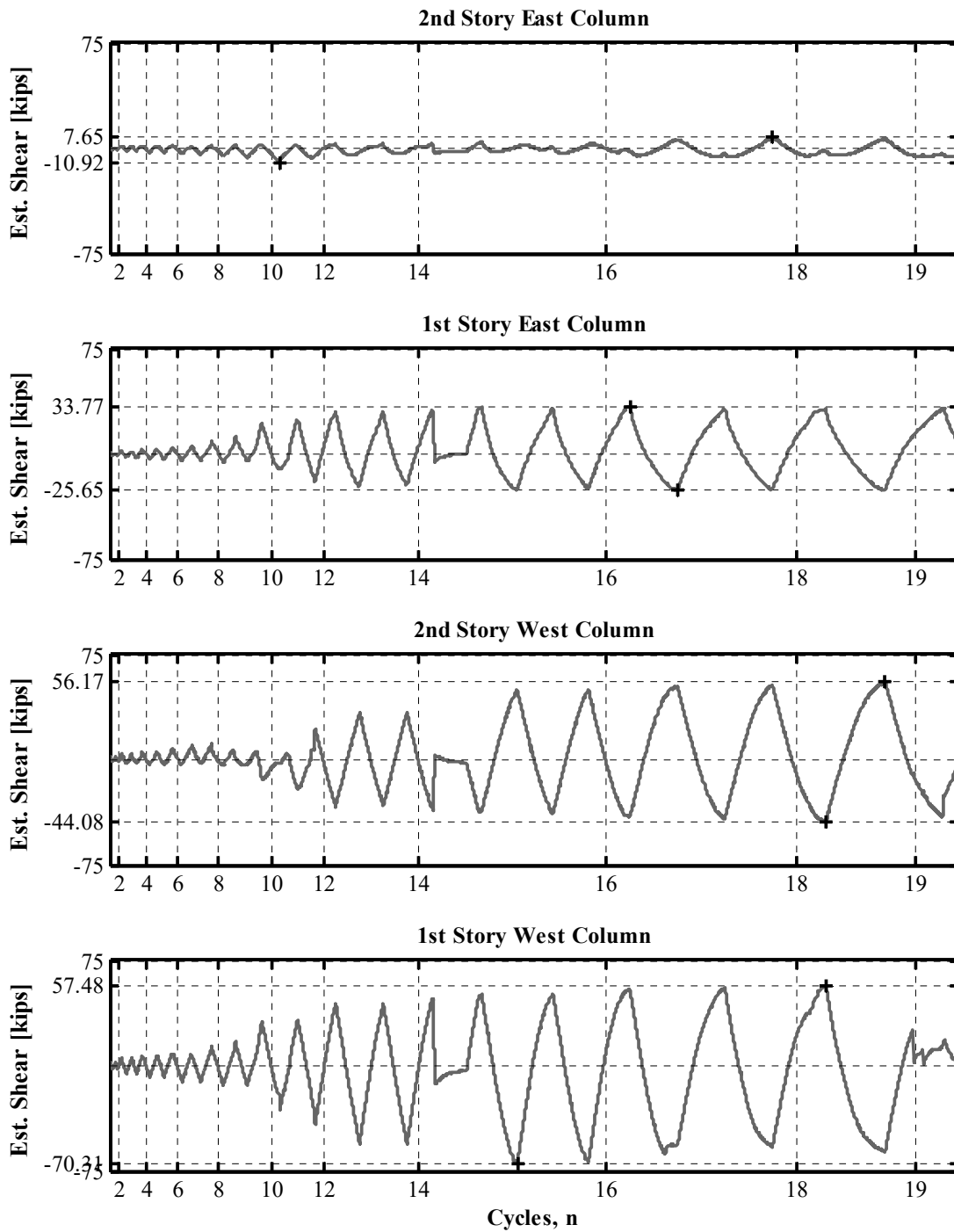


Figure B.28 NCBF-B-2 column estimated shear time histories.

Appendix C Plots of the NCBF-B-3SB Test

C.1 RESPONSE HISTORY PLOTS

The following plots show the maximum and minimum values of selected variables derived from the instrumentation. Time is broken into cycles to reflect the slow, static nature of the quasi-static test. Global plots of the story shears and drifts are shown in Section C.1.1. The derived axial force, shears, moments, and rotations at specified sections of the members are shown for the braces, beams, and columns in Sections C.1.2, C.1.3, and C.1.4, respectively. Labels used in the plots are defined by the values in Table C.1

Table C.1 NCBF-B-3SB: values used for labels in plots.

Design axial capacity		Location	F_y (ksi) ¹	T_n (kips) ²	C_n (kips) ³
HSS6×6×1/2		First-story west brace	59.6	448	340
HSS8×8×5/8		Second-story west brace	64.6	754	666
			P_y (kips) ⁶	T_{max} (kips) ⁶	C_{max} (kips) ⁶
BRB		First-story east brace	230	327	357
Design moment		Location	F_y (ksi) ¹	M_y (kip-in) ⁴	M_p (kip-in) ⁵
W10×54	Strong axis	West column	60.5	3630	4029
	Weak axis	East column		1246	1894
W14×53		Beam	56.5	4396	4921
HSS6×6×1/2		First-story west brace	59.6	960	1180
HSS8×8×5/8		Second-story west brace	64.6	2358	2888

¹ From steel mill certificates provided by Schuff Steel

² Design tensile capacity from AISC 360 [2010] using a nominal yield strength of 46ksi

³ Design compression buckling capacity from AISC 360 [2010] for concrete-filled tubes (CFT) using the length of the brace from the shop drawings with an effective length factor of $k = 1$ and a nominal yield strength of 46 ksi

⁴ Yielding moment: $M_y = F_y S$, where S is the elastic section modulus

⁵ Plastic moment: $M_p = F_y Z$, where Z is the plastic section modulus

⁶ T_{max} and C_{max} correspond to the maximum compression and tension capacity of the BRB as specified by StarSeismic ($T_{max} = \omega P_y$; $C_{max} = \beta \omega P_y$, where P_y is the force required to yield the steel core of 5 in.²)

C.1.1 Global Plots

The following section shows the plots for the global response parameters of each story, including story shears and displacements. Maximum and minimum values are called out on each plot.

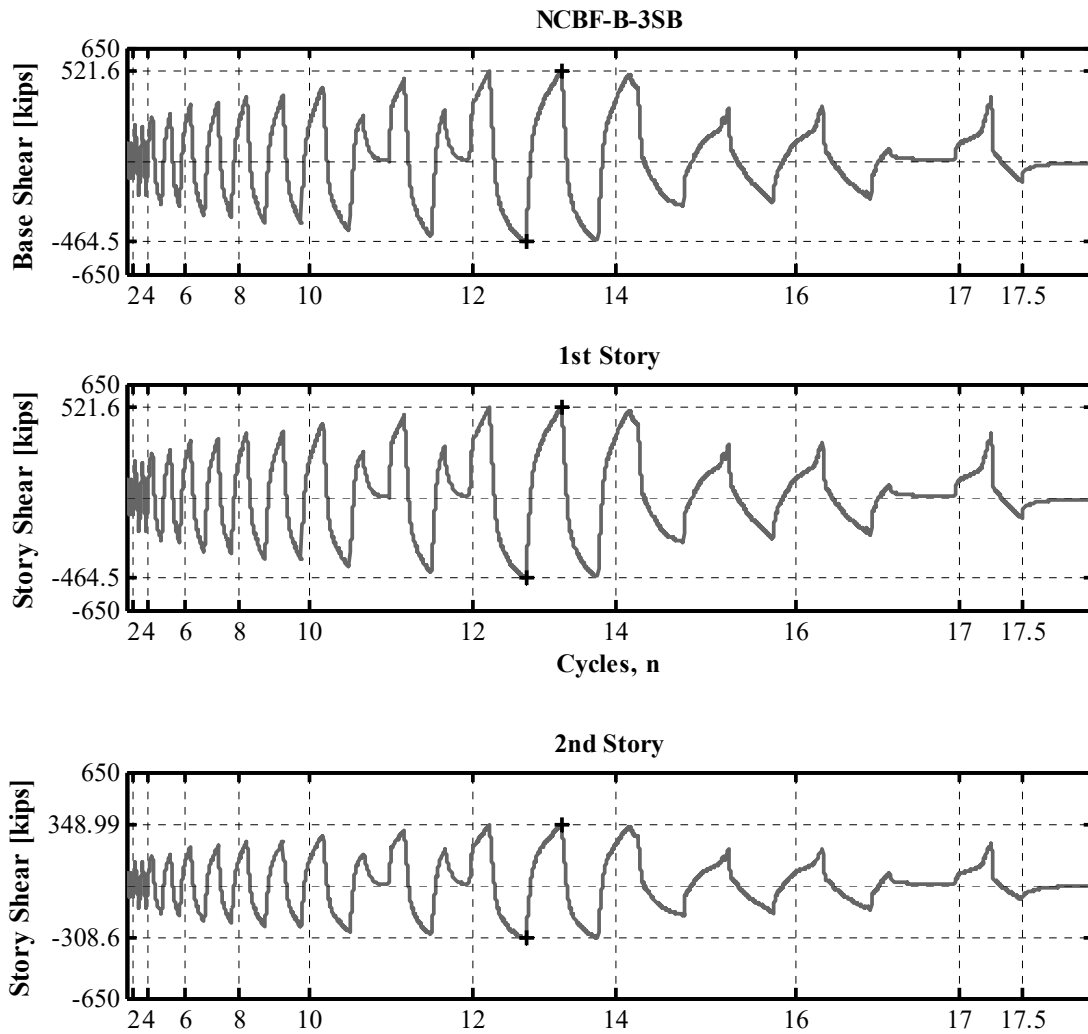


Figure C.1 NCBF-B-3SB story shear time histories.

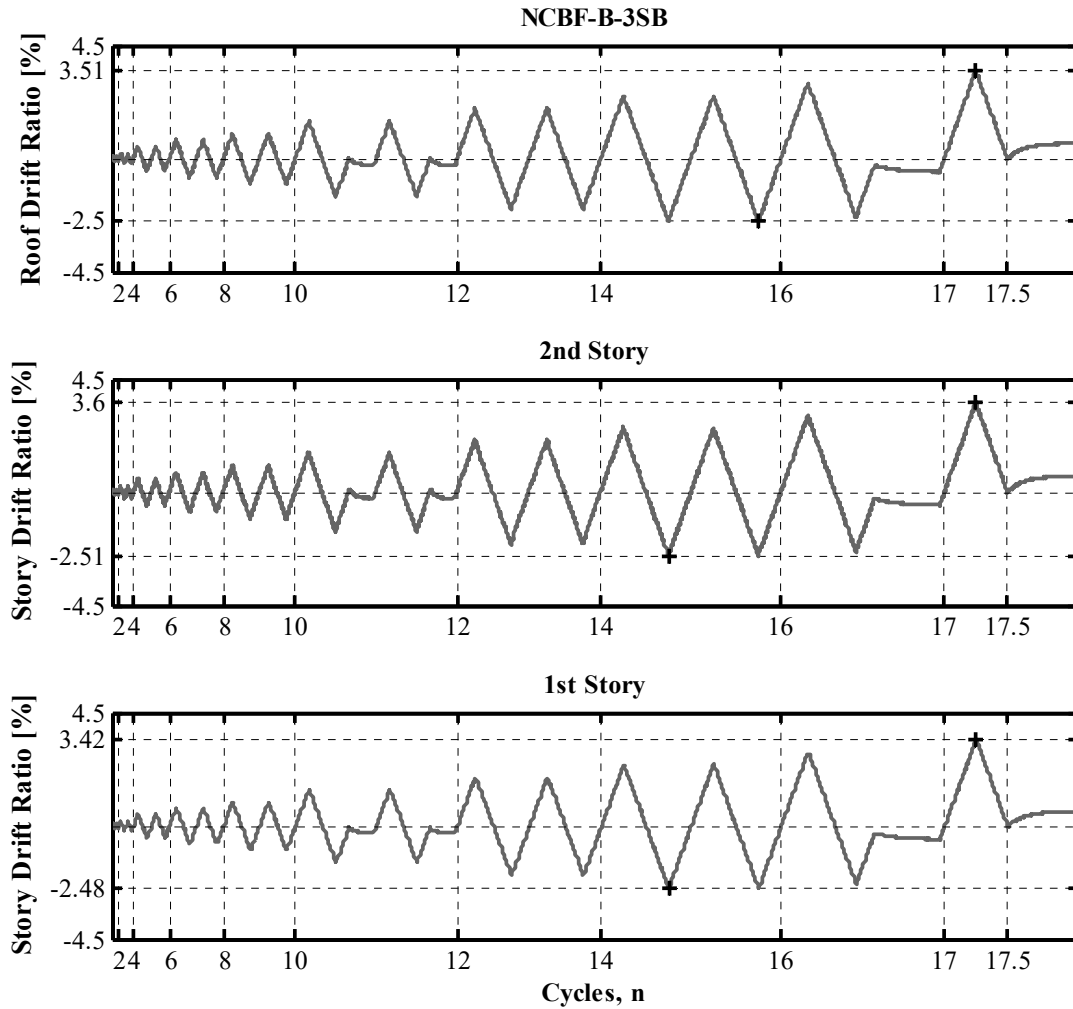


Figure C.2 NCBF-B-3SB story drift ratio time histories.

C.1.2 Brace Plots

The following section shows the plots for the brace response parameters. Plots include the response history for the brace estimated axial force, out-of-plane displacement, axial deformation, estimated moments, end rotations, and estimated shears. Maximum and minimum values are called out on each plot.

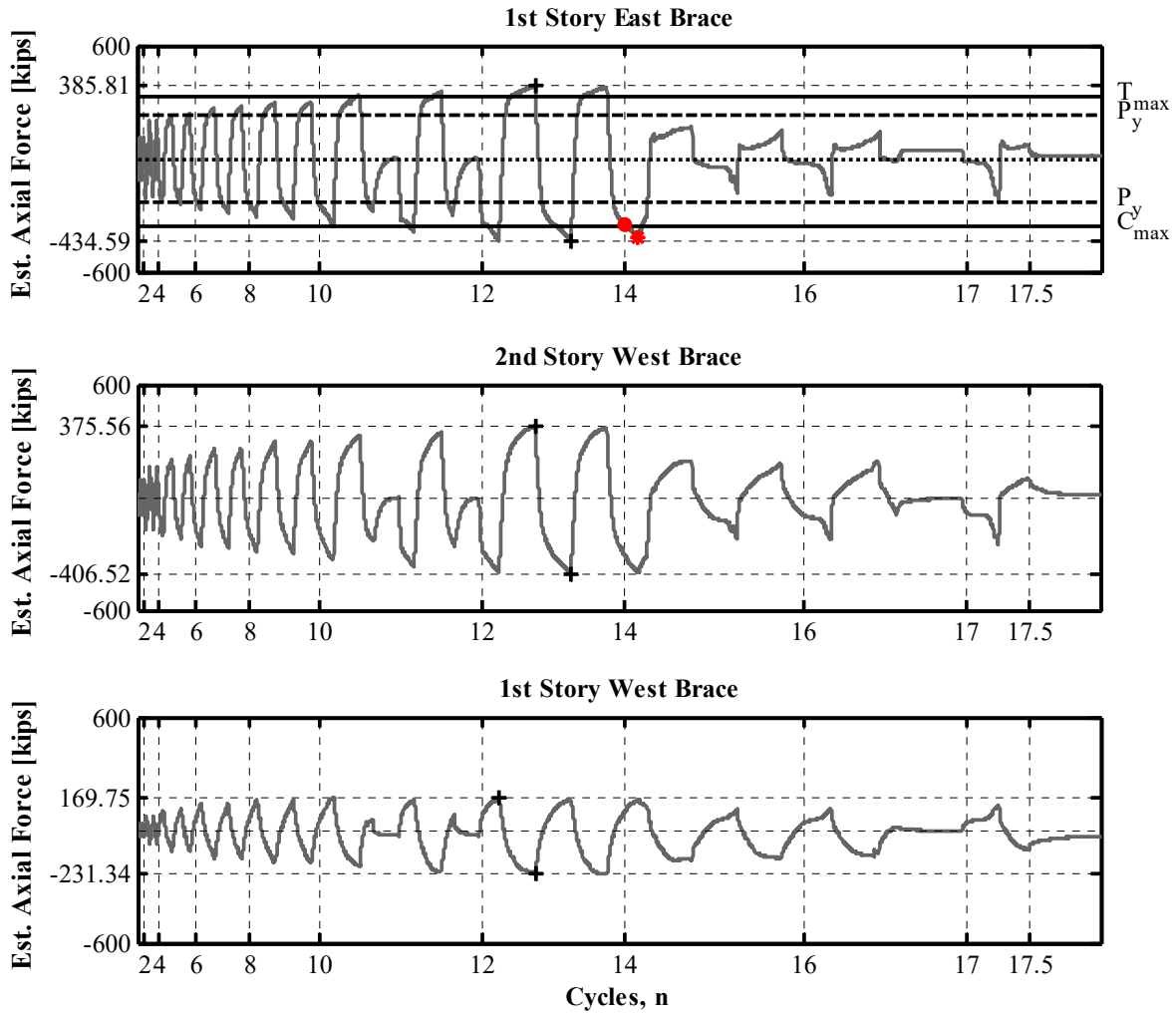


Figure C.3 NCBF-B-3SB estimated brace axial force time histories.

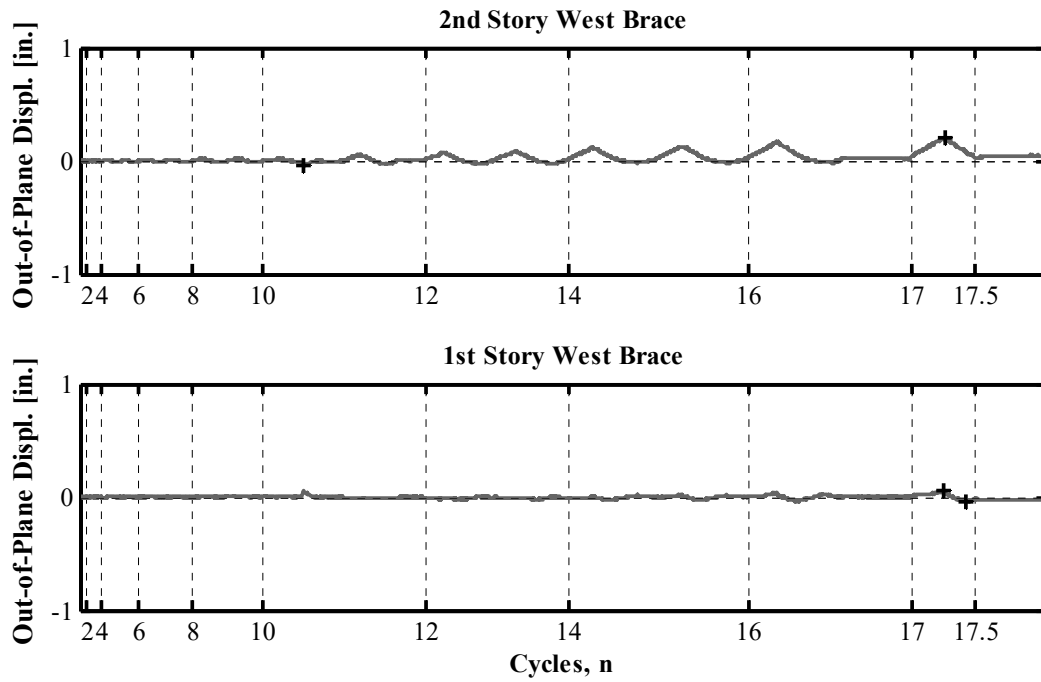


Figure C.4 NCBF-B-3SB brace out-of-plane displacement time histories.

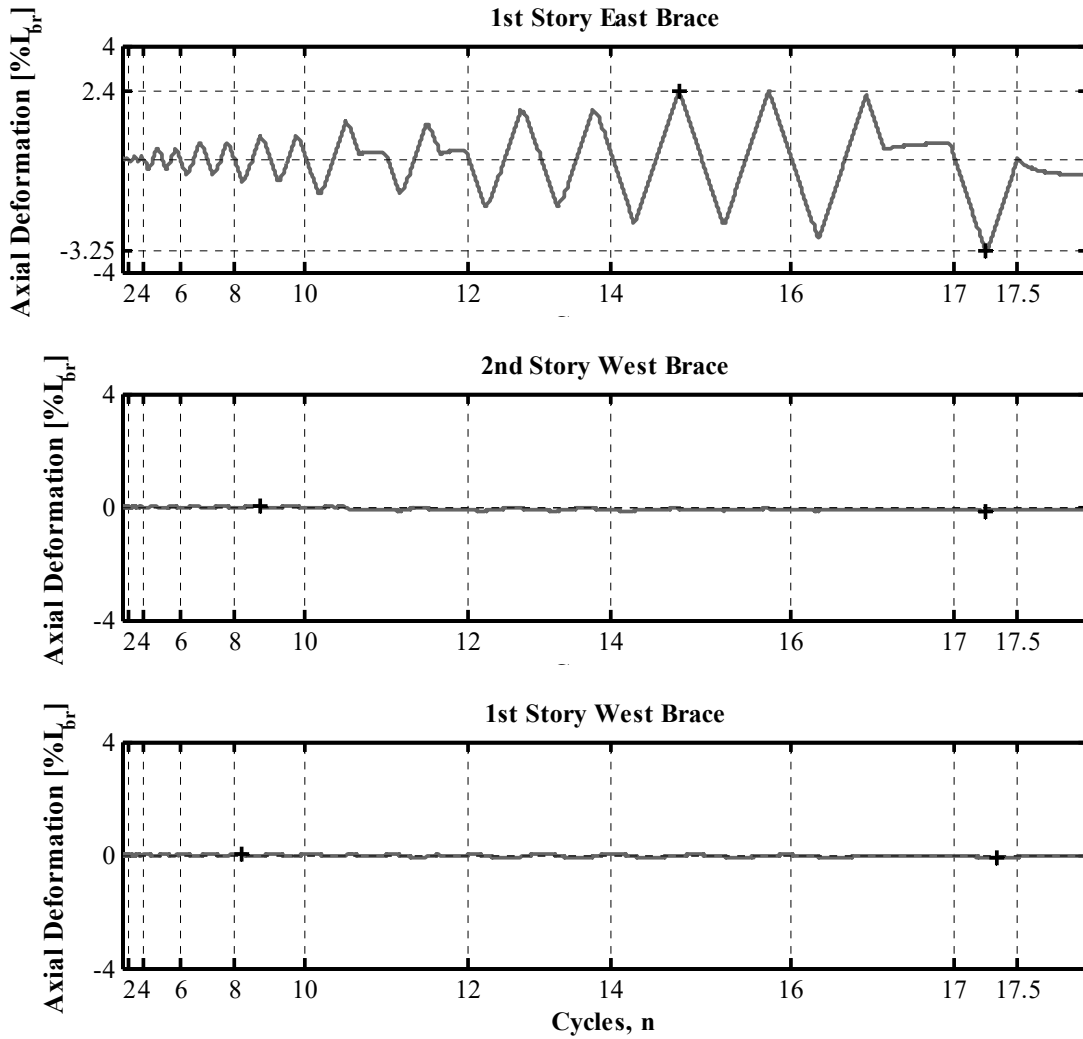


Figure C.5 NCBF-B-3SB Brace axial deformation time histories (L_b is the work-point-to-work-point length).

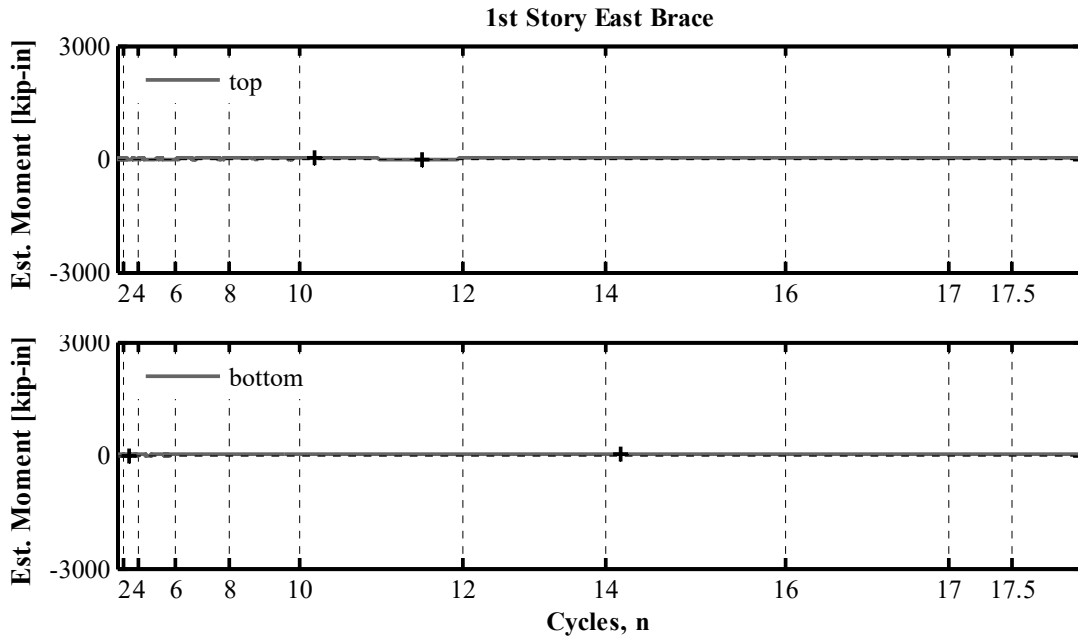


Figure C.6 NCBF-B-3SB first-story east brace estimated moment time histories (measured at top and bottom ¼-points of brace length).

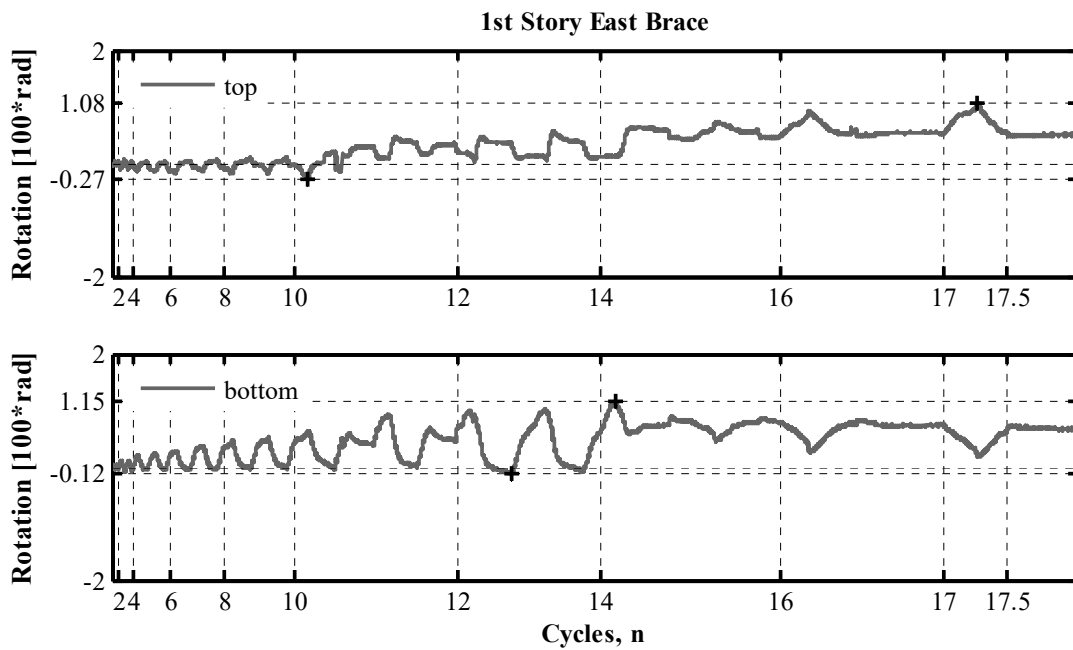


Figure C.7 NCBF-B-3SB first-story east brace out-of-plane end rotation time histories.

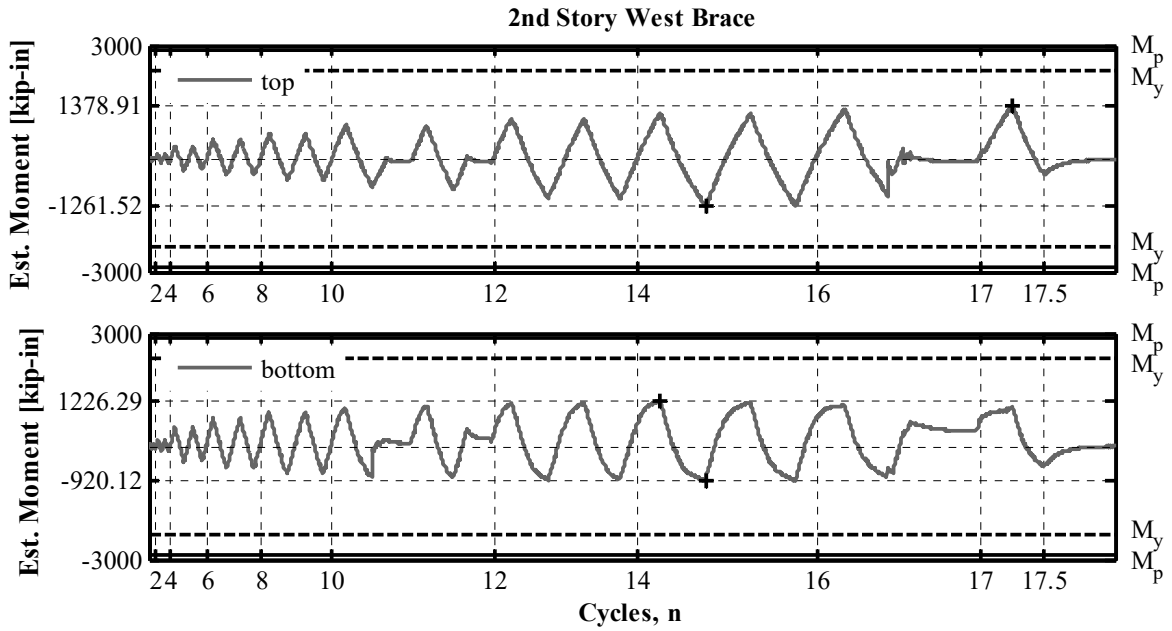


Figure C.8 NCBF-B-3SB second-story west brace estimated moment time histories (measured at top and bottom $\frac{1}{4}$ points of brace length).

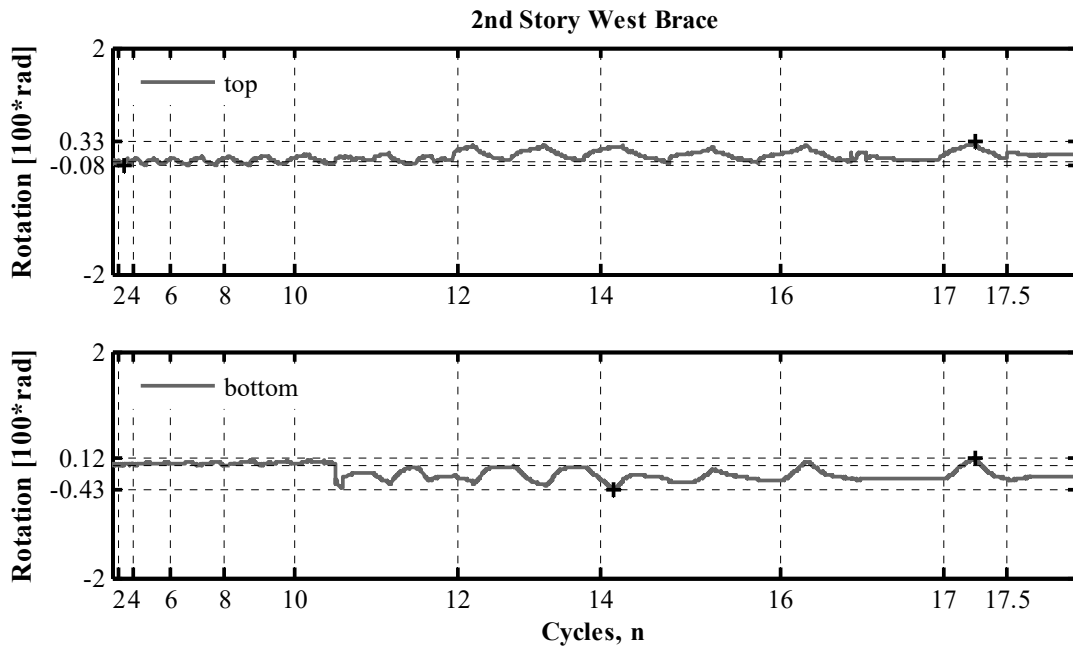


Figure C.9 NCBF-B-3SB second-story west brace out-of-plane end rotation time histories.

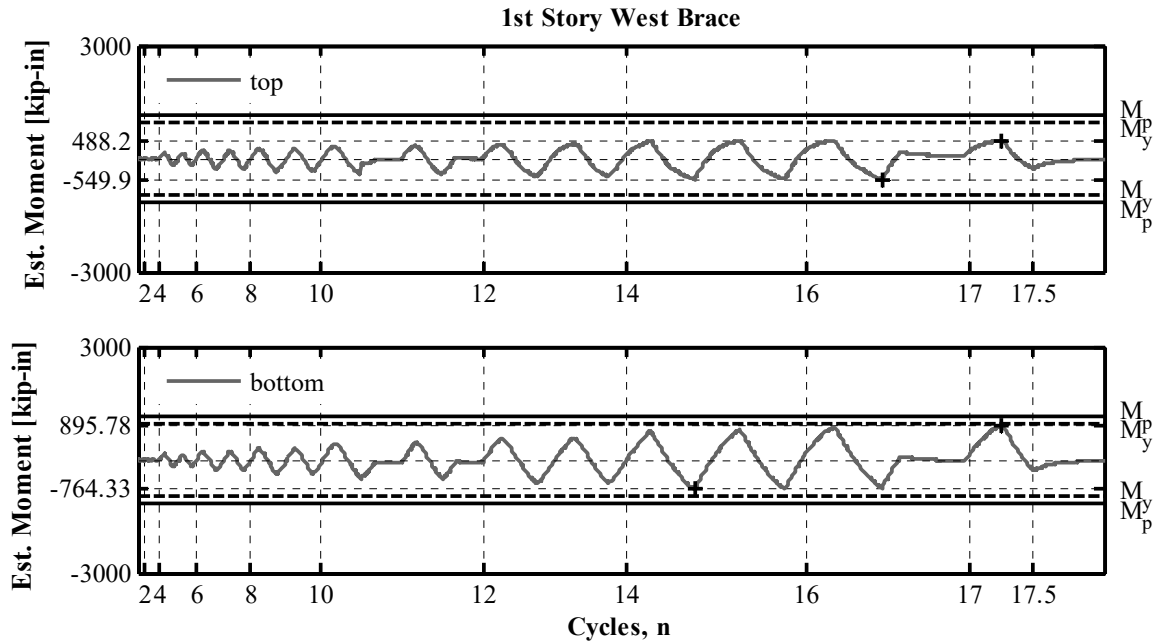


Figure C.10 NCBF-B-3SB first-story west brace estimated moment time histories (measured at top and bottom $\frac{1}{4}$ -points of brace length).

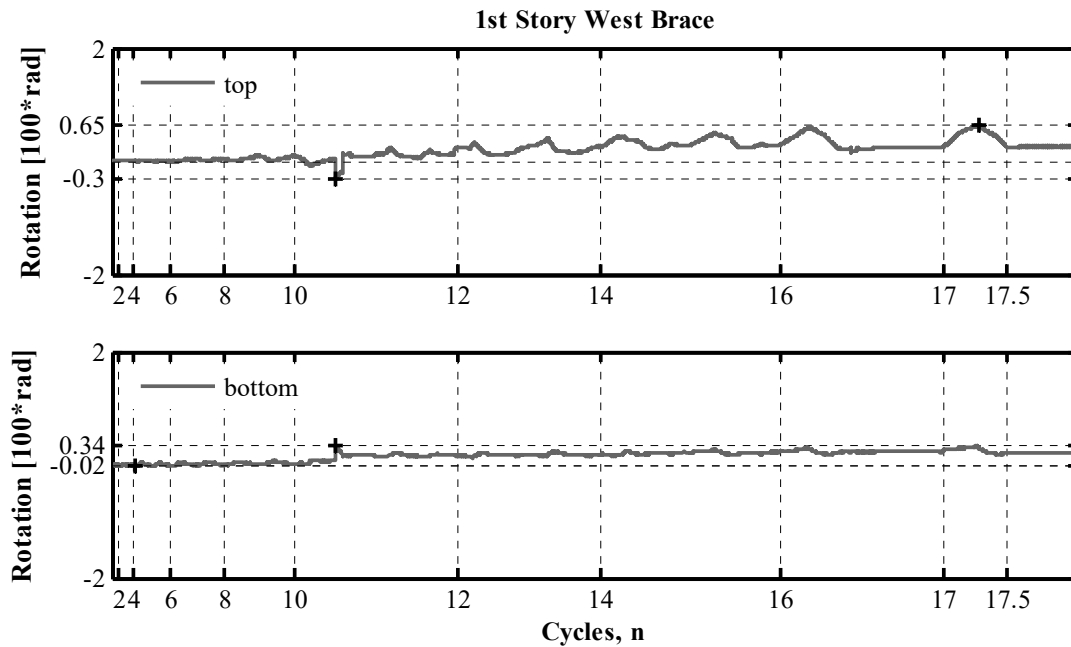


Figure C.11 NCBF-B-3SB first-story west brace out-of-plane end rotation time histories.

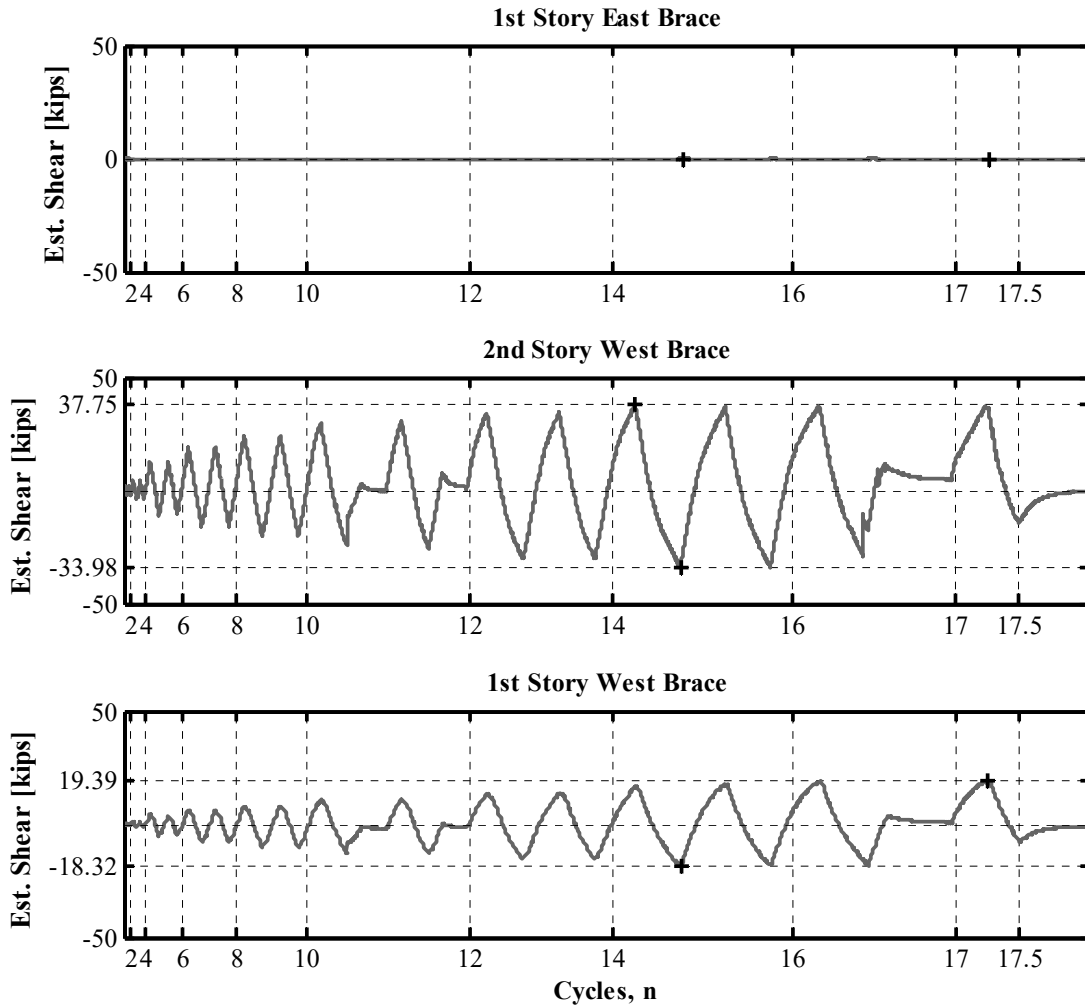


Figure C.12 NCBF-B-3SB brace estimated shear time histories.

C.1.3 Beam Plots

The following section shows the plots for the brace response parameters. Plots include the response history for the beam estimated unbalanced load, mid-span displacement, estimated moments, axial deformation, end rotations, and shears. Maximum and minimum values are called out on each plot.

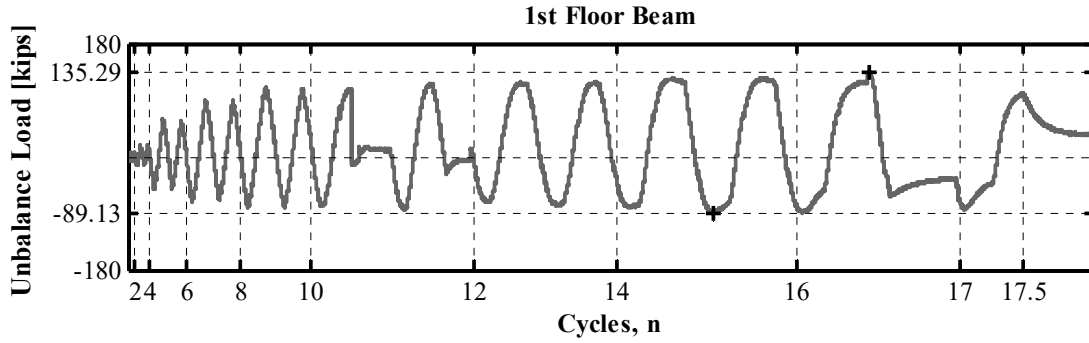


Figure C.13 NCBF-B-3SB first-floor beam estimated unbalanced load history.

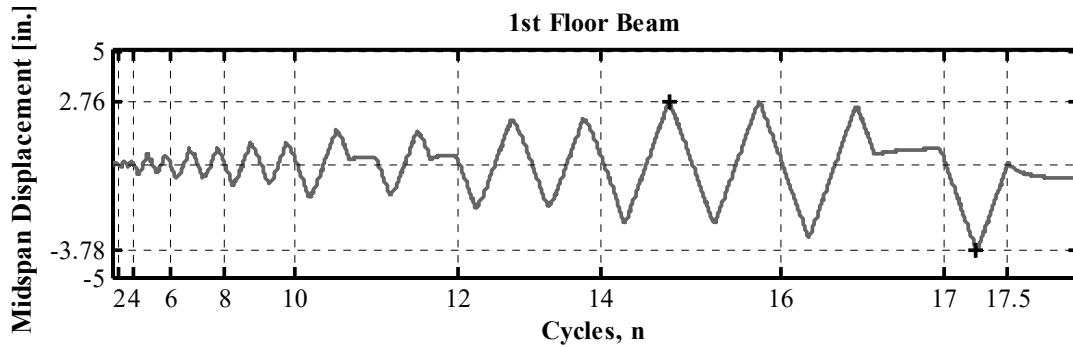


Figure C.14 NCBF-B-3SB first-floor beam vertical mid-span displacement history.

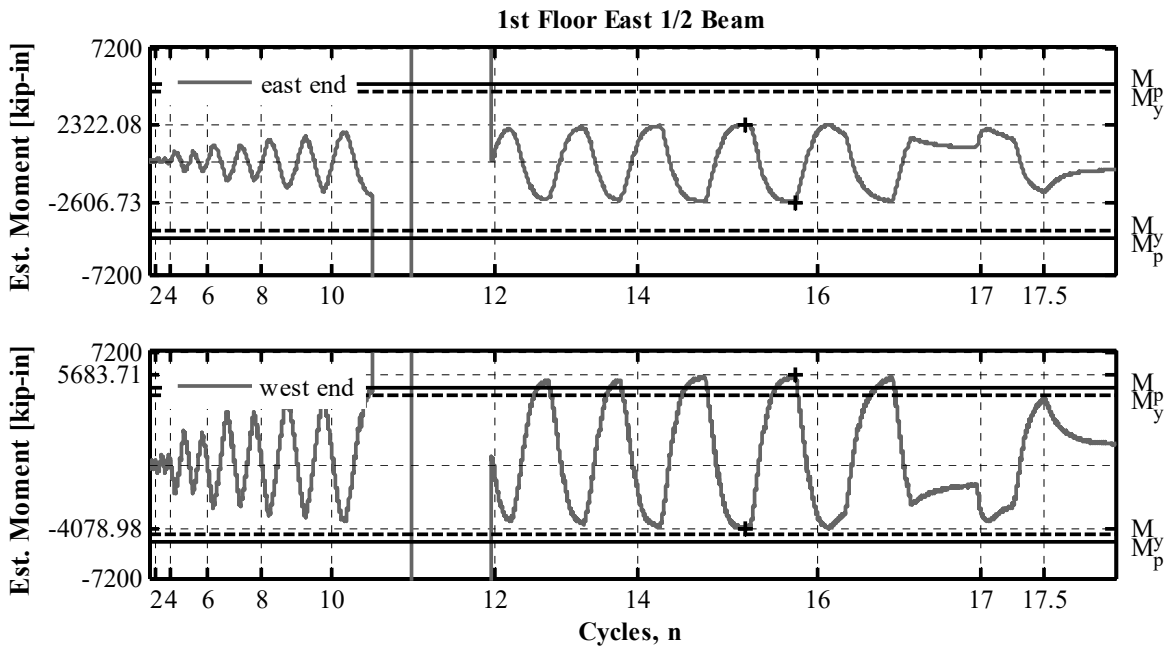


Figure C.15 NCBF-B-3SB first-floor east 1/2 beam estimated moment history (measured at 3 ft-0 in. from the east end and 1 ft-6 in. from the west end).

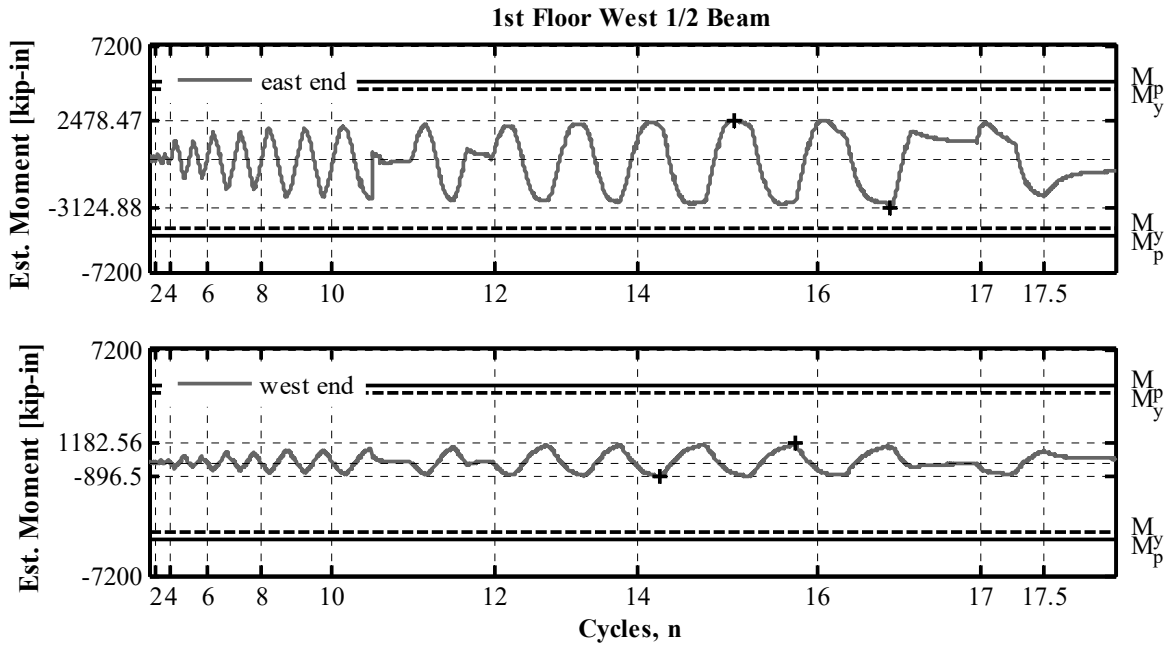


Figure C.16 NCBF-B-3SB first-floor west 1/2 beam estimated moment history (measured at 1 ft-6 in. from the east end and 3 ft-0 in. from the west end).

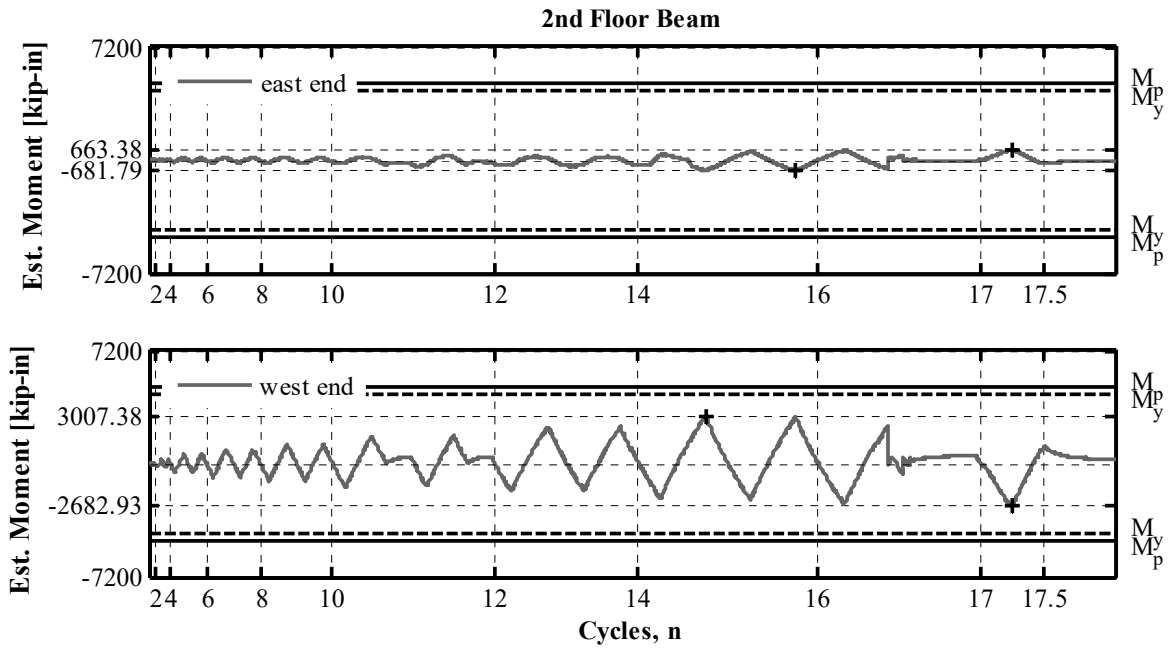


Figure C.17 NCBF-B-3SB second-floor beam estimated moment history (measured at 3 ft-0 in. from the east end and 3 ft-0 in. west of the beam midpoint).

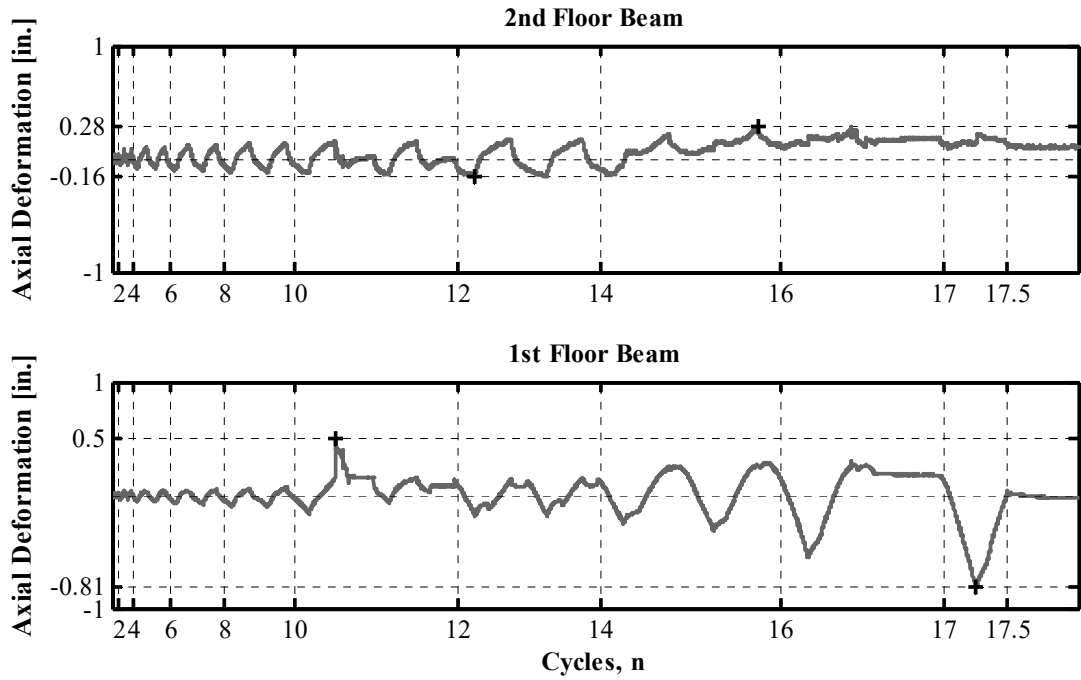


Figure C.18 NCBF-B-3SB beam axial deformation time histories.

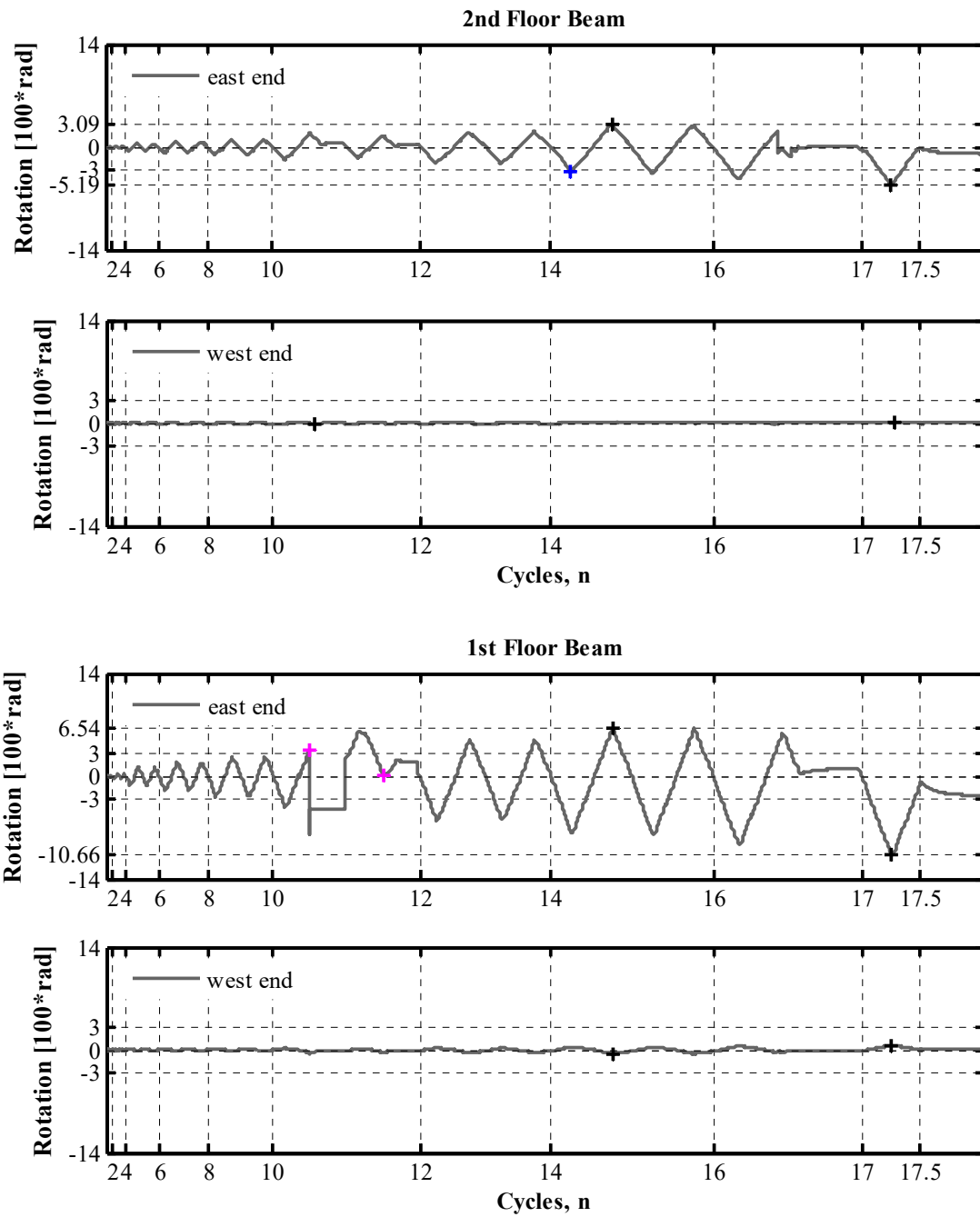


Figure C.19 NCBF-B-3SB first-floor beam end rotation time histories.

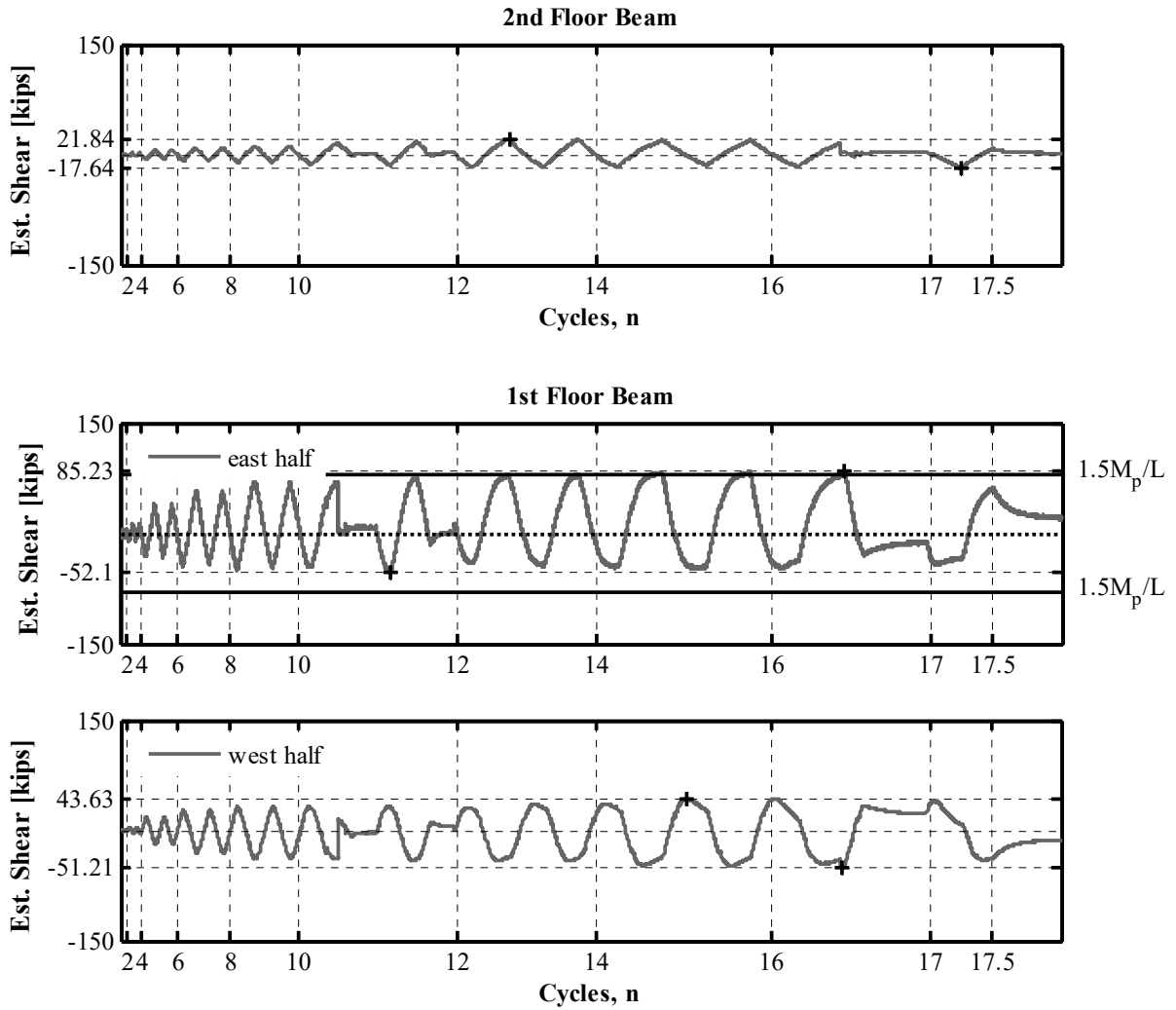


Figure C.20 NCBF-B-3SB beam estimated shear time histories (where L is the distance from the beam end to the edge of the middle connection).

C.1.4 Column Plots

The following section shows the plots for the column response parameters. Plots include the response history for the column estimated axial force, estimated moments, and estimated shear. Maximum and minimum values are called out on each plot.

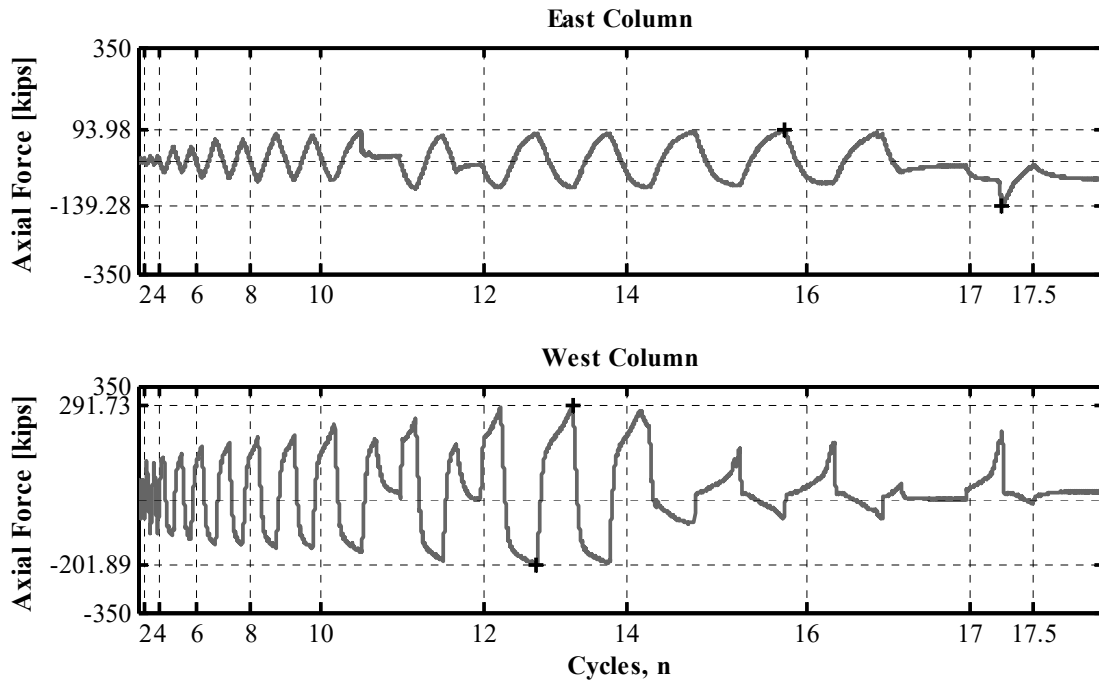


Figure C.21 NCBF-B-3SB column estimated axial force time histories.

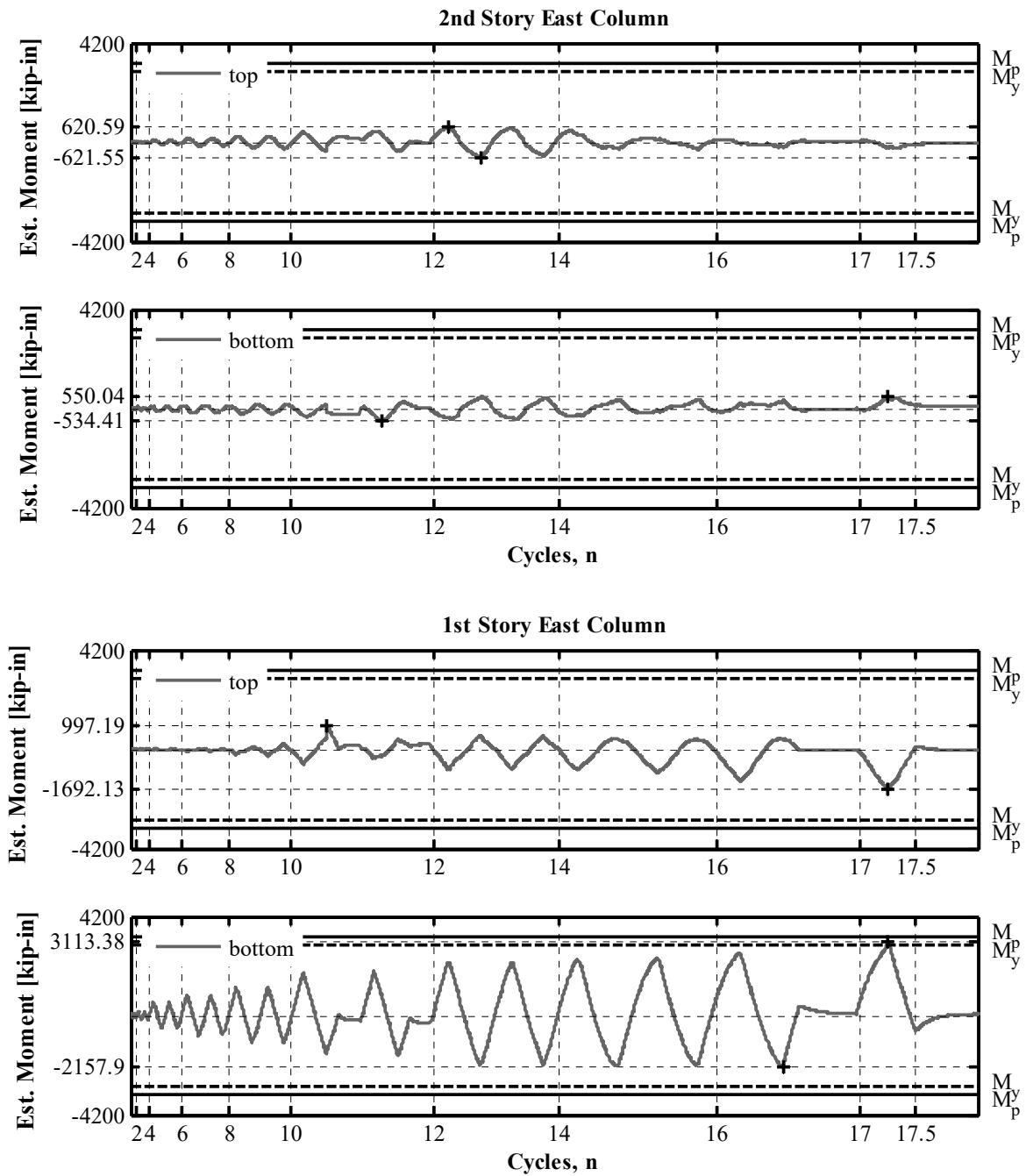


Figure C.22 NCBF-B-3SB east column estimated moment history (measured at 3 ft-0 in and 4 ft-0 in. from the column ends).

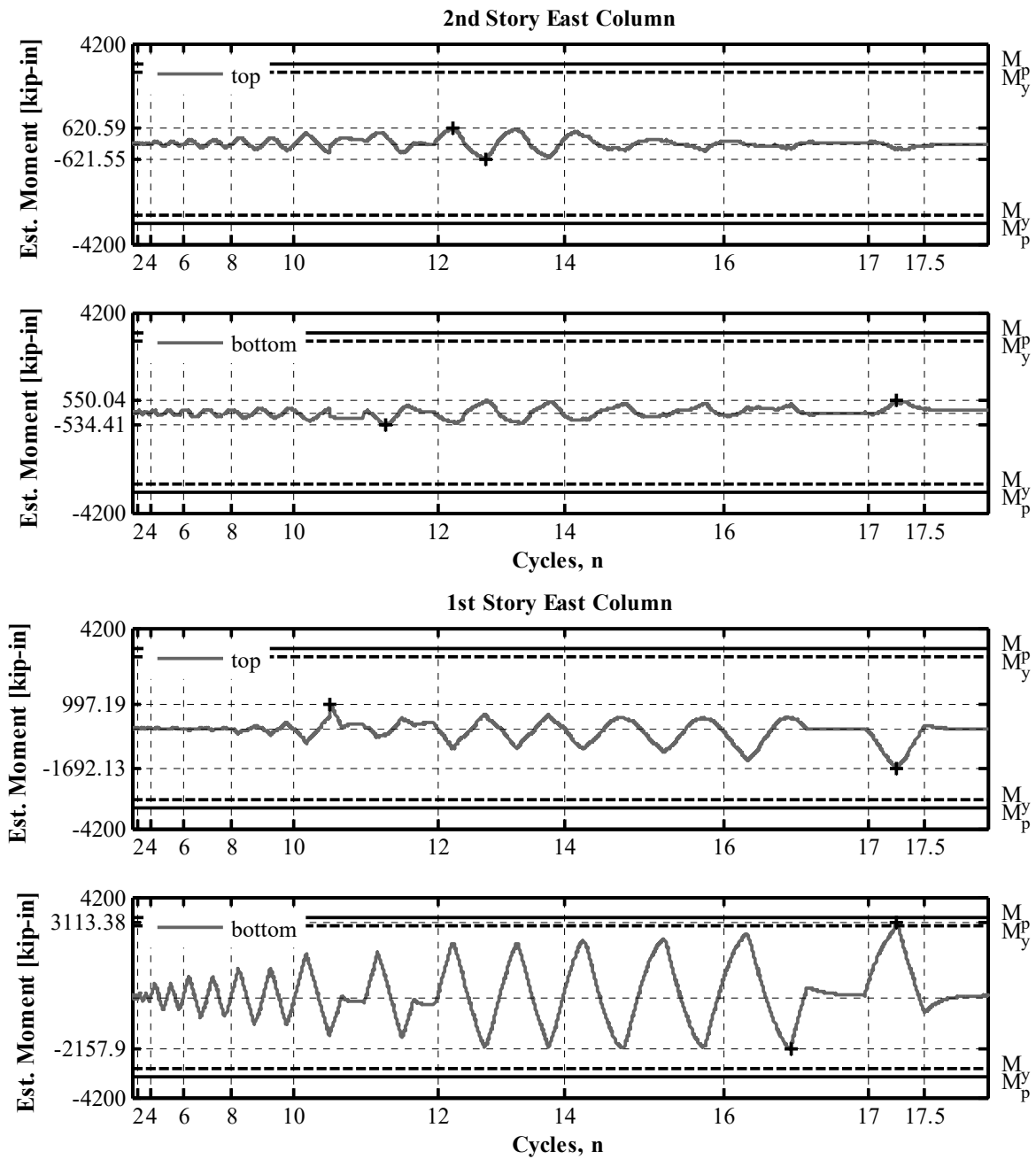


Figure C.23 NCBF-B-3SB west column estimated moment history (measured at 3 ft-0 in. and 4 ft-0 in from the column ends).

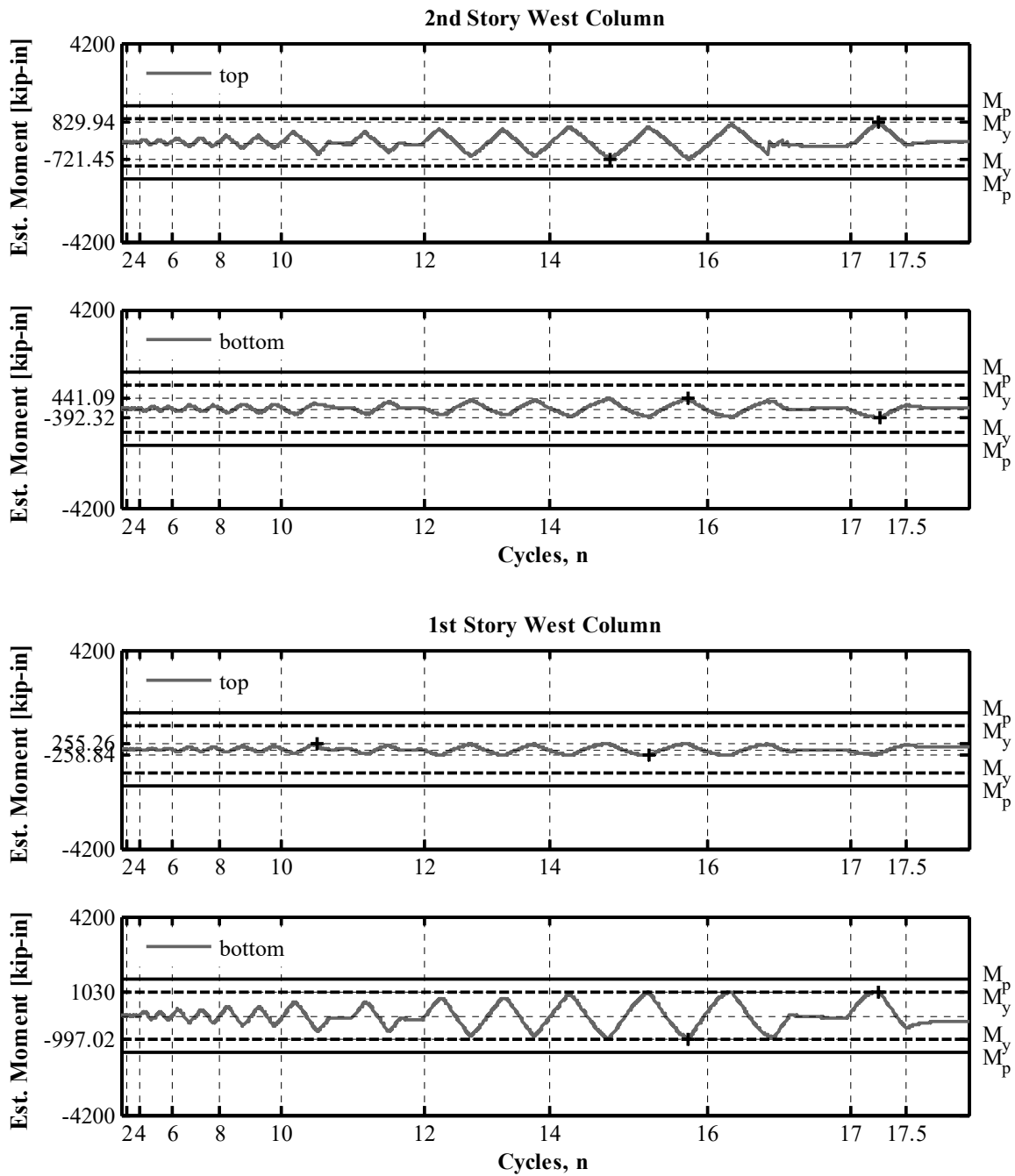


Figure C.24 NCBF-B-3SB Column estimated shear time histories.

PEER REPORTS

PEER reports are available as a free PDF download from <https://peer.berkeley.edu/peer-reports>. Printed hard copies of PEER reports can be ordered directly from our printer by following the instructions also available at <https://peer.berkeley.edu/peer-reports>. For other related questions about the PEER Report Series, contact the Pacific Earthquake Engineering Research Center, 325 Davis Hall; Mail Code 1792, Berkeley, CA 94720. Tel.: (510) 642-3437; and Email: peer_center@berkeley.edu.

- PEER 2017/11** *Preliminary Studies on the Dynamic Response of a Seismically Isolated Prototype Gen-IV Sodium-Cooled Fast Reactor (PGSFR)*. Benshun Shao, Andreas H. Schellenberg, Matthew J. Schoettler, and Stephen A. Mahin. December 2017.
- PEER 2017/10** *Development of Time Histories for IEEE693 Testing and Analysis (including Seismically Isolated Equipment)*. Shakhzod M. Takhirov, Eric Fujisaki, Leon Kempner, Michael Riley, and Brian Low. December 2017.
- PEER 2017/09** *"R" Package for Computation of Earthquake Ground-Motion Response Spectra*. Pengfei Wang, Jonathan P. Stewart, Yousef Bozorgnia, David M. Boore, and Tadahiro Kishida. December 2017.
- PEER 2017/08** *Influence of Kinematic SSI on Foundation Input Motions for Bridges on Deep Foundations*. Benjamin J. Turner, Scott J. Brandenberg, and Jonathan P. Stewart. November 2017.
- PEER 2017/07** *A Nonlinear Kinetic Model for Multi-Stage Friction Pendulum Systems*. Paul L. Drazin and Sanjay Govindjee. September 2017.
- PEER 2017/06** *Guidelines for Performance-Based Seismic Design of Tall Buildings, Version 2.02*. TBI Working Group led by co-chairs Ron Hamburger and Jack Moehle: Jack Baker, Jonathan Bray, C.B. Crouse, Greg Deierlein, John Hooper, Marshall Lew, Joe Maffei, Stephen Mahin, James Malley, Farzad Naeim, Jonathan Stewart, and John Wallace. May 2017.
- PEER 2017/05** *Recommendations for Ergodic Nonlinear Site Amplification in Central and Eastern North America*. Youssef M.A. Hashash, Joseph A. Harmon, Okan Ilhan, Grace A. Parker, and Jonathan P. Stewart. March 2017.
- PEER 2017/04** *Expert Panel Recommendations for Ergodic Site Amplification in Central and Eastern North America*. Jonathan P. Stewart, Grace A. Parker, Joseph P. Harmon, Gail M. Atkinson, David M. Boore, Robert B. Darragh, Walter J. Silva, and Youssef M.A. Hashash. March 2017.
- PEER 2017/03** *NGA-East Ground-Motion Models for the U.S. Geological Survey National Seismic Hazard Maps*. Christine A. Goulet, Yousef Bozorgnia, Nicolas Kuehn, Linda Al Atik, Robert R. Youngs, Robert W. Graves, and Gail M. Atkinson. March 2017.
- PEER 2017/02** *U.S.–New Zealand–Japan Workshop: Liquefaction-Induced Ground Movements Effects, University of California, Berkeley, California, 2–4 November 2016*. Jonathan D. Bray, Ross W. Boulanger, Misko Cubrinovski, Kohji Tokimatsu, Steven L. Kramer, Thomas O'Rourke, Ellen Rathje, Russell A. Green, Peter K. Robinson, and Christine Z. Beyzaei. March 2017.
- PEER 2017/01** *2016 PEER Annual Report*. Khalid M. Mosalam, Amarnath Kasalanati, and Grace Kang. March 2017.
- PEER 2016/10** *Performance-Based Robust Nonlinear Seismic Analysis with Application to Reinforced Concrete Bridge Systems*. Xiao Ling and Khalid M. Mosalam. December 2016.
- PEER 2016/08** *Resilience of Critical Structures, Infrastructure, and Communities*. Gian Paolo Cimellaro, Ali Zamani-Noori, Omar Kamouh, Vesna Terzic, and Stephen A. Mahin. December 2016.
- PEER 2016/07** *Hybrid Simulation Theory for a Classical Nonlinear Dynamical System*. Paul L. Drazin and Sanjay Govindjee. September 2016.
- PEER 2016/06** *California Earthquake Early Warning System Benefit Study*. Laurie A. Johnson, Sharyl Rabinovici, Grace S. Kang, and Stephen A. Mahin. July 2016.
- PEER 2016/05** *Ground-Motion Prediction Equations for Arias Intensity Consistent with the NGA-West2 Ground-Motion Models*. Charlotte Abrahamson, Hao-Jun Michael Shi, and Brian Yang. July 2016.
- PEER 2016/04** *The Mw 6.0 South Napa Earthquake of August 24, 2014: A Wake-Up Call for Renewed Investment in Seismic Resilience Across California*. Prepared for the California Seismic Safety Commission, Laurie A. Johnson and Stephen A. Mahin. May 2016.
- PEER 2016/03** *Simulation Confidence in Tsunami-Driven Overland Flow*. Patrick Lynett. May 2016.
- PEER 2016/02** *Semi-Automated Procedure for Windowing time Series and Computing Fourier Amplitude Spectra for the NGA-West2 Database*. Tadahiro Kishida, Olga-Joan Ktenidou, Robert B. Darragh, and Walter J. Silva. May 2016.

- PEER 2016/01** *A Methodology for the Estimation of Kappa (κ) from Large Datasets: Example Application to Rock Sites in the NGA-East Database and Implications on Design Motions.* Olga-Joan Ktenidou, Norman A. Abrahamson, Robert B. Darragh, and Walter J. Silva. April 2016.
- PEER 2015/13** *Self-Centering Precast Concrete Dual-Steel-Shell Columns for Accelerated Bridge Construction: Seismic Performance, Analysis, and Design.* Gabriele Guerrini, José I. Restrepo, Athanassios Vervelidis, and Milena Massari. December 2015.
- PEER 2015/12** *Shear-Flexure Interaction Modeling for Reinforced Concrete Structural Walls and Columns under Reversed Cyclic Loading.* Kristijan Kolozvari, Kutay Orakcal, and John Wallace. December 2015.
- PEER 2015/11** *Selection and Scaling of Ground Motions for Nonlinear Response History Analysis of Buildings in Performance-Based Earthquake Engineering.* N. Simon Kwong and Anil K. Chopra. December 2015.
- PEER 2015/10** *Structural Behavior of Column-Bent Cap Beam-Box Girder Systems in Reinforced Concrete Bridges Subjected to Gravity and Seismic Loads. Part II: Hybrid Simulation and Post-Test Analysis.* Mohamed A. Moustafa and Khalid M. Mosalam. November 2015.
- PEER 2015/09** *Structural Behavior of Column-Bent Cap Beam-Box Girder Systems in Reinforced Concrete Bridges Subjected to Gravity and Seismic Loads. Part I: Pre-Test Analysis and Quasi-Static Experiments.* Mohamed A. Moustafa and Khalid M. Mosalam. September 2015.
- PEER 2015/08** *NGA-East: Adjustments to Median Ground-Motion Models for Center and Eastern North America.* August 2015.
- PEER 2015/07** *NGA-East: Ground-Motion Standard-Deviation Models for Central and Eastern North America.* Linda Al Atik. June 2015.
- PEER 2015/06** *Adjusting Ground-Motion Intensity Measures to a Reference Site for which $V_{S30} = 3000$ m/sec.* David M. Boore. May 2015.
- PEER 2015/05** *Hybrid Simulation of Seismic Isolation Systems Applied to an APR-1400 Nuclear Power Plant.* Andreas H. Schellenberg, Alireza Sarebanha, Matthew J. Schoettler, Gilberto Mosqueda, Gianmario Benzoni, and Stephen A. Mahin. April 2015.
- PEER 2015/04** *NGA-East: Median Ground-Motion Models for the Central and Eastern North America Region.* April 2015.
- PEER 2015/03** *Single Series Solution for the Rectangular Fiber-Reinforced Elastomeric Isolator Compression Modulus.* James M. Kelly and Niel C. Van Engelen. March 2015.
- PEER 2015/02** *A Full-Scale, Single-Column Bridge Bent Tested by Shake-Table Excitation.* Matthew J. Schoettler, José I. Restrepo, Gabriele Guerrini, David E. Duck, and Francesco Carrea. March 2015.
- PEER 2015/01** *Concrete Column Blind Prediction Contest 2010: Outcomes and Observations.* Vesna Terzic, Matthew J. Schoettler, José I. Restrepo, and Stephen A. Mahin. March 2015.
- PEER 2014/20** *Stochastic Modeling and Simulation of Near-Fault Ground Motions for Performance-Based Earthquake Engineering.* Mayssa Dabaghi and Armen Der Kiureghian. December 2014.
- PEER 2014/19** *Seismic Response of a Hybrid Fiber-Reinforced Concrete Bridge Column Detailed for Accelerated Bridge Construction.* Wilson Nguyen, William Trono, Marios Panagiotou, and Claudia P. Ostertag. December 2014.
- PEER 2014/18** *Three-Dimensional Beam-Truss Model for Reinforced Concrete Walls and Slabs Subjected to Cyclic Static or Dynamic Loading.* Yuan Lu, Marios Panagiotou, and Ioannis Koutromanos. December 2014.
- PEER 2014/17** *PEER NGA-East Database.* Christine A. Goulet, Tadahiro Kishida, Timothy D. Ancheta, Chris H. Cramer, Robert B. Darragh, Walter J. Silva, Youssef M.A. Hashash, Joseph Harmon, Jonathan P. Stewart, Katie E. Wooddell, and Robert R. Youngs. October 2014.
- PEER 2014/16** *Guidelines for Performing Hazard-Consistent One-Dimensional Ground Response Analysis for Ground Motion Prediction.* Jonathan P. Stewart, Kioumars Afshari, and Youssef M.A. Hashash. October 2014.
- PEER 2014/15** *NGA-East Regionalization Report: Comparison of Four Crustal Regions within Central and Eastern North America using Waveform Modeling and 5%-Damped Pseudo-Spectral Acceleration Response.* Jennifer Dreiling, Marius P. Isken, Walter D. Mooney, Martin C. Chapman, and Richard W. Godbee. October 2014.
- PEER 2014/14** *Scaling Relations between Seismic Moment and Rupture Area of Earthquakes in Stable Continental Regions.* Paul Somerville. August 2014.
- PEER 2014/13** *PEER Preliminary Notes and Observations on the August 24, 2014, South Napa Earthquake.* Grace S. Kang and Stephen A. Mahin, Editors. September 2014.
- PEER 2014/12** *Reference-Rock Site Conditions for Central and Eastern North America: Part II – Attenuation (Kappa) Definition.* Kenneth W. Campbell, Youssef M.A. Hashash, Byungmin Kim, Albert R. Kottke, Ellen M. Rathje, Walter J. Silva, and Jonathan P. Stewart. August 2014.

- PEER 2014/11** *Reference-Rock Site Conditions for Central and Eastern North America: Part I - Velocity Definition.* Youssef M.A. Hashash, Albert R. Kottke, Jonathan P. Stewart, Kenneth W. Campbell, Byungmin Kim, Ellen M. Rathje, Walter J. Silva, Sissy Nikolaou, and Cheryl Moss. August 2014.
- PEER 2014/10** *Evaluation of Collapse and Non-Collapse of Parallel Bridges Affected by Liquefaction and Lateral Spreading.* Benjamin Turner, Scott J. Brandenberg, and Jonathan P. Stewart. August 2014.
- PEER 2014/09** *PEER Arizona Strong-Motion Database and GMPEs Evaluation.* Tadahiro Kishida, Robert E. Kayen, Olga-Joan Ktenidou, Walter J. Silva, Robert B. Darragh, and Jennie Watson-Lamprey. June 2014.
- PEER 2014/08** *Unbonded Pretensioned Bridge Columns with Rocking Detail.* Jeffrey A. Schaefer, Bryan Kennedy, Marc O. Eberhard, and John F. Stanton. June 2014.
- PEER 2014/07** *Northridge 20 Symposium Summary Report: Impacts, Outcomes, and Next Steps.* May 2014.
- PEER 2014/06** *Report of the Tenth Planning Meeting of NEES/E-Defense Collaborative Research on Earthquake Engineering.* December 2013.
- PEER 2014/05** *Seismic Velocity Site Characterization of Thirty-One Chilean Seismometer Stations by Spectral Analysis of Surface Wave Dispersion.* Robert Kayen, Brad D. Carkin, Skye Corbet, Camilo Pinilla, Allan Ng, Edward Gorbis, and Christine Truong. April 2014.
- PEER 2014/04** *Effect of Vertical Acceleration on Shear Strength of Reinforced Concrete Columns.* Hyerin Lee and Khalid M. Mosalam. April 2014.
- PEER 2014/03** *Retest of Thirty-Year-Old Neoprene Isolation Bearings.* James M. Kelly and Niel C. Van Engelen. March 2014.
- PEER 2014/02** *Theoretical Development of Hybrid Simulation Applied to Plate Structures.* Ahmed A. Bakhaty, Khalid M. Mosalam, and Sanjay Govindjee. January 2014.
- PEER 2014/01** *Performance-Based Seismic Assessment of Skewed Bridges.* Peyman Kaviani, Farzin Zareian, and Ertugrul Taciroglu. January 2014.
- PEER 2013/26** *Urban Earthquake Engineering.* Proceedings of the U.S.-Iran Seismic Workshop. December 2013.
- PEER 2013/25** *Earthquake Engineering for Resilient Communities: 2013 PEER Internship Program Research Report Collection.* Heidi Tremayne (Editor), Stephen A. Mahin (Editor), Jorge Archbold Monterossa, Matt Brosman, Shelly Dean, Katherine deLaveaga, Curtis Fong, Donovan Holder, Rakeeb Khan, Elizabeth Jachens, David Lam, Daniela Martinez Lopez, Mara Minner, Geffen Oren, Julia Pavicic, Melissa Quinonez, Lorena Rodriguez, Sean Salazar, Kelli Slaven, Vivian Steyert, Jenny Taing, and Salvador Tena. December 2013.
- PEER 2013/24** *NGA-West2 Ground Motion Prediction Equations for Vertical Ground Motions.* September 2013.
- PEER 2013/23** *Coordinated Planning and Preparedness for Fire Following Major Earthquakes.* Charles Scawthorn. November 2013.
- PEER 2013/22** *GEM-PEER Task 3 Project: Selection of a Global Set of Ground Motion Prediction Equations.* Jonathan P. Stewart, John Douglas, Mohammad B. Javanbarg, Carola Di Alessandro, Yousef Bozorgnia, Norman A. Abrahamson, David M. Boore, Kenneth W. Campbell, Elise Delavaud, Mustafa Erdik, and Peter J. Stafford. December 2013.
- PEER 2013/21** *Seismic Design and Performance of Bridges with Columns on Rocking Foundations.* Grigorios Antonellis and Marios Panagiotou. September 2013.
- PEER 2013/20** *Experimental and Analytical Studies on the Seismic Behavior of Conventional and Hybrid Braced Frames.* Jiun-Wei Lai and Stephen A. Mahin. September 2013.
- PEER 2013/19** *Toward Resilient Communities: A Performance-Based Engineering Framework for Design and Evaluation of the Built Environment.* Michael William Mieler, Bozidar Stojadinovic, Robert J. Budnitz, Stephen A. Mahin, and Mary C. Comerio. September 2013.
- PEER 2013/18** *Identification of Site Parameters that Improve Predictions of Site Amplification.* Ellen M. Rathje and Sara Navidi. July 2013.
- PEER 2013/17** *Response Spectrum Analysis of Concrete Gravity Dams Including Dam-Water-Foundation Interaction.* Arnkjell Løkke and Anil K. Chopra. July 2013.
- PEER 2013/16** *Effect of Hoop Reinforcement Spacing on the Cyclic Response of Large Reinforced Concrete Special Moment Frame Beams.* Marios Panagiotou, Tea Visnjic, Grigorios Antonellis, Panagiotis Galanis, and Jack P. Moehle. June 2013.
- PEER 2013/15** *A Probabilistic Framework to Include the Effects of Near-Fault Directivity in Seismic Hazard Assessment.* Shrey Kumar Shahi, Jack W. Baker. October 2013.

- PEER 2013/14** *Hanging-Wall Scaling using Finite-Fault Simulations*. Jennifer L. Donahue and Norman A. Abrahamson. September 2013.
- PEER 2013/13** *Semi-Empirical Nonlinear Site Amplification and its Application in NEHRP Site Factors*. Jonathan P. Stewart and Emel Seyhan. November 2013.
- PEER 2013/12** *Nonlinear Horizontal Site Response for the NGA-West2 Project*. Ronnie Kamai, Norman A. Abramson, Walter J. Silva. May 2013.
- PEER 2013/11** *Epistemic Uncertainty for NGA-West2 Models*. Linda Al Atik and Robert R. Youngs. May 2013.
- PEER 2013/10** *NGA-West 2 Models for Ground-Motion Directionality*. Shrey K. Shahi and Jack W. Baker. May 2013.
- PEER 2013/09** *Final Report of the NGA-West2 Directivity Working Group*. Paul Spudich, Jeffrey R. Bayless, Jack W. Baker, Brian S.J. Chiou, Badie Rowshandel, Shrey Shahi, and Paul Somerville. May 2013.
- PEER 2013/08** *NGA-West2 Model for Estimating Average Horizontal Values of Pseudo-Absolute Spectral Accelerations Generated by Crustal Earthquakes*. I. M. Idriss. May 2013.
- PEER 2013/07** *Update of the Chiou and Youngs NGA Ground Motion Model for Average Horizontal Component of Peak Ground Motion and Response Spectra*. Brian Chiou and Robert Youngs. May 2013.
- PEER 2013/06** *NGA-West2 Campbell-Bozorgnia Ground Motion Model for the Horizontal Components of PGA, PGV, and 5%-Damped Elastic Pseudo-Acceleration Response Spectra for Periods Ranging from 0.01 to 10 sec*. Kenneth W. Campbell and Yousef Bozorgnia. May 2013.
- PEER 2013/05** *NGA-West 2 Equations for Predicting Response Spectral Accelerations for Shallow Crustal Earthquakes*. David M. Boore, Jonathan P. Stewart, Emel Seyhan, and Gail M. Atkinson. May 2013.
- PEER 2013/04** *Update of the AS08 Ground-Motion Prediction Equations Based on the NGA-West2 Data Set*. Norman Abrahamson, Walter Silva, and Ronnie Kamai. May 2013.
- PEER 2013/03** *PEER NGA-West2 Database*. Timothy D. Ancheta, Robert B. Darragh, Jonathan P. Stewart, Emel Seyhan, Walter J. Silva, Brian S.J. Chiou, Katie E. Wooddell, Robert W. Graves, Albert R. Kottke, David M. Boore, Tadahiro Kishida, and Jennifer L. Donahue. May 2013.
- PEER 2013/02** *Hybrid Simulation of the Seismic Response of Squat Reinforced Concrete Shear Walls*. Catherine A. Whyte and Bozidar Stojadinovic. May 2013.
- PEER 2013/01** *Housing Recovery in Chile: A Qualitative Mid-program Review*. Mary C. Comerio. February 2013.
- PEER 2012/08** *Guidelines for Estimation of Shear Wave Velocity*. Bernard R. Wair, Jason T. DeJong, and Thomas Shantz. December 2012.
- PEER 2012/07** *Earthquake Engineering for Resilient Communities: 2012 PEER Internship Program Research Report Collection*. Heidi Tremayne (Editor), Stephen A. Mahin (Editor), Collin Anderson, Dustin Cook, Michael Erceg, Carlos Esparza, Jose Jimenez, Dorian Krausz, Andrew Lo, Stephanie Lopez, Nicole McCurdy, Paul Shipman, Alexander Strum, Eduardo Vega. December 2012.
- PEER 2012/06** *Fragilities for Precarious Rocks at Yucca Mountain*. Matthew D. Purvance, Rasool Anooshehpour, and James N. Brune. December 2012.
- PEER 2012/05** *Development of Simplified Analysis Procedure for Piles in Laterally Spreading Layered Soils*. Christopher R. McGann, Pedro Arduino, and Peter Mackenzie-Helnwein. December 2012.
- PEER 2012/04** *Unbonded Pre-Tensioned Columns for Bridges in Seismic Regions*. Phillip M. Davis, Todd M. Janes, Marc O. Eberhard, and John F. Stanton. December 2012.
- PEER 2012/03** *Experimental and Analytical Studies on Reinforced Concrete Buildings with Seismically Vulnerable Beam-Column Joints*. Sangjoon Park and Khalid M. Mosalam. October 2012.
- PEER 2012/02** *Seismic Performance of Reinforced Concrete Bridges Allowed to Uplift during Multi-Directional Excitation*. Andres Oscar Espinoza and Stephen A. Mahin. July 2012.
- PEER 2012/01** *Spectral Damping Scaling Factors for Shallow Crustal Earthquakes in Active Tectonic Regions*. Sanaz Rezaeian, Yousef Bozorgnia, I. M. Idriss, Kenneth Campbell, Norman Abrahamson, and Walter Silva. July 2012.
- PEER 2011/10** *Earthquake Engineering for Resilient Communities: 2011 PEER Internship Program Research Report Collection*. Heidi Faison and Stephen A. Mahin, Editors. December 2011.
- PEER 2011/09** *Calibration of Semi-Stochastic Procedure for Simulating High-Frequency Ground Motions*. Jonathan P. Stewart, Emel Seyhan, and Robert W. Graves. December 2011.
- PEER 2011/08** *Water Supply in regard to Fire Following Earthquake*. Charles Scawthorn. November 2011.

- PEER 2011/07** *Seismic Risk Management in Urban Areas*. Proceedings of a U.S.-Iran-Turkey Seismic Workshop. September 2011.
- PEER 2011/06** *The Use of Base Isolation Systems to Achieve Complex Seismic Performance Objectives*. Troy A. Morgan and Stephen A. Mahin. July 2011.
- PEER 2011/05** *Case Studies of the Seismic Performance of Tall Buildings Designed by Alternative Means*. Task 12 Report for the Tall Buildings Initiative. Jack Moehle, Yousef Bozorgnia, Nirmal Jayaram, Pierson Jones, Mohsen Rahnama, Nilesh Shome, Zeynep Tuna, John Wallace, Tony Yang, and Farzin Zareian. July 2011.
- PEER 2011/04** *Recommended Design Practice for Pile Foundations in Laterally Spreading Ground*. Scott A. Ashford, Ross W. Boulanger, and Scott J. Brandenberg. June 2011.
- PEER 2011/03** *New Ground Motion Selection Procedures and Selected Motions for the PEER Transportation Research Program*. Jack W. Baker, Ting Lin, Shrey K. Shahi, and Nirmal Jayaram. March 2011.
- PEER 2011/02** *A Bayesian Network Methodology for Infrastructure Seismic Risk Assessment and Decision Support*. Michelle T. Bensi, Armen Der Kiureghian, and Daniel Straub. March 2011.
- PEER 2011/01** *Demand Fragility Surfaces for Bridges in Liquefied and Laterally Spreading Ground*. Scott J. Brandenberg, Jian Zhang, Pirooz Kashighandi, Yili Huo, and Minxing Zhao. March 2011.
- PEER 2010/05** *Guidelines for Performance-Based Seismic Design of Tall Buildings*. Developed by the Tall Buildings Initiative. November 2010.
- PEER 2010/04** *Application Guide for the Design of Flexible and Rigid Bus Connections between Substation Equipment Subjected to Earthquakes*. Jean-Bernard Dastous and Armen Der Kiureghian. September 2010.
- PEER 2010/03** *Shear Wave Velocity as a Statistical Function of Standard Penetration Test Resistance and Vertical Effective Stress at Caltrans Bridge Sites*. Scott J. Brandenberg, Naresh Bellana, and Thomas Shantz. June 2010.
- PEER 2010/02** *Stochastic Modeling and Simulation of Ground Motions for Performance-Based Earthquake Engineering*. Sanaz Rezaeian and Armen Der Kiureghian. June 2010.
- PEER 2010/01** *Structural Response and Cost Characterization of Bridge Construction Using Seismic Performance Enhancement Strategies*. Ady Aviram, Božidar Stojadinović, Gustavo J. Parra-Montesinos, and Kevin R. Mackie. March 2010.
- PEER 2009/03** *The Integration of Experimental and Simulation Data in the Study of Reinforced Concrete Bridge Systems Including Soil-Foundation-Structure Interaction*. Matthew Dryden and Gregory L. Fenves. November 2009.
- PEER 2009/02** *Improving Earthquake Mitigation through Innovations and Applications in Seismic Science, Engineering, Communication, and Response*. Proceedings of a U.S.-Iran Seismic Workshop. October 2009.
- PEER 2009/01** *Evaluation of Ground Motion Selection and Modification Methods: Predicting Median Interstory Drift Response of Buildings*. Curt B. Haselton, Editor. June 2009.
- PEER 2008/10** *Technical Manual for Strata*. Albert R. Kottke and Ellen M. Rathje. February 2009.
- PEER 2008/09** *NGA Model for Average Horizontal Component of Peak Ground Motion and Response Spectra*. Brian S.-J. Chiou and Robert R. Youngs. November 2008.
- PEER 2008/08** *Toward Earthquake-Resistant Design of Concentrically Braced Steel Structures*. Patxi Uriz and Stephen A. Mahin. November 2008.
- PEER 2008/07** *Using OpenSees for Performance-Based Evaluation of Bridges on Liquefiable Soils*. Stephen L. Kramer, Pedro Arduino, and HyungSuk Shin. November 2008.
- PEER 2008/06** *Shaking Table Tests and Numerical Investigation of Self-Centering Reinforced Concrete Bridge Columns*. Hyung IL Jeong, Junichi Sakai, and Stephen A. Mahin. September 2008.
- PEER 2008/05** *Performance-Based Earthquake Engineering Design Evaluation Procedure for Bridge Foundations Undergoing Liquefaction-Induced Lateral Ground Displacement*. Christian A. Ledezma and Jonathan D. Bray. August 2008.
- PEER 2008/04** *Benchmarking of Nonlinear Geotechnical Ground Response Analysis Procedures*. Jonathan P. Stewart, Annie On-Lei Kwok, Youssef M. A. Hashash, Neven Matasovic, Robert Pyke, Zhiliang Wang, and Zhaohui Yang. August 2008.
- PEER 2008/03** *Guidelines for Nonlinear Analysis of Bridge Structures in California*. Ady Aviram, Kevin R. Mackie, and Božidar Stojadinović. August 2008.
- PEER 2008/02** *Treatment of Uncertainties in Seismic-Risk Analysis of Transportation Systems*. Evangelos Stergiou and Anne S. Kiremidjian. July 2008.
- PEER 2008/01** *Seismic Performance Objectives for Tall Buildings*. William T. Holmes, Charles Kircher, William Petak, and Nabih Youssef. August 2008.

- PEER 2007/12** *An Assessment to Benchmark the Seismic Performance of a Code-Conforming Reinforced Concrete Moment-Frame Building.* Curt Haselton, Christine A. Goulet, Judith Mitrani-Reiser, James L. Beck, Gregory G. Deierlein, Keith A. Porter, Jonathan P. Stewart, and Ertugrul Taciroglu. August 2008.
- PEER 2007/11** *Bar Buckling in Reinforced Concrete Bridge Columns.* Wayne A. Brown, Dawn E. Lehman, and John F. Stanton. February 2008.
- PEER 2007/10** *Computational Modeling of Progressive Collapse in Reinforced Concrete Frame Structures.* Mohamed M. Talaat and Khalid M. Mosalam. May 2008.
- PEER 2007/09** *Integrated Probabilistic Performance-Based Evaluation of Benchmark Reinforced Concrete Bridges.* Kevin R. Mackie, John-Michael Wong, and Božidar Stojadinović. January 2008.
- PEER 2007/08** *Assessing Seismic Collapse Safety of Modern Reinforced Concrete Moment-Frame Buildings.* Curt B. Haselton and Gregory G. Deierlein. February 2008.
- PEER 2007/07** *Performance Modeling Strategies for Modern Reinforced Concrete Bridge Columns.* Michael P. Berry and Marc O. Eberhard. April 2008.
- PEER 2007/06** *Development of Improved Procedures for Seismic Design of Buried and Partially Buried Structures.* Linda Al Atik and Nicholas Sitar. June 2007.
- PEER 2007/05** *Uncertainty and Correlation in Seismic Risk Assessment of Transportation Systems.* Renee G. Lee and Anne S. Kiremidjian. July 2007.
- PEER 2007/04** *Numerical Models for Analysis and Performance-Based Design of Shallow Foundations Subjected to Seismic Loading.* Sivapalan Gajan, Tara C. Hutchinson, Bruce L. Kutter, Prishati Raychowdhury, José A. Ugalde, and Jonathan P. Stewart. May 2008.
- PEER 2007/03** *Beam-Column Element Model Calibrated for Predicting Flexural Response Leading to Global Collapse of RC Frame Buildings.* Curt B. Haselton, Abbie B. Liel, Sarah Taylor Lange, and Gregory G. Deierlein. May 2008.
- PEER 2007/02** *Campbell-Bozorgnia NGA Ground Motion Relations for the Geometric Mean Horizontal Component of Peak and Spectral Ground Motion Parameters.* Kenneth W. Campbell and Yousef Bozorgnia. May 2007.
- PEER 2007/01** *Boore-Atkinson NGA Ground Motion Relations for the Geometric Mean Horizontal Component of Peak and Spectral Ground Motion Parameters.* David M. Boore and Gail M. Atkinson. May 2007.
- PEER 2006/12** *Societal Implications of Performance-Based Earthquake Engineering.* Peter J. May. May 2007.
- PEER 2006/11** *Probabilistic Seismic Demand Analysis Using Advanced Ground Motion Intensity Measures, Attenuation Relationships, and Near-Fault Effects.* Polsak Tothong and C. Allin Cornell. March 2007.
- PEER 2006/10** *Application of the PEER PBEE Methodology to the I-880 Viaduct.* Sashi Kunnath. February 2007.
- PEER 2006/09** *Quantifying Economic Losses from Travel Forgone Following a Large Metropolitan Earthquake.* James Moore, Sungbin Cho, Yue Yue Fan, and Stuart Werner. November 2006.
- PEER 2006/08** *Vector-Valued Ground Motion Intensity Measures for Probabilistic Seismic Demand Analysis.* Jack W. Baker and C. Allin Cornell. October 2006.
- PEER 2006/07** *Analytical Modeling of Reinforced Concrete Walls for Predicting Flexural and Coupled-Shear-Flexural Responses.* Kutay Orakcal, Leonardo M. Massone, and John W. Wallace. October 2006.
- PEER 2006/06** *Nonlinear Analysis of a Soil-Drilled Pier System under Static and Dynamic Axial Loading.* Gang Wang and Nicholas Sitar. November 2006.
- PEER 2006/05** *Advanced Seismic Assessment Guidelines.* Paolo Bazzurro, C. Allin Cornell, Charles Menun, Maziar Motahari, and Nicolas Luco. September 2006.
- PEER 2006/04** *Probabilistic Seismic Evaluation of Reinforced Concrete Structural Components and Systems.* Tae Hyung Lee and Khalid M. Mosalam. August 2006.
- PEER 2006/03** *Performance of Lifelines Subjected to Lateral Spreading.* Scott A. Ashford and Teerawut Juirnarongrit. July 2006.
- PEER 2006/02** *Pacific Earthquake Engineering Research Center Highway Demonstration Project.* Anne Kiremidjian, James Moore, Yue Yue Fan, Nesrin Basoz, Ozgur Yazali, and Meredith Williams. April 2006.
- PEER 2006/01** *Bracing Berkeley. A Guide to Seismic Safety on the UC Berkeley Campus.* Mary C. Comerio, Stephen Tobriner, and Ariane Fehrenkamp. January 2006.
- PEER 2005/17** *Earthquake Simulation Tests on Reducing Residual Displacements of Reinforced Concrete Bridges.* Junichi Sakai, Stephen A Mahin, and Andres Espinoza. December 2005.

- PEER 2005/16** *Seismic Response and Reliability of Electrical Substation Equipment and Systems.* Junho Song, Armen Der Kiureghian, and Jerome L. Sackman. April 2006.
- PEER 2005/15** *CPT-Based Probabilistic Assessment of Seismic Soil Liquefaction Initiation.* R. E. S. Moss, R. B. Seed, R. E. Kayen, J. P. Stewart, and A. Der Kiureghian. April 2006.
- PEER 2005/14** *Workshop on Modeling of Nonlinear Cyclic Load-Deformation Behavior of Shallow Foundations.* Bruce L. Kutter, Geoffrey Martin, Tara Hutchinson, Chad Harden, Sivapalan Gajan, and Justin Phalen. March 2006.
- PEER 2005/13** *Stochastic Characterization and Decision Bases under Time-Dependent Aftershock Risk in Performance-Based Earthquake Engineering.* Gee Liek Yeo and C. Allin Cornell. July 2005.
- PEER 2005/12** *PEER Testbed Study on a Laboratory Building: Exercising Seismic Performance Assessment.* Mary C. Comerio, Editor. November 2005.
- PEER 2005/11** *Van Nuys Hotel Building Testbed Report: Exercising Seismic Performance Assessment.* Helmut Krawinkler, Editor. October 2005.
- PEER 2005/10** *First NEES/E-Defense Workshop on Collapse Simulation of Reinforced Concrete Building Structures.* September 2005.
- PEER 2005/09** *Test Applications of Advanced Seismic Assessment Guidelines.* Joe Maffei, Karl Telleen, Danya Mohr, William Holmes, and Yuki Nakayama. August 2006.
- PEER 2005/08** *Damage Accumulation in Lightly Confined Reinforced Concrete Bridge Columns.* R. Tyler Ranf, Jared M. Nelson, Zach Price, Marc O. Eberhard, and John F. Stanton. April 2006.
- PEER 2005/07** *Experimental and Analytical Studies on the Seismic Response of Freestanding and Anchored Laboratory Equipment.* Dimitrios Konstantinidis and Nicos Makris. January 2005.
- PEER 2005/06** *Global Collapse of Frame Structures under Seismic Excitations.* Luis F. Ibarra and Helmut Krawinkler. September 2005.
- PEER 2005/05** *Performance Characterization of Bench- and Shelf-Mounted Equipment.* Samit Ray Chaudhuri and Tara C. Hutchinson. May 2006.
- PEER 2005/04** *Numerical Modeling of the Nonlinear Cyclic Response of Shallow Foundations.* Chad Harden, Tara Hutchinson, Geoffrey R. Martin, and Bruce L. Kutter. August 2005.
- PEER 2005/03** *A Taxonomy of Building Components for Performance-Based Earthquake Engineering.* Keith A. Porter. September 2005.
- PEER 2005/02** *Fragility Basis for California Highway Overpass Bridge Seismic Decision Making.* Kevin R. Mackie and Božidar Stojadinović. June 2005.
- PEER 2005/01** *Empirical Characterization of Site Conditions on Strong Ground Motion.* Jonathan P. Stewart, Yoojoong Choi, and Robert W. Graves. June 2005.
- PEER 2004/09** *Electrical Substation Equipment Interaction: Experimental Rigid Conductor Studies.* Christopher Stearns and André Filiatrault. February 2005.
- PEER 2004/08** *Seismic Qualification and Fragility Testing of Line Break 550-kV Disconnect Switches.* Shakhzod M. Takhirov, Gregory L. Fenves, and Eric Fujisaki. January 2005.
- PEER 2004/07** *Ground Motions for Earthquake Simulator Qualification of Electrical Substation Equipment.* Shakhzod M. Takhirov, Gregory L. Fenves, Eric Fujisaki, and Don Clyde. January 2005.
- PEER 2004/06** *Performance-Based Regulation and Regulatory Regimes.* Peter J. May and Chris Koski. September 2004.
- PEER 2004/05** *Performance-Based Seismic Design Concepts and Implementation: Proceedings of an International Workshop.* Peter Fajfar and Helmut Krawinkler, Editors. September 2004.
- PEER 2004/04** *Seismic Performance of an Instrumented Tilt-up Wall Building.* James C. Anderson and Vitelmo V. Bertero. July 2004.
- PEER 2004/03** *Evaluation and Application of Concrete Tilt-up Assessment Methodologies.* Timothy Graf and James O. Malley. October 2004.
- PEER 2004/02** *Analytical Investigations of New Methods for Reducing Residual Displacements of Reinforced Concrete Bridge Columns.* Junichi Sakai and Stephen A. Mahin. August 2004.
- PEER 2004/01** *Seismic Performance of Masonry Buildings and Design Implications.* Kerri Anne Taeko Tokoro, James C. Anderson, and Vitelmo V. Bertero. February 2004.

- PEER 2003/18** *Performance Models for Flexural Damage in Reinforced Concrete Columns.* Michael Berry and Marc Eberhard. August 2003.
- PEER 2003/17** *Predicting Earthquake Damage in Older Reinforced Concrete Beam-Column Joints.* Catherine Pagni and Laura Lowes. October 2004.
- PEER 2003/16** *Seismic Demands for Performance-Based Design of Bridges.* Kevin Mackie and Božidar Stojadinović. August 2003.
- PEER 2003/15** *Seismic Demands for Nondeteriorating Frame Structures and Their Dependence on Ground Motions.* Ricardo Antonio Medina and Helmut Krawinkler. May 2004.
- PEER 2003/14** *Finite Element Reliability and Sensitivity Methods for Performance-Based Earthquake Engineering.* Terje Haukaas and Armen Der Kiureghian. April 2004.
- PEER 2003/13** *Effects of Connection Hysteretic Degradation on the Seismic Behavior of Steel Moment-Resisting Frames.* Janise E. Rodgers and Stephen A. Mahin. March 2004.
- PEER 2003/12** *Implementation Manual for the Seismic Protection of Laboratory Contents: Format and Case Studies.* William T. Holmes and Mary C. Comerio. October 2003.
- PEER 2003/11** *Fifth U.S.-Japan Workshop on Performance-Based Earthquake Engineering Methodology for Reinforced Concrete Building Structures.* February 2004.
- PEER 2003/10** *A Beam-Column Joint Model for Simulating the Earthquake Response of Reinforced Concrete Frames.* Laura N. Lowes, Nilanjan Mitra, and Arash Altoontash. February 2004.
- PEER 2003/09** *Sequencing Repairs after an Earthquake: An Economic Approach.* Marco Casari and Simon J. Wilkie. April 2004.
- PEER 2003/08** *A Technical Framework for Probability-Based Demand and Capacity Factor Design (DCFD) Seismic Formats.* Fatemeh Jalayer and C. Allin Cornell. November 2003.
- PEER 2003/07** *Uncertainty Specification and Propagation for Loss Estimation Using FOSM Methods.* Jack W. Baker and C. Allin Cornell. September 2003.
- PEER 2003/06** *Performance of Circular Reinforced Concrete Bridge Columns under Bidirectional Earthquake Loading.* Mahmoud M. Hachem, Stephen A. Mahin, and Jack P. Moehle. February 2003.
- PEER 2003/05** *Response Assessment for Building-Specific Loss Estimation.* Eduardo Miranda and Shahram Taghavi. September 2003.
- PEER 2003/04** *Experimental Assessment of Columns with Short Lap Splices Subjected to Cyclic Loads.* Murat Melek, John W. Wallace, and Joel Conte. April 2003.
- PEER 2003/03** *Probabilistic Response Assessment for Building-Specific Loss Estimation.* Eduardo Miranda and Hesameddin Aslani. September 2003.
- PEER 2003/02** *Software Framework for Collaborative Development of Nonlinear Dynamic Analysis Program.* Jun Peng and Kincho H. Law. September 2003.
- PEER 2003/01** *Shake Table Tests and Analytical Studies on the Gravity Load Collapse of Reinforced Concrete Frames.* Kenneth John Elwood and Jack P. Moehle. November 2003.
- PEER 2002/24** *Performance of Beam to Column Bridge Joints Subjected to a Large Velocity Pulse.* Natalie Gibson, André Filiatrault, and Scott A. Ashford. April 2002.
- PEER 2002/23** *Effects of Large Velocity Pulses on Reinforced Concrete Bridge Columns.* Greg L. Orozco and Scott A. Ashford. April 2002.
- PEER 2002/22** *Characterization of Large Velocity Pulses for Laboratory Testing.* Kenneth E. Cox and Scott A. Ashford. April 2002.
- PEER 2002/21** *Fourth U.S.-Japan Workshop on Performance-Based Earthquake Engineering Methodology for Reinforced Concrete Building Structures.* December 2002.
- PEER 2002/20** *Barriers to Adoption and Implementation of PBEE Innovations.* Peter J. May. August 2002.
- PEER 2002/19** *Economic-Engineered Integrated Models for Earthquakes: Socioeconomic Impacts.* Peter Gordon, James E. Moore II, and Harry W. Richardson. July 2002.
- PEER 2002/18** *Assessment of Reinforced Concrete Building Exterior Joints with Substandard Details.* Chris P. Pantelides, Jon Hansen, Justin Nadauld, and Lawrence D. Reaveley. May 2002.
- PEER 2002/17** *Structural Characterization and Seismic Response Analysis of a Highway Overcrossing Equipped with Elastomeric Bearings and Fluid Dampers: A Case Study.* Nicos Makris and Jian Zhang. November 2002.

- PEER 2002/16** *Estimation of Uncertainty in Geotechnical Properties for Performance-Based Earthquake Engineering.* Allen L. Jones, Steven L. Kramer, and Pedro Arduino. December 2002.
- PEER 2002/15** *Seismic Behavior of Bridge Columns Subjected to Various Loading Patterns.* Asadollah Esmaeily-Gh. and Yan Xiao. December 2002.
- PEER 2002/14** *Inelastic Seismic Response of Extended Pile Shaft Supported Bridge Structures.* T.C. Hutchinson, R.W. Boulanger, Y.H. Chai, and I.M. Idriss. December 2002.
- PEER 2002/13** *Probabilistic Models and Fragility Estimates for Bridge Components and Systems.* Paolo Gardoni, Armen Der Kiureghian, and Khalid M. Mosalam. June 2002.
- PEER 2002/12** *Effects of Fault Dip and Slip Rake on Near-Source Ground Motions: Why Chi-Chi Was a Relatively Mild M7.6 Earthquake.* Brad T. Aagaard, John F. Hall, and Thomas H. Heaton. December 2002.
- PEER 2002/11** *Analytical and Experimental Study of Fiber-Reinforced Strip Isolators.* James M. Kelly and Shakhzod M. Takhirov. September 2002.
- PEER 2002/10** *Centrifuge Modeling of Settlement and Lateral Spreading with Comparisons to Numerical Analyses.* Sivapalan Gajan and Bruce L. Kutter. January 2003.
- PEER 2002/09** *Documentation and Analysis of Field Case Histories of Seismic Compression during the 1994 Northridge, California, Earthquake.* Jonathan P. Stewart, Patrick M. Smith, Daniel H. Whang, and Jonathan D. Bray. October 2002.
- PEER 2002/08** *Component Testing, Stability Analysis and Characterization of Buckling-Restrained Unbonded Braces™.* Cameron Black, Nicos Makris, and Ian Aiken. September 2002.
- PEER 2002/07** *Seismic Performance of Pile-Wharf Connections.* Charles W. Roeder, Robert Graff, Jennifer Soderstrom, and Jun Han Yoo. December 2001.
- PEER 2002/06** *The Use of Benefit-Cost Analysis for Evaluation of Performance-Based Earthquake Engineering Decisions.* Richard O. Zerbe and Anthony Falit-Baiamonte. September 2001.
- PEER 2002/05** *Guidelines, Specifications, and Seismic Performance Characterization of Nonstructural Building Components and Equipment.* André Filiatrault, Constantin Christopoulos, and Christopher Stearns. September 2001.
- PEER 2002/04** *Consortium of Organizations for Strong-Motion Observation Systems and the Pacific Earthquake Engineering Research Center Lifelines Program: Invited Workshop on Archiving and Web Dissemination of Geotechnical Data, 4-5 October 2001.* September 2002.
- PEER 2002/03** *Investigation of Sensitivity of Building Loss Estimates to Major Uncertain Variables for the Van Nuys Testbed.* Keith A. Porter, James L. Beck, and Rustem V. Shaikhutdinov. August 2002.
- PEER 2002/02** *The Third U.S.-Japan Workshop on Performance-Based Earthquake Engineering Methodology for Reinforced Concrete Building Structures.* July 2002.
- PEER 2002/01** *Nonstructural Loss Estimation: The UC Berkeley Case Study.* Mary C. Comerio and John C. Stallmeyer. December 2001.
- PEER 2001/16** *Statistics of SDF-System Estimate of Roof Displacement for Pushover Analysis of Buildings.* Anil K. Chopra, Rakesh K. Goel, and Chatpan Chintanapakdee. December 2001.
- PEER 2001/15** *Damage to Bridges during the 2001 Nisqually Earthquake.* R. Tyler Ranf, Marc O. Eberhard, and Michael P. Berry. November 2001.
- PEER 2001/14** *Rocking Response of Equipment Anchored to a Base Foundation.* Nicos Makris and Cameron J. Black. September 2001.
- PEER 2001/13** *Modeling Soil Liquefaction Hazards for Performance-Based Earthquake Engineering.* Steven L. Kramer and Ahmed-W. Elgamal. February 2001.
- PEER 2001/12** *Development of Geotechnical Capabilities in OpenSees.* Boris Jeremić. September 2001.
- PEER 2001/11** *Analytical and Experimental Study of Fiber-Reinforced Elastomeric Isolators.* James M. Kelly and Shakhzod M. Takhirov. September 2001.
- PEER 2001/10** *Amplification Factors for Spectral Acceleration in Active Regions.* Jonathan P. Stewart, Andrew H. Liu, Yoojoong Choi, and Mehmet B. Baturay. December 2001.
- PEER 2001/09** *Ground Motion Evaluation Procedures for Performance-Based Design.* Jonathan P. Stewart, Shyh-Jeng Chiou, Jonathan D. Bray, Robert W. Graves, Paul G. Somerville, and Norman A. Abrahamson. September 2001.
- PEER 2001/08** *Experimental and Computational Evaluation of Reinforced Concrete Bridge Beam-Column Connections for Seismic Performance.* Clay J. Naito, Jack P. Moehle, and Khalid M. Mosalam. November 2001.

- PEER 2001/07** *The Rocking Spectrum and the Shortcomings of Design Guidelines.* Nicos Makris and Dimitrios Konstantinidis. August 2001.
- PEER 2001/06** *Development of an Electrical Substation Equipment Performance Database for Evaluation of Equipment Fragilities.* Thalia Agnanos. April 1999.
- PEER 2001/05** *Stiffness Analysis of Fiber-Reinforced Elastomeric Isolators.* Hsiang-Chuan Tsai and James M. Kelly. May 2001.
- PEER 2001/04** *Organizational and Societal Considerations for Performance-Based Earthquake Engineering.* Peter J. May. April 2001.
- PEER 2001/03** *A Modal Pushover Analysis Procedure to Estimate Seismic Demands for Buildings: Theory and Preliminary Evaluation.* Anil K. Chopra and Rakesh K. Goel. January 2001.
- PEER 2001/02** *Seismic Response Analysis of Highway Overcrossings Including Soil-Structure Interaction.* Jian Zhang and Nicos Makris. March 2001.
- PEER 2001/01** *Experimental Study of Large Seismic Steel Beam-to-Column Connections.* Egor P. Popov and Shakhzod M. Takhirov. November 2000.
- PEER 2000/10** *The Second U.S.-Japan Workshop on Performance-Based Earthquake Engineering Methodology for Reinforced Concrete Building Structures.* March 2000.
- PEER 2000/09** *Structural Engineering Reconnaissance of the August 17, 1999 Earthquake: Kocaeli (Izmit), Turkey.* Halil Sezen, Kenneth J. Elwood, Andrew S. Whittaker, Khalid Mosalam, John J. Wallace, and John F. Stanton. December 2000.
- PEER 2000/08** *Behavior of Reinforced Concrete Bridge Columns Having Varying Aspect Ratios and Varying Lengths of Confinement.* Anthony J. Calderone, Dawn E. Lehman, and Jack P. Moehle. January 2001.
- PEER 2000/07** *Cover-Plate and Flange-Plate Reinforced Steel Moment-Resisting Connections.* Taejin Kim, Andrew S. Whittaker, Amir S. Gilani, Vitelmo V. Bertero, and Shakhzod M. Takhirov. September 2000.
- PEER 2000/06** *Seismic Evaluation and Analysis of 230-kV Disconnect Switches.* Amir S. J. Gilani, Andrew S. Whittaker, Gregory L. Fenves, Chun-Hao Chen, Henry Ho, and Eric Fujisaki. July 2000.
- PEER 2000/05** *Performance-Based Evaluation of Exterior Reinforced Concrete Building Joints for Seismic Excitation.* Chandra Clyde, Chris P. Pantelides, and Lawrence D. Reaveley. July 2000.
- PEER 2000/04** *An Evaluation of Seismic Energy Demand: An Attenuation Approach.* Chung-Che Chou and Chia-Ming Uang. July 1999.
- PEER 2000/03** *Framing Earthquake Retrofitting Decisions: The Case of Hillside Homes in Los Angeles.* Detlof von Winterfeldt, Nels Roselund, and Alicia Kitsuse. March 2000.
- PEER 2000/02** *U.S.-Japan Workshop on the Effects of Near-Field Earthquake Shaking.* Andrew Whittaker, Editor. July 2000.
- PEER 2000/01** *Further Studies on Seismic Interaction in Interconnected Electrical Substation Equipment.* Armen Der Kiureghian, Kee-Jeung Hong, and Jerome L. Sackman. November 1999.
- PEER 1999/14** *Seismic Evaluation and Retrofit of 230-kV Porcelain Transformer Bushings.* Amir S. Gilani, Andrew S. Whittaker, Gregory L. Fenves, and Eric Fujisaki. December 1999.
- PEER 1999/13** *Building Vulnerability Studies: Modeling and Evaluation of Tilt-up and Steel Reinforced Concrete Buildings.* John W. Wallace, Jonathan P. Stewart, and Andrew S. Whittaker, Editors. December 1999.
- PEER 1999/12** *Rehabilitation of Nonductile RC Frame Building Using Encasement Plates and Energy-Dissipating Devices.* Mehrdad Sasani, Vitelmo V. Bertero, James C. Anderson. December 1999.
- PEER 1999/11** *Performance Evaluation Database for Concrete Bridge Components and Systems under Simulated Seismic Loads.* Yael D. Hose and Frieder Seible. November 1999.
- PEER 1999/10** *U.S.-Japan Workshop on Performance-Based Earthquake Engineering Methodology for Reinforced Concrete Building Structures.* December 1999.
- PEER 1999/09** *Performance Improvement of Long Period Building Structures Subjected to Severe Pulse-Type Ground Motions.* James C. Anderson, Vitelmo V. Bertero, and Raul Bertero. October 1999.
- PEER 1999/08** *Envelopes for Seismic Response Vectors.* Charles Menun and Armen Der Kiureghian. July 1999.
- PEER 1999/07** *Documentation of Strengths and Weaknesses of Current Computer Analysis Methods for Seismic Performance of Reinforced Concrete Members.* William F. Cofer. November 1999.
- PEER 1999/06** *Rocking Response and Overturning of Anchored Equipment under Seismic Excitations.* Nicos Makris and Jian Zhang. November 1999.

- PEER 1999/05** *Seismic Evaluation of 550 kV Porcelain Transformer Bushings.* Amir S. Gilani, Andrew S. Whittaker, Gregory L. Fenves, and Eric Fujisaki. October 1999.
- PEER 1999/04** *Adoption and Enforcement of Earthquake Risk-Reduction Measures.* Peter J. May, Raymond J. Burby, T. Jens Feeley, and Robert Wood. August 1999.
- PEER 1999/03** *Task 3 Characterization of Site Response General Site Categories.* Adrian Rodriguez-Marek, Jonathan D. Bray and Norman Abrahamson. February 1999.
- PEER 1999/02** *Capacity-Demand-Diagram Methods for Estimating Seismic Deformation of Inelastic Structures: SDF Systems.* Anil K. Chopra and Rakesh Goel. April 1999.
- PEER 1999/01** *Interaction in Interconnected Electrical Substation Equipment Subjected to Earthquake Ground Motions.* Armen Der Kiureghian, Jerome L. Sackman, and Kee-Jeung Hong. February 1999.
- PEER 1998/08** *Behavior and Failure Analysis of a Multiple-Frame Highway Bridge in the 1994 Northridge Earthquake.* Gregory L. Fenves and Michael Ellery. December 1998.
- PEER 1998/07** *Empirical Evaluation of Inertial Soil-Structure Interaction Effects.* Jonathan P. Stewart, Raymond B. Seed, and Gregory L. Fenves. November 1998.
- PEER 1998/06** *Effect of Damping Mechanisms on the Response of Seismic Isolated Structures.* Nicos Makris and Shih-Po Chang. November 1998.
- PEER 1998/05** *Rocking Response and Overturning of Equipment under Horizontal Pulse-Type Motions.* Nicos Makris and Yiannis Roussos. October 1998.
- PEER 1998/04** *Pacific Earthquake Engineering Research Invitational Workshop Proceedings, May 14–15, 1998: Defining the Links between Planning, Policy Analysis, Economics and Earthquake Engineering.* Mary Comerio and Peter Gordon. September 1998.
- PEER 1998/03** *Repair/Upgrade Procedures for Welded Beam to Column Connections.* James C. Anderson and Xiaojing Duan. May 1998.
- PEER 1998/02** *Seismic Evaluation of 196 kV Porcelain Transformer Bushings.* Amir S. Gilani, Juan W. Chavez, Gregory L. Fenves, and Andrew S. Whittaker. May 1998.
- PEER 1998/01** *Seismic Performance of Well-Confined Concrete Bridge Columns.* Dawn E. Lehman and Jack P. Moehle. December 2000.

PEER REPORTS: ONE HUNDRED SERIES

- PEER 2012/103** *Performance-Based Seismic Demand Assessment of Concentrically Braced Steel Frame Buildings.* Chui-Hsin Chen and Stephen A. Mahin. December 2012.
- PEER 2012/102** *Procedure to Restart an Interrupted Hybrid Simulation: Addendum to PEER Report 2010/103.* Vesna Terzic and Božidar Stojadinovic. October 2012.
- PEER 2012/101** *Mechanics of Fiber Reinforced Bearings.* James M. Kelly and Andrea Calabrese. February 2012.
- PEER 2011/107** *Nonlinear Site Response and Seismic Compression at Vertical Array Strongly Shaken by 2007 Niigata-ken Chuetsu-oki Earthquake.* Eric Yee, Jonathan P. Stewart, and Kohji Tokimatsu. December 2011.
- PEER 2011/106** *Self Compacting Hybrid Fiber Reinforced Concrete Composites for Bridge Columns.* Pardeep Kumar, Gabriel Jen, William Trono, Marios Panagiotou, and Claudia Ostertag. September 2011.
- PEER 2011/105** *Stochastic Dynamic Analysis of Bridges Subjected to Spatially Varying Ground Motions.* Katerina Konakli and Armen Der Kiureghian. August 2011.
- PEER 2011/104** *Design and Instrumentation of the 2010 E-Defense Four-Story Reinforced Concrete and Post-Tensioned Concrete Buildings.* Takuya Nagae, Kenichi Tahara, Taizo Matsumori, Hitoshi Shiohara, Toshimi Kabeyasawa, Susumu Kono, Minehiro Nishiyama (Japanese Research Team) and John Wallace, Wassim Ghannoum, Jack Moehle, Richard Sause, Wesley Keller, Zeynep Tuna (U.S. Research Team). June 2011.
- PEER 2011/103** *In-Situ Monitoring of the Force Output of Fluid Dampers: Experimental Investigation.* Dimitrios Konstantinidis, James M. Kelly, and Nicos Makris. April 2011.
- PEER 2011/102** *Ground-Motion Prediction Equations 1964–2010.* John Douglas. April 2011.
- PEER 2011/101** *Report of the Eighth Planning Meeting of NEES/E-Defense Collaborative Research on Earthquake Engineering.* Convened by the Hyogo Earthquake Engineering Research Center (NIED), NEES Consortium, Inc. February 2011.
- PEER 2010/111** *Modeling and Acceptance Criteria for Seismic Design and Analysis of Tall Buildings.* Task 7 Report for the Tall Buildings Initiative - Published jointly by the Applied Technology Council. October 2010.
- PEER 2010/110** *Seismic Performance Assessment and Probabilistic Repair Cost Analysis of Precast Concrete Cladding Systems for Multistory Buildings.* Jeffrey P. Hunt and Božidar Stojadinovic. November 2010.
- PEER 2010/109** *Report of the Seventh Joint Planning Meeting of NEES/E-Defense Collaboration on Earthquake Engineering. Held at the E-Defense, Miki, and Shin-Kobe, Japan, September 18–19, 2009.* August 2010.
- PEER 2010/108** *Probabilistic Tsunami Hazard in California.* Hong Kie Thio, Paul Somerville, and Jascha Polet, preparers. October 2010.
- PEER 2010/107** *Performance and Reliability of Exposed Column Base Plate Connections for Steel Moment-Resisting Frames.* Ady Aviram, Božidar Stojadinovic, and Armen Der Kiureghian. August 2010.
- PEER 2010/106** *Verification of Probabilistic Seismic Hazard Analysis Computer Programs.* Patricia Thomas, Ivan Wong, and Norman Abrahamson. May 2010.
- PEER 2010/105** *Structural Engineering Reconnaissance of the April 6, 2009, Abruzzo, Italy, Earthquake, and Lessons Learned.* M. Selim Günay and Khalid M. Mosalam. April 2010.
- PEER 2010/104** *Simulating the Inelastic Seismic Behavior of Steel Braced Frames, Including the Effects of Low-Cycle Fatigue.* Yuli Huang and Stephen A. Mahin. April 2010.
- PEER 2010/103** *Post-Earthquake Traffic Capacity of Modern Bridges in California.* Vesna Terzic and Božidar Stojadinović. March 2010.
- PEER 2010/102** *Analysis of Cumulative Absolute Velocity (CAV) and JMA Instrumental Seismic Intensity (I_{JMA}) Using the PEER–NGA Strong Motion Database.* Kenneth W. Campbell and Yousef Bozorgnia. February 2010.
- PEER 2010/101** *Rocking Response of Bridges on Shallow Foundations.* Jose A. Ugalde, Bruce L. Kutter, and Boris Jeremic. April 2010.
- PEER 2009/109** *Simulation and Performance-Based Earthquake Engineering Assessment of Self-Centering Post-Tensioned Concrete Bridge Systems.* Won K. Lee and Sarah L. Billington. December 2009.
- PEER 2009/108** *PEER Lifelines Geotechnical Virtual Data Center.* J. Carl Stepp, Daniel J. Ponti, Loren L. Turner, Jennifer N. Swift, Sean Devlin, Yang Zhu, Jean Benoit, and John Bobbitt. September 2009.

- PEER 2009/107** *Experimental and Computational Evaluation of Current and Innovative In-Span Hinge Details in Reinforced Concrete Box-Girder Bridges: Part 2: Post-Test Analysis and Design Recommendations.* Matias A. Hube and Khalid M. Mosalam. December 2009.
- PEER 2009/106** *Shear Strength Models of Exterior Beam-Column Joints without Transverse Reinforcement.* Sangjoon Park and Khalid M. Mosalam. November 2009.
- PEER 2009/105** *Reduced Uncertainty of Ground Motion Prediction Equations through Bayesian Variance Analysis.* Robb Eric S. Moss. November 2009.
- PEER 2009/104** *Advanced Implementation of Hybrid Simulation.* Andreas H. Schellenberg, Stephen A. Mahin, Gregory L. Fenves. November 2009.
- PEER 2009/103** *Performance Evaluation of Innovative Steel Braced Frames.* T. Y. Yang, Jack P. Moehle, and Božidar Stojadinovic. August 2009.
- PEER 2009/102** *Reinvestigation of Liquefaction and Nonliquefaction Case Histories from the 1976 Tangshan Earthquake.* Robb Eric Moss, Robert E. Kayen, Liyuan Tong, Songyu Liu, Guojun Cai, and Jiaer Wu. August 2009.
- PEER 2009/101** *Report of the First Joint Planning Meeting for the Second Phase of NEES/E-Defense Collaborative Research on Earthquake Engineering.* Stephen A. Mahin et al. July 2009.
- PEER 2008/104** *Experimental and Analytical Study of the Seismic Performance of Retaining Structures.* Linda Al Atik and Nicholas Sitar. January 2009.
- PEER 2008/103** *Experimental and Computational Evaluation of Current and Innovative In-Span Hinge Details in Reinforced Concrete Box-Girder Bridges. Part 1: Experimental Findings and Pre-Test Analysis.* Matias A. Hube and Khalid M. Mosalam. January 2009.
- PEER 2008/102** *Modeling of Unreinforced Masonry Infill Walls Considering In-Plane and Out-of-Plane Interaction.* Stephen Kadsiewicz and Khalid M. Mosalam. January 2009.
- PEER 2008/101** *Seismic Performance Objectives for Tall Buildings.* William T. Holmes, Charles Kircher, William Petak, and Nabih Youssef. August 2008.
- PEER 2007/101** *Generalized Hybrid Simulation Framework for Structural Systems Subjected to Seismic Loading.* Tarek Elkhoraibi and Khalid M. Mosalam. July 2007.
- PEER 2007/100** *Seismic Evaluation of Reinforced Concrete Buildings Including Effects of Masonry Infill Walls.* Alidad Hashemi and Khalid M. Mosalam. July 2007.

The Pacific Earthquake Engineering Research Center (PEER) is a multi-institutional research and education center with headquarters at the University of California, Berkeley. Investigators from over 20 universities, several consulting companies, and researchers at various state and federal government agencies contribute to research programs focused on performance-based earthquake engineering.

These research programs aim to identify and reduce the risks from major earthquakes to life safety and to the economy by including research in a wide variety of disciplines including structural and geotechnical engineering, geology/seismology, lifelines, transportation, architecture, economics, risk management, and public policy.

PEER is supported by federal, state, local, and regional agencies, together with industry partners.



PEER Core Institutions

University of California, Berkeley (Lead Institution)
California Institute of Technology
Oregon State University
Stanford University
University of California, Davis
University of California, Irvine
University of California, Los Angeles
University of California, San Diego
University of Nevada, Reno
University of Southern California
University of Washington

PEER reports can be ordered at <https://peer.berkeley.edu/peer-reports> or by contacting

Pacific Earthquake Engineering Research Center
University of California, Berkeley
325 Davis Hall, Mail Code 1792
Berkeley, CA 94720-1792
Tel: 510-642-3437
Email: peer_center@berkeley.edu

ISSN 1547-0587X